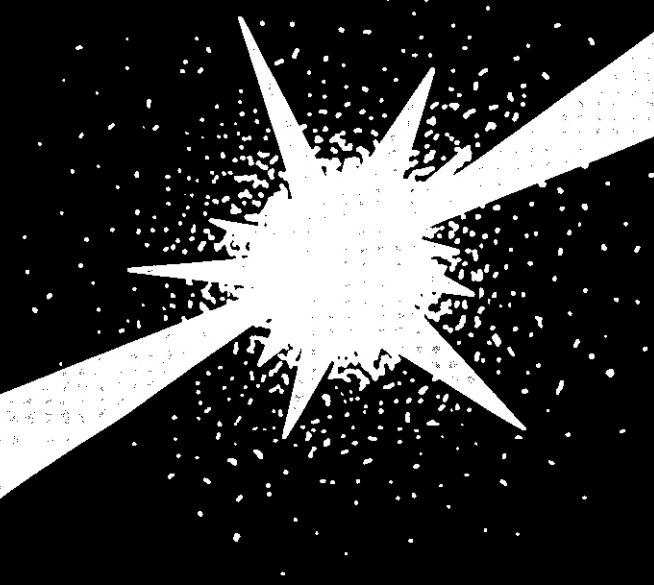
DOE/ER-0313/10

Fusion Reactor Materials

Semiannual Progress Report for Period Ending March 31, 1991



U. S. Department of Energy
Office of Fusion Energy

This report has been reproduced directly from the bast available copy.

Available to DOE and DOE contractors from the Office of Scientific and Technical Information, P.O. Box 62, Oak Ridge, TN 37831; prices available from (615) 576-8401, FTS 626-8401

Available to the public from the National Technical information Service, U.S. Department of Commerce. 5285 Port Royal Rd., Springfield. VA 22161.

This report was prepared as an account of work sponsored by an agency of the United States Government. Neither the United States Government nor any agency thereof, nor any of their employees, makes any warranty. express or implied, or assumes any legal liability or responsibility for the accuracy, completeness, or usefulness of any information, apparatus, product, or process disclosed, or represents that its use would not infringe privately owned rights. Reference herein to any specific commercial product, process. or service by trade name. trademark. manufacturer. or otherwise. does not necessarily constitute or imply its endorsement, recommendation. or favoring by the United States Government or any agency thereof. The views and opinions of authors expressed herein do not necessarily state or reflect those of the United States Government or any agency thereof.

DOE/ER-0313/10
Distribution
Categories
UC-423. -424

FUSION REACTOR MATERIALS SEMIANNUAL PROGRESS REPORT FOR THE PERIOD ENDING MARCH 31, 1991

Date Published: JULY 1991

Prepared for
DOE Office of Fusion Energy
(AT 15 02 03 A)

Prepared by
OAK RIDGE NATIONAL LABORATORY
Oak Ridge, Tennessee 37831
Managed by
MARTIN MARIETTA ENERGY SYSTEMS, INC
for the
U.S. DEPARTMENT OF ENERGY
under Contract DE-AC05-84OR21400

FOREWORD

This is the tenth in a series of semiannual technical progress reports on fusion reactor materials. This report combines research and development activities which were previously reported separately in the following progress reports:

- Alloy Development for Irradiation Performance
- Damage Analysis and Fundamental Studies
- Special Purpose Materials

These activities are concerned principally with the effects of the neutronic and chemical environment on the properties end performance of reactor materials; together they form one element of the overall materials program being conducted in support of the Magnetic Fusion Energy Program of the U.S. Department of Energy. The other major element of the program is concerned with the interactions between reactor materials and the plasma and is reported separately.

The Fusion Reactor Materials Program is a national effort involving several national laboratories, universities, and industries. The purpose of this series of reports is to provide a working technical record for the use of the program participants, end to provide a means of communicating the efforts of materials scientists to the rest of the fusion community, both nationally and worldwide.

This report has been compiled and edited under the guidance of A. F. Rowcliffe and Frances Scarboro, Oak Ridge National Laboratory. Their efforts, and the efforts of the many persons who made technical contributions, are gratefully acknowledged. F. W. Wiffen, Reactor Technologies Branch, has responsibility within DOE for the programs reported on in this document.

R. Price, Chief
Reactor Technologies Branch
Office of Fusion Energy

Reports previously listed in this series are as follows:

DOE/ER-0313/1	Period ending September 30, 1986
DOE/ER-0313/2	Period ending March 31, 1987
DOE/ER-0313/3	Period ending September 30, 1987
DOE/ER-0313/4	Period ending March 31, 1988
DOE/ER-0313/5	Period ending September 30, 1988
DOE/ER-0313/6	Period Ending March 31, 1989
DOE/ER-0313/7	Period Ending September 30, 1989
DOE/ER-0313/8	Period Ending March 31, 1990
DOE/ER-0313/9	Period Ending September 30, 1990

FOREWORD iii

1.0 IRRADIATION FACILITIES, TEST MATRICES, AND EXPERIMENTAL METHODS 1

1.1 DESIGN AND FABRICATION OF HFIR-MFE-JP TARGET IRRADIATION CAPSULES - (Oak Ridge National Laboratory and Midwest Technical, Inc.) 3

New uninstrumented HFIR target capsule designs were completed ior irradiating 12.5-mm-diameter stainless steel fracture roughness specimens to a damage level of approximately 3 displacements per atom (dpa) at temperatures of 60-125 and 250-300°C. Two planned low temperature capsules of identical design, designated HFIR-MFE-JP-18 and HFIR-MFE-JP-19, will each contain 32 fracture toughness specimens directly cooled by reactor cooling water. A single helium-filled elevated temperature capsule, designated HFIR-MFE-JP-17, will contain a slack of 86 fracture toughness specimen. Included in each capsule will be companion transmission electron microscopy (TEM) and SS-3 tensile specimens. Fabrication and assembly of capsules JP-17, -18, and -19 is scheduled for completion by August 1991.

1.2 FABRICATION AND OPERATION OF HFIR-MFE RB* SPECTRALLY TAILORED IRRADIATION CAPSULES -(Oak Ridge National Laboratory and Midwest Technical, Inc.) 5

Fabrication and operation of four NFIR-MFE RB* capsules (60, 200, 330, and 400°C) to accommodate MFE specimens previously irradiated in spectrally tailored experiments in the ORR are proceeding satisfactorily. With the exception of the 60°C capsule, where the test specimens are in direct contact with the reactor cooling water, the specimen temperatures (monitored by 21 thermocouples) are controlled by varying the thermal conductance of a small gap region between the specimen holder and the containment tube. Irradiation of the 60 and 330°C capsules was started on July 17, 1990. As of March 31,195'1, these two capsules had completed 7 cycles of their planned 28-cycle (formerly 14-cycle) irradiation to a damage level of 20 displacements per atom (dpa). Fabrication of pans for the other two (200 and 400°C capsules) is wmplete. Assembly of the 200 and 400°C capsules is scheduled for completion by mid FY 1992; operation of these two capsules will follow the first two (60 and 330°C).

1.3 REEVALUATION OF FABRICATION TECHNIQUE FOR MINIATURE TENSILE SPECIMENS - (University of Missouri-Rolla and Pacific Northwest Laboratory) 7

The present punching process and two potential alternatives for fabricating miniature tensile specimens were evaluated. Three fabrication processes were considered: punching, electrical discharge machining (EDM), and chemical milling. Evaluation criteria included dimensional control and reproducibility, induced microstructural alteration, cost, and the validity of the resultant tensile data. It was demonstrated using annealed 304 stainless steel that punching not only led to substantial specimendeformation but also exhibited the largest dimensional variability. EDM and chemical milling produced specimens with dimensions that were acceptable from bath standpoints. While EDM and chemical milling produced comparable tensile data, chemical milling was more expensive per specimen for the produnion of only a small number of specimens. EDM was therefore Selected for all future fabrication of miniature tensile specimens.

2. DOSIMETRY, DAMAGE PARAMETERS AND ACTIVATION CALCULATIONS 15

2.1 REAC*3 NUCLEAR DATA LIBRARIES (Westinghouse Hanford Company) 17

The purpose of this work is to provide the means of calculating activation in fusion devices.

2.2 INDUCED RADIOACTIVITY OF ELEMENTS IRRADIATED IN FFTF/MOTA AND EBR-2 (Pacific Northwest Laboratory and Westinghouse Hanford Company) 19

Calculations of decay rates of radionuclides in 36 elements irradiated in FFTF/MOTA core center and EBR-2 mid-core and top-core positions have been made using REAC*2. Tables of the results have been made and are being used in compiling test specimen waste disposal documentation.

3.0 MATERIALS ENGINEERING AND DESIGN REQUIREMENTS 23

No contributions.

4.0 FUNDAMENTAL MECHANICAL BEHAVIOR 25

No contributions.

5.0 RADIATION EFFECTS: MECHANISTIC STUDIES, THEORY AND MODELING 27

5.1 DEFECT PRODUCTION AND ATOMIC MIXING IN HIGH ENERGY COLLISION CASCADES: A MOLECULAR DYNAMICS STUDY (Lawrence Livermore National Laboratory) 29

We have performed molecular dynamics computer simulation studies of 25 keV displacement cascades in Cu at low temperature. At this energy we observe the splitting of a cascade into subcascades and show that displacement cascades in metals may lead to the formation of vacancy and interstitial dislocation loop. We discuss a new mechanism of defect production based on the observation of interstitial prismatic dislocation loop punching from cascades at 10 K. We also show that below the subcascade threshold, atomic mixing in the cascade is recoil-energy dependent. We obtain a mixing efficiency that is proportional to the square root of the recoil energy.

5.2 A SIPA-BASED THEORY OF IRRADIATION CREEP IN THE LOW SWELLING RATE REGIME (Whiteshell Nuclear Research Establishment and Pacific Northwest Laboratory) 49

A model is presented which describes the major facets of the relationships between irradiation creep. void swelling and applied stress. The increasing degree of anisotropy in distribution of dislocation Burger's vectors with stress levels plays a major role in this model. Although bcc metals are known to creep and swell at lower rates than fcc metals. it is predicted that the creep-swelling coupling coefficient is actually larger.

5.3 SWELLING AND MICROSTRUCTURE OF HIGH PURITY NICKEL IRRADIATED WITH FAST NEUTRONS IN EBR-II (University of Illinois and Pacific Northwest Laboratory) 56

No summary.

5.4 POSTIRRADIATION STRENGTH AND DEFORMATION OF FERRITIC Fe-Cr BINARY ALLOYS - (Pacific Northwest Laboratory) 63

Six binary Fe-Cr alloys with chromium levels ranging from 3 to 18% were tensile tested at room temperature following irradiation at 365, 403, and 574°C to doses of 7.4, 31.1, and 34.3 dpa, respectively. Irradiation at 365 and 403°C produced significant strengthening at all chromium levels, with concurrent reductions in ductility. Strength levels were insensitive to composition, irradiation temperature or neutron exposure. Irradiation at 574°C produced strength increases at only the two highest chromium levels. The results are attributed to dislocation loop and void development at 365 and 403°C, and phase instability at 574°C. NO evidence for channel fracture was found.

6.0 DEVELOPMENT OF STRUCTURAL ALLOYS 71

6.1 FERRITIC STAINLESS STEELS 71

6.1.1 HEAT TREATMENT EFFECTS ON TOUGHNESS OF 9Cr-1MoVNb and 12Cr-1MoVW STEELS IRRADIATED AT 365°C (Oak Ridge National Laboratory) 73

The 9Cr-1MoVNb and 12Cr-1MoVW steels were austenitired at 1040 and 1100°C to produce two different prior-austenite grain sizes. Pieces of the steels with these different heat treatments were then given different tempering treatments (1 h at 760 and 2.5 h 780°C). Charpy impact specimens with these different heat treatments were irradiated in FFTF at 365°C up to 5 dpa. For 9Cr-1MoVNb steel in the unirradiated mndition, the smaller the prior-austenite grain size, the lower the ductile-brittle transition temperature (DBTT). Also, the higher the tempering temperature, the lower the DBTT prior to irradiation. Regardless of the starting value, however. the DBTI shift during irradiation was the same for all specimens. This means that heat treatment can be used to insure a lower DBTT before and after irradiation. The 12Cr-1MoVW steel showed little effect of heat treatment on DBTI in the unirradiated condition, and the shift in DBTI was relatively constant. Thus, heat treatment cannot be used to reduce the effect of irradiation on the DBTT.

6.1.2 IRRADIATION RESPONSE OF F82H, A REDUCED ACTIVATION Fe-8Cr-2W MARTENSITIC STEEL (University of Tokyo, Pacific Northwest Laboratory, and Nippon Kokan K.K.) 78

Miniature tensile and microscopy specimens of the tungsten-stabilized martensitic steel F82H were examined after irradiation in FFTF to fluences as high as 37 dpa at temperatures ranging from 365 to 750°C. Tensile tests performed at room temperature revealed a small amount of hardening at or below 405°C and significant softening at the higher irradiation temperatures. Electron microscopy results were Consistent with the tensile data. The tempered manensile structure was quite stable below 405°C. The manensile lath structure recovered slightly at 550°C accompanied by the coarsening of Carbide particles, while above 670°C, the manensile lath structure was eliminated. Cavity formation was observed only below 405°C. The maximum welling measured was as high as 0.14% at 405°C. Analysis of precipitate extraction replicas showed superior phase stability during irradiation. Precipitates identified in the irradiated specimens were $M_{23}C_6$ and Laves. the Same as were identified following thermal aging. Other precipitates were not observed.

6.2 AUSTENITIC STAINLESS STEEL 87

6.2.1 SOME IMPLICATIONS OF RADIATION-INDUCED PROPERTY CHANGES IN AUSTENITIC STAINLESS STEELS ON ITER FIRST-WALL DESIGN AND PERFORMANCE (Oak Ridge National Laboratory, Japan Atomic Energy Research Institute, and Argonne National Laboratow) 89

New data on radiation-induced hardening, low-temperature creep and potential susceptibility (sensitization) to aqueous mrrosion have been obtained on various heats of austenitic stainless steel (including type 316) irradiated at 60 to 400°C to 7 to 13 dpa. The data were obtained from spectrally tailored reactor experiments, whose radiationdamage parameters are similar to those in the proposed International Thermonuclear Experimental Reactor (ITER) first-wall (FW) and blanket design. Austenitic stainless steels were found to increase significantly in strength at 60 to 330°C, to have higher irradiation-creep rates at 60°C than at 200 to 400°C, and to show radiation-induced changes in electrochemical properties at 200 to 400°C. These data on several radiation-induced property changes suggest that type 316 steel may be an adequate material for the FW of ITER. However. there is a definitely a need for new data on franure-toughness and on fatique behavior below 400°C, as well as more data on irradiation-creep and effects of irradiation on corrosíon properties, to better define temperature and dose dependencies for more detailed design analyses. Cold-working should remain an optional as-fabricated mndition for the FW of ITER. Many properties of SA and CW 316 become Similar after irradiation at 60 to 400°C. The higher initial yield-strength of CW 316 will allow higher design stress and elastic strain limits.

6.2.2 SWELLING AND MICROSTRUCTURAL ANALYSIS OF U.S.-PCA AUSTENITIC STAINLESS STEEL IRRADIATED AT 60 TO 400°C IN ORR SPECTRAL-TAILORED EXPERIMENTS -- (Oak Ridge National Laboratory) 99

Specimens of solution-annealed (SA) and 25% cold-worked (CW) PCA austenitic stainless steel were irradiated in ORR-MFE-4 at 330 and 400°C to 13 dpa. and in ORR-MFE-6J/7J at 60, 200, 330 and 4WC to 7.4 dpa. Swelling measured by the ORNL precision densitometer of CW PCA irradiated at 400°C was negligible after 7.4 and 13 dpa. whereas SA PCA showed 0.3 to 0.4% swelling after 13dpa. At 330°C. both SA and CW PCA showed about 0.2% swellingafter 13dpa. Transmission electron microsmpy (TEM) analysis of the cavity microstructure showed many voids in SA PCA irradiated at 400°C, while only tiny helium bubbles were fouhd in the other specimens irradiated at 330 to 400°C. No cavities were detectable in CW PCA irradiated at 60 or 200°C. Fine MC precipitates were found in SA and CW PCA specimens at 330 and 400°C, hut not at lower temperatures. Both SA and CW PCA contained mixtures of larger Frank loops and dislocation networks at 330 and 400°C, whereas the dislocation structure of CW PCA was dominated by tiny "black-dot" loops at 60 and 200°C. The CW PCA showed significant radiation-induced recovery of the initial dislocation network structure at all temperatures; no large Frank loops were found at 60°C, while the maximum mncentration of larger loops was observed at 330°C.

6.2.3 STATUS OF MOTA IRRADIATION EXPERIMENTS ON REDUCED ACTIVATION AUSTENITIC ALLOYS (Pacific Northwest Laboratory, Westinghouse Hanford Company, Oak Ridge National Laboratory, Hokkaido University, Nagoya University, Ispra Establishment, and Baikov Institute) 109

A number of collaborative international experiments are being conducted to assess the feasibility of Fe-Cr-Mn austenitic steels for fusion service. A review is presented of the current status of these various efforts. The first time irradiation of an Fe-Cr-Mn steel in the form of pressurized lubes is highlighted.

6.2.4 PHASE STABILITY IN THERMALLY AGED Fe-Cr-Mn ALLOYS (Northwest College and University Association for Science, Washington State University, and Pacific Northwest Laboratory) 113

Fe-Cr-Mn alloys have been proposed as a structural material for fusion reactors that will exhibit reduced long-term radioactivity. However, Fe-Cr-Mn ternary equilibrium has nor previously been well defined at temperatures below 650°C. The current experiment characterized phase evolution and equilibrium in three alloys; Fe-15Cr-15Mn, Fe-10Cr-30Mn and Fe-30Mn in the 20% cold-worked mndition aged from 300 to 700°C for 1,000 to 30,000 hours at temperatures from 300 to 600°C. Results indicate thato phase formation is extremely sluggish, and cold-working and long aging times are required to initiate σ phase formation in alloys not previously predicted to exhibit such precipitation. σ phase appears to form on high diffusivitypaths such as recrystallizing grain fronts and grain boundary triple paints. Three isothermal Sections at 300, 500 and 600°C were constructed from the experimental data that extend the temperature range of the Fe-Cr-Mn ternary diagram to lower temperatures than previously published.

6.3 REFRACTORY METAL ALLOYS 133

6.3.1 CORRELATION OF MICROSTRUCTURE AND SWELLING BEHAVIOR OF VANADIUM ALLOYS IRRADIATED IN FFTF/MOTA AT 420°C (Argonne National Laboratory and Tohoku University) 135

Microstructural evolutions in V, V-Cr, V-Ti, V-Ti-Cr, and V-Ti-Si alloys have been characterized by TEM after irradiation at 420°C in FFTF/MOTA. The results have been correlated with swelling behavior of the alloys to provide a better understanding of the superior resistance of some of the high-Ti heats to void swelling.

6.3.2 TENSILE PROPERTIES OF VANADIUM AND VANADIUM-BASE ALLOYS (Argonne National Laboratory) **145**

Tensile property data are presented for unalloyed vanadium and 18 vanadium alloys that are considered candidates for structural material in a magnetic fusion reactor. The compositions of these candidate alloys are principally those vanadium binary and ternary alloys with Cr, Ti, and Si additions. The dependence of the tensile properlies for these materials on temperature (25-700°C), Cr concentration (0-15%), Ti concentration (0-20%), and Si concentration (0.05-1.28%) is presented in the form of tables. graphs. and parametric equations. The strengthening of V by Cr, Ti, and Si additions is discussed with emphasis on the role of interanion of these alloying additions with interstitial impurities (i.e., O, N, and C).

6.3.3 REVISED CALCULATIONS FOR THE DYNAMIC HELIUM CHARGING EXPERIMENT IN FFTF/MOTA 2B -(Pacific Northwest Laboratory) 156

Calculations of the initial tritium loading, lithium isotopic ratio. and helium pressure have been revised for the planned dynamic helium charging experiment (DHCE) in FFTF/MOTA-2B based on current neutronic information regarding the neutron flux spectrum.

6.3.4 STATUS OF THE DYNAMIC HELIUM CHARGING EXPERIMENT (DHCE) IN FFTF/MOTA (Argonne National Laboratory, Tohoku University, Pacific Northwest Laboratory, and Westinghouse Hanford Company) 159

Preparation of the DHCE experiment has been completed and it has been inserted into MOTA 2B for irradiation in FFTF. The experiment will produce helium in test specimens of vanadium alloys to simulate a fusion environment.

6.4 COPPER ALLOYS 165

6.4.1 MICROSTRUCTURAL EXAMINATION OF PURE COPPER AND CUJNI IRRADIATED WITH FISSION OR SPALLATION NEUTRONS (Pacific Northwest Laboratory, Risø National Laboratory, and Los Alamos National Laboratory) **167**

Specimens of pure copper and a copper alloy containing 5 atomic percent nickel have been examined by transmission electron microscopy following irradiation by neutrons in a mixed thermal reactor, a fast reactor and a spallation neutron source. Radiation damage microstructures have been investigated in order to identify microstructural differences and to determine suitability of copper alloys for high heat flux substructure applications in a fusion device. Most conditions developed void swelling, and all were found to contain defect clusters on a fine scale. Damage accumulation in Cu-5Ni was found to be significantly different from that observed in pure copper. Based on limited comparisons of irradiation at 335°C, high energy spallation neutrons do not appear to have any significant effect on swelling at low dose. The results of this study confirm the need for improved temperalure control of irradiation experiments in order to correlate radiation damage lo fusion conditions.

6.4.2 STATUS OF COPPER IRRADIATION EXPERIMENTS (Pacific Northwest Laboratory, University of Missouri-Rolla, Risø National Laboratory, University of Illinois, Tohoku University, Oak Ridge National Laboratory, and SCM Metal Products) 186

A variety of FFTF irradiation studies and out-of-reactor studies are in progress to determine the response of copper alloys to the environment anticipated for fusion service. An updated review of these various studies is presented.

6.4.3 NEUTRON-INDUCED CHANGES IN DENSITY OF COPPER ALLOYS (Pacific Northwest Laboratory and Westinghouse Hanford Company) **192**

Density change measurements have been completed on the Generation 2.0 copper alloy experiment at 411°C after reaching 100 dpa. The Glidcop alloy CuAl25 continues to exhibit excellent resistance to void swelling. Welding and high oxygen levels both degrade the swelling resistance of oxide dispersion-strengthened alloys. The alloy Cu-2.0 Be also resists swelling and appears to be densifying in response to the continued formation of the transmutant nickel.

6.4.4 RADIATION-INDUCED CHANGES IN ELECTRICAL CONDUCTIVITY OF A WIDE RANGE OF COPPER ALLOYS (Pacific Northwest Laboratory, University of Illinois, and Tohoku University) 199

A wide variety of radiation-induced changes in electrical conductivity was observed in a series of irradiation experiments conducted on mpper alloys in FFTF/MOTA. The behavior of each alloy was found to depend on the alloy composition, starting state, irradiation temperature. and the sometimes complex interanion of three radiationdriven processes. These processes are transmutation, void swelling, and solute redistribution.

6.4.5 BRAZING OF COPPER-LUMINA ALLOYS (Auburn University and Oak Ridge National Laboratory) **206**

An induction braze has been developed to join copper-alumina alloys to eliminate the requirement for either plating the joining surfaces prior to brazing or the use of an inert cover gas or a vacuum pump to prevent excessive oxidation. Preliminary tensile tests of induction lap joints and fatigue tests of induction brazed butt joints have been conducted. A theoretical study of the diffusion of silver into the alloy has been compared to experimental EDX analysis

7.0 ENVIRONMENTAL EFFECTS ON STRUCTURAL MATERIALS **213**

7.1 ENVIRONMENTAL EFFECTS ON SIC/SIC COMPOSITES FOR FUSION STRUCTURAL APPLICATIONS (Pacific Northwest Laboratory) **215**

The chemical stability of SiC/SiC composites in fusion relevant environments has been evaluated from the database available in the literature for monolithic SiC. The results of this assessment suggests that the primary chemical reactions that will limit the stability of these materials are: 1) Li reduction of surface and grain boundary glass phases in a liquid Li coolant, 2) impurity effecu on oxidation and the oxidation of the fiber/matrix interfacial layer in a He coolant and 3) H_2 reduction of the "passive" SiO_2 layer and the reaction of the H_2 with SiC to form gaseous reaction products. Strength degradation has been observed for each of these reactions under cenain wnditions, but the database is insufficient to predict whether similar property changes will occur in fusion relevant environments. Clearly, more experimental data is needed to evaluate the stability of SiC/SiC composites for long-term exposures in fusion relevant environments.

7.2 EFFECT OF GAMMA IRRADIATION ON STRESS-CORROSION BEHAVIOR OF AUSTENITIC STAINLESS STEEL UNDER ITER-RELEVANT CONDITIONS (Pacific Northwest Laboratory) **231**

This study wupled with other published data supports the conclusion that gamma irradiation will not induce Stress corrosion cracking if the oxygen activity in the ITER water coolant is maintained at a low level. This conclusion is based on stress corrosion cracking tests conduned at 100°C in deionized water with 10 ppm Cl^- on solution annealed and sensitized Type 316 SS and PCA The material was sensitized to about 5 C/cm^2 and fatigue crack growth tests were conducted in an autoclave exposed to a ^{60}Co source with tests conducred at 0, 2.3 x 10^2 and 6.5 x 10^3 rad/h. The material and water chemistry conditions were chosen to represent the worst case condition expected in an ITER resulting from poor welding and water chemistry control. Crack growth rates were found to decrease by about a factor of 2 in the presence of both gamma fluxes. Average crack velocities were 2.0 and 1.5 x 10^{-5} mm/cycle for Type 316 SS and PCA, respectively, in the absence of gamma irradiation and 1.3 and 0.74 x 10^{-5} mm/cycle at both gamma fluxes. These results suggest, for the limited conditions examined in this study, that radiolysis alone will not cause stress corrosion cracking of slightly sensitized Type 316 SS or PCA in water with 10 ppm Cl^- at 100°C. Other conditions that have not been examined and may cause crack growth include: radiolysis effects in high O_2 activity water. hydrogen induced cracking of radiation hardening Type 316 SS and PCA and irradiation-assisted Stress corrosion cracking (IASCC).

7.3 RADIATION-INDUCED SEGREGATION IN IRRADIATED TYPE 304 ALLOYS FOR THE ICG-IASCC ROUND ROBIN -- (Oak Ridge National Laboratory) **237**

Grain boundary RIS in two neutron-irradiated type 304 stainless steels has been investigated by X-ray microanalysis. In the wnventional alloy (LC), narrow (≤5 nm width) RIS zones depleted in chromium and iron and enriched in silicon, phosphorus, and nickel were observed near grain boundaries. For the higher purity alloy (QC), similar width (≤6 nm) RIS zones depleted in chromium and iron and enrichment in nickel were observed at boundaries. though at reduced magnitudes relative to those in the LC material. No significant segregation of siliwn or phosphorus was observed in the QC material. RIS zones associated with faulted dislocation loops in the LC material were detected and shown to be depleted in chromium and enriched in nickel and iron relative to the matrix.

7.4 AQUEOUS STRESS CORROSION OF CANDIDATE AUSTENITIC STEELS FOR ITER STRUCTURAL APPLICATIONS (Argonne National Laboratory) **241**

Hydrogen embritllement of candidate first-wall materials (e.g., stainless steel, or SS) is a key issue for ITER because of hydrogen production due to (n,p) transmutation reactions; hydrogen generation of up to 2500 appm is anticipated. Material composition, changer in composition caused by transmutation reanions. irradiation damage, environment. and expected loading wnditions were reviewed to assess the relative importance of various degradation processes for a fusion reactor first wall. The stability of austenite with regard to creation of deformation- or stress-induced manensile, α', was considered in relation to SCC and hydrogen-assisted crack growth in SSs at low temperatures (<150°C).

7.5 PRELIMINARY ASSESSMENT OF AQUEOUS CORROSION OF NIOBIUM ALLOYS FOR STRUCTURAL APPLICATIONS IN THE ITER DIVERTOR (Argonne National Laboratory) 248

Niobium and Nb-base alloys are under consideration as candidate materials for the ITER divertor structure. Unalloyed Nb and binary alloys of Nb-2.5Ti, Nb-2.5Zr, Nb-2.5Hf, Nb-2.5V, Nb-2.5Ta, Nb-2.4Mo, Nb-2.5W, Nb-2.5Fe, Nb-2.5Ti, and ternary alloys of Nb-2.5Ti-2.5Ta, Nb-2.5Ti-2.5Mo, Nb-2.5Hf-2.5Mo (expressed in terms of atomic percent alloy addition) were exposed to high-puny water with < 30 ppb dissolved oxygen in a refreshed Stainless steel autoclave (with a 1300-psi overpressure) to determine the extent of oxidation as a function of time at 300°C. Corrosion data are presented for pure Nb and for ten binary and three ternary Nb-base alloys exposed for up to 2906 h. All alloys exhibited weight gains except Nb-2.5Ni, Nb-2.5Ta, and Nb-2.5Fe, which lost weight after 0, 1500, and 2200 h, respectively. Of the alloys that gained weight, the V and Mo additions were the most effective in minimizing weight gain. The ternary alloys incorporating Mo were superior in terms of bath resistance to weight gain and embrittlement.

..... 257

8.0 SOLID BREEDING MATERIALS

8.1 IRRADIATION EXPERIMENT DESIGN FOR IN SITU TRITIUM RECOVERY FOR Li_2O and Li_2ZrO_3: BEATRIX-II, PHASE II (Pacific Northwest Laboratory, Japan Atomic Energy Research Institute, AECL Chalk River, and Westinghouse Hanford Company) 259

BEATRIX-II is an irradiation experiment designed to study the in situ tritium release behavior from selected ceramic solid breeder materials. The second irradiation cycle of the experiment. Phase II, will include a temperature change capsule with a ring specimen of Li_2O and a temperature gradient capsule with Li_2ZrO_3 spheres. The temperalure change capsule is designed to achieve temperatures in the range from 485 to 650°C while the temperature gradient capsule will include a temperature range from 450 to 1200°C. The effect of specimen temperature, sweep gas composition, irradiation damage, and sweep gas flow rate on the tritium recovery behavior will be determined in a fast neutron flux to burnups of *8%.*

8.2 IN SITU TRITIUM RECOVERY FROM Li_2O IRRADIATED UNDER A LARGE TEMPERATURE GRADIENT BEATRIX-II SOLID SPECIMEN (Japan Atomic Energy Research Institute, Pacific Northwest Laboratory, and AECL Chalk River) 270

BEATRIX-II is an in situ tritium recovery experiment to determine the tritium release characteristics of Li_2O in a fast neutron flux A large diameter specimen of Li_2O has been irradiated under a steep temperature gradient to 4% burnup in a variety of sweep gas compositions and now rates. Decreasing tne amount of hydrogen in the sweep gas significantly decreases the tritium recovery rate. During irradiation the temperature of the specimen has remained stable and the results suggest that Li_2O is a viable fusion solid breeder material

8.3 INVESTIGATION OF TRITIUM RELEASE AND RETENTION IN LITHIUM ALUMINATE - (Argonne National Laboratory and Commisariat a L'Energie Atomique) 280

Tritium release from single crystal lithium aluminate has been investigated by a series of isothermal anneal and constant rate heating experiments. The results of these experiments indicate that after anneals at low temperature, a large fraction of the tritium present before the anneal remains in the sample. We have modeled this behavior based on first order release from three types of sites. At low temperature the release is dominated by one site. while the tritium in the other sites is retained in the solid. Dopants appear to alter the distribution of tritium between the sites. Adding MgO decreases the fraction of tritium released at 777°C, while inneasing the fractions released at *538* and 950°C.

8.4 DESORPTION CHARACTERISTICS OF THE $LiAlO_2$-H_2-H_2O(g) SYSTEM - (Argonne National Laboratory) . 284

The energetics and kinetics of the evolution of H_2O and H_2 from $LiAlO_2$ have been studied by the temperature programmed desorption technique. After treating the sample with helium containing 990, 495, or 247 vppm H_2 at *923* K, H_2O and H_2 evolution was observed during 473 to 1073 K (200 to 800°C) ramps at rates of 5.6 K/min. The sweep gas was either pure helium or the same He-H_2 mixture that was used in the preliminary treatment. The H_2O and H_2 desorption peaks were shown to be the sums of first-order subpeaks which had reproducible activation energies and pre-exponential terms. For H_2O desorption. these peaks, of types labeled B. C, and D had activation energies of 22, 28, and *32* kcal/mol. (Earlier work identified type A peaks with an activation energy of 18 kcal/mol.) Enhancement of desorption of H_2O in rate and quantity by H_2 in the sweep gas was confirmed. It appears that the effectiveness of H_2 in this enhancement is not in modifying the activation energy and pre-exponential term for a given kind of site. but rather in changing the populations of sites participating in the desorption processes so that sites with lower activation energies are increasingly involved. Only C and D subpeaks were involved in H_2 desorption and they had activation energies close to and perhaps only 1 kcal/mol higher than the analogous peaks for H_2 evolution.

9.0 CERAMICS 291

9.1 MICROSTRUCTURE OF Al_2O_3 AND $MgAl_2O_4$ PREIMPLANTED WITH H, He, C AND IRRADIATED WITH Ar^+ IONS (Japan Atomic Energy Research Institute, Oak Ridge National Laboratory and Harwell Laboratory) 293

Polycrystalline spinel ($MgAl_2O_4$) and alumina (Al_2O_3) were irradiated under three, different sets of ion irradiation conditions in order to examine the effecu of displacement damage and transmutation product formation on their microstructural evolution. Specimens were implanted with H, He and C alone, or irradiated with 4 MeV Ar^+ ions alone, or preimplanted with H, He, C and subsequently irradiated with 4 MeV Ar^+ ions. Irradiated specimens were observed with transmission electron microscopy following irradiation to damage levels of 0.6 to 30 dpa at 260 to 630°C for spinel and 0.6 to 18 dpa at 260 to 810°C for alumina. In both spinel and alumina. no radiation effecu were observable in specimens implanted with H, He and C alone. and the preinjected transmutation products did not have a significant effect on dislocation loop size or density in Ar^+ irradiated specimens. In alumina, cavities were formed in all of the observed Ar^+ irradiated specimens for both the preimplanted H, He and C case and the Ar^+ alone case. In spinel, cavity formation was only observed in preimplanted specimens irradiated with Ar^+ ions at relatively high temperatures and/or doses.

9.2 MICROSTRUCTURAL CHANGES IN OXIDE CERAMICS FOLLOWING LIGHT ION IRRADIATION (Oak Ridge National Laboratory) 302

Irradiation of ceramics such as Al_2O_3 and $MgAl_2O_4$ with energetic light ions causes a suppression in the nucleation of dislocation loop. The results of recent electron microscope studies on ion irradiated oxide ceramics are summarized. It is proposed that the anomalous suppression of dislocation loop formation may be associated with the high proponion of energy lost to electronic ionization events compared to displacement damage events during light ion irradiation.

9.3 PREPARATION OF $MgAl_2O_4$ SPINEL CONTAINING CONTROLLED AMOUNTS OF ^{17}O ISOTOPE (Oak Ridge National Laboratory) 310

Magnesium aluminate spinel ($MgAl_2O_4$) with an ^{17}O enrichment ($^{17}O/O_{Tot}$) of about 23 at. % was prepared by reacting fine mixtures of aluminum hydroxide (enriched with ^{17}O) and MgO of normal isotopic content. The material was prepared for experiments in which the radiation damage produced in a fusion reactor is simulated by fission reactor exposures. The powder mixtures were obtained by hydrolyzing, with water containing the ^{17}O isotope, a mixture of aluminum isopropoxide and MgO powder. The mixture was convened into pure spinel by a series of heat treatmenu and grindings. Essentially fully dense bodies, which contained about 45% of the ^{17}O isotope initially present in the water, were successfully fabricated provided that all thermal treatmenu were conducted in argon or vacuum atmospheres.

9.4 IRRADIATION OF CONVENTIONAL AND ISOTOPICALLY TAILORED CERAMICS IN HFIR (Oak Ridge National Laboratory, Rensselaer Polytechnic Institute, and Los Alamos National Laboratory) 314

Al_2O_3 and $MgAl_2O_4$ specimens containing ^{17}O isotope concentrations of 0 to 25 at. % ($^{17}O/O_{TOT}$) have been prepared for irradiation in HFIR in order to investigate the effects of helium formation on their microstructure and dielectric and mechanical properties. SiC/SiC flexure ban, ceramic fibers and a wide range of commercial ceramic TEM disks has also been included in the irradiation capsules. The specimens will be irradiated at temperatures of 100, 350, and 600°C in two irradiation capsules that will receive respective maximum neutron fluences of 2.4×10^{26} and 7.2×10^{26} n/m² (E > 0.1 MeV).

9.5 IRRADIATION OF CERAMICS IN FFTF (Oak Ridge National Laboratory and Rensselaer Polytechnic Institute) 317

A wide range of advanced structural ceramics have been prepared and shipped to FFTF for irradiation to a nominal fluence $\sim 6 \times 10^{26}$ n/m² (E > 0.1 MeV) at temperatures of 420 to 800°C. Most of the ceramics will be irradiated as TEM disks, but SiC/SiC flexural bars, electrical conductivity disks, and bundles of commercial ceramic fibers will also be irradiated in separate irradiation capsules.

9.6 CROSS SECTIONAL MEASUREMENT OF ELASTIC MODULUS FOR ION BEAM DAMAGED SILICON CARBIDE - (Oak Ridge National Laboratory and Rensselaer Polytechnic Institute) 320

The application of a microindentation technique to measure the elastic modulus of carbon beam implanted silicon carbide is presented. Samples of Chemically Vapor Deposited (CVD) Silicon Carbide/Nicalon composites have been implanted to a damage level of 30 dpa at room temperature. The samples were then prepared in cross section and the microstructure was analyzed and modulus was measured along the damage path of the carbon ions. Both CVD silicon carbide and Nicalon silicon carbide was seen to amorphize at room temperature with the threshold for the CVD being approximately 15 dpa. Amorphization of Nicalon silicon carbide fiber was seen to occur over the entire range of the carbon path implying a much lower threshold for amorphization. Elastic moduli were seen to decrease significantly (from 440 GPa to 280 GPa) for the CVD material with the minimum modulus corresponding to the maximum damage region of the carbon beam. The modulus of Nicalon showed the opposite behavior. The modulus for the fiber was increased over most of the damaged region from an undamaged value of 170 GPa to a maximum of 210 GPa.

9.7 IN-SITU MEASUREMENT OF RADIATION INDUCED CONDUCTIVITY IN CERAMICS (Los Alamos National Laboratory) **328**

Recent data by E R. Hodgson[1,2] and by G. P. Pells[3,4] shows enhanced dielectric loss and electrical breakdown in ceramics during irradiation with protons and electrons and while subject to an externally applied DC electric field. We have investigated this radiation-induced conductivity effect at frequencies between 100 Hz and 10 MHz by irradiating sapphire with 3 MeV protons at 300 K Calculations of energy deposition and displacement damage in the sapphire were made using TRIM 90 on an IBM-AT. Results show an immediate increase in loss tangent at onset of irradiation that depends on both frequency and time.

9.8 CORROSION AND ELECTRICAL PROPERTIES OF CERAMIC INSULATORS AFTER EXPOSURE TO FLOWING LITHIUM AT 400°C - (Argonne National Laboratory) **330**

Based on a preliminary survey of more than 15 oxides and nitrides, four ceramic materials (CaO, MgO, Y_2O_3, and BN) were identified as candidates for insulator coating development. These compounds were fabricated by a variety of techniques and exposed to flowing lithium at 400°C to assess chemical compatibility. Yttrium oxide exhibited excellent mrrosion resistance in flowing liquid Li at 400°C; its mrrosion rate was calculated to be 0.042 m/yr. Resistivity measurements were taken before and aher Li exposure to determine the effects of Li on the electrical properties of Y_2O_3. No deterioration in the resistivity muld be measured; in both cases the resistivity was $>10^{12}$ Ω-m. Boron nitride coatings on V-20Ti Substrates were fabricated by the newly developed ion-beam-assisted-deposition process. These coatings are expected to exhibit better compatibility with liquid Li than the previously RF-sputtered coatings. The resistivity of in-situ-formed $(V,Ti)_xN$ reanion-product layers on various V-base alloys, including V-7Cr-5Ti, V-2.5Ti-1Si, and V-20Ti, is being determined.

1.0 IRRADIATION FACILITIES, TEST MATRICES, AND EXPERIMENTAL METHODS

DESIGN AND FABRICATION OF HFIR-MFE-JP TARGET IRRADIATION CAPSULES - A. W. Longest, D. W. Heatherly, K. R. Thorns (Oak Ridge National Laboratory), and J. E. Corum (Midwest Technical, Inc.).

OBJECTIVE

The objective of this work is to design and fabricate irradiation capsules for irradiating magnetic fusion energy (MFE) first-wall materials in the High Flux Isotope Reactor (HFIR) target positions. Japanese and U.S. specimens will be irradiated to determine fracture toughness of austenitic stainless steels after irradiation to 3 dpa at temperatures of 60-125 and 250-300°C.

SUMMARY

New uninstrumented HFIR target capsule designs were completed for irradiating 12.5-mm-diameter stainless steel fracture toughness specimens to a damage level of approximately 3 displacements per atom (dpa) at temperatures of 60-125 and 250-300°C. Two planned low temperature capsules of identical design, designated HFIR-MFE-JP-18 and HFIR-MFE-JP-19, will each contain 32 fracture toughness specimens directly cooled by reactor cooling water. A single helium-filled elevated temperature capsule, designated HFIR-MFE-JP-17, will contain a stack of 86 fracture toughness specimen. Included in each capsule will be companion transmission electron microscopy (TEM) and SS-3 tensile specimens.

Fabrication and assembly of capsules JP-17, -18, and -19 is scheduled for completion by August 1991.

PROGRESS AND STATUS

Introduction

A series of fracture-toughness-specimen irradiation capsules are being designed and fabricated as part of the U.S./Japan collaborative program for testing MFE first-wall materials in mixed-spectrum fission reactors. The test specimens will he irradiated in HFIR target capsules designed for 60-125°C and 250-300°C specimen temperatures.

These capsules are designed to accommodate 12.5-mm diameter stainless steel Disk-Shaped Compact DC(T) specimens of standard proportions; also, companion TEM and SS-3 tensile specimens are accommodated. The capsules are uninstrumented and are intended to provide early irradiation data on low-temperature fracture toughness properties of candidate first-wall materials. Spectral tailoring of the neutron flux is deemed unnecessary for the planned 2-cycle irradiation to a damage level of approximately 3 dpa. In the HFIR target region, the helium production-to-atom displacement ratio in austenitic stainless steels in a short irradiation of 1 to 2 cycles is reasonably close to the ratio (14 appm/dpa) expected in a fusion reactor first wall.

60-125°C Capsules

Two planned uninstrumented low-temperature capsules of identical design, designated HFIR-MFE-JP-18 and HFIR-MFE-JP-19, will each contain 32 12.5-mm-diameter fracture toughness specimens (total of real specimens plus one or more dummy specimens holding TEM specimens), 8 SS-3 tensile specimens, and up to 75 TEM specimens per dummy fracture toughness specimen. These capsules are of the shrouded type with the fracture toughness specimens directly cooled on their flat faces by downward-flowing reactor cooling water. They will be irradiated in interior HFIR target positions.

Predicted temperatures over the crack region of the fracture toughness specimens range from approximately 60-85°C near the ends of the 50-cm test length to 65-125°C near the middle. The crack region is defined here as the region of the specimen between radii of 0.14 and 0.41 cm; the postirradiation-testing crack surface is expected to be bounded by these radii.

Construction drawings for capsules JP-18 and -19 have been issued and parts fabrication is in progress. Assembly is scheduled to be completed by August 1991.

250-300°C Capsule

A single uninstrumented helium-filled elevated temperature capsule, designated HFIR-MFE-JP-17, will contain a stack 86 12.5-mm-diameter fracture toughness specimens (total of real specimens plus one or more dummy specimens holding TEM specimens), 12 *SS-3* tensile specimens, and up to 75 TEM specimens per dummy fracture toughness specimen, all within a tight-fitting aluminum cladding tube. Also, one or more of the fracture toughness specimens near the ends of the 50-cm test length may be replaced by copper alloy specimens. This capsule is of the shrouded type and will be cooled by reactor cooling water flowing downward between the cladding tube and shroud tube. Capsule JP-17 will be irradiated in one of the six HFIR peripheral target positions; these positions accommodate slightly larger capsules than do the interior target positions.

Capsule JP-17 features a unique thermal design in that, over the middle portion of the test length, aluminum cooling spacers of varying thicknesses are employed between the fracture toughness specimens to achieve predicted specimen temperatures for the crack region between 250-300°C. Near each end, where the heat generation rate falls below the point where the cooling spacers are needed, it was decided to allow specimen temperatures to decrease below the desired range rather than complicate the design by attempting to compensate for the rapidly falling heat generation rate.

Construction drawings for capsule JP-17 have been completed and are being issued. Assembly is scheduled for completion by August 1991.

FUTURE WORK

Assembly of capsules JP-17, -18, and -19 is scheduled for completion by August 1991.

FABRICATION AND OPERATION OF HFIR-MFE RB* SPECTRALLY TAILORED IRRADIATION CAPSULES -
A. W. Longest, D. W. Heatherly, E. D. Clemmer (Oak Ridge National Laboratory), and J. E. Corum (Midwest Technical, Inc.).

OBJECTIVE

The objective of this work is to fabricate and operate irradiation capsules for irradiating magnetic fusion energy (MFE) first-wall materials in the High Flux Isotope Reactor (HFIR) removable beryllium (RB*) positions. Japanese and US. MFE specimens are being transferred to RB* positions following irradiation to 7.5 dpa at temperatures of 60, 200, 330, and 400°C in Oak Ridge Research Reactor (ORR) experiments ORR-MFE-6J and -7J.

SUMMARY

Fabrication and operation of four HFIR-MFE RB* capsules (60,200,330, and 400°C) to accommodate MFE specimens previously irradiated in spectrally tailored experiments in the ORR are proceeding satisfactorily. With the exception of the 60°C capsule, where the test specimens are in direct contact with the reactor cooling water, the specimen temperatures (monitored by 21 thermocouples) are controlled by varying the thermal conductance of a small gap region between the specimen holder and the containment tube.

Irradiation of the 60 and 330°C capsules was started on July 17, 1990. As of March 31,1991, these two capsules had completed 7 cycles of their planned 28-cycle (formerly 14-cycle) irradiation to a damage level of 20 displacements per atom (dpa). Fabrication of parts for the other two (200 and 400°C capsules) is complete. Assembly of the 200 and 400°C capsules is scheduled for completion by mid FY 1992; operation of these two capsules will follow the first two (60 and 330°C).

PROGRESS AND STATUS

Introduction

A series of spectrally tailored irradiation capsules are being fabricated and operated as part of the U.S./Japan collaborative program for testing MFE first-wall materials in mixed-spectrum fission reactors. The test specimens are being irradiated in the RB* facility' of the HFIR.

Four HFIR-MFE RB* capsules were designed to accommodate Japanese and US. MFE specimens previously irradiated to 7.5 dpa at temperatures of 60, 200, 330, and 400°C in the ORR in spectrally tailored experiments ORR-MFE-6J and **-75.** Details of these ORR experiments, including descriptions of the test matrix, mechanical property specimens, and techniques of spectral tailoring, have been reported elsewhere?' Hafnium liners are being used in the HFIR-MFE RB* experiments to tailor the neutron spectrum to closely match the helium production-to-atom displacement ratio (14 appm/dpa) expected in a fusion reactor first wall.

The HFIR-MFE RB* capsules are being irradiated in pairs (first the 60 and 330°C capsules, then the 200 and 400°C capsules) to a damage level of 20 dpa. The target exposure level was given as 16 dpa in the last progress report', at which point the test specimens were to be removed, examined, and approximately one-half of them re-encapsulated into two dual-temperature capsules (60/200 and 330/400°C) for further irradiation. However, in a recent renew of the irradiation program, it was decided to extend the first four irradiations to 20 dpa and omit the planned dual-temperature capsules.

60°C Capsule

The 60°C capsule, designated HFIR-MFE-60J-1, is an uninstrumented capsule with the test specimens in contact with the reactor cooling water. Capsule design, assembly, and details of the specimen loading were described previously.'

Irradiation of this capsule began July 17, 1990, at the start of HFIR cycle 289. As of March 31, 1991, 7 cycles of its planned 28-cycle irradiation to a damage level of 20 dpa had been completed. Specimen operating temperatures in this capsule are predicted to be within 10°C of 60°C.

330°C Capsule

The 330°C capsule, designated HFIR-MFE-330J-1, is an instrumented and singly contained capsule where the specimen temperatures are monitored by 21 thermocouples and controlled by adjusting the thermal conductance of a small gas gap region between the specimen holder outer sleeve and the containment tube. This capsule is cooled with 49°C reactor cooling water flowing downward over the containment tube surface. Capsule design, assembly, and details of the specimen loading were described previously.[6,7]

Irradiation of this capsule began on July 17, 1990, at the start of HFIR cycle 289. As of March 31, 1991, 7 cycles of its planned 28-cycle irradiation to a damage level of 28 dpa had been completed. Measured temperatures from the 21 thermocouples in the aluminum alloy specimen holder indicate that specimen operating temperatures are within 25°C of 330°C which satisfies the temperature criterion for these experiments.

200 and 400°C Capsules

The 200 and 400°C capsule designs were described previously[8] and are basically the same as that of the 330°C capsule. The main differences in the three capsule designs are associated with (1) the number and spacing of the specimen holder slots and holes to accommodate the different specimen loadings, (2) the width of the temperature control gas gap region between the specimen holder outer sleeve and containment tube to obtain the desired specimen temperatures, and (3) the test piece included in the aluminum plug and holder above the test specimen holder to obtain extra information.

Fabrication of parts for both capsules is complete. Assembly of the capsules is scheduled for completion by mid FY 1992. Operation of these two capsules will follow the first two (60 and 330°C).

FUTURE WORK

Assembly of the 200 and 400°C capsules is scheduled to be completed in FY 1992.

REFERENCES

1. K R. Thoms et al., "HFIR Irradiation Facilities Improvements - Completion of the HIFI Project," J. Nucl. Mater., 155-157 (1988) 1340-45.

2. J. L. Scott et al., pp. 12-20 in ADIP Semiann. Prog. Rep., March 31, 1985, DOE/ER-0045/14, U.S. DOE, Office of Fusion Energy.

3. J. L. Scott et al., Second Annual Prog. Rep. on United Sales-Japan Collaborative Testing in the High Flux Isotope Reactor and the Oak Ridge Research Reactor, Sept. 30, 1985, ORNL/TM-10102.

4. A. W. Longest et al., "Design, Fabrication, and Operation of HFIR-MFE RB* Spectrally Tailored Irradiation Capsules," in Fusion Reactor Materials Semiann. Prog. Rep., Sept. 30, 1990, DOE/ER-0313/9, U.S. DOE, Office of Fusion Energy.

5. A. W. Longest et al., "Design and Fabrication of HFIR-MFI? RB* Spectrally Tailored Irradiation Capsules," in Fusion Reactor Materials Semiann. Prog. Rep., March 31, 1988, DOE/ER-0313/4, U.S. DOE, Office of Fusion Energy.

6 A. W. Longest et al., "Design and Fabrication of HFIR-MFE RB* Spectrally Tailored Irradiation Capsules," in Fusion Reactor Materials Semiann. Prog. Rep., Sept. 30, 1987, DOE/ER-0313/3, U.S. DOE, Office of Fusion Energy.

7. A. W. Longest et al., "Design and Fabrication of HFIR-MFE RB* Spectrally Tailored Irradiation Capsules," in Fusion Reactor Materials Serniann. Pmg. Rep., Sept. 30, 1988, DOE/ER-03135, US. DOE, Office of Fusion Energy.

8. A W. Longest et al., "Design and Fabrication of HFIR-MFE RB* Spectrally Tailored Irradiation Capsules," in Fusion Reactor Materials Serniann. Pmg. Rep., March 31, 1989, DOE/ER-0313/6, U.S. DOE, Office of Fusion Energy.

REEVALUATION OF FABRICATION TECHNIQUE FOR MINIATURE TENSILE SPECIMENS - M. A. Blotter, University of Missouri-Rolla, and M. L. Hamilton, Pacific Northwest Laboratory[a]

PURPOSE

The purpose of this work is to develop an improved fabrication method for miniature tensile specimens

SUMMARY

The present punching process and two potential alternatives for fabricating miniature tensile specimens were evaluated. Three fabrication processes were considered: punching, electrical discharge machining (EDM), and chemical milling. Evaluation criteria included dimensional control and reproducibility, induced microstructural alteration, cost, and the validity of the resultant tensile data. It was demonstrated using annealed 304 stainless steel that punching not only led to substantial specimen deformation but also exhibited the largest dimensional variability. EDM and chemical milling produced specimens with dimensions that were acceptable from both standpoints. While EDM and chemical milling produced comparable tensile data, chemical milling was more expensive per specimen for the production of only a small number of specimens. EDM was therefore selected for all future fabrication of miniature tensile specimens.

PROGRESS AND STATUS

Introduction

Miniature specimens used for mechanical testing have been a mainstay of the fusion materials program for many years and will continue to be used extensively in future research. Periodic review and improvement in the fabrication, handling, and testing techniques are necessary to ensure that such specimens continue to produce valid data. Flat miniature tensile specimens with the dimensions shown in Figure 1 were originally designed to be punched from sheet stock rolled to the desired specimen thickness. The primary advantages of this technique were its rapidity and its low cost.' Specimens were fabricated on site without the delays associated with using an off site vendor or the expense of machining or tooling up for each production batch.

The main disadvantage of fabrication by punching is that the act nf punching produces unavoidable deformation in the specimen; even under optimum conditions, the best specimens exhibit some cupping (see Figure 2). Although cupping is most pronounced in very soft or very tough materials, its effects can

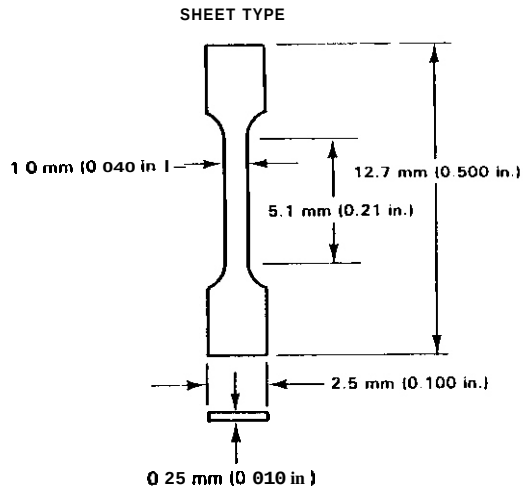


Figure 1. Dimensions of miniature tensile specimen.

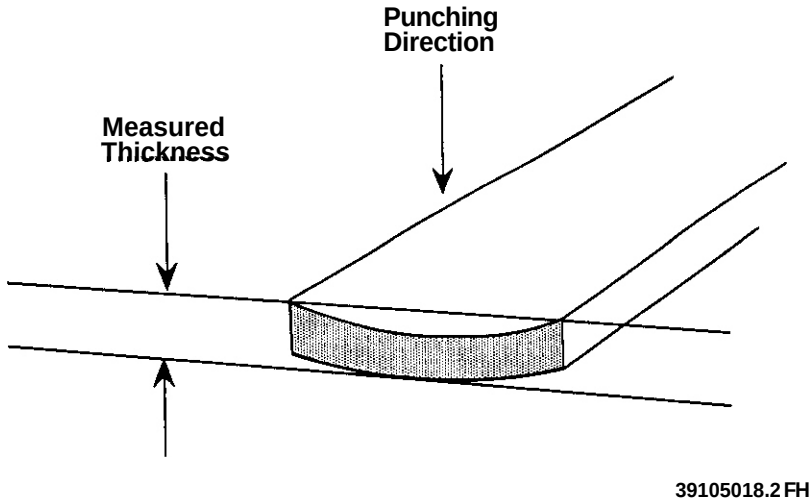


Figure 2. Development of cupping during punching operation.

(a) Pacific Northwest Laboratory is operated for the U.S. Department of Energy by Battelle Memorial Institute under Contract DE-AC06-76RLO 1830.

frequently be ameliorated by performing the requisite heat treatments after the punching operation. This was considered acceptaole in the past, particularly when coupled with a polishing operation to deburr deformed specimens. Despite some severe deformation problems with punched specimens, it has been possible to generate reproducible results for the changes in tensile behavior caused by irradiation.'

To produce good specimens consistently, the punch and die must be kept sharp. In addition, the appropriate clearance between punch and die is sensitive to the material being punched and must be optimized for each alloy. If the punch clearance and sharpness are not optimal, the cupping can be more severe and a burr will remain that must be polished away. The same punches and dies were used for many different alloys, and the punches were sharpened periodically as needed. Punches can be sharpenec only a limited number of times, however, and the punch and die sets were occasionally damaged with use over the years. New punch and die sets would have been required to ccntinue punching miniature tensile specimens. Given the need for new punch and die sets and the difficulties that have been experienced with some punched miniature tensile specimens, it was decided that several techniques to fabricate miniature tensile specimens would be evaluated before one was selected for future specimen fabrication. Three techniques were considered potentially feasible on the basis of both cost and ease of fabrication: punching, chemical milling, and electrical discharge machining (EDM).

Chemical milling is a photo-chemical etching technique that is frequently used to make high precision components for a number of industries, and was attractive due to its low cost and relatively rapid turn around time for the production of large numbers of specimens. It entails masking the surface, stripping the mask from the areas to be etched away, chemically etching away the undesired regions, and removing the mask. While part outlines can be achieved with a large degree of accuracy, the edges eaten away are known to be somewhat uneven and undercut, depending on material, shape, size and thickness.

EDM is the most expensive of the three techniques on a per specimen basis, but held the most promise for distortion-free, reproducible specimens. EDM is a means of shaping conductive materials by arc erosion. It is particularly well suited to cutting internal shapes and delicate pieces. In this technique, a tool is held a small distance from the workpiece while an electrical input builds up a charge and raises the voltage across the gap between the two, which is filled with a dielectric fluid. When the potential reaches a certain level, a discharge occurs between the closest points on the two surfaces. A minute amount of metal is melted and expelled in a globular form where the spark strikes the workpiece, leaving a small crater. This is repeated 20,000-300,000 times per second with the spark positioned by a servo-control device.

When the miniature tensile test system was originally developed and the punch and die sets were new, control specimens were punched from solution annealed 304 stainless steel. These specimens were used to verify the test system operation at the start of each testing sequence. Over the years, the supply of these control specimens had diminished to the point that fabrication of new controls was necessary. The procurement of new standards was therefore coupled with the reevaluation of the Fabrication technique. The specimen dimensions are shown in tigure 1.

Exoerimental Procedure

Two punch and die sets were ordered to allow the consideration of different clearances that might be appropriate for different materials of interest. The punch and die sets were made from hardened D2 tool steel. Tolerances of 0.3 and 1 mils were selected for the two sets based on the punching experience of the company that machined them. The set with the larger clearance was used to punch specimens from the same sheet of 304 stainless steel that had been used to punch the earlier control specimens. Punched specimens for this experiment were used in an as-punched condition, since the polishing operation typically used to deburr the miniature tensile specimens is known to both remove some of the artifacts of punching that were of interest here and to introduce additional variability.

No vendors were willing to bid on the initial requisition for chemically milled specimens due to the tight tolerances requested on the width of the specimen gauge section. The original drawing specified a width of 40 mils +1.0/-0.0 mils. One company (Hutchinson Technology in Hutchinson, MN) was willing to make specimens on a prototype basis after the tolerance on the gauge width was increased to +1.5/-0.0 mils. Due to a paucity of the original 304 stainless steel sheet stock, only a small number of chemically milled specimens were made from the original solution annealed sheet stock. A number of additional specimens were made from vendor-supplied 304 stainless steel to fully investigate the validity of the fabrication technique. The vendor indicated that the vendor-supplied 304 was in a "fully hardened" condition.

A wire EDM process was used to fabricate specimens by the third technique. The machine shop (JW Industries of Alburqueque, NM) claimed that dimensions could be held to within 0.2 mils. Specimens were made only from the original 304 sheet stock. Anticipating the success of the EDM technique, enough specimens were made to provide control specimens for a number of upcoming test sequences.

Three types of examinations were performed on each specimen type to determine the effect of production process on the quality of the specimens. The gauge dimensions were measured to determine the gauge measurements that would typically be used to calculate cross sectional area in tensile tests. Cptical microscopy

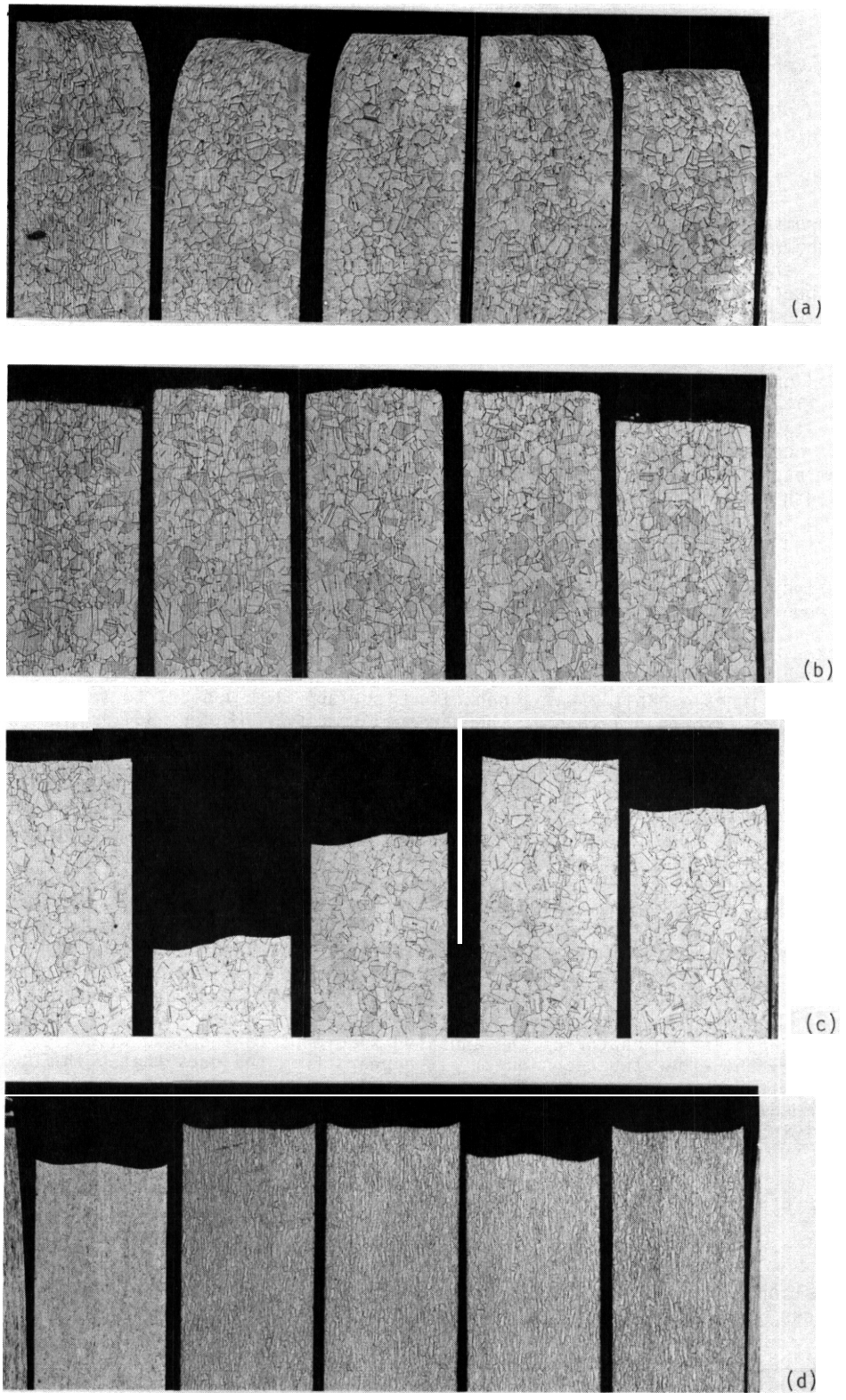


Figure 3. Transverse sections showing specimen edges for each fabrication type at 100x: a) punched, b) EDM, c) chemically milled (PNL-supplied material), and d) chemically milled (vendor-supplied material).

was performed on transverse specimen sections to determine 1)whether there was evidence of microstructural change at the specimen edges, and 2)the variability in specimen cross section associated with each technique. Quantitative evidence for material distortion was obtained by comparing Knoop hardness measurements taken on the transverse specimen sections at both the cut edge and in the body of the specimen.

Tensile tests were performed on each specimen type to determine the effect of production process on the subsequent tensile data. The variability of the tensile data was evaluated for each production process.

Results

Dimensional measurements. Using a digital micrometer accurate to 0.05 mils, three measurements each of the gauge thickness and width were obtained on five specimens produced by each technique. The contact surfaces of the micrometer were a cone point and a knife edge, which allowed accurate thickness measurements to be made even on the punched specimens. The cone point was placed inside thn punched "cup" while the knife edge was placed on the convex specimen surface to eliminate any potential distortion in the measurement caused by the burr. The average dimensions and their variability are given in Table 1. It is evident that while punching produced the most uniform measurements of specimen width, it also gave rise to the largest variability in measured gauge thickness, presumably due to the cupping of the specimen during the punching operation (see Figure 2). Conversely, chemical milling produced the least distortion in the measured specimen thickness but the largest variability in gauge width. This variability is a result of the chemical milling process, which is accomplished by photographically etching the sheet stock from both sides, producing a slight bevel from each surface to the center of the sheet thickness. It is worth noting that the variability in width produced by chemical milling is more significant for hardened steel than for solution annealed steel, most likely because the larger stored energy of the hardened steel probably increases the nonuniformity of the etching process.

Optical metallography. The same five specimens of each type that were used for the dimensional measurements were sectioned, mounted, and polished to reveal a transverse section through the gauge section. Figure 3 shows the appearance of the edges on the transverse sections for each fabrication process. The punched edges shown in Figure 3a are obviously somewhat deformed, although they are not in need of deburring; this condition demonstrates that the clearance between the punch and die was reasonable for the 304 steel. The chemically etched specimens exhibit a wavy, nonuniform surface that appears to be more variable in the solution annealed specimens (Figure 3c) than in the hardened specimens (Figure 3d). This observation is consistent with the tendency of finer-grained materials to etch more smoothly.[4] The EDM specimens shown in Figure 3b exhibit a relatively good squared off edge with a minimal amount of what is probably nonadherent debris in the vicinity of the edge. Such debris can result when material at the melted edge of the specimen does not fall away from the specimen completely. The debris was more visible when the metallographic mount was examined in the microscope than it is in the photograph. Neither the chemically milled nor the EDM specimens show evidence of microstructural change at the machined edges.

Hardness measurements. Knoop hardness was measured on the transverse metallography sections at both the specimens' edge and center using a 200 gram load. Two measurements were made on each specimen at each location. The average hardness values are given in Table 1. The hardness measurements are almost identical at the edges and centers of the annealed specimens produced by chemical milling and by EDM. It is evident that the punching operation severely deformed the microstructure at the edges of the specimens, even for the relatively good specimens that were produced with the new punch and die. The punching operation also caused the hardness in the center of the annealed specimens to increase slightly relative to the specimens produced by the other two techniques. It appears from the data that both EDM and chemical milling cause a small difference in hardness between the center and the machined edge. The reason for this decrease is not immediately obvious, although it is probably related to the relaxation of the microstructure allowed by the melting or etching that occurred at the specimen edges.

Table 1. Average Dimensions, Hardness and Cross Sectional Area of Miniature Tensile Specimens

Production Process	Dimensions		Hardness		Oeviation in Cross Sectional area (%)
	Thickness (mils)	Width (mils)	Edge (KHN)	Center (KHN)	
PNL-supplied material (solution annealed 304 stainless steel)					
Punching	10.20 ± 0.10	40.45 ± 0.05	357 ± 18	173 ± 5	3.8 ± 1.6
EDM	10.45 ± 0.05	40.75 ± 0.10	157 ± 8	163 ± 2	0.8 ± 0.4
Chemical milling	10.25 ± 0.05	40.35 ± 0.20	151 ± 5	161 ± 4	1.4 ± 0.9
Vendor-supplied material (hardened 304 stainless steel)					
Chemical milling	9.90 ± 0.05	40.65 ± 0.25	402 ± 9	428 ± 9	1.7 ± 0.4

Variability in cross sectional area determination. Strength calculstions require an accurate determination of the cross sectional area of a specimen. Current tensile test procedures require only the neasurement of specimen thickness, with an assumed gauge width of 40.4 mils based on earlier assessments of punched specimens. It is recognized, however, that there is some error associated with the current procedures, given the tendency for the specimens to become cupped during punching and the potential nonuniformity of the deburring operation that follows punching. Several types of area calculations were performed to assess both the variability in the actual cross sectional area. and the validity of the standard area calculation (i.e., the product of measured thickness and width) for each fabrication technique.

Photomicrographs at 100x of the transverse specimen sections shown in Figure 3 were xeroxed to enlargements of 150x. Cut-outs corresponding to the cross sectional area at the maximum measured width were weighed and compared to cut-outs corresponding to the actual cross sectional area. The average percentage difference between the two represents the deviation in area, ΔA_0, that would occur for area calculations using the dimensional measurements obtained prior to a tensile test, assuming that the measurement device contacts the points of greatest thickness. These deviations are also given in Table 1. The largest error in cross sectional area was obtained with punched specimens, while the least was obtained with EDM specimens. The error in cross sectional area associated with chemical milling was intermediate, and was virtually the same for solution-annealed or cold worked material. If the area deviations were large, as is the case for the punched specimens, the value $1-\Delta A_0$ could be used as a multiplicative normalization factor that might provide a better determination of cross sectional area than that calculated directly from the dimensional measurements, if a value for ΔA_0 were obtained for each batch of specimens fabricated.

Tensile data. Tensile tests were performed on five specimens of each type. A nominal gauge length of 0.2 inches was assumed for all specimens. The tensile data are given in Table 2. Although the ultimate strength of the punched specimens is almost identical to that of the EDM and chemically milled specimens, the yield strength is about 15% higher and the ductility is significantly lower.

The values of gauge width and thickness were determined for each specimen as the average of three measurements each. The measurements were performed between ball surfaces in an LVDT device that had been used previously for similar measurements. The dimensions obtained in this manner were not consistent with those obtained with the cone point and knife edge micrometer, and exhibited more variability as well. The width measurement is particularly difficult to obtain between ball surfaces because the positioning is not stable and requires continuous operator contact, an undesirable condition with irradiated specimens. For these reasons, use of the ball surfaces for dimensional measurements will be discontinued in the future and replaced with a conventional micrometer.

Discussion

The measured widths given in Table 1 are all within the specifications of the drawing shown in Figure 1. In the worst case, a 1% variability in the thickness was introduced during the punching operation. From a dimensional standpoint alone, therefore, all three of the fabrication techniques could be considered acceptable. The punched specimens produced in this experiment, however, are known to be superior in quality to others produced more typically.[2,3] In addition, the clearance between the punch and die is not necessarily appropriate for other alloys, and continued use of punching for specimen production would require some effort to optimize the clearance for a range of alloys. It is likely that the dimensional quality of punched specimens would degrade with time in a way similar to that observed previously. The necessary addition of a polishing operation to deburr punched specimens, as has been done previously, introduces even more variability in specimen dimensions due to the difficulty of uniformly and reproducibly deburring specimens. Thus punching the specimens is the least desirable option from the standpoint of dimensional control and reproducibility.

Table 2. Average Tensile Data Determined on Miniature Tensile Specimens of 304 Stainless Steel

Production Process	Yield Strength (ksi)	Ultimate Strength (ksi)	Uniform Elongation (%)	Total Elongation (%)	Equivalent Cold Work level (%)
PNL-supplied material (solution annealed 304 stainless steel:					
Punching	44.4 ± 2.4	92.4 ± 0.9	46.6 ± 1.4	49.9 ± 1.4	3
Chemical milling	37.8 ± 0.4	91.3 ± 0.6	66.5 ± 3.3	73.2 ± 2.3	1
EDM	38.1 ± 1.3	90.8 ± 0.3	59.6 ± 1.7	68.0 ± 2.5	1
Previously punched	55.5 ± 2.4	101.5 ± 1.1	35.5 ± 2.9	38.5 ± 3.0	5
Vendor-supplied material (hardened 304 stainless steel)					
Chemical milling	109.0 ± 5.5	134.0 ± 1.5	7.1 ± 1.3	7.1 ± 1.3	25

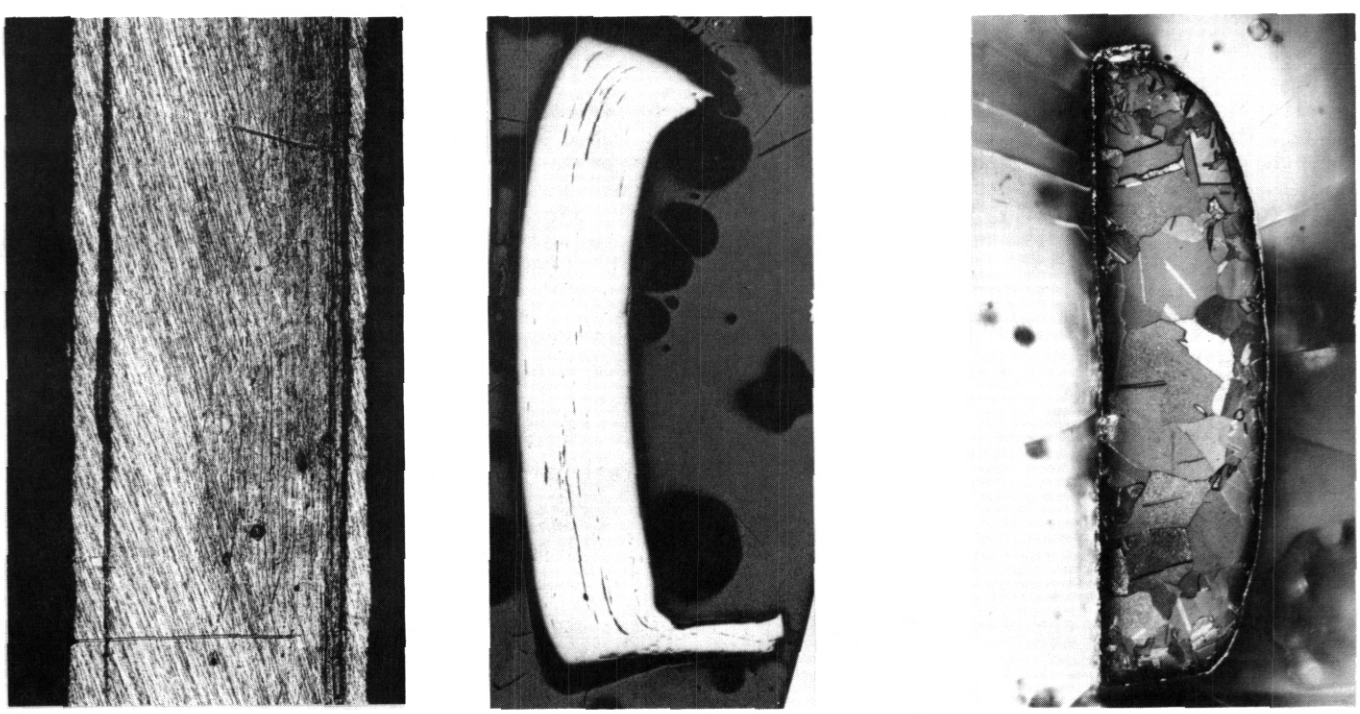
If the sharpness of the punch and the clearance between punch and die are not optimized, the edges of the specimens can crack or be deformed excessively, potentially invalidating the tensile results. Cracked specimens can lead to premature failure.' while smeared edges represent regions of different microstructure with potentially different tensile behavior.[3] While annealing treatments applied after the punching operation can restore the microstructure of specimens deformed during punching, smeared specimens tend to cup excessively when they are punched, resulting in a nonuniform cross section.

Post-fabrication heat treatment has been successful at removing the effects of deformation: no difference in hardness was observed after heat treatment between the specimen edge and center in the PE16 specimen shown in Figure 4a, despite the obvious band that remained as an artifact indicating the size of the sheared zone produced during the punching operation.[3] The burr that existed before polishing in these specimens is shown in Figure 4b. Punching soft materials can also lead to significant nonuniformity in the specimen cross section; Figure 4c shows a deburred specimen of Marz copper with large differences between the two curved edges. The nonuniform, non-square edges shown in the specimens in Figure 4 can lead to errors in cross sectional area determinations of up to several percent.

The metallography shown in Figures 1 and 4 and the hardness and tensile data given in Tables 1 and 2 demonstrate that punching is likely to alter the structure at the edges of the specimens. Punching could therefore only be considered acceptable if the specimens produced were heat treated following fabrication to remove the deformation remaining at the specimen edges after punching.

It is difficult to assess the effects of cracks that can be produced at the specimen edges; certainly it is impossible to remove them after they are introduced. One example of such cracks, produced in specimens of A212B, is given in Figure 5 (before deburring).' While such cracks do not typically lead to errors in the determination of cross sectional area, they are likely to lead to premature fracture of the specimen.

The condition of the 304 sheet stock supplied to the vendors by PNL was not known precisely; it was initially believed to be in a slightly cold worked condition on the basis of tensile data obtained previously from miniature tensile specimens punched from the same sheet. The current data were evaluated to verify this condition. The variability in the tensile data on the 304 specimens was assessed in terms of equivalent cold work level using Figure 6 as follows: Trend lines were drawn through the strength data provided in references 5 and 6 as a function of cold work level. Only minimum values from the ASTM specification



(a) (b) (c)

Figure 4. Miniature tensile specimen of PE16 showing (a) band delineating the size of the sheared zone that resulted from punching, (b) the degree of cupping that lead to the sheared zone. (c) Marz copper specimen showing nonuniformity of curved edges.

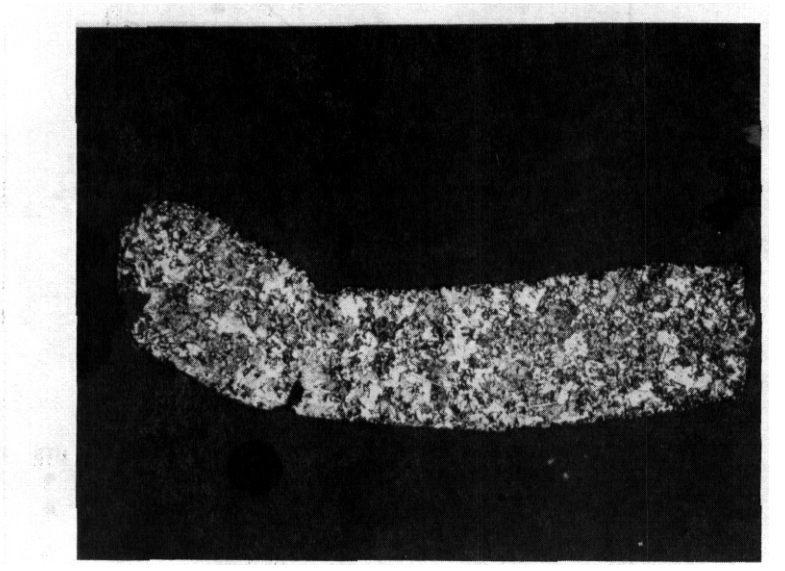


Figure 5. Cracks produced during punching of miniature tensile specimens of A212B pressure vessel steel.

were available for the solution annealed condition (i.e., 0% cold work level). No information on variability was available for these data. The tensile values from the current experiment were then located on these trend lines; an equivalent cold work level was extracted as the abscissa coordinate corresponding to the yield strength on the trend line. The equivalent cold work values are given in Table 2. Error bars are shown only for those cases where the error was larger than the size of the data point itself. The fact that the ultimate strengths were somewhat higher than would be expected for the cold work level that was determined is consistent with the observations of earlier experimenters.'

The tensile data generated in this experiment indicated that the sheet stock provided by PNL was probably nominally in the solution annealed condition. The yield strength data from the EDM and chemically milled specimens suggest that the 304 sheet stock supplied by PNL was in a solution annealed condition, since the value given for the 0% cold work level in Figure 6 is merely the ASTM specification for the minimum strength of 304 stainless steel. The tensile data on the new punched specimens imply that punching even the best quality 304 specimens that are achievable induces the equivalent, of about 1% cold work, whereas the data on the old punched specimens imply that the punching process previously in use typically induced the equivalent of about 5% cold work. In addition, more scatter was observed in the tensile data generated from punched specimens than from EDM or chemically milled specimens. Similar behavior is undoubtedly exhibited by other materials, particularly when the punch and die clearances are not optimized.

The final factor to be considered in the selection of an improved fabrication process was cost. Punching is obviously the cheapest if no optimization of punch and die clearances is explored, but the optimization that should be explored with this technique has the potential for being quite costly in both dollars and time. It should be possible to punch specimens from any material of the same quality as was obtained in the current work if the clearances were optimized. The cost for EDM specimens depends on the number of specimens being made, but appears to be roughly $10 each. Chemical milling involved a set-up charge of about $500 and would cost about $500 for each future batch of specimens for lots of up to 1000 specimens. Since only small numbers of these specimens are typically manufactured at any one time, the cost savings potentially available with chemical milling would not be realized, and this process would conceivably be more expensive than the EDM technique. Thus the technique selected for the fabrication of all future miniature tensile specimens is EDM.

CONCLUSIONS

The EDM technique was selected for future fabrication of miniature tensile specimens. Although chemical milling would be cheaper for large numbers of specimens, it is likely to be more costly for the small number of specimens typically made at one time in the fusion materials program. Punching was judged unacceptable

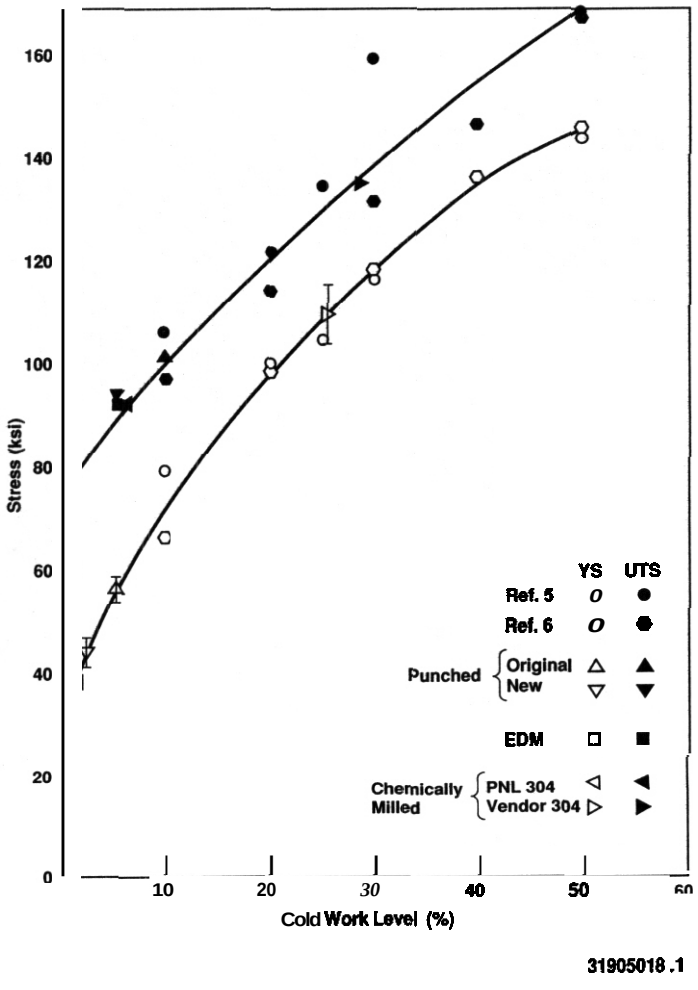


Figure 6. Assignment of equivalent cold work levels for test specimens relative to strengths given in References 5 and 6.

for the fabrication of miniature tensile specimens on the basis of dimensional variability and the likelihood of specimen deformation, unless a potentially costly investment in punch and die clearance optimization is made.

REFERENCES

1. N. F. Panayotou, S. D. Atkin, R. J. Puigh, and B. A. Chin, "Design and Use of Nonstandard Tensile Specimens for Irradiated Materials Testing," The Use of Small-Scale Specimens for Testing Irradiated Material, ASTM STP 888, W. R. Corwin and G. E. Lucas, Eds., ASTM, Philadelphia, 1986, pp. 201-219.

2. M. L. Hamilton and H. L. Heinisch, "Tensile Properties of Neutron Irradiated A212B Pressure Vessel Steel," Effects of Radiation on Materials: 14th International Symposium (Volume II), ASTM STP 1046, N. H. Packan, R. E. Stoller, and A. S. Kumar, Eds., American Society for Testing and Materials, Philadelphia, 1990, pp. 45-54.

3. M. L. Hamilton, "Precipitation Strengthening in a Nickel-Base Superalloy," Masters' Thesis, Washington State University, 1985.

4. L. E. Doyle, Manufacturing Processes and Materials for Engineers, 2nd edition, Prentice-Hall, 1969.

5. R. A. Moen and D. R. Duncan, "Cold Work Effects: A Compilation of Data for Types 304 and 316 Stainless Steel," HEDL-TI-76005, March 1976.

6. O. Peckner and I. M. Bernstein, Handbook of Stainless Steels, 1977, McGraw-Hill.

2.0 DOSIMETRY, DAMAGE PARAMETERS AND ACTIVATION CALCULATIONS

REAC*3 NUCLEAR DATA LIBRARIES - F. M. Mann and D. E. Lessor, Westinghouse Hanford Company,[a] HO-36, P.O. Box 1970, Richland, WA 99352

PURPOSE

The libraries (transport cross section, transmutation cross section, and decay data) associated with the REAC*3 nuclear transmutation code system are described.

SUMMARY

The purpose of this work is to provide the means of calculating activation in fusion devices.

PROGRESS AND STATUS

Introduction

In order to calculate neutron activation and the resultant dose, a series of libraries are needed. The neutrons must be transported from their source to the point where transmutation occurs (which requires a neutron transport cross section library). The probability for transmutation must be calculated (which requires a transmutation cross section library). The decay of the transmutation product must be followed, including the production of photons (which requires a decay data library). Finally the photons must be followed to the point of interest (which requires a photon transport cross section library).

The REAC*3 nuclear transmutation code system[1] contains modern versions of each of these data

Transport Cross Section Library

The NJOY nuclear data processing system (Version 89)[2] was used to process about 300 materials from the latest versions of the Evaluated Nuclear Data File (ENDF/B-V and ENDF/B-VI).[3] Except for a few isotopes in the fission oroduct region not reached from fission. all ENDF/B-VI evaluations were orocessed. Pointwise ENDF (PENDF) and groupwise ENDF (GENDF) tapes were created. The specifications for the' PENDF tapes were reached after consultation with Bob MacFarlane of the Los Alamos National Laboratory (LANL). Resonance reconstruction was done to 0.2% and then Dooler broadened to 300, 400. 600. 900. and 1200 K. Cross sections for actinide isotopes were further broadened to 1600, *2000,* 3000, and 4000 K. Bound effects were included. Also calculated were KERMA and damage energy parameters. The GENDF tapes were generated in an 89 neutron group structure and a 20 photon group structure. The neutron group structure is the same below 4 eV as that of the standard 69 group WIMS structure.[4] Two flux weightings were used, one typical of thermal reactors and the other typical of fast reactor cores. A minimum of 6 sigma-0's were used for each material with the most important actinides having 8 sigma-0's. Cross sections for the MCNP[5] ACE tapes were created for all evaluations except for the ENDF/B-VI evaluations from the Oak Ridge National Laboratory (ORNL), which used the R-matrix resonance formalism. Plots of the total, capture, fission, (n,2n), (n,p), (n,alpha) cross sections were created from PENDF tapes whenever the reactions were present.

Transmutation Cross Section Library

A new transmutation cross section library is being created in ENDF/B-VI format.[6] About 500 non-actinide isotopes will be present with evaluations extended in most cases to 40 MeV. Cross sections to the first and second isomeric states are included whenever these states are present in the product isotopes. All transmuting reactions in ENDF/B-VI have been placed in this library. In particular, (n,gamma) evaluations were processed into a fine group structure (399 groups). The REAC-ECN-5[7] activation cross section library which is also known as EAF-1 is being used for target isotopes having short half-lives. Also experimental and systematic data in the REAC-ECN-5 library are being used for normalization.

After creation as a pointwise library, the library will be processed into various group structures.

Decay Data Library

A new decay data library has also been formed in ENDF/B-VI format. This library consists of evaluations created by Charles Reich of the Idaho National Engineering Development Laboratory (INEL) for ENDF/B-VI and data from the Evaluated Nuclear Structure Data File (ENSOF) (May 1990).[8] Once Tal England *of* LANL completes the ENDF/B-VI decay data file of the fission products, his evaluations will replace those currently in the library. Table 1 shows the contents of the current library and of that expected this fall.

(a) Westinghouse Hanford Company is operated for the U.S. Department of Energy under Contract DE-AC-6-87RL0930,

Table 1. Source of Data for Decay Data Libraries

Source	Number of Isotopes Current Status	Fall 1991
Stable isotopes	262	262
C. Reich (INEL)	724	--
ENDF/B-VI	--	977
ENSOF (90)	1316	1279
Table of Isotopes	459	370
Total	2761	2888

As the libraries are designed to have data for all isotopes between the neutron-drip and proton-drip lines, some data will have only half-life and branching information from the Table of Isotopes.[9]

Summary

Three types of nuclear data libraries will soon be complete for use with the REAC transmutation code system: a transport cross section library, a transmutation cross section library, and a decay data library. Extensive documentation for each of the libraries is planned.

REFERENCES

1. F. M. Mann, "REAC*2: User's Manual and Code Description," WHC-EP-0282, Westinghouse Hanford Company, Richland, WA, December, 1989.

2. R. E. MacFarlane, D. W. Muir, and R. M. Boicourt, "The NJOY Nuclear Data Processing System, Volume I: User's Manual," "LA-9309-M, Vol. I," Los Alamos National Laboratory, Los Alamos, NM, May 1982.

3. The ENDF/B libraries are produced by the Cross Section Evaluation Working Group and are maintained by the National Nuclear Data Center, Brookhaven National Laboratory, Upton, NY.

4. R. E. MacFarlane and D. W. Muir, "The NJOY Nuclear Data Processing System, Volume III: The GROUPR. GAMINR. and MODER Modules," "LA-9303-M, Vol. III," Los Alamos National Laboratory, Los Alamos, NM, October, 1987.

5. J. F. Briesmeister, Editor, "MCNP- A General Monte Carlo Code for Neutron and Photon Transport," Version 3A, LA-7936-M, Rev. 2, Los Alamos National Laboratory, Los Alamos, NM, 1986.

6. P. F. Rose and C. L. Dunford, Editors, "Data Formats and Procedures for the Evaluated Nuclear Data File, ENDF-6," ENDF, Version 6, ENDF-102, National Nuclear Data Center, Brookhaven National Laboratory, Upton, NY, 1990.

7. J. Kopecky and H. Gruppelaar, "The REAC-ECN-3 Data Library with Activation and Transmutation Cross Sections for Use in Fusion Reactor Technology," Proceedings of the International Conference on Nuclear Data for Science and Technology, Mito, Japan, 1988, p. 245. Published by Saikon Publishing Co., Ltd., Tokyo, Japan.

8. The ENSDF data are produced by the International Nuclear Data Project and are maintained by the National Nuclear Data Center, Brookhaven National Laboratory, Upton, NY.

9. C. M. Lederer and V. S. Shirley, Editors, "Table of Isotopes," Seventh Edition, Wiley-Interscience, New York, NY, 1978.

INDUCED RADIOACTIVITY OF ELEMENTS IRRADIATED IN FFTF/MOTA AND EBR-2 - H. L. Heinisch (Pacific Northwest Laboratory)[a], F. M. Mann and D. E. Lessor (Westinghouse Hanford Company)

PURPOSE

The purpose of this work is to provide information for evaluating the residual induced radioactivity of materials irradiated in FFTF/MOTA and EBR-2 irradiation facilities.

SUMMARY

Calculations of decay rates of radionuclides in 36 elements irradiated in FFTF/MOTA core center and EBR-2 mid-core and top-core positions have been made using REAC*2. Tables of the results have been made and are being used in compiling test specimen waste disposal documentation.

PROGRESS AND STATUS

Residual induced radioactivity of test materials is an unavoidable consequence of radiation effects experiments performed in nuclear reactors. Knowledge of the activity level of the specimens and the associated irradiation hardware is essential to planning the experiment, performing the tests and disposing of the waste materials. Gamma dose rates are measured directly during storage and handling as part of ALARA procedures, but for aspects such as waste disposal, detailed laboratory analysis is needed to fully characterize the quantity of each radioactive isotope in a test specimen.

Calculations provide a reliable, yet inexpensive method of estimating the concentrations of all the radioactive isotopes in an irradiated material. Characterization of residual radioactivity of test specimens required for handling and waste disposal is routinely done at Hanford using the REAC*2 computer code system'. To avoid doing calculations on a case by case basis, tables of decay rates have recently been compiled for the radionuclides of 36 elements irradiated in FFTF/MOTA and in EBR-2. Samples of this information are given in Tables 1 and 2 for FFTF/MOTA and EBR-2, respectively.

Decay rates were calculated with REAC*2 for 250 day irradiations in FFTF/MOTA Level 3 (core center) at a total neutron flux of 5.45 x 10^{15} n/cm^2 (72% having E > 0.1 MeV). This results in a total neutron fluence of 1.2 x 10^{23} n/cm^2, about 35 dpa in steel. Decay rates were also calculated for irradiation in EBR-2 Row 2 Midplane for 40 days at a total neutron flux of 2.1 x 10^{15} n/cm^2 (93% having E > 0.1 MeV) to a total neutron fluence of 7.2 x 10^{21} n/cm^2 (about 5 dpa in steel) and for 40 days in EBR-2 Row 2 Top-of-Core at a total neutron flux of 2.80 x 10^{14} n/cm^2 (35% having E > 0.1 MeV) to a total neutron fluence of 9.6 x 10^{20} n/cm^2 (about 0.25 dpa in steel).

In the tables decay rates are given for the individual radionuclides in each element that together contribute 99% or more of the total activity. Oecay rates are given in Ci/g of the pure element. Radionuclides decaying by beta emission are identified. The tables contain decay rates after decay times of 0.5, 1, 2, 3, 4, and 5 years out of reactor.

The tables have been useful in documenting radioisotope levels in activated test specimens and in the waste products of their preparation and testing. When disposing of irradiated test materials, the decay rates of the radionuclides for each element in the specimen are obtained from the table corresponding to the greatest decay time that is less than the real time out of reactor. The results are linearly scaled for specimens exposed in multiple irradiations. The total contribution of each radionuclide present is evaluated, and those contributing at least 1% to the total activity of a specimen are noted in the records.

Uncertainty in the calculations depends on the elements involved and the uncertainties in the irradiation information. Calculations require nuclear reaction cross sections and decay data, the neutron flux spectrum, irradiation time and power history, and the material composition. In principle, the largest uncertainty in such calculations originates from uncertainty in the cross sections, where uncertainties can range from less than a percent to a factor of two or more, depending on the reaction. Cross sections for most of the reactions involving common alloying elements are well known. Irradiation times are well-known, and, because the irradiations are for materials experiments, the compositions are usually well-known. Uncertainties in the neutron fluence and spectrum, including differences in neutron flux spectra of these facilities over the years, are not considered significant within the scope of these calculations. Differences are assumed to be accounted for by the assumption that the dose for a typical run in a "generic" spectrum for each facility is an upper limit for any real, single irradiation.

(a) Pacific Northwest Laboratory is operated for the U.S. Department of Energy by Battelle Memorial Institute under Contract DE-AC06-76RLO 1830.

Table 1. Decay Rates of Radionuclides of Selected Elements, in Ci/g of the Pure Element, After Irradiation to 1.2×10^{23} Total n/cm^2 in FFTF/MOTA, Level 3 (core center). Only radionuclides contributing at least 1% to the total activity are listed for each element. The letter B following the isotope name indicates radionuclides that undergo beta decay.

Element	Isotope	Decay Rates in Ci/g After Decay Times of 0.5 year	1 year	2 years	3 years	4 years	5 years
Ti	Sc 46 B	2.61×10^{-02}	5.76×10^{-03}	2.81×10^{-04}	1.37×10^{-05}	6.67×10^{-07}	
	Ca 45 B	1.43×10^{-03}	6.63×10^{-04}	1.43×10^{-04}	3.08×10^{-05}	6.65×10^{-06}	1.43×10^{-06}
	H 3 B			4.85×10^{-06}	4.58×10^{-06}	4.33×10^{-06}	4.09×10^{-06}
V	V 49	4.12×10^{-05}	2.81×10^{-05}	1.31×10^{-05}	6.09×10^{-06}	2.83×10^{-06}	1.32×10^{-06}
	H 3 B	2.07×10^{-06}	2.01×10^{-06}	1.90×10^{-06}	1.79×10^{-06}	1.70×10^{-06}	1.60×10^{-06}
Cr	Cr 51	1.90×10^{-02}	1.96×10^{-04}				
	V 49	3.01×10^{-04}	2.05×10^{-04}	9.54×10^{-05}	4.44×10^{-05}	2.07×10^{-05}	9.62×10^{-06}
	H 3 B		7.17×10^{-06}	6.78×10^{-06}	6.41×10^{-06}	6.06×10^{-06}	5.13×10^{-06}
Mn	Mn 54	8.88×10^{-03}	5.92×10^{-03}	2.63×10^{-03}	1.17×10^{-03}	5.20×10^{-04}	2.31×10^{-04}
Fe	Fe 55	2.48×10^{-01}	2.18×10^{-01}	1.68×10^{-01}	1.30×10^{-01}	1.00×10^{-01}	1.76×10^{-02}
	Mn 54	2.25×10^{-01}	1.50×10^{-01}	6.67×10^{-02}	2.97×10^{-02}	1.32×10^{-02}	5.86×10^{-03}
co	Co 60 B	$1.88 \times 10^{+01}$	$1.76 \times 10^{+01}$	$1.54 \times 10^{+01}$	$1.35 \times 10^{+01}$	$1.19 \times 10^{+01}$	$1.04 \times 10^{+01}$
Ni	Co 58 B	$2.50 \times 10^{+00}$	4.20×10^{-01}	1.18×10^{-02}			
	Fe 55	*1.14* $\times 10^{-02}$	6.80×10^{-02}	5.25×10^{-02}	4.05×10^{-02}	3.13×10^{-02}	2.42×10^{-02}
	Co 60 B		2.34×10^{-02}	2.06×10^{-02}	1.80×10^{-02}	1.58×10^{-02}	1.39×10^{-02}
	co 57			3.53×10^{-03}	1.39×10^{-03}	5.47×10^{-04}	
	Ni 63 B			6.02×10^{-03}	5.97×10^{-03}	5.93×10^{-03}	5.89×10^{-03}

TABLE 2. Decay Rates of Radionuclides of Selected Elements, in Ci/g of the Pure Element, after Irradiation to 7.2×10^{21} total n/cm^2 in EBR-2, Row 2 Midplane. Only radionuclides contributing at least 1% to the total activity are listed for each element. The letter B following the isotope name indicates radionuclides that undergo beta decay.

Element	Isotope	Decay Rates in Ci/g After Decay Times of 0.5 year	1 year	2 years	3 years	4 years	5 years
Ti	Sc 46 B	7.24×10^{-03}	1.60×10^{-03}	7.79×10^{-05}	3.80×10^{-06}	1.85×10^{-07}	
	Ca 45 B	3.27×10^{-04}	1.52×10^{-04}	3.21×10^{-05}	7.06×10^{-06}	1.52×10^{-06}	3.29×10^{-07}
	H 3 B			1.14×10^{-06}	1.08×10^{-06}	1.02×10^{-06}	9.64×10^{-07}
V	V 49	1.04×10^{-05}	7.10×10^{-06}	3.30×10^{-06}	1.54×10^{-06}	7.16×10^{-07}	3.33×10^{-07}
	H 3 B	4.78×10^{-07}	4.65×10^{-07}	4.39×10^{-07}	4.15×10^{-07}	3.92×10^{-07}	3.71×10^{-07}
Cr	Cr 51	1.44×10^{-03}	1.49×10^{-05}				
	V 49	6.81×10^{-05}	4.64×10^{-05}	2.16×10^{-05}	1.01×10^{-05}	4.68×10^{-06}	2.18×10^{-06}
	H 3 B		1.71×10^{-06}	1.68×10^{-06}	1.59×10^{-06}	1.50×10^{-06}	1.42×10^{-06}
Mn	Mn 54	2.48×10^{-03}	1.65×10^{-03}	7.34×10^{-04}	3.26×10^{-04}	1.45×10^{-04}	6.44×10^{-05}
Fe	Mn 54	3.70×10^{-02}	2.47×10^{-02}	1.10×10^{-02}	4.87×10^{-03}	2.17×10^{-03}	9.62×10^{-04}
	Fe 55	7.42×10^{-03}	6.52×10^{-03}	5.03×10^{-03}	3.89×10^{-03}	3.00×10^{-03}	2.32×10^{-03}
co	Co 60 B	1.59×10^{-01}	1.49×10^{-01}	1.31×10^{-01}	1.15×10^{-01}	1.01×10^{-01}	8.81×10^{-02}
	Fe 59 B	5.31×10^{-03}					
	Co 58 B	3.28×10^{-03}					
Ni	Co 58 B	7.10×10^{-01}	1.19×10^{-01}	3.35×10^{-03}	9.44×10^{-05}		
	Fe 55	1.15×10^{-02}	1.01×10^{-02}	7.81×10^{-03}	6.03×10^{-03}	4.66×10^{-03}	3.60×10^{-03}
	Co 60 B		3.33×10^{-03}	2.92×10^{-03}	2.56×10^{-03}	2.24×10^{-03}	1.97×10^{-03}
	co 57		2.04×10^{-03}	8.02×10^{-04}	3.16×10^{-04}	1.24×10^{-04}	
	Ni 63 B			1.43×10^{-04}	1.42×10^{-04}	1.41×10^{-04}	1.40×10^{-04}

FUTURE WORK

Calculations for positions above and below the core in FFTF/MOTA will be made and included in a final report. Effective ways of including this information in a computer data base are being considered.

REFERENCES

1. F. M. Mann, REAC*2: Users Manual and Code Description, WHC-EP-0282 (1989)

3.0 MATERIALS ENGINEERING AND DESIGN REQUIREMENTS

No contributions.

4.0 FUNDAMENTAL MECHANICAL BEHAVIOR

No contributions.

5.0 RADIATION EFFECTS: MECHANISTIC STUDIES, THEORY, AND MODELING

DEFECT PRODUCTION AND ATOMIC MIXING IN HIGH ENERGY COLLISION CASCADES: A MOLECULAR DYNAMICS STUDY - T. Diaz de la Rubia and M. W. Guinan (Lawrence Livermore National Laboratory)

OBJECTIVE

The purpose of this work was to develop an efficient molecular dynamics code utilising the vector architecture of the Cray-2 supercomputer and apply it to the study of high energy collision cascades. This was accomplished with international collaboration under the auspices of the IEA Working Group on Radiation Effects Theory and Modeling.

SUMMARY

We have performed molecular dynamics computer simulation studies of 25 keV displacement cascades in Cu at low temperature. At this energy we observe the splitting of a cascade into subcascades and show that displacement cascades in metals may lead to the formation of vacancy and interstitial dislocation loops. We discuss a new mechanism of defect production based on the observation of interstitial prismatic dislocation loop punching from cascades at 10 K. We also show that below the subcascade threshold, atomic mixing in the cascade is recoil-energy dependent. We obtain a mixing efficiency that is proportional to the square root of the recoil energy.

PROGRESS AND STATUS

Introduction

The nature of the damage that ensues in a metal upon its irradiation with energetic particles has been a topic of interest for over **40** years.[1,2] Initially, this interest resulted from the need to understand radiation effects in materials in a nuclear reactor environment; today it is driven by these same concerns and by the emergence of energetic ion beams as a common tool in non-equilibrium processing and modification of materials.[3]

Essential to gathering a knowledge of radiation damage in solids is understanding the cascade of atomic displacements that results when an energetic particle (e.g., a heavy ion or a fast neutron) penetrates a solid. Displacement cascades present a difficult problem to study by either theoretical or experimental means. Their many-body and highly non-linear nature precludes **use** of treatments based on the linearized Boltzmann transport equation and the binary collision approximation; such collisional models consider only the interaction between moving and stationary atoms.[4,5] Experimentally, the small size ($\approx 3 \times 10^5$ A3) and very short lifetime ($\approx 10^{-11}$ s) of cascades has hampered attempts to dynamically resolve their evolution. Models based on applications of the heat transport equation[6] are limited by the inhomogeneous nature and extreme thermal gradients imposed in the core of the cascade. Caro et al.[7] have recently proposed a model that employs results from molecular dynamics simulation to establish the time scale of the heat transport, thereby avoiding explicit definition of the thermal diffusivity in the cascade. This approach is nevertheless limited in its scope since no information on defect production and clustering may be obtained.

Molecular dynamics computer simulation (MD) has been used as a tool to study the structure and dynamics of energetic displacement cascades for the last 30 years. The early pioneering work of Gibson et al.[8] demonstrated that Frenkel defect production in electron irradiated metals proceeds via replacement collision sequences (RCSs) along close-packed directions. These seminal studies, performed at Brookhaven around 1960 with recoil atom energies up to 400 eV, set the stage for higher energy MD studies. Until recently, however, progress in the field has been slow mainly because of the large number of atoms required to perform these simulations, and also because of the lack of reliable interatomic potentials to describe the energetics of metals. This slow progress is illustrated in Fig. 1 where we show the energy of the primary knock-on atom (PKA) employed in simulations of cascades in bulk systems (in reduced energy units[9]) versus the year of the study. This figure is not intended to provide an exhaustive review of MD investigations of particle- solid interaction phenomena and besides the work of the Brookhaven group already mentioned, it includes the work of the Argonne-Illinois-Livermore group.[10-14] Also included for comparison is an average threshold energy of subcascade

formation in fcc metals obtained by Heinisch[15] in binary collision approximation studies. This subcascade energy is of interest to MD simulations since above this threshold cascades are expected to break up into individual subcascades.16

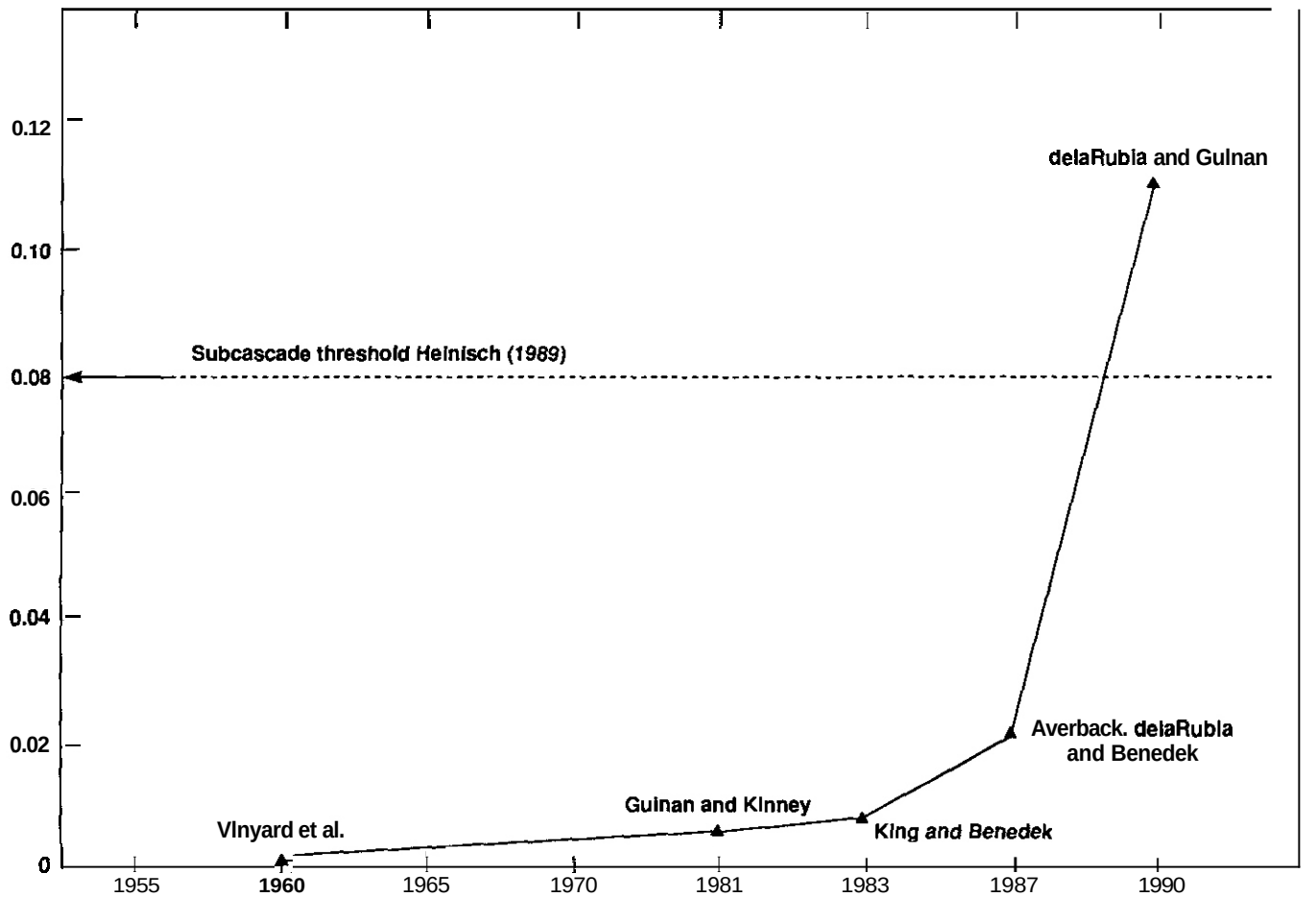


Fig. 1. Maximum reduced energy employed in molecular dynamics studies of collision cascades as a function of the year the studies were carried out. The dotted line is the threshold for the formation of subcascades obtained in binary collision studies.

As can be seen from Fig. 1, 20 years elapsed from the time of the Brookhaven study until the next MD simulations of cascades in bulk metals were performed. In this work, Guinan and Kinney[10] simulated events in W at energies up to 10 keV. They employed computational cells that contained 60,000 atoms and showed that atomic motion during the thermal spike phase of the cascade leads to point defect recombination and therefore to low defect production efficiency (number of defects produced relative to the predictions of linear-cascade models[17,18]) in cascades. Their results were in good qualitative agreement with experimental studies which had shown that the defect production efficiency, ξ, for cascade-producing irradiation of metals reaches a constant value of 1/3 for average recoil energies in the subcascade regime.[19]

The recent surge in the availability and power (CPU-speed and memory) of supercomputers has made the use of MD plausible for radiation damage studies at even higher reduced energy. MD studies of 5 keV cascades in Cu and Ni (corresponding to the 1987 point in Fig. 1) led to a model of formation of the primary state of radiation damage in metals based on the concept of local melting during the thermal spike phase of the cascade.[12,13] Within this simple "liquid droplet" model, defect production, point defect clustering and the amount of atomic rearrangement produced in a displacement cascade (i.e., ion beam mixing) are all governed by the extent and lifetime of the melt zone and therefore by the melting

behavior of the material under study. Due to the limited recoil atom energy (maximum of 5 keV) employed in those studies, ideas put forth in the model are based on extrapolation of results to higher energies where subcascade formation becomes important. Furthermore, the nature of the pair potentials employed sheds some questions into the reliability of some qualitative aspects of the results.

In order to increase the PKA energy in MD simulations we have developed a new code, termed MOLDYCASK, that takes advantage of the vector architecture of Cray supercomputers.20 This code has enabled us to perform MD simulations of energetic displacement cascades in Cu at energies as high as 25 keV (ε=0.11 in reduced energy units) with more realistic isotropic many-body potentials of the EAM type.[21,22] It makes use of the model of Caro and Victoria23 to describe lattice-electron interactions.

We present results of 1, 2.5, 5, 10, and 25 keV PKA cascades in copper. Also included are results of dimer-recoil (E_{Tot}=10 keV) events. At the highest reduced energy treated in these simulations (ε= 0.11), the break-uo of a cascade into individual isolated subcascades is seen to take place. The collapse of a displacement cascade to a vacancy dislocation loop is observed and more significantly, prismatic dislocation loops are seen to appear near the edge of the molten zone of 25 keV and dimer-recoil cascades. We have recently proposed that a new, cooperative mechanism, not related to RCSs but rather akin to dislocation loop punching24 is responsible for this interstitial prismatic dislocation loop formation.[14] We analyze evidence for this new mechanism of defect production and discuss its consequences regarding the microstructural evolution of metals in high-radiation environments.

The results display an energy dependence of atomic mixing in the cascade. The degree of clustering of vacancies and SIAs in the cascades is also observed to be energy (and energy density) dependent. The results reproduce the correct magnitude of ξ in cascades and shed new light into defect production mechanisms.

Molecular Dynamics Model

The MOLDYCASK code employs the vectorized link cell method (VLC) of Heyes and Smith25 as modified by M.W. Finnis[26] to find the neighbors of a given atom in the computational crystal. With this technique, the calculation of the forces on all atoms in a MD step can be fully vectorized on a Gray-2. The VLC method gains its speed from the splitting of the computational crystal into "link cells" of side length slightly larger than the cut-off distance of the interaction potential. Extensive use of Cray-specific vector operations greatly enhances the code's performance. The advantages of this technique become most evident when the number of atoms in the MD crystal exceeds several thousands. For large numbers of atoms, the VLC offers considerable computational speed and low memory requirements.

In the MD studies to be described below, we have employed crystals containing up to 500,000 atoms for the case of the 25 keV events. With this crystal size the code performs a complete MD step (including I/O operations) in 111 seconds of CPU.

The cascades were initiated by imparting kinetic energy to one atom in the crystal. The direction of this primary knock-on atom (PKA) was chosen at random although it was insured that it was away from a channeling or a close-packed direction. Simulations were also performed for dimer recoils with a total energy of 10 keV. In this case, a pair *of* nearest neighbors endowed with 5 keV/atom is employed as the primary knock-on. For simplicity, and to maximize overlap effects at this energy, the initial direction of travel of the 2 recoiling atoms in the dimer was chosen to differ by only 5". Henceforth, these events will be referred to as di-5 keV cascades. All events were performed in computational crystals coupled (via Langevin dynamics applied to the boundary atoms) to a thermal reservoir at a constant ambient temperature of 10 K. Energy that arrived at the boundary layers was prevented from reentering the crystal via the periodic boundary conditions by virtue of a damping coefficient applied to the atoms in the boundary link cells. Details of this procedure have been given elsewhere.[20]

The embedded atom method (EAM) potentials of Foiles, Baskes and Daw[22] have been shown to accurately reproduce many equilibrium properties of fcc metals and are used, in a modified version, throughout this work. In order to treat the highly non- equilibrium atomic configurations and distances

encountered in the course of these simulations, we modified these potentials to improve the description of the pressure derivative of the bulk modulus20 and to correctly characterize high energy scattering.27 It has been shown that the EAM potential for Cu reproduces the threshold displacement energy correctly28 and therefore our modification does not alter the characteristics of the potential for energies below 40 eV. At very high energy the pair potential contribution to the total energy is chosen to reproduce the scattering from a Moliere potential and the embedding function is forced to become a constant. In this manner, the EAM potential is effectively transformed into a pair potential at high energy.

The electronic energy loss has been included in our simulations by means of the model of Caro and Victoria.[23] In this model, based on the local density approximation to the electronic energy loss,[29] the high energy electronic stopping enters the motion of the atoms in the MD crystal via the Langevin equation of motion. Furthermore, the model reproduces the correct limit of the electron-phonon coupling at low energy for weakly coupled metals such as Cu. We have previously employed this model to investigate the effect of electron-phonon coupling on the dynamics of thermal spikes in Cu in reference[27] where details of its implementation are given.

Cascade Structure

Previous MD studies of 5 keV displacement cascades in Cu and Ni[12,13,30] with pair potentials showed that local melting takes place at the core of the cascade. It was concluded that the melting point is the physical quantity that determines the behavior of a metal under cascade-producing irradiation. The present study confirms the melting behavior of the cascade and provides the first dynamical simulation evidence for subcascade formation and interaction. Moreover. the large damage energy density deposited in the local melt region of the 25 keV and dimer-recoil cascades is shown to give rise to new defect production phenomena not observed before.

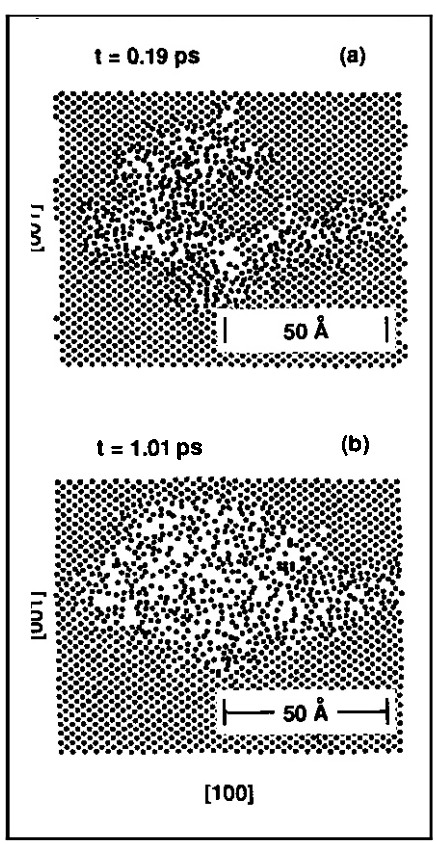


Fig. 2. Evidence for the formation of subcascades in a 25 keV event in Cu. The filled circles represent positions in an (010) plane of width a012 at 0.19 ps (a) and 1.01 ps (b).

Evidence for the break-up of a high energy cascade into subcascades and their subsequent interaction is presented in Fig. 2 where a snapshot of the atom positions in a (010) plane of width a012 are shown (a_0 is the lattice parameter of the perfect crystal). The plane cuts across the centroid of a 25 keV cascade defined as the "center of gravity" of the kinetic energy distribution in the crystal. Figure 2a shows such a cut 0.2 ps after the initiation of the primary recoil event. A region in which a large degree of crystalline order is preserved is seen surrounded by two "lobes" of highly disordered material. At a later time, 1.02 ps, figure 2b shows that the two original subcascades have overlapped to form a single melt zone. This represents the first time that the dynamical interaction between subcascades has been observed in an MD simulation. From these results it may be expected that for irradiations of low melting temperature materials where a large amount of damage energy is deposited, a molten tube connecting subcascades may be formed.

In Fig. 3, we show similar planar projections across the center of a second 25 keV cascade at 3 different times. Atoms with total energy larger than that required to bring them from 0 K to the liquid phase,i.e., Q+L = 0.48 eV where L is the latent heat of melting of Cu, are shown as filled circles. As can be seen from the figure, the disordered region has a sharp interface in with the rest of the crystal. No subcascade break-up is observed in this case. Note the changing size and shape of the of the molten region.

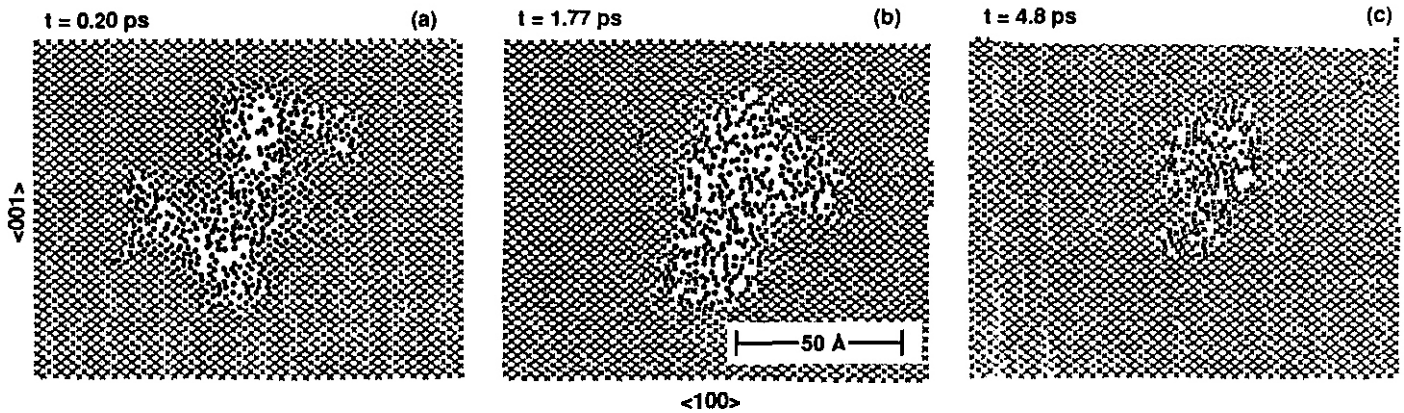


Fig. 3. Time development of the molten zone in a second 25 keV cascade in Cu. The x's are the positions of atoms in an (010) plane of width $a_0/2$. Atoms with a total energy > 0.48 eV (see text) are plotted as filled circles. Positions are shown at 0.20ps (a), 1.77 ps (b) and 4.8 ps (c).

In order to study the local atomic structure of the cascade region, we calculate the square of the magnitude of the planar structure factor, $|S_p(k)|^2$, for regions of (010) planes that contain 250 atoms in the core area of the cascade. This quantity, where **k** is a primitivelattice vector in the plane, is highly sensitive to local order and takes a value of 1 for a perfect crystal at 0 K and fluctuates near a value of 0 for a crystal with no long range order. Fig. 4 shows the average value of $|S_p(k)|^2$ for 12 planes centered on the centroid of the cascade at several times. No long range order is appreciable at times longer than about 0.25 ps until late in the event. It is interesting to note however, that at 0.2 ps $|S_p(k)|^2$ fluctuates near a value *of* 0.1 indicating, as expected, that the cascade core has not yet reached a true molten state.

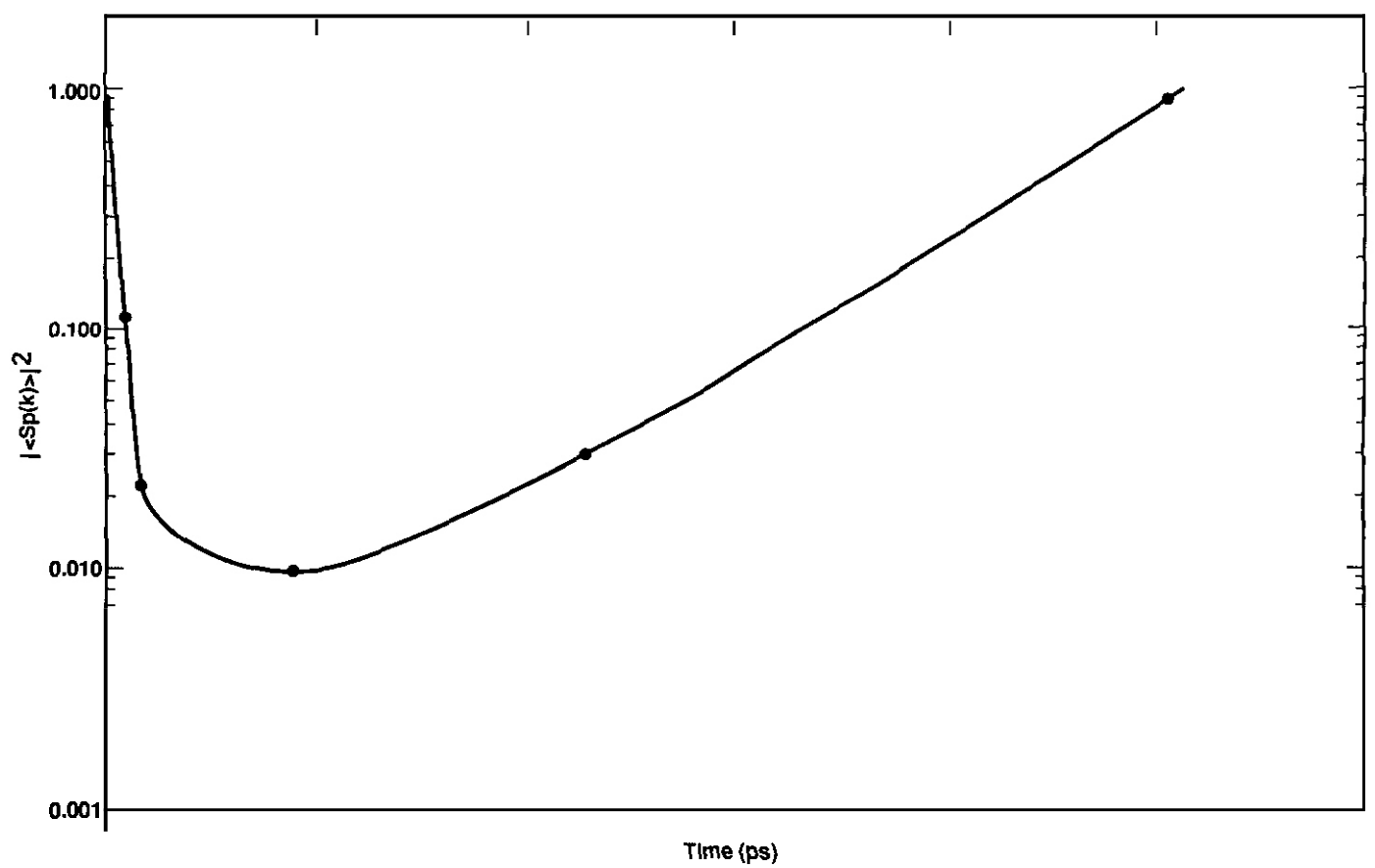


Fig. 4. Average of the square of the planar structure factor for 250 atoms at the cascade core.

Cascade Kinetics

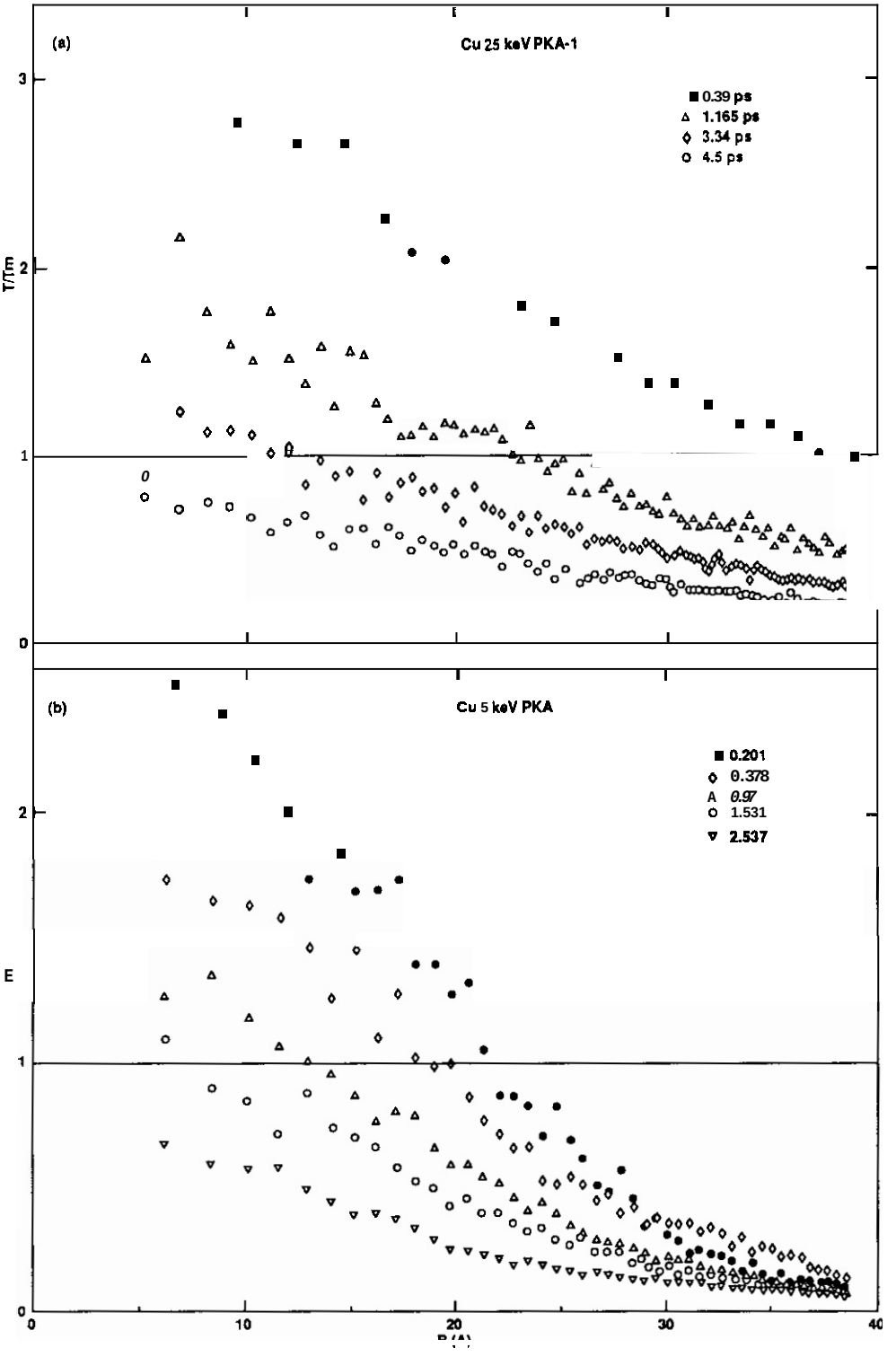


Fig. 5. Radial temperature distributions for two cascades as a function of distance from the centroid of the cascade region at several times . a) a 25 keV cascade at 0.39-4.5 ps and b) a 5 keV cascade at 0.20-2.5 ps.

temperature (normalized to the experimental value of the melting point of Cu), for the 25 keV cascade corresponding to figures 3a-c. The temperature remains above the melting point for over 3 ps. However, for the 5 keV event, figure 5b shows that the temperature in the cascade region falls below the melting point at ~1.5 ps. At early times (0.2-0.4 ps) the cooling rate achieved in the core of the 25 keV displacement cascades is 1 x 10^{15} K/s and the temperature gradient is ~90 K/Å in the central region. At later times, the different cooling rates of the cascades are highlighted by the results presented in Fig. 6 where the average temperature in the cascade core (R<15 Å) is shown for 5, 10, di-5 and 25 keV events.

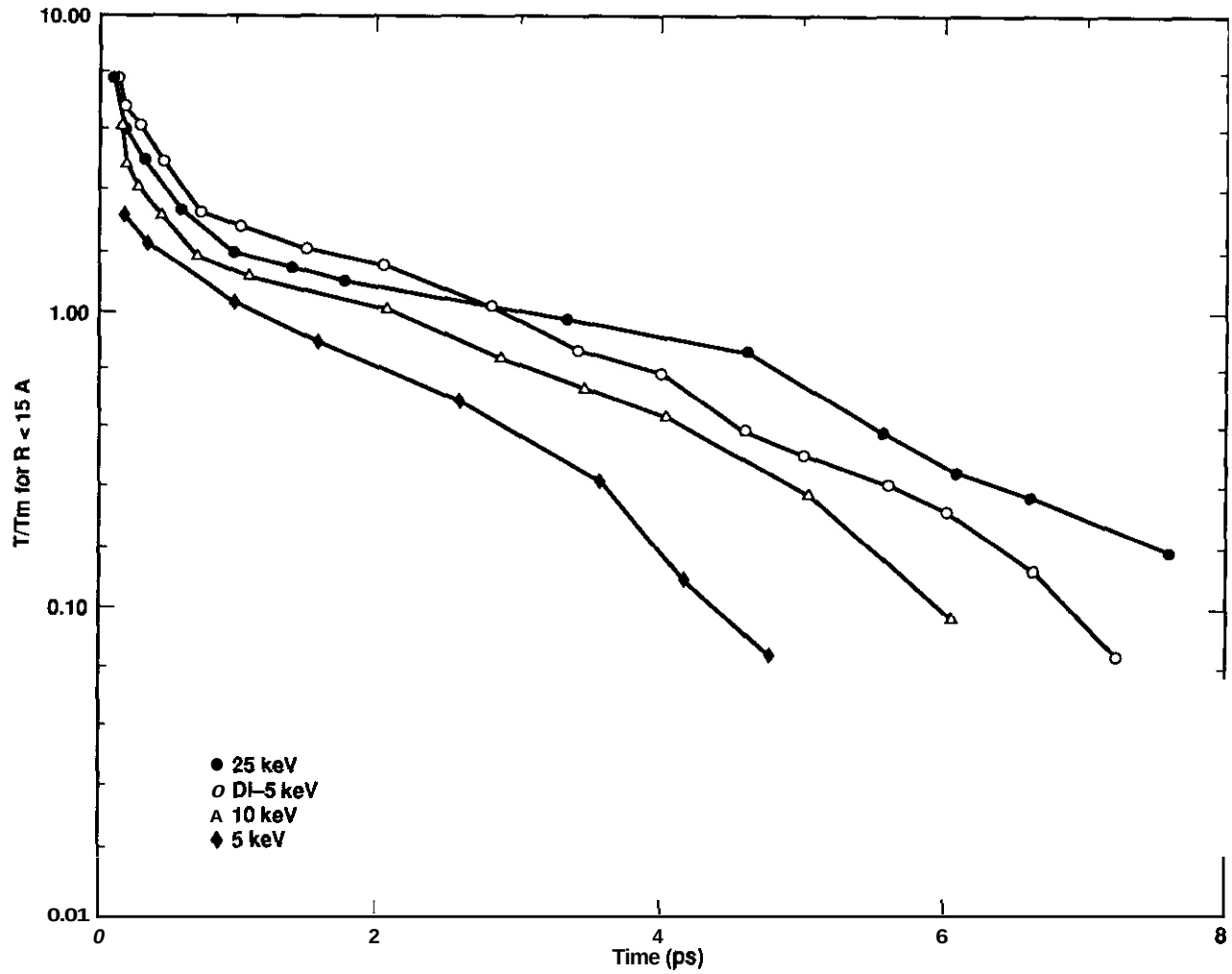


Fig. 6. The logrithm of the reduced temperature, T/T_m, of the core regions (r < 15 Å) of four cascades as a function of time.

The process of melting a solid is usually accompanied by a corresponding reduction in the atomic density of the melt. In Fig. 7, we plot the atomic density (normalized to the perfect crystal value) for the core (R<15 Å) of the same 25 keV cascade at several times. The atomic density in the molten zone is substantially decreased during the cascade lifetime. It is the existence of this free volume in the liquid that results in the large diffusion coefficients typically observed in liquid metals. As will be shown below, atomic diffusion in this locally molten zone generates a large amount of atomic rearrangement during the lifetime of the displacement cascade.

The large cooling rates and temperature gradients described above result, as expected, in a large degree of undercooling in the melt region. In figure 5a, it can be seen that by 4.6 ps the crystal temperature is everywhere below the melting point. However, inspection of figure 3c shows that a large disordered region is still present near the center of the cascade. This is further confirmed by the very low value of $|Sp(k)|^2$ at 4.6 ps seen in figure 4.

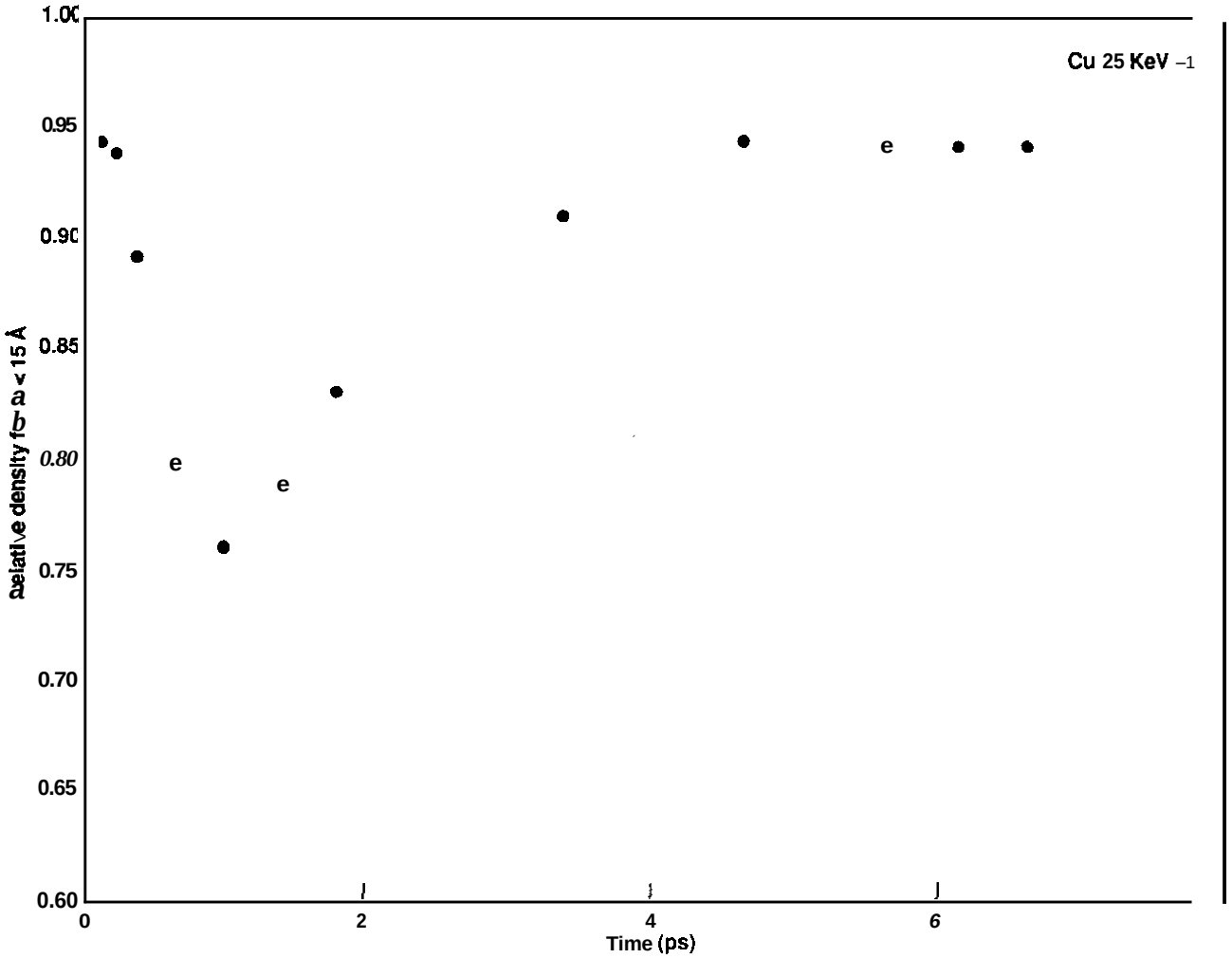


Fig. 7. Relative density in the core (r < 15 Å) of a 25 keV cascade as a function of time.

For sufficiently high interfacial undercooling during the rapid quenching of a pure metal melt, the formation of structures departing widely from those at equilibrium is expected.[31] Following the analysis of reference 31, we estimate that for the 25 keV discussed above the scaled interfacial undercooling at the crystallization front at ≈4.6 ps is $\Delta T_i/T_l = 0.26$ where $\Delta T_i = T_l - T_i$ and T_l and Ti are the liquidus and interfacial temperatures, respectively, This value is over a factor of 2 larger than the estimates of Lin and Spaepen [32] following laser melting of pure Fe.

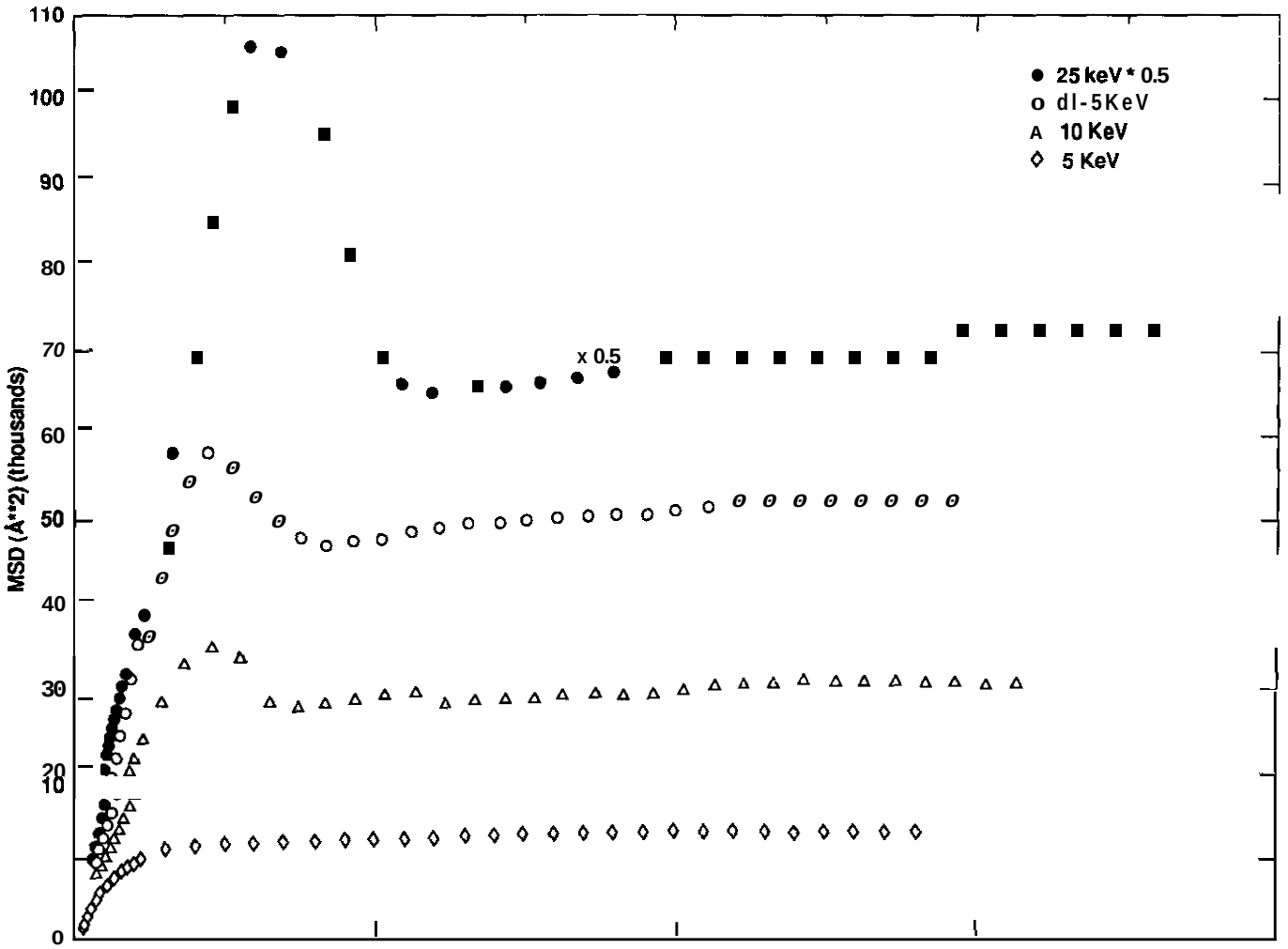
Atomic Mixing

In order to study the amount of atomic rearrangement that takes place during the lifetime of a displacement cascade we calculate the total mean square displacement for the atoms in an MD crystal, which we define as

$$< R^2(t) > = \sum_{i=1}^{N} [r_i(t) - r_i(0)]^2$$

where $r_i(0)$ denotes the perfect lattice position of atom i, and $r_i(t)$ indicates its displaced position at time t.

In Fig. 8 we show the mean square displacement for the atoms in the computational crystal of 5, 10, di-5 and 25 keV cascades. For clarity of presentation, the data for the 25 keV event have been scaled by a factor of 0.5. A marked difference in the dynamics of these cascades is clearly visible. In the case of the 25 keV and dimer cascades a large contribution to R^2 arises from the expansion of the crystal outside the cascade region at 1 ps. Although part of this distortion is recovered during the cooling stage of the cascade, a much larger magnitude of the total mean square displacement is observed for these cascades compared to the 5 and 10 keV events.



observed experimentally33 but this is not unreasonable since isolated subcascades are not expected in Cu until higher recoil energies are reached.

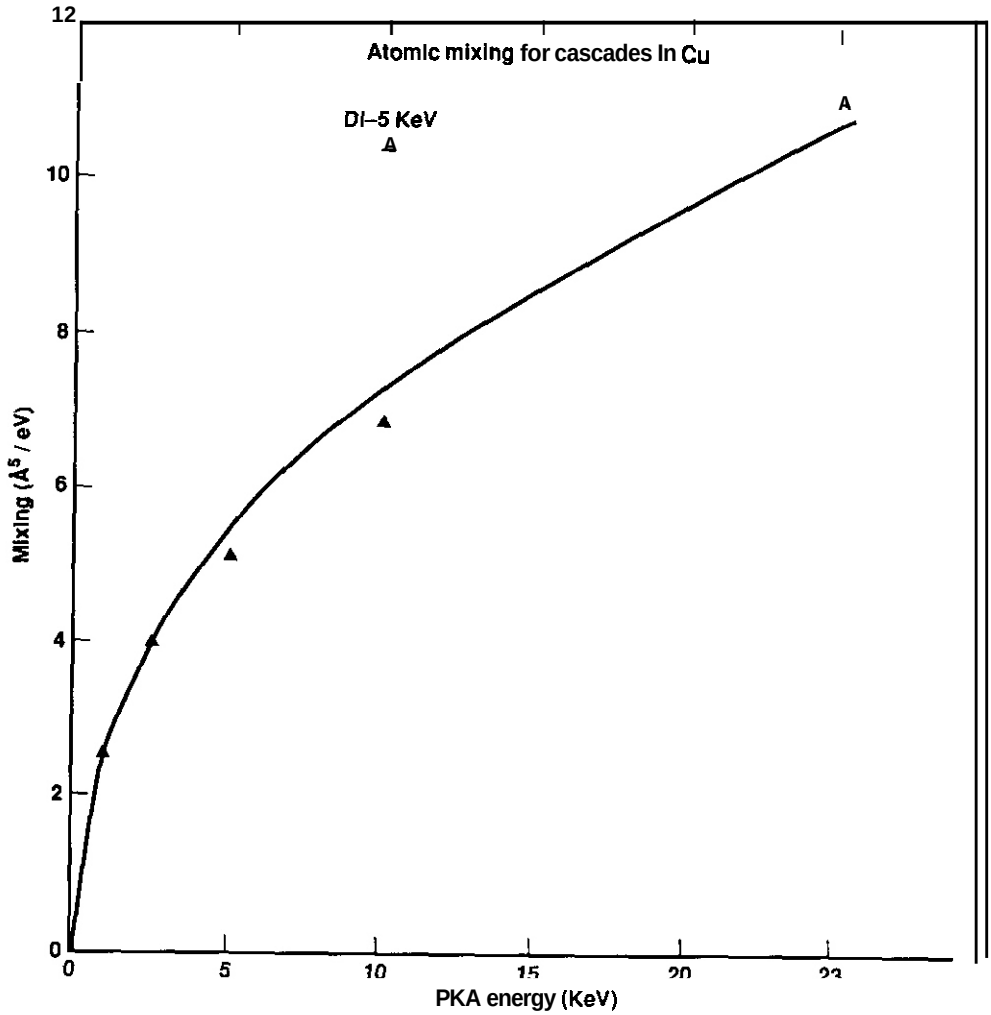


Fig. 9. Normalized value of the mixing parameter for cascades in Cu. The fit to the data is reflects the dependence of the atomic mixing on the square root of the PKA energy.

More important is the increase in atomic mixing with PKA energy. This reflects the long lifetime and high energy density of the melt zone found in the 25 and di-5 keV PKA events. Energy density is defined by considering the radius of gyration of the region of the crystal in which total atom energies exceed 0.48 eV (i.e., the molten zone). The time at which this definition is applied is arbitrarily chosen as 0.25 ps (i.e., near the end of the collisional phase) for all events. The energy density in the 5, 10, di-5 and 25 keV cascades is 0.54, 0.68, 0.97 and 0.96 eV/atom, respectively. We note that atomic mixing in the di-5 keV cascades is almost a factor of two larger than in the 10 keV monomer events and very similar in magnitude to the 25 keV events. A fit through the data, excluding the di-5 keV cascade, results in a magnitude of atomic mixing that scales ≈ as the 1/2 power of the cascade energy.

This observation that the mixing is energy dependent in this regime is consistent with the model that assigns individual liquid droplets to different subcascades. It is not until the energy range where subcascades are formed is reached that mixing becomes energy independent. Further experimental evidence supporting the local-melt model of ion beam mixing has recently been presented by Klatt et al.[34] who irradiated a series of AgPd alloys of varying compositions. Ag and Pd were chosen because of their similar mass and atomic number and the fact that they show complete solid solubility across the entire composition range. By changing the content of one component in the alloy, the melting point of the system was varied from that of pure Ag (1234 K) to that of pure Pd (1825 K). The results showed a monotonic increase in the mixing efficiency with decreasing melting point of the alloy. The

quantitative results of the experiments are in excellent agreement with calculations based on diffusion in the molten region of the cascade.[33]

Defect Production and Clustering

In the absence of nuclear transmutation effects, defect production and clustering in energetic displacement cascades determine, to a large extent, the response of a material to a high-radiation environment.

Fig. 10 shows the primary state of damage resulting from 5, 10, di-5 and 25 keV cascades in Cu. The usual pattern, originally described by Seeger[35] of a vacancy-rich core region surrounded by a cloud of SIAs can be seen. While small clusters that contain 2 or 3 SIAs are seen in all cases, figures 10c,d reveal the presence of several large clusters of SIAs. As we will *see* below these large SIA clusters are formed as the result 0f a new, cooperative mechanism of defect production.[14]

The absolute number of defects observed in the monomer PKA events agrees well with the experimental observation of a defect production efficiency, ξ=1/3 for cascade-producing irradiation in Cu.[19] The average number of Frenkel pairs observed at the end of the events is 14, 27, and 59, for **5,** 10 and 25 keV events, respectively. These correspond to x=0.26, .23, and 0.20 respectively36 Although the statistics gathered in these studies do not permit an accurate comparison to experiment, the mechanisms by which the reduced ξ arises may be inferred from the simulations. As discussed in previous papers[12,13,30], the low value of ξ results from the absorption of RCSs in the volume of the molten core of the cascade. Only those SIAs transported by RCSs beyond the molten zone survive at the end of the cascade. Under experimental conditions where highly non-linear spike effects are important, e.g., in 40 keV di-atomic molecule irradiation of W[37], ξ has been found to approach unity. In the dimer-recoil events discussed here, the ratio of defects produced (per recoil) to that produced in the monomer 5 keV events is 1.2. This number is lower than the value of 1.55 found by Seidman et al.[37]; this is not unexpected since the recoil energy in our dimer cascades is well below the subcascade threshold. The trend towards an increased ξ in highly non-linear cascades is reproduced. The new defect production mechanism revealed by these studies helps explain some of these experimental results. Its consequences will be discussed in more detail below.

Recent MD studies by Foreman et al[38-40] of low energy cascades (up to 2 keV) in Cu with a many-body potential have largely confirmed previous 5 keV results with pair potentials regarding the ejection of SIAs by RCSs from the molten core of the cascade. Also, the previously observed clustering of small numbers of SIAs as the result of the elastic interaction among SIAs ejected from the cascade core via RCSs[12] has been confirmed. These studies have also provided very good statistical information on the absolute number of defects produced in low energy cascades in Cu.

Cascade collapse

Although pair potential studies of *5* keV cascades in Cu and Ni[12,13] provided extensive evidence for vacancy clustering the results of this work are the first theoretical confirmation of experimental results that show cascade collapse to vacancy dislocation loops at ambient temperature below annealing stage I.

Analysis of the spatial configuration of the vacancies at the end of a 25 keV cascade reveals a dislocation loop that contains 14 vacancies in a (111) plane. Figure 1l a shows the empty lattice sites where the vacancies are located. Figure l l b shows the positions of the atoms in the (-110) plane normal to section AA in figure l l a. As can be seen from this figure, the vacancies form a Frank loop with the Burgess vector b=a0/3[111].

Experimental evidence shows that in many metals energetic displacement cascades collapse into vacancy dislocation loops even at irradiation temperatures below stage I.[41] Seidman and co-workers observed highly supersaturated vacancy-rich regions in heavy ion irradiated W and Pt in the FIM[37,42] The large amount of vacancy clustering led them to suggest that vacancy clusters precipitate in the cascade core and subsequently grow by absorption of additional vacancies during the thermal spike.

Other workers have suggested an alternative mechanism for vacancy clustering based on thermotransport of vacancies towards, and **SIAs** away from the center of the cascade, aided by high thermal gradients in the core region.[43,44] These mechanisms both require high vacancy mobility during the thermal spike

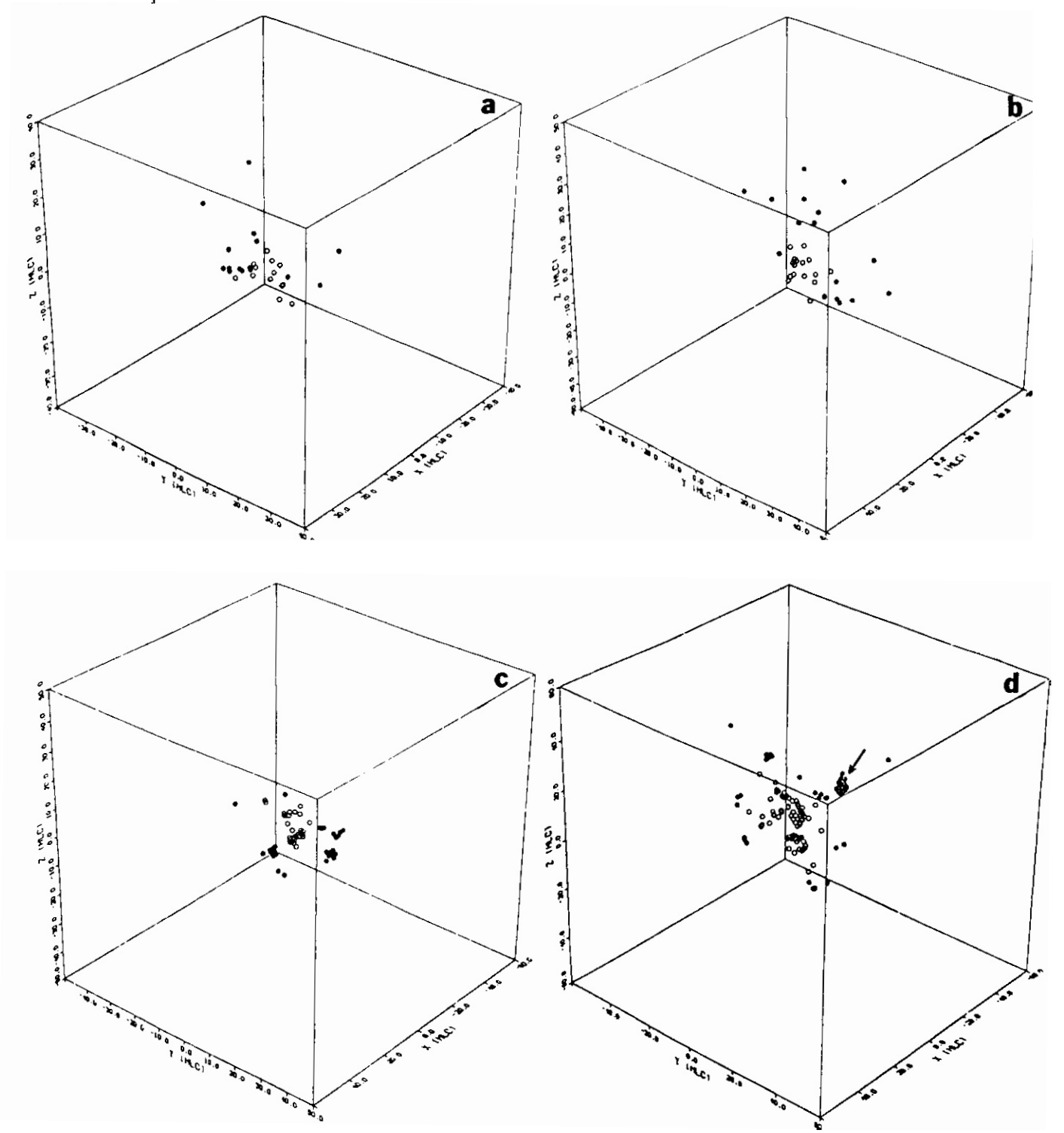


Fig. 10. Primary state of damage resulting from (a) 5 keV, (b) 10 keV, (c) di-5 keV, and (d) 25 keV cascades in copper. Filled circles (•) indicate self-interstitial atoms and open circles (o) vacancies. The arrow in figure 10d indicates the position of an interstitial cluster of 17 sites.

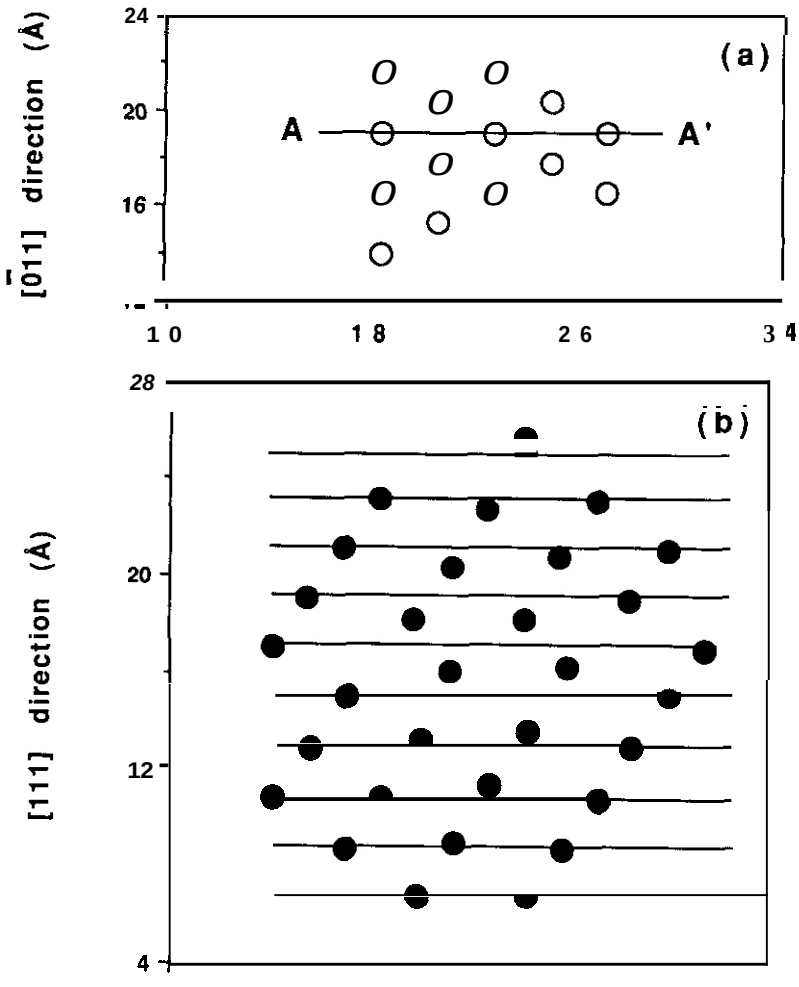


Fig.11. (a) Lattice sites of a vacancy dislocation loop produced in a 25 keV cascade in Cu. (b) Location of atoms in section A-A normal to the (111) plane of (a). The loop has an a013 [i l l] Burgers vector.

The present as well as our previous MD studies suggest a different, although related mechanism, in which vacancies cluster near the center of a displacement cascade as a result of the rapid resolidification of the molten core of the cascade.[45] The resolidification kinetics-based interpretation of cascade collapse is borne out of the lower atomic density found in the molten zone of the cascade than in the surrounding matrix. For materials with low melting point, for cascades with high energy density, or for events in a lattice at high ambient temperature, the resolidification process should proceed slowly and therefore the cascade collapse probability should be large under these conditions.

Although detailed calculations based on these premises are now under way, the present results support these ideas. For **25** and di-5 keV cascades large clustering of vacancies was observed. This is in contrast to monomer **5** and 10 keV PKA events where the number of vacancy clusters observed was substantially smaller. The fraction of defects (both vacancies and SIAs) found in clusters (larger than 3) in all these events is given in Fig. 12. For each energy, an average is taken over the two events simulated. **As** the energy density in the cascade increases, there appears to be a trend towards both, a larger fraction of defects in clusters as well ***as*** larger defect clusters. Fig. 13 shows the size of the largest vacancy and **SIA** clusters for all these events. The larger reduction in atomic density in the core of the cascade and longer lifetime of the dimer and **25** keV events are consistent with the mechanisms of cascade collapse described above. As we shall see below, the production of large SIA clusters and in some cases interstitial prismatic dislocation loops, results from a new, cooperative mechanism of defect production.

Interstitial loop punching - A new mechanism of defect production

The spatial distribution of **SIAs** that surrounds the cascade core is not well understood. It is commonly assumed that Frenkel pairs are produced as isolated point defects free to migrate above stage I annealing. Whether SIAs can be found in clusters following low temperature (below stage **I)** irradiation of metals has been a topic of controversy for many years. Previous MD studies as well as the cascades described here have shown that the large elastic interaction of **SIAs** may lead to clustering of RCS's ejected from the cascade core. Evidence for this process has been presented before[12] and is also depicted in Fig.14 where the replacement "cloud" (i.e., all the lattice sites in which an atomic replacement has taken place during the lifetime of the cascade) resulting from a 5 keV PKA event is

shown. Clearly visible are RCS trails leading to SIAs that are well separated from the edge of the disorder region. Also evident are small clusters of SIAs that result from the interaction of RCSs.

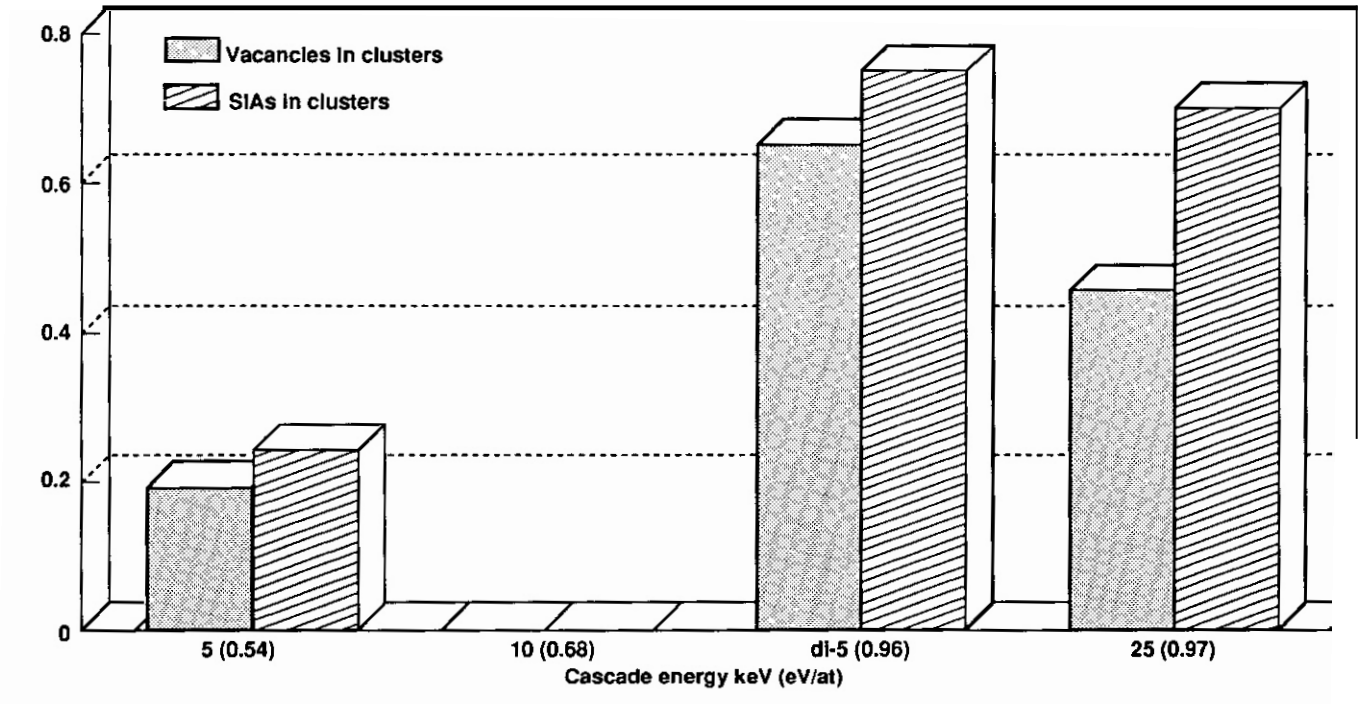


Fig. 12 Fraction of vacancies and SIAs in clusters > 3 for the cascades depicted in figure 10

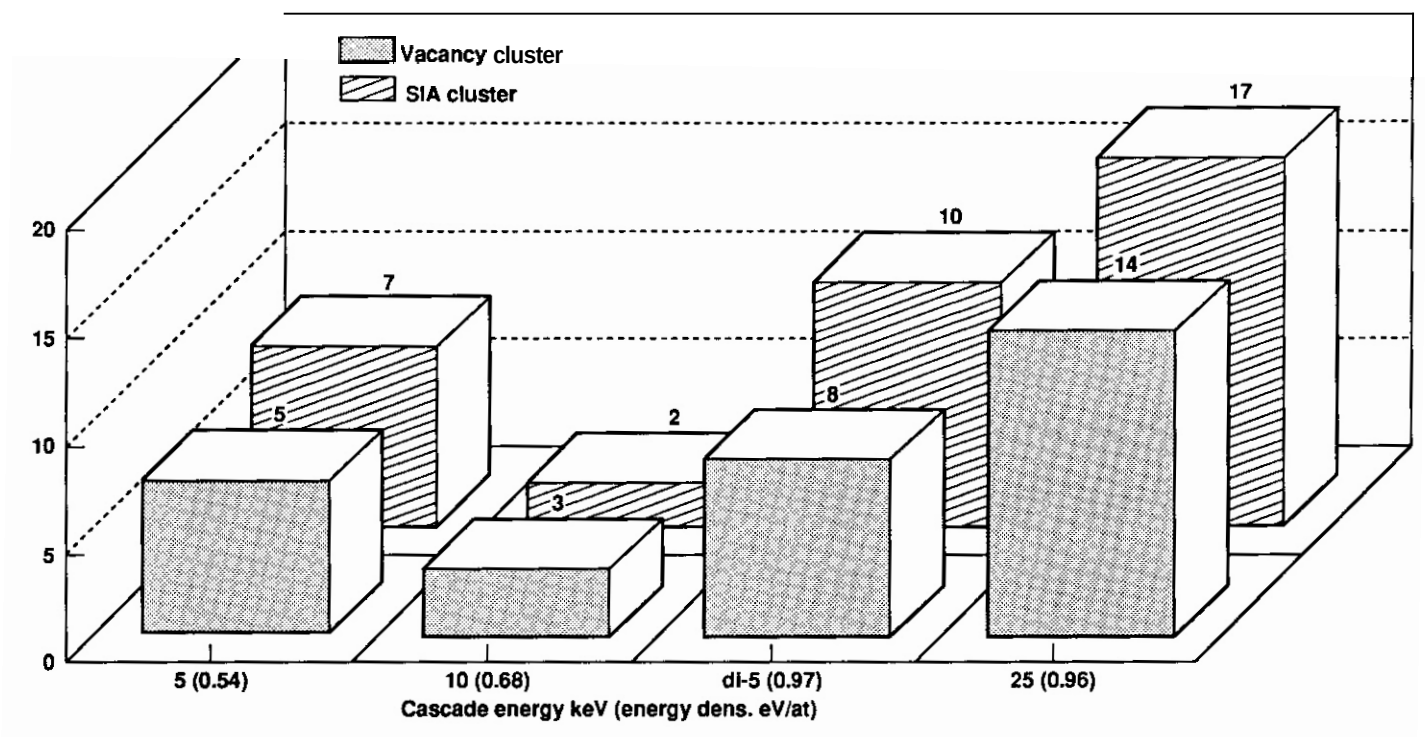


Fig. 13. Size of the largest defect clusters in the cascades depicted in figure 10.

Diffuse X-ray scattering experiments provide evidence for the formation of SIA clusters in cascades produced by low dose neutron irradiation of Cu at 77 K.[46] At this temperature SIAs in Cu are mobile and their clustering could be a result of long range diffusion. Earlier experiments at liquid He

temperature in which **SIA** clusters were identified by diffuse X-ray scattering employed very high neutron doses; therefore questions remained as to the effect of cascade overlap on the observed distribution of defects.[47,48] Transmission electron microscopy studies at low temperature provide evidence for **SIA** clustering in 14 MeV neutron irradiated Au and Cu but experimental uncertainties remain.[49]

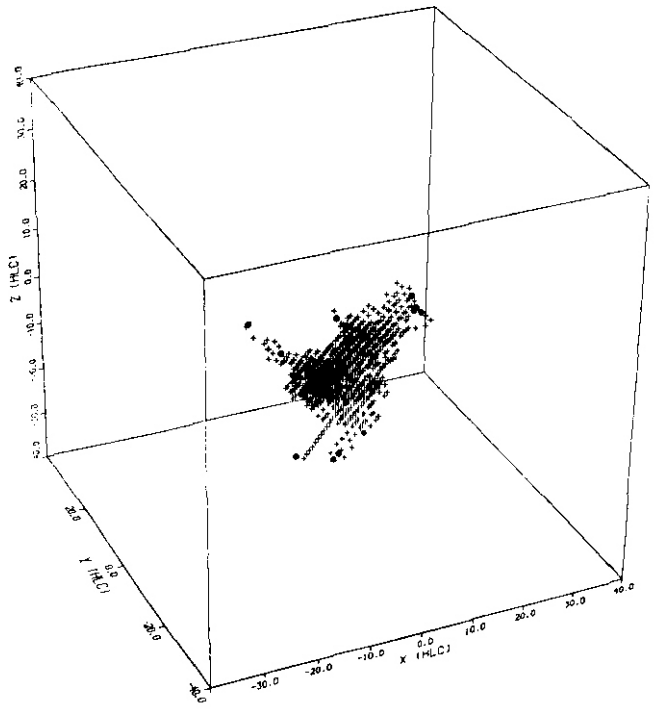
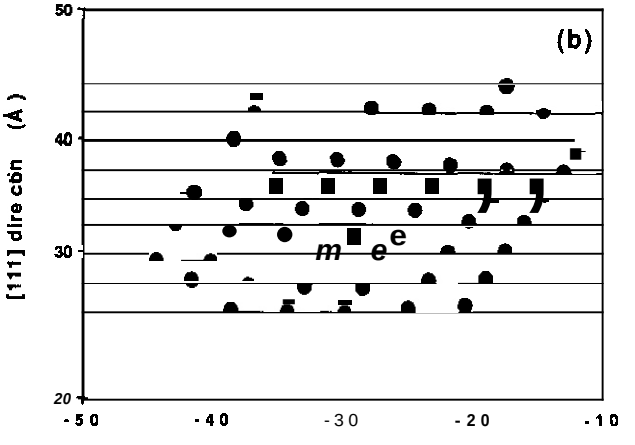


Fig. 14. Replacement "cloud" and RCS trails leading to **SIAs** outside the cascade core at the end of a **5** keV cascade.

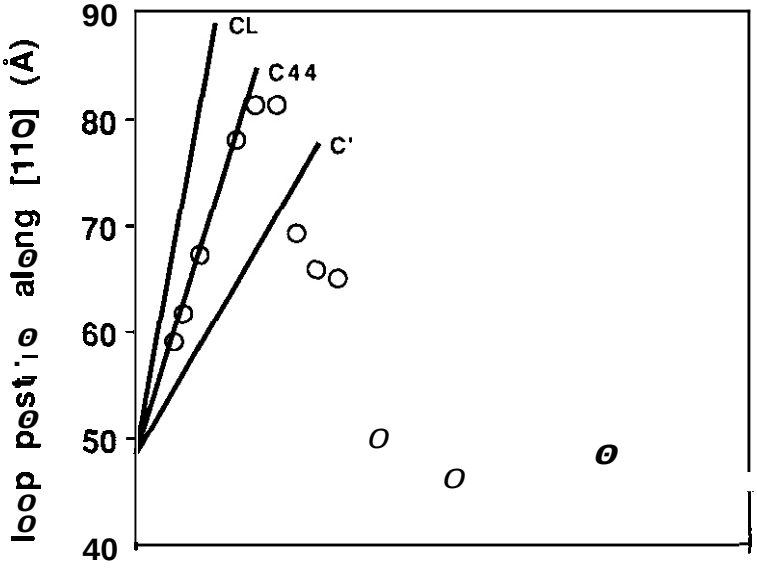
The largest SIA cluster found in figure 10d (indicated by an arrow in the figure) reveals the presence of 17 nearest neighbor **SIAs.** The individual **SIAs** are oriented along the [110] direction and at the end of the event are all observed to lie on a single (111) plane forming a prismatic dislocation loop. Fia. 15a shows the lattice sites, defined as those that contain two atoms per Wigner-Seitz cell, containing these **SIAs.** Figure 15b, shows the actual positions of atoms in the (-110) plane normal to section AA' in figure 15a. The SIAs in the cluster form a prismatic dislocation loop with Burgers vector b=a0/2[110]. The lines in figure 15b indicate the original positions of the (111) planes. By looking at a grazing angle at figure 15b, the interstitial loop is clearly visible. Such an i-loop expected to glide easily under the influence

direction

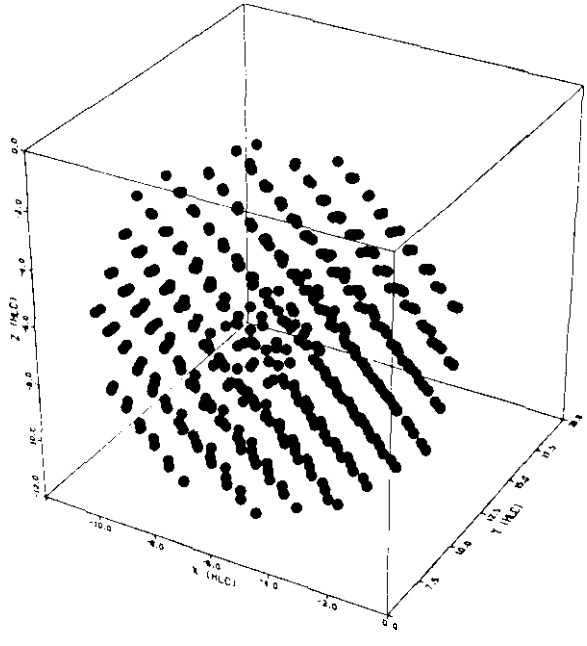


Later the transient thermal stresses produced by the outgoing shock-waveso relax as the cascade cools and the **SIAs** in the cluster glide back along the [110] direction towards the center of the cascade. **Due** to the high speed of the resolidification front the **SIA** cluster remains separated from the liquid-solid interface and is not absorbed by the molten region. During the ejection and relaxation, all the **SIAs** remain confined within a few adjacent (111) planes and at longer times coalesce into a single (111) plane.

Further evidence for the formation of i-loops in high energy displacement cascades in Cu is presented in



RCS's are important for events of all energies, i.e., from near threshold recoils (≈20 eV) to PKA energies in the keV range. The length of RCSs is not well known but MD studies in Cu show their average length in 5 keV cascades to be =23 Å.[28] In W However, RCSs were found to have lengths of the order of 160 Å.[51] As the size of the cascade increases with primary recoil energy a larger fraction of RCS's produced during the collisional phase is absorbed in the molten core of the cascade. These point defects become delocalized in the melt and lose their identity. The Frenkel pair production efficiency therefore decreases with increasing PKA energy as observed experimentally. Above 5-10 keV,



the pressure in the cascade zone produced by a given energy density,[50] and on the shear moduli which determine the pressure required to punch a dislocation loop.[24] As the energy density (and thus the pressure in the highly compressed region of the cascade periphery) increases, the probability of punching a dislocation loop increases and a larger fraction of SIAs are produced in clusters relative to those produced as isolated **SIAs** via RCSs.

The process of i-loop punching in nascent cascades has important consequences regarding the microstructural evolution of irradiated metals. The fraction of point defects free to migrate over long distances will be strongly dependent on this i-loop formation and the interpretation of such processes as radiation induced precipitation and void swelling will be affected by this new mechanism. Since SIA clusters are expected to be stable up to very high temperatures (above operating temperatures in fission or fusion reactor environments), i-loop production in nascent cascades may lead to large excess vacancy fluxes at elevated temperatures where vacancy dislocation loops are unstable but i-loops are not. Woo and Singh have recently shown that interstitial clustering in cascades can lead to an anomalously high rate of void swelling by adding a large bias term in the chemical rate theory equations that govern microstructural evolution.[53]

CONCLUSIONS

We have presented recent results of energetic displacement cascade studies in Cu with realistic interatomic potentials. Our simulations employ a new MD code, termed MOLDYCASK developed under the auspices of the IEA, that makes efficient use of the vector architecture of Cray supercomputers. These studies are the first ever to simulate cascades at PKA energies in the subcascade threshold regime where direct comparison to fast neutron and heavy ion irradiation experiments is possible. Our results have shown, for the first time in a dynamical simulation, that cascades may collapse to vacancy dislocation loops. Moreover, based on the results of our 25 keV cascade studies, we have postulated a new, cooperative mechanism of defect production not related to RCSs but rather based on punching of interstitial prismatic dislocation loops from the core of the molten zone of the cascade. We have proposed that this new mechanism of defect production may have profound implications regarding the primary state of damage and the microstructural evolution of metals in high-radiation environments,

We have also discussed the energy dependence of the atomic mixing parameter in cascades and have shown that the mixing efficiency in the cascade increases towards a constant, asymptotic value at energies beyond the subcascade formation threshold. Our results have confirmed the "liquid droplet" model of atomic mixing in cascades and have shown that for diatomic molecule irradiation where highly non-linear overlap effects, and therefore high homologous temperatures in the cascade core are expected, atomic mixing increases over that obtained in monomer recoil cascades.

FUTURE WORK

We are beginning studies of late transition metal alloys and intermetallic compounds. In the future we make use of three-body potentials in the study of semiconducting compounds.

AKNOWLEDGEMENTS

We wish to thank **M.** Finnis for fully vectorizing the MOLDY6 code at Livermore, S. Foiles for providing EAM fitting routines, and A. Caro and S. Pronnecke for implementing the electronic loss model. This work was performed under the auspices of the U.S. Department of Energy, Office of Fusion Energy, Reactor Technology Branch by Lawrence Livermore National Laboratory under contract W-7405-Eng-48.

REFERENCES

1. F. Seitz and J.S. Koehler, in: Solid State Physics, eds. **F.** Seitz and D. Turnbull (Academic, New York,1956) Vol. 2.

2. ***See,*** e.g., Proceedings of International Conference on Vacancies and Interstitials in Metals and Alloys, edited by C. Abromeit and **H.** Wollenberger, Mater. Sci. Forum 15-18, 1987.

3. See, e.g., Surface Chemistry and Beam Solid Interactions, edited by H. Atwater, F. A. Houle, and D. Lowndes (Mater. Res. Soc. Symp. Proc. 201, Pittsburgh, PA 1991).

4. P. Sigmund, Rev. Roumaine Phys. 17, 823. 969, and 1079 (1972).

5. J.F. Ziegler, J.P. Biersack and U. Littmark, "The Stopping and Range of Ions in Solids" (Pergammon Press, NY. 1985).

6. G.H. Vineyard, Rad. Eff. 32, 91 (1976)

7. M. Caro, A. Ardelea and A. Caro, J. Mater. **Res.** 5, 2652 (1990)

8. J. B. Gibson, A. N. Goland, M. Milgram, and G. H. Vineyard, Phys. Rev. 120, 1229 (1960)

9. J. Lindhard, V. Nielsen, and M. Scharff, Mat.-Fys. Medd. K. Dan. Vidensk. Selsk. 36, No 10 (1968).

10. M.W. Guinan and J.H. Kinney. J. Nucl. Mater. 103&104, 1319 (1981).

11. W.E. King and R. Benedek, Phys. Rev. B23, 6335 (1981). J. Nucl. Mater. 117, 26 (1983)

12. T. Diaz de la Rubia, R. S. Averback, R. Benedek, and W. E. King, Phys. Rev. Lett. 59, 1930 (1987).

13. T. Diaz de la Rubia, R. S. Averback, H. Hsieh, and R. Benedek, J. Mater. Res. 4, 579 (1989).

14. T. Diaz de la Rubia and **M.W.** Guinan, Accepted for publication in **Phys.** Rev. Lett. **(1991).**

15. H. Heinisch. Rad. Eff. Def. Sol. 113, 53 (1990).

16. K.L. Merkle, in: Radiation Damage in Metals, eds. N.L. Peterson and S.D. Harkness (ASM, Metals Park, OH. 1976), p. 58.

17. P. Sigmund, Rad. Eff. 1, 15 (1969).

18. M. J. Norgett, M. T. Robinson, and I. M. Torrens, Nucl. Eng. Design, 33, 50 (1975)

19. R. S. Averback, R. Benedek, and K. L. Merkle, Phys. Rev. B 18, 4156 (1978)

20. T. Diaz de la Rubia and M.W. Guinan, J. Nucl. Mater. 174, 151 (1990).

21. M. Daw and M.I. Baskes, Phys. Rev. B29, 6433 (1984).

22. S. Foiles, M. Baskes, and M. S. Daw, Phys. Rev. B 33, 7983 (1986)

23. A. Caro and M. Victoria, Phys. Rev. A 40, 2287 (1989)

24. **W.** G. Wolfer, Phil. Mag. **A** 58, 285 (1988).

25. D.M. Heyes and W. Smith, in: Information Quarterly for Computer Simulation of Condensed Phases, 26 (Science and Engineering Research Council, Daresbury Laboratory, Daresbury, Warrington WA4AD, England, 1987) p. 68.

26. M.W. Finnis, MOLDY6 - A Molecular Dynamics Program for Simulation of Pure Metals, Harwell Report AERE-R-13182, (1989).

27. S. Pronnecke. A. Caro, M. Victoria, T. Diaz de la Rubia, and M. W. Guinan. J. Mater. Res. 6,483 (1991).

28. T. Diaz de la Rubia, Ph.D. Thesis, State University of New York at Albany, Albany, NY (1989)

29. P. M. Echenique, R. M. Nieminen. and R. H. Ritchie, Solid State Commun. 37, 779 (1981).

30. T. Diaz de la Rubia, R.S. Averback. R. Benedek and I. Robertson, Rad. Eff. Def. Sol. 113,39 (1990).

31. D. Turnbull, in: Second Israel Materials Engineering Conference, edited by A. Grill and S.I. Rokhlin, (Beer-Sheva, Israel 1984).

32. C.J. Lin and F. Spaepen, in: Chemistry and Physics of Rapidly Solidified Materials, edited by B.J. Berkowitz and R.O. Scattergood (TMS-AIME, 1983).

33. **S-J.** Kim, M-A. Nicolet, R.S. Averback and D. Peak, Phys. Rev. B37, 38 (1988).

34. J. Klatt and R.S. Averback, R. Benedek and I. Robertson, Appl. Phys. Lett. 55, 1295 (1989).

35. A. Seeger, in: Radiation Damage in Solids, (IAEA, Vienna, 1962), Vol 1, p. 107.

36. The defect production efficiency *is* defined as the defect production normalized by the NRT value assuming an average threshold displacement energy for Cu of 30 eV. The damage energy was taken to be $\sim 0.9\ E_{PKA}$ in accordance with the energy loss obtained by application of the electronic losses model described in the text.

37. D. Pramanik and D.N. Seidman, J. Appl. Phys. 54, 6352 (1983)

38. C. A. English, W. J. Phythian, and A. J. E. Foreman, J. Nucl. Mater. 174, 135 (1990)

39. A.J.E. Foreman, C.A. English, and W.J. Phytian, Harwell Report AEA-TRS-2028, (1991)

40. A.J.E. foreman, W.J. Phythian, and C.A. English, Harwell Report AEA-TRS-2031, (1991)

41. *See,* e.g., C. A. English and M. L. Jenkins, Mats. Science Forum, 15-18. 1003 (1987)

42. D. Pramanik and D.N. Seidman, Nucl. Instr. & Meth. 209/210, 453 (1983)

43. **V.I.** Protasov and **V.G.** Chudinov, **Rad. Eff.** 66, 1 (1982)

44. V.G. Kapinos and P.A. Platonov, Rad. Eff. 103, 45 (1987).

45. R.S. Averback, T. Diaz de la Rubia, H. Hsieh and R. Benedek, in: Proceedings of International Conference on Ion Beam Modification of Materials (Knoxville, TN, 1990) to be published in Nucl. Instr. & Meth. B.

46. P. Ehrhart and R. S. Averback, Phil. Mag. A 60, 283 (1989).

47. B. von Guerard, D. Grass, and J. Peisl, Phys. Rev. Lett. 44, 262 (1980)

48. G. Wallner, H. Franz, R. Rausch, A. Schmalzbauer, and J. Peisl, Mater. Sci. Forum 15-18, 907 (1987).

49. Y. Shimomura, M. W. Guinan, H. Fukushima, P. A. Hahn, and M. Kiritani, J. Nucl. Mater. 155-157, 1181 (1988).

50. M. W. Guinan, J. Nucl. Mater. 53, 171 (1978).

51. C-Y. Wei and D. N. Seidman, Phil. Mag. A 43, 1419 (1981)

52. *See.,* e.g., V.M. Agranovich and V.V. Kirsanov, in: Physics of Radiation Effects in Crystals, eds. R.A. Johnson and A.N. Orlov (North-Holland, Amsterdam, 1986) **p.** 117.

53. C. H. Woo and B. N. Singh, Phys. Stat. Sol. **(b)** 159, 609 (1990)

A SIPA-BASED THEORY OF IRRADIATION CREEP IN THE LOW SWELLING RATE REGIME - C. H. Woo, Whiteshell Nuclear Research Establishment, F. A. Garner, Pacific Northwest Laboratory[a]

OBJECTIVE

The objective of this effort is to provide a fundamental understanding of the relationship between irradiation creep and swelling.

SUMMARY

A model is presented which describes the major facets of the relationships between irradiation creep, void swelling and applied stress. The increasing degree of anisotropy in distribution of dislocation Burger's vectors with stress level plays a major role in this model. Although bcc metals are known to creep and swell at lower rates than fcc metals, it is predicted that the creep-swelling coupling coefficient is actually larger.

PROGRESS AND STATUS

Introduction

A recent series of irradiation creep studies conducted on austenitic and ferritic steels in the EBR-II and FFTF fast reactors at ~400°C have shown that a simple relationship exists between irradiation creep and void swelling.[1-4] Regardless of the duration of the transient regime of swelling, the instantaneous creep rate is the sum of two terms, one independent of swelling and one directly proportional to the instantaneous swelling rate. The creep-swelling coupling coefficient is remarkably independent of the composition and thermomechanical condition in the austenitic steels, being -0.6×10^{-2} MPa^{-} for all steels studied. The coupling coefficient measured for the HT9 ferritic steel is somewhat larger at -0.9×10^{-2} MPa^{-1}.[1] There appears to be an upper stress limit, however, beyond which the creep rate no longer increases.'

We show in this paper that such behavior can be described by a theory which postulates that stress-induced preferential absorption (SIPA) of interstitial atoms is the major creep mechanism. This produces an increasingly anisotropic dislocation microstructure with increasing stress and dpa levels. SIPA produces a stress-induced bias differential among dislocations which are oriented differently with respect to the external stress (i.e., it's principal axes). This results in anisotropic dislocation climb and loop growth, the velocities of which are a function of their orientation. The end result is an anisotropic dislocation structure composed of unequal densities of dislocation and loops with the various possible Burger's vectors. This situation has been observed experimentally.[5-10]

Under the combined action of irradiation and an external deviatoric stress on a specimen, SIPA produces a deviatoric strain rate. This is made up of two components: a) a direct component where the deviatoric strain originates from the difference in climb rates of aligned (with respect to the deviatoric stress vector) and non-aligned dislocations; and b) an indirect component where the deviatoric strain originates from the climb of the anisotropic dislocation structure created by SIPA. The former effect, i.e., item a), has been analyzed by a number of authors based on a variety of effects of stress on point-defect jump processes"-" and is described by the generic name of SIPA creep. The latter effect, i.e., item b), is predicted and analyzed by Woo[17] under the name of "SIPA-Induced Growth (SIG)."

Although most authors have devoted attention to SIPA creep, the indirect strain rate due to SIG, at least in the transient regime, has been shown to contribute very significantly to the total deviatoric strain rate caused by SIPA. In fact, it *is* often many times larger that due to the direct contribution of SIPA creep. Nevertheless, it is seldom included in other analyses as a strain contribution associated with the SIPA mechanism.

In the following, we consider the steady-state case and derive an expression for the total strain rate due to the SIPA mechanism. This will be used to compare with the experimental observations. It will be shown that the total strain rate due to SIPA, including SIG, matches closely the characteristics of irradiation creep in stainless steels at low to moderate stress levels and relatively low temperatures. both quantitatively and qualitatively.

Steadv-State Dislocation Structure

Let us adopt a simple model. A uniaxial tensile stress is applied to a specimen whose dislocation structure consists of three classes, one aligned with the external stress (class 1) and two non-aligned (classes 2 and 3). Let us suppose that the dislocations annihilate by the climb of dipoles." We restrict

---

(a) Pacific Northwest Laboratory is operated for the U.S. Department of Energy by Battelle Memorial Institute under Contract DE-AC06-76RLO 1830.

ourselves in this analysis to a temperature range below the peak swelling regime, in which the production bias[19] is unimportant. The conservation equations of the line density ρ_n of the nth class is thus given by

$$\dot{\rho}_n = \dot{\lambda}_n - \alpha_D \rho_n^2 \tag{1}$$

where the dot over variables means the time derivative. In Equation (1) $\dot{\lambda}_n$ is the dislocation line (nth class) production rate by the growth of interstitial loops and $\alpha_D \rho^2$ is the line destruction rate by interacting dipoles, α_D being the reaction cross section. The loop line growth rate can be derived from the climb velocity[16,17] and is given by

$$\dot{\lambda}_n = \frac{\rho_n}{b\rho r_n} \left(aqK \Delta\phi \frac{\sigma}{\mu} [\cos^2\theta_n - \textstyle\sum_k f_k \cos^2\theta_k] \, t \, \dot{S} \right) \tag{2}$$

where b = magnitude of the Burgers vector

ρ_n = total dislocation density

r_n = loop radius of the nth class

a = production efficiency, i.e., fraction of the dpa rate that corresponds to free defects

q = ratio of the dislocation sink strength to the total sink strength

$\Delta\phi$ = point defect property associated with the *SIPR effect*[16]

θ_n = angle between the loop plane normal of the nth class and the stress direction

f_k = fraction of line density due to the kth class

$\dot{S}$ = total rate of accumulation of interstitials at the interstitial loops (= rate of accumulation of vacancies at the voids in the present case).

At steady state $\dot{\rho}_n = 0$ and from Equations (1) and (2), we obtain the steady state dislocation density of the nth class:

$$\rho_n = \frac{1}{\alpha_D b\rho r_n} \left\{ aqK\Delta\phi \frac{\sigma}{\mu} [\cos 2\theta_n - \sum_k f_k \cos 2\theta_k] \, t \, \dot{S} \right\} \tag{3}$$

so that

$$f_n = \frac{1}{\alpha_D b\rho^2 r_n} \left\{ aqK\Delta\phi \frac{\sigma}{\mu} [\cos^2\theta_n - \sum_k f_k \cos^2\theta_k] + \dot{S} \right\} \tag{4}$$

Substituting $\theta_1 = 0$ and $\theta_2 = \theta_3 = \pi/2$, we obtain from Equation (4)

$$\begin{cases} f_1 = \dfrac{1}{\alpha_D b\rho^2 r_1} \left\{ aqK\Delta\phi \dfrac{\sigma}{\mu} (1 - f_1) + \dot{S} \right\} \\ f_2 = f_3 = \dfrac{1}{2 r_2} \left\{ -f_1 aqK\Delta\phi \dfrac{\sigma}{\mu} \, t \, \dot{S} \right\} \\ f_1 + f2 + f_3 = 1 \end{cases} \tag{5}$$

It has been shown, experimentally, that stress mainly affects the steady-state loop number density, and not so much the loop size.[5-7] Therefore, we make the simplifying assumption here that $r_1 = r_2$. Then Equation (5) can be simplified to a quadratic equation in f_1:

$$3\tau f_1^2 - (3i \, t \, 2\tau) f_1 \, t \, \dot{S} \, t \, \tau = 0 \tag{6}$$

where we have defined

$$\tau = aqK\Delta\phi\frac{\sigma}{\mu} \tag{7}$$

The solution of Equation (6) yields

$$f_1 = \frac{1}{3} + \frac{\dot{S}}{2\tau}\left[1 - \left(1 - \frac{8\tau^2}{9\dot{S}^2}\right)^{1/2}\right] \tag{8}$$

The other solution is discarded as it causes f to decrease as τ, i.e., as σ increases, which is deemed to be physically unrealistic.

Strain Rate Due to SIG

From Equation (8), f, reaches a maximum when

$$\tau = \tau_{max} = \frac{3}{2\sqrt{2}}\,\dot{S} \tag{9}$$

and

$$f_1 = f_1^{max} = \frac{1 + \sqrt{2}}{3} \tag{10}$$

The value of f_1^{max} is less than 1 because the climb velocity difference between the aligned and non-aligned dislocations reduces as f_2 decreases and vanishes as f_2 approaches zero.

Equation (9) represents a condition in which a value of the stress exists where a maximum anisotropy of the dislocation structure and hence maximum value of SIPA is reached. Increase of stress beyond this value will not increase the strain rate caused by SIPA, i.e., the SIG strain rate saturates. Thus this saturation stress σ_{max} is given by

$$aqK\Delta\phi\frac{\sigma_{max}}{\mu} = \frac{3}{2\sqrt{2}}\,\dot{S} \tag{11}$$

Assuming a simple model of swelling driven by dislocation bias, p, it can be easily shown that

$$\dot{S} \approx pq\,(1 - q)aK \tag{12}$$

where 1 - q is the fraction of sink strength due to voids.

Equations (11) and (12) combine to give

$$\sigma_{max} = \frac{3}{2\sqrt{2}}\,\frac{p(1-q)\mu}{\Delta\phi} \tag{13}$$

For SIPA due to elasto-diffusion,[16] $\Delta\phi$ is given by

$$A4 = \frac{3}{16}\beta\,[P_i(1-p_i) - P_v(1-p_v)] \tag{14}$$

where β is the reciprocal of the product of the Boltzmann constant and the absolute temperature. P_j (j = i, v for interstitials and vacancies, respectively) is related to the point-defect saddle-point relaxation volume and p_j is related to the anisotropy of the corresponding point-defect configurations. The values of P_j and p, can be obtained from Schober[20] for Cu and α-Fe. Using the following values for p, q and μ

p = 0.3[21]
q = 0.9
$\mu = 7 \times 10^4$ MPa

we obtain values of σ_{max} from Equation (13)

$$\sigma_{max} = \begin{cases} 170\ \text{MPa}^{(a)} \text{ for Cu} \\ 57\ \text{MPa}^{(a)} \text{ for } \alpha\text{-Fe} \end{cases} \quad (15)$$

Using Equations (8) and (12) we can also calculate the SIG strain rate. In this regard the deviatoric strain rate associated with the climb of an anisotropic dislocation structure is given by

$$\dot{\epsilon}_{SIG} = (\sum_k f_k \cos\theta_k - \tfrac{1}{3})\,\dot{S} \quad (16)$$

In the present model, after substituting θ_1, θ_2 and θ_3, we have

$$\dot{\epsilon}_{SIG} = (f_1 - \tfrac{1}{3})\,\dot{S} \quad (17)$$

We can linearize Equation (8) by fitting a straight line to Equation (8) at $\tau = 0$ and $\tau = \tau_{max}$. We then obtain from Equation (10)

$$f_1 \approx \tfrac{1}{3} + \tfrac{\sqrt{2}}{6}\,\frac{\sigma}{\sigma_{max}} \quad (18)$$

which gives the exact values cf $f_1 = 1/3$ at $\sigma = 0$ and $f_1 = (1 + \sqrt{2})/3$ at $\sigma = \sigma_{max}$.

Using Equation (18), we can derive from Equation (17),

$$\dot{\epsilon}_{SIG} = \frac{\sqrt{2}}{3}\,\frac{\sigma}{\sigma_{max}}\,\dot{S} \quad (19)$$

This can be put in the form

$$\dot{\epsilon}_{SIG} = D\dot{S}\sigma$$

with

$$D = \frac{\sqrt{2}}{3}\,\frac{1}{\sigma_{max}}. \quad (20)$$

The value of D can be obtained from Equation (15)

$$D = \begin{cases} 0.3 \times 10^{-2}\ \text{MPa}^{-1} \text{ for fcc Cu} \\ 0.9 \times 10^{-2}\ \text{MPa}^{-1} \text{ for bcc Fe} \end{cases} \quad (21)$$

If we assume that the point-defect properties of stainless steel may be approximated by fcc Fe, then $\Delta\phi$ for stainless steel may be expected to be less than that for bcc Fe because of the stronger anisotropy of the bcc lattice. From this point of view, the value of D for stainless steels, namely, -0.6×10^{-2} MPa^{-1} can be obtained from a reasonable value of $\Delta\phi \approx 30$. It should be noted here that, if the origin of the SIPA mechanism is based on the point-defect diaelastic polarizability, [i.e., the second-order homogeneity interaction[11-13]] the value of D obtained would be one to two orders of magnitude too small.

Strain Rate Due to SIPA Creep

The creep rate due to SIPA caused by elasto-diffusion has been derived[16] and is given by

$$\dot{\epsilon}_{SIPA} = \tfrac{1}{2} a_n K \Delta\phi \frac{\sigma}{\mu}\,[\sum_n f_n \cos 4\theta_n - (\sum_n f_n \cos 2\theta_n)^2] \quad (22)$$

In the present model, substituting values of θ_1, θ_2 and θ_3, we obtain

$$\dot{\epsilon}_{SIPA} = B_0\sigma \quad (23)$$

(a) Under the biaxial stress conditions of a pressurized tube, this is equivalent to a hoop stress of 227/(1-S) MPa for Cu and 76/(1-S) MPa for α-Fe.

where

$$B_0 = f_I(1-f_I)\, aK\Delta\phi \frac{1}{\mu} \tag{24}$$

Using Equation (21), we can write

$$B_0/D = \left(\frac{aK\Delta\phi}{\mu}\,\sigma_{max}\right)\frac{3}{\sqrt{2}}\, f_I(1-f_I) \tag{25}$$

Substituting Equation (11) into Equation (25), we obtain

$$B_0/D = \frac{9}{4}\, f_I(1-f_I)\, s/q \tag{26}$$

We have shown in the last section that $(1 \pm \sqrt{2})/3 > f_I > 1/3$, so that equation (26) can be written as

$$0.6\,\dot{S} > B_0/D > 0.2\,\dot{S} \tag{27}$$

Assuming a value of $\dot{S} \sim 10^{-3}$ dpa^{-1} (typical of 400°C irradiation in austenitic steels), we have

$$0.6 \times 10^{-3}\ \text{dpa}^{-1} > B_0/D > 0.2 \times 10^{-3}\ \text{dpa}^{-1} \tag{28}$$

Unlike the value of D, the ratio B_0/D is not sensitive to the point defect properties and is expected to hold for a large range of metals and alloys. The value of this ratio, as estimated in Equation (28), also agrees very well with experimental measurements.[4]

Summary

The results of the foregoing calculation can now be summarized.

1. The total deviatoric strain rate $\dot{\epsilon}$ caused by SIPA can be written as observed experimentally,[1-4] in the following form

$$\dot{\epsilon}/\sigma = B_0 \pm D\dot{S}, \tag{29}$$

where B_0 arises from SIPR creep and $D\dot{S}$ is due to SIG.

2. The value of D can be calculated according to the foregoing theory, if certain point-defect dipole-tensors are known. For Cu and α-Fe, where such information is available from computer simulation, we have

$$D = \begin{cases} 0.3 \times 10^{-2}\ \text{MPa}^{-1} & \text{for fcc-Cu} \\ 0.9 \times 10^{-2}\ \text{MPa}^{-1} & \text{for bcc-Fe} \end{cases} \tag{30}$$

The experimentally observed value of D for austenitic stainless steel of 0.6×10^{-2} MPa^{-1} can be obtained based on a reasonable assumption of the point-defect dipole-tensor in austenitic steels.

3. The ratio B_0/D in Equation (29) can be calculated from the foregoing theory. It is found to be in the range

$$0.6 \times 10^{-3}\ \text{dpa}^{-1} > B_0/D > 0.2 \times 10^{-3}\ \text{dpa}^{-1} \tag{31}$$

for a swelling rate of 10^{-3} dpa^{-1}. This ratio, unlike D, is independent of the point-defect properties required for the calculation of D and is in good agreement with existing experimental data,[1-4] where B_0/D lies in the range 0.36×10^{-3} dpa^{-1} to 0.67×10^{-3} dpa^{-1}.

4. Equation (29) is valid only below a maximum stress σ_{max}. Any further increase of the stress beyond this point will not cause an increase in the SIPA-induced strain rate. The SIPA creep is then said to be saturated. We emphasize however, that this does not preclude the contribution from other creep mechanisms at higher stress. The value of the stress for maximum stain rate is related to D; and in the present calculation is estimated to be about 160 MPa for the hoop stress of a pressurized tube. Such an upper limit has been observed in 304 stainless steel.[2]

5. The saturated strain rate is related to the swelling rate by

$$\dot{\epsilon}_{max} \simeq \frac{(1.2)\sqrt{2}}{3} \dot{S} \tag{33}$$

so that for a pressurized tube at saturation

$$(\Delta\dot{D}/D)_{max} \simeq 2.7\ (\Delta\dot{D}/D)_{unstressed} \simeq \dot{S} \tag{34}$$

As shown in Table 1 this relationship has been observed in the diametrical strain rates of pressurized tubes in a number of experiments.

TABLE 1. Comparison of Experimental Results with Prediction that $(\Delta\dot{D}/D)_{max}/\dot{S} \simeq 1.0$

Alloy	Condition	Reactor	Stress Level	$(\Delta\dot{D}/D)/\dot{S}$	Reference
304L	Annealed	EBR-II	0,188 MPa	1.08	2
316	20% Cold worked	EBR-II	0,343 MPa	1.10	4
316	20% Cold worked	EBR-II	0,206 MPa	0.94[b]	4
D9[a]	20% Cold worked	FFTF	0,200 MPa	0.76[c]	1
PCA[a]	20% Cold worked	FFTF	0,200 MPa	1.11	1,3

(a) D9 and PCA ar Ti-modified 316 type steels.
(b) After temperature changes from 550 to 400°C.
(c) This value represents an underestimate due to failure nf the stressed tube following its measurement at the previous discharge.

6. A characteristic of SIPA is the sensitivity of the dislocation structure to the stress state. Garner and Gelles[11] review a number of experiments which demonstrate this sensitivity.

7. As a result of SIG, the "creep" due to SIPA has a memory, i.e., the strain rate would persist, even when the applied stress is removed. As a result, creep continues until the established anisotropy of the dislocation structure is replaced by a new isotopic one. Examples of this behavior are also presented by Garner and Gelles.[11]

References

1. M. B. Toloczko, F. A. Garner and C. R. Eiholzer, Fusion Reactor Materials Semiannual Progress Report, DOE/ER-0313/9 (1990) in press; also in this semiannual report.

2. D. L. Porter, F. A. Garner and G. D. Hudman, J. Nucl. Mater. (Proceedings ICFRM-4, in press).

3. F. A. Garner and R. J. Puigh, J. Nucl. Mater. (Proceedings ICFRM-46, in press).

4. F. A. Garner and D. L. Porter, J. Nucl. Mater. 155-157 (1988) 1006, also D. L. Porter, E. L. Wood, F. A. Garner, ASTM STP 1046 (1990) 551.

5. H. R. Brager, F. A. Garner, and G. L. Guthrie, J. Nucl. Mater. 66 (1977) 301.

6. F. A. Garner, W. G. Wolfer, and H. R. Brager, ASTM STP 683, eds. J. A. Sprague and D. Kramer, (1979) 160.

7. D. S. Gelles, F. A. Garner, and H. R. Brager, ASTM STP 725, eds. O. Kramer, H. R. Brager, and J. S. Perrin (1981) 680.

8. D. S. Gelles, ASTM STP 870, eds. F. A. Garner and J. S. Perrin (1985) 98.

9. D. S. Gelles, F. A. Garner, and B. L. Adams, in Damage Analysis and Fundamental Studies Quarterly Progress Report, DOE/ER-0046/11 (1982) 81.

10. F. A. Garner and O. S. Gelles, J. Nucl. Mater. 159 (1988) 286.

11. P. T. Heald and M. V. Speight, Phil. Mag. 29 (1974) 1075.

12. W. G. Wolfer and M. Ashkin, J. Appl. Phys. 47 (1976) 791.

13. R. Bullough and J. R. Willis, Phil. Mag. 31 (1975) 855.

14. E. J. Savino, Phil. Mag. 36 (1977) 323.

15. P. H. Dederichs, and K. Schroeder, Phys. Rev. 817 (1978) 2524.

16. C. H. Woo, J. Nucl. Mater. 120 (1984) 55.

17. C. H. Woo, Phil. Mag. 42 (1980) 551.

18. B. B. Glasgow and W. G. Wolfer, ASTM STP 870, eds. F. A. Garner and J. S. Perrin (1985) 98.

19. C. H. Woo and B. N. Singh, Phys. Stat. Sol. (b) 159 (1990) 609.

20. H. R. Schober, J. Phys. F7 (1977) 1127.

21. B. C. Skinner and C. H. Woo, Phys. Rev. 30 (1984) 3084.

Swelling and Microstructure of High Purity Nickel Irradiated with Fast Neutrons in EBR-II-
J. F. Stubbins, University of Illinois and F. A. Garner, Pacific Northwest Laboratory[a]

OBJECTIVE

The objective of this effort is to provide an understanding of the radiation-induced evolution of microstructure in pure nickel, a metal often used in fission-fusion correlations.

PROGRESS AND STATUS

Introduction

In an earlier report,(1) a review was presented of the parametric sensitivity of void swelling in nickel, a metal often selected in fission-fusion correlation studies as a model material for studying neutron spectral effects. It was shown that nickel's response to radiation is often dominated by its tendency to saturate in swelling. At moderate dpa levels. this tendency often overshadows the influence of other variables and calls into question the validity of uncritically using nickel for comparative irradiations conducted in widely disparate irradiation environments.

Figure 1 shows the swelling response of pure nickel to thermomechanical starting condition and irradiation temperature as observed in a recent experiment. These data were presented in an earlier report and were derived from an experiment conducted in EBR-II to a nominal level of 14 dpa.(1) Reevaluation of the exposure levels has shown that seven of the nine specimens were irradiated at 14 dpa, but two (annealed and cold-worked conditions at 600°C) were irradiated at a somewhat lower elevation in EBR-II. These two specimens reached only 12 dpa.

Note that the cold-worked and the cold-worked and aged conditions yield swelling values that are relatively insensitive to irradiation temperature, declining very slowly at higher temperatures. The annealed condition, however, yields swelling that is essentially the same as that of the other two conditions at 425°C but is strongly sensitive to irradiation temperature above 425°C. Given the consistency of the data at 12 and 14 dpa for the cold worked and the cold worked and aged conditions, it appears that saturation of swelling for these conditions must occur well below 12 dpa and is only slightly sensitive to irradiation temperature. It is not certain whether the annealed condition has reached a saturation state at either 500 or 600°C. A second discharge of this experiment at higher fluence is now being examined and should answer this question. Saturation definitely appears to have been reached at 425°C, however.

Since most fission-fusion correlation experiments are based on microstructural comparisons involving voids, dislocations and loops, it was decided to examine the microstructures of these specimens in order to provide an understanding of the saturation process.

Exoerimental

Hiqh purity (99.999%) nickel in three thermomechanical treatment conditions was irradiated in EBR-II in the AA-14 fusion materials experiment at irradiation temperatures of 425, 500, and 600°C to doses of 12-14 dpa. The tnermomechanical treatment conditions were solution annealed, cold worked, and cold worked and aged. The specific treatment conditions are given in Table 1.

Swelling values for the 12-14 dpa discharge were determined using immersion density measurements accurate to ±0.16% swelling. The microstructures of both the initial and irradiated material conditions were determined using a JEOL JEM 1200EX transmission electron microscope operated at 120 kV. Specimen thicknesses were established by means of stereo pairs. The data for specimens irradiated to 12-14 dpa at 425 and 600°C have been analyzed and are presented here. Analysis of the 500°C data at 12-14 dpa is still in progress. Density measurements for the second discharge will be completed shortly.

---

[a] Pacific Northwest Laboratory is operated for the U.S. Department of Energy by Battelle Memorial Institute under Contract DE-AC06-76RLO 1830.

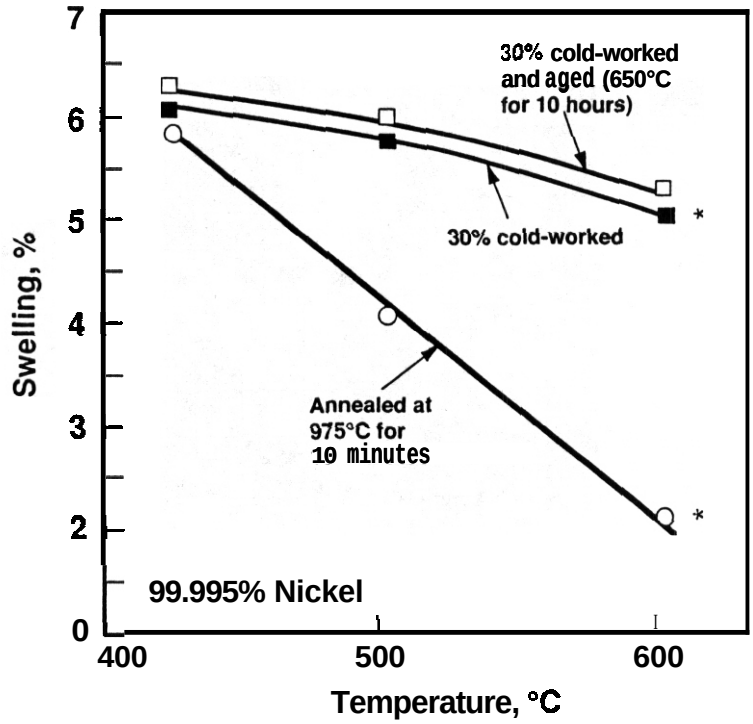


Figure 1. Swelling of pure nickel observed after 12-14 dpa in EBR-II as a function of irradiation temperature and starting condition. All data taken at 14 dpa with the exception of two data at 12 dpa, each marked with an asterisk.

Table 1
Thermalmechanical Treatment Conditions for Nickel

Alloy Code	Condition	Treatment History
BN	Solution Annealed (SA)	975°C for 10 min/water quench
BP	Cold Worked (CW)	30% cold rolled
BR	Cold Worked and Aged (CWA)	30% cold rolled/650°C for 10 h/ water quench

Results

Micrographs showing the initial dislocation microstructures for the three thermomechanical treatment conditions are presented in Figure 2, and the dislocation densities are tabulated in Table 2. The presence of a non-trivial dislocation structure in the solution annealed state was surprising and is probably a consequence of the use of rapid quenching after annealing. A number of dislocation loops are evident in the structure, an observation that is consistent with microstructures typically developed by rapid quenching. In general, there were no dislocation cells or highly pinned networks of dislocations in the annealed specimen in contrast with that of the other two specimen conditions. The aged condition contained small dislocation cells with internal dislocation-free areas, whereas the cold worked condition contained moderately high densities of dislocations inside the cells.

After irradiation, the dislocation densities have fallen in all specimens, especially in the solution annealed condition at 600°C. At each temperature the dislocation densities in the cold worked and the cold worked and aged conditions have converged at each irradiation temperature. These convergence values decrease slightly with temperature.

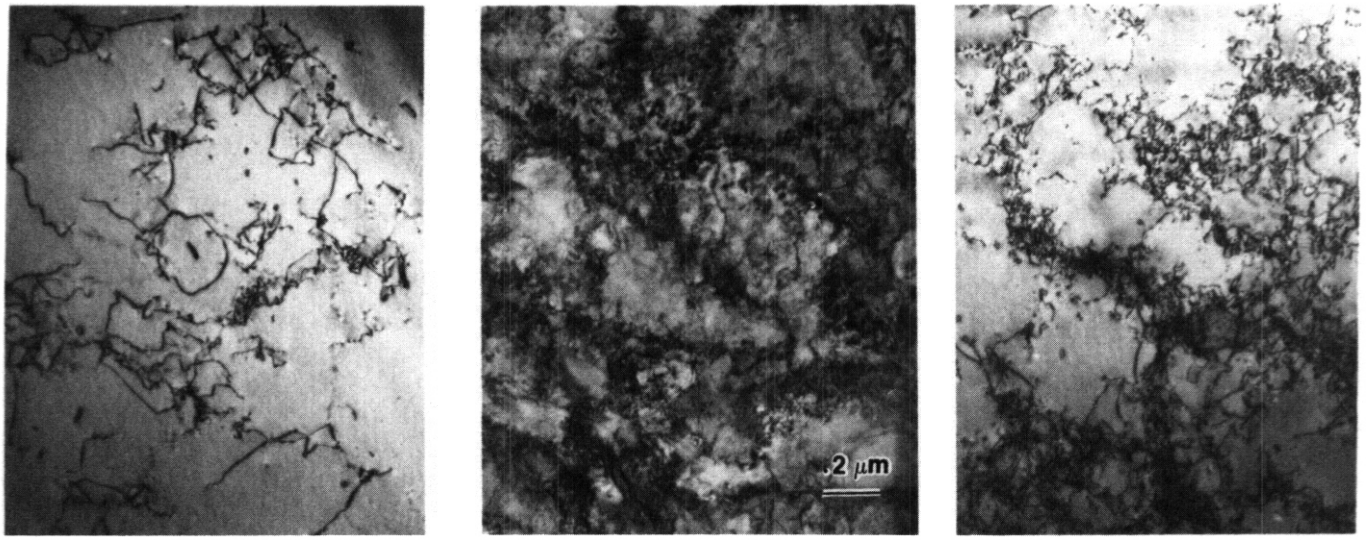


Figure 2. Micrographs of starting dislocation structures of (a) annealed and quenched, (b) cold worked, and (c) cold worked and aged pure nickel.

A comparison of the irradiation-produced microstructures at 425°C is shown in Figure 3, and at 600% in Figure 4 (note the difference in magnification in these two sets of micrographs). The low void density in the solution annealed material at 600°C is clearly evident, as are the smaller average void sizes in the solution-annealed material at both temperatures.

Microstructural parameters for both the unirradiated and irradiated material conditions are presented in Table 2. A detailed analysis of the distribution in the void population following irradiation is shown in Figure 5 where the void number densities are plotted as a function of size. The void population in the cold worked and in the cold worked and aged materials involves a large range of sizes at both temperatures that was not observed in the annealed material.

Table 2
Microstructural Parameters

Condition	Immersion Density Swelling (%)	TEM Measured Swelling (%)	Void Density 10^{19} (m^{-3})	Mean Void Diameter (nm)	Dislocation Density (10^{13} m^{-2})
Solution Annealed					
Unirradiated	--	--	--	--	4.6
425°C to 14 dpa	5.8	4.1	25.4	62	3.0
600°C to 12 dpa	2.0	1.8	1.3	124	t0.2
Cold Worked					
Unirradiated	--	--	--	--	>20
425°C to 14 dpa	6.1	1.6	7.6	111	1.8
600°C to 12 dpa	5.1	7.0	0.48	268	-1
Cold Worked and Aged					
Unirradiated	--	--	--	--	14
425°C to 14 dpa	6.3	5.2	20.0	72	2
600°C to 14 dpa	5.3	7.6	0.78	241	~0.8

The void data presented in Table 2 and Figure 5 also show that the cold worked and aged material at both temperatures develops a void structure that is intermediate to that of the other two conditions. Cold working leads to the lowest void number densities at both irradiation temperatures, but the largest void sizes. The solution annealed material has the highest void densities and the smallest void sizes at both irradiation temperatures. The intermediate void sizes and number densities of the cold worked and aged material, however, are associated with the highest swelling levels. It is considered particularly significant that at 425°C, the postirradiation microstructure and the swelling of the annealed and the aged

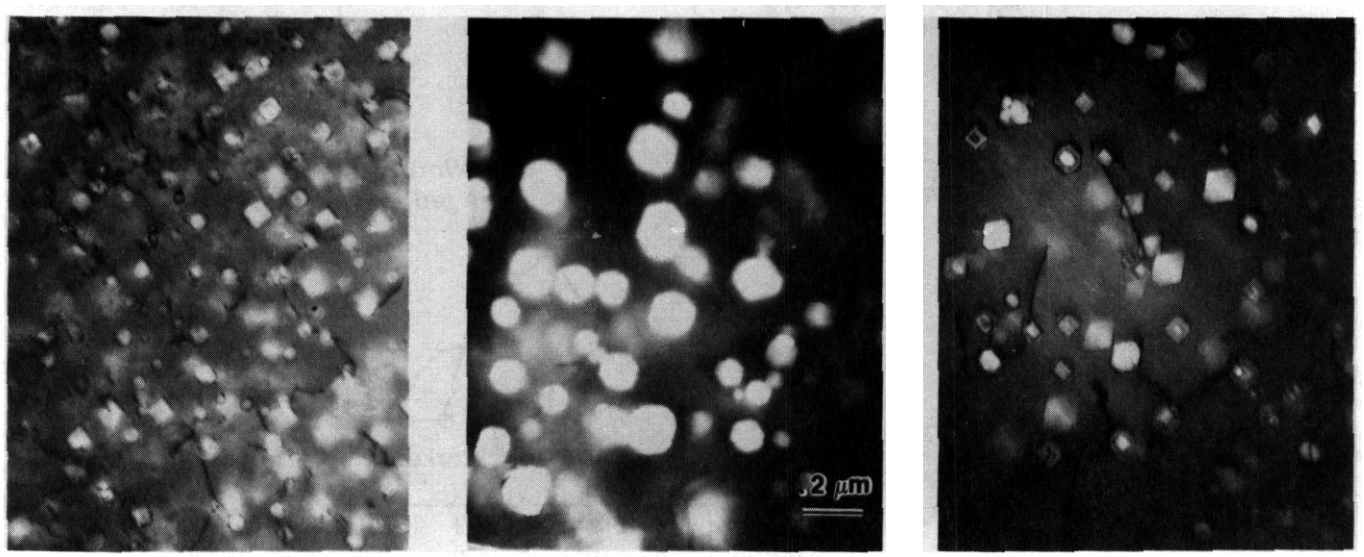


Figure 3. Irradiation-produced microstructures at 425°C for (a) annealed, (b) cold worked, and (c) cold worked and aged pure nickel.



Figure 4. Irradiation-produced microstructures at 600°C for (a) annealed, (b) cold worked, and (c) cold worked and aged pure nickel. Note the difference in magnification compared to that of Figure 3.

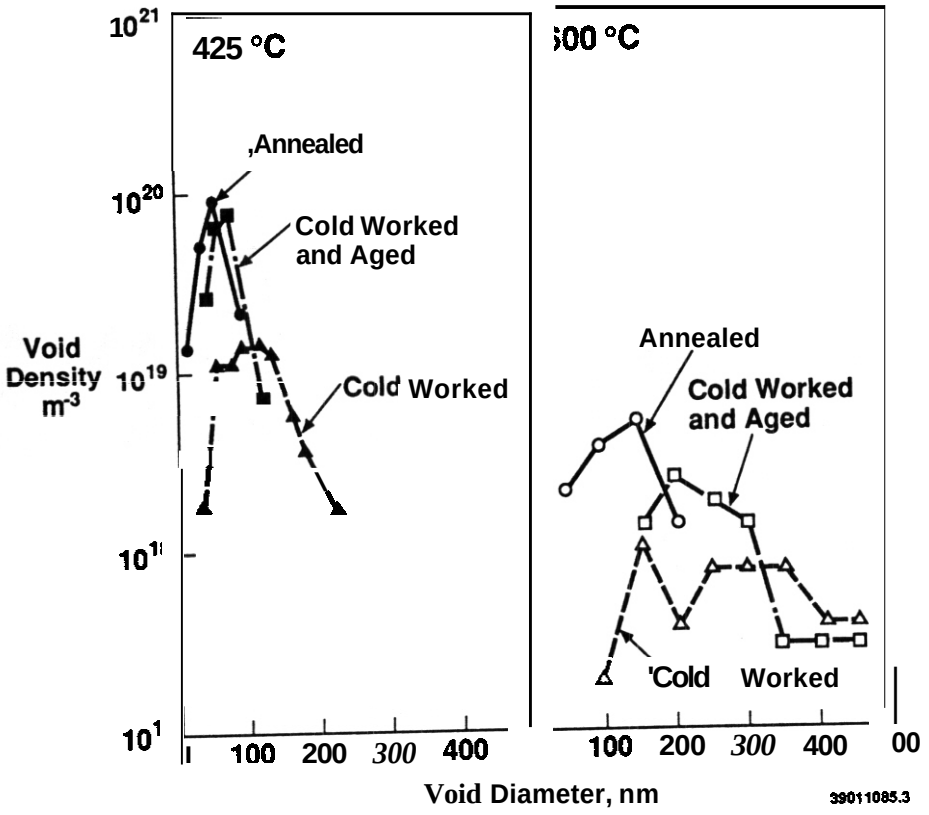


Figure 5. Influence of temperature and starting condition on void distributions in irradiated nickel.

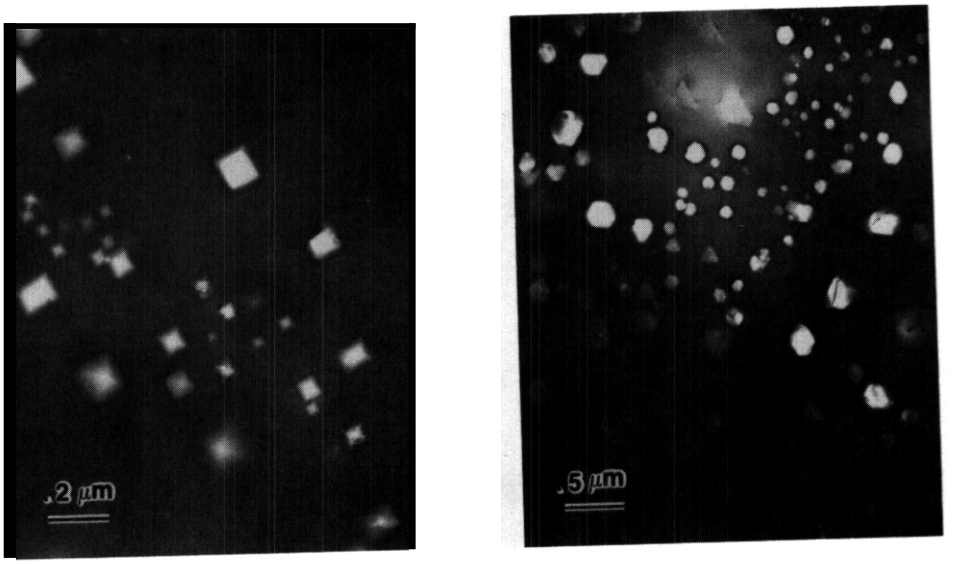


Figure 6. Heterogeneity observed in the void population in the (a) cold worked condition after irradiation at 600°C and (b) the cold worked and aged condition after irradiation at 500°C.

specimens are rather comparable, but at 600°C this is not true. This probably reflects the strong dependence of Frank loop density on irradiation temperature. At the lower temperature the loop microstructure is known to be the most dense and therfore probably the most persistent, resisting the tendency toward collapse in density that accompanies unfaulting and interaction of loops.

While the void population in the annealed condition was very homogeneous, those of the cold worked and the cold worked and aged conditions were quite heterogeneous and contained a wide variability in size and number distribution in a given volume. This is emphasized in Figure 6 where two material conditions are shown, each with large local variations in void size and density in a relatively small region. This also leads to a larger uncertainty in void size and density determinations for those conditions. The heterogeneity probably arises from the heterogeneity of the starting dislocation and cell network, as illustrated in Figure 2.

The interaction of voids with the dislocation population is also evident in Figure 6. It was common at all irradiation conditions to find dislocations connecting voids. with almost no independent dislocations that were not associated with voids.

It appears that those material conditions that had either preexisting or easily developed and persistent loop microstructures all evolved to essentially the same saturation microstructure at a given temperature. For those cases where dislocation networks were harder to form, especially at highar temperatures, saturation microstructures either failed to develop or were still in the process of developing at 12-14 dpa. Examination of the second discharge of this experiment at higher fluence is underway and may illuminate which of these two possibilities was occuring. It does appear, however, that by using the microstructural data we can identify the major reasons for the behavior observed in this experiment.

First, nickel has a relatively high stacking fault energy. One consequence of this is that dislocations are not stabilized against glide by separation into partials and stacking faults. Therefore, during cold working, nickel does not develop dislocation densities that approach those of stainless steel ($\geq 3 \times 10^{15}$ m^{-2})[2] since the higher level of glide leads to greater levels of dislocation annihilation. When the mobility of dislocations is enhanced by radiation-induced point defects, the density falls faster and even further. The dislocations formed either by quenching or by Frank loop unfaulting in annealed material glide and annihilate at rates at 600°C that do not allow the attainment of a high saturation density. It has been shown that the saturation density at a given irradiation temperature and displacement rate is determined by the competition of various loss and production mechanisms of dislocation line length.[2] The loss rate associated with glide and annihilation events is probably affected by the high stacking fault energy much more than is the production rate.

Second, it appears that voids, once formed, thereafter become the most effective agents in maintaining the dislocation density, trapping the ends of dislocations at void surfaces. It is probably the case that only in starting conditions where voids can nucleate prior to the complete collapse of the dislocation network can a saturation density be reached and maintained. Even then the density of dislocations will be temperature dependent, decreasing somewhat as the void density decreases with irradiation temperature. On the other hand, the voids probably also serve as internal surfaces that attract, annihilate and thereby reduce any "excess" length of individual dislocations between voids. Thus the onset of swelling probably contributes to the collapse in dislocation density.

Discussion

If the saturation level of swelling is related to the time averaged dislocation density in the early phase of the irradiation, then it would be expected that the most swelling would occur in conditions where heavily pinned networks existed prior to irradiation or at lower irradiation temperatures where loop nucleation would proceed at higher and more stable levels. It is quite possible that the steepness of a swelling curve for a annealed and slow cooled condition with irradiation temperature might be somewhat different from that shown in Figure 1 for the annealed and quenched condition. Aging of heavily pinned cold worked structures provides small open areas within the dislocation cells that may enhance void nucleation a small amount in the early stage of the irradiation and thus lead to slightly more swelling than attained in cold-worked material.

It is obvious, however, that the postirradiation dislocation densities observed here for all conditions and temperatures are at least one order of magnitude lower than that observed in typical stainless steels at this temperature (3.8×10^{14} m^{-2}).[2] This radiation induced collapse in dislocation density probably accounts for the saturation in swelling. It has been shown that if the void sink strength is much larger than the dislocation sink strength, then the swelling rate will strongly decrease.[3] Stainless steels do not exhibit such a collapse in density and have not exhibited saturation behavior at any relevant swelling level (<~80%). It has also been suggested that swelling saturation may in part result as a consequence of dislocation segments that are relatively short and that terminate on both ends on void surfaces.[3] The microstructural observations of this study are consistent with both of these proposals.

If it is assumed that voids with larger diameters have been growing longer and that voids nucleate easiest at higher dislocation densities, then the void and dislocation data derived in these studies are consistent

with these assumptions at both irradiation temperatures. This suggests that voids nucleate relatively early in the irradiation but only grow while the dislocation density is relatively high. The dislocation density probably falls with irradiation at a rate dependent on both the initial dislocation density and the irradiation temperature, and when it reaches the low saturation value dictated by the current void density, the growth of voids stops.

Conclusions

Void nucleation in pure nickel during irradiation probably proceeds while the dislocation density is relatively high. This condition can be reached most easily in either of two sets of conditions. First, in annealed nickel, it may occur at relatively low irradiation temperatures where loop nucleation rates and therefore loop stability are the highest and most persistent. Second, it also occurs when the starting dislocation density is relatively high and strongly pinned in dislocation cell walls produced during cold working. Aging leads to reduction of the dislocation density within the cells but retains the cell walls themselves. This leads to a slightly higher level of swelling.

The population of dislocations will eventually collapse regardless of the starting state since the high stacking fault energy of nickel precludes the formation of partial dislocations with their stronger level of pinning. This causes easy glide and annihilation of dislocation line length. The collapse in turn leads to an imbalance of sink strengths and a strong reduction of the void growth rate. In highly pinned starting structures, the dependence of the saturation levels of both dislocations and void swelling are only slightly sensitive to temperature. In unpinned structures, however, the temperature dependence is very strong, probably reflecting the temperature dependence of loop size and density and the resultant influence on dislocation evolution.

Future Work

Analysis of the 500°C microstructural data will proceed. Measurement of the density changes produced by irradiation at the higher displacement level will also be completed.

References

1. Garner, F. A., "Influence of Material and Environmental Variables on the Neutron-Induced Swelling of Nickel." Fusion Reactor Materials Semiannual Prowess Report, DOE/ER-03138, March 31, 1990, pp. 125-135.

2. Garner, F. A., and W. G. Wolfer, "A Model for the Evolution of Network Dislocation Density in Irradiated Metals." ASTM STP 782 (1982) pp. 1073-1087.

3. Wolfer, W. G., J. Nucl. Mater., 122-123 (1984) 367-378.

POSTIRRADIATION STRENGTH AND DEFORMATION OF FERRITIC Fe-Cr BINARY ALLOYS - M. L. Hamilton and D. S. Gelles (Pacific Northwest Laboratory)

PURPOSE

The purpose of this effort is to investigate the irradiation-induced changes in strength and deformation mode in fundamental binary Fe-Cr alloys to gain insight into the behavior of more complex ferritic/martensitic alloys.

SUMMARY

Six binary Fe-Cr alloys with chromium levels ranging from 3 to 18% were tensile tested at room temperature following irradiation at 365, 403 and 574°C to doses of 7.4, 37.7 and 34.3 dpa, respectively. Irradiation at 365 and 403°C produced significant strengthening at all chromium levels, with concurrent reductions in ductility. Strength levels were insensitive to composition, irradiation temperature or neutron exposure. Irradiation at 574°C produced strength increases at only the two highest chromium levels. The results are attributed to dislocation loop and void development at 365 and 403°C, and phase instability at 574°C. No evidence for channel fracture was found.

PROGRESS AND STATUS

Introduction

Ferritic/martensitic steels continue to be considered for application as structural materials in irradiation environments. Commercially processed alloys are being evaluated as well as complex experimental alloys under the auspices of the Fusion Materials Program under the Office of Fusion Energy in the U.S. Department of Energy. Since it is not possible to duplicate for testing purposes the irradiation conditions anticipated in a fusion device, significant effort is devoted to understanding the fundamental irradiation response of ferritic materials to facilitate extrapolation to a fusion environment from the available fission environment. Experiments on simple alloys are therefore included in the Fusion Materials Program to allow comparison with the behavior of more complex alloys. This study is part of that effort and presents the first post-irradiation tensile data reported for simple Fe-Cr binary alloys.

It has been demonstrated that void swelling plays a significant role in controlling the mode of deformation in highly irradiated austenitic alloys.[1,2] Elongated voids in such alloys are associated with channel fracture, where deformation is confined almost exclusively to narrow deformation channels.[3] An earlier study revealed the presence of similar elongated voids in deformation slip bands of an irradiated TEM disk of a binary Fe-6Cr alloy, suggesting that a similar phenomenon may operate in ferritic alloys. Since typical ferritic alloys are inherently resistant to swelling, however, investigation of the effect of swelling on deformation in ferritic alloys is difficult. Reasonable levels of void swelling can develop in simple Fe-Cr binary alloys,[3-6] however, and an experiment was therefore initiated using these alloys to investigate the possibility that channel fracture can occur in body centered cubic systems.

As part of an effort to provide baseline data on fundamental ferritic alloys and to understand the potential contribution of channel fracture to deformation in ferritic alloys, binary Fe-Cr alloys ranging from 3 to 18% chromium were irradiated in the form of miniature tensile specimens in the Fast Flux Test Facility (FFTF). Tensile tests were performed at room temperature on the first set of specimens discharged following irradiation, and the fracture surfaces were examined for evidence of channel fracture.

ExDerimental Procedure

Six Fe-Cr alloys were fabricated with chromium levels ranging from 3 to 18% in increments of 3%.[3] One hundred pound heats of the alloys were extruded to bars 1 cm in diameter and cold rolled to 0.508 mm (0.020 in.) thick sheet (0.635 mm [0.025 in.] for the 12Cr alloy). Chemical overcheck analyses revealed that the Fe-3Cr alloy was contaminated with small amounts of Ni, P, Mn, C, N and O.[5] Miniature tensile specimens were punched from the sheet and heat treated after being deburred and engraved with identification codes. The heat treatment comprised one hour at 1040°C followed by two hours at 760°C.[6] The nominal gauge dimensions of the specimens were 5.1 mm long x 1.0 mm wide (0.2 in. long x 0.040 in. wide).

Three identical sets of specimens were irradiated in the FFTF at 365, 403 and 574°C; the first set of specimens was discharged to respective exposures of 7.4, 37.7, and 34.3 dpa. The major difference between irradiation at 365 and 403°C was in flux and therefore in neutron exposure rather than in temperature. Tensile tests were conducted at room temperature using a tensile testing machine designed specifically for miniature specimens.[7] All tests were conducted at a constant crosshead speed with an initial strain rate of 1×10^{-4} sec^{-1}. Two to five tests were conducted for each irradiation condition. The data were analyzed manually to determine the 0.2% offset yield strength, the ultimate strength, and the uniform and total elongations.

Results

Tensile tests. The average tensile data are given in Table 1 for each irradiation condition. Figures 1 and 2 show the tensile data for the four irradiation conditions as a function of chromium level. Irradiation at 574°C had very little effect on the tensile behavior of these alloys except for the two highest chromium levels, where significant strengthening was observed, with a concurrent reduction in ductility. There was virtually no difference between irradiation at 365°C to 7 dpa and irradiation at 403°C to 38 dpa. Irradiation at these temperatures produced significant strengthening at all chromium levels with a concurrent reduction in ductility. At these temperatures, the observed increase in strength ranged from a factor of 2 to a factor of 6.

Previous tests performed on unirradiated specimens in the same alloy series' produced yield and ultimate strengths about 15 MPa higher on the average than the current tests, implying a slight variability in the results from one testing iteration to another. Such variability could be due to maintenance procedures, etc. The previous data were therefore not included in considerations of the current data, which were all generated during the same testing sequence.

Fractography. The unirradiated specimens exhibited large reductions in area at failure, frequently necking down to a knife edge. The irradiated specimens with 12% chromium or less all failed in a ductile manner regardless of the irradiation temperature, exhibiting either a knife edge or cup and cone type of fracture surface. The 18Cr alloy failed by cleavage at all irradiation temperatures except in one specimen irradiated at 574°C, where a large amount of cracking was observed during the test. The 15Cr alloy failed in a ductile manner after irradiation at 574°C but exhibited some specimen-to-specimen variability at the two lower irradiation temperatures, failing sometimes in a ductile manner and sometimes by cleavage. The average values of ductility do not reflect the variability observed at these two chromium levels; it is seen more clearly by examining the individual data points shown in Figures 3 and 4.

Discussion

This effort was intended in part to determine whether ferritic alloys could exhibit channel fracture due to the presence of void swelling. The data obtained earlier on similar TEM disks demonstrated that 0.2% void

Table 1. Tensile Data on Binary Fe-Cr Ferritic Alloys

Cr Level (%)	Irradiation Temperature Dose (°C)/(dpa)	Average Tensile Data YS (MPa)	UTS	UE (%)	TE (%)
3	--	205	309	23.0	31.2
3	365/ 7.4	451	527	2.6	9.5
3	403/37.3	531	621	0.9	8.1
3	574/34.3	125	263	27.8	38.5
6	--	110	245	21.1	28.8
6	365/ 7.4	490	537	0.6	6.5
6	403/37.3	494	530	0.6	7.0
6	574/34.3	92	238	21.4	30.0
9	--	114	279	23.8	33.3
9	365/ 7.4	509	594	0.7	7.0
9	403/37.3	484	553	0.7	7.9
9	574/34.3	111	270	22.5	27.8
12	--	160	319	24.5	37.7
12	365/ 7.4	520	755	1.0	11.3
12	403/37.3	673	684	0.6	7.9
12	574/34.3	148	314	22.8	36.5
15	--	133	249	16.8	22.1
15	365/ 7.4	558	620	3.0	5.4
15	403/37.3	583	613	1.0	6.7
15	574/34.3	434	498	8.3	14.3
18	--	169	243	18.7	23.6
18	365/ 7.4	557	612	0.5	0.9
18	403/37.3	533	529	0.2	0.2
18	574/34.3	484	507	2.0	5.0

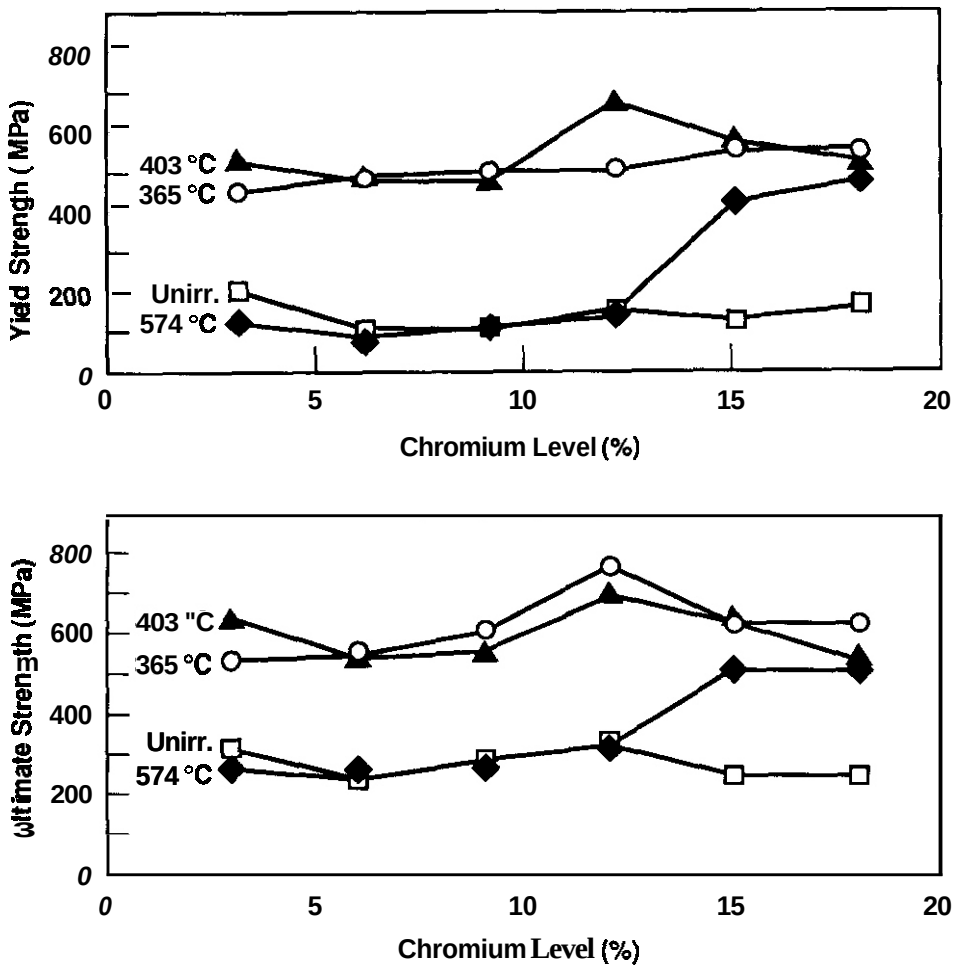


Figure 1. Yield and ultimate tensile strength for Fe-Cr binary alloys irradiated at various temperatures plotted as a function of chromium content. Neutron exposure levels were 7.4, 37.7 and 34.3 dpa at 365, 403 and 574°C, respectively.

swelling was expected in these alloys.[3] Swelling on the order of 2% therefore does not induce channel fracture, at least in simple alloys. Identical specimens continuing their irradiation to higher dose levels will be available at a later date to extend these results to higher swelling levels.

These results also provide a basis for understanding the effects of irradiation on more complicated martensitic steels. Irradiation hardening to levels of 500 MPa was exhibited by each of these simple ferritic alloys, as shown in Figure 1, and this hardening is expected to be a direct result of dislocation loop and void development, regardless of composition. Furthermore, irradiation hardening in these simple ferritic alloys appears to be insensitive not only to composition but also to irradiation temperature and dose in the vicinity of 400°C. The hardening to levels significantly above 500 MPa that is observed in the more complex martensitic steels,[9] and that exhibits a strong temperature dependence in the vicinity of 400°C, can therefore be attributed to more complex alloying effects than are present in the simple binary alloys examined here.

The binary alloys containing 15 and 18% chromium developed high strength after irradiation at 574°C and generally fractured by cleavage. This behavior is probably a result of the phase evolution in the Fe-Cr binary system. Formation of σ phase and phase separation to form α', a chromium-rich body centered cubic phase, has been seen in binary Fe-Cr alloys thermally aged at 400 - 450°C.[10] Alpha prime has also been identified in both binary and complex alloys containing 12% chromium and higher following irradiation at about 420°C.[12] The present results indicate that α' and/or σ precipitation also occurs at temperatures as high as 574°C in binary alloys with 15% or more chromium. Such precipitation is often responsible for hardening and embrittlement, and provides an explanation for the observed cleavage fracture mode.

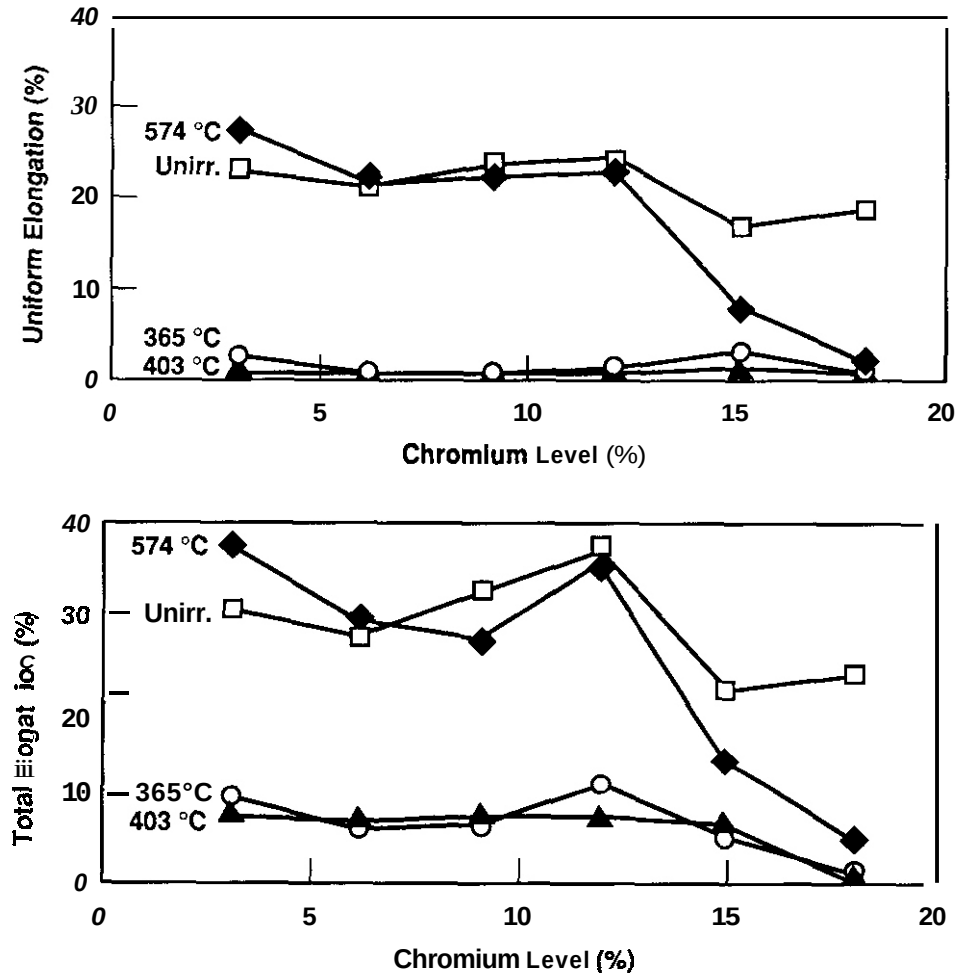


Figure 2. Uniform and total elongation for Fe-Cr binary alloys irradiated at various temperatures plotted as a function of chromium content. Neutron exposure levels were **7.4, 37.7** and **34.3** dpa at **365, 403** and 574°C, respectively.

Two somewhat unusual and unanticipated phenomena were observed in the tensile traces. **It** is known that binary Fe-XCr alloys can exhibit the upper and lower yield point phenomenon frequently observed in body centered cubic alloys,** depending on the purity of the materials used. This feature of a tensile trace results from Luders band propagation from stress concentrations along the gauge length after dislocations are unlocked from the interstitial atmospheres pinning them. The majority of the unirradiated specimens tested in this experiment, as well as a few of the 3Cr specimens irradiated at 574°C, exhibited a yield 'plateau' similar to that typically observed after the upper yield, but without an actual upper yield point preceding the plateau. This phenomenon is shown schematically in Figure 5a. **If** the upper yield point was exceeded at the localized stress concentration that initiated the propagation of the Luders bands, then the upper yield point would not be observed in the test trace. Alternatively, **if** the load drop associated with the upper yield point was relatively small, **it** is possible that **it** was obscured by the relative softness of the tensile machine.

A second and perhaps related phenomenon was the appearance of distinct 'bumps' in some of the tensile traces that occurred at the maximum load almost immediately after the yield point (see schematic in Figure 5b). This phenomenon was most prevalent in the 6 and 9Cr alloys following irradiation at **365** and **403°C.** This phenomenon has also been observed by one of the authors in simple austenitic specimens after irradiation, in both the current specimen geometry as well as in another miniaturized geometry. No explanation of these bumps is immediately forthcoming.

The heat treatment that was used allowed relatively large grain sizes to develop in some instances, yielding in the best case about 10 grains across the specimen thickness and in the worst case only about 1.5 grains across the thickness. The grain sizes are given in Table 2 for each composition. There was some concern

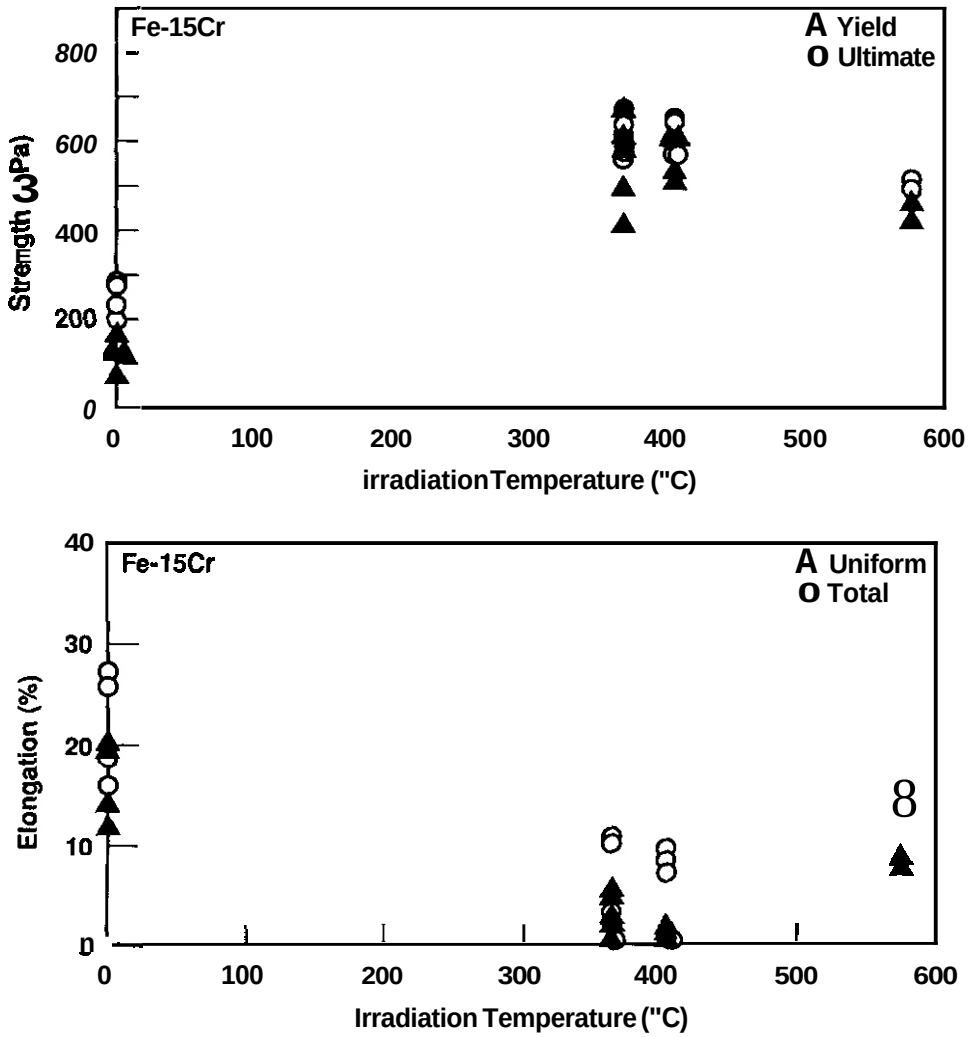


figure 3. Strength and elongation for Fe-15Cr as a function of irradiation temperature showing results for all specimens tested. Neutron exposure levels were 7.4, 37.7 and 34.3 dpa at 365, 403 and 574°C, respectively.

that the larger grain sizes would invalidate the tensile results. The data obtained on unirradiated specimens, however, are in reasonably good agreement with those of several other authors[12-14] despite a difference of up to a factor of ten in grain size between the specimens in the various studies. In addition, the fracture surfaces showed no indication that the failure itself was influenced by grain boundaries, although specimen surfaces in the large grained materials exhibited some markings away from the failure that are probably grain boundaries (see Figure 6). It appears, therefore, that the larger grain size of some of the specimens did not adversely affect the experiment.

CONCLUSIONS

Six binary Fe-Cr alloys with chromium levels ranging from 3 to 18% were tensile tested at room temperature following irradiation at 365, 403 and 574°C to doses of 7.4, 37.7 and 34.3 dpa, respectively. Irradiation at 365 and 403" produced significant strengthening at all chromium levels, with concurrent reductions in ductility. Strength levels were insensitive to composition, irradiation temperature or neutron exposure. Irradiation at 574°C produced strength increases at only the two highest chromium levels. The results are attributed to dislocation loop and void development at 365 and 403°C, and phase instability at 574°C.

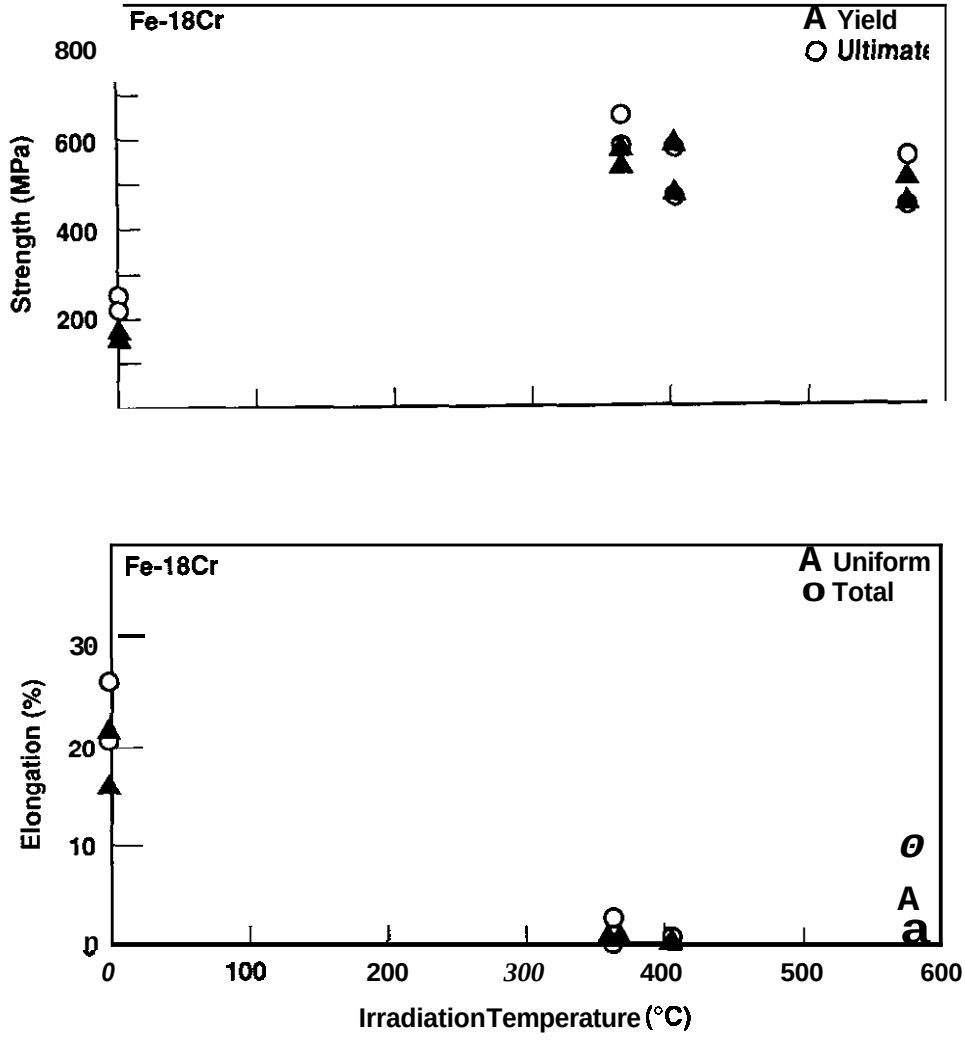


Figure 4. Strength and elongation for Fe-18Cr as a function of irradiation temperature showing results for all specimens tested. Neutron exposure levels were 7.4, 37.7 and 34.3 dpa at 365, 403 and 574°C, respectively.

FUTURE WORK

Additional specimens will become available at higher neutron exposures after further irradiation in the FFTF. Tensile tests will be performed at room temperature on these specimens as they are discharged from reactor. Electron microscopy will be attempted on deformed specimen gauge sections to determine whether elongated voids are indeed present or not.

REFERENCES

1. R. L. Fish, J. L. Straalsund, C. W. Hunter and J. J. Holmes, "Swelling and Tensile Property Evaluations of High-Fluence EBR-II Thimbles," in Effects of Radiation on Substructure and Mechanical Properties of Metals and Alloys, ASTM STP 529, American Society for Testing and Materials, 1973, pp. 149-164.

2. M. L. Hamilton, F. H. Huang, W. J. S. Yang and F. A. Garner, "Mechanical Properties and Fracture Behavior of 20% Cold Worked 316 Stainless Steel Irradiated to Very High Neutron Exposures," Influence of Radiation in Material Properties: 13th International Symposium (Part 11), ASTM STP 956, F. A. Garner, C. H. Henager, Jr., and N. Igata, Eds., American Society for Testing and Materials, Philadelphia, 1987, pp. 245-270.

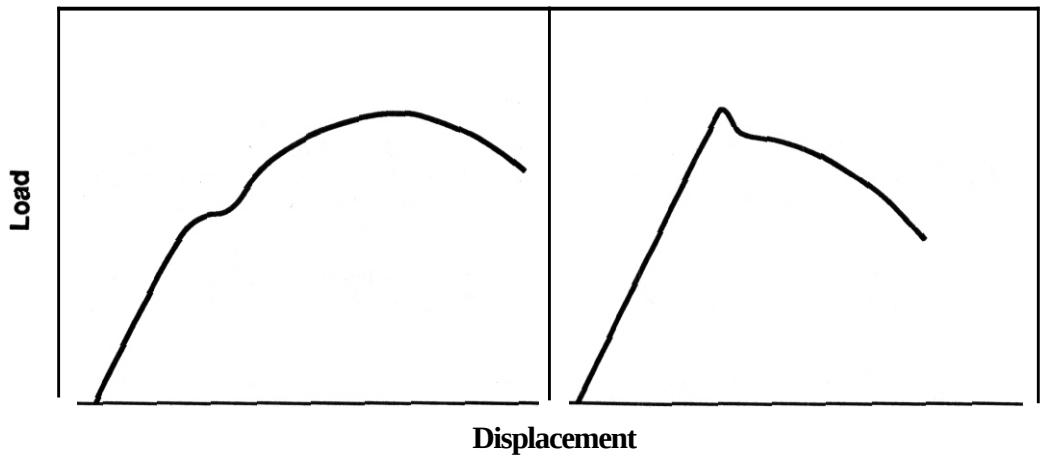


Figure 5. Schematics of load-displacement traces obtained for irradiated Fe-Cr binary alloys showing a) yield plateau and b) maximum load response associated with the yield point.

Table 2. Grains in Fe-Cr Tensile Specimens

	Number of Grains Across Thickness
Fe-3Cr	5-6
Fe-6Cr	3
Fe-9Cr	4.5
Fe-12Cr	10
Fe-15Cr	5
Fe-18Cr	1.5

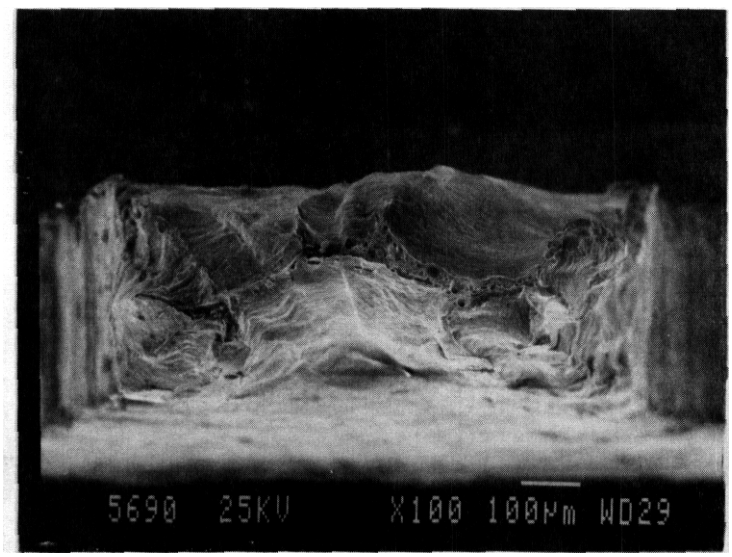


Figure 6. Fracture surface of an unirradiated specimen of Fe-6Cr showing what is almost a knife edge failure unaffected by a coarse grain size.

3. D. S. Gelles, "Neutron Irradiation Damage in Ferritic Fe-Cr Alloys," Effects of Radiation on Materials: 14th International Symposium, Vol. I, ASTM STP 1046, N. H. Packan, R. E. Stoller, and A. S. Kumar, Eds., American Society for Testing and Materials, Philadelphia, 1989, pp. 73-97.

4. E. A. Little and D. A. Stow, Met. Sci. (1980). 89.

5. D. S. Gelles and R. L. Meinecke, "Swelling in Simple Ferritic Alloys Irradiated to High Fluence," Alloy Development for Irradiation Performance Progress Report for Period Ending September 1983, DOE/ER-0045/11, 1984, p. 103.

6. D. S. Gelles, J. Nucl. Mat. 108 & 109 (1982) pp. 515-526.

7. N. F. Panayotou, S. D. Atkin, and R. J. Puigh, "Design and Use of Nonstandard Tensile Specimens for Irradiated Materials Testing," The Use of Small Scale Specimens for Testing Irradiated Material, ASTM STP 888, W. R. Corwin and G. E. Lucas, Eds., American Society for Testing and Materials, Philadelphia, 1986, pp. 201-219.

8. M. F. Maxon, H. L. Heinisch and D. S. Gelles, "The Tensile Properties of Fe-Cr Binary Alloys Using Miniature Specimens," Fusion Reactor Materials Semiannual Progress Report for Period Ending September 30, 1987, DOE/ER-0313/3, 1988, p. 60.

9. R. L. Klueh and P. J. Maziasz, "Helium Effects on Neutron-Irradiated Cr-Mo Ferritic Steels: A Review of Recent Results." in Effects of Radiation on Materials: 14th International Symposium, Vol. I, ASTM STP 1046, H. H. Packan, R. E. Stoller and A. S. Kumar, Eds., American Society for Testing and Materials, Philadelphia, 1989, pp. 246-262.

10. Metals Handbook, 8th Edition, Vol. 8, American Society for Metals, Metals Park, OH, 1973, p. 291.

11. D. S. Gelles and L. E. Thomas, "Effects of Neutron Irradiation on Microstructure in Experimental and Commercial Ferritic Alloys," in Proceedings of Topical Conference on Ferritic Alloys for Use in Nuclear Energy Technologies, J. W. Davis and D. J. Michel, Eds., The Metallurgical Society of AIME, Warrendale, PA, 1984, pp. 559-568.

12. M. J. Kelley and N. S. Stoloff, Met. Trans. A 7A (1976) pp. 331-333.

13. G. T. Horne, R. B. Roy and H. W. Paxton, J.I.S.I., February 1963, pp. 161-167.

14. W. P. Rees, B. E. Hopkins and H. R. Tipler, J.I.S.I, May 1954, pp. 93-115.

6.0 DEVELOPMENT OF STRUCTURAL ALLOYS

6.1 Ferritic Stainless Steels

HEAT TREATMENT EFFECTS ON TOUGHNESS OF 9Cr-1MoVNb AND 12Cr-1MoVW STEELS IRRADIATED AT 365°C -- R. L. Kiueh and D. J. Alexander (Oak Ridge National Laboratory)

OBJECTIVE

The goal of this study is to evaluate the impact behavior of irradiated ferritic steels and relate the change in properties to the heat treatment of the steel.

SUMMARY

The 9Cr-1MoVNb and 12Cr-1MoVW steels were austenitized at 1040 and 1100°C to produce two different prior-austenite grain sizes. Pieces of the steels with these different heat treatments were then given different tempering treatments (1 h at 760 and 2.5 h 780°C). Charpy impact specimens with these different heat treatments were irradiated in FFTF at 365°C up to 5 dpa. For 9Cr-1MoVNb steel in the unirradiated condition, the smaller the prior-austenite grain size, the lower the ductile-brittle transition temperature (DBTT). Also, the higher the tempering temperature, the lower the DBTT prior to irradiation. Regardless of the starting value, however, the DBTT shift during irradiation was the same for all specimens. This means that heat treatment can be used to insure a lower DBTT before and after irradiation. The 12Cr-1MoVW steel showed little effect of heat treatment on DBTT in the unirradiated condition. and the shift in DBTT was relatively constant. Thus, heat treatment cannot be used to reduce the effect of irradiation on the DBTT for this steel.

PROGRESS AND STATUS

Introduction

Ferritic/martensitic steels are relatively immune to void swelling and are being considered as possible structural materials for the first wall and blanket structure of future magnetic fusion reactors. A major concern involves the effect of irradiation on toughness. Toughness changes are observed by studying the Charpy impact behavior before and after irradiation of steels in a fission reactor. Irradiation can cause a large increase in the ductile-brittle transition temperature (DBTT) and a decrease in the upper-shelf energy (USE). Even if the DBTT is suitably low before irradiation, it can be well above room temperature after irradiation.'.'

Charpy impact behavior can be affected by the heat treatment the steel received. Prior-austenite grain size can affect the DBTT and USE; the smaller the grain size, the lower the DBTT and the higher the USE. The prior-austenite grain size depends on the austenitization temperature, Tempering also affects the behavior: the higher the tempering temperature or the longer the tempering time at a given temperature, the lower the DBTT and the higher the USE.

There do not appear to have been any studies on the effect of heat treatment on the Charpy impact properties after irradiation. In this experiment. Charpy impact specimens of 9Cr-1MoVNb (modified 9Cr-1 Mo steel) and 12Cr-1MoVW (the Sandvik HT9 composition) steels were given different heat treatments and then irradiated in the Fast Flux Test Facility (FFTF). The results were compared with results for the same steels in the unirradiated condition.

Experimental Procedure

The 9Cr-1MoVNb steel was taken from an argon-oxygen decarburized (AOD) and electroslag-remelted (ESR) heat (Heat 30176) processed by CarTech into 1-in. plate. The 12Cr-1MoVW steel was from an AOD/ESR melt which was processed into hot-rolled plate (National Fusion Heat 9607-R2). The compositions of the steels are given in Table 1. Pieces of 15.9-mm-thick plate was rolled to 9.5-mm-thick plate for heat treatment to obtain the specimens.

Plates 88.9 by 152 by 9.5 mm were normalized and tempered. Two plates of 9Cr-1MoVNb and two plates of 12Cr-1MoVW were austenitized 1 h at 1040°C and air cooled, and a similar number of plates were austenitized 1 h at 1100°C and air cooled. Then one plate from each steel with each normalization treatment was tempered 1 h at 760°C and 2.5 h at 780°C.

Subsize Charpy specimens were irradiated and tested. These were essentially one-third the standard size and measured 3.3 by 3.3 by 25.4 mm and contained a 0.51-mm-deep 30" V-notch with a 0.05- to 0.08-mm-root radius. All specimens were taken from the center of the normalized-and-tempered 9.5-mm-thick plate along the rolling direction with the notch running transverse to the rolling direction (L-T orientation).

Table 1. Chemical **Composition** of **Steels**

	9Cr-1MoVNb (Heat 30116)	12Cr-1MoVW (Heat 9607-R2)
C	0.092	0.20
Mn	0.48	0.51
P	0.012	0.016
S	0.004	0.007
si	0.15	0.26
Ni	0.09	0.54
Cr	8.32	11.65
Mo	0.86	1.02
V	0.20	0.29
Cb	0.06	0.01
Ti	0.001	t0.01
co	0.017	0.09
C"	0.03	0.03
41	0.006	
Al	0.011	0.009
B	0.0003	0.009
B	0.0006	0.001
W	<0.01	0.51
As	0.001	0.004
Sn	0.002	0.001
Zr	<0.001	0.002
Pb	<0.001	
Sb	<0.001	
N_2	0.055	0.041
O_2	0.010	0.013
H_2	0.0001	0.013

Specimens were irradiated in the FFTF in the Materials Open Test Assembly (MOTA) in the MOTA-1E experiment. Six Charpy specimens from each heat and each heat treatment were irradiated in the below-core specimen canister of MOTA. This is a sodium "weeper" that operates at ≈365°C, which is slightly above the coolant ambient temperature. All of the 9Cr-1MoVNb steel specimens were irradiated to a fluence of about 1.3 x 10" n/m^2 (>0.1 MeV), which produces a damage dose of ≈5 dpa. The 12Cr-1MoVW steels were in a different position in the reactor and received about 1.1 x 10^{26} n/m^2, ≈4 dpa. Less than 1 appm He formed in the specimens during irradiation.

Details on test procedure for the subsize Charpy specimens have been published.' Individual Charpy data sets were fitted with a hyperbolic-tangent function to obtain the transition temperature and upper-shelf energy.

Results and discussion

Prior-austenite grain size was determined by the austenitization temperature, and Table 2 gives estimated grain sizes for the two different temperatures used. There was only a small difference in average grain diameter for the 9Cr-1MoVNb steel: 20 and 29 μm for the 1040 and 1100°C austenitizing temperatures. A larger difference was observed for the 12Cr-1MoVW steel: 32 and 153 μm for austenitization temperatures of 1040 and 1100°C, respectively.

Results for the Charpy tests for the steels in the normalized-and-tempered and irradiated conditions are given in Table 3. In addition to giving the DBTT and **USE** for both conditions, the shift in DBTT (ΔDBTT) and change in **USE** (ΔUSE) are also given (**AUSE** is given in both joules and as the percent change of the unirradiated value)

For the 9Cr-1MoVNb steel, grain size affected the DBTT of the unirradiated steel. This can be seen by comparing DBTT values for the two austenitizing temperatures for a common tempering temperature. A large difference is seen after the 760°C temper, with a lesser difference after the 780°C temper, indicating that the 780°C temper has a greater effect than the 760°C temper, as expected. This effect of tempering is verified by examining the results for the two tempering temperatures for a given austenitization temperature. For the steel austenitized at 1100°C. where grain size will play a smaller role, tempering at 780°C has a larger effect than the 760°C temper. The **USE** of the 9Cr-1MoVNb steel in the unirradiated condition appears to be little affected by heat treatment.

After the 9Cr-1MoVNb steel was irradiated to ≈5 dpa, the ΔDBTT for the four different heat treatments are essentially the same. The difference of 10°C could perhaps indicate a slight effect of prior austenite grain size, as both steels austenitized at 1100°C had the largest ΔDBTT. These results would indicate that tempering had no effect on ΔDBTT. The change in USE was also fairly constant.

Table 2. Estimated Prior-Austenite Grain Sizes of 9Cr-1MoVNb and 12Cr-1MoVW Steels

Austenitization Temperature (°C)	Average Grain Diameter (μm)	ASTH Grain Size Number
	9Cr-1MoVNb Steel	
1040	20	8
1100	29	7
	12Cr-1MoVW Steel	
1040	32	7
1100	153	3–4

The 12Cr-1MoVW steel in the unirradiated condition shows a somewhat different behavior from the 9Cr-1MoVNb steel (Table 3). There was no apparent effect of prior-austenite grain size. That is, the DBTT values were the same for the steel given the two different austenitizing treatments and then tempered at 760°C. There was a difference when the steels were tempered at 780°C, but the difference was opposite to that expected from a grain size effect. **The** specimen austenitized at 1040°C and tempered at 780°C had a DBTT similar to that of the two steels tempered at 760°C, but the steel austenitized at 1100°C and tempered at 780°C had a somewhat lower DBTT (19°C lower). For a prior-austenite grain size effect, a higher DBTT is expected. Therefore, this difference **must** be due the higher tempering temperature. The results indicate that there is no prior-austenite grain size effect on the DBTT of 12Cr-1MoVW steel. The USE of the 12Cr-1MoVW in the unirradiated condition did not appear to be affected by heat treatment (Table 3). although there was more scatter than for 9Cr-1MoVNb.

Irradiation of the 12Cr-1MoVW steel to ≈4 dpa caused a ΔDBTT for all heat treatments over twice that observed for the 9Cr-1MoVNb steel (Table 3). After irradiation, the difference in DBTT for the four different heat treatments was less than it was before irradiation, and this difference in DBTT values was less than observed for the 9Cr-1MoVNb steel. The ΔDBTT values for all but one of the heat treatments were similar; the three with similar values were the steels that had similar DBTT

Table 3. Effect of Irradiation at 365°C on Charpy Behavior of 9Cr-1MoVNb and 12Cr-1MoVW Steels

Heat Treatment	DBTT, °C		USE, J		ΔDBTT	ΔUSE
	Unirradiated	Irradiated	Unirradiated	Irradiated	°C	J (%)
9Cr-1MoVNb Steel						
1040/1h/AC;760/1h	-64	-19	10.5	7.6	45	2.9 (38)
1040/1h/AC;780/2.5h	-80	-37	10.6	8.2	43	2.4 (29)
1100/1h/AC;760/1h	-17	36	10.0	7.3	53	2.7 (37)
1100/1h/AC;780/2.5h	-61	-6	10.6	8.9	55	1.7 (19)
12Cr-1MoVW Steel						
1040/1h/AC;760/1h	-32	97	6.0	3.6	129	2.4 (40)
1040/1h/AC;780/2.5h	-35	95	7.6	3.4	130	4.2 (55)
1100/1h/AC;760/1h	-34	100	5.4	2.5	134	2.9 (54)
1100/1h/AC;780/2.5h	-51	107	6.2	3.9	158	2.3 (37)

DBTT was determined at 112 the upper shelf.

values before irradiation. The steel with a somewhat higher DBTT was the steel with the lowest DBTT before irradiation, which means that it showed the largest shift during irradiation. These results indicate that heat treatment has little effect on the DBTT of the 12Cr-1MoVW steel in either the unirradiated or irradiated condition. Considering the scatter, the change in the USE also appears little affected by heat-treatment. In general, the percent change in USE for the 12Cr-1MoVW steel was greater than for 9Cr-1MoVNb steel.

The lack of a prior-austenite grain size *effect* in 12Cr-1MoVW steel compared to the 9Cr-1MoVNb steel may indicate that the precipitate in the microstructure controls the fracture behavior of the 12Cr-1MoVW. This steel contains twice as much carbon as the 9Cr-1MoVNb steel, and in the normalized-and-tempered condition, the 12Cr-1MoVW contains over twice as much precipitate (3.8 wt % precipitate in the 12Cr-1MoVW compared to 1.5 wt % in 9Cr-1MoVNb).[9] This difference in precipitation can be Seen in Fig. 1, where carbide extraction replicas of the 9Cr-1MoVNb and 12Cr-1MoVW steels are shown after a similar normalization-and tempering treatment for both steels. These photomicrographs, taken from the work of Vitek and Klueh,[9] show how the large amount of precipitate in the 12Cr-1MoVW could well determine the fracture process.

One interpretation of the results is that for 9Cr-1MoVNb steels, heat treatment could be used to minimize the effect of irradiation on ΔDBTT. This follows from the observation that the specimens with the smaller grain size had a lower DBTT in the unirradiated condition. and the ADBTT was the same regardless of the heat treatment. Thus, the lowest DBTT after irradiation is guaranteed by starting with the lowest possible DBTT before irradiation. Reduction of DBTT should be accomplished while at the same time keeping the strength as high as possible. Lowering the grain size further would be the best way to accomplish this, aithough as seen in Table 2, grain size changed only slightly with the austenitizing temperatures used for this study.

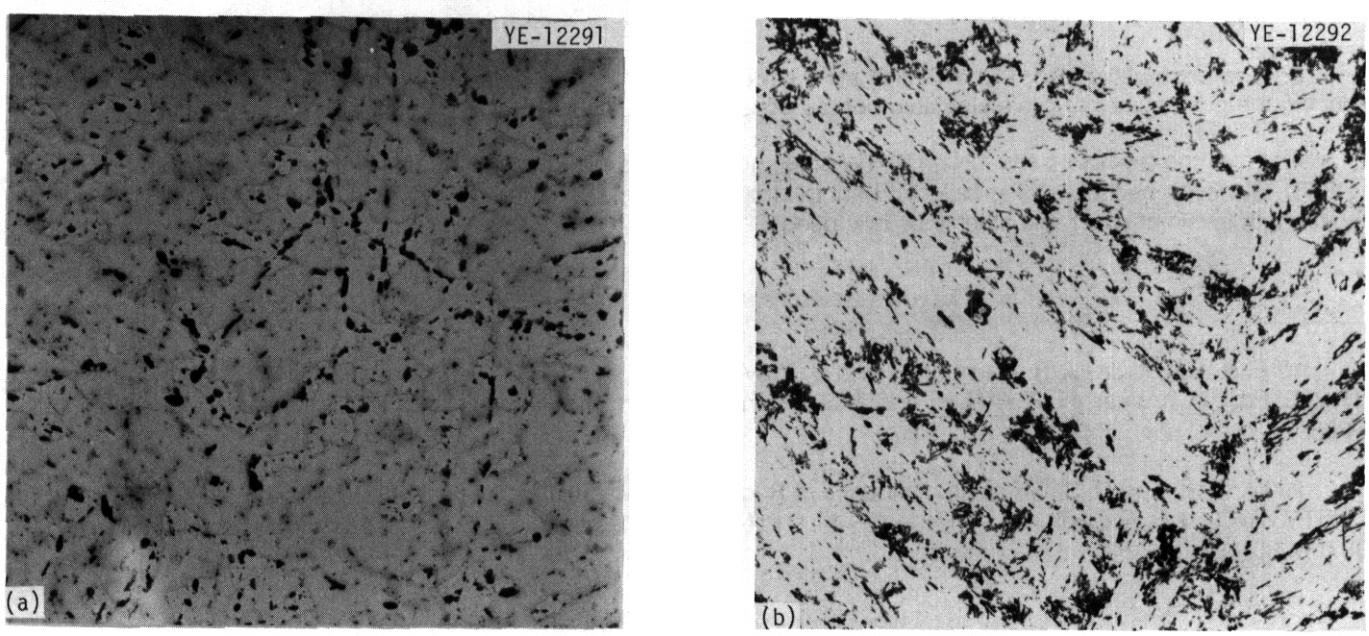


Fig. 1. Extraction replicas of normalized-and-tempered (a) 9Cr-1MoVNb (1040°C/0.5h/AC + 780°C/2.5 h/AC) and (b) 12Cr-1MoVW (1050°C/0.5h/AC + 780°C/2.5 h/AC) steels. Taken from reference 9.

A different interpretation is required for the 12Cr-1MoVW steel. Here it appears that heat treatment has little effect on DBTT. The results indicate that it would therefore be appropriate to use the lower tempering temperature, because this would improve the strength of the steel with essentially no effect on toughness. The 780°C tempering temperature has been used extensively in the past, but 760°C (or less) should be acceptable.

Previous studies of 9Cr-1MoVNb and 12Cr-1MoVW steels irradiated in fast reactors indicated that the shift in DBTT saturated with increasing fluence.[2,10] Hu and Gelles[2] irradiated 9Cr-1MoVNb and 12Cr-1MoVW steels at 390°C in EBR-II. The ΔDBTT for 9Cr-1MoVNb was 52 and 54°C after irradiation to 13 and 26 dpa, respectively, and for 12Cr-1MoVW shifts of 124 and 144°C were observed for the same fluences. Similarly, 12Cr-1MoVW irradiated at 365°C to ≈10 and 17 dpa in FFTF resulted in a ΔDBTT of 161°C at both fluences.[10] For the latter experiment, the steels were austenitized at 1050°C and tempered 2.5 h at 780°C. Both of these studies used half-size specimens, instead of the third-size specimens of the present experiment. However, third-size specimens were also irradiated at 365°C to 10 dpa in the second study,[10] and the ΔDBTT was 151°C, essentially the same as for the half-size specimens, although the DBTT before irradiation for the third-size specimens was lower. This result and others indicated that specimen size does not affect ΔDBTT.[10]

The magnitude of the ΔDBTT values for the 9Cr-1MoVNb and 12Cr-1MoVW steels observed in the present study is similar to those observed in previous studies. Based on the previous results at 365°C, however, it appears that saturation was probably not achieved in the present experiment, where irradiation was to only about 5 and 4 dpa for the 9Cr-1MoVNb and 12Cr-1MoVW steels, respectively. Such saturation studies are required to determine if the conclusions on austenite grain size apply to saturation. Specimens are presently being irradiated in FFTF to determine the behavior when saturation occurs.

Summary and conclusion

Charpy specimens of 9Cr-1MoVNb and 12Cr-1MoVW steels were heat treated to produce two different prior-austenite grain sizes. and specimens with these different grain sizes were given two different tempering treatments. Specimens were tested as heat treated and after irradiation in FFTF at 365°C. The 9Cr-1MoVNb was irradiated to ≈5 dpa and the 12Cr-1MoVW to ≈4 dpa. The following summarizes the observations and conclusions.

1. As heat treated, the DBTT of the 9Cr-1MoVNb steel depended on the austenitizing temperature (prior-austenite grain size) and to a lesser extent on tempering temperature. The shii in DBTT caused by irradiation for this steel was relatively independent of heat treatment. This meant that after irradiation. the relative difference in DBTT for the steel given the different heat treatments was similar to what it was before irradiation.

2. Prior-austenite grain size had little effect on the DBTT of the 12Cr-1MoVW steel, and tempering temperature had only a slight effect. The shift in DBTT was again relatively independent of heat treatment: the shift for the 12Cr-1MoVW steel was over twice that for 9Cr-1MoVNb steel.

3. The observations for 9Cr-1MoVNb steel suggest that the effect of irradiation on DBTT can be ameliorated by reducing the prior-austenite grain size as much as possible.

4. From the results on the 12Cr-1MoVW steel, no method is obvious to reduce the effect of irradiation on the shift in DBTT. However, because of the lack of a heat treatment effect on DBTT, the steel can be used without tempering to the low strength levels at which the steel is usually used.

References

1. F. A. Smidt. Jr.. J. R. Hawthorne, and V. Provenzano. in: Effects of Radiation on Materials: Tenth Conference, STP 725, Eds. D. Kramer. H. R. Brager, and J. S. Perrin (American Society for Testing and Materials, Philadelphia, 1981) p. 269.

2. W. L. Hu and D. S. Gelles, in: Influence of Radiation on Material Properties: 13th International Symposium (Part II), ASTM STP 956, F. A. Garner, C. H. Henager. Jr., and N. Igata, Eds. (American Society for Testing Materials, Philadelphia, 1987) p. 83.

3. D. S. Gelles, J. Nud. Mater. **149 (1987) 192.**

4. J. M. **Viek,** W. R. Corwin, R. L. Klueh, and J. R. Hawthorne, J. Nucl. Mater. **141-143 (1986) 948.**

5. W. R. Corwin, J. M. **Viek.** and R. **L.** Klueh, J. Nucl. Mater. **149 (1987) 312.**

6. R. L. Klueh, J. M. **Viek. W. R.** Corwin. and D. J. Alexander, J. Nud. Mater. **155157 (1988) 973.**

7. R. L. Klueh and D. J. Alexander, J. Nucl. Mater. to be published.

8. D. J. Alexander, R. K. Nanstad, W. R. Corwin. and J. T. Hutton, Applications of Automation Technology to Fatigue and Fracture Testing, ASTM STP 1092, A. A. Braun. N. E Ashbaugh. and F. M. Smith, Eds. (American Society for Testing and Materials, Philadelphia. 1990) p. 83.

9. J. M. **Viek** and R. **L.** Klueh, Met. Trans. **14A (1983) 1047.**

10. R. L. Klueh and D. J. Alexander, in: Proceedings of **the 15th** Symposium ***on*** Effects of Radiation on Materials (American Society for Testing and Materials, Philadelphia) to be published.

IRRADIATION RESPONSE OF F82H, A REDUCED ACTIVATION Fe-8Cr-2W MARTENSITIC STEEL - Y. Kohno (University of Tokyo), 0. S. Gelles (Pacific Northwest Laboratory), A. Kohyama (University of Tokyo), M. Tamura (Nippon Kokan K.K.) and M. L. Hamilton (Pacific Northwest Laboratory)

OBJECTIVE

The objective of this work is to determine the applicability of F82H, a tungsten-stabilized, martensitic stainless steel, as a low activation material for fusion reactor structural components.

SUMMARY

Miniature tensile and microscopy specimens of the tungsten-stabilized martensitic steel F82H were examined after irradiation in FFTF to fluences as high as 37 dpa at temperatures ranging from 365 to 750°C. Tensile tests performed at room temperature revealed a small amount of hardening at or below 405°C and significant softening at the higher irradiation temperatures. Electron microscopy results were consistent with the tensile data. The tempered martensite structure was quite stable below 405°C. The martensite lath structure recovered slightly at 550°C, accompanied by the coarsening of carbide particles, while above 670°C, the martensite lath structure was eliminated. Cavity formation was observed only below 405°C. The maximum swelling measured was as high as 0.14% at 405°C. Analysis of precipitate extraction replicas showed superior phase stability during irradiation. Precipitates identified in the irradiated specimens were $M_{23}C_6$ and Laves, the same as were identified following thermal aging. Other precipitates were not observed.

PROGRESS AND STATUS

Introduction

The development of low activation alloys has been incorporated into the goals of fusion materials development to minimize the quantity of highly activated material generated in fusion machine components, thereby increasing the acceptability of fusion power.' Certain elemental additions must be carefully controlled in alloys to achieve this goal; in particular, Cu, Ni, Mo, Nb and N, with Nb restricted most severely. The alloy compositions being considered for low activation ferritic or martensitic steels are based on three commercially important alloy classes: 2.25Cr, 9Cr and 12Cr steels. Since these classes of steel contain about 1% Mo and frequently some Nb, the design of low activation alternatives requires substitutes for these two elements. W and V are the leading candidates to replace the Mo, while Ta can be considered a substitute for the Nb. Mn and C are added for austenite stabilization to obtain a fully martensitic 12Cr steel without the addition of Ni. Three classes of low activation ferritic/martensitic alloys are therefore possible: 1) low Cr bainitic alloys, 2) 7 - 9Cr martensitic alloys and 3) 12Cr stabilized martensitic alloys. Development efforts have been directed towards low activation steels in all three classes.

The low activation martensitic alloys in the 7 - 9Cr range exhibited better mechanical behavior after irradiation in FFTF/MOTA than the comparable versions of the other two classes of ferritic/martensitic alloys.' The dose dependence of the tensile properties of the 7 - 9Cr alloys was intermediate to that of the other classes of alloys, with the yield strength and total elongation being almost dose independent. The impact behavior of the 7 - 9Cr alloys also showed better resistance to irradiation than the low activation versions of the other two classes. The irradiation-induced shift in ductile brittle transition temperature (DBTT) was much smaller and the upper shelf energy (USE) was generally higher. The 7 - 9Cr alloys therefore appear the most promising of the low activation alloys for fusion reactor applications. This class of alloys also exhibits reasonable phase stability during irradiation and sufficient high temperature strength. However, the void swelling resistance of this alloy class is not as good as that of other low activation ferritic/martensitic alloys.

An effort to develop an improved low activation martensitic steel in the 7 - 9Cr range has been made in both Japan[3-5] and the U.S.[6-8] One of the candidates in this class of alloys is F82H, with a nominal composition of Fe-8Cr-2W-0.1C-V,Ta,B. It was designed in Japan jointly by the Japanese Atomic Energy Research Institute (JAERI) and the steel company Nippon Kokan (NKK). Both microscopy and tensile specimens of this steel were irradiated recently in FFTF with the objective of investigating changes in tensile behavior and microstructure, including characterization of the void swelling following neutron irradiation.

ExDerimental Procedures

Table 1 gives the actual chemical composition and the pre-irradiation heat treatment for F82H. Transmission electron microscopy (TEM) specimens 3 mm in diameter were punched from 0.076 and 0.178 mm (0.003 and 0.007 inch) thick sheets. The specimens were irradiated in the FFTF/MOTA IF during FFTF cycle 10 in one below-core and four in-core positions at nominal irradiation temperatures of 365 (below core), 405, 550, 670 and 750°C. The TEM specimen codes and corresponding irradiation conditions are provided in Table 2. Microstructural examination was performed using JEM-2000FX and JEM-1200EX microscopes. Microchemical analysis on

Table 1. The Chemical Composition and Starting Condition of F82H

C	Si	Mn	P	S	Ni	Cr	Mo	W	V	Nb	Ta	Ti	B	Al	N
0.093	0.09	0.49	0.005	0.001	0.01	7.65	0.00	2.0	0.18	0.00	0.040	--	0.0034	0.01	0.002

Heat treatment: normalized t tempered (1040°C/0.5hr t 740°C/2hr).

Table 2. Irradiation Conditions for F82H

Specimen Codes (0.003", 0.007")	Irradiation Temperature (°C)	Neutron Fluence (n/cm^2)(a)	Displacement Damage (dpa)
376V, 376U	365	1.78×10^{22}	6.7
396V, 396U	405	7.71×10^{22}	35.8
4A6V, 4A6U	550	8.00×10^{22}	37.0
4B6V, 4B6U	670	6.12×10^{22}	28.3
4E6V, 4E6U	750	8.02×10^{22}	37.1

(a) E > 0.1 MeV.

extraction replicas obtained in each specimen condition was performed using EDX systems on the TEMs. Miniature tensile specimens having a gauge length of 5.1 nm (0.21 inch) were punched from sheet stock approximately 0.43 mm (0.017 inch) thick, heat treated, and irradiated under the same conditions as the TEM disks. Tensile tests were performed at room temperature following irradiation using a horizontal test frame designed specifically for this specimen geometry.[9]

Results and Discussion

Electron microscopy. The microstructure of F82H prior to irradiation consisted of tempered martensite laths.[10,11] Negligible delta ferrite was present, and only the $M_{23}C_6$-type of carbide precipitation was identified, primarily along prior austenite grain boundaries. Other precipitation, such as tantalum or vanadium carbides or Laves phase, was not found in unirradiated specimens. The average prior austenite grain size was 120 μm.

Figure 1 shows the post-irradiation microstructure at relatively low magnification for each irradiation temperature. The tempered martensite structure is stable after irradiation below 405°C. However, a slight recovery of the martensite lath structure can be identified after irradiation at 405°C. At low irradiation temperatures, the size and distribution of the carbides show no distinct change compared with the unirradiated condition. At 550°C, however, coarsening or a partial elimination of the lath structure was clearly exhibited along with coarsening of the carbides. A distinct change in the matrix structure was evident after irradiation at 670 and 750°C, where the lath structure was destroyed and the precipitate density was reduced. The high temperature results could conceivably be the result of decarburization since the specimens were irradiated in open packets through which liquid sodium coolant flowed during irradiation.

The temperature dependence of cavity fownation is shown in Figure 2. Cavity formation typical of void swelling was clearly observed for irradiation below 405°C. A few tiny bubbles were formed above 550°C, most of which were observed on grain boundaries. Cavity distribution was very nonuniform at 365 and 405°C, and cavities tended to agglomerate in the central areas of martensite laths. The cavities were also aligned in rows, indicating that they nucleated preferentially on dislocations. Table 3 sunmarizes the quantitative measurements of the cavity microstructure following irradiation at 365 and 405°C. The average cavity number density in cavity-rich regions of the specimen irradiated 405°C was estimated to be about 2.3×10^{20} m^{-3}, whereas it was estimated to be about 6.8×10^{19} m^{-3} in the specimen irradiated at 365°C. The lower value at 365°C may be due to the lower level of displacement damage relative to the 405°C irradiation. The average cavity diameters were estimated to be 22.7 and 12.7 nm at 405 and 365°C, respectively. Both the cavity number density and cavity size were very small above 550°C, and therefore cavity swelling was negligible. From Table 3 it can be seen that swelling remained very low for exposures as high as 30 dpa. Although it is very low, the swelling observed in F82H at 405°C was about twice as high as was observed in a similar material, GA3X (Fe-7.5Cr-1.95W-0.3V-0.15C), irradiated in FFTF at 426°C.[6]

Compositional analysis of the individual particles on precipitate extraction replicas was performed for each irradiation condition. The results are sumnarized in Table 4. In the unirradiated condition and following irradiation at 365, 405, 550 and 670°C, $M_{23}C_6$ remained the primary extracted phase, whereas all precipitate

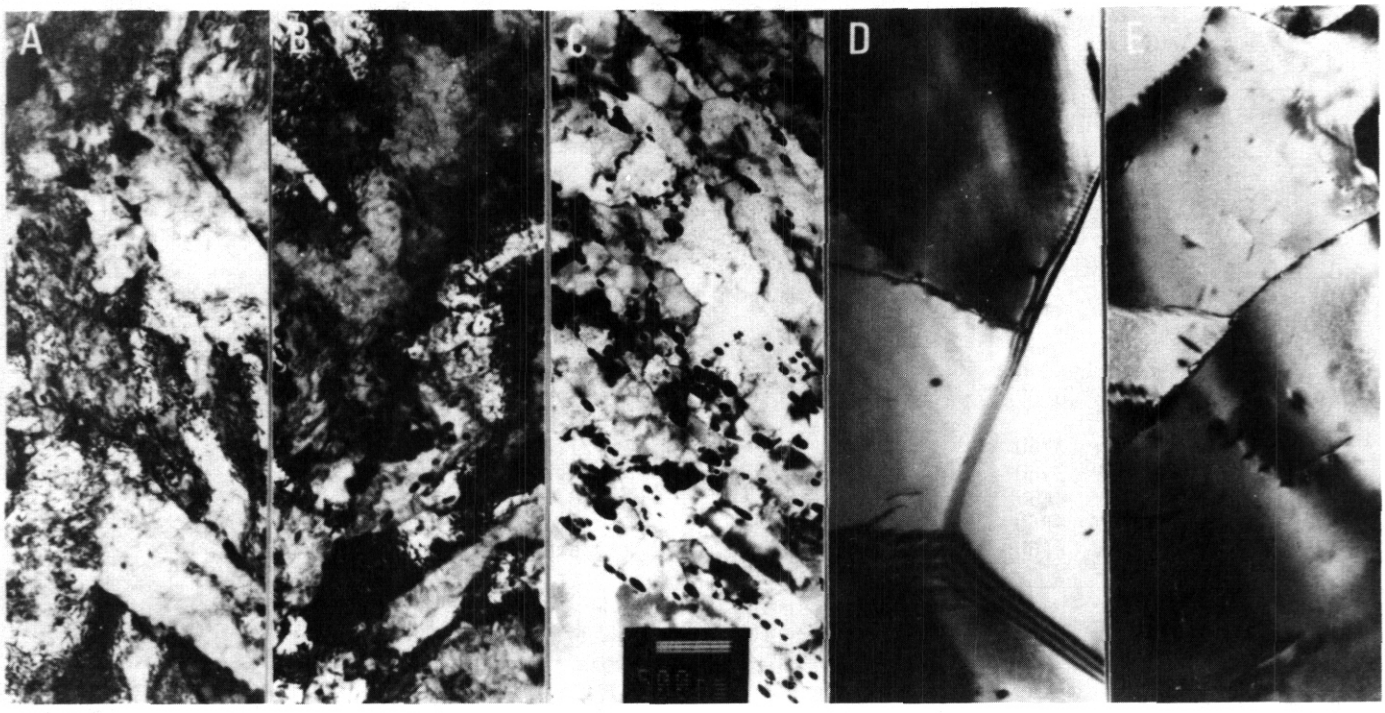


Figure 1. Microstructure of F82H irradiated in FFTF/MOTA at (a) 365°C to 6.7 dpa, (b) 405°C to 35.8 dpa, (c) 550°C to 37.0 dpa, (d) 670°C to 28.3 dpa, and (e) 750°C to 37.1 dpa.

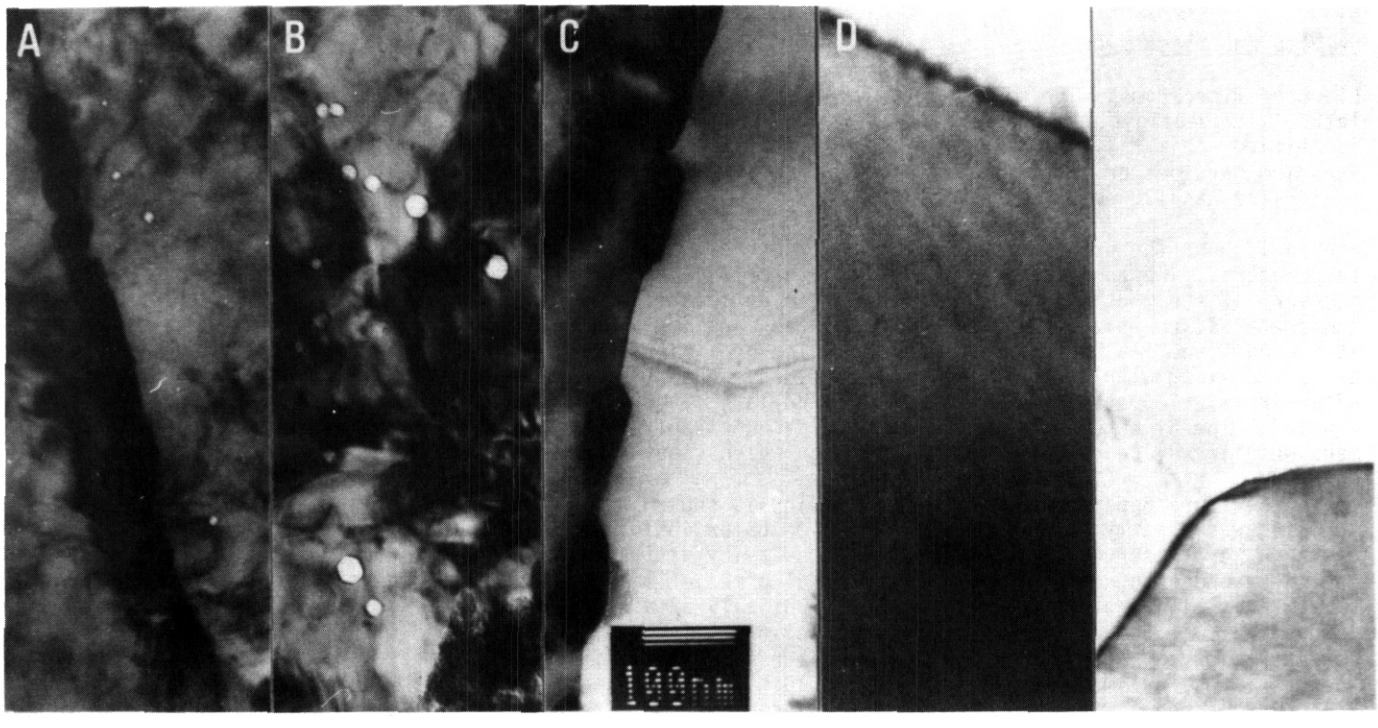


Figure 2. Cavity microstructure of F82H irradiated in FFTF/MOTA at (a) 365°C to 6.7 dpa, (b) 405°C to 35.8 dpa, (c) 550°C to 37.0 dpa, (d) 670°C to 28.3 dpa, and (e) 750°C to 37.1 dpa.

particles analyzed after 750% irradiation were tungsten-rich Laves phase with no $M_{23}C_6$ identified. The absence of carbide precipitation at 750°C is consistent with the possibility of decarburization during irradiation at high temperature.

Tamura et al. analyzed the precipitation response of F82H to thermal aging at 400 to 650°C for times up to 36 Msec.[11] They identified Laves phase precipitation in aged F82H in addition to $M_{23}C_6$ and provided the

Table 3. Quantitative Measurements for Cavity Microstructure in F82H Irradiated in FFTF

Irradiation Parameters		Cavity Parameters		
Temperature (°C)	Fluence (dpa)	Swelling (%)	Density (m^{-3})	Diameter (nm)
365	6.7	0.0073	6.8×10^{19}	12.7
405	35.8	0.14	2.3×10^{20}	22.7

Table 4. Precipitate Compositions for F82H as Determined by Extraction Replicas

Specimen Condition		Major Elements (wt%) Fe	Cr	W	Other	Number	Tentative I.D.
Unirradiated	6U,6V	28.5-33.4	40.4-52.1	17.5-25.8	--	28	$M_{23}C_6$
365°C	376V	27.2-32.9	40.8-47.7	19.0-26.7	--	24	$M_{23}C_6$
405°C	396V	28.6-33.8	46.0-52.2	17.5-21.0	--	21	$M_{23}C_6$
550°C	4A6V	18.4-28.6	44.1-58.3	20.1-32.3	--	22	$M_{23}C_6$
670°C	486V	27.2-32.6	44.9-55.2	16.5-23.0		18	$M_{23}C_6$
		28.9-35.7	57.3-57.6	--	7.0-13.4Si	3	?
750°C	4E6V-1	37.5-57.1	6.9- 9.8	33.2-54.7	--	13	Laves
	4E6V-2	36.1-47.4	6.9- 9.4	41.8-55.1	--	21	Laves

time-temperature-precipitation behavior of Laves phase shown in Figure 3, where the shaded area represents Laves phase precipitation together with $M_{23}C_6$. The results obtained from irradiated specimens in this work are also plotted in Figure 3 as circles at an aging time of 2.9×10^4 ks, which is equivalent to the 335 effective full power days of irradiation in FFTF. The open or filled circles represent an identification of only $M_{23}C_6$ or only Laves, respectively. It is likely that the nose temperature for Laves precipitation

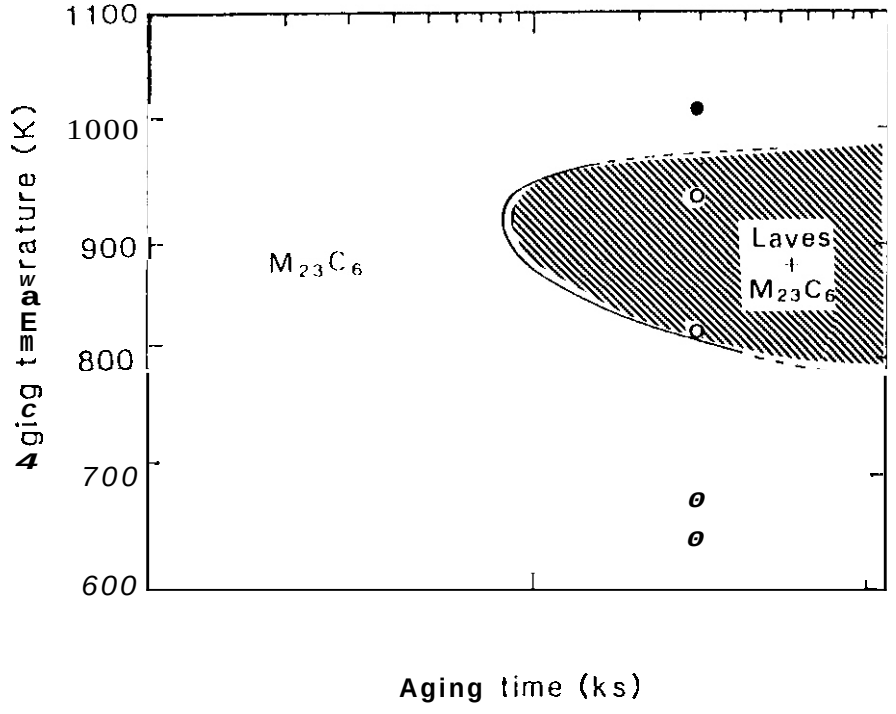


Figure 3. Time-temperature-precipitation diagram for Laves phase in F82H. Phases identified in irradiated specimens are indicated by open ($M_{23}C_6$ only) or filled (Laves only) circles at an aging time equivalent to the duration of the irradiation.

shifts with irradiation to a temperature higher than that observed in the thermally aged condition. Such a response was recently observed by Maziasz and Klueh in an Fe-9Cr-Mo,V,Nb steel."

It is worth noting that F82H exhibits better phase stability than other tungsten- or manganese-stabilized steels: neutron irradiation produces no change in the precipitation behavior of F82H, but this is not the case for other similar steels.[6,13,14] lntermetallic chi phase formation during irradiation was reported in the manganese-stabil ized steel, Fe-12Cr-6.6Mn-1Mo-0.1C-Nb,V,[13,14] and in the tungsten-stabilized steel, Fe-7.5Cr-1.95W-0.3V-0.15C.[6] Chi phase is considered detrimental to mechanical properties in these steels.

Tensile testing. The tensile data from the F82H tensile specimens are given in Table 5 and shown graphically in Figures 4 and 5. Note that the temperature axis in these figures corresponds to the test temperature for the tests on unirradiated material, while it represents the irradiation temperature for tests performed at room temperature on irradiated material. As shown in the figures, the specimens tested in the current study exhibited slightly higher strength and lower ductility than was observed in unirradiated material by researchers in Japan using larger specimens (gauge length and diameter were 30 mm [1.18 in] and 6 mm [0.24 in], respectively).[10,11] No explanation is immediately forthcoming for this difference besides the difference in specimen sizes, which is not expected to cause such variation. Table 5 also gives the strain hardening coefficients (n) that were determined by linear regression to fit the equation $\sigma = K\varepsilon^n$. The values of n are shown graphically in Figure 6. The large increase in n that occurred at the higher irradiation temperatures is consistent with the observed variations in the yield and ultimate strengths.

Table 5. Tensile Data on F82H at Room Temperature

Specimen ID	Irradiation Temperature (°C)	Neutron Exposure (dpa)	Thickness (mils)	Yield Strength (MPa)	Ultimate Strength (MPa)	Uniform Elongation (%)	Total Elongation (%)	Strain Hardening Coefficient
Unirradiated Controls								
#1-4M6U			14.3	657	865	1.5	6.0	--
#2-4B6U			14.4	704	826	1.2	4.4	0.090
#4-4Z6U			16.8	706	778	1.0	5.3	0.060
#6-XX6U[a]			13.9	647	776	1.7	4.4	--
Average			14.8	679	811	1.4	5.0	0.075
Irradiated F82H Specimens								
376U-2	365	6.7	16.6	689	766	2.9	5.8	0.049
376U-6	365	6.7	16.4	704	769	1.3	7.6	--
376U-8	365	6.7	15.7	699	805	3.0	7.2	0.060
Average			16.2	697	780	2.4	6.9	0.055
396U-0	405	35.8	16.2	674	777	3.3	7.6	0.062
396U-07	405	35.8	16.2	668	750	3.4		0.052
Average			16.2	671	764	3.4	7.8	0.057
4A6U-2	550	37.0	16.4	471	723	5.0	9.2	0.142
4A6U-3	550	37.0	15.8	469	710	5.0	9.9	0.142
Average			16.1	470	717	5.0	9.5	0.142
4B6U-1	670	28.3	15.7	248	437	15.0	25.4	0.177
4B6U-2	670	28.3	16.5	257	447	15.5	24.3	0.170
Average			16.1	253	442	15.3	24.8	0.174
4E6U-2	750	37.1	15.5	203	341	20.6	30.2	0.156
4E6U-3	750	37.1	15.3	222	368		26.4	0.151
Average			15.4	213	355	19.1	28.3	0.154

(a) ID code not noted.

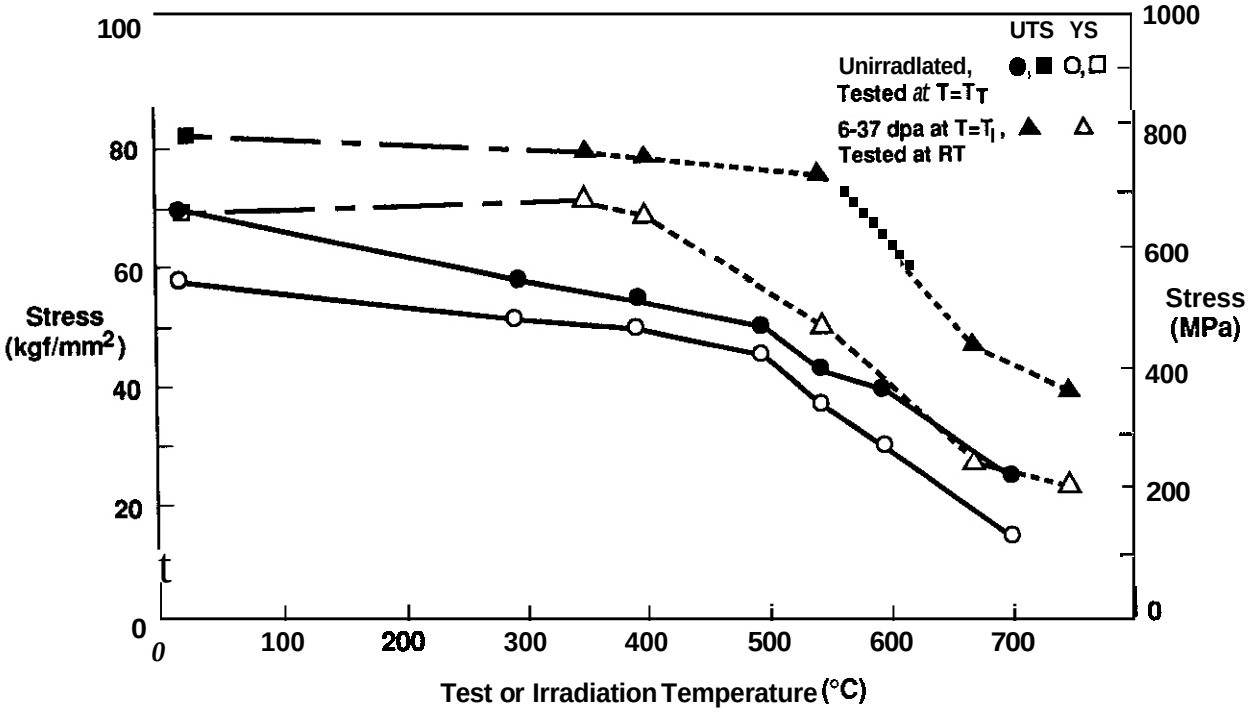


Figure 4. Strength of F82H. Tests on unirradiated specimens were performed at the corresponding temperature on the abcissa.[10] Elevated temperature tests were performed in Japan on slightly larger specimens." Tests on irradiated specimens were performed at room temperature following irradiation at the temperature indicated on the abcissa.

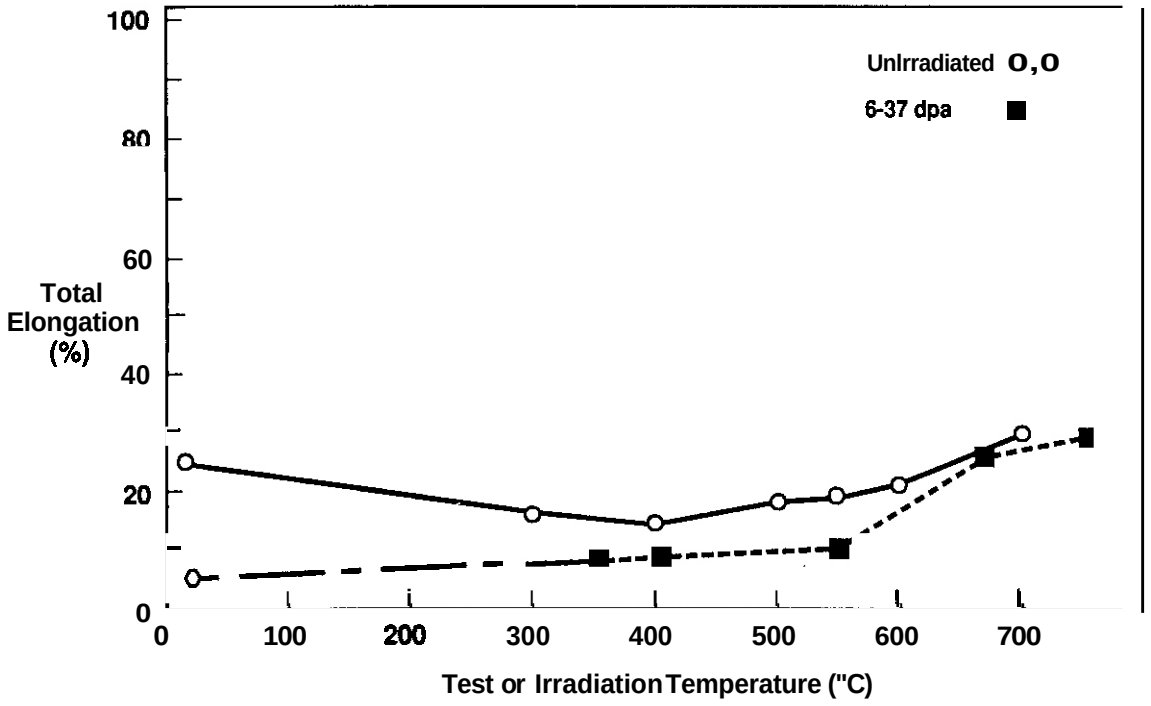


Figure 5. Ductility of F82H. Tests on unirradiated specimens were performed at the corresponding temperature on the abcissa.[10] Elevated temperature tests were performed in Japan on slightly larger specimens." Tests on irradiated specimens were performed at room temperature following irradiation at the temperature indicated on the abcissa.

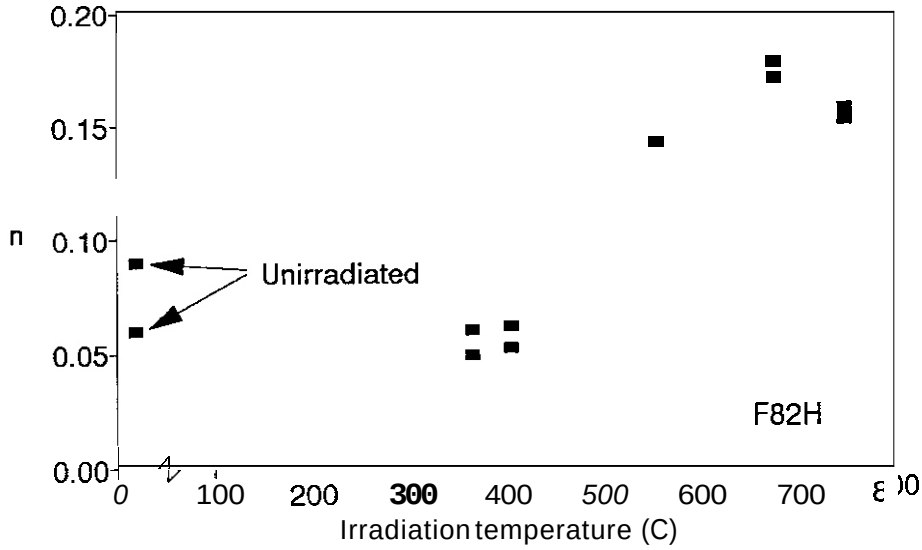


Figure 6. Work hardening of F82H.

Despite the differences in the tensile properties between the U.S. and Japanese specimens, the tensile behavior of the irradiated specimens was consistent with the observed microstructural evolution. No change in strength, ductility, or work hardening coefficient was observed after irradiation at 365 and 405°C, consistent with the fact that virtually no changes in the microstructure were observed at these temperatures. The strength dropped and the ductility increased as the irradiation temperature was increased above 550°C, consistent with the recovery of the lath structure observed in electron microscopy. Such recovery was also responsible for the increase in the work hardening coefficient observed at the higher irradiation temperatures. The recovery of the microstructure and the concomitant decrease in strength would be expected to limit the application of the alloy to temperatures below about 600°C.

CONCLUSIONS

The tempered martensite structure in F82H was quite stable during neutron irradiation at temperatures below 405°C. At higher temperatures, recovery of the martensite lath structure occurred accompanied by the coarsening of carbide particles. The tempered martensite structure was eliminated above 670°C. Cavity formation was observed only for irradiation at 405°C and below. Maximum swelling was measured to be as high as 0.14% at 405°C. Phase stability during irradiation was very good. The only precipitates identified were $M_{23}C_6$ and laves, which were also identified in thermally aged conditions. The stability of the microstructure was reflected in the tensile behavior of the alloy following irradiation. No change in strength or ductility was observed after low temperature irradiation to about 30 dpa. As the martensite structure recovered during irradiation at higher temperatures, the strength dropped and the ductility increased.

FUTURE WORK

Additional TEM disks and miniature tensile specimens are continuing irradiation in FFTF to higher neutron exposures, along with Charpy impact specimens. Examination of these specimens will be performed after the next discharge of specimens from the FFTF/MOTA.

REFERENCES

1. R. W. Conn et al., Report of the DOE Panel on low Activation Materials for Fusion Applications, UCLA/PPG-728, June 1983.

2. D. S. Gelles, in Reduced Activation Materials for Fusion Reactors, R. L. Klueh, D.S. Gelles, M. Okada, N. H. Packan, Eds., ASTM STP-1047 (1990) 113.

3. "Radiation Effects in Low Activation Steels", Report of Monbusho Grant-in-Aid for Fusion Science, Y. Hosoi, Ed., 1989 (in Japanese).

4. T. Noda, F. Abe, H. Araki and M. Okada, J. Nucl Mater., 141-143 (1986) p. 1102.

5. F. Abe, T. Noda, H. Araki and M. Okada, ibid. ref. 2, p. 130.

6. O. S. Gelles, C. Y. Hsu and T. A. Lechtenberg, Fusion Reactor Materials, DOE/ER-0313/3 (1987) p. 150.

7. R. L. Klueh, D. S. Gelles and T. A. Lechtenberg, ibid. ref. 4, p. 1081.

8. R. L. Klueh and P. J. Maziasz, ibid. ref. 2, p. 140.

9. N. F. Panayotou, S. O. Atkin, R. J. Puigh, and B. A. Chin, "Design and Use of Nonstandard Tensile specimens for Irradiated Materials Testing," The Use of Small-scale Specimens for Testing Irradiated Material, ASTM STP 888, W. R. Corwin and G. E. Lucas, Eds., ASTM, Philadelphia, 1986, pp. 201.

10. M. Tamura, H. Hayakawa', M. Tanimura, A. Hishinuma and T. Kondo, ibid. ref. 4, p. 1067.

11. M. Tamura, H. Hayakawa, A. Yoshitake, A. Hishinuma and T. Kondo, J. Nucl. Mater., 155-157 (1988) p. 620.

12. P. J. Maziasz and R. L. Klueh, "Comparison of The Effects of Long-Term Thermal Aging and HFIR Irradiation on The Microstructural Evolution of 9Cr-1Mo-VNb Steel", Presented at the 15th ASTM symposium on Effect of Radiation on Materials, Nashville, TN, June 1990, to be published in conference proceedings.

13. A. Kohyama and D. S. Gelles, FFTF/MOTA Annual Progress Report for Fusion Year 1987, National Institute for Fusion Science, Nagoya, 1988, p. 100.

14. Y. Kohno, A. Kohyama and D. S. Gelles, FFTF/MOTA Annual Progress Report for Fusion Year 1988, National Institute for Fusion Science, Nagoya, 1989, p. 210.

6.2 Austenitic Stainless Steels

SOME IMPLICATIONS OF RADIATION-INDUCED PROPERTY CHANGES IN AUSTENITIC STAINLESS STEELS ON ITER FIRST-WALL DESIGN AND PERFORMANCE -- P. J. Maziasz, A. F. Rowcliffe, M. L. Grossbeck, G.E.C Bell, E. E. Bloom, and D. C. Lousteau (Oak Ridge National Laboratory), A. Hishinuma and T. Kondo (Japan Atomic Energy Research Institute), and R. F. Mattas and D. **L.** Smith (Argonne National Laboratory)

OBJECTIVE

The objective of this program is to collect the property change data and the best available insight on underlying mechanisms to provide input on the behavior of irradiated type **316** austenitic stainless steel to the ITER project.

SUMMARY

New data on radiation-induced hardening, low-temperature creep and potential susceptibility (sensitization) to aqueous corrosion have been obtained on various heats of austenitic stainless steel (including type **316)** irradiated at **60** to 400°C to 7 to **13** dpa. The data were obtained from spectrally tailored reactor experiments, whose radiation-damage parameters are similar to those in the proposed International Thermonuclear Experimental Reactor (ITER) first-wall (FW) and blanket design. Austenitic stainless steels were found to increase significantly in strength at **60** to 330°C, to have higher irradiation-creep rates at 60°C than at 200 to 400°C, and to show radiation-induced changes in electrochemical properties at 200 to 400°C. These data on several radiation-induced property changes suggest that type **316** steel may be an adequate material for the FW of ITER. However, there is definitely a need for new data on fracture-toughness and on fatigue behavior below 400°C, as well as more data on irradiation-creep and effects of irradiation on corrosion properties, to better define temperature and dose dependencies for more detailed design analyses. Cold-working should remain an optional as-fabricated condition for the FW of ITER. Many properties of SA and CW **316** become similar after irradiation at **60** to 400°C. The higher initial yield-strength of CW **316** will allow higher design stress and elastic strain limits.

PROGRESS AND STATUS

Introduction

The International Thermonuclear Experimental Reactor (ITER), currently in the conceptual design phase, is a collaborative effort between four major parties - the European Community, the Soviet Union, the United States, and Japan. The ITER project is an attempt to provide a common next-step in large fusion devices beyond existing large tokamak experiments that include TFTR (U.S.), JET (E.C.) and JT-60 (Japan). ITER has much in common with the earlier Next European Torus (NET) design project,'.' but ITER is more aggressive in terms of its technology phase and the demands that irradiation exposure will place on the first-wall (FW) and blanket structural materials. The ITER reference FW material is type **316** austenitic stainless steel. Type **316** was chosen primarily because of the large amount of worldwide experience with this steel for reactor core component and structural applications in the fission reactor industry.' However, the FW irradiation conditions anticipated for ITER push type **316** stainless steel into a new regime of radiation damage for which only limited data are available to answer important design questions.'"

The spectrally-tailored experiments conducted in the Oak Ridge Research Reactor (ORR) by the U.S. and U.S./Japan Collaborative Fusion Materials Programs provide some of the most relevant data to date for ITER.'' One purpose of this paper is to summarize the most recent data on radiation-induced property changes in austenitic stainless steels from these experiments. Another purpose is to consider the implications of the available data on austenitic stainless steels for current materials performance requirements and critical issues emerging from the ITER design studies. Finally, this report addresses some of the data needed from future reactor experiments.

ITER First-Wall Materials Parameters

A summary of current materials parameters being assumed and specified for design and performance of the ITER FW is given in Table **1.**[1,3,4] A schematic cross-section of the first wall is shown in Fig. **1,** with two sheets of steel surrounding a channel of cooling water. The reference FW material for ITER is type **316** stainless steel in the solution-annealed (SA) condition: whereas type **316L** (low-carbon) was selected for NET.' Cold-worked type **316** and a manganese-stabilized austenitic steel are also being considered as alternate FW materials.'

Table 1. ITER first wall materials parameters (technology phase, normal operation)

Material	Type 316 SS
Neutron wall loading. MW/m²	1
Damage rate. dpa/s	(3–4)
Damage levels	
dpa	10–50
appm Heldpa	10–15
appm H/dpa	52
Temperature. °C	90–350
Number of pulses, × 10^{-4}	(2–6)
Total burn time, h	>21,000
Primary stress limit (S_m)	213 yield strength or 1/3 ultimate tensile strength
Secondary stress limit	3 × S_m
Coolant pressure. MPa	1–2

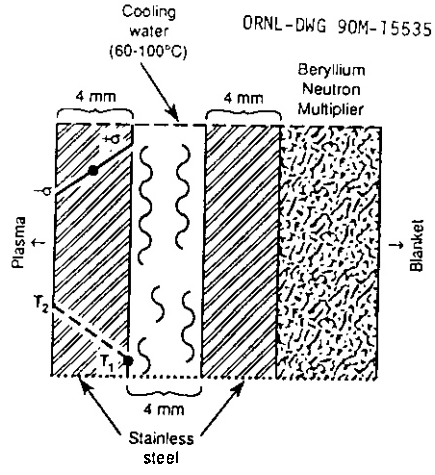


Fig. 1 A schematic cross-section of the first-wall, including double walls of steel surrounding a channel of cooling water. The temperature and related secondary stress gradient expected during plasma burn cycles are also indicated.

The maximum limit for primary stress (S_m, Table 1) is derived from Section 3, Division 2 of the **ASME** boiler and pressure vessel code; the maximum secondary stress is usually limited to three times the primary stress ($3S_m$). The coolant water temperatures range from 60°C inlet to 100°C outlet. During the plasma burn cycle, heat fluxes will produce the temperature profile shown in Fig. 1, which in turn will produce a stress gradient due to differential thermal expansion. T_1 should be close to the local coolant temperature, while T_2 will vary during the plasma burn cycles. T_2 may be as high as 350°C.[1] Detailed neutronic, thermal and stress analyses for ITER have not yet been completed. However, thermomechanical studies for NET performed on a similar FW configuration define maximum cyclic strain limits (due to peak thermal stresses caused by peak FW surface heat fluxes ranging from 0.3-0.5 MW/m^2) as about 0.4% total strain (elastic + plastic) during the physics phase, and about 0.2% during the technology phase.[1] These correspond to the maximum allowable strains that allow a fatigue life of 10^4 to 10^5 cycles for SA 316L at 425°C.

Radiation-Induced Property Chanees in Austenitic Stainless Steels

Spectrally-Tailored Experiments

Data described here have been derived from two spectrally-tailored irradiation experiments conducted in the Oak Ridge Research Reactor (ORR), MFE-4 and MFE-6J/7J. Detailed descriptions of these experiments, and of the spectral-tailoring technique can be found elsewhere.[1,3] Spectral-tailoring involves changing the materials that surround the experimental subassembly in mixed-spectrum fission reactors like ORR to change the ratio of fast to thermal neutron fluxes irradiating the specimens. The fast neutrons (E>0.1 MeV) produce displacement damage (dpa) while the thermal neutrons produce helium atoms via a two-step transmutation reaction with ^{58}Ni. The ORR-MFE-4 experiment was conducted by the U.S. Fusion Materials Program at temperatures of 330, 400, 500 and 600°C to a peak dose of 13 dpa, with 12 appm He/dpa in type 316 (12-13 wt % Ni) and 18 appm Heidpa in PCA (16 wt % Ni) austenitic stainless steels. The ORR-MFE-6J/7J experiment was conducted under the U.S./Japan Collaborative Agreement for fusion materials testing,[3] at temperatures of 60, 200, 330 and 400°C to a dose of 7 dpa, with Y appm Heidpa in type 316 and 12 appm He/dpa in PCA.[4]

Various heats of austenitic stainless steel were irradiated in these experiments, including U.S. and Japanese heats of type 316 (Fe, 16-18Cr, 12-14Ni, 2.5Mo, 2Mn, in wt %) or Ti-modified PCA type (Fe, 14Cr, 16Ni, 2Mo, 2Mn) stainless steels? Various kinds of specimens were irradiated, with the as-fabricated metallurgical condition usually being either solution-annealed (SA) or 15 to 25% cold-worked (CW).

Hardening

The major effect of irradiation below 500°C on the tensile properties of austenitic stainless steels tested at the irradiation temperature is hardening. Hardening generally describes the large increases in yield strength ***(YS)*** that correlate with reduced ductility [uniform elongation (UE) and total elongation (TE)]. Radiation-induced hardening is caused by the point-defects and microstructural evolution produced during irradiation. Hardening only produces emhrittlement when it becomes so severe that materials fail in the elastic regime (lower strength, no ductility).

Plots of YS, UE and TE as functions of irradiation temperature are shown in Fig. 2; all tests were carried out at the irradiation temperature. After irradiation, both SA and CW austenitic stainless steels become very strong, with YS values in the range of 700 to 1000 MPa at 60 to 330°C [Fig. 2(a)] and ***YS*** about the same as the ultimate tensile strength (UTS).[9] The CW material is initially much stronger than SA material, and remains 100 to **200** MPa stronger after irradiation. Steels irradiated in ORR-MFE-6JDJ appear to be strongest at 330°C. The data from ORR-MFE-6J/7J at 7 dpa agree reasonably well with design curves of the **YS** after 10 dpa, for many SA and CW steels irradiated in a variety of fission reactors.[1,3]

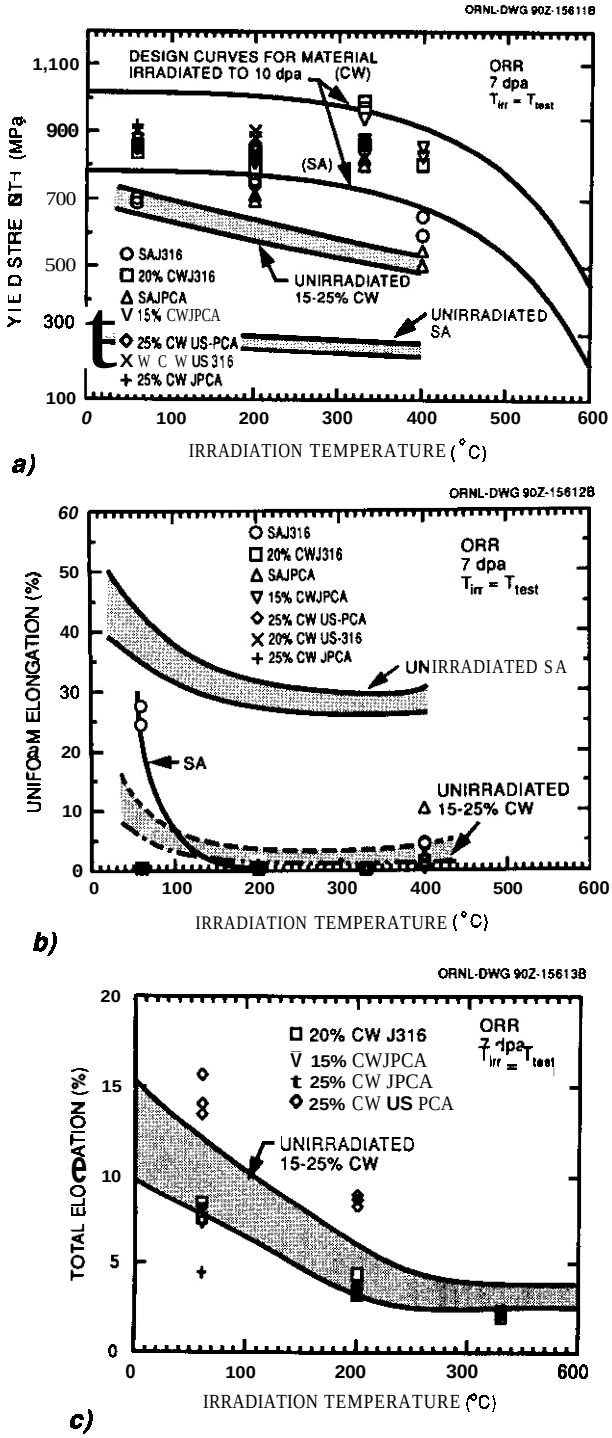


Fig. 2 a.) Yield stress (YS), b.) uniform elongalion (UE), and c.) total elongation (TE) as functions of irradiation temperature for various heats of austenitic stainless steel irradiated in ORR-MFE-6J/7J.[9] The design curves for YS in a.) were generated from other data described elsewhere.[1]

Ductility, as measured by UE, is <1% in CW steel after irradiation at 60 to 330°C in ORR, and is similar for SA steels at 200 to 330°C [Fig. 2(b)]. Irradiation more severely reduces UE in SA material because it is initially much more ductile than CW material. The UE of unirradiated CW steel is much lower than SA steel, and can be as low as 1% in steels like 25% CW PCA at 100 to 400°C.[11] However, TE values for CW material irradiated at 60 to 330°C are 2 to 15%, about the same as found in unirradiated CW material [Fig. 2(c)]. The decline in TE with increasing temperature at 60 to 330°C is consistent with maximum hardening occurring at 330°C. Low UE values suggest limited work-hardening capability in the irradiated steels. However, the higher TE values (Fig. 2) indicate that even after irradiation to 7 dpa, these alloys retain a substantial capacity for plastic deformation. A ductile-transgranular 'fracture mode has been observed in similar steels irradiated in HFIR at 60°C[12] and 400°C[13] to 10 to 20 dpa, which also had very low UE.

Irradiation-Creeo

Irradiation-creep generally describes deformation that would not occur unless the material was exposed to both displacement damage and stress. This radiation-induced phenomenon is linear with stress and weakly dependent on temperature. It arises from the complex interactions between the point defects and the dislocation microstructure during irradiation. The existing data base is derived primarily from irradiation-creep experiments performed in fast breeder reactors (FBR) at temperatures of 400°C and above and at Heldpa ratios of 0.5 to 1 appm He/dpa.[14,15]

Data from pressurized-tube specimens of CW PCA stainless steel irradiated at 400°C in ORR experiments spectrally-tailored to produce Heldpa ratios in the range of 12 to 18 appm/dpa are shown in Fig. 3. The ORR data clearly fall above those obtained from similar specimens irradiated in FFTF with a Heldpa ratio of about 0.3 appm/dpa.[16] These data suggest that helium enhances the irradiation-creep rate, although issues involved in the interpretation are not completely resolved;[16] irradiation-creep is sensitive to damage rate, and possibly other spectral effects as well.

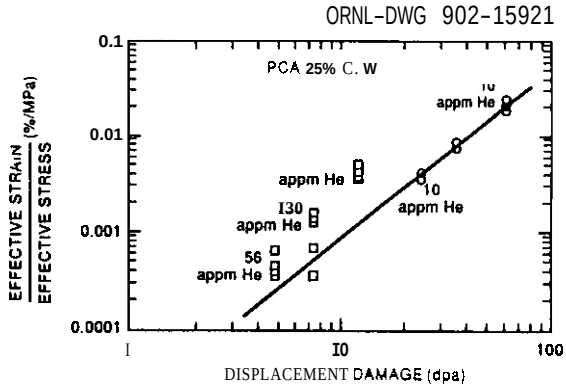


Fig. 3 Iradiation-creep data from pressurized tube specimens of 25% CW PCA austenitic steel irradiated in ORR (MFE-4 and -6J/7J)[7] and FFTF[16] at about 400°C.

Recent data from the ORR-MFE-6J/7J experiment show an unusual temperature dependence of in-reactor creep strains at 60 to 400°C (Fig. 4).[18] Irradiation-creep strains at 60°C were higher than those found at 200 to 400°C. Other steels in the same experiment, including a simple Fe-Cr-Ni ternary alloy, and J316 and JPCA austenitic and HT-9 martensiticlfemtic steels also exhibit enhanced creep at 60°C. A model based upon transient interstitial absorption **by** dislocations has been proposed to explain this phenomenon."

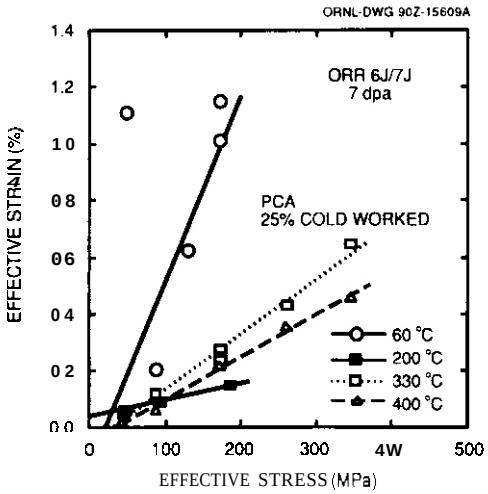


Fig. 4 Radiation-creep data from pressurized tube specimens of 25% CW PCA austenitic Steel irradiated in ORR-MFE-6J/7J at 60-400°C to about 7 dpa (12 appm Heidpa)."

Radiation-Induced Effects on Selected Corrosion Proverties

Irradiation-assisted stress-corrosion cracking (IASCC) is a major form of environmental degradation for austenitic stainless steels in water-cooled fission reactors.[19] IASCC has also recently become a major concern for fusion reactors like ITER which feature a water-cooled austenitic stainless steel FW.[20,21] IASCC has been found in type 304 stainless steel irradiated at 288°C to <1 dpa, manifesting itself as intergranular stress-corrosion cracking (IGSCC). IGSCC is suggested to be caused either by segregation of impurities like S, P and Si to the grain boundaries, or by Cr depletion at the grain boundaries so that grain boundaries are no longer "stainless" (<12% Cr) or "sensitized." While precipitation of Cr-rich carbides can cause sensitization during thermal aging, Cr-depletion at grain boundaries during irradiation is generally caused by radiation-induced solute-segregation (RIS).

Inazumi and Bell[20] have developed a technique for applying the electrochemical potentiokinetic reactivation (EPR) method for detecting Cr-depletion to miniature specimens (3-mm-diam disks). The EPR technique is described in detail elsewhere.[20-22] EPR quantitatively measures the degree of sensitization in terms of a reactivation charge per unit of "active area" (P_a, C/cm^2). In thermally aged specimens, P_a is calculated using the grain boundary area, but in neutron-irradiated specimens, RIS causes attack at both grain boundary and matrix microstructural features, so that the entire specimen becomes "active area."

Recent EPR data by Inazumi and Bell[23] on disks of 25% CW PCA stainless steel irradiated in ORR-MFE-6J/7J to 7.4 dpa show significant radiation-induced changes in corrosion behavior at 200 to 400°C relative to control material, but no change at 60°C (Fig. **5).** P_a is several orders of magnitude greater after ORR irradiation at 400°C, and similar to that found for SA and CW PCA irradiated in FFTF at 420°C to 9 dpa.[21] Subsequent X-ray microcompositional analysis using analytical electron microscopy (AEM) confirmrd Cr depletion at grain boundaries which was caused by (RIS)." Surface examination of the EPR-tested disks showed clear grain boundary attack after ORR irradiation at 400°C, only matrix etching with no attack at grain boundaries at 200°C, and no etching effects at 60°C (Fig. 6).

Radiation-Induced Swelling

Swelling due to radiation-induced voids is a major concern for the FW of fusion devices at temperatures of 400°C and above, and has been the focus of considerable alloy development effort?"'' Recent data from ORR-MFE-4 have shown that helium-enhanced void swelling at 500°C can be significant after only 11 to 13 dpa in advanced alloys like the titanium-modified PCA stainless steel.' Through the 1980s, the FW temperatures in various fusion reactor design concepts have progressed toward 350°C and below, as currently anticipated for ITER."' Data at 7 to **13** dpa have been obtained for various austenitic stainless steels (SA and CW conditions) irradiated in spectrally-tailored experimrnts which reproduce the Heidpa ratio and dpa rate anticipated for the FW of ITER. These data have been used to develop the preliminary swelling equation shown in

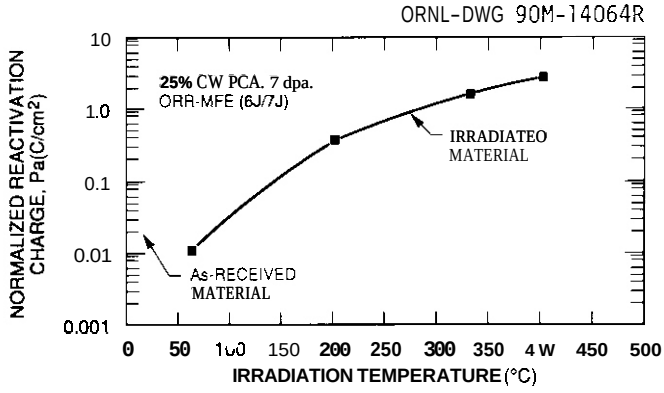


Fig. **5** The reactivation charge per unit of "activated' area (P_a), as measured by EPR testing of miniaturized specimens of 25% CW PCA austenitic steel irradiated ORR-MFE-6J/7J to 7 dpa" plotted as a function of irradiation temperature. The P_a value for unirradiated control material is also shown.

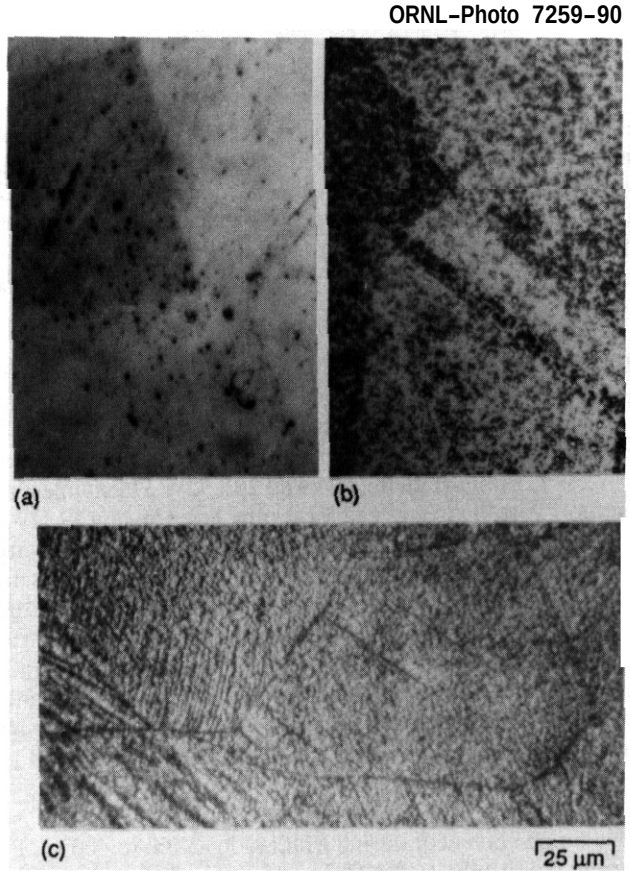


Fig. 6 Optical microscopy of the surface of disc specimens of 25% CW PCA irradiated to 7 dpa in ORR-MFE-6J/7J after EPR testing.[22] a.) T_{irr}=60°C no etching within grains or at grain boundaries. b.) T_{irr}=200°C, etching of grain interiors only. c.) T_{irr}=400°C, etching within grains and at boundaries.

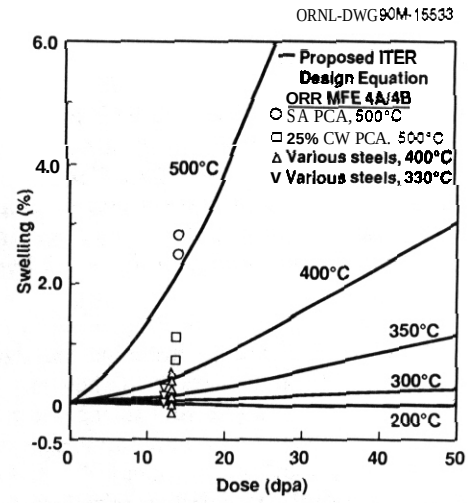


Fig. 7 Proposed ITER swelling equation for austenitic stainless steels irradiated at fusion relevant He/dpa ratios and damage rates (R.E. Stoller, ORNL). Swelling data at 11-13 dpa is from ORR-MFE-4.[11]

Fig. 7. The incubation dose and swelling rate parameters of the bilinear swelling equation, developed by the U.S. Breeder Reactor Materials Program, have been adjusted so that the equation fits the data from the spectrally-tailored experiments. This proposed equation indicates that, provided FW temperatures do not exceed 400°C, swelling of SA 316 or SA PCA austenitic stainless steels will be limited to about 2% after 35 dpa.

If ITER FW temperatures reach 400°C or above, void swelling cannot be dismissed as a concern. Transmission electron microscopy (TEM) of PCA stainless steel disks irradiated in ORR-MFE-4 to 13 dpa at 400°C clearly show the advantage of CW material with regard to void swelling resistance (Fig. 8). SA PCA with large voids shows about 0.4% swelling, while CW PCA with only a dense dispersion of very small helium bubbles shows none. Often concerns about welding and/or sensitization to aqueous corrosion encourage the choice of low-carbon austenitic stainless steels like type 316L in the SA condition. However, data from both FBR and mixed-spectrum reactor irradiation experiments show that low-carbon austenitic stainless steels are much less resistant to void swelling than steels containing 0.4 to 0.6 wt % C, particularly in the SA condition.[4,29]

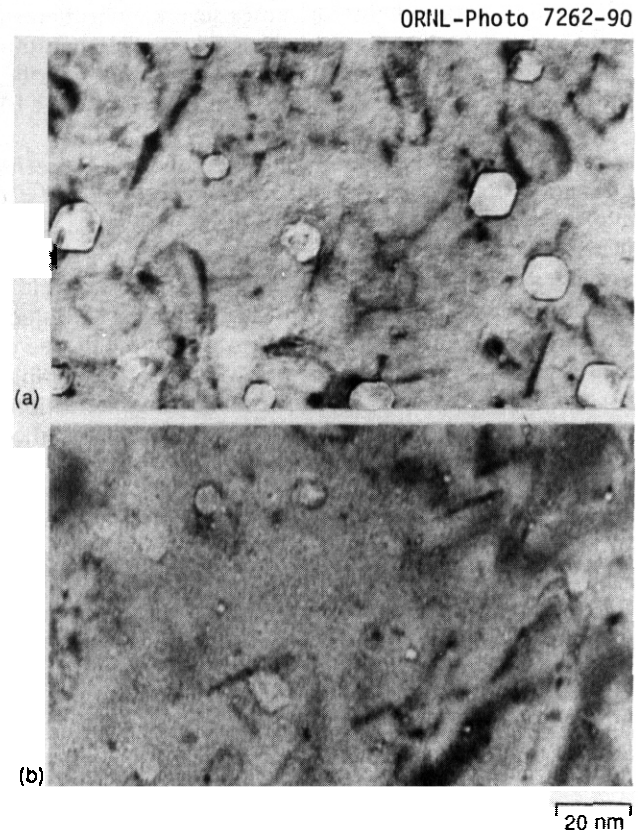


Fig. 8 TEM showing a.) large voids in SA PCA and b.) fine helium bubbles in 25% CW PCA, irradiated in ORR-MFE-4 at 400°C to 13 dpa.

Implications of Current Data on ITER First-Wall Design and Performance Issues

Performance Issues

Several recent review papers by Boutard,[3] Rowcliffe et al.[4] and Grossbeck et al.[18] have summarized available data on the effects of irradiation on various properties of austenitic stainless steels, and have identified some critical issues related to their use as the FW material for ITER. There is some concern about radiation-hardening causing such low ductility at irradiation temperatures of 300°C and below, and about a related loss of fracture toughness. Boutard[3] put particular emphasis on low-cycle fatigue behavior at <250°C and crack propagation, and expressed concerns about hydrogen embrittlement and IASCC. Irradiation creep at lower temperatures is an important phenomenon which has not yet been taken into account in design studies.[4,18]

With regard to radiation-hardening, the data summarized here suggest that the austenitic stainless steels irradiated at 60 to 400°C have not become embrittled; they have such low UE because they have little capacity for additional strain-hardening since they have already become very strong due to the irradiation-produced dislocation structure. With regard to impact and toughness behavior, a plane-strain fracture toughness parameter K_{IC} can be calculated from tensile data using a modified-Krafft model when failure is localized but ductile.[30,31] Calculations of K_{IC} at 250°C for unirradiated SA and 20% CW 316 stainless steel and for those materials irradiated in mixed-spectrum fission reactors[10,18] as a function of dose are given in Fig. 9. While irradiation reduces the fracture toughness, K_{IC} values saturate with dose and remain in the 50 to 75 MPa-m$^{1/2}$ range to about 50 dpa, with CW and SA materials achieving similar saturation values. These results are consistent with actual fracture-toughness data obtained for FBR irradiated SA and 20% CW 316 steel at 380 to 427°C at 8 to 12 dpa[32] and up to 85 dpa.[31] At the highest FBR dose levels, microstructural evolution and RIS produce an unstable austenite matrix that either partially decomposes to ferrite during irradiation, or forms strain-induced martensite during post-irradiation testing at room temperature. This microstructural behavior causes severe embrittlement, with a brittle "quasi-cleavage" failure mode at lower temperatures and "channel" fracture closer to the irradiation temperature. However, these specimens irradiated to 85 dpa still show K_{IC} values of about 80 MPa-m$^{1/2}$ after testing at 32 to 425°C. Further detailed design analysis is required to determine exactly what level of fracture-toughness will be satisfactory for the ITER FW.

Another important mechanical properties concern is low cycle fatigue behavior during irradiation at 100 to 400°C. Post-irradiation, strain-controlled fatigue data on 20% CW 316 steel irradiated in HFIR at 430°C to 15 dpa indicated a reduction in low-cycle fatigue life by a factor of 3 to 10, and a slight reduction in the endurance limit relative to unirradiated material.[33] It is important that an endurance limit for irradiated material was found at a total strain level of 0.15%; the fatigue life of irradiated material should be adequate if strains are held below this value. It is also important to note that reduced fatigue life was attributed to radiation-induced hardening by dislocation loops, not helium embrittlement. Fatigue resistance at lower irradiation temperatures is a concern due to the degree of radiation-hardening that occurs. But in-reactor fatigue may also be significantly different than the behavior observed during long-term post-irrradiation tests. Post-irradiation fatigue data must be complemented by in-reactor testing. The interaction of cyclic stresses (and temperatures) with the transient point defect concentrations and the dynamic microstructural evolution produced during irradiation may affect the mechanisms that cause deformation as well as crack nucleation and growth during in-reactor fatigue. For example, irradiation-creep could extend fatigue life by reducing stress, particularly the stress intensity at crack tips. Furthermore, radiation-hardening will increase the elastic strain limit, making small fatigue strains elastic rather than plastic and less damaging. Data from in-reactor fatigue experiments being conducted at 250°C to 2 dpa will shortly be available from the European Technology Programme.[34]

While the high rate of irradiation-creep observed at 60°C is somewhat surprising, it should not cause problems unless deformation strains become too large. Irradiation-creep should be beneficial for relieving stresses,[18] which would improve the situation with regard to problems associated with fatigue resistance, void swelling, and IASCC. However, if creep relieves the secondary stress gradient during irradiation (Fig. 1), a reverse stress gradient will be present in the FW during shutdown when the plasma is quenched. Evaluating such behavior during the service lifetime will definitely require both more detailed design analysis and more detailed materials data.

Finally, the current data showing no electrochemical attack of the 14Cr-16Ni PCA steel after irradiation at 60°C is encouraging with regard to concerns about IASCC for the stainless steel FW in contact with water at 60 to 100°C (Fig. 1). The etching observed during EPR testing of specimens irradiated at 200 to 400°C indicates that grain-boundary attack only occurred at 400°C. IASCC could adversely affect fatigue life if cracks initiated on the coolant side of the FW then cause material irradiated at higher temperatures to come in contact with coolant water. It is important to understand the effects of (RIS) and the potential for IASCC for austenitic steels irradiated at 100 to 150°C since there is such a large change in behavior between 60 and 200°C. Moreover, matrix pitting as observed at 200°C could be deleterious if it makes the material prone to transgranular stress corrosion cracking during irradiation.

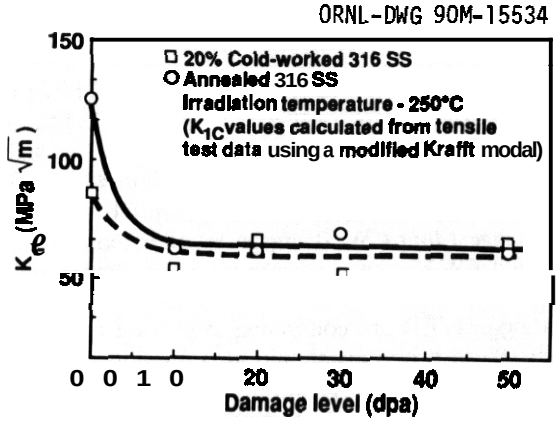


Fig. 9 Calculated fracture-toughness at 250°C using a modified Krafft model following Hamilton:' based on tensile data from 20%CW 316 steel irradiated in various mixed-spectrum reactors at 250°C.[10]

Fabrication Issues

Usually this topic includes specifying the physical metallurgical variables of alloy composition and the final thermomechanical condition of the as-fabricated material, as well as recommendations regarding welding/joining practice. The current choice of FW material for ITER is SA type 316 stainless steel, with CW type 316 being considered as an alternate choice.) In genereal, austenitic stainless steels are processed by various hot-, warm-, or cold-wrought steps into final product form prior to the final solution-annealing treatment. Neither solution-annealing nor cold-working is a precisely defined metallurgical state. SA material can be "dead-soft" (minimum YS) or mill-annealed with some small amount of strain for straightening or final conditioning that corresponds to 5 to 10% CW. Boutard has called attention to the fact that if the FW is fabricated from SA 316, cyclic fatigue during the Physics Phase of operation will plastically deform and harden the FW, so that material will not be strictly in a SA or 20 to 25% CW condition when irradiation begins.[3] The use of the much higher initial YS of CW austenitic steel will allow design stress limits to take advantage of the high strength that irradiated material will eventually possess. In addition, the higher initial strength of CW material may allow FW to be thinner, which would reduce stresses caused by thermal gradients. Finally, increased YS should allow the strains produced by thermal expansion to be elastic rather than plastic, which is beneficial for fatigue resistance.

With regard to welding prior to irradiation, both SA aind CW J316 have been welded satisfactorily by electron-heam (EB, autogenous) and tungsten-arc, inert gas (TIG, filler-metal) techniques prior to irradiation in the ORR-MFE-6J/7J experiment?' Both weld-joint (EB, TIG) specimens [gage section consisting mainly of heat-affected-zone (HAZ) plus weld-metal] and weld-metal (TIG) specimens of SA and CW J316 were irradiated at 60 to 400°C. The tensile properties of these various welded specimens were intermediate to those observed for irradiated SA and CW base-metal snecimens. Similar results were found for earlier experiments on 20% CW 316 TIG-welded with 16-8-2 filler metal and irradiated in HFIR at 5 to 10 dpa at 60°C.[12] Therefore, it appears that initially good welds will continue to remain good during irradiation. One concern about the use of CW material is that the HAZ will be softer than the base-metal. However, initial fatigue strains produced during the Physics Phase will most likely harden the softer-regionsto produce more uniform strength. Repair welding of irradiated material may also be an important maintenance issue. Work by Lin et al.[35] on welding of type 316 stainless steel preimplanted (tritium trick method) with various amounts of helium showed that as little as 25 appm He produced cracking in the HAZ, as shown in Fig. 10. Material that contained only 0.2 appm He was weldable. Weld repair may still be possible after the earliest shake-down runs of ITER, and special weld-overlay methods with low heat input may help avert intergranular helium embrittlement in the HAZ at 1 to 2 appm He. However, such difficulties with in-service weld repair will place a greater emphasis on making good initial welds.

ORNL-Photo 7263-90

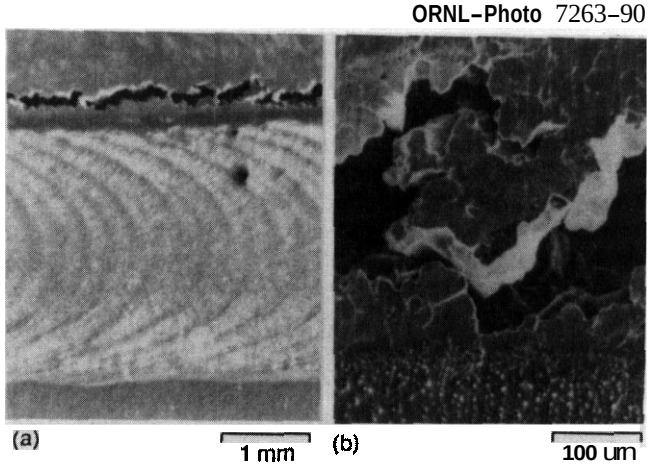


Fig. 10 a.) lower magnification optical microscopy showing cracking in the heat-affected-zone and b.) higher magnification scanning electron microscopy showing intergranular cracks in as-welded type 316 stainless steel containing 2.5 appm He.[35]

SUMMARY AND PERSPECTIVE

New data on austenitic stainless steels irradiated in spectral-tailoring experiments in ORR at 60 to 400°C to 7 to 13 dpa show significant effects of irradiation on properties. Irradiation causes rapid hardening of the steels at 60 to 330°C, but does not induce brittle behavior. Irradiation induces a significant adverse change in electrochemical behavior at 200 to 400°C, but not at 60°C. Irradiation surprisingly induces higher rates of radiation-creep at 60°C than are found at 200 to 400°C. Swelling appears to be minimal during irradiation at 350°C and below. Together, these data point to the potential for type 316 to perform satisfactorily as the FW material for ITER. The data further suggest that CW 316 may be better than SA 316 from the standpoint of higher initial YS and of better void swelling resistance if FW irradiation temperatures exceed 350°C.

Ongoing national programs by the four major parties participating in ITER are continuing to provide the information needed for the conceptual design studies. During the next few years, these programs should also provide significant new radiation effects data on fracture toughness and IASCC, and extend the mechanical properties data base on irradiated steels to higher doses. The present data base on the properties of irradiated material is insufficient to allow the detailed performance analyses which will be required in the engineering design phase of ITER. A well coordinated, international effort will be needed to define the most appropriate reactor irradiation conditions, the reactor facilities, and the testing methodologies, and to develop a comprehensive data base on prototypic commercial heats of austenitic stainless steel.

Although SA 316 is the logical first choice as a fabrication option, a range of alternate options should also continue to be studied. While the 15 to 25% CW condition provides high initial YS, intermediate CW levels of 5 to 15% might produce a better combination of YS and UE during irradiation. Rather than simple, conventional SA or CW treatments, specialized thennomechanical processing like the SAR (strained, aged and recrystallized) treatment developed at JAERI to minimize IASCC may be attractive for type 316. The ultrafine grain size produced by the SAR treatment may also provide better ductility and toughness at similar levels of strength after irradiation. Goals should include both meeting minimum requirements as well as attempting to achieve maximum performance.

ACKNOWLEDGMENTS

Research was sponsored by the Office of Fusion Energy, U.S. Department of Energy, under Contract DE-AC05-84OR21400 with Martin Marietta Energy Systems, Inc., at the Oak Ridge National Laboratory, and under Contract W-31-109-ENG-38 with the Argonne National Laboratory, and by the Collaborative Research program between the Japan Atomic Energy Institute (JAERI) and the Office of Fusion Energy.

REFERENCES

1. M. Chazalon et al., "Next European Torus In-Vessel Components: Fusion Technology, 14, 82 (1988)

2. P. Schiller and J. Nihoul, "Projected Materials Requirements for the Next European Torus and for Longterm Tokamak-Based DEMO Fusion Devices: J. Nucl. Mater., 155-157, 41 (1988).

3. J. L. Boutard, "Structural Material Requirements and Related Research and Development for ITER In-Vessel Components," ICFRM-4 Proc. (Dec., 1989); to be published in J. Nucl. Mater. in 1991.

4. A. F. Rowcliffe et al., "Radiation Effects at Fusion Reactor He:dpa Ratios: Overview of U.S./Japan Spectral Tailoring Experiments," ibid. ref. 3.

5. R. E. Stoller et al., "Swelling Behavior of Austenitic Stainless Steels in a Spectrally Tailored Reactor Experiment: Implications for Near-Term Fusion Machines," J. Nucl. Mater., 155-157, 1328 (1988).

6. M. L. Grossbeck and K. R. Thorns, "ORR-MFE-4: Spectral Tailoring Experiment to Simulate the He/dpa Ratio of a Fusion Reactor," ADIP Quart. Proe. Rep., June, 1980, DOE/ER-0045/3, pp. 10-24.

7. M. L. Grossbeck and J. A. Horak, "Irradiation Creep in Type 316 Stainless Steel and US PCA with Fusion Reactor He/dpa Levels," J. Nucl. Mater., 155-157, 1001 (1988).

8. J. L. Scott et al. "Program of United States-Japan Collaborative Testing in HFIR and ORR," J. Nucl. Mater., 141-143, 996 (1986).

9. M. L. Grossbeck et al., 'Tensile Properties of Austenitic Stainless Steels Irradiated in the ORR Spectral Tailoring Experiment ORR-MFE-6J and -7J," Fusion Reactor Materials Semiannu. Proe. Reut., March 1989, DOE/ER-0313/6, pp. 259-268.

10. M. L. Grossbeck, "Empirical Relations for Tensile Properties of Austenitic Stainless Steels Irradiated in Mixed Spectrum Reactors," ihid ref. 3.

11. D. N. Braski, 'Tensile Properties of Unirradiated PCA From Room Temperature to 700°C," J. Nucl. Mater., 122&123, 338 (1984).

12. F. W. Wiffen and P. J. Maziasz, 'The Influence of Neutron Irradiation at 55°C on the Properties of Austenitic Stainless Steels," J. Nucl. Mater., 103&104, 821 (1981).

13. P. J. Maziasz and D. **N.** Braski, "Modificationof the Grain Boundary Structure of the Austenitic PCA Stainless Steel to Improve Helium Embrittlement Resistance," J. Nucl. Mater., 141-143, 973 (1986).

14. K. Ehrlich, "Irradiation Creep and Interrelation with Swelling in Austenitic Stainless Steels," J. Nucl. Mater., 100, 149 (1981).

15. W. A. Coghlan, "Review of Recent Irradiation Creep Results," Internat. Metals Rev., 31, 245 (1986).

16. R. J. Puigh, 'The In-Reactor Deformation of the PCA Alloy," J. Nucl. Mater., 141-143, 954 (1986).

17. M. **L.** Grossheck, K. Ehrlich and C. Wassilew, "An Assessment of Tensile, Irradiation Creep, Creep Rupture, and Fatigue Behavior in Austenitic Stainless Steels With Emphasis on Spectral Effects," to he publ. in J. Nucl. Mater. in 1990.

18. M. L. Grossheck, L. K. Mansur and M. P. Tanaka,"Irradiation Creep in Austenitic Stainless Steels at 60-400°C with a Fusion Reactor Helium to dpa Ratio," Effects of Radiation on Materials: 14th International Symposium, ASTM **STP** 1046, vol. 11, Philadelphia, PA, p. 537 (1990).

19. A. J. Jacobs and ***G.*** P. Wazadlo, Proc. Internat. Conf. on Nuclear Power Plant Aging, Availability Factor and Reliability Analysis, ASM-International, Metals Park, OH, p. 173 (1985).

20. T. Inazumi, G.E.C. Bell and K. Kiuchi, "ElectrochemicalEvaluation of Sensitization in Austenitic Stainless Steels Using Miniaturized Specimens," ihid ref. 3.

21. T. Inazumi et al., "Evaluationof Radiation-Induced Sensitization of Austenitic Stainless Steels Using Electrochemical Potentiokinetic Reactivation Technique," to be publ. in Corrosion in 1990.

22. W.L. Clark, V.M. Romero and J.C. Danko, General Electric Company Report, GEAP-21382 (1976).

23. T. Inazumi and G.E.C. Bell, "Radiation-Induced Sensitization of PCA Under Spectrally Tailored Irradiation Conditions," Fusion Reactor Materials Semiannu. Proe. Reot., March 1990, DOE/ER-0313/8, pp. 272-278.

24. R. **E.** Gold et al., "MaterialsTechnology for Fusion: Current Status and Future Requirements,"Nucl. Technol./Fusion, 1, 169 (1981).

25. P. J. Maziasz, "Swellingand Swelling Resistance Possibilities of Austenitic Stainless Steels in Fusion Reactors,"J. Nucl. Mater., 122&123, 472 (1984).

26. P. J. Maziasz, "A Perspective on Present and Future Alloy Development Efforts on Austenitic Stainless Steels for Fusion Reactor Application," J. Nucl. Mater., 133&134, 134 (1985).

27. M. P. Tanaka et al., "MicrostructuralDevelopment of Austenitic Stainless Steels Irradiated in HFIR," J. Nucl. Mater., 155-157, 801 (1988).

28. S. Hamada et al., "The Microstructural Evolution and Swelling Behavior of Type 316 Stainless Steel Irradiated in HFIR," Effects of Radiation on Materials: 14th International Symposium, ASTM STP 1046, vol. I, Philadelphia, PA, p. 172 (1989).

29. P. J. Maziasz et al., "Some Effects of Thermal-Mechanical Pretreatment and Alloy Compositional Variation on Swelling of Austenitic Stainless Steel Irradiated in HFIR," Fusion Reactor Materials Semiannu. Proe. Rept., March 1987, DOE/ER-0313/2, pp. 188-204.

30. G. **E. Lucas** and **D.** S. Gelles, 'The Influence **of** Irradiation on Fracture and Impact Properties **of** Fusion Reactor Materials," J. Nucl. Mater., 155-157, **164 (1988).**

31. M. L. Hamilton et al., "Mechanical Properties and Fracture Behavior **of 20%** Cold-Worked **316** Stainless Steel Irradiated to Very High Neutron Exposures," Influence of Radiation on Materials Prooerties: **13th** International Symposium (Part II), ASTM STP **956,** Philadelphia, PA, p. **245 (1987).**

32. D. J. Michel and R. **A.** Gray, "Effects **of** Irradiation on the Fracture Toughness **of** FBR Structural Materials," J. Nucl. Mater., **148, 194 (1987).**

33. M. L. Grossheck and K. C. Liu, "Fatigue Behavior **of** Type **316** Stainless Steel Irradiated in a Mixed Spectrum Fission Reactor Forming Helium," Nucl. Technol., 58, **538 (1982).**

34. In-pile fatigue testing being conducted by W. Vandermeulen, SCK-CEN Mol. Belgium European Technology Programme: Task PSM **6.1.**

35. H. T. Lin, M. L. Grossbeck and B. A. Chin, "Cavity Microstructures and Kinetics during Gas Tungsten Arc Welding **of** Helium-Containing Stainless Steel, Met. Trans. **A,** 21A, ***2585*** (1990).

SWELLING AND MICROSTRUCTURAL ANALYSIS OF U.S.-PCA AUSTENITIC STAINLESS STEEL IRRADIATED AT 60 TO 400°C IN ORR SPECTRAL-TAILORED EXPERIMENTS

P.J. Maziasz (Oak Ridge National Laboratory)

OBJECTIVE

Microstructural analysis of neutron irradiated austenitic stainless steels and correlation with changes in mechanical properties.

SUMMARY

Specimens of solutioc-annealed (SA) and 25% cold-worked (CW) PCA austenitic stainless steel were irradiated in ORR-MFE-4 at 330 and 400°C to 13 dpa, and in ORR-MFE-6J/7J at 60,200,330 and 400°C to 7.4 dpa. Swelling measured by the ORNL precision densitometer of CW PCA irradiated at 400°C was negligible after 7.4 and 13 dpa, whereas SA PCA showed 0.3 to 0.4% swelling after 13 dpa. At 330°C, both SA and CW PCA showed about 0.2% swelling after 13 dpa. Transmission electron microscopy (TEM) analysis of the cavity microstructure showed many voids in SA PCA irradiated at 400°C, while only tiny helium bubbles were found in the other specimens irradiated at 330 to 400°C. No cavities were detectable in CW PCA irradiated at 60 or 200°C. Fine MC precipitates were found in SA and CW PCA specimens at 330 and 400°C, but not at lower temperatures. Both SA and CW PCA contained mixtures of larger Frank loops and dislocation networks at 330 and 400°C, whereas the dislocation structure of CW PCA was dominated by tiny '%lack-dot"loops at 60 and 200°C. The CW PCA showed significant radiation-induced recovery of the initial dislocation network structure at all temperatures; no large Frank loops were found at 60°C, while the maximum concentration of larger loops was observed at 330°C.

PROGRESS AND STATUS

Introduction

Spectrally tailored experiments have comprised a major portion of the overall effort on fission reactor irradiation experiments by the U.S. Fusion Materials Program (FMP) since about 1980.[1] Spectral-tailoring was achieved in the Oak Ridge Research Reactor (ORR) by periodically changing the materials surrounding the experimental subassembly in the reactor core to alter the ratio of fast to thermal neutron fluxes. In nickel-bearing alloys like type 316 and PCA austenitic stainless steel, this has the direct effect of altering the ratio of helium/dpa generation. The He/dpa ratio achieved in the ORR experiments became approximately linear with dose and ranged from 12 to 18 appm/dpa, close to the values expected in a fusion reactor first-wall?' The spectrally tailored ORR-MFE-4 experiment was conducted by the U.S. FMP at temperatures of 330 to 600°C to doses of of 11 to 13 dpa. The subsequent ORR-MFE-6J/7J experiment, irradiated at temperatures of 60 to 400°C to a dose of 7.4 dpa, was conducted under the collaborative agreement between the U.S. (ORNL) and the Japanese (JAERI) fusion materials programs."

A variety of new radiation-induced property changes with important implications for fusion have been observed for austenitic stainless steels in the spectrally tailored experiments. These include: (a) void swelling rates (measured by precision densitometry) that are very sensitive to He/dpa ratio, and appear maximum at about 12 to 18 appm He/dpa at 500°C,[3] (b) higher irradiation-creep rates in ORR at 400 to 500°C than those observed during fast reactor irradiations: (c) larger strains due to irradiation-Cree? at 60°C than at 200 to 400°C,[5] (d) high levels of radiation-induced hardening accompanied by very low values of uniform elongation at 60 to 330°C,[6] and (e) radiation-induced sensitivity to electrochemical attack after irradiation at 200 to 400°C, but not at 60°C, as measured by the electrochemical potentiokinetic reactivation (EPR) method.[7,8] All of these property change data have been obtained from the titanium-modified PCA austenitic stainless steel, but as yet, there has been no systematic study of the microstructural evolution in this or any other related steel at this combination of low dose and lower irradiation temperatures, and at the fusion-relevant He/dpa ratio. Therefore, the specific purpose of this work is to characterize and analyze the microstructure of PCA specimens available from these spectrally tailored experiments via transmission electron microscopy (TEM). The broader purpose of this and follow-on work will be to correlate microstructural behavior with the data on property changes to reveal underlying mechanisms, and to compare the microstructural data on the US. PCA with that of JPCA and type 316 stainless steels.

Experimental

The composition of the austenitic PCA (K-280 heat) stainless steel is given in Table 1. Standard 3-mm-diam TEM disks were punched from 0.25-mm-thick sheet stock that was cold rolled either 25% or 50% after a solution-annealing treatment of 1 h at 1175°C. Disks from the 25% cold-worked (CW) condition sheet remained in that condition, while disks from the 50% CW sheet were given a final solution-annealing (SA) treatment for 0.5 h at 1100°C.

Table 1. Composition of PCA, Heat No. K280 (wt %)

Fe	NI	Cr	Tl	C	Mo	Mn	S1	P	S	E	N
Bal	16.2	14.0	0.24	0.05	2.3	1.8	0.4	0.01	0.003	0.001	0.01

SA and CW PCA specimens were irradiated in the spectrally-tailored ORR-MFE-4 at temperatures of **330** and 400°C to **13** dpa and **230** appm He. Only CW PCA specimens were irradiated in the ORR-MFE-6J/7J experiment at 60, 200, **330** and 400°C to 7.4 dpa and 130 appm He. Density change measurements were made on TEM disks prior to electropolishing using the ORNL precision densitometer. However, because swelling values were quite low and close to the accuracy limits for the densitometer? measurements were confined to the group of specimens irradiated at **330** and 400°C. Microstructural analysis was performed on the JEM 2000FX analytical electron microscope (AEM), using standard techniques to obtain quantitative data for the cavity. dislocation and precipitate components.

Results

The TEM data will be presented primarily in terms of temperature dependence. Data at 330 and 400°C also include dose dependence from 7.4 to **13** dpa and comparison of SA and CW material at each temperature. Density change measurements on specimens irradiated at **330** and 400°C are given in Table 2. The concentrations of the microstructural components are plotted versus irradiation temperature in Fig. 1 and versus dose at **330** and 400°C in Fig. 2. Quantitative data on sizes and concentrations of dislocation loops, cavities and precipitates from TEM analysis are given in Table **3.** Quantitative data on the total dislocation concentration as well as the portions due to network, large Frank loop and 'black-dot" loop components of the dislocation structure are given in Table 4, and plotted as functions of irradiation temperature in Fig. 3 and as functions of dose in Fig. **4.**

Table 2. Summary of Density Change Measured Swelling for PCA Irradiated at 330 to 400°C in the Spectrally Tailored ORR-MFE-4A, -4B, -6J and -75 Experiments

Alloy	Irradiation Conditions: Temperature (°C)	Irradiation Conditions: Dose (dpa)	$\Delta V/V_0$, %
SA PCA	400	13	0.38 0.33
25% *N* PCA	400	13	−0.05 0.02
25% CW PCA	400	7.4	−0.08 −0.03
SA PCA	330	13	0.18 0.24
25% CW PCA	330	13	0.16 0.22

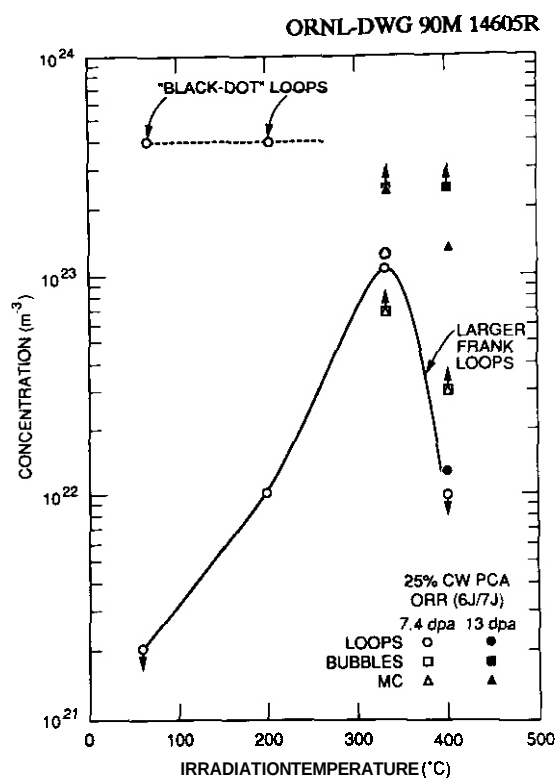


Fig. 1. Temperature dependence of the concentrations of various microstructural components in 25% CW PCA irradiated in the spectrally tailored WR MFE-6J, -75 (7.4 dpa) and NFE-4 (13 dpa) experiments.

ORNLDWG 91M-6423

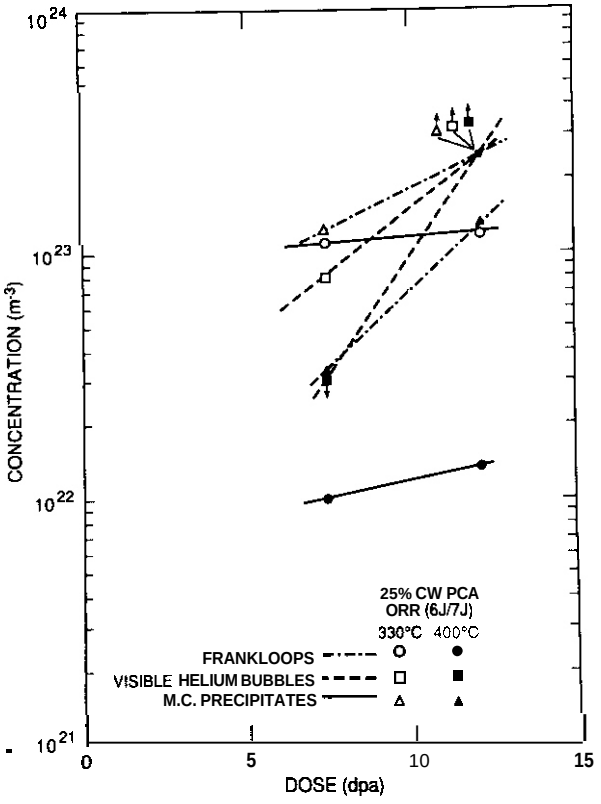


Fig. 2. Dose dependence of the concentrations of various microstructural components in 25% CW PCA irradiated in the spectrally tailored ORR MFE-6J, -7J (7.4 dpa) and MFE-4 (13 dpa) experiments at 330 and 400°C.

ORNLDWG 90M 14606R

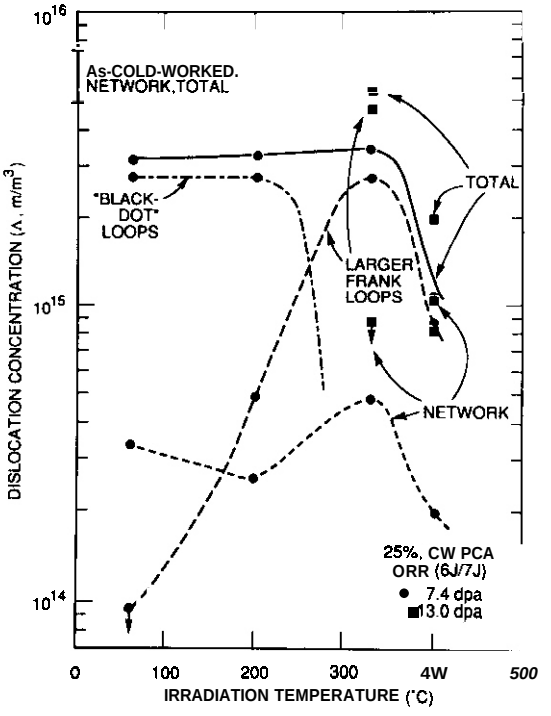


Fig. 3. Temperature dependence of the dislocation concentration from various components of the dislocation microstructure in 25% CW PCA irradiated in the Spectrally tailored ORR MFE-6J, -7J (7.4 dpa) and WE-4 (13 dpa) experiments.

60°C

Only a very high concentration (4×10^{23} m^{-3}) of tiny 'black-dot" loops were produced by irradiation in **CW PCA** after **7.4** dpa (Figs. **1** and **5)**. No cavities or precipitates were detectable, and very few large Frank interstitial loops were found (Figs. 1 and **6).** There was also significant recovery of the as-cold-worked dislocation network (over 10 times less) during irradiation (Fig. **3).** However, the contribution made by the tiny loops to the total dislocation concentration produced only a slight net decrease in dislocation content during irradiation relative to as-cold-worked material.

200°C

A very high concentration of fine **(1.4-3** nm) 'black-dot" loops was observed in **CW PCA,** together with recovery of the network dislocation structure, similar to the results at **60°C** (Figs. 1 and **5)**. No cavities or precipitates were found. **A** modest density (5×10^{20} m^{-3}) of larger (4-23 nm) Frank interstitial loops was found (Figs. **1** and 6), but these made only a small contribution to the total dislocation concentration. The total dislocation content after irradiation at 200°C was about the same as found at **60°C,** and again was dominated by the contribution from the "black-dot" loops (Fig. **3).**

330°C

CW PCA irradiated at **330°C** to **7.4** dpa contained a much higher concentration (1.1×10^{23} m^{-3}) of larger Frank loops than the specimens irradiated at lower temperatures to the same dose (Figs. **1** and 6). There was little change in Frank loop concentration or size range (smallest to largest) (Fig. 2 and Table **3)** with increasing dose from **7.4** to 13 dpa, but there was a small increase in the size of the average loop (Table **4).** The concentration of network dislocations after **7.4** dpa was higher than at lower irradiation temperatures, but irradiation still caused recovery of the dislocation network structure relative to as-cold-worked material (Fig. **3).** The network concentration increased with dose (Fig. **4).** No 'black-dot" loops were observed at **330°C** at either dose. Instead, high concentrations of tiny helium bubbles and similarly tiny **MC** precipitate particles were

Table 3. summary of Microstructural Observations from PCA Irradiated at 60 to 400°C in the Spectrally Tailored ORR-MFE-4A and -4B and -6J and -75 Experiments

Alloy	Irradiation Conditions: Temperature (°C)	Irradiation Conditions: Dose (dpa)	Dislocations: Loops (diameter, concentration) (m^{-3})	Dislocations: Type	Cavities: Voids (dimeter, concentration)	Cavities: Bubbles (dimeter, (concentration]	Precipitation: Phase	Precipitation: (diameter, concentration)
SA PCA	400	13	11.2 to 44 nm 1.6×10^{21} m^{-3}	Frank	5 to 10 nm 5.2×10^{21} m^{-3}	1.4 to 3 nm 1.5×10^{23} m^{-3}	MC	1 to 6 nm ~5 to 7 $\times 10^{22}$ m^{-3}
SA PCA	330	13	4 to 23 nm 6.3×10^{22} m^{-3}	Frank	None	1.9 nm $>2.5 \times 10^{23}$ m^{-3}	MC	~2 nm
25% CW PCA	400	13	7 to 37 nm 1.3×10^{22} m^{-3}	Frank	A few patches 6 to 10 nm	1.4 to 4 nm $>2.5 \times 10^{23}$ m^{-3}	MC	2 to 5 nm 1.3×10^{23} m^{-3}
25% CW PCA	330	13	2 to 21 nm 1.2×10^{23} m^{-3}	Frank	None	1 to 2 nm $>2.5 \times 10^{23}$ m^{-3}	MC	~2 nm $>2.5 \times 10^{23}$ m^{-3}
25% CW PCA	400	7.4	4 to 62 nm $<1 \times 10^{22}$ m^{-3}	Frank	A few patches 5 to 10 nm	<1 to 2 nm $>3 \times 10^{22}$ m^{-3}	MC	3 to 4 nm $2–4 \times 10^{22}$ m^{-3}
25% CW PCA	330	7.4	2 to 25 nm 1.1×10^{23} m^{-3}	Frank	None	1 to 2 nm $>8 \times 10^{22}$ m^{-3}	MC	2 to 3 nm 1.2×10^{23} m^{-3}
25% CW PCA	200	7.4	1.4 to 3 nm ~4 $\times 10^{23}$ m^{-3} 4 to 23 nm ~1 $\times 10^{22}$ m^{-3}	"Black-dot" Frank	None	None	None	None
25% CW PCA	60	7.4	1.5 to 3 ~4 $\times 10^{23}$ m^{-3} 14 to 19 nm $<2 \times 10^{21}$ m^{-3}	"Black-dot" Frank	None	None	None	None

Table 4. Summary of Concentration Data for us-PCA Irradiated in Spectrally Tailored Experiments OUR-MFE-4A and -40 and -6J and -75

Alloy/ Condition	Irradiation Conditions: Temperature (°C)	Irradiation Conditions: Dose (dpa)	Dislocation concentration (Ω m/m^3): Network	Dislocation concentration (Ω m/m^3): "Black-Dot" Loops	Dislocation concentration (Ω m/m^3): Larger Frank Loops (line length/m^3)	Dislocation concentration (Ω m/m^3): Total	Number Density of Large Loops (m^{-3})
SA-PCA	As-annealed		4×10^{12}	None	None	4×10^{12}	
SA-PCA	400	13	1.8×10^{15}	None	1×10^{15} (25 nm)[a]	~3×10^{15}	$1.3 \times 10^{**}$
SA-PCA	330	13	9×10^{14}	None	3.1×10^{15} (16.5 nm)[a]	~4×10^{15}	6.0×10^{22}
25% CW-PCA	As-cold worked		25×10^{15}	None	None	25×10^{12}	0
25% CW-PCA	400	13	1.1×10^{15}	None	8.4×10^{14} (21 nm)[a]	~2×10^{15}	1.3×10^{22}
25% CW-PCA	400	7.4	2×10^{14}	None	9×10^{14} (29 nm)[a]	1.1×10^{15}	9.9×10^{21}
25% CW-PCA	330	13	$<9 \times 10^{14}$	None	1.7×10^{15} (12.4 nm)[a]	4.7– 5.6×10^{15}	1.2×10^{23}
25% N-PCA	330	7.4	4.5×10^{14}	None	3.1×10^{15} (9 nm)[a]	3.5×10^{15}	1.1×10^{23}
25% CU-PCA	200	7.4	2.6×10^{14}	2.8×10^{15} (2.2 nm)[a]	5×10^{14} (16.5 nm)[a]	~3.6×10^{15}	9.6×10^{21}
25% CW-PCA	60	7.4	3.4×10^{14}	2.8×10^{15} (2.2 nm)[a]	$<1 \times 10^{14}$ (16.5 nm)[a]	~3.1×10^{15}	1.9×10^{21}

** Average diameter of loops in this size class

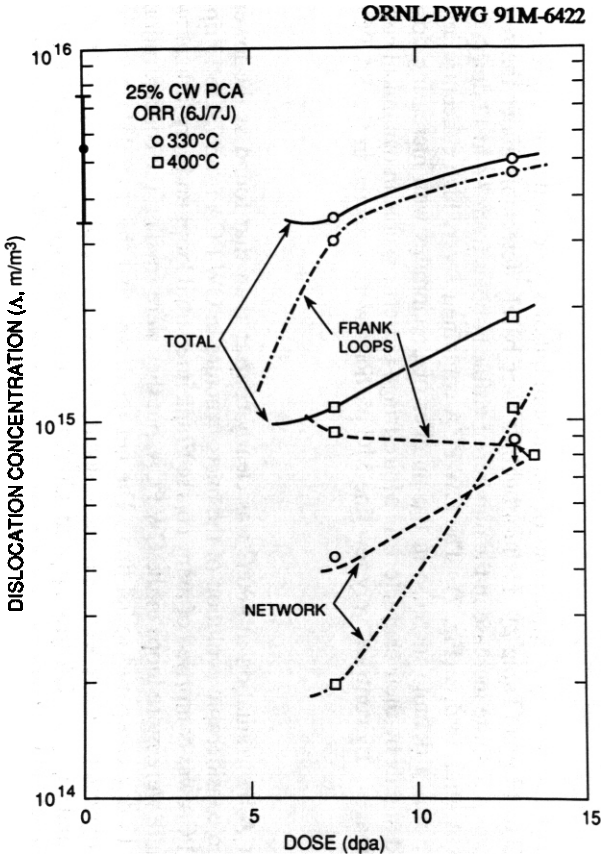


Fig. 4. Dose dependence of the dislocation concentration from various components of the dislocation microstructure in 25% CW PCA irradiated in the spectrally tailored ORR MFE-6J, -7J (7.4 dpa) and MFE-4 (13 dpa) experiments at 330 and 400°C.

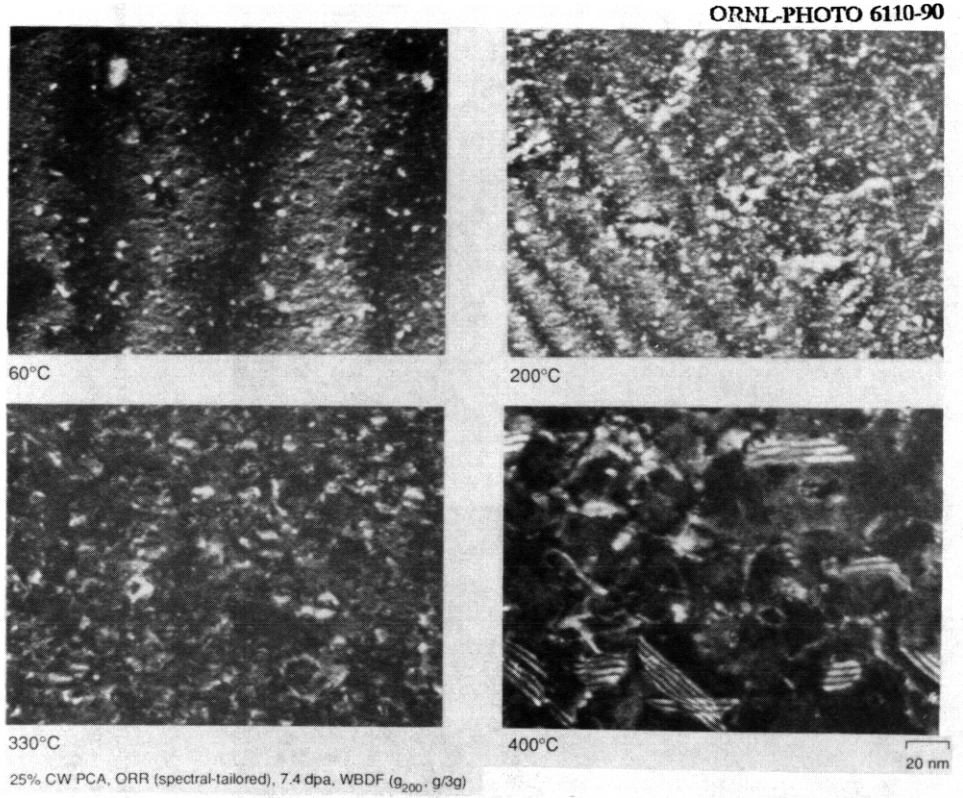


Fig. 5. Weak-beam dark-field TEM imaging of the dislocation microstructure of 25% CW PCA irradiated at 60 to 400°C (conditions indicated). Small bright dots at 60 and 200°C are strain images of tiny "black-dot" loops, whereas the small matrix contrast features at 330°C appear due to strain associated with tiny helium bubbles (probably highly overpressured) and MC precipitates.

ORNL-PHOTO 6111-90

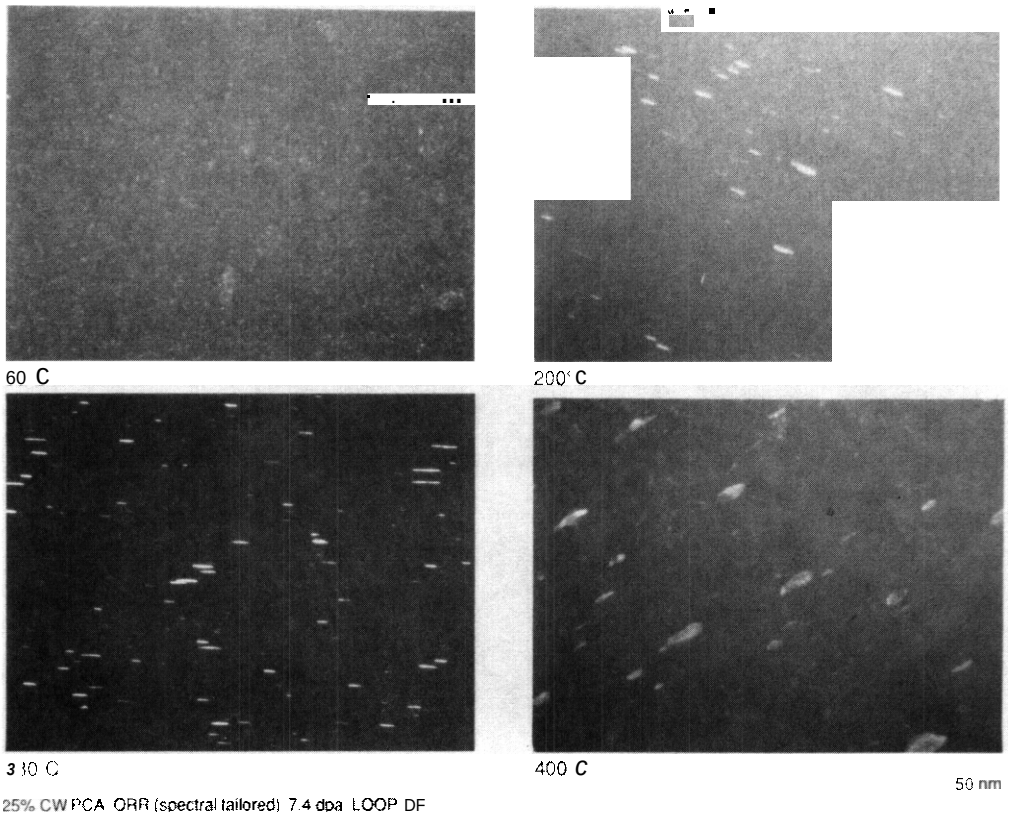


Fig. 6. Dark-flald T M using tha <111> satellite streaks around g_{200} reflections to image the fault plana of largar Frank Interstitial loops in 25% CW PCA Irradlated at 60 to 400°C (conditions Indicated).

uniformly dispersed in the matrix; both types of tiny microstructural defects were visible during weak-beam dark-field imaging (Fig. 4). The total dislocation concentration after 7.4 dpa was about the same as observed at 60 and 200°C, hut increased after 13 dpa to nearly the level found in as-cold-worked material, mainly due to the increase in network dislocations and the growth of Frank loops with dose (Figs. 2 and 4). The dislocation microstructure found in SA PCA irradiated to 13 d p was similar to that of the CW PCA, but the Frank loop structure was somewhat coarser, and there were slightly more network dislocations in the SA PCA (Table 4).

Although no voids were detected, the abundant dispersions of tiny helium bubbles produced about 0.2% swelling in both SA and CW PCA irradiated at 330°C to 13 dpa (Table 2). Helium bubbles were barely detectable above the resolution limit in CW PCA at both doses, but there was a definite increase in the number of visible bubbles from 7.4 to 13 dpa (Fig. 2). Helium bubbles were slightly larger in SA PCA after 13 dpa (Fig. 7). The CW PCA contained a very high concentration of fine MC precipitates at both doses, and there was a definite increase in the number of precipitates with increasing dose. The MC particles were detected and identified mainly hy their characteristic Moire fringe patterns visible in dynamical contrast images as well as in weak-beam dark-field images. By contrast, very few fine MC particles were detected in the SA PCA.

400°C

The microstructure in CW PCA by irradiation at 400°C was clearly coarser than that found at the lower irradiation temperatures (Fig. 5). There was also considerable evolution of the microstructure in CW PCA from 7.4 to 13 d p . After 7.4 dpa, the dislocation structure of CW PCA was comprised of many coarse Frank interstitial loops and very little network (Tables 3 and 4, and Fig. 5). After 13 dpa, there were more loops in the CW PCA, hut they were smaller; the concentration of network dislocations was five times higher at 13 dpa compared to 7.4 dpa. The net result was that the total dislocation concentration of CW PCA doubled as the dose increased, hut there were still less dislocations in the irradiated material than were found in the ascold-worked material (Figs. 3 and 4). SA PCA irradiated at 400°C to 13 dpa has more network dislocation, and more and larger Frank loops than found in CW PCA. Therefore, the total dislocation content of the SA PCA was about three times greater than found in CW PCA after 13 dpa (Table 4).

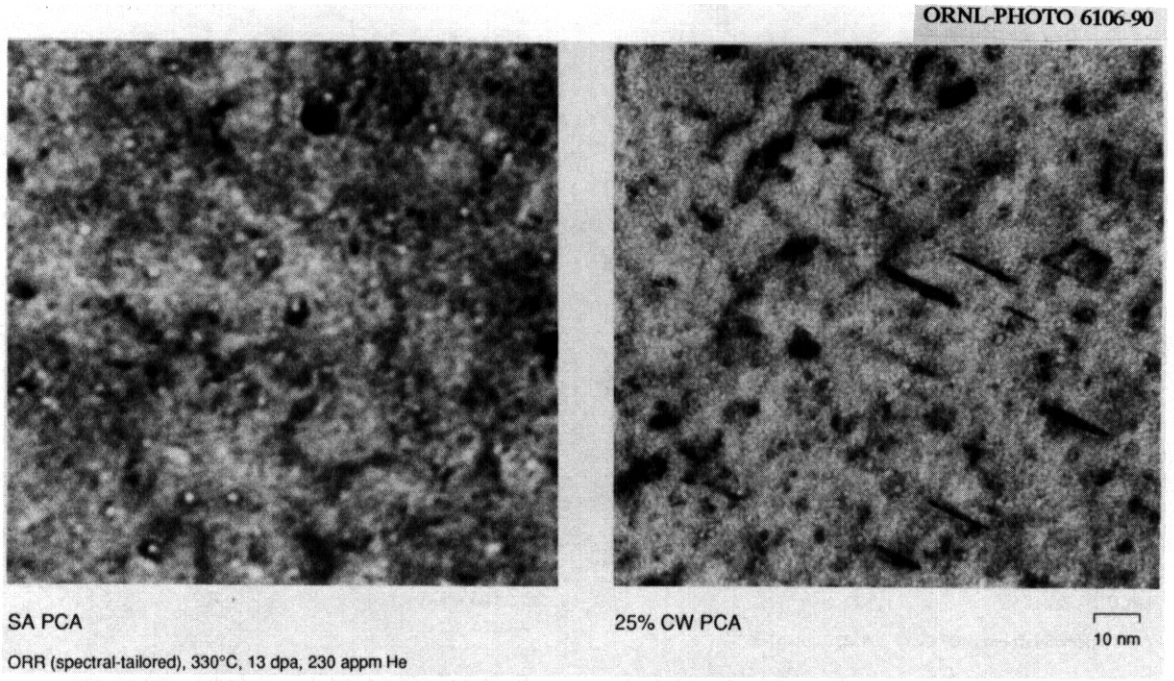


Fig. 7. TEM of the tiny helium bubbles formed in SA and 25% CW PCA during irradiation in ORR at 330°C to 13 dpa.

The CW PCA irradiated to 7.4 dpa contained many ($>3 \times 10^{22}$ m^{-3}) fine (<1-2 nm) helium bubbles, together with a few sparse patches of larger (6-10 nm) voids. The fine helium bubbles were almost completely associated with a uniform and equally fine dispersion of MC particles. After 13 dpa, the concentrations of tiny helium bubbles and MC precipitate particles both increased by a factor of 10, and yet there was no detectable change in the void component of the microstructure. The bubble concentration at 400°C after 13 dpa was still less than half that found at 330°C. Density change measurements showed no detectable swelling of CW PCA at either dose (Table 2).

The microstructure of SA PCA irradiated to 13 dpa was roughly similar to that of CW PCA, except that the SA PCA contained many more large voids (Fig. 8). There were slightly more and larger Frank loops, and more network dislocations in the SA PCA, and there were fewer fine helium bubbles and a discernibly coarser distribution of small MC particles. The swelling of SA PCA was 0.3 to 0.4%, more than found in CW PCA mainly because there were more voids.

Discussion

While the data on the PCA austenitic stainless steel irradiated in these ORR spectrally tailored experiments at 60 to 400°C to 7.4 to 13 dpa are unique, there are some microstructural data on other heats of austenitic stainless steel irradiated in other mixed-spectrum reactors in this temperature range that are relevant for comparison. 20% CW type 316 (heat X-15893) stainless steel and SA and 20% CW "P7" (a high-purity austenitic stainless alloy) were irradiated at 250 to 550°C in an earlier spectrally tailored experiment, ORR-MFE-2, to <5 dpa and <40 appm He.[9,10] In the 20% CW type 316, no cavities or precipitates were detectable at 250, 290, or 450°C after 5 dpa.[9] However, these specimens were examined in 1982 using a JEOL 100°C TEM with more limited practical resolution and visibility at higher magnification than the modern JEOL 2000FX AEM used in this work, so these data should be viewed accordingly. Likewise Brager and Garner found "small defect clusters" in SA and 20% CW P7 alloy, after irradiation at 350°C to 3 dpa, but they were not able to identify these?' With regard to dislocation structure, only qualitative information is available on the specimens irradiated in ORR-MFE-2. Large Frank loops were observed in all of the P7 and type 316 specimens. In the 20% CW 316, a similar dense mixture of large Frank loops (8-25 nm diam), network, and "black-dot" loop damage were reported for the dislocation microstructure at 250 to 450°C. However, the "%lack-dot" loops observed at 450°C using weak-beam dark-field imaging may have been strain around overpressurized helium bubbles that were too small to resolve in bright-field. It is, therefore, significant in this work on the 25% CW PCA that tiny bubbles and MC precipitates can be clearly resolved at 330°C, and can be distinguished from "%lack-dot" loop damage that appears at 200°C and below. The previous ORR data is generally quite consistent with the data reported here, except that the Frank loops found in 25% CW PCA at 400°C and 7.4 dpa are somewhat larger than those found in 20% CW 316 at 450°C and 5 dpa.

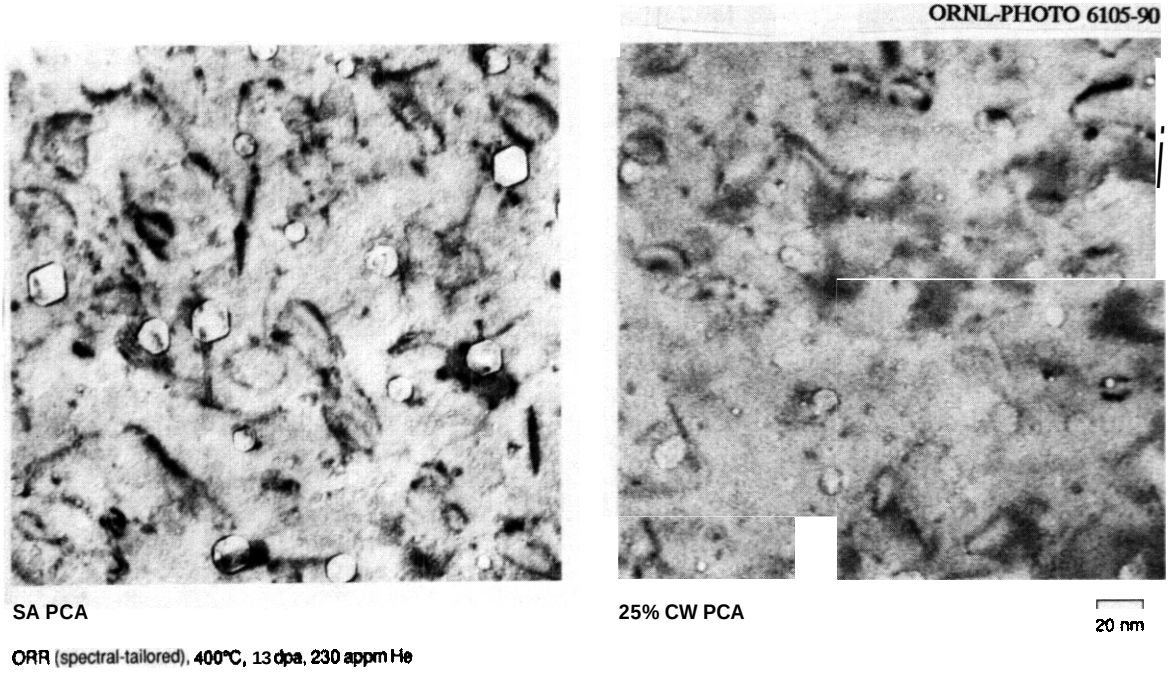


Fig. 8. Comparison of cavity microstructures in SA and 25% CW PCA irradiated In ORR at 400°C to 13 dpa. Note the many larger votdr In tha SA PCA.

There is a considerable amount of previous quantitative microstructural data on cavity and precipitation evolution in SA and CW 316 (N-lot, J316 and DO-heat), PCA and JPCA austenitic stainless steels irradiated in more recent HFIR experiments[9-11] at 300 and 400°C, and some data on some of these steels and type 316+Ti (R1-heat) steel irradiated in older HFIR experiments[12,13] at 55 and 325-450°C. There are also some other mixed-spectrum reactor data on SA 348 (niobium-stabilized) stainless steel irradiated at 350°C to 33 to 39 dpa in ATR and at 300°C to 44 dpa in ETR.[18] Although no helium bubbles or MC precipitates were detected in SA PCA or 20% CW 316 (N-lot) after HFIR irradiation at 300 to 400°C to 10 dpa, tiny helium bubbles were detected in SA and 25% CW PCA, and in 20% CW 316 (N-lot) at both temperatures after 44 dpa. Fine MC was observed at 400°C, but not at 300°C in the 25% CW PCA irradiated to 44 dpa.[11] In later collaborative HFIR experiments with the Japanese, fine helium bubbles were easily detectable at 33 and 57 dpa in SA and in 20-25% CW J316, JPCA and PCA steels at 300 and 400°C, at least in part due to use of a better JEOL 2000FX AEM.[12,13] In the present work, bubble sizes and concentrations and MC precipitate sizes in CW PCA after ORR irradiation to 7 to 13 dpa at 330 to 400°C were comparable to those observed after higher dose irradiation in HFIR at 300 to 400°C, but many more fine MC precipitates were observed in the steels irradiated in ORR (1-2 x 10^{23} compared to 1-2 x $10^{22}/m^{-3}$). In previous HFIR experiments on CW 316+Ti, a very high concentration of fine MC particles was detectable after 8.5 dpa at 325 to 350°C, but helium bubbles were not.[12] Thomas and Beeston[18] observed very high concentrations of very fine helium bubbles in SA 348 irradiated in both ATR and ETR reactors at 300 to 350°C to 33 to 44 dpa, but they found no MC precipitation. They found fine G-phase precipitation after ATR irradiation at 350°C, but found none in the specimens irradiated in ETR at 300°C.

With regard to dislocation evolution, most steels irradiated in mixed-spectrum fission reactors have large Frank loops after irradiation at 300 to 400°C.[9-13,15-18] However, there is little systematic data on dislocation network evolution at these temperatures. Quantitatively, the 25% CW U.S. PCA irradiated in HFIR at 300 to 400°C to 34 dpa had many more Frank loops than similarly irradiated 20% CW JPCA,[12] and the loop data for CW U.S. PCA irradiated to lower doses in ORR is consistent with the higher dose data from HFIR. Previous data on 20% CW 316 and 316+Ti irradiated at 55°C in HFIR showed dense dispersions of "blackdot" loops and network dislocations, but few or no larger Frank loops,[14,15] consistent with the ORR data on 25% CW PCA in this work. Although previous HFIR data at 55°C showed recovery of the network dislocation structure in CW 316 and 316+Ti, the network concentrations observed in the current ORR experiments on CW PCA are much lower. The transition from low-temperature 'blackdot" loop damage at 200°C to the high-temperature microstructural features (i.e., helium bubbles and MC precipitates) at 330°C is much clearer in this data than in previous data.[11] Thomas and Beeston observed unidentified fine defects after irradiation at 350°C, but these defects did not appear to be "black-spot"loops.

Finally, there are some recent quantitative data on the dislocation microstructure of SA 316 irradiated in RTNS-II (D-T fusion neutrons) and in OWR (mixed spectrum fission neutrons) to very low doses of 0.001 to 0.03 dpa at 90 and 290°C.[19] Qualitatively, they observe only "blackdot" interstitial loops, with no evidence of dislocation network or larger Frank loops.

The concentration of tiny loops that they observe ranges from 10 times less to several times more than found in this work, with strong dependencies on temperature and dose but only a weak dependence on neutron energy spectrum. Their data are consistent with data from this work in terms of the upper temperature limit **of** the 'black-dot" loop regime being <330°C. However, quantitative differences between the data also probably reflect the fact that they observed loop nucleation in 'virgin" SA 316 material. Our data, particularly the dose dependencies at 330 and 400°C, suggest that considerable microstructural evolution has occurred, even after only 7.4 dpa. It is particularly important to note the considerable (and somewhat surprising) recovery of the as-cold-worked network dislocation structure that has occurred during irradiation in CW PCA at 60 to 400°C. This most likely is an important necessary process that needs to occur prior to or while tiny loops nucleate. The dose dependencies, particularly at 400°C, clearly show that dislocation evolution has advanced to the stage at which Frank loops unfault to generate a new dislocation network structure as irradiation progresses.

Conclusions

1. Voids and bubbles were observed in SA and 25% CW PCA after irradiation in ORR to 13 dpa at 400°C. There is considerable evolution of the visible bubble microstructure at 330 and 400°C from 7.4 to 13 dpa, but there is no conversion of the high concentrations of tiny bubbles to voids at 330°C. No cavities were observed in 25%CW PCA after 7.4 dpa at 60 and 200°C.

2. Immersion density change measurements showed 0.3 to 0.4% swelling in SA PCA after only 13 dpa at 400°C, but no swelling in 25%CW PCA. At 330°C, both SA and 25%CW PCA showed about 0.2% swelling after 13 dpa.

3. Both SA and 25% CW PCA contained fine MC particles after 13 dpa at 330 and 400°C. Dense dispresions of very fine MC particles were almost exclusively associated with the equal fine dispersions of helium bubbles in the 25% CW PCA. No MC was detectable at 60 or 200°C after 7.4 dpa.

4. Both SA and 25% CW PCA had dislocation structures that were mixtures of network and larger Frank loops after irradiation at 330 and 400°C. The network dislocation structure in the 25% CW PCA showed considerable recovery relative to the as-cold-worked condition. At 400°C there was considerable evolution of the dislocation structure with dose, with both the concentration of loops and network dislocations increasing from 7.4 to 13 dpa. By comparison, there was little additional loop nucleation from 7.4 to 13 dpa at 330°C, and the modest increase in dislocation concentration with dose was due to loop growth and an increase in the dislocation network concentration. After 13 dpa, the SA PCA had more loops and more network dislocations relative to 25% CW PCA at 330 and 400°C.

5. 25% CW PCA contained very high concentrations of tiny "black-spot" loops after irradiation at 60 and 200°C to 7.4 dpa. Many larger Frank loops were found at 200°C, but very few were observed at 60°C. There is much more radiation-produced recovery of the network at 60 and 200°C than observed at 330 and 400°C. However, the total dislocation concentration is only slightly less than in as-cold-worked material, mainly due to the contribution of the abundant 'black-dot" loops.

Future Work

Future work will include correlating the quantitative microstructural data with property change data to gain insight into mechanisms governing the properties behavior.

REFERENCES

1. M. L. Grossbeck and K. R. Thoms, "ORR-MFE-4 Spectral Tailoring Experiment to Simulate the He/dpa Ratio of a Fusion Reactor," ADIP Quart. Proe. Rep., June. 1980, DOE/ER-0045/3, pp. 10-24.

2. M. L. Grossbeck and J. A. Horak, "Irradiation Creep in Type 316 Stainless Steel and US PCA with Fusion Reactor He/dpa Levels," J. Nucl. Mater., 155-157, 1001 (1988).

3. R. E. Stoller et al., "Swelling Behavior of Austenitic Stainless Steels in a Spectrally Tailored Reactor Experiment: Implications for Near-Term Fusion Machines," J. Nucl. Mater., 155-157, 1328 (1988).

4. J. L. Scott et al. "Program of United States-Japan Collaborative Testing in HFIR and ORR," J. Nucl. Mater., 141-143, 996 (1986).

5. M. L. Grossbeck. L. K. Mansur and M. P. Tanaka."Irradiation Creep in Austenitic Stainless Steels at 60-400°C with a Fusion Reactor Helium to dpa Ratio," Effects of Radiation on Materials: 14th International Symposium, ASTM 1046, vol. II, Philadelphia, PA, p. 537 (1990).

6. M. L. Grossbeck et al., 'Tensile Properties of Austenitic Stainless Steels Irradiated in the ORR Spectral Tailoring Experiment ORR-MFE-6J and -7J," Fusion Reactor Materials Semiannu. Proe. Rept., March 31. 1989, DOE/ER-0313/6, pp. 259-268.

7. T. Inazumi et al., "Evaluation of Radiation-Induced Sensitization of Austenitic Stainless Steels Using Electrochemical Potentiokinetic Reactivation Technique," to be publ. in Corrosion in 1990.

8. T. Inazumi and G.E.C. Bell, "Radiation-Induced Sensitization of PCA Under Spectrally Tailored Irradiation Conditions," Fusion Reactor Materials Semiannu. Proe. Rept., March 31. 1990, DOE/ER-0313/8, pp. 272-278.

9. P. J. Maziasz, "Microstructural Development of 20%-Cold-Worked Type 316 Stainless Steel Irradiated in ORR at 250 to 500°C," ADIP Ouart. Proe. Reut.. Seatember 1982, DOE/ER-0045/9, pp. 78-88.

10. H. R. Brager and F. A. Garner, 'The Influence of Cold Work Level. Solute and Helium Content on the Swelling of "Pure" AISI 316 (Fe-17Cr-16.7Ni-2.5Mo)," Effects of Radiation on Materials:' Eleventh Conference, ASTM 782, Am. Soc. for Testing and Matls., Philadelphia, PA, p. 152 (1982).

11. P. J. Maziasz and D. N. Braski, "Improved Swelling Resistance for PCA Austenitic Stainless Steel Under HFIR Irradiation Through Microstructural Control," J. Nucl. Mater., 122&123, 311 (1984).

12. M. P. Tanaka, S. Hamada, A. Hishinuma, and P. J. Maziasz, "Microstructural Development of Austenitic Stainless Steels Irradiated in HFIR," J. Nucl. Mater. 155-157, 801 (1988).

13. S. Hamada et al., 'The Microstructural Evolution and Swelling Behavior of Type 316 Stainless Steel Irradiated in HFIR," Effects of Radiation on Materials: 14th Internat. Symp., ASTM STP 1046, vol. I, p. 172 (1989).

14. F. W. Wiffen and P. J. Maziasz, 'The Influence of Neutron Irradiation at 55°C on the Properties of Austenitic Stainless Steels," J. Nucl. Mater. 103&104, 821 (1981).

15. P. J. Maziasz, "MicrostructuralDevelopment in 20%-Cold-Worked Types 316 and 316+Ti Stainless Steels Irradiated in HFIR Temperature and Fluence Dependence of the Dislocation Component," ADIP Ouart. Prop. Rent.. Sentember 30.1981. DOE/ER-0045/7, pp. 54-97.

16. P. J. Maziasz, J. A. Horak and B. L. Cox, 'The Influence of Both Helium and Neutron Irradiation on the Precipitation in 20% Cold-Worked Austenitic Stainless Steel," Phase Stability During Irradiation, TMS-AIME, Warrrendale, PA, p. 271 (1981).

17. P. I. Maziasz, Effects of Helium Content on Microstructural Development in Type 316 Stainless Steel Under Neutron Irradiation, ORNL-6121 (November 1984).

18. L. E. Thomas and J. M. Beeston, 'The Microstructure of Neutron Irradiated Type-348 Stainless Steel and Its Relationship to Creep and Hardening," J. Nucl. Mater., 107, 159 (1982).

19. H. L. Heinisch, T. Muroga and M. Kiritani, "Microstructure-TensileProperty Correlation of 316SS in Low Dose Neutron Irradiations," Fusion Reactor Materials Semiannu. Proe. Rept., March 31, 1990, DOE/ER-0313/8, pp. 51-57.

STATUS OF MOTA IRRADIATION EXPERIMENTS ON REDUCED ACTIVATION AUSTENITIC ALLOYS - F. A. Garner and M. L. Hamilton [Pacific Northwest Laboratory)[a] C. R. Eiholzer (Westinghouse Hanford Company) R. L. Klueh (Oak Ridge National Laboratory) H. Takahashi and S. Ohnuki (Hokkaido University) K. Miyahara (Nagoya University) P. Schiller (Ispra Establishment) L. I. Ivanov (Baikov Institute)

OBJECTIVE

The objective of this effort is to determine the suitability for fusion applications of austenitic steels based on the Fe-Cr-Mn system that result in reduced long term radioactivation.

SUMMARY

A number of collaborative international experiments are being conducted to assess the feasibility of Fe-Cr-Mn austenitic steels for fusion service. A review is presented of the current status of these various efforts. The first time irradiation of an Fe-Cr-Mn steel in the form of pressurized tubes is highlighted.

STATUS AND ACCOMPLISHMENTS

Introduction

Austenitic steels based on the Fe-Cr-Mn system are being explored for potential application to fusion environments. A series of experiments designed to explore the swelling and phase stability of these alloys were conducted earlier in FFTF cycles 7-10 and the results have been published in references 1-8. Conclusions derived from these earlier studies led to the initiation of other experiments conduced in FFTF cycles 9-12. The status of these experiments is presented below. All of these studies are being conducted as collaborative international studies.

Influence of Nickel on Radiation-Induced Evolution of Fe-Cr-Mn Allovs

The results of early irradiation experiments demonstrated that Fe-Cr-Mn alloys are less stable during irradiation than comparable Fe-Cr-Ni alloys. This instability arises in part from the radiation-induced segregation of iron and the concurrent outflow of manganese from microstructural sinks. Based on the results of earlier studies on Fe-Cr-Ni alloys, it was hypothesized that nickel additions to Fe-Cr-Mn alloys would lead to simultaneous segregation of iron and nickel, the latter serving to reduce the formation of undesirable phases. The validity of this hypothesis was demonstrated earlier in irradiation studies of Fe-15Cr-15Mn-XNi and Fe-17Cr-19Mn-0.5Si-XNi alloys. Although nickel is normally avoided on the basis of low activation considerations, most manganese-stabilized commercial alloys that are currently available contain nickel at some level.

Three separate series of irradiation experiments on Fe-Cr-Mn-Ni alloys were conducted in FFTF cycle 9, and microscopy analysis was performed at Pacific Northwest Laboratory (PNL) by researchers from Hokkaido University. These experiments involved Fe-15Cr-15Mn-XNi and Fe-10Cr-30Mn-XNi (X = 0, 5, 10, 15 wt%) and Fe-17Cr-19Mn-0.5Si-XNi (X = 0.03, 1.47, 5.90) with 0.1C, 0.02P and 0.1N. The 15Cr and 17Cr alloys have been examined recently and the results reported in references 9 and 10, respectively. It was shown that nickel additions not only increase the phase stability as proposed, but also increase the swelling initially. This latter finding is a consequence of nickel causing reduced formation of the lower swelling ferrite phase.

In the current study, the influence of nickel on radiation-induced microstructural evolution of Fe-10Cr-30Mn-XNi alloys (X = 0, 5, 10, 15 wt%) is being explored. Higher manganese alloys in this range are being studied by several groups of researchers. These alloys were irradiated in the annealed condition in FFTF at 420°C (25 dpa), 470°C (17 dpa), and 550°C (20 dpa). Density measurements, electron microscopy and EDS analysis were performed recently on both irradiated and thermally aged specimens.

While this work is still in progress, it is possible to summarize its major conclusions. The austenite phase in these alloys was found to be relatively stable, particularly when compared with that of the Fe-15Cr-15Mn-XNi alloys reported earlier. This stability is due in part to both the presence and segregation of nickel, as well as to the higher manganese content. In the absence of nickel, small amounts of alpha phase formed on grain boundaries during irradiation, increasing in amount with increasing irradiation temperature. Sigma phase also formed frequently on grain boundaries during irradiation, increasing in amount with increasing irradiation temperature. In addition, sigma phase often formed on the boundaries between the alpha and austenite phase. Void formation occurred in the austenitic phase of all four alloys at each of the three temperatures studied, but not in either the alpha or the sigma phases. In

---

(a) Pacific Northwest Laboratory is operated for the U.S. Department of Energy by Battelle Memorial Institute under Contract DE-AC06-76RLO 1830.

general, the void density increased with nickel content. The measured changes in bulk density were found to reflect the dependence on nickel content of both phase stability and void swelling. The analysis of this work will continue with documentation occurring in the next reporting period.

Phase Stability Studies

Researchers who conducted several out-of-reactor studies (3, 11-14) have reached the conclusion that the Fe-Cr-Mn phase diagram of Schafmeister and Ergang needed modification, especially for the formation of ferrite and sigma phases. The previously cited studies conducted in reactor have also supported this conclusion but noted that the inverse Kirkendall effect operating during neutron irradiation leads to pronounced segregation of iron and out-migration of manganese from various microstructural sinks. This phenomenon accelerates and further modifies the phase evolution of Fe-Cr-Mn alloys compared to that which occurs out-of-reactor. To explore the impact of composition on phase evolution in reactor, a number of joint U.S./Japan studies are in progress.

In a joint study between Nagoya University and PNL, four Fe-12Cr-XMn alloys (X = 15, 20, 25, 30 wt%) were irradiated in the annealed condition in the FFTF-MOTA to exposures ranging from 17 to 30 dpa at temperatures of 370, 420, 520 and 600°C. The objective of this investigation is to determine the effect of manganese level and irradiation temperature on both the phase stability and microstructural evolution of these alloys. Particular emphasis was directed toward the location of the boundaries of the three phase ($\gamma+\alpha+\sigma$) regime. Analysis is still in progress, but some preliminary results are now available.

At the 15Mn level, the alloy exists in the three phase regime at all irradiation temperatures studied, with the amount of blocky iron-rich α-ferrite phase increasing at lower temperatures. At 20% Mn and above the ferritic phase was not observed, indicating that such manganese levels successfully stabilize the austenite phase. However, sigma and sometime chi phases were formed at these higher manganese levels. Voids were found to develop only in the austenite phase, but the details of the void microstructure appear to be relatively insensitive to the manganese content.

Another joint study between PNL and the National Research Institute for Metals (NRIM) in Tsukuba, Japan explores the evolution of sigma phase in annealed Fe-10Cr-30Mn-0.5Si alloys as a function of carbon content during irradiation at 420, 520 and 600°C in FFTF cycles 11 and 12. (See Table 1 for composition of the alloys.) Cycle 11 has just been completed and the specimens will be examined for changes in density and microstructure in the next reporting period.

In addition to the above experiment, additional specimens were placed in cycle 12 (MOTA 2B) at 365, 420, 520 and 600°C. Alloy NRIM-3 (Table 1) was irradiated in both the 20% cold worked and annealed conditions to explore the influence of cold work. Cold working is known to accelerate formation of sigma phase, which is also sensitive to carbon content.' A candidate alloy based on the results of out-of-reactor developmental studies at NRIM on this alloy series was also placed in MOTA 28. Its composition is Fe-10.10Cr-28.24Mn-1.85W-0.20V-0.20Ti-0.16C-0.008B and it is being irradiated in the annealed condition.

Table 1. Composition (wt%) of NRIM Alloys in FFTF Cycles 11 and 12

	C	Cr	Mn	Si	S	P	Cu	Sb	O	N
NRIM-1	0.003	10.09	28.4	0.46	0.010	<0.002	0.0005	0.0001	0.0064	0.0051
NRIM-2	0.033	10.11	28.2	0.46	0.010	<0.002	0.0005	0.0001	0.0071	0.0082
NRIM-3	0.110	9.81	29.94	0.49	0.009	<0.002	0.0002	0.0001	0.005	0.001
NRIM-4	0.263	9.86	30.09	0.48	0.009	t0.002	0.0002	0.0001	0.003	0.001
NRIM-5	0.546	9.92	30.77	0.46	0.010	<0.002	0.0002	0.0001	0.002	0.002

Irradiation of Second Generation AMCR Alloys

In the early FFTF irradiation studies on commercial alloys it was shown that AMCR alloy supplied by Creusot-Marrel (Fe-10Cr-18Mn-0.7Ni-0.6Si-0.06N-0.2C) exhibited somewhat better performance than the other alloys investigated. Researchers at the Ispra Establishment developed a series of lower activation variations on this steel which was inserted for irradiation in FFTF cycles 11 and 12 at 420, 520 and 600°C. (See Table 2 for the composition of these steels.) Cycle 11 has just been completed and these specimens will be examined in the next reporting period.

Table 2. Composition (wt.%) of ISPRA Second Generation AMCR Alloys

	Cr	Mn	Ni	Mo	C	N	Si	S	P	Cu	Al	Nb	V	W	Ta	Qb	Co	B
A	12.5	10 5	2	<0.1	0.10	<0.05	0.5	<0.01	<0.02	<0.1	<0.05	<0 001	3.75	1.4	<0.005	<0.001	<0.1	<0.005
B	12 5	10.5	<0 25	<0 I	0.30	<0.05	0.5	<0 01	<0.02	<0.1	<0.05	<0.001	0.75	1.4	<0.005	<0.001	<0.1	<0.005
C	12.5	11.5	2	<0.1	0.10	<0.05	0.5	<0.01	<0.02	<0.1	<0.05	<0.001	<0.1	2.0	<0.005	<0.001	<0.1	<0.005
0	10.0	17.5	<0.25	<0.1	030	<0.05	0.5	<0.01	<0.02	<0.1	<0.05	<0.001	<0.1	2.0	<0.005	<0.001	<0.1	<0.005
E	I7 0	10.5	2	<0.1	0.10	<0.05	0.5	<0.01	<0 02	<0.1	<0.05	<0.001	0 75	2.0	<0 005	<0.001	<0.1	<0.005

Irradiation of Soviet Candidate Steels

A joint U.S./U.S.S.R. development and irradiation study is being conducted with participation of the Baikov Institute in Moscow and the Oak Ridge and Pacific Northwest Laboratories. The Soviet side provided two groups of materials to the U.S. side. The first group involved sheets and rods of a steel designated 10Kh12G20V and was supplied to Oak Ridge National Laboratory. This material was derived from a vacuum induction melting heat with composition Fe-20.10Mn-12.15Cr-0.95W-0.01Ti-0.005V-0.32Si-0.10C. TEM disks 0.01-inch thick were prepared at Oak Ridge from the originally received 0.033-inch thick sheet. The specimens were placed in cycle 12 (MOTA 2B) in both the 20% cold worked and annealed (0.5 hr at 1100°C) conditions. Irradiation will proceed at 365, 400, 520 and 600°C.

The second group of material was sent to PNL in the form of annealed 4.6 mm diameter Cubes with 0.2 mm thick walls. The composition of this material wss Fe-19.0Mn-13.0Cr-1.0W-0.32Si 0.09C with 0.012S and 0.024P. Before the material was fabricated into pressurized tubes, a burst test was conducted at 600°C. The tube failed at a pressure of 2700 psi, equivalent to a midwall stress of 29 ksi (200 MPa). Working with Westinghouse Hanford Company, 1.0" long pressurized tubes were fabricated for insertion into MOTA 28. irradiation will proceed at 420, 520 and 600°C at hoop stresses of 0, 30, 60, 100 and 140 MPa. The stresses were chosen based on the burst test result and strength data supplied by the Soviet side. This is the first time pressurized tubes made from Fe-Cr-Mn steels will be irradiated.

FUTURE WORK

Based on recent decisions in the U.S. fusion materials community and an independent decision reached at a recent IEA sponsored workshop (Culham, U.K., April 1991), no new initiatives involving austenitic Fe-Cr-Mn steels will be pursued by Western and Japanese national laboratories. Wherever appropriate, however, work in progress will be completed and evaluated. It is anticipated, however, that some Soviet laboratories and Japanese university groups will continue to study austenitic Fe-Cr-Mn steels.

REFERENCES

1. H. R. Brager, F. A. Garner, D. S. Gelles and M. L. Hamilton, J. Nucl. Mater., 133-134 907 (1985).

2. F. A. Garner, H. R. Brager, D. S. Gelles and J. M. McCarthy, J. Nucl. Mater., 148 294 (1987).

3. F. A. Garner, F. Abe and T. Noda, J. Nucl. Mater., 155-157 870 (1988).

4. J. M. McCarthy and F. A. Garner, J. Nucl, Mater., 155-157 877 (1988).

5. J. M. McCarthy, J. Nucl. Mater., 176 (1990) in press.

6. F. A. Garner, H. R. Brager and H. Takahashi 176 (1990) in press.

7. F. A. Garner and J. M. McCarthy, ASTM STP 1047 (1990) pp. 19-29.

8. J. M. McCarthy, Fusion Reactor Materials Semiannual Prowess Report DOE/ER-0313-6 pp. 103-108 (1989).

9. S. Ohnuki, F. A. Garner, H. Takahashi and J. M. McCarthy, Fusion Reactor Semiannual Proqress Reoort DOE/ER-0313/8 pp. 139-145 (1990).

10. H. Takahashi, S. Ohnuki and F. A. Garner, Fusion Reactor Semiannual Prowess Report DOE/ER-0313/9 pp. 146-154 (1991).

11. Y. Okazaki, M. Machizuki, K. Miyahara and Y. Hosoi, ASTM STP 1047 pp. 80-92 (1990)

12. R. L. Klueh and P. J. Maziasz, ASTM STP **1047** pp. **7-18 (1990).**

13. Y. Murata, K. Kazuhiro, Y. Matsumoto and M. Morinaga, ISIJ International, 30 **927 (1990).**

14. W. Schüle, **E.** Lang and A. Panzarasa, Ispra Establishment Report EUR **11759** EN **(1988).**

15. P. Schafmeister and R. Ergang, Arch. Eisenhuttenwes., 12 507 **(1939).**

PHASE STABILITY IN THERMALLY AGED Fe-Cr-Mn ALLOYS - J. I. Cole and J. J. Hoyt (Northwest College and University Association for Science and Washington State University) and D. S. Gelles (Pacific Northwest Laboratory][a]

OBJECTIVE

The object of this work is to determine the thermal aging response of Fe-Cr-Mn alloys in order to provide comparison with irradiation behavior. This task is involved in the development of low activation austenitic steels.

SUMMARY

Fe-Cr-Mn alloys have been proposed as a structural material for fusion reactors that will exhibit reduced long-term radioactivity. However, Fe-Cr-Mn ternary equilibrium has not previously been well defined at temperatures below 650°C. The current experiment characterized phase evolution and equilibrium in three alloys: Fe-15Cr-15Mn, Fe-10Cr-30Mn and Fe-30Mn in the 20% cold-worked condition aged from 300 to 700°C for 1,000 to 30,000 hours at temperatures from 300 to 600°C. Results indicate that σ phase formation is extremely sluggish, and cold-working and long aging times are required to initiate σ phase formation in alloys not previously predicted to exhibit such precipitation. σ phase appears to form on high diffusivity paths such as recrystallizing grain fronts and grain boundary triple points. Three isothermal sections at 300, 500 and 600% were constructed from the experimental data that extend the temperature range of the Fe-Cr-Mn ternary diagram to lower temperatures than previously published.

PROGRESS AND STATUS

Introduction

Austenitic stainless steels play an important role in modern engineering. The three major constituents present in austenitic steels, Fe, Cr and Ni, provide a combination of corrosion resistance, strength and formability that is extremely desirable for many applications. Chromium induces passivation which provides high corrosion resistance, and nickel stabilizes the austenite phase, improving alloy formability. Because of their excellent properties, Fe-Cr-Ni austenitics had been considered as the material of choice for first wall and blanket materials in nuclear fusion reactors. However, when exposed to high fluence neutrons, Fe-Cr-Ni alloys produce extremely long-lived and highly radioactive transmutation products. As a result, a recent emphasis has been placed on the development of an Fe-Cr-Mn austenitic alloy which would exhibit greatly reduced long-term radioactivity. In contrast to Fe-Cr-Ni alloys, a more limited amount of information is available on the ternary phase equilibrium in the Fe-Cr-Mn system, mainly due to the limited applications in which it would be superior to Fe-Cr-Ni. Now that a need for low activation Fe-Cr-Mn alloys has been realized, additional data on the ternary phase equilibrium is required.

The purpose of this study is to characterize the phase evolution and phase equilibrium of two simple Fe-Cr-Mn ternary alloys and one simple Fe-Mn binary alloy as a function of aging time and temperature. The alloys in a 20% cold worked condition were aged in the temperature range of 300 to 700°C (573K to 973K) for times between 1,000 and 30,000 hours. These materials were aged by H. R. Brager and F. A. Garner as part of their irradiation study on reduced activation materials. The long aging times were used to ensure the attainment of phase equilibrium. Characterization of the alloys was done using optical microscopy, magnetic measurements, microhardness tests, and electron microscopy. The final results were compared with the known literature. Finally, isothermal sections based on experimental data were constructed.

ExDerimental Procedure

The present investigation characterized the microstructure of 3 alloys, with nominal compositions Fe-15Cr-15Mn, Fe-10Cr-30Mn and Fe-30Mn; the actual compositions, determined analytically, are given in Table 1. The alloys were cast as button melts in a standard electric arc furnace. Following casting, the alloys were cold-rolled in a succession of steps, each step followed by annealing at 1050°C for 1/2 hour and then air cooling. The final sheets, in unannealed 20% cold worked condition, were approximately 1/2 in. by 1 in. by 0.0012 in. The sheets were wrapped in bundles with tantalum wire and encapsulated in quartz tubes with 1/4 atmosphere of argon. The target aging temperatures and times were 400, 500, 600 acd 700°C for 1,000 hours and 300, 400, 500 and 600°C for 10,000 and 30,000 hours, or approximately 3.5 years. The actual times varied for the individual furnaces and are given in Table 2. The quartz tube holding the 400°C samples broke during aging; therefore the maximum aging time for the 400°C samples was around 5000 hours. The total test matrix contained 33 samples.

(a) Pacific Northwest Laboratory is operated for the U.S. Department of Energy by Battelle Memorial Institute under Contract DE-AC06-76RLO 1830.

Table 1. Compositions (in Weight Percent) of the Three Alloys Examined as Determined by the Oregon Metallurgical Corporation, Albany, Oregon

	Fe-15Cr-15Mn	Fe-10Cr-30Mn	Fe-30Mn
C	0.02	0.035	0.054
N	0.007	0.003	0.005
V	0.01	0.01	0.01
Fe	remainder	remainder	remainder
Cr	13.2	9.2	0.01
Ni	0.02	0.01	0.02
Si	0.1	0.1	0.1
cu	0.03	0.03	0.03
Mn	14.5	31.6	31.8

Table 2. Actual Aging Times for the Fe-15Cr-15Mn, Fe-10Cr-30Mn and the Fe-30Mn Alloys Aged at 300, 400, 500, 600 and 700°C

Temperature (°C)	Aging Times (hours)
300	9,215 and 28,653
40G	1,000 and 5,000
500	1,000, 8,927 and 27,384
600	1,000, 9,231 and 27,646
700	1,000

Magnetic measurements were obtained on the aged specimens using a ferrite indicator to determine qualitatively the volume fraction of ferrite present in the material. Five to ten, 3 mm transmission electron microscopy (TEM) discs were punched from the original 0.25 mm sheets. These discs were used for both optical and electron microscopy. Punching caused the discs to be cup-shaped, indicating deformation at the disc edges. Two discs for each sample were prepared in a single metallographic mount for optical examination and microhardness measurements, one facing flat and one on edge. The samples were ground through 600 grit sandpaper and polished on Buehler automatic polishers using standard polishing procedures. The Fe-30Mn samples had to be polished in oil rather than water because of their tendency to pit and oxidize. Careful attention was paid to the amount of grinding and polishing done because the thin TEM samples were easily worn away. The etchants used were, for Fe-15Cr-15Mn and Fe-10Cr-30Mn, Villela's etch swabbing for 5 to 20 sec; and for Fe-30Mn, 2% Nital swabbing for 30 to 60 sec. Microhardness measurements were made on the as-polished samples because it was found that the microstructure of the etched samples obscured the edges of the hardness indentatlon. Measurements were made on the samples mounted on edge to ensure the indenter did not penetrate completely through the extremely thin samples. Five to six measurements were made on each sample with a Vickers indenter and a 500 g load. The length and width of the indentations were measured in filar units and converted to Vickers hardness using conversion tables based on the system magnification.

Image analysis of selected photomicrographs was done on an Apple Macintosh personal computer. The second phase precipitate area fractions and particle sizes were determined for the Fe-10Cr-30Mn samples exhibiting precipitation. This was done by digitizing the image of the photomicrograph which could then be processed to isolate the features of the image to be measured, in this case the second phase. The program automatically computes the area fraction, and measures the size of each feature and generates a size distribution profile based on an entered magnification. Image analysis was determined to be unusable with the Fe-15Cr-15Mn alloy due to the complexity of the microstructure.

The samples used for electron microscopy were prepared as thin samples. The punched discs were further ground to approximately 0.05 mm using 600 grit grinding paper. Following grinding, the samples were thinned

using a Tenupol-3 jet electropolisher. Two electropolishing solutions were tried. One used a 5:1 mixture of methanol:H_2SO_4 and the other 90% perchloric:10% glacial acetic acids. Polishing conditions were 35 V and 0.5 amp at a flow rate of 6 and sensitivity of 9.5. Both solutions worked with similar results. Approximately 5 samples were thinned for each individual specimen. Extra care was required to completely dry the Fe-30Mn samples to avoid oxidization.

Characterization of the alloys was performed using a JEOL 1200EX electron microscope equipped with a double tilt goniometer, an energy dispersive X-ray (EDX) detector for EDX analysis and an acquired scanned image device (ASID) for operation in scanning transmission electron microscopy (STEM) mode. Each of the samples were characterized using EOX analysis, and selected area diffraction of the individual phases within the samples. Selected area diffraction (SAD) was performed in the transmission electron microscopy (TEM) mode to determine crystal structure. The diffraction patterns generated using the SAD technique were identified with the aid of a computer program called Diffract for the Apple Macintosh computer. The program required the entry of microscope voltage, crystal structure (position of the atoms and type) and the camera length. With this information the program generated scaled diffraction patterns for the entered parameters. An initial calculation of the lattice parameters was done by indexing an actual pattern by hand. The camera length was calibrated using a polycrystalline Al standard. A series of diffraction patterns were generated for low index zone axes. BY comparing the computer generated patterns to the actual' photographic negatives of the individual phases, the crystal structures were readily identified.

The compositional analysis of the materials using EDX analysis in STEM mode was performed using "free lens control" of the first and second condenser lens strength which gave control of the beam size and convergence angle, and thus, some control over the intensity of the characteristic x-rays emitted. A position that was, by visual inspection, in a single phase field and near the edge of the sample was chosen. The beam was placed on the selected region and the free lens controls adjusted to achieve a count rate greater than 300 counts per second (cps) without overloading the x-ray detector. A computer program was used that collected a spectrum for a period of 60 seconds, saved the spectrum to disk, and calculated the weight percentages.

The program that determined the weight percentages used a modified verrion of the Cliff-Lorimer equation

$$\frac{C_A}{C_B} = K_A \frac{I_A}{\sum I, \; t \; I, \; t \; \ldots}$$

where the intensities after background subtraction are used. One additional difficulty was correcting for the overlapping peaks Mn-K, with Fe-K_α and Cr-K_β with Mn-K_α. A factor of $K_\alpha = (0.16)K_\beta$ was used to correct for overlapping peaks. The constants K_{Mn}, K_{Fe} and K_{Cr} were calculated from an Fe-10Cr-30Mn sample solution treated for 2 hours at 1150°C. This sample was single phase and the compositions as determined analytically were used along with the relative intensities after background subtraction to calculate the K factors. Ten separate calculations of the K factors were made and averaged. The calculated K factors were K_{Mn} = 1.06, K_{Fe} = 1.01 and K_{Cr} = 0.89. The calibrated factors were entered into the program and used throughout the EDX analysis.

Results

To clearly portray the phase evolution and phase equilibrium in the three alloys investigated, the results of each alloy will be described individually. The parameters discussed will include microstructural changes during aging, recovery and recrystallization characteristics, and compositions of the individual phases within each of the alloys, in anticipation of the eventual construction of isothermal sections for the equilibrium phase diagram.

Fe-15Cr-15Mn

The Fe-15Cr-15Mn alloys exhibited the most complex microstructures. Optical micrographs of the Fe-15Cr-15Mn alloys aged for 1,000, 5,000, 10,000 and 30,000 hours for 300, 400, 500, 600 and 700°C are shown in Figures 1 through 5. The micrographs indicate that what initially appears to be a lath structure (darker features) is transforming to large block-like precipitates with aging time. The micrographs when combined with the magnetic and hardness measurements, shown in Table 3 and 4, respectively, indicate the nature of the phase evolution taking place. The lath structure was identified as deformation-induced martensite, while the block-like precipitates were σ phase. A cursory identification of the phases present within each of the Fe-15Cr-15Mn samples is presented in Table 5 and was later confirmed by electron microscopy.

The micrographs indicate that martensite is present in the samples aged for less than 10,000 hours at 500°C and below. The martensite could either be epsilon (HCP) or α' (BCT). Epsilon martensite forms from the γ phase upon quenching and then transforms to α' during deformation. The alloys aged at 600 and 700°C contain no martensite and appear to have reached equilibrium within the first 1,000 hours of aging. In addition, these alloys lacked magnetism, indicating an absence of ferrite. Thus, the two phase lamellar structure was identified as γ t σ and the lighter regions were determined to be single phase γ. The general consistency

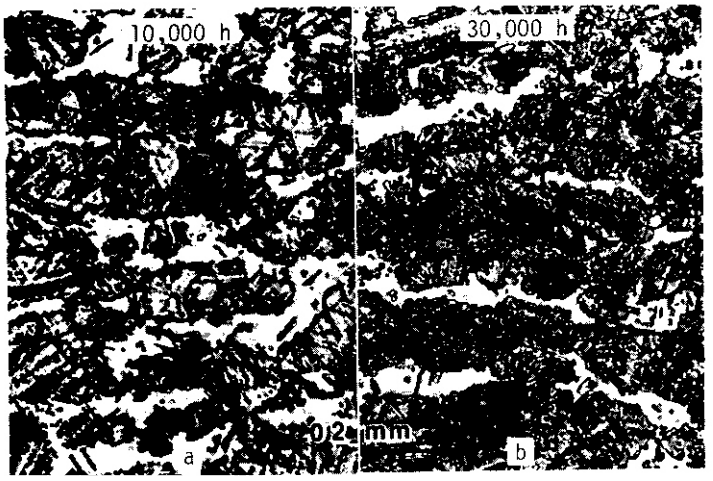


Figure 1. Fe-15Cr-15Mn aged for 10,000 and 30,000 hours at 300°C.

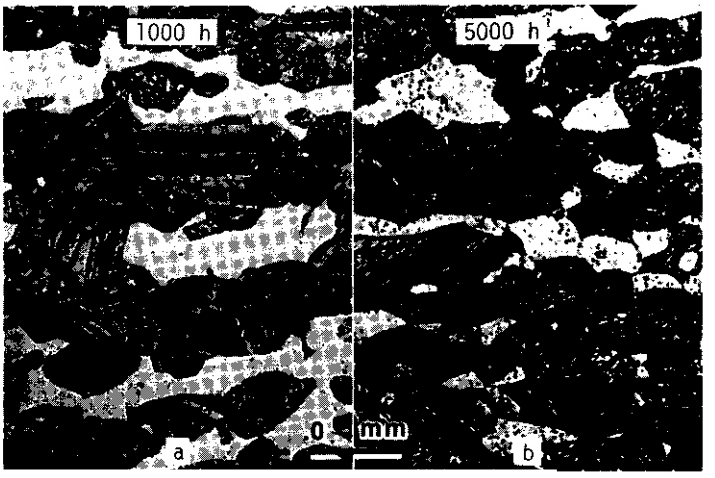


Figure 2. Fe-15Cr-15Mn aged for 1,000 and 5,000 hours at 400°C.

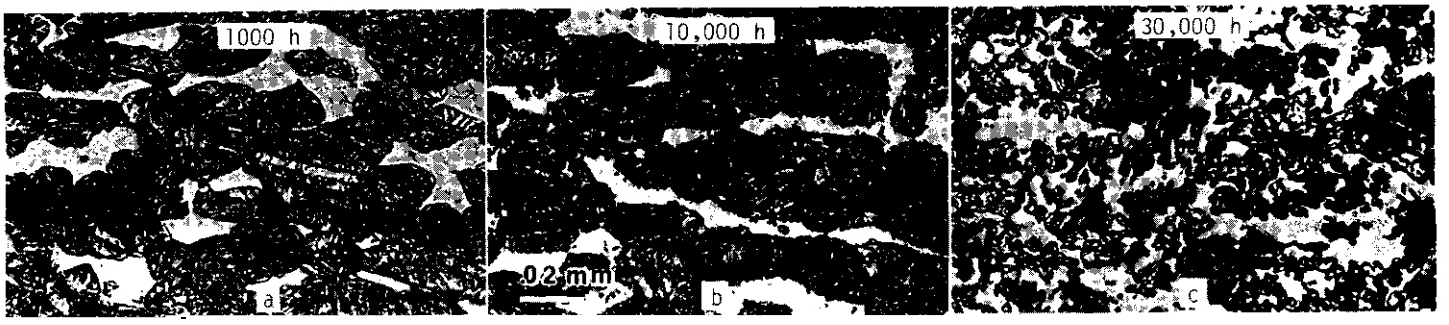


Figure 3. Fe-15Cr-15Mn aged for 1,000, 10,000 and 30,000 hours at 500°C.

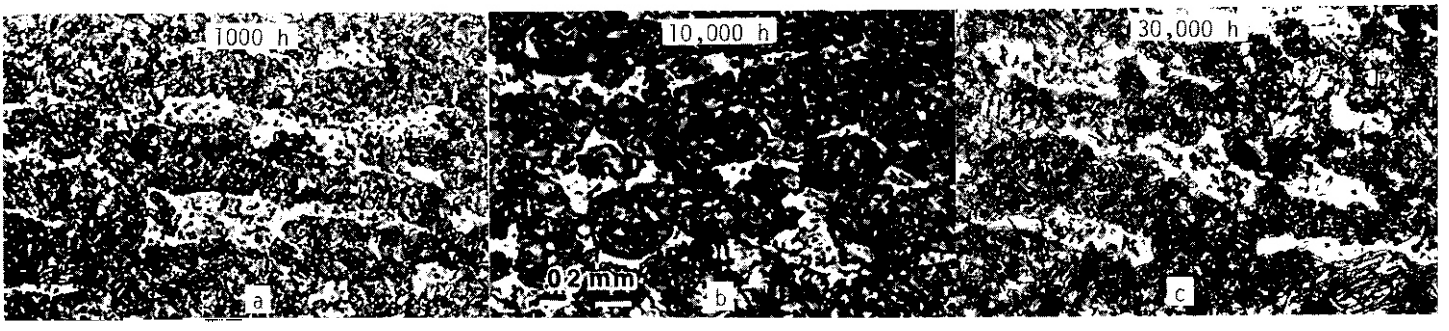


Figure 4. Fe-15Cr-15Mn aged for 1,000, 10,000 and 30,000 hours at 600°C.

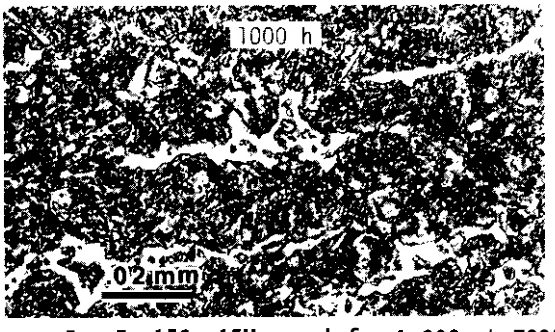


Figure 5. Fe-15Cr-15Mn aged for 1,000 at 700°C.

Table 3. Magnetic Measurements of Ferrite (in Weight Percent) in the Fe-15Cr-15Mn Alloys

TemDerature	Treatment Times 1.000 hrs	5.000 hrs	10,000 hrs	30,000 hrs
300°C			7.5-10.0	7.5-10.0
400°C	17.5-20.0	20-25.0		
500°C	12.5-15.0		10-12.5	7.5-10.0
600°C	0.0		0.0	0.0
700°C	0.0			

Table 4. Vickers (VHN) Hardness of the Fe-15Cr-15Mn Alloys

TemDerature	Treatment Times 1.000 hrs	5,000 hrs	10,000 hrs	30.000 hrs
300°C			355	352
400°C	380	395		
500°C	348		333	285
600°C	340		337	344
700°C	288			

Table 5. Identification of Phases Present in the Fe-15Cr-15Mn Alloys

TemDerature	Treatment Times 1.000 hrs	5.000 hrs	10,000 hrs	30,000 hrs
300°C			σ,γ,α,M	σ,γ,α
400°C	σ,γ,M	σ,γ,M		
500°C	σ,γ,M		σ,γ,α	σ,γ,α
600°C	σ,γ		σ,γ	σ,γ
700°C	σ,γ			

of the hardness measurements indicate that although the martensite is disappearing with time, the formation of brittle σ negates any significant change in hardness due to the disappearance of martensite.

The 30,000 hour microstructures and magnetic measurements, for the temperatures investigated, indicate that the Fe-15Cr-15Mn composition is very near the $\alpha+\gamma+\sigma/\gamma+\sigma$ phase boundary. At 300 and 500°C, three phases, $\alpha+\gamma+\sigma$, are present; the 600°C sample contains only $\sigma+\gamma$. Overall, it appears that the σ phase forms at the expense of α and then coarsens with increased time and temperature, completely transforming the α to σ at 600°C.

The compositions of the individual phases, as determined by EOX analysis, are given in Tables 6 through 8. The standard deviations were calculated based on the averages of 10-15 measurements. Typical EDX spectra obtained from the individual phases α, σ and γ are shown in Figure 6. The spectra frequently exhibited sulfur peaks which were determined to be residual sulfur from the H_2SO_4 in the electrolytic solution.

Figure 7 shows the electron diffraction patterns of the individual phases α, σ and γ generated using selected area diffraction.

The phase identification and compositions determined by EDX analysis confirm the observations made using optical microscopy. In addition to the phases listed in Table 5, there were found extremely small particles which appeared to be some type of carbide. Because their volume fraction was so low, the particles were not considered in the study beyond noting they existed. The martensitic structure in the alloys had a

Table 6. Fe-15Cr-15Mn Phase Compositions (in Weight Percent) After 1000 Hours of Aging

	Cr	Standard Deviation	Mn	Standard Deviation	Fe	Standard Deviation
400°C Aging Temuerature						
γ	12.84	0.47	13.52	1.02	73.64	1.26
α	18.28	0.53	12.61	0.57	69.11	0.35
500°C Aging Temuerature						
γ	13.76	0.73	14.82	0.94	71.42	2.45
α	19.59	1.22	12.18	1.34	68.23	1.27
600% Aging Temuerature						
σ	26.80	1.28	13.26	0.47	59.93	1.09
γ	10.95	0.72	14.11	1.20	74.95	1.46
700°C Aging Temperature						
σ	26.66	0.59	13.36	0.81	59.97	0.81
γ	12.28	0.87	14.67	0.99	73.05	2.36

Table 7. Fe-15Cr-15Mn Phase Compositions (in Weight Percent) After 10,000 Hours of Aging

	Cr	Standard Deviation	Mn	Standard Deviation	Fe	Standard Deviation
300°C Aging Temperature						
σ	27.02	1.38	17.86	1.80	55.12	1.98
γ	13.02	0.38	15.41	0.80	71.57	3.02
α	10.07	1.08	3.99	0.54	85.93	1.42
400°C Aging TemDerature						
γ	12.72	0.61	14.91	1.01	72.37	2.26
α	17.74	1.28	12.27	1.11	69.99	2.30
500°C Aging TemDerature						
σ	26.80	0.54	17.42	0.58	55.78	0.56
γ	12.51	0.34	15.36	0.44	72.13	0.54
α	11.99	1.49	4.69	0.92	83.32	2.34
600°C Aging TemDerature						
σ	27.96	0.56	13.51	0.62	58.53	0.28
γ	11.13	0.38	14.45	1.33	74.42	1.30

composition close to that of the austenite. Figure 8 shows a TEM micrograph of the martensite structure. Except for the samples at 300 and 400°C, all of the samples appeared to have reached equilibrium at 10,000 hours of aging, indicated by the negligible change in composition of the individual phases between 10,000 and 30,000 hours of aging.

Other deformation-induced features were present in the microstructure in addition to the martensite. Figure 9 shows a series of stacking faults in the austenite. The darker particles are σ phase. The σ and ferrite grains exhibit relatively low dislocation density compared to the austenite, particularly at the lower temperatures and shorter aging times.

Overall, the electron microscopy indicated that at 1,000 hours of aging there were large regions of α, γ and martensite, and upon further aging the α recrystallized and σ formed profusely within the α. Following recrystallization, the α and σ grains were nearly the same size. The lamellar structure in the optical micrographs of the three-phase alloys aged at 300 and 500°C for 30,000 hours was identified as α+γ+σ. Above 600°C, α had completely transformed to σ, forming a σ+γ lamellar structure after 1000 hours.

Table 8. Fe-15Cr-15Mn Phase Compositions (in Weight Percent) After 30,000 Hours of Aging

	Cr	Standard Deviation	Mn	Standard Deviation	Fe	Standard Deviation
300°C Aging Temperature						
α	27.56	1.14	18.41	0.82	54.03	1.67
γ	13.27	0.52	15.40	0.88	71.33	1.44
α	9.82	1.36	4.45	1.18	85.73	3.21
500°C Aging Temperature						
σ	26.47	1.22	17.71	0.77	55.82	1.02
γ	13.24	0.50	15.27	0.96	71.49	1.55
α	10.31	2.00	4.73	1.32	84.96	3.87
600°C Aging Temperature						
σ	26.97	0.90	13.60	0.40	59.43	1.09
γ	11.84	1.94	14.35	1.28	73.80	1.73

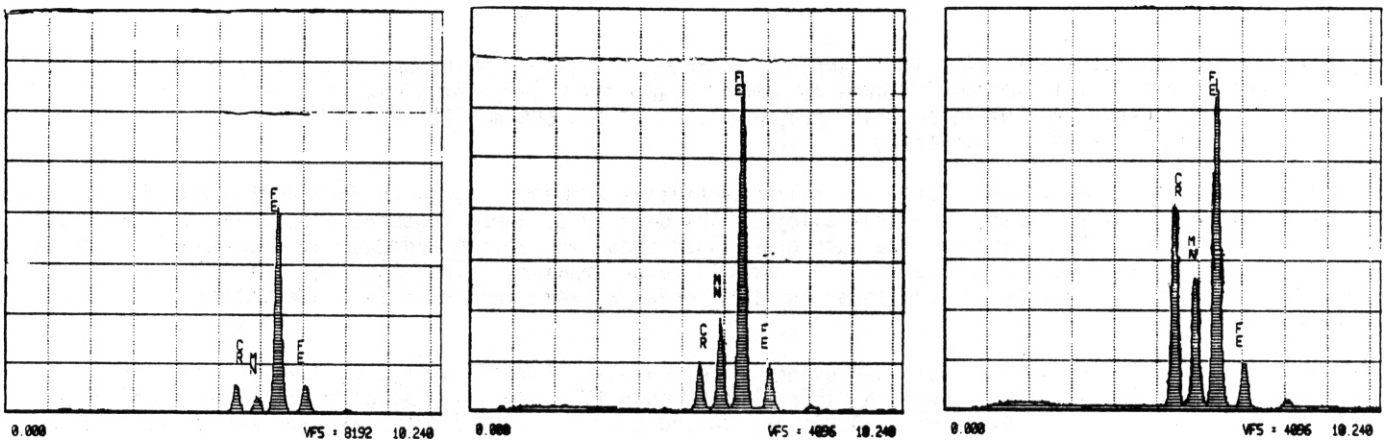


Figure 6. EDX spectra of the α, γ and σ phases of Fe-15Cr-15Mn aged for 30,000 hours at 500°C.

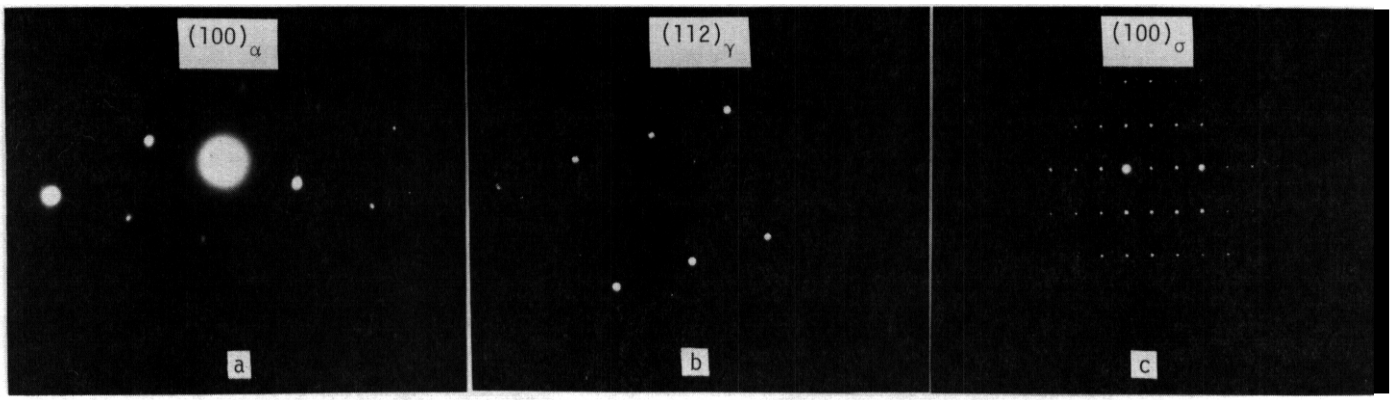


Figure 7. Diffraction patterns of the α, γ and σ phases of Fe-15Cr-15Mn aged for 30,000 hours at 500°C.

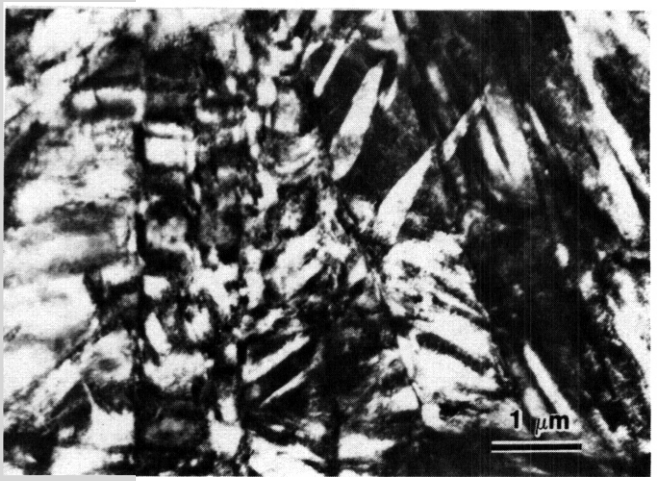


Figure 8. Martensite in the Fe-15Cr-15Mn alloy aged at 500°C for 1,000 hours.

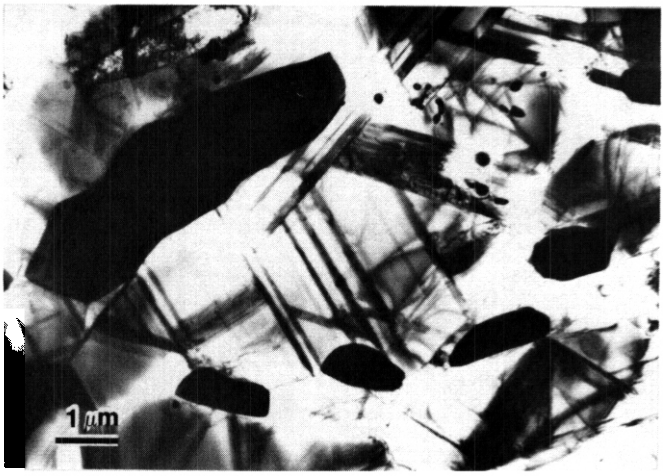


Figure 9. Stacking faults observed in the austenite phase of the Fe-15Cr-15Mn sample aged at 600°C for 30.000 hours.

Fe-10Cr-30Mn

Optical micrographs of the Fe-10Cr-30Mn sample are shown in Figures 10 through 14. The'alloys exhibit a significarit amount of deformation features at 300, 400 and 500°C and substantial second phase precipitation at the grain boundaries and grain boundary triple points in the 600 and 700°C samples. All eleven of the Fe-10Cr-30Mn samples were nan-magnetic.

The deformation features are most likely epsilon martensite and twinning which form during rapid cooling or during deformation of high manganese iron alloys. The density of these features decreases with increasing time and higher aging temperature. The hardness values shown in Table 9 indicate an increase in hardness in the samples following the precipitation of σ which is to be expected. The alloy aged at 500°C exhibited some recrystallization and the precipitates on the boundaries were not explicitly identified but appeared a type of carbide.

The particle size distributions, obtained using image analysis, for the alloys aged at 600 and 700°C exhibiting σ phase precipitation are shown in Figures 15 through 17. The data indicates there is negligible coarsening of the precipitates between 10,000 and 30,000 hours. The uniform size and absence of precipitate coarsening with aging time indicate that the mechanism of precipitate growth has slowed considerably with aging time in the Fe-10Cr-30Mn alloys. At 700°C for 1,000 hours of aging the particles are smaller than the particles formed at 600°C, as is the volume fraction of particles.

The compositions of the alloys aged for 30,000 hours are shown in Table 10. The 300 and 500°C samples were single phase austenite while the 600°C sample contained austenite and σ. Within experimental error, the

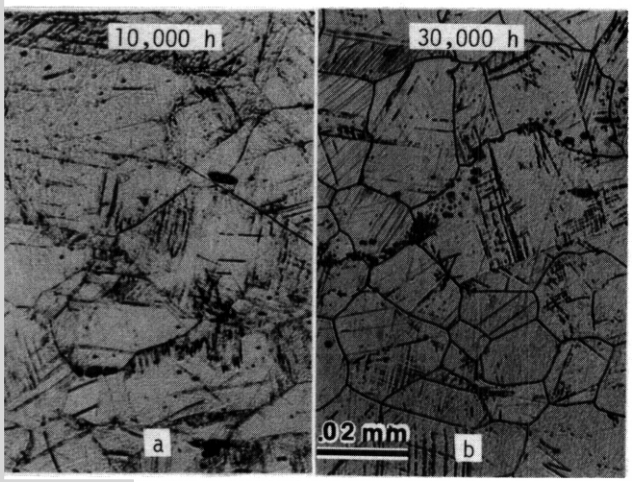


Figure 10. Fe-10Cr-30Mn aged for 10,000 and 30.000 hours at 300°C.

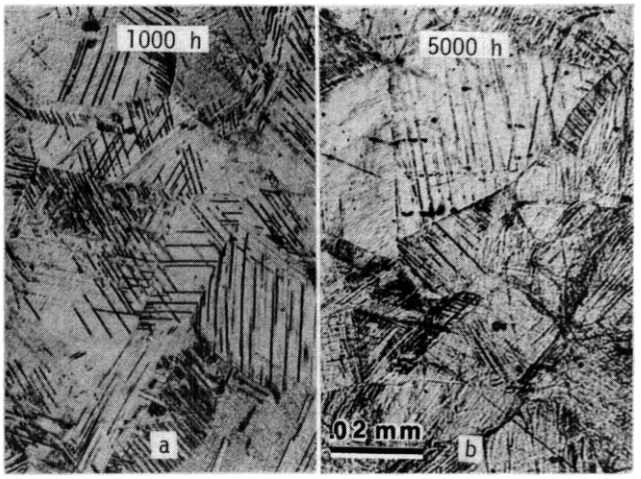


Figure 11. Fe-10Cr-30Mn aged for 1,000 and 5,000 hours at 400°C.

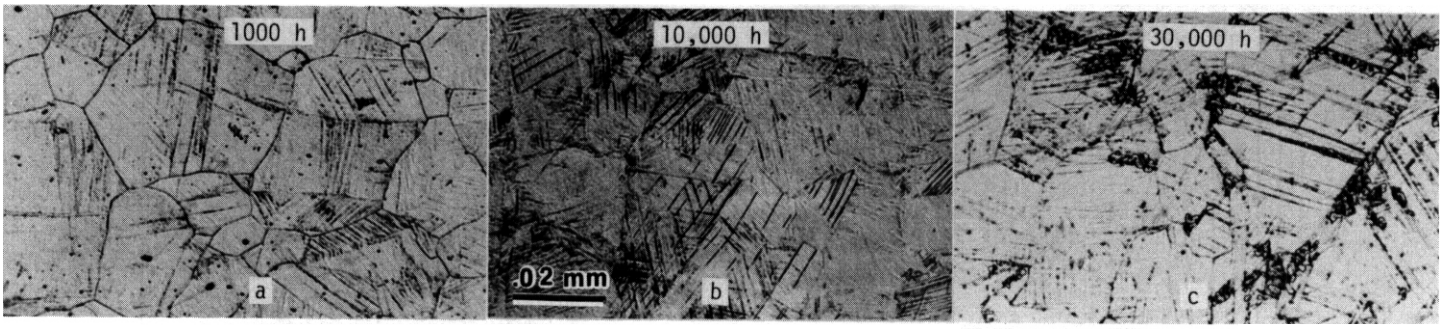


Figure 12. Fe-10Cr-30Mn aged for 1,000, 10,000 and 30,000 hours at 500°C.

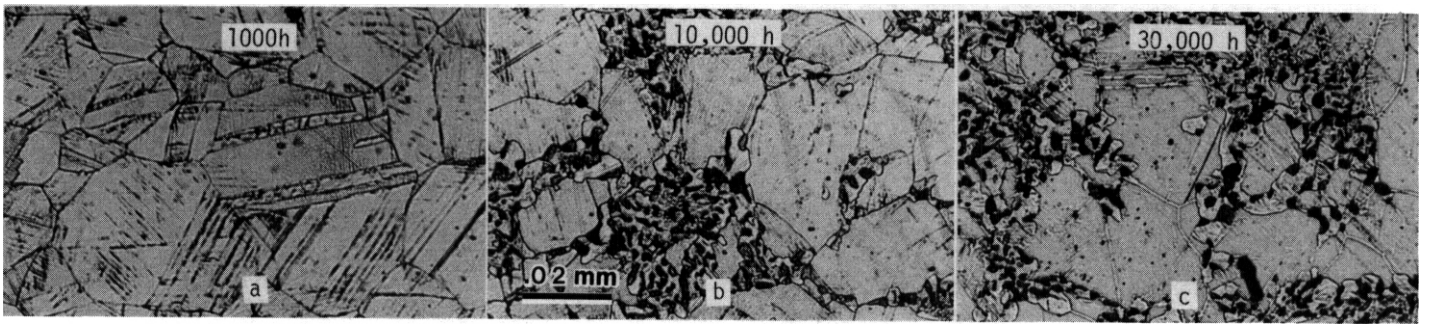


Figure 13. Fe-10Cr-30Mn aged for 1,000, 10,000 and 30,000 hours at 600°C.

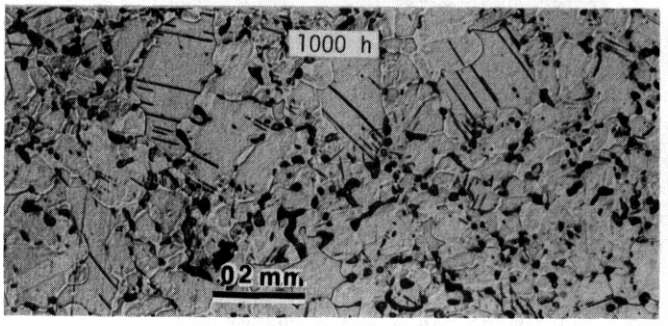


Figure 14. Fe-10Cr-30Mn aged for 1,000 at 700°C.

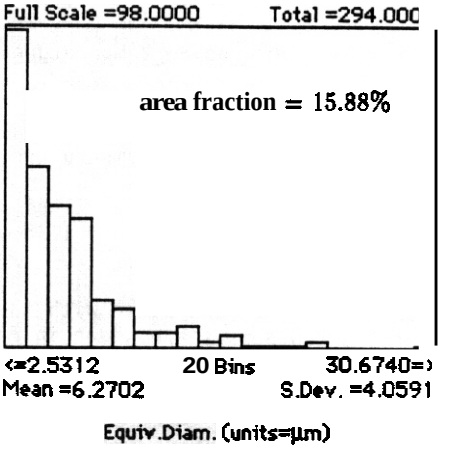


Figure 15. Particle size distribution of the σ phase in the Fe-10Cr-Mn aged at 600°C for 10,000 hours.

Table 9. Vickers Hardness (VHN) of the Fe-10Cr-30Mn Alloys

	Treatment Times			
Temperature	1,000 hrs	5,000 hrs	10,000 hrs	30,000 hrs
300°C			250	193
400°C	270	243		
500°C	244		209	286
600°C	173		206	263
700°C	169			

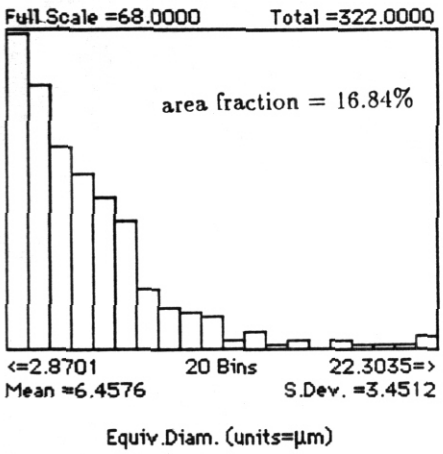


Figure 16. Particle size distribution of the σ phase in the Fe-10Cr-Mn aged at 600°C for 30,000 hours.

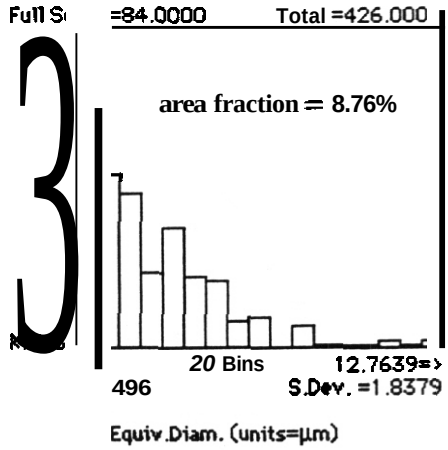


Figure 17. Particle size distribution of the σ phase in the Fe-10Cr-Mn aged at 700°C for 1,000 hours.

Table 10. Fe-10Cr-30Mn Phase compositions After 30,000 Hours of Aging

	Cr	Standard Deviation	Mn	Standard Deviation	Fe	Standard Deviation
400°C aging temperature.						
γ	10.10	1.75	31.86	1.65	58.04	3.22
500°C aging temperature.						
γ	8.864	0.57	31.23	1.12	59.92	1.20
600°C aging temperature.						
σ	10.99	1.86	35.14	0.93	53.87	1.54
γ	8.14	1.36	30.55	1.42	61.30	2.21

single phase determinations agree with the overall composition given in Table 1. The electron diffraction patterns of the two phases are shown in Figure 18. Typical spectra of the γ and σ phases are shown in Figure 19.

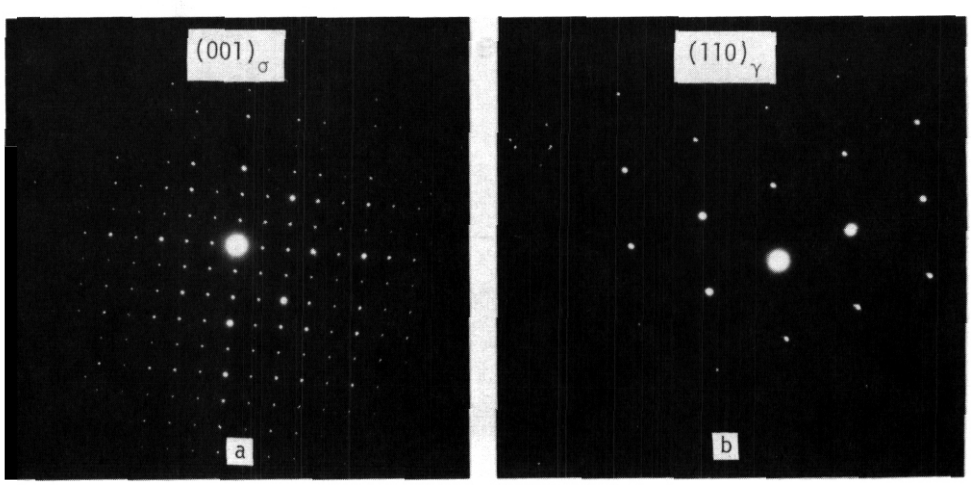
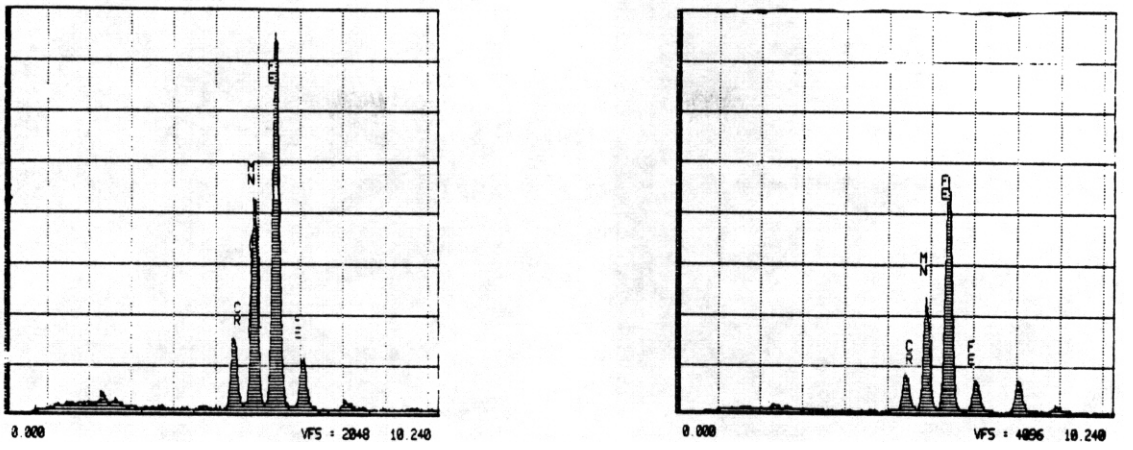


Figure 18. Diffraction patterns of the σ and γ phases of Fe-10Cr-30Mn aged for 30,000 hours at 600°C.



σ γ

Figure 19. EDX spectra of the σ and γ phases in Fe-10Cr-30Mn aged for 30,000 hours at 600°C.

The σ phase was preferentially etched during electropolishing, in the Fe-10Cr-30Mn alloys leaving many holes where the σ phase had existed. The σ phase was definitely precipitating on grain boundaries as shown in the TEM micrograph of Figure 20. Such data would support the supposition that σ is able to form only on such high diffusivity interfaces. Figure 21 illustrates the high density of extended stacking faults within the single phase austenite sample aged at 400°C for 1,000 hours. The material within the faults protruded into the hole produced by thinning as the surrounding material of higher energy was preferentially etched away.

Fe-30Mn

All thermomechanical treatment conditions produced a non-magnetic single phase in the Fe-30Mn samples. Figures 22 through 26 illustrate the microstructures of each of the conditions. The Fe-30Mn samples exhibited epsilon martensite formation similar to the Fe-10Cr-30Mn alloys. In addition, recrystallizing grains appear in samples aged at 600°C and above, and for all the samples aged for 30,000 hours. Hardness measurements given in Table 11 suggest such a process of recrystallization. One can see a noticeable decrease in hardness when comparing those microstructures exhibiting recrystallized grains to those that do not.

The EDX derived compositions for the Fe-30Mn samples aged for 30,000 hours are shown in Table 12. Except for the 500°C condition, the compositions obtained are within experimental error of the overall composition given in Table 1. The single phase was determined to be austenite using selected area diffraction. Figure 27 shows what appears to be a recrystallizing grain within a severely deformed matrix.

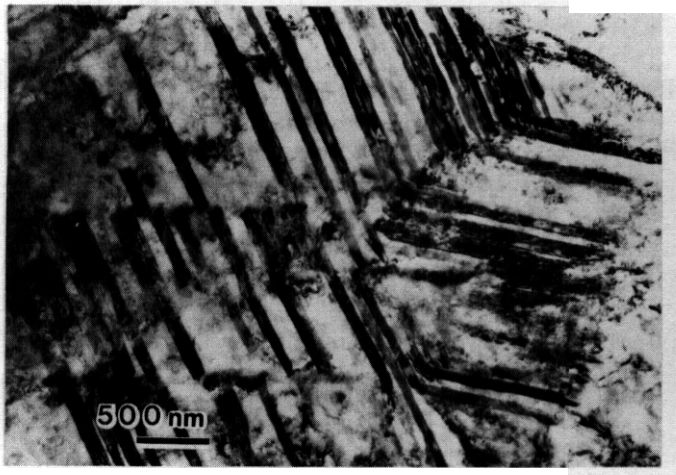


Figure 20. TEM micrograph of σ precipitation on a grain boundary during aging of an Fe-10Cr-30Mn alloy aged for 1,000 hours at 700°C.



Figure 21. Extended stacking faults in the austenite phase of an Fe-10Cr-30Mn alloy aged at 400°C for 1,000 hours.

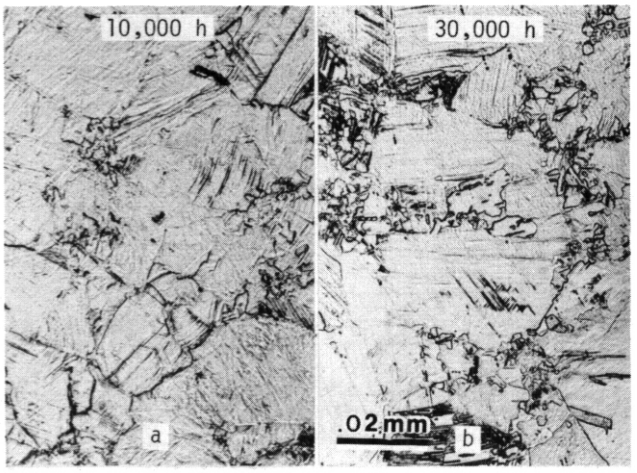


Figure 22. Fe-30Mn aged for 10,000 and 30,000 hours at 300°C.

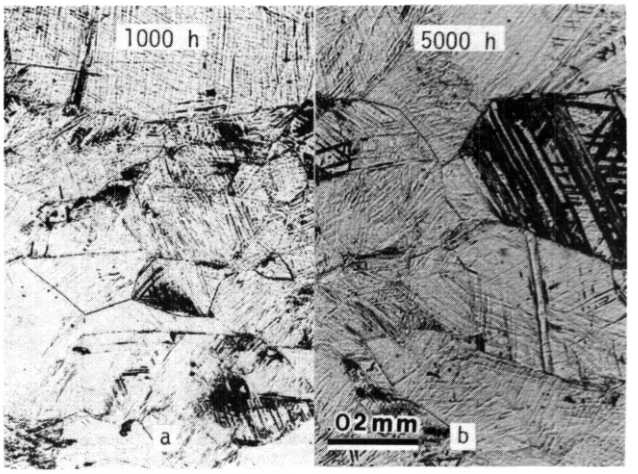


Figure 23. Fe-30Mn aged for 1,000 and 5,000 hours at 400°C.

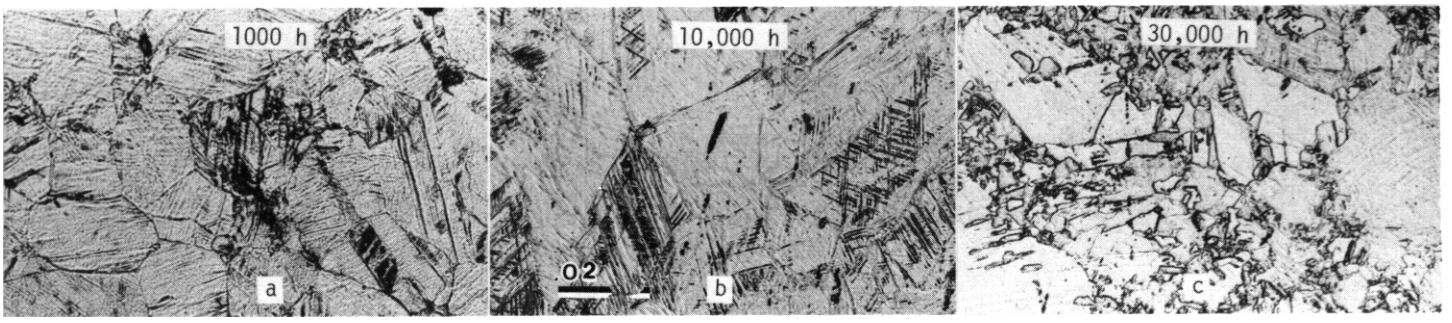


Figure 24. Fe-30Mn aged for 1,000, 10,000 and 30,000 hours at 500°C.

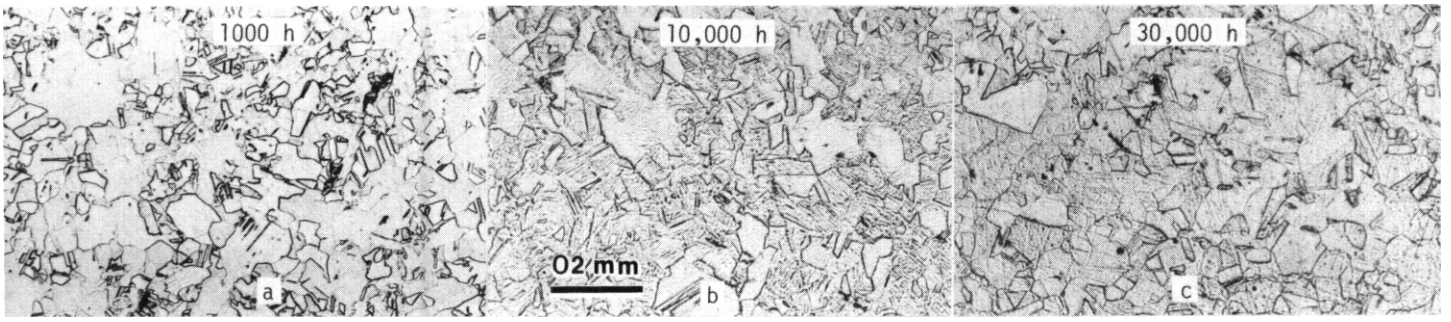


Figure 25. Fe-30Mn aged for 1,000, 10,000 and 30,000 hours at 600°C.

Table 11. Vickers Hardness (VHN) of the Fe-30Mn Alloys

	Treatment Times			
Temperature	1,000 hrs	5,000 hrs	10.000 hrs	30.000 hrs
300°C			226	212
400°C	255	293		
500°C	271		213	193
600°C	144		166	163
700°C	114			

Table 12. Fe-30Mn Phase Compositions (in Weight Percent) After 30,000 Hours of Aging

	Mn	Standard Deviation	Fe	Standard Deviation
300°C Aaina Temoerature				
γ	31.36	0.50	68.70	0.50
500°C Aaina Temoerature				
γ	31.05	0.41	68.95	0.42
600°C Aaina Temoerature				
γ	31.34	0.95	68.66	0.90

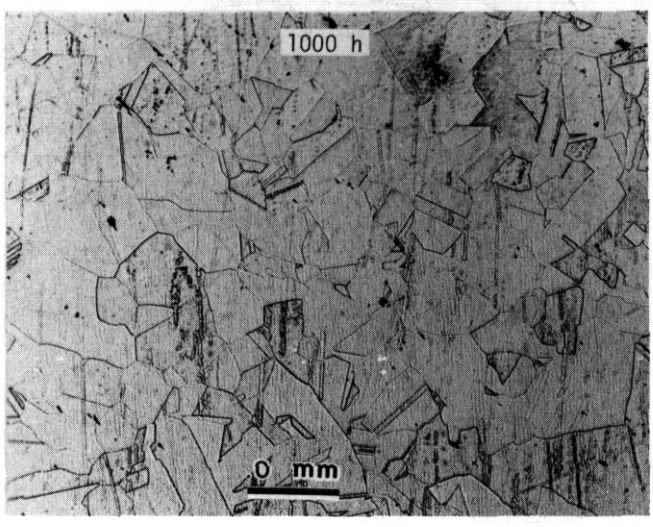
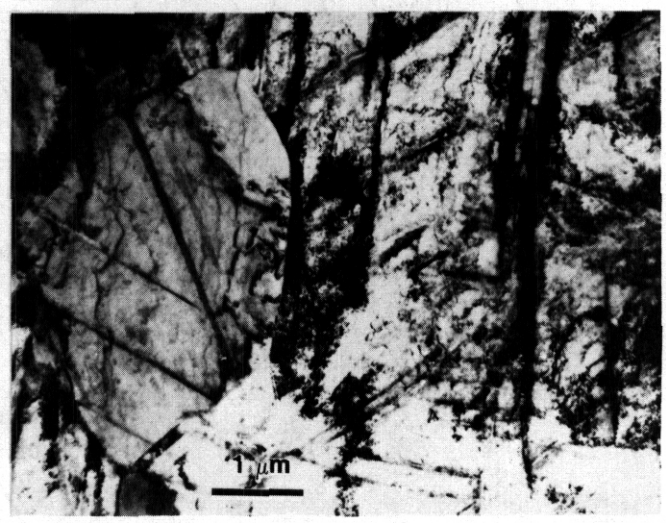


Figure 26. Fe-30Mn aged for 1,000 at 700°C.



Fiaure 27. TEM micrograph of recrystallizina grain within deformed austenite matrix of the Fe-30Mn alloy aged for 30,000 hours at 500°C.

Discussion

Fe-Cr-Mn Phase Oiaaram

Figure 28 shows an isothermal section constructed from the 600°C compositional data. Data points with connected solid tie-lines define the composition measurements from the base compositions while the dashed lines are interpolations based on the Fe-Cr and Fe-Mn binary diagrams.[1,2] Figure 29 illustrates the Fe-Cr-Mn diagram derived at 500°C. Once again, the dashed lines indicate interpolations based on the binary diagrams. The diagram suggests that as the temperature is reduced, the three phase $\sigma+\gamma+\alpha$ triangle is moving towards higher Mn. The single phase σ region has also retreated to higher levels of chromium. The Fe-10Cr-30Mn sample is now single phase austenite indicating the γ phase boundary has moved to higher levels of Cr. The isotherm at 300°C is shown in Figure 30. In the binary Fe-Cr diagram, a eutectoid reaction σ to $\alpha+\alpha'$ occurs at approximately 420°C. As a consequence, a three phase triangle $\alpha+\alpha'+\sigma$ should exist between the three phase triangle $\sigma+\gamma+\alpha$ and the Fe-Cr edge, but may shift to lower temperatures. The single phase austenite field extends to between 10 and 15% Cr at 300°C. In viewing the three isotherms in Figures 28 through 30 as a whole, some general comments can be made. As the temperature is increased, the $\sigma+\gamma/\sigma+\gamma+\alpha$ phase boundary appears to be moving towards lower manganese content, making σ phase more stable in higher manganese compositions. The γ phase field appears to be constricting as temperature increases as a consequence of the expanded σ phase field.

Comparison with Previous Work

Overall, the results of the present study confirm that the phase diagrams developed in the earliest studies in the Fe-Cr-Mn system do not accurately describe the phase equilibrium. A review of several earlier studies on the phase equilibrium diagrams of Fe-Cr-Mn was made by Rivlin and Raynor.[3] However, more recent

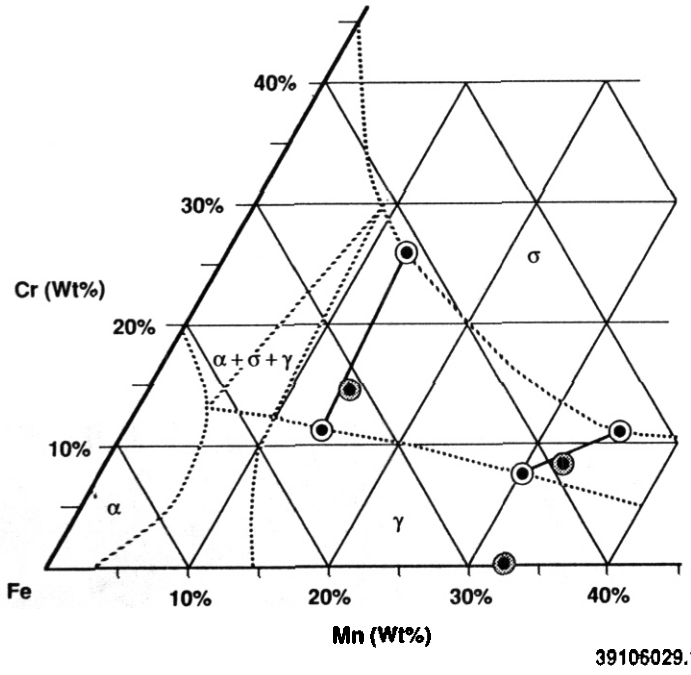


Figure 28. 600°C isotherm derived for Fe-Cr-Mn system.

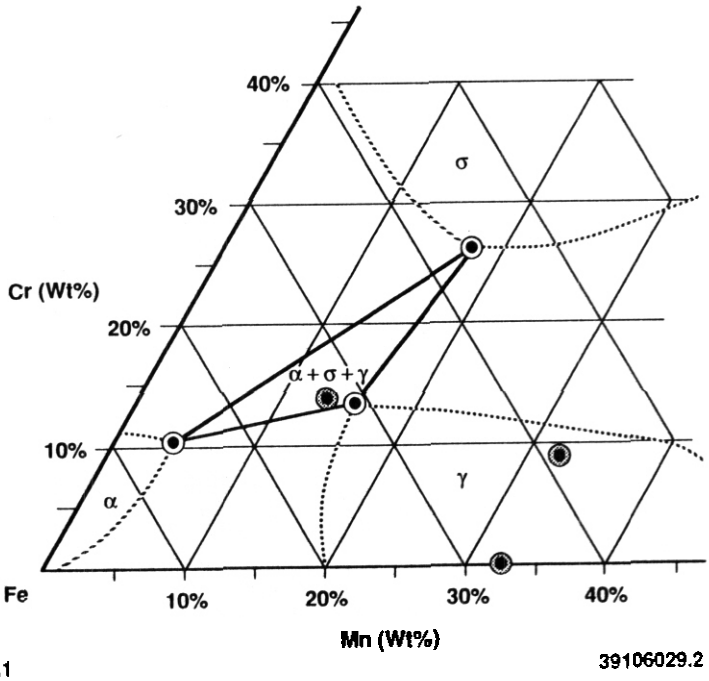


Figure 29. 500°C isotherm derived for Fe-Cr-Mn system.

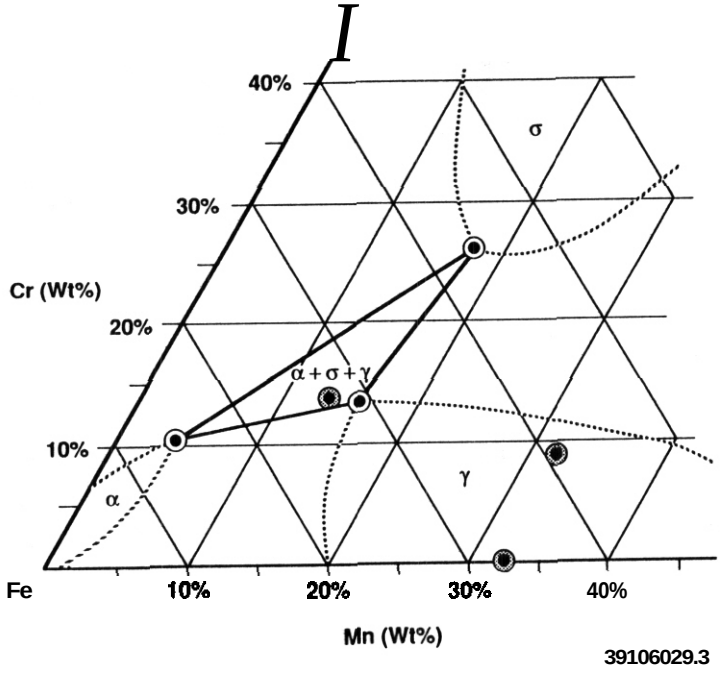


Figure 30. 300°C isotherm derived for Fe-Cr-Mn system.

studies, done under the auspices of the Fusion Materials program, contradict several aspects of this earlier work.[4-6] Summary and comparison of the various studies are in order.

The binary Fe-Cr diagram has been fairly well established and is presented in Figure 31.' The austenite phase field is severely restricted and the σ that forms congruently from α at 820°C has a fairly narrow composition range. Even in the binary, the long times required for σ formation result in an ambiguity concerning the eutectoid temperature due to the small difference in the Gibb's free energy of the competing phases.' The Fe-Mn diagram is given in Figure 32.[2] Increased Mn stabilizes the austenite phase field, while at higher manganese content an α manganese phase forms.

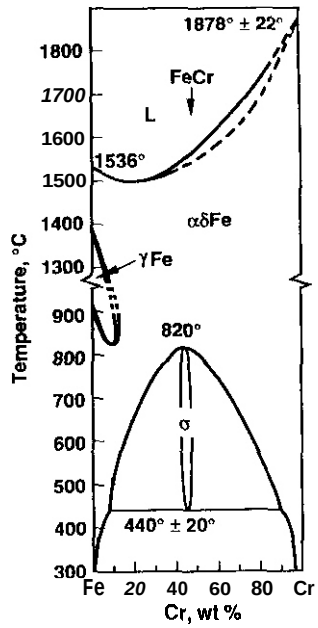
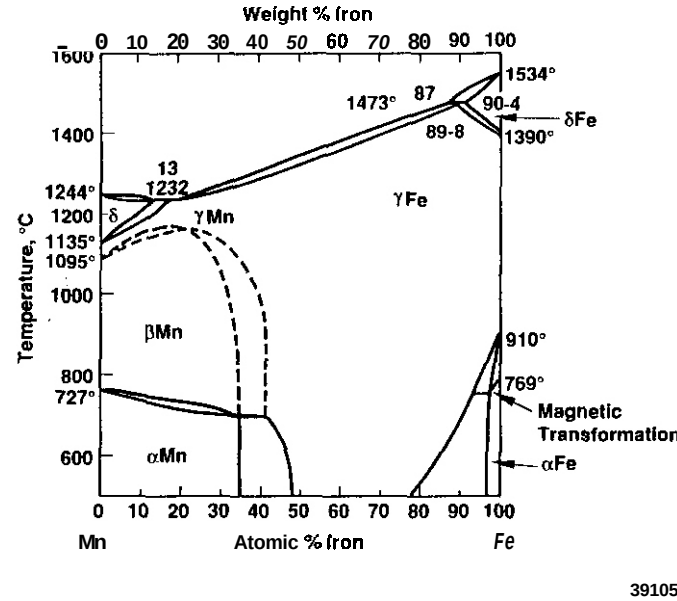


Figure 31. Fe-Cr phase diagram.'



39105031.1

Figure 32. Fe-Mn phase diagram.'

The earlier investigations compiled by Rivlin and Raynor' were far from complete and generally limited to the Fe-rich corner of the phase diagram. Many of the alloys used were of questionable purity and were aged in the annealed condition for relatively short periods of time. This combination of undesirable factors leads to a great deal of uncertainty on whether true equilibrium was obtained in the studies.

One of the earlier studies by Burgess and Forgeng derived an isothermal section at 650°C, shown in Figure 33.[8] This diagram was assembled from optical microscopy and magnetic measurements data on commercially pure alloys (carbon between 0.05 and 0.16%, silicon between 0.15 and 0.62%) aged in the annealed condition for an unstated period of time. The presence of Mn expands the σ phase field. In addition, the chromium content of the austenite is independent of the manganese content within the two-phase $\gamma+\sigma$ region.

An isotherm at 700°C was proposed by Schafmeister and Ergang, shown in Figure 34.[9] However, the indicated σ phase boundaries are in contradiction with the accepted Fe-Cr binary, shown in Figure 31. The conclusion was made that the location of the three phase triangle $\alpha+\sigma+\gamma$ is only approximate.

A fairly detailed study of the two-phase α/γ equilibrium in these alloys was performed by Kirchner and Uhrenius, and produced isotherms in the temperature range of 750°C to 950°C.[10] The alloys were aged for times ranging from 1 week to 7 months in the annealed condition. Experimental results were employed in a regular solution model in calculating the phase boundary lines. Initial materials were very pure and compositions of individual phases were determined using an electron probe microanalyzer. The thermodynamic calculations, although consistent within the individual isotherms, could not be reasonably correlated across the whole temperature range of the study. These calculations were assumed to be accurate and were used as a measuring stick for other studies. The isotherms at 750% and 800°C are shown in Figure 35. It should be noted that there was no evidence of σ phase formation in these alloys.

Rivlin and Raynor also produced an isotherm at 750°C,[1] shown in Figure 36. The $\alpha\delta$Fe/γFe boundaries derived by Kirchner and Urhenius were combined with σ phase data interpolated from vertical sections derived by Grigor'ev and Gruzdeva.[11] However, the data sets were not completely compatible and interpolations (dashed lines) were made based on the available data.

As mentioned previously, more recent studies done on Fe-Cr-Mn alloys as part of the Fusion Materials program contradict the previous studies considerably. This contradictory data indicates that true equilibrium was not achieved in the earlier studies or that the impurity contents were too high to provide a valid representation of the simple ternary Fe-Cr-Mn system.

As an offshoot of the studies of phase evolution in irradiated materials, Garner et al. characterized the microstructure of an Fe-10Cr-30Mn alloy in annealed and cold-worked conditions aged for times between 3.6 and 3600 ks at 923K.[8] Formation of σ only occurred in the cold-worked condition and not in the annealed state. The available evidence indicated that the formation of σ phase occurred only at the boundaries of

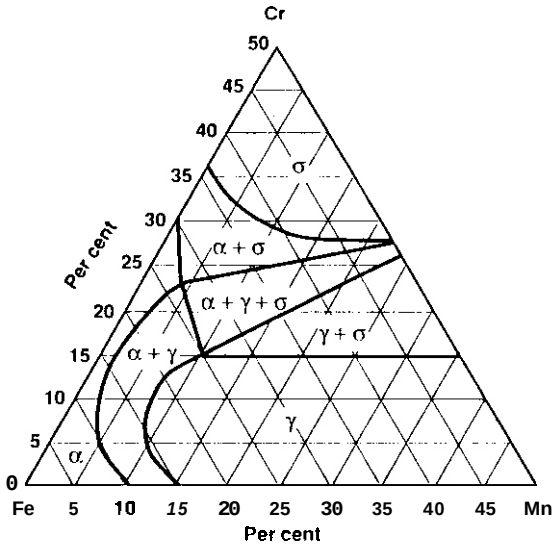


Figure 33. Isothermal section for Fe-Cr-Mn at 650°C derived by Burgess and Forgeng.[3]

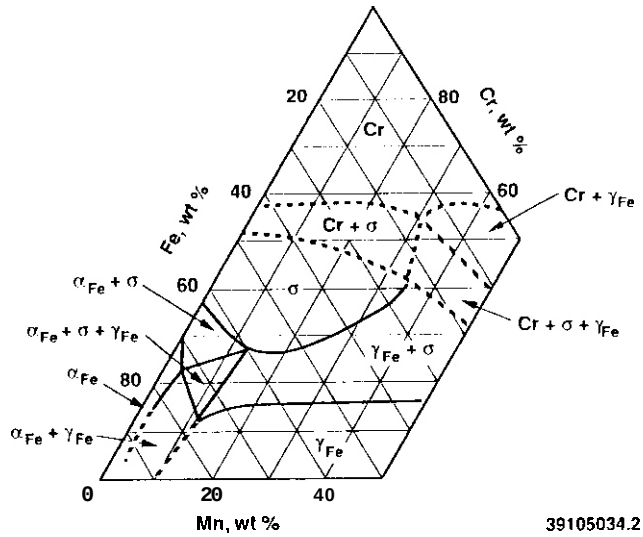


Figure 34. 700°C isotherm for Fe-Cr-Mn system derived hy Schafmeister and Ergang.[3]

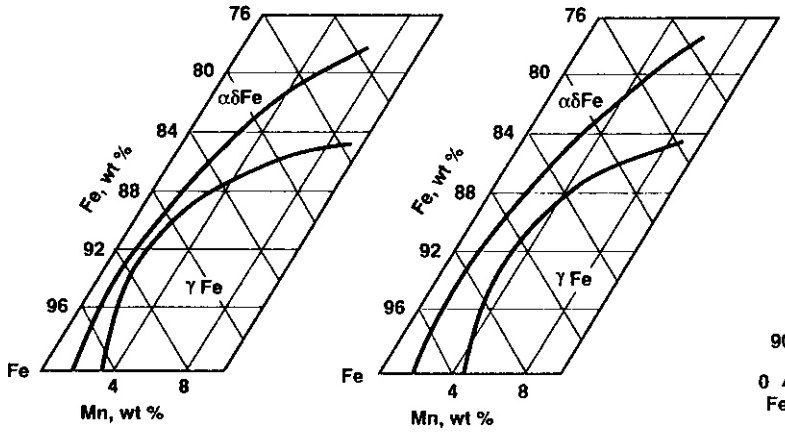


Figure 35. $\alpha\delta$Fe/γFe boundaries at 800°C and 750°C.[10]

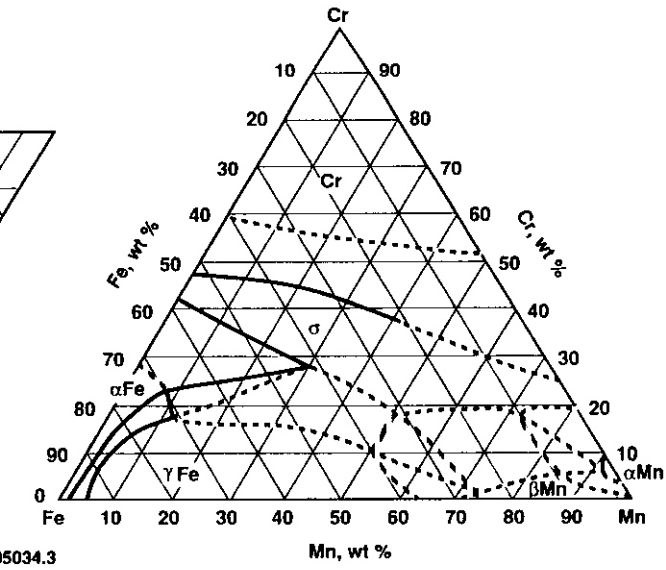


Figure 36. 750°C Fe-Cr-Mn isotherm compiled by Rivlin and Raynor.[1]

the recrystallizing grains. Once the boundary passed beyond the particle, its growth was restricted. EDX analysis indicated the composition of the σ phase was 15-23%Cr, 47-50%Fe and 30%Mn in the 30% cold-worked condition. One conclusion of the study was that formation of σ phase could only occur at recrystallizing grain fronts or grain boundary triple points. From the 650°C isotherm of Burgess and Forgeng, shown in Figure 33, it can be seen that the bulk composition of the Fe-10Cr-30Mn exhibition σ phase precipitation alloy falls well within the single-phase austenite region, indicating a significant discrepancy.

Further studies on cold-worked Fe-Cr-Mn alloys were performed by Okaraki et al.[5] Levels of 50% cold work followed by aging at 650°C for Fe-12Cr-Mn samples were found to accelerate the formation of σ. The formation sequence was 6 to $\delta+\gamma$ to $\delta+\gamma+\sigma$ for 10Mn, 6 to $\gamma+\sigma$ (lamellar structure) for 15-20%Mn, and δ to σ (direct transformation) for 25-30%Mn. Additionally, there appeared to be a consistency to the composition of σ (the Mn t Cr content approximately equal to 42%).

As a final example of the most recent studies on the Fe-Cr-Mn system, an isotherm at 650°C was developed experimentally by Murata et al.[6] The alloys were prepared from 99.9% pure starting materials and aged in the 50% cold worked condition. Figure 37 depicts the isothermal section constructed for this study. In comparison with the diagram by Burgess and Forgeng, Figure 33, the $\gamma+\sigma$ phase field extends to chromium levels as low as about 5%. Aspects of the present study correspond closely with this Japanese study. However, the present study extends to lower temperatures, making direct comparisons difficult. No previous investigations on the Fe-Cr-Mn equilibrium below 650°C could be found in the published literature. The isothermal section in Figure 31 indicates that the austenite phase field is much more restricted than that of the Burgess and Forgeng diagram at 650°C shown in Figure 33. The data agrees more with the diagram by Murata et al. shown in Figure 37, yet even this diagram has several discrepancies. The composition of the $\alpha+\sigma/\alpha$ boundary at the Fe-Cr binary edge is approximately 28% in the Murata et al. diagram. Looking at the Fe-Cr binary of Figure 31, one can see that the composition should be around 20%. In addition, the $\alpha+\sigma/\alpha$ boundary appears to extend into the three-phase $\alpha+\sigma+\gamma$ triangle while the $\gamma/\gamma+\alpha$ phase boundary doesn't. This violates the phase rule. As drawn, the 600°C isothermal section derived for this study does not violate the phase rule. The σ phase field extends to lower chromium content in the current study than the Murata et al. study also. However, because only one average composition, Fe-10Cr-30Mn, was investigated, not a great deal of certainty can be placed on the location of the σ boundary.

Although not directly related to thermal equilibrium of the simple ternary system, a study done by Klueh and Masiasz attempted to determine a stable austenitic phase for Fe-Cr-Mn-C based on a modified Schaeffler diagram.[12,13] The study provides some insight into how effective Mn is as an austenite stabilizer. The Schaeffler diagram was originally devised to predict the stable phases in Fe-Cr-Ni weld metal based on chromium and nickel equivalents given by the equations[14]

$$\text{Ni equiv.} = (\text{Ni}) + (\text{Co}) + 0.5(\text{Mn}) + 0.3(\text{Cu}) + 25(\text{N}) + 30(\text{C})$$

$$\text{Cr equiv.} = (\text{Cr}) + 2(\text{Si}) + 1.5(\text{Mo}) + 5(\text{V}) + 5.5(\text{Al}) + 1.75(\text{Nb}) + 1.5(\text{Ti}) + 0.75(\text{W})$$

where the concentrations of the respective elements in parentheses are given in weight percent. Figure 38 shows both the original diagram developed for Fe-Cr-Ni superimposed on the diagram revised for Fe-Cr-Mn-C based on the experimental results. The overall conclusion of the study was that manganese is a much weaker austenite stabilizer against the formation of δ-ferrite and a stronger stabilizer against the formation of martensite. The diagram indicates that lower chromium and higher manganese content; must be used to maintain a stabile austenite structure.

Phase Evolution

The sluggish nature of the phase evolution in the alloys tends to confirm the mechanism proposed by Garner et al. that σ phase formation can only occur at recrystallizing grain fronts and at grain boundary triple points. Only those alloys exhibiting aspects of recrystallization, also showed σ phase precipitation. Figures 4 and 5 illustrate the precipitation of σ on the grain boundaries.

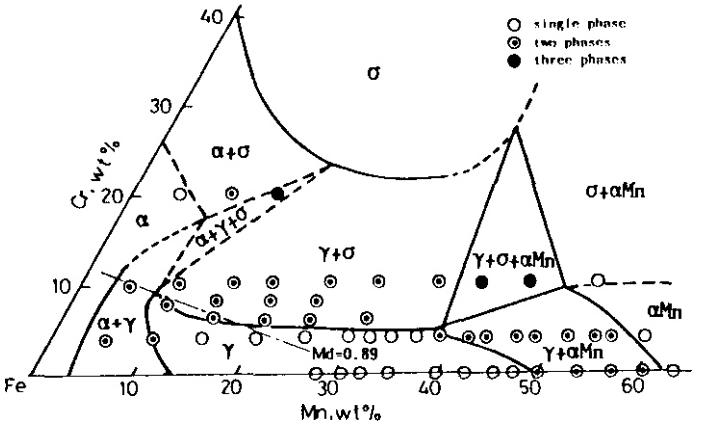


Figure 37. 650°C isotherm derived by Murata et al.[6]

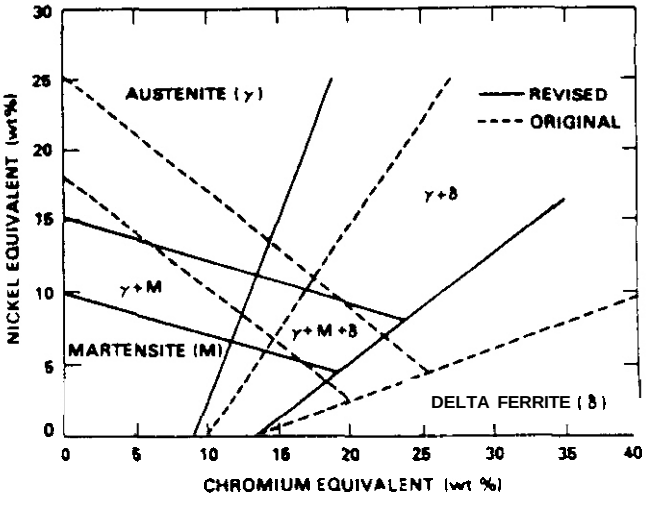


Figure 38. Modified Schaeffler diagram for the Fe-Cr-Mn system."

The photomicrographs of the 33 alloys also indicate that the recrystallization process is extremely slow below 600°C in the high Mn alloys. The profuse precipitation of σ in the Fe-15Mn-15Cr alloys made the recrystallization nature of these alloys unclear. However, in the Fe-10Cr-30Mn and Fe-30Mn alloys, formation of recrystallizing grains is evident. In the Fe-10Cr-30Mn alloys, recrystallization is only evident above 600°C for 10,000 and 30,000 hours of aging. The recrystallizing grains appear to be initiating the precipitation of σ along the grain fronts. The Fe-30Mn alloy exhibits recrystallizing grains in the 300, 500 and 600°C samples aged for 30,000 hours. Above 600°C recrystallizing grains appear starting with only 1,000 hours of aging and grain growth is occurring. The results suggest that the recrystallization process is slowed by the addition of chromium.

Some important points become evident in examining the results of the present investigation. The possibility that prior cold-working of Fe-Cr-Mn alloys can initiate the precipitation of brittle σ phase in alloys expected to be totally austenitic is a major concern. Such precipitation would also lead to chromium depletion of the matrix, thus reducing the alloy's corrosion resistance. In addition, the formation of ferrite and chi during irradiation must be prevented if these alloys are to be used as a reduced activation material in fusion reactor environments. The challenge appears to be the development of an alloy and a feasible thermomechanical treatment schedule that will prevent deleterious phase evolution.

Irradiation Effects

Studies indicate Fe-Cr-Mn exhibits tendencies to develop different secondary phases during irradiation than during thermal aging.[15,16] Many examples were found of ferrite formation at point defect sinks due to radiation induced segregation of iron. However, an examination of an Fe-5Cr-15Mn alloy irradiated at 420°C to 9 dpa revealed that, upon irradiation, the single-phase austenite transformed to α martensite (bct) and retained austenite and within the α martensite was manganese-rich chi phase (bcc) formed by radiation induced segregation. Also, in the more pertinent case of Fe-15Cr-15Mn, chi that was rich in chromium formed during irradiation. Epsilon martensite (hcp) was also seen to form in the austenite grains. The formation of epsilon martensite decreased with increasing Mn. Ferrite formation decreased with increased Mn and then increased again at about 35% manganese. Therefore, whereas sigma phase forms during thermal aging, chi phase is found following irradiation, and radiation induced segregation leads to ferrite formation.

CONCLUSIONS

1. Previous diagrams developed for the Fe-Cr-Mn system by Burgess and Forgeng and by Schafmeister and Ergang do not accurately predict equilibrium in the system due to the slow nature of σ phase formation. σ phase can form in Fe-Cr-Mn alloys of lower chromium content than the earlier diagrams suggest. Formation is on recrystallizing grain boundaries and grain boundary triple points during long-term thermal aging of cold-worked materials. The more recent diagram by Murata and coworkers is in closer agreement with the present results.

2. The isotherms at 600, 500 and 300°C derived in the current experiment indicate that the σ phase field expands with increased temperature while the γ phase field constricts. The diagrams indicate that σ phase will form in alloys whose chromium content is as low as 8.8% at 600°C.

3. In an Fe-15Cr-15Mn alloy the microstructural evolution follows a path of $\alpha+\gamma+M$ to $\alpha+\gamma+\sigma$ when aged between 300 and 500°C from 1,000 to 30,000 hours. At 600 and 700°C the microstructure has attained equilibrium in the first 1,000 hours of aging.

4. The addition of chromium to a Fe-30Mn alloy appears to slow the process of recrystallization. An Fe-30Mn alloy aged at 500°C shows evidence of recrystallization at 1,000 hours of aging, while an Fe-10Cr-30Mn alloy does not exhibit recrystallization until 10,000 hours of aging.

REFERENCES

1. G.V. Raynor and V.G. Rivlin, Bulletin of Alloy Phase Diagrams Vol. 2, No. 1 (1981) pp 99-100.

2. A. Hellawell, "The Equilibrium Diagram of the System Iron Manganese," Annotated Equilibrium Diagrams No. 26, 1956, London, The Institute of Metals.

3. V.G. Rivlin and G.V. Raynor, Eds. International Metals Review, Vol. 28, No. 1 (1983).

4. F.A. Garner, F. Abe and T. Noda, Journal of Nuclear Materials, 155-157 (1988) 870-876.

5. Y. Okazaki, M. Machizuki, K. Miyahara and Y. Hosoi, Reduced Activation Materials for Fusion Reactors, ASTM STP 1047, R.L. Klueh, D.S. Gelles, M. Okada, and N.H. Packan, Eds. ASTM, Philadelphia (1990), pp. 80-92

6. Y. Murata, K. Kazuhiro, Y. Matsumoto and M. Morinaga, ISIJ International Vol. 30, No. 11 (1990), 927-936.

7. F. Muller and O. Kubaschewski, High Temperatures.-High pressures, 1 (1969) 543-551.

8. C.O. Burgess and W.D. Forgeng, Trans. AIME, 131 (1938) 277-299.

9. P. Schafmeister and R. Ergang, Arch. Eisenhuttenwes., 12 (10) (1939) 507-510.

10. G. Kirschner and B. Uhrenius, Acta Metall., 22 (1974) 523-532.

11. A. Grigor'ev and B. Gruzdeva, Akad Nauk Gruz. (Bull. Acad. Sci. Georgian SSR), 49 (3) (1968) 641-646.

12. R.L. Klueh, P.J. Maziasz and E.H. Lee, Materials Science and Engineering A, 102 (1988) 115-124.

13. P.J. Maziasz and R.L. Klueh, Reduced Activation Materials for Fusion Reactors, ASTM STP 1047, R.L. Klueh, D.S. Gelles, M. Okada, and N.H. Packan, Eds., ASTM, Philadelphia (1990), pp. 56-79.

14. H. Schneider, Foundry Trade Journal, 108 (1960) 563-564.

15. F.A. Garner, H.R. Brager, D.S. Gelles and J.M. McCarthy, Journal of Nuclear Materials, 148 (1987) 294.

16. J.M. McCarthy and F.A. Garner, Journal of Nuclear Materials, 155-157 (1988) 877.

FUTURE WORK

This work is completed

6.3 Refractory Metal Alloys

CORRELATION OF MICROSTRUCTURE AND SWELLING BEHAVIOR OF VANADIUM ALLOYS IRRADIATED IN FFTF/MOTA AT 420°C

H. M. Chung. B. A. Loomis (Argonne National Laboratory). and K. Abe (Tohoku University, Japan)

OBJECTIVE

Microstructures of vanadium-base alloys are profoundly modified during neutron irradiation. The objective of this work is to characterize the microstructural evolution of several candidate vanadium alloys after irradiation in FFTF/MOTA and to correlate the results with swelling properties of the alloys, thereby providing an insight to develop an optimized alloy.

SUMMARY

Microstructural evolutions In V, V-Cr, V-Ti, V-Ti-Cr. and V-Ti-Si alloys have been characterized by TEM after irradiation at 420°C in FFTF/MOTA. The results have been correlated with swelling behavior of the alloys to provide a better understanding of the superior resistance of some of the high-Ti heats to void swelling.

INTRODUCTION

The swelling behavior of vanadium-based alloys (V-Ti, V-Cr. V-Cr-Ti, and V-TI-Si) after neutron irradiation at 420 and 600°C in the Materials Open Test Assembly (MOTA) of the Fast Flux Test Facility (FFTF) has been reported in a series of previous papers.[1-5] Results of these investigations showed that irradiation-induced swelling of vanadium-based alloys can be effectively inhibited by addition of >5 wt.% TI in the alloy. For example, swelling of V-TI alloys containing 5-20% Ti and V-15Ti-7.5Cr alloy was <1% in comparison with swelling as high as 3-4% for V. V-14Cr, V-15Cr-1Ti, and V-3Ti-1Si alloys upon irradiation at 420°C up to 114 dpa (Fig. 1).[1] However, mechanism of the superior inhibition of swelling of the high-Ti alloys is not well understood at present. In this investigation. microstructural evolution of these alloys was characterized by transmission electron microscopy (TEM), and the results were correlated with void-swelling behavior of the alloys to provide a better understanding of the role of Ti content.

MATERIALS AND PROCEDURES

Procedures of preparation of alloy specimens in this investigation have been described in an earlier report.[1] Chemical composition of as-fabricated alloys investigated by TEM has been reported previously.[1] For determination of swelling [density change). disk-shaped specimens ~3 mm in diameter and ~0.3 mm in thickness were obtained from cold-worked sheets. The specimens were irradiated in FFTF/MOTA during cycle 7-10 at 420°C to neutron fluences (E > 0.1 MeV) ranging from 3×10^{22} n cm^{-2} (17 dpa) to 1.9×10^{23} n cm^{-2} (114 dpa). The specimens were sealed inside Li^7-filled TZM/Mo capsules during irradiation to prevent contamination by O, N, and C impurities dissolved in the sodium coolant of the FFTF.

Irradiated specimens were jet-thinned for TEM In a solution of 15% sulfuric acid-72% methanol-13% butyl cellosolve maintained at -5°C. TEM was conducted with a JEOL 100CX scanning transmission electron microscope operating at 100 keV. Vanadium reflections were used as a standard in each selected-area diffraction (SAD) pattern to calculate reciprocal lattice spacings of precipitates.

RESULTS

Vanadium

Some of the unirradiated heats of V contained unknown, nearly spherically shaped precipitates 30-150 nm in diameter. This type of precipitate, designated as Type A in Fig. 2, was obtained from Heat BL-12. It appeared that heats containing high oxygen concentrations (e.g., BL-12, O ~1670 wt. ppm) developed more of this type of precipitates during solidification. In other heats. the precipitates were negligible except on grain boundaries (e.g., BL-20, O ~570 wt.ppm).

Grain growth was generally excessive. Breakaway grain growth (i.e., secondary recrystallization) was observed in both unirradiated V and in various alloys. Grain boundaries of the specimens in which breakaway grain growth was observed were frequently pinned by the Type A precipitates (Fig. 2).

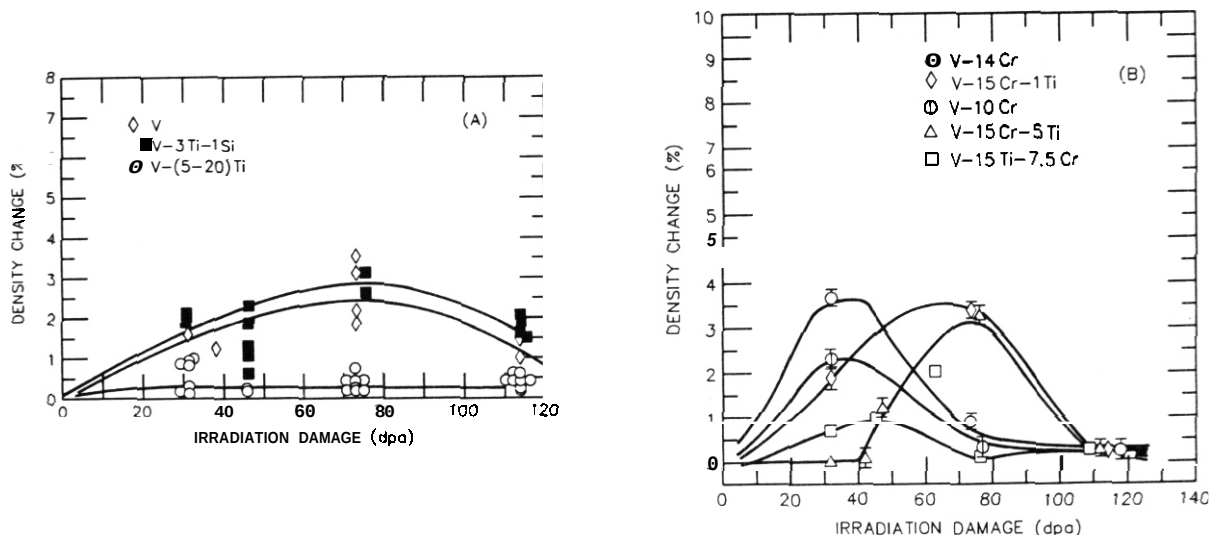


Fig. 1. Density change (swelling) vs. irradiation damage for (A) V, V-Ti. and V-Ti-Si alloys; (B) V-Cr and V-Cr-Ti alloys irradiated at 420°C.

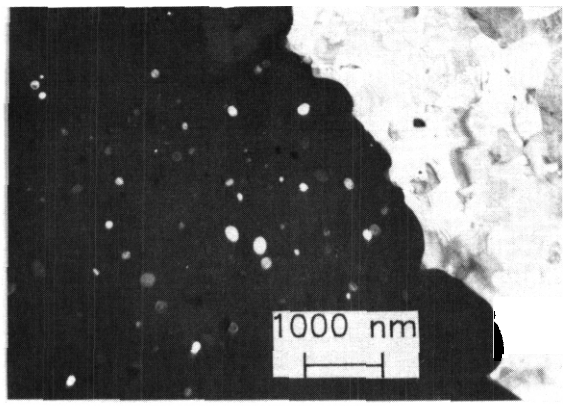


Fig. 2. Type A precipitates (dark-field image) and breakaway grain growth observed in unirradiated V (BL-12).

Vanadium specimens from Heat BL-36 that were irradiated to 38 and 73 dpa contained high density of very fine microvoids 3-6 nm in size. Size and density of the microvoids were similar for the two fluence levels. Density and size of microvoids produced in specimens of Heat BL-20 at 31 dpa were similar to those of the BL-36 irradiated to 38 dpa. Number density of microvoids in Heat BL-20 increased approximately 2.5 times as irradiation was increased to 114 dpa (Fig. 3). Voids near a grain boundary were ~2-3 times larger than those away from grain boundaries.

Besides the microvoids, V specimens irradiated to 31-114 dpa contained dislocations, dislocation tangles, and black-dot defects in high density (Fig. 4A). Black-dot defects ranged in size from ~5 to 10 nm, i.e., somewhat larger than microvoids. Because of these irradiation-induced imperfections, microstructure imaged in bright-field was usually very complex.

The SAD patterns (e.g., Figs. 4B and 4C) that correspond to the complex structures (such as Fig. 4A) also indicate the presence of several phases. Many spurious reflections were observed in such SAD patterns, indicating precipitation of unknown secondary phase or phases. This type of precipitates, designated as Type B. were observed only in irradiated specimens of V. However, the unknown Type B precipitates could be artifact phases (e.g., hydrides) produced during specimen preparation.

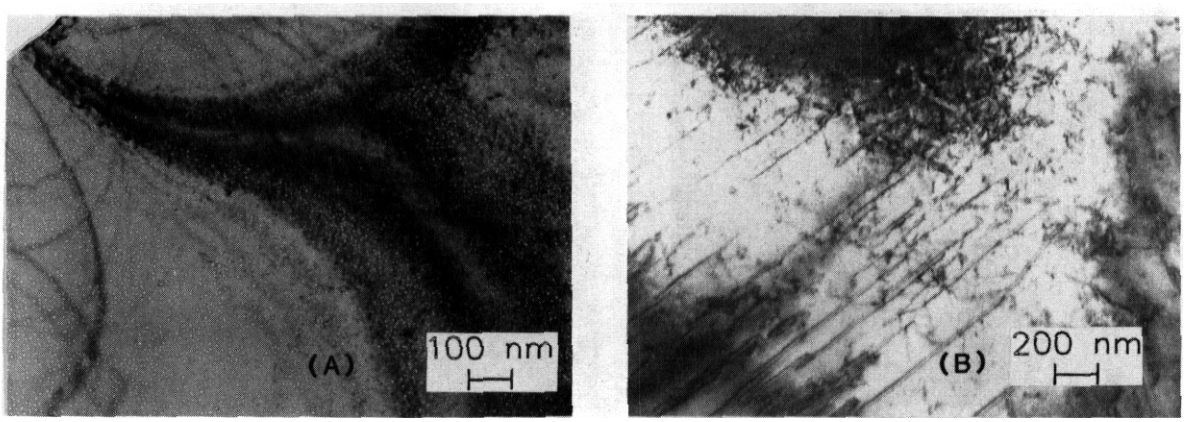


Fig. 3. Microvoids (A) and dislocations (B) observed in V specimen (BL-20) irradiated at 420°C to 114 dpa.

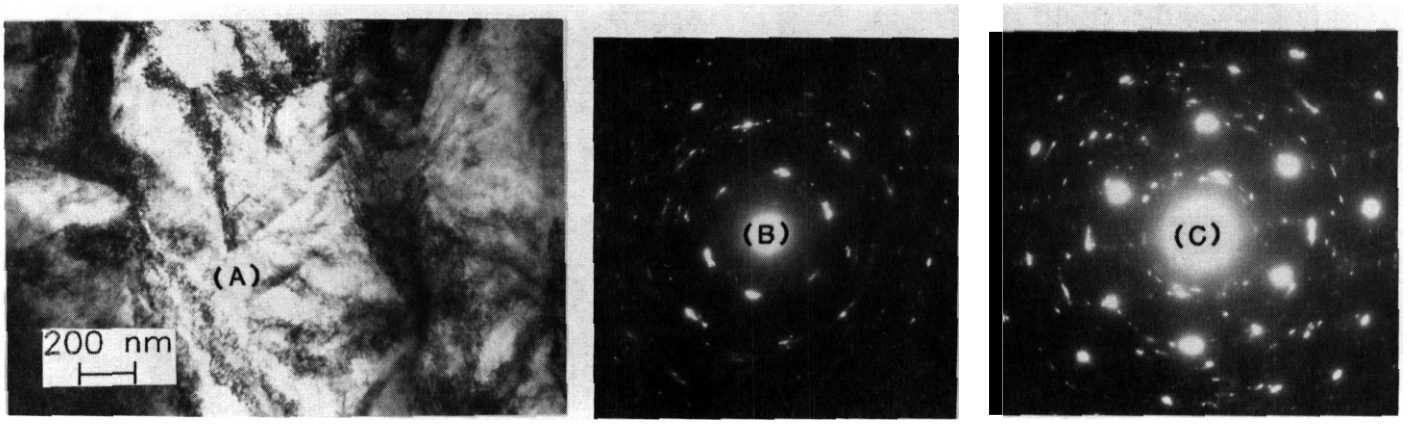


Fig. 4. Complex structure containing microvoids. dislocation tangles, and unidentified plate-like precipitates observed in V specimen (BL-20) irradiated at 420°C to 31 dpa (A) and corresponding *SAD* pattern (B). The pattern of (B) and a similar *SAD* pattern obtained for 73 dpa (C) indicate precipitation of an unknown phase, designated as Type B precipitate.

V-Cr Alloys

V-10Cr alloy specimens irradiated to 114 dpa were characterized by a high density of black-dot defects, short dislocations, and dislocation loops (Fig. 5A). In contrast to the V specimens irradiated to a similar dose, dislocation tangles in the V-10Cr specimen were negligible. Also, examination of bright-field images and SAD patterns showed no evidence of precipitates (Fig. 5B). Microvoid size (i.e., 4-7 nm) was similar to that in V specimens irradiated to a similar fluence; however, number density was lower by a factor of 4-5 (e.g., smaller than that shown in Fig. 3A).

V-Ti Alloys

V-Ti alloys containing 9- (BL-34). 18- (BL-15), and 20-wt.% Ti (BL-16) were examined after irradiation up to 114 dpa. Swelling of these heats determined from density measurements was minimal, i.e., <1%. In accordance with the swelling data, number density of voids in these alloys was very low. This is shown in Figs. 6A and 6B, in which the void distributions in V-18Ti and V-20Ti specimens, irradiated to 46 and 114 dpa. respectively. are visible. However, void size was significantly larger (15-70 nm) than that in the V or V-Cr alloys (3-7nm).

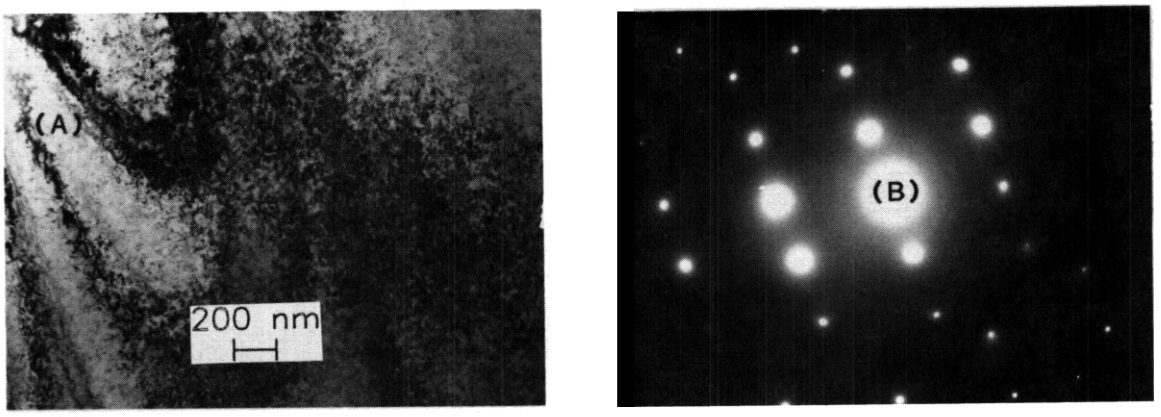


Fig. 5. Dislocation loops. black-dot defects, and dislocation tangles (A) and SAD pattern indicating negligible precipitates (B) in V-10Cr (BL-35) irradiated at 420°C to 114 dpa. Void formation was negligible.

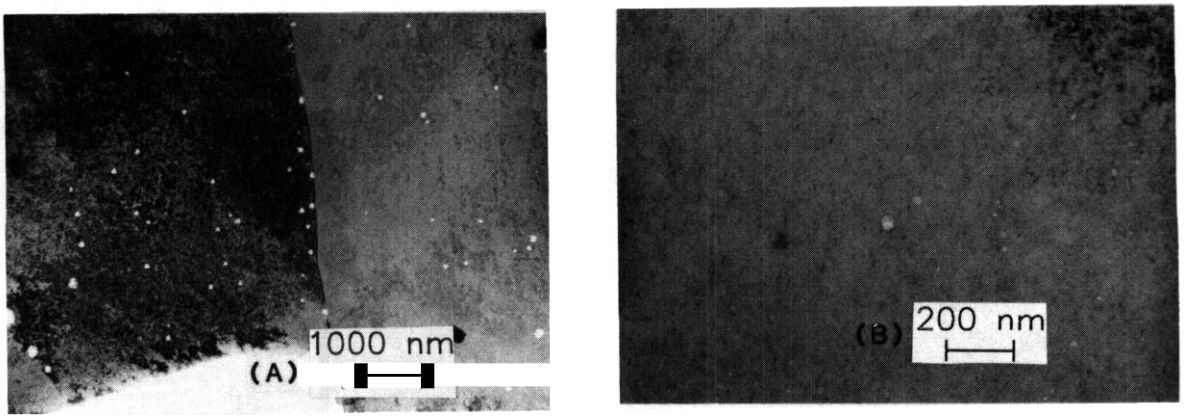


Fig. 6. Voids in V-18Ti (BL-15) (A) and voids and Type 11 precipitates in V-20Ti (BL-16) (B) irradiated at 420°C to 46 and 114 dpa, respectively.

A high density of dislocation loops and short dislocations was observed in the V-18Ti and V-20Ti specimens after irradiation to 46-114 dpa. However, dislocation tangles and long dislocations were largely absent, a situation similar to that of the V-10Cr alloy.

Four types of precipitates were observed in the V-18Ti and V-20Ti alloys irradiated to 114 dpa. Each type is described below.

Type I Precipitates

Both V-18Ti and V-20Ti specimens irradiated to 46 and 114 dpa. respectively. were characterized by profuse precipitation of a very fine (~3-10 nm) spherical phase (Fig. 7). From bright-field imaging alone, it was difficult to either observe the precipitates or distinguish them from black-dot defects, which have similar sizes and exhibit similar contrast (Fig. 7A). Therefore, it was necessary to examine SAD patterns (Fig. 7B) and to obtain dark-field images (Fig. 7C) to determine the size and distribution of the precipitates. Type I precipitates have been reported previously for V-Ti, V-Cr-Ti, V-Ti-Si alloys irradiated at 600°C to 21-84 dpa,[2,3] although those observations were based primarily on bright-field imaging. It appeared that the density of precipitates contained in the V-18Ti specimen (oxygen content 830 wt.ppm) irradiated to 46 dpa was higher than that of a V-20Ti specimen (oxygen content 390 wt.ppm) irradiated to 114 dpa.

Type II Precipitates

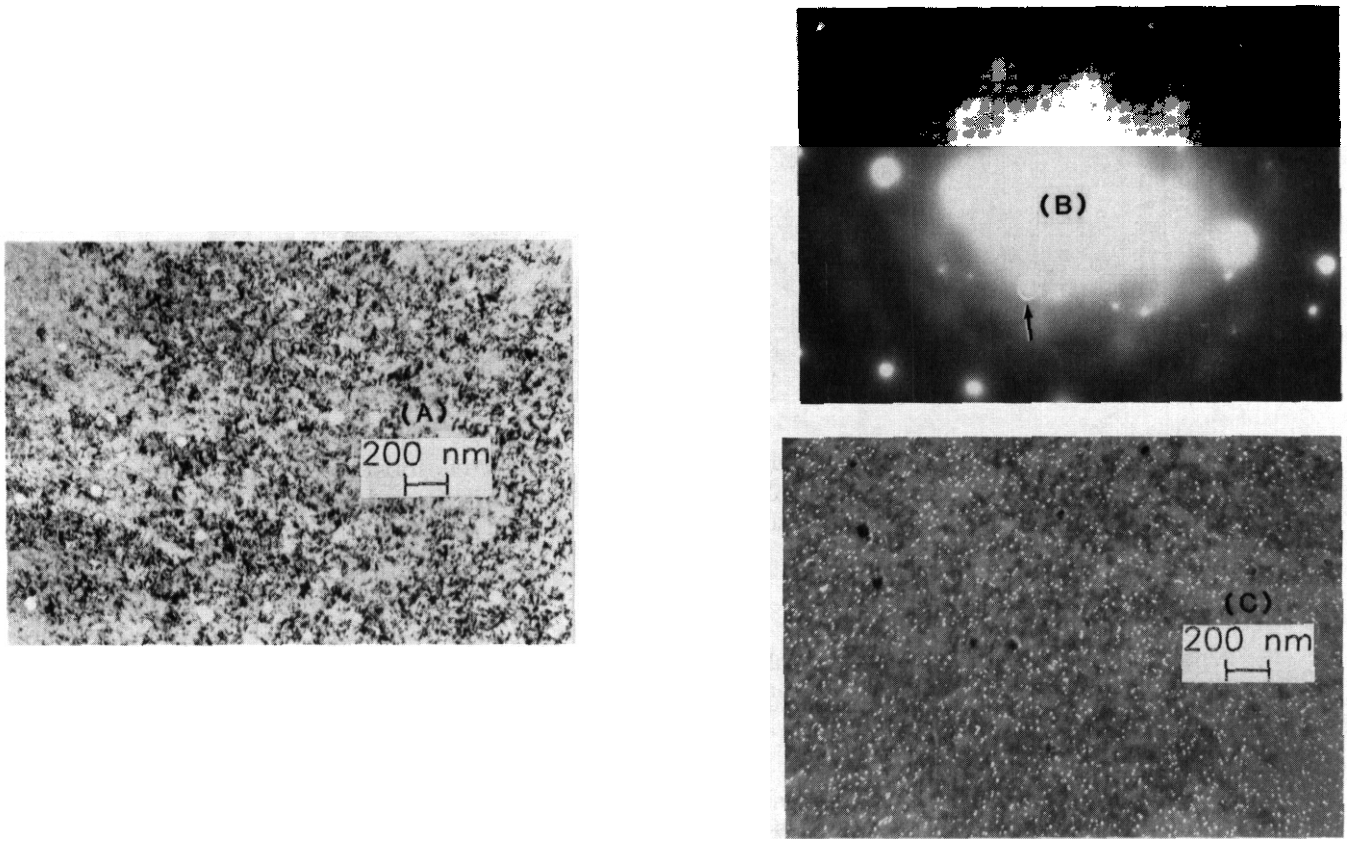


Fig. 7. Bright-field image of V-18Ti (BL-15) irradiated to 46 dpa, showing dense dislocation loops, short dislocations. relatively large voids, black-dot defects, and fine Type I precipitates (A); SAD pattern of (A) showing reflections from the Type I precipitates (B); and dark-field image (C) of the Type I precipitates produced from the encircled reflection in (B).

The morphology of this short needle-like precipitate (~5 nm in diameter and ~30 nm in length). is visible in Fig. 6B. In the present study, it was observed in the V-20Ti alloy irradiated to 114 dpa but not in V-18Ti alloy irradiated to 46 dpa. Similar precipitates have been also reported for V-15Cr-5Ti, V-10Cr-5Ti, and V-3Ti-1Si alloys after irradiation at 600°C to 21-84 dpa[2,3] and for V-13Cr-5Ti alloy after irradiation to 14-17 dpa at 600°C.[6] This type of precipitate is typically observed in conjunction with the fine spherical precipitates of Type 1. This suggest that Type II may be in fact Type I precipitates preferentially formed on short dislocations.

Type III Precipitates

The morphology of this type of precipitate is blocky, ranging from 100 to 1000 nm in size It was observed in unirradiated and irradiated V-Ti. V-Cr-Ti, and V-Ti-Si alloys, indicating that it formed during alloy fabrication. Some of examples of this type precipitate in V-Ti alloys are shown in bright- and dark-field contrasts in Fig. 8. In previous reports,[2,3,6] this type of precipitate was believed to be TiO_2 in V-Ti, V-Cr-Ti, and V-Ti-Si alloys irradiated at 600°C. Spectra obtained from energy-dispersive spectroscopy (EDS) of these precipitates showed a Ti-rich composition. Also, the lattice spacings of the dark-field-imaging reflections and SAD patterns appeared to be consistent with rutile structure of TiO_2 (tetragonal. a = 0.4594 nm. c = 0.2958 nm) but not consistent either with brookite (orthorhombic, a = 0.925 nm. b = 0.546 nm. c = 0.516 nm) or with anatase (tetragonal, a = 0.378 nm. c = 0.950 nm) modification of TiO_2. Therefore. this type of precipitate seems to be the rutile form of TiO_2.

Type IV Precipitates

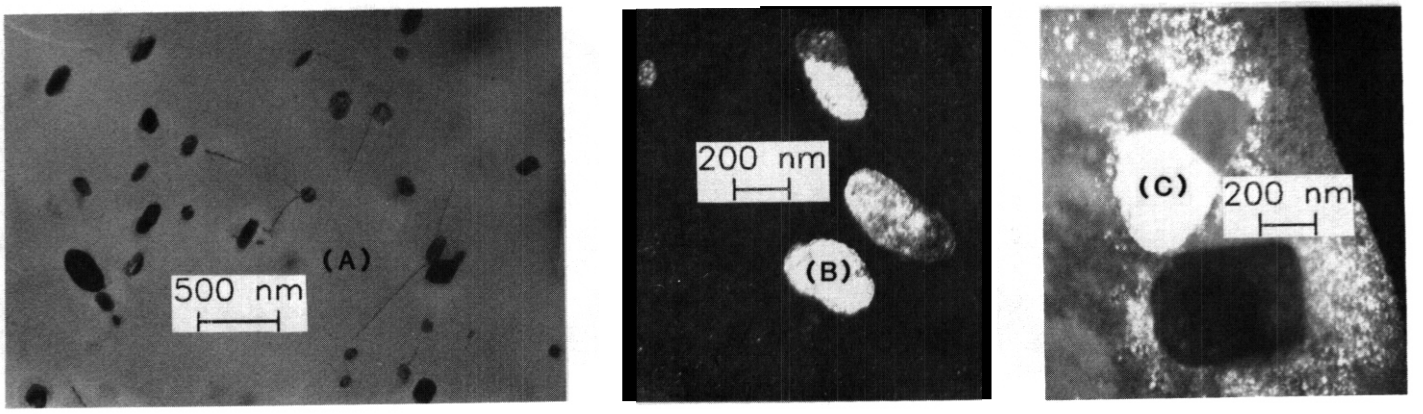


Fig. 8. Type III precipitates, believed to be rutile form of TiO_2, observed in (A) unirradiated V-9Ti (BL-34); (B) V-18Ti (BL-15) irradiated to 46 dpa: and (C) V-20Ti (BL-16) irradiated to 114 dpa. (B) and (C) are in dark-field contrast.

Type IV precipitate was observed only on grain boundaries (e.g., V-18Ti specimen irradiated to 46 dpa). Examples of bright- and dark-field images of the precipitate shown in Figs. 9A and 9B, respectively.

Nature of Precipitates

Of the four types of precipitates, it seems that Types I and II precipitates are irradiation-induced in nature, while Types III and IV precipitates are thermally produced during solidification or annealing of the alloys. Type I precipitate seems to be influenced more by specimen chemical composition than by fluence (dose) at an irradiation temperature of 420°C.

V-Ti-Si Alloys

Both unirradiated and irradiated specimens of V-3Ti-0.5Si and V-3Ti-1Si alloys were found to contain another type of precipitates that apparently formed during solidification or annealing. These Type V precipitates (Figs. 10A and 10B) are nearly spherical and 50-300 nm in size. EDS spectra of the precipitates indicated a Ti-rich composition (Fig. 10C). Examination of several SAD patterns of the precipitates indicated that diffraction characteristics were consistent with those of TiO phase (fcc, NaCl-type structure, a = 0.424 nm).

The size and distribution of voids produced in a V-3Ti-1Si specimen after irradiation to 114 dpa are shown in Fig. 11A; size (i.e., ~7-20 nm) and number density of voids in the figure indicate a significant swelling and seem to be consistent with the 1.5-2% swelling shown in Fig. 1. In Fig. 11A, the voids are denuded near Type V precipitate. indicating that precipitate/matrix interface may act as a sink for vacancies and microvoids. Fig. 11B shows structure of short dislocations produced in the V-3Ti-1Si specimen irradiated to 114 dpa.

V-Cr-Ti Alloys

Unirradiated and irradiated V-Cr-Ti alloys contained some Type III precipitates that are believed to be rutile TiO_2 (Figs. 12A and 12B). Frequently, the precipitates were observed wrapped in dislocations (Fig. 12B). This feature was reported for V-20Ti alloy irradiated at 600°C.[2,3]

Bright-field and SAD characteristics of V-15Cr-1Ti and V-15Cr-5Ti alloys indicated that some amount of Type I precipitates were produced after irradiation to 114 dpa (Fig. 12C). Both V-15Cr-1Ti and V-15Cr-5Ti alloys irradiated to 114 dpa were characterized by a high density of black-dot defects, short dislocations, and dislocation loops. The V-Cr alloys exhibit similar characteristics. Void formation in both types of alloys was negligible, which seems to be consistent with the low swelling of the specimens (i.e., ~0.3 % for a dpa of 114. Fig. 1).

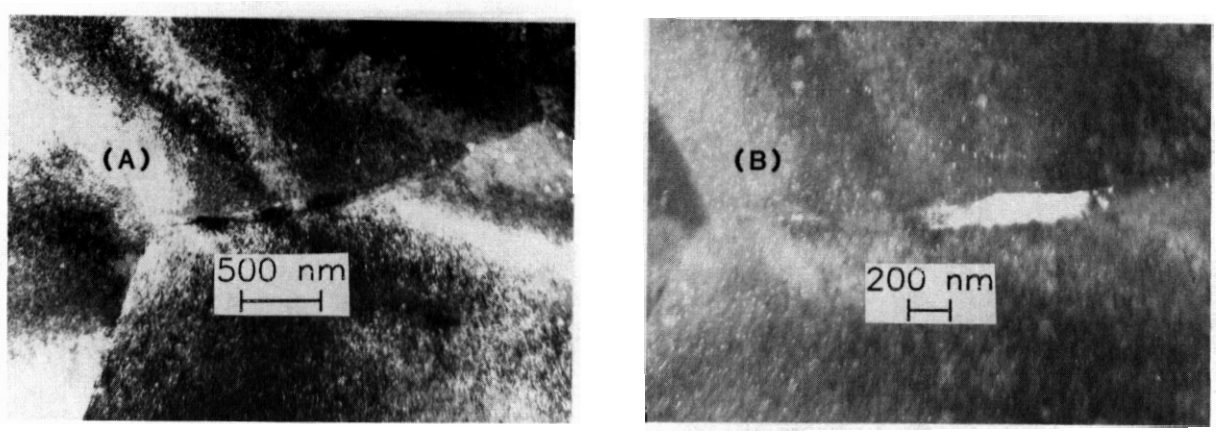


Fig. 9. Bright- (A) and dark-field (B) morphologies of ***Type*** **IV precipitates observed on** grain **boundary of V-18Ti (BL-15) irradiated to 46 dpa.**

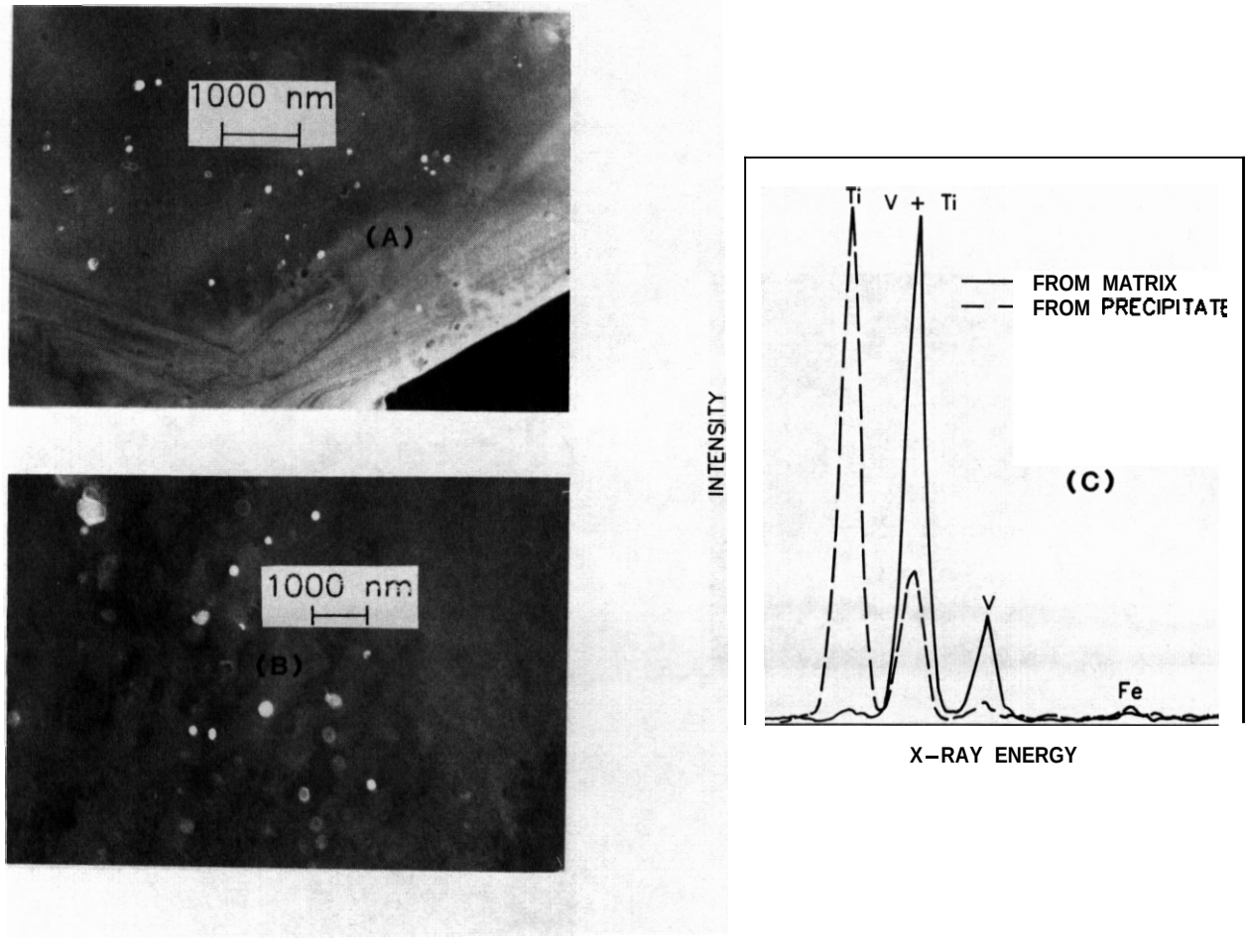


Fig. 10. Dark-field images of Type **V precipitates *in* unirradiated** V-3Ti-0.5Si **(BL-42) (A) and V-3Ti-1Si (BL-27) irradiated to 114 dpa (B). EDS spectra showing a Ti-rich composition** of **the precipitates are shown in (C).**

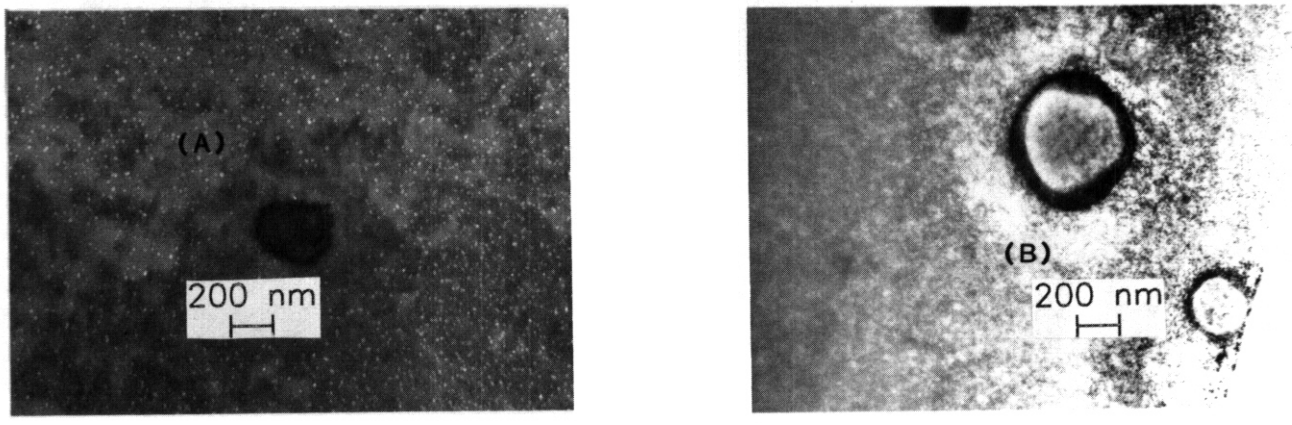


Fig. 11. Voids **(A)** and dislocations (B) in V-3Ti-1Si (BL-27) irradiated to **114** dpa. Note smaller number of voids near a Type V precipitate in (A).

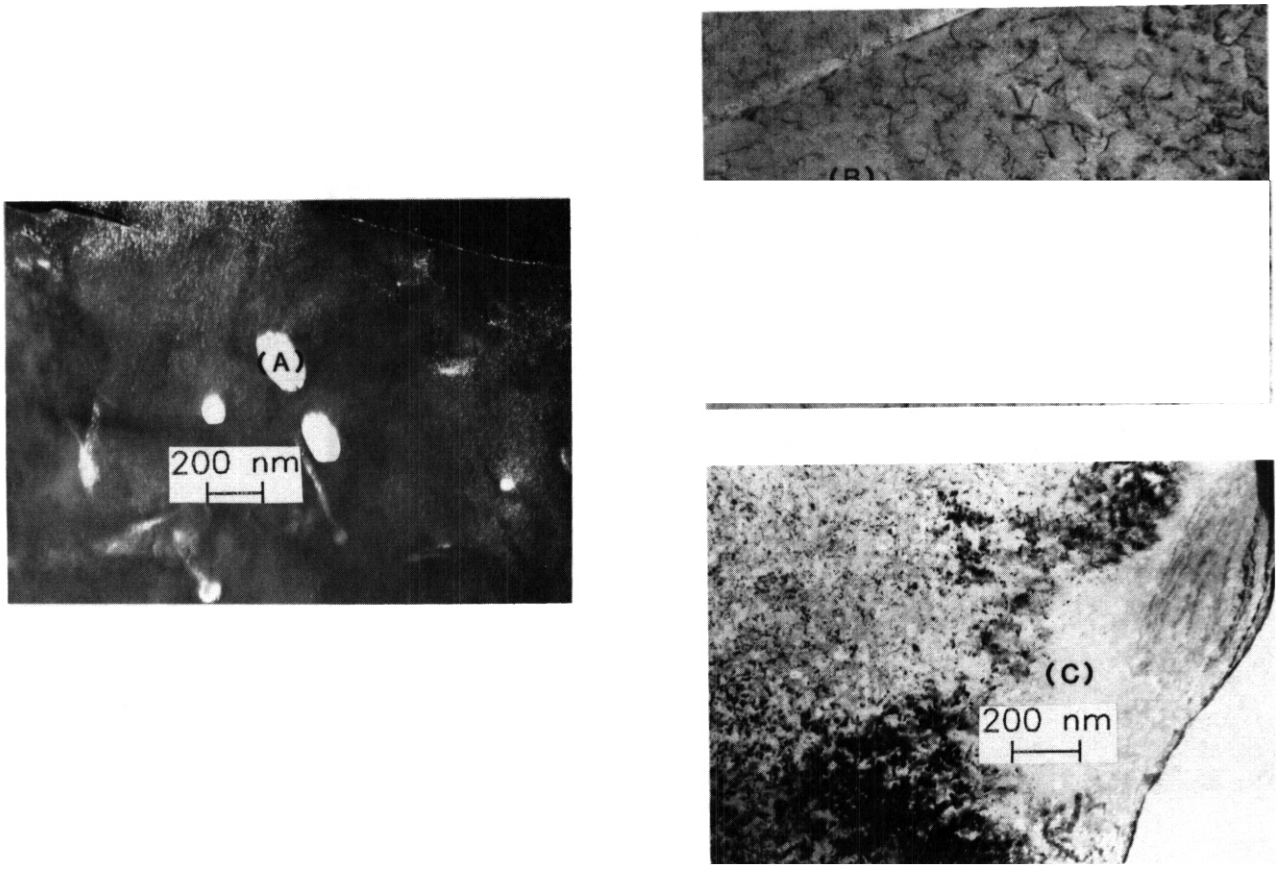


Fig. 12. Type III precipitates in unirradiated V-7.5Cr-15Ti (BL-10) (A); similar precipitates "wrapped **with** dislocations in V-15Cr-5Ti (BL-24) irradiated to 114 dpa (B); and short dislocations, dislocation loops, black-dot defects, Type I precipitates, and negligible voids in V-15Cr-1Ti (BL-26) irradiated to 114 dpa (C).

DISCUSSION

The results of TEM characterization of each specimen, i.e., volume fraction of voids estimated on the basis of size and number density of voids and foil thickness. are consistent with the swelling behavior summarized in Fig. 1. For example, significant density changes in V and V-3Ti-1Si alloys irradiated to 114 dpa (Fig. 1A) are consistent with the relatively large volume fraction of voids shown in Figs. 3A and 11A, respectively. The negligible swelling in V-18Ti, V-20Ti, V-10Cr, and V-15Cr-1Ti alloys irradiated to 114 dpa is likewise consistent with the negligible number of voids. As expected, this observation is similar to that for alloys irradiated at 600°C.[2,3]

The very small density change and minimal void formation in V-18Ti and V-20Ti at all damage levels appear to be associated with the significant precipitation of the very fine Type I particles (e.g., Fig. 7C). However, to confirm similar trend for other types of alloys (e.g., V-15Ti-7.5Cr), correlation must be obtained between void formation and dark-field distribution of Type I Precipitates. As pointed out earlier. Type I precipitates cannot be identified from bright-field imaging. and a misleading quantification could be obtained without dark-field imaging. The needle-like Type II precipitates were negligible in specimens irradiated at 420°C in comparison with those irradiated at 600°C. Void formation therefore does not seem to be associated with Type II, at least for irradiation at 420°C. Also, resistance to void formation does not appear to be directly associated with precipitation of either Type III, IV, or V phases, i.e., relatively large and sparse precipitates in comparison with Type I. Type III and V precipitates appear to be TiO_2 and TiO, respectively. and form during solidification or annealing rather than during irradiation.

In a previous investigation, the absence of void formation in ion-irradiated V-Ti and V-Ti-Cr alloys was attributed to precipitation of Ti_3O particles,[7] which may incorporate vacancy defects within the precipitate structure. Because of their small size (i.e., 3-10 nm), surface-to-volume ratio of Type I precipitates is extremely large. Therefore. it is expected that the large interfaces areas created by copious Type I precipitates can act as a sink for a large number vacancies created during irradiation, which suppresses nucleation and growth of voids. An alternative mechanism of suppression of void nucleation may be trapping of vacancy defects by Ti and oxygen atoms. i.e., irradiation-induced formation of vacancy/Ti-O clusters, which eventually lead to precipitation of some form of titanium oxide.

It is not clear that Type I precipitates observed in this study are indeed Ti_3O phase, as in the case of the ion-irradiated vanadium alloys. Further study is being conducted to identify the precipitates by dark-field/SAD analysis and electron-energy-loss spectroscopy. If Type I precipitates are indeed some form of irradiation-induced oxides of titanium. it seems that inhibition of void swelling will be influenced not only by minimum titanium content (e.g., >5 wt.%) but also by a minimum level of oxygen impurity in the alloy. Similar consideration suggests that the fabrication-related formation of the blocky Type III and V precipitates believed to be titanium oxides) will also influence inhibition of void formation indirectly.

CONCLUSIONS

Characteristics of void formation and precipitation in V. V-Ti, V-Cr. V-Ti-Cr, and V-Ti-Si alloys were examined by TEM after irradiation in FFTF/MOTA at 420°C up to 114 dpa. Three types of precipitates (i.e., Type III, IV, V) involving blocky TiO_2 or TiO apparently form by thermal processes. Minimal void swelling of vanadium alloys containing >5 wt.% Ti appears to be associated with irradiation-induced precipitation of a very fine particle-like (3-10 nm in size) phase. Vacancies produced during irradiation may be trapped by Ti and an impurity [probably O) complex: hence. void nucleation is suppressed in such alloys.

FUTURE WORKS

The crystal structure of the very fine precipitates that suppress void swelling will be determined from diffraction characteristics and electron energy-loss spectroscopy. Distribution of the precipitates will be determined from dark-field imaging for V-Ti. V-Ti-Cr, and V-Ti-Si alloys irradiated to various damage levels. The number density of the precipitates will be correlated with size and density of voids. Similar Correlation will be also obtained for alloys irradiated at 600°C to identify mechanism of inhibition of void swelling. TEM microstructural characteristics will be also correlated with ductility degradation of the alloys irradiated at 420. 520, and 600°C.

REFERENCES

1. B. A. Loomis. K. Abe. L. J. Nowicki, H. Chung, and D. L. Smith, "Swelling Dependence of Neutron-Irradiated Vanadium Alloys on Temperature, Neutron Fluence. and Tbermomecbanical Treatment." Fusion Reactor Materials Semiannual Progress Report for Period Ending September 30. 1990, DOE/ER-0313/9, *Oak* Ridge National Laboratory. *Oak* Ridge, TN, in press.

2. B. A. Loomis and D. L. Smith. "Relationship of Microstructure and Tensile Properties for Neutron-Irradiated Vanadium Alloys." Fusion Reactor Materials Semiannual Progress Report for Period Ending March 31, 1990, DOE/ER-0313/8, *Oak* Ridge National Laboratory, Oak Ridge, TN. August 1990, pp. 225-235.

3. B. A. Loomis and D. L. Smith, "Relationship of Microstructure and Tensile Properties for Neutron-Irradiated Vanadium Alloys," Proc. Fifteenth International Symposium on the Effects of Radiation on Materials, Nashville, TN, June 17-21, 1990, in press.

4. B. A. Loomis and D. L. Smith, 'Tensile Properties for Neutron-Irradiated Vanadium Alloys." Fusion Reactor Materials Semiannual Progress Report for Period Ending September 30. 1989, DOE/ER-0313/7, Oak Ridge National Laboratory, Oak Ridge. TN. pp. 203-209.

5. S. Ohnuki, D. S. Gelles, B. A. Loomis, F. A. Gamer, and H. Takahashi. "Microstructural Examination of Simple Vanadium Alloys Irradiated in the FFTF/MOTA," Fusion Reactor Materials Semiannual Progress Report for Period Ending September 30, 1989, DOE/ER-0313/7, *Oak* Ridge National Laboratory, *Oak* Ridge, TN, pp. 177-189.

6. D. S. Gelles. S. Ohnuki. B. A. Loomis. H. Takahashi. and F. A. Gamer, "Microstructural Explanation for Irradiation Embrittlement for V-15Cr-5Ti," Fusion Reactor Materials Semiannual Progress Report for Period Ending September 30, 1989. DOE/ER-0313/7, Oak Ridge National Laboratory, *Oak* Ridge. TN. pp. 193-202.

7. B. A. Loomis. B. J. Kestel, and S. B. Gerber. "Solute Segregation and Microstructural Evolution in Ion-Irradiated Vanadium-Base Alloys." Proc. 13th Int'l. Conf. on Radiation-Induced Changes in Microstructure. ASTM STP 955. Part I. Philadelphia, 1987, pp. 730-742.

TENSILE PROPERTIES OF VANADIUM AND VANADIUM-BASE ALLOYS* - B. A. Loomis, L. J. Nowicki, and D. L. Smith (Argonne National Laboratory).

OBJECTIVE

The objective of this research is to determine the composition of a vanadium-base alloy with the optimal combination of mechanical properties, swelling resistance, corrosion resistance, fabricability, and weldability for use as a structural material in the environment of a magnetic fusion reactor.

SUMMARY

Tensile property data are presented for unalloyed vanadium and 18 vanadium alloys that are considered candidates for structural material in a magnetic fusion reactor. The compositions of these candidate alloys are principally those vanadium binary and ternary alloys with Cr, Ti, and Si additions. The dependence of the tensile properties for these materials on temperature (25-700°C), Cr concentration (0-15%), Ti concentration (0-20%), and Si concentration (0.05-1.28%) is presented in the form of tables, graphs, and parametric equations. The strengthening of V by Cr, Ti, and Si additions is discussed with emphasis on the role of interaction'of these alloying additions with interstitial impurities (i.e., O, N, and C).

PROGRESS AND STATUS

Introduction

The tensile properties of unalloyed V and V-1Ti, V-3Ti, V-5Ti, V-10Ti, V-5Cr-5Ti, V-7Cr-5Ti, V-10Cr-10Ti, V-3Ti-0.54Si, V-3Ti-0.99Si, and Vanstar-7 alloys were determined for test temperatures of 25-700°C. These tensile-property data complement the data that were reported previously for V-20Ti, V-10Cr-5Ti, V-12Cr-5Ti, V-15Cr-5Ti, V-7.5Cr-15Ti, and V-3Ti-0.25Si alloys by Loomis et al. In this report, the tensile-property data from Ref. 1 and the more recently acquired data are compiled in the form of tables, graphs, and parametric equations for use as a reference resource. The strengthening of V by Cr, Ti, and Si additions is discussed, with emphasis on the role of interaction of these alloying additions with interstitial impurities (i.e., O, N, and C).

Materials and Procedures

Unalloyed vanadium and vanadium alloys with nominal compositions of V-1Ti, V-3Ti, V-5Ti, V-10Ti, V-5Cr-5Ti, V-7Cr-5Ti, V-10Cr-10Ti, V-3Ti-0.54Si, V-3Ti-0.99Si, and V-9Cr-3Fe-1Zr (Vanstar-7) were obtained in the form of ≈50% cold-worked sheet with thickness of ~0.9 mm. Chemical analyses of the materials, performed by the Analytical Department of the Teledyne Wah Chang Albany Company, are presented in Table 1. Tensile specimens with a gauge length of 7.62 mm and a gauge width of 1.52 mm were machined from the as-received sheet. The surfaces of tensile specimens were mechanically ground and polished to a surface finish of ≈0.3 μm. The polished tensile specimens were recrystallized by annealing for 1 h in a vacuum of 2×10^{-5} Pa. The V-5Cr-5Ti, V-7Cr-5Ti, V-10Cr-10Ti, and Vanstar-7 alloys were annealed at 1125°C. The V-3Ti, V-5Ti, V-10Ti, V-3Ti-0.54Si, and V-3Ti-0.99Si alloys were annealed at 1100°C, and the unalloyed vanadium and V-1Ti alloy were annealed at 1050°C. These annealing temperatures resulted in an average, recrystallized grain diameter of ≈0.020 mm in the specimens.

The tensile specimens were tested at a tensile strain rate of 0.0011 s^{-1} and a crosshead speed of 0.008 $mm \cdot s^{-1}$. All of the tensile tests were conducted in an environment of flowing argon (3×10^{-5} $m^3 \cdot s^{-1}$) of 99.9999% purity. The temperature of the specimens was determined by use of a chromel-alumel thermocouple that was arc-welded to the edge of the specimen, and the temperature of the specimens during the tensile test was controlled to ±1°C. The tensile specimens were heated to the test temperature at a rate of $0.2°C \cdot s^{-1}$.

ExDerimental Results

The yield strength (YS), ultimate tensile strength (UTS), uniform elongation (E_u), and total elongation (E) for the unalloyed vanadium and the vanadium alloys (Table 1) at 25-700°C are presented in Appendix 1.

1. Serrated Yielding

The load-elongation curves for the unalloyed V and the V alloys (Table 1) exhibited serrated yielding during tensile deformation at 320 and 420°C but not at 25, 100, and 225°C. In the case of the V specimen tested at 300°C, serrated yielding was observed in the load-elongation curve. At 520°C, V-Ti, V-Cr-Ti, and V-Ti-Si alloys containing 1, 3, 5, and 10% Ti (nominal composition) underwent serrated yielding, whereas un-

*Work supported by the Office of Fusion Energy, U.S. Department of Energy, under Contract W-31-109-Eng-38.

Table 1. Vanadium and Vanadium Alloy Compositions

Nominal Composition	ANL No.	Concentration (wt.%)			Concentration (ppm)			
		Cr	Ti	Fe	O	N	C	Si
V	BL-51				570	49	56	370
V-1Ti	BL-50		1.0		230	130	235	1050
V-3Ti	BL-52	-	3.1	0.04	210	310	300	500
V-5Ti	BL-46		4.6		300	53	85	160
V-10Ti	BL-12		9.8	0.63	1670	390	450	245
V-20Ti	BL-15	-	17.1	0.04	830	160	380	480
V-5Cr-5Ti	EL-47	4.1	4.3		350	220	200	870
V-7Cr-5Ti	BL-49	7.9	5.7		400	150	127	360
V-10Cr-5Ti	BL-43	9.2	4.9	0.02	230	31	100	340
V-12Cr-5Ti	EL-40	10.9	5.0	0.04	470	80	90	270
V-15Cr-5Ti	BL-23	12.9	5.9	0.04	400	490	280	1230
V-15Cr-5Ti	BL-24	13.5	5.2	0.05	1190	360	500	390
V-15Cr-5Ti	EL-41	14.5	5.0	0.02	330	96	120	400
V-10Cr-10Ti	BL-44	9.9	9.2	0.04	300	87	150	270
V-7.5Cr-15Ti	BL-10	7.2	14.5	0.09	1110	250	400	400
V-3Ti-0.25Si	EL-27	-	3.1	0.04	210	310	300	2500
V-3Ti-0.54Si	BL-42		3.1	0.02	580	190	140	5400
V-3Ti-0.99Si	BL-45		2.5	0.01	345	125	90	9900
Vanstar-7'	EL-28	9.7	-	3.50	280	520	640	

'Alloy contains 1.3% Zr.

alloyed V and the V-20Ti and Vanstar-7 alloys did not exhibit serrated yielding. At 600°C, vanadium alloys containing 5% Ti, i.e., V-5Ti and V-(5-15)Cr-5Ti alloys, exhibited serrated yielding, whereas unalloyed V and V-Ti and V-Ti-Si alloys containing 1, 3, 10, 15, and 20% Ti and the Vanstar-7 alloy did not. At 650°C, the V-5Cr-5Ti alloy exhibited serrated yielding, but the V-20Ti, V-(12-15)Cr-5Ti, and V-7.5Cr-15Ti alloys did not. At 700°C, the unalloyed V and the V alloys did not exhibit serrated yielding.

2. Temperature Dependence of YS and UTS

The general dependence of YS on temperature for the unalloyed V and V alloys (Table 1) is shown by curve IV in Fig. 1. The YS decreased with an increase of temperature from 25°C to ≈325°C and then either did not change significantly or underwent a small decrease with an increase of temperature from 325°C to 700°C. The general dependence of UTS on temperature for the unalloyed V and V alloys is shown by curves I, II, and III in Fig. 1. The UTS decreased with an increase of temperature from 25°C to ≈225°C and then increased with an increase of test temperature to 420°C, followed by either a decrease of UTS above 520-600°C (I), no significant change or a further increase of the UTS with increase of temperature to 700°C (11), or a substantial decrease of UTS above 420°C (III).

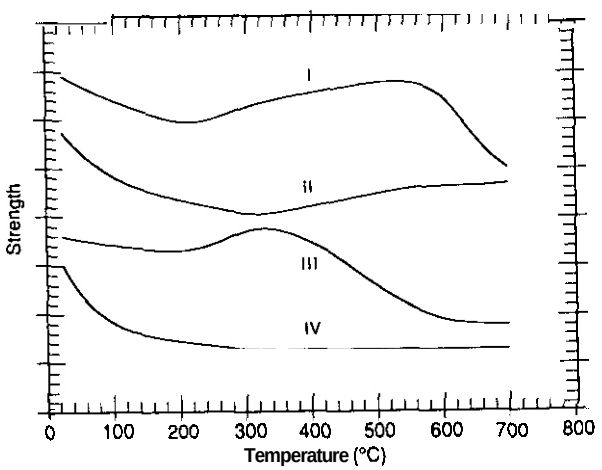


Fig. 1. General YS and UTS temperature dependence.

The dependence of *UTS* on temperature for V-1Ti, V-3Ti-(0.25-0.99)Si, V-10Ti, V-20Ti, V-15Cr-5Ti (BL23), V-10Cr-10Ti, V-7.5Cr-5Ti, and Vanstar-7 alloys was similar to I. The temperature dependence of UTS for V-3Ti, V-5Ti, and V-(5-15)Cr-5Ti (BL24 and BL41) alloys was similar to II, and the temperature dependence for unalloyed V was similar to III. Hence, the temperature dependence of UTS exhibited by the V-Ti and V-Cr-Ti alloys was dependent on Ti concentration, i.e., 0-3% Ti (I), 3-5% Ti (II), and 5-20% Ti (I), with no apparent influence of the Cr concentration. Moreover, the temperature dependence of UTS exhibited by an alloy was changed by solute addition, e.g., Si addition to the V-15Cr-5Ti (BL23) alloy. Based on the data in Appendix 1, these distinctive types of temperature dependence for UTS are shown in Figs. 2 (I) and (111), 3 (II), 4 (I) and (II), 5 (I), and 6 (I).

3. Dependence of YS and UTS on Ti, Cr, and Si Concentration

The dependence of YS and UTS on Ti concentration (C_{Ti}) in V-(0-20)Ti alloys, Cr concentration (C_{Cr}) in V-(0-15)Cr-5Ti alloys, and Si concentration (C_{Si}) in V-3Ti-(0-1.28)Si alloys is shown in Figs. 7, 8, and 9, respectively. The average value of the maximum and minimum YS and UTS data (Appendix 1) in the temperature

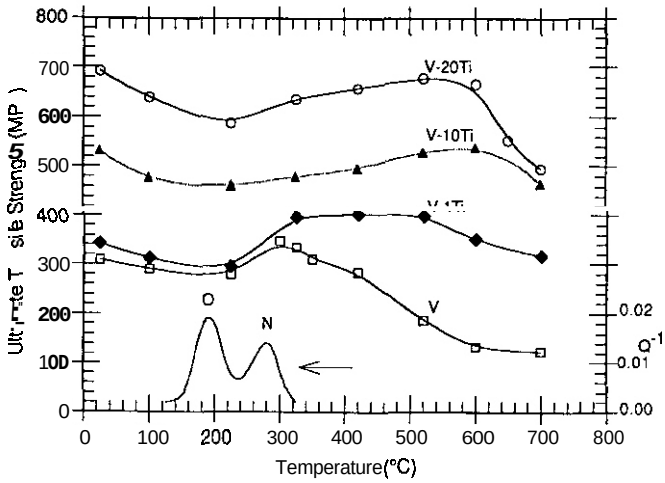


Fig. 2. Temperature dependence of **UTS** for V and **V-(1-20)Ti** alloys and internal friction for V from Ref. 2.

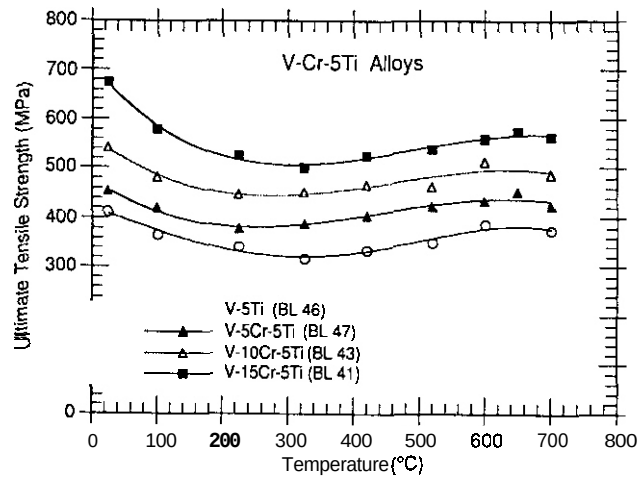


Fig. 3. Temperature dependence of **UTS** for V-(0-15)Cr-5Ti alloys.

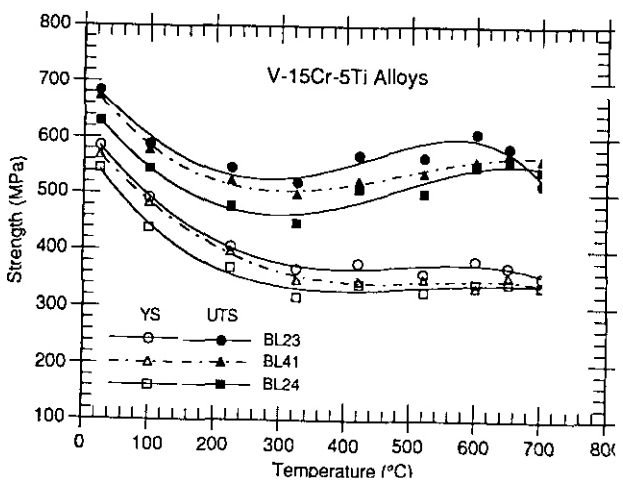


Fig. 4. Temperature dependence of **YS** and **UTS** for **V-15Cr-5Ti** alloys.

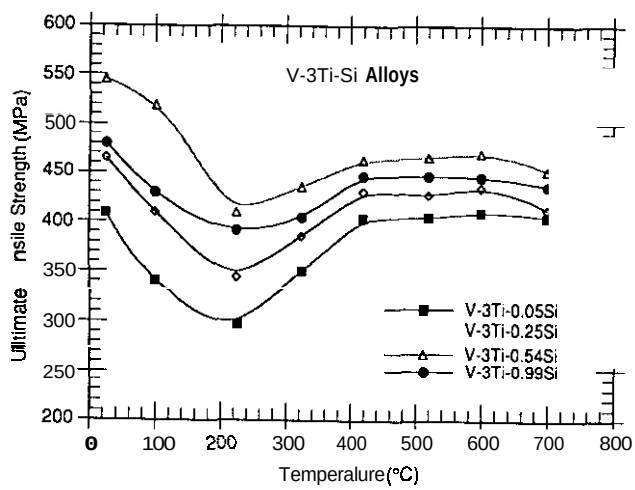


Fig. 5. Temperature dependence of UTS for **V-3Ti-(0.05-0.99)Si** alloys.

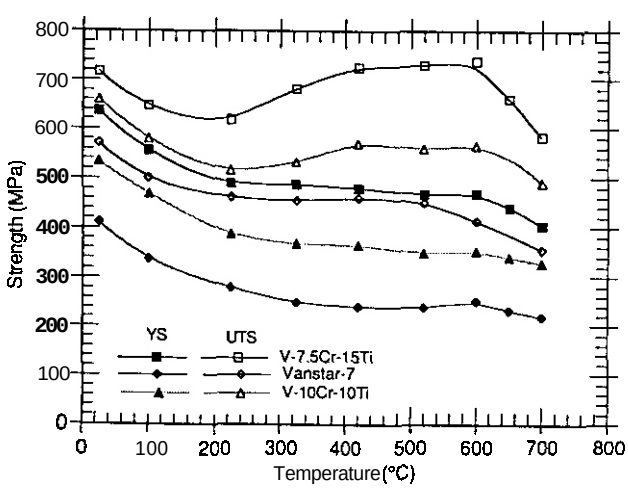


Fig. 6. Dependence of YS and **UTS** on temperature for **V-base** alloys.

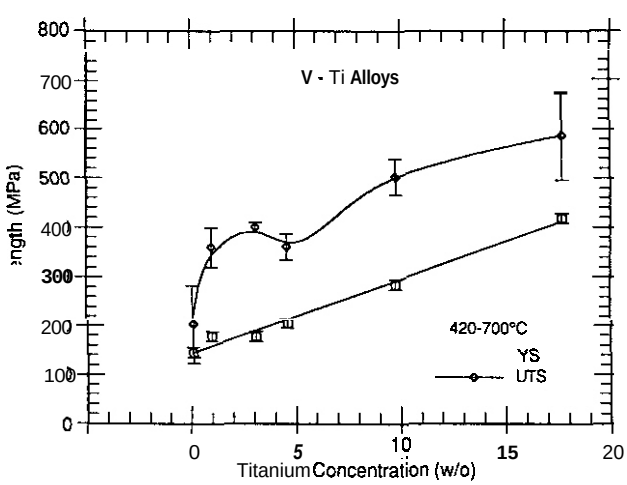
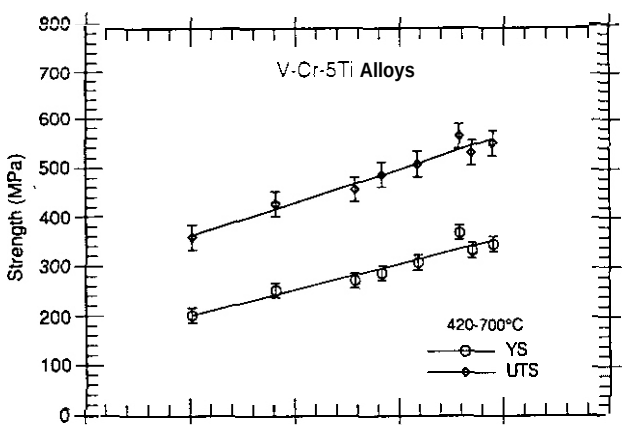
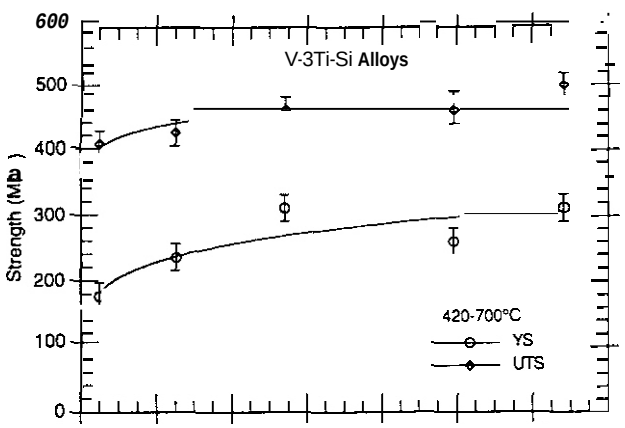
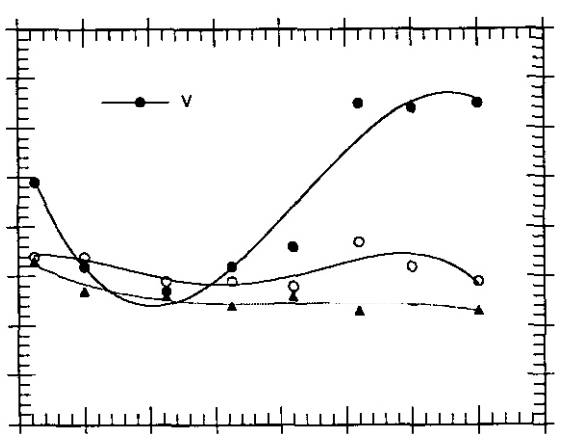


Fig. 7. Dependence of YS and **UTS** on C_{Ti} for V-Ti alloys.







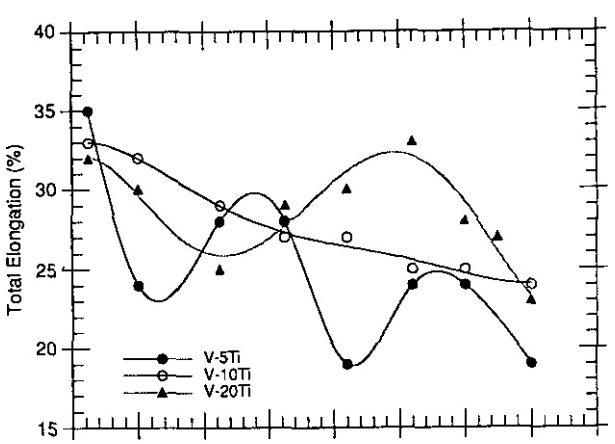


Fig. 10. Dependence of E, on temperature for V, V-1Ti, and V-3Ti.

Fig. 11. Temperature dependence of E for V-5Ti, V-10Ti, and V-20Ti alloys.

5. Dependence of E_f and E_f on Ti, Cr, and Si Concentration

The dependence of E_u and E_f on C_{Ti} in V-(0-20)Ti alloys, C_{Cr} in V-(0-15)Cr-5Ti alloys, and C_{Si} in V-3Ti-(0.05-1.28)Si alloys at 600°C is shown in Figs. 15, 16, and 17, respectively. The data for the V-Ti alloys show that E_f and E_f for V decrease with an increase of C_{Ti} to ≈3% and that E_f and E_f are essentially unchanged with increase of C_{Ti} from 3% to 20% (Fig. 15). The V-Cr-5Ti and V-3Ti-Si alloys appear to have minimum E_f and E_f for alloy compositions of ≈5% Cr and 0.5% Si (Figs. 16 and 17).

6. Parametric Equations for Tensile Properties

The dependence of YS, UTS, E_u, and E_f on temperature (T), C_{Cr}, C_{Ti}, and C_{Si} for the unalloyed vanadium and vanadium alloys listed in Table 1 is formulated by the equations in Appendix 2. These equations were obtained by the use of the data in Appendix 1. The YS and UTS equations have an accuracy of ±5%, and the E_f and E_f equations have an accuracy of ±10%.

DISCUSSION OF RESULTS

The YS of the V and V alloys at 25-700°C was primarily dependent on the complex interactions between intrinsic dislocations and stress fields associated with the substitutional alloying atoms (i.e., Cr, Ti, Si, Fe, and Zr), interstitial atoms (i.e., O, N, and C), and intrinsic precipitates, e.g., VO and TiO (Ref. 5), because the YS did not change significantly at temperatures >225°C.

The dependence of UTS on temperature for the unalloyed V and the V alloys exhibited a minimum UTS at 225-320°C, followed by an increase of UTS with increase of temperature to temperatures in the range of 420-700°C, depending on the material. The increase of UTS for the unalloyed V and the V alloys was associated with serrated yielding in the load-elongation curves. Therefore, the increase of UTS at >325°C for unalloyed V and V alloys is attributed primarily to stress-induced diffusion of O and N (and possibly C) to dislocations because of serrated yielding and internal friction peaks reported for O and N (at 181 and 265°C, respectively) in V (Fig. 2).[2,6]

Moreover, in addition to solution strengthening of the V alloys by Ti, it seems evident that the stress-induced diffusion of O and N atoms and their interaction with Ti atoms to form Ti-(O,N) complex and/or precipitates contributed significantly to the UTS for V-Ti, V-Ti-Si, and V-Ti-Cr alloys. Because we have not completed comprehensive analyses of the intrinsic and/or stress-induced precipitates in the alloy microstructures, we cannot elucidate on the different temperature dependence of UTS for the alloys, i.e., the general dependence in Fig. 1. It is our expectation that the average diameter, average spacing, composition, and crystallographic compatibility (i.e., coherency or noncoherency) of the Ti-O precipitates were significant factors in determining the temperature dependence of UTS for the alloys. An understanding of the necessity for 3-5%Ti in V-Ti and V-Ti-Cr alloys for high temperature (>520°C) tensile strength (and creep strength) is of paramount importance for the selection of a V alloy for use in a fusion reactor. In contrast to Ti solute, it is believed that the effect of Cr and Si on the UTS for V-Ti-Si and V-Ti-Cr alloys was to provide an increment of solid solution strengthening.

CONCLUSIONS

1. The temperature dependence of UTS for V-Ti and V-Ti-Cr alloys is dependent on Ti concentration with no apparent influence of Cr concentration.
2. The increase of YS and UTS for V-(1-20)Ti alloys is ~16 MPa/1% Ti and ≈19 MPa/1% Ti, respectively.
3. The increase of YS and UTS for V-(0-15)Cr-5Ti alloys is ≈10 MPa/1% Cr and 13 MPa/1% Cr, respectively.
4. The increase of YS and UTS for V-3Ti-(0.05-1.28)Si alloys is ~84 MPa/1% Si and ~64 MPa/1% Si, respectively.
5. The presence of relatively high (1230 ppm) Si concentration in V-15Cr-5Ti alloy resulted in significant strengthening of the alloy to ≈600°C.
6. The V-(0-15)Cr-5Ti and V-3Ti-(0-1.3)Si alloys have minimum E_f and E_f for alloy compositions of ~5% Cr and 0.5% Si, respectively.

FUTURE WORK

The average diameter, average spacing, composition, and crystallographic compatibility (i.e., coherency or noncoherency) of the intrinsic and stress-induced precipitates will be determined.

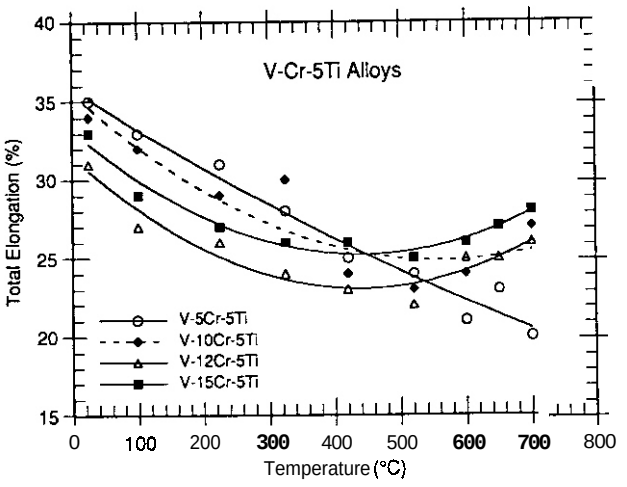


Fig. 12. Temperature dependence of E_t for V-(5-15)Cr-5Ti alloys.

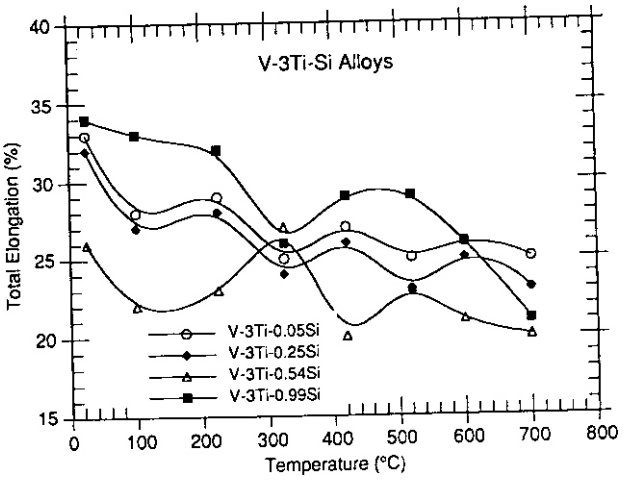


Fig. 13. Temperature dependence of E_t for V-3Ti-(0.05-0.99)Si alloys.

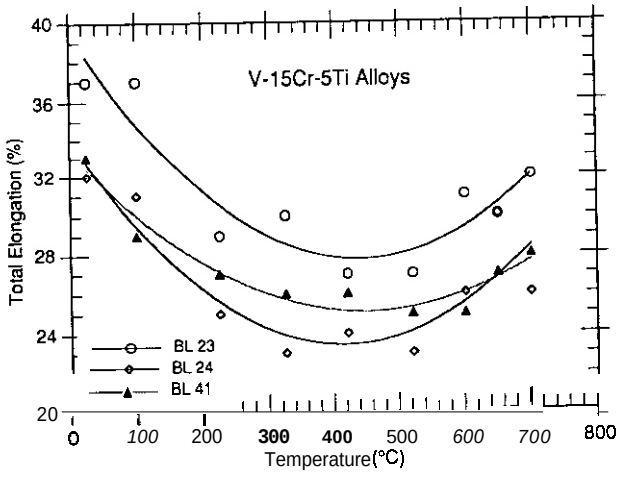


Fig. 14. Temperature dependence of E_t for V-15Cr-5Ti alloys.

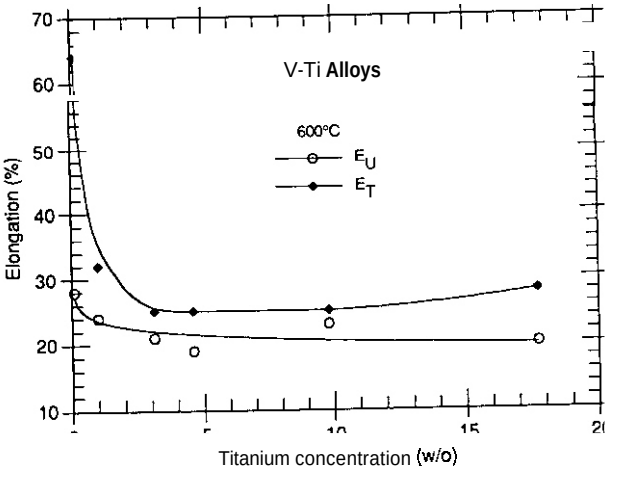


Fig. 15. Dependence of E_t and E_u on C_{Ti} for V-(0-20)Ti alloys.

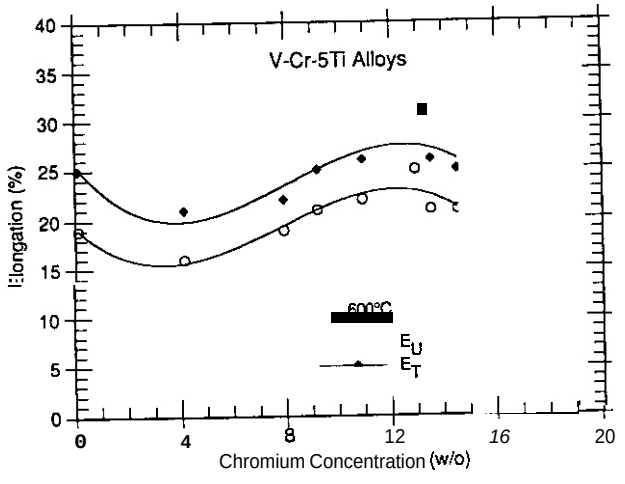


Fig. 16. Dependence of E_t and E_u on C_{Cr} for V-(0-15)Cr-5Ti alloys.

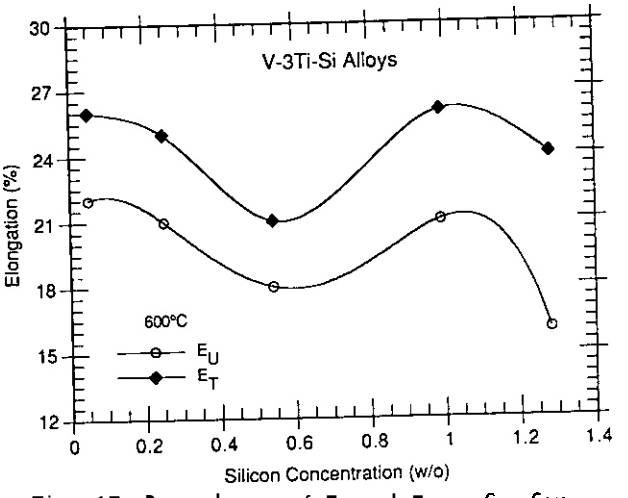


Fig. 17. Dependence of E_u and E_t on C_{Si} for V-3Ti-(0.05-1.3)Si alloys.

REFERENCES

1. E. A. Loomis, R. H. Lee, D. L. Smith, and J. R. Peterson, "Strength, Ductility, and Ductile-Brittle Transition Temperature for MFR Candidate Vanadium Alloys," J. Nucl. Mater., 155-157 (1988) 631-638.

2. R. W. Powers. "Internal Friction in Oxygen-Vanadium and Nitrogen-Vanadium Solid Solutions," Acta Met. 2 (1954) 604-607.

3. B. A. Loomis and D. L. Smith, "Response of Unirradiated and Neutron-Irradiated Vanadium Alloys to Charpy-Impact Loading," to be published in the proceedings of Fourth International Conference on Fusion Reactor Materials, December 4-8, 1989, Kyoto, Japan.

4. D. N. Braski, "The Tensile Properties and Swelling of Several Vanadium Alloys After Irradiation to 40 dpa in FFTF," in: Alloy Development for Irradiation Performance, Semiannual Progress Report for Period Ending March 31, 1986, DOE/ER-0045/16, pp. 60-64.

5. K. H. Kramer, "Ausscheidungsvorgange in Rein-Vanadin und Vanadin-Titan Legierungen," J. Less Common Met., 21 (1970) 365.

6. R. W. K. Honeycombe, in: The Plastic Deformation of Metals (St. Martins, New York, 1968) p. 144.

Appendix 1. Tensile Properties for V and V Alloys.

Alloy	ANL I.D.	Test Temp. (°C)	Strength		Elongation	
			Yield (MPa)	Tensile (MPa)	Uniform (%)	Total (%)
V	BL 51-1	25	259	309	28	49
V	BL 51-10	100	220	290	24	32
V	BL 51-5	225	175	279	21	28
V	BL 51-9	300	181	348	26	32
V	BL 51-4	325	153	335	24	32
V	BL 51-8	350	138	310	24	32
V	BL 51-2	420	167	283	25	36
V	BL 51-7	520	134	187	34	65
V	BL 51-3	600	124	134	28	64
V	BL 51-6	700	124	124	28	64
V-1Ti	BL 50-2	25	268	343	23	34
V-1Ti	BL 50-8	120	236	317	23	34
V-1Ti	BL 50-4	225	188	275	20	28
V-1Ti	BL 50-7	325	174	396	23	29
V-1Ti	BL 50-3	420	198	402	22	28
V-1Ti	BL 50-6	520	181	398	28	37
V-1Ti	BL 50-5	600	174	351	24	32
V-1Ti	BL 50-9	700	157	317	21	29
V-3Ti	BL 52-1	25	295	409	24	
V-3Ti	BL 52-7	100	210	340	22	27
V-3Ti	BL 52-6	225	180	298	22	28
V-3Ti	BL 52-5	325	177	350	20	24
V-3Ti	BL 52-2	420	183	404	20	26
V-3Ti	BL 52-3	520	170	405	19	23
V-3Ti	BL 52-4	600	177	410	21	25
V-3Ti	BL 52-8	700	183	405	19	23
V-3Ti-0.25Si	BL 27-1	25	367	465	24	33
V-3Ti-0.25Si	BL 27-14	100	300	410	22	27
V-3Ti-0.25Si	BL 27-6	225	235	344	22	28
V-3Ti-0.25Si	BL 27-5	325	227	386	20	24
V-3Ti-0.25Si	BL 27-2	420	242	431	20	26
V-3Ti-0.25Si	BL 27-3	520	228	428	19	23
V-3Ti-0.25Si	BL 27-4	600	230	435	21	25
V-3Ti-0.25Si	BL 27-10	700	224	413	19	23
V-3Ti-0.54Si	BL 42-1	25	473	545	20	26
V-3Ti-0.54Si	BL 42-6	100	405	519	19	22
V-3Ti-0.54Si	BL 42-2	225	317	410	18	23
V-3Ti-0.54Si	BL 42-3	325	300	436	21	27
V-3Ti-0.54Si	BL 42-4	420	328	463	16	20
V-3Ti-0.54Si	BL 42-5	520	312	466	18	23
V-3Ti-0.54Si	BL 42-8	600	308	470	18	21
V-3Ti-0.54Si	BL 42-9	700	291	452	17	20

Appendix 1 (cont'd)

Alloy	ANL I.D.	Test Temp. (°C)	Strength Yield (MPa)	Strength Tensile (MPa)	Elongation Uniform (%)	Elongation Total (%)
V-3Ti-0.99Si	BL 45-10	25	421	480	25	34
V-3Ti-0.99Si	BL 45-5	105	355	430	26	33
V-3Ti-0.99Si	BL 45-4	225	286	392	26	32
V-3Ti-0.99Si	BL 45-2	325	259	405	21	26
V-3Ti-0.99Si	BL 45-6	420	274	447	24	29
V-3Ti-0.99Si	BL 45-6	520	274	447	24	29
V-3Ti-0.99Si	BL 45-1	600	241	446	21	26
V-3Ti-0.99Si	BL 45-3	700	260	437	17	21
V-5Ti	BL 46-1	25	336	412	22	35
V-5Ti	BL 46-6	108	294	366	16	24
V-5Ti	BL 46-10	160	259	342	20	25
V-5Ti	BL 46-3	225	217	317	23	28
V-5Ti	BL 46-5	330	214	342	22	28
V-5Ti	BL 46-2	420	215	334	15	19
V-5Ti	BL 46-8	520	195	350	20	24
V-5Ti	BL 46-7	600	195	388	19	25
V-5Ti	BL 46-4	700	203	376	17	19
V-10Ti	BL 12-1	25	435	532	25	33
V-10Ti	BL 12-8	100	314	477	25	32
V-10Ti	BL 12-6	225	326	463	23	28
V-10Ti	BL 12-5	325	310	479	21	27
V-10Ti	BL 12-2	420	308	496	21	27
V-10Ti	BL 12-7	520	303	529	21	25
V-10Ti	BL 12-3	600	298	538	23	25
V-10Ti	BL 12-4	700	262	466	19	24
V-20Ti	BL 15-1	25	628	692	22	32
V-20Ti	BL 15-4	100	525	640	22	30
V-20Ti	BL 15-6	225	437	588	20	25
V-20Ti	BL 15-5	325	436	636	24	29
V-20Ti	BL 15-3	420	443	658	24	30
V-20Ti	BL 15-2	520	445	678	29	33
V-20Ti	BL 15-4	600	417	667	20	28
V-20Ti	BL 15-8	650	400	554	20	29
V-20Ti	BL 15-7	700	393	496	15	23
V-5Cr-5Ti	BL 47-9	25	387	454	25	34
V-5Cr-5Ti	BL 47-10	100	325	420	25	33
V-5Cr-5Ti	BL 47-5	225	272	379	26	31
V-5Cr-5Ti	BL 47-3	337	254	388	20	28
V-5Cr-5Ti	BL 47-2	420	250	405	21	25
V-5Cr-5Ti	BL 47-8	520	244	423	19	24
V-5Cr-5Ti	BL 47-4	600	256	434	16	21
V-5Cr-5Ti	BL 47-7	650	264	453	19	23
V-5Cr-5Ti	BL 47-6	700	266	414	17	20
V-7Cr-5Ti	BL 49-3	25	425	521	26	36
V-7Cr-5Ti	BL 49-9	108	393	489	23	30
V-7Cr-5Ti	BL 49-10	175	318	404	12	13
V-7Cr-5Ti	BL 49-8	225	236	347	17	23
V-7Cr-5Ti	BL 49-6	325	261	429	18	26
V-7Cr-5Ti	BL 49-4	420	287	470	20	25
V-7Cr-5Ti	BL 49-5	600	285	486	19	22
V-7Cr-5Ti	BL 49-7	700	271	487	21	26
V-10Cr-5Ti	BL 43-9	25	440	541	23	33
V-10Cr-5Ti	BL 43-10	100	387	482	20	32
V-10Cr-5Ti	BL 43-3	225	334	448	22	29
V-10Cr-5Ti	BL 43-6	325	312	452	21	30
V-10Cr-5Ti	BL 43-1	420	300	467	20	25
V-10Cr-5Ti	BL 43-4	520	297	463	18	23
V-10Cr-5Ti	BL 43-5	600	297	512	21	25

Appendix 1 (cont'd)

Alloy	ANL I.D.	Test Temp. (°C)	Strength		Elongation	
			Yield (MPa)	Tensile (MPa)	Uniform (%)	Total
V-10Cr-5Ti	BL 43-7	700	277	488	21	27
V-12Cr-5Ti	BL 40-12	25	491	573	23	
V-12Cr-5Ti	BL 40-13	100	402	500	21	27
V-12Cr-5Ti	BL 40-14	225	347	464	21	26
V-12Cr-5Ti	BL 40-5	325	304	448	17	24
V-12Cr-5Ti	BL 40-2	433	321	501	18	24
V-12Cr-5Ti	BL 40-3	520	303	488	17	22
V-12Cr-5Ti	BL 40-4	600	299	519	22	26
V-12Cr-5Ti	BL 40-2	650	310	529	20	25
V-12Cr-5Ti	BL 40-1	700	299	513	25	26
V-15Cr-5Ti	BL 23-15	25	533	627		37
V-15Cr-5Ti	BL 23-14	100	483	589	25	37
V-15Cr-5Ti	BL 23-6	225	407	548	23	29
V-15Cr-5Ti	BL 23-5	325	368	522	23	30
V-15Cr-5Ti	BL 23-12	420	379	571	21	27
V-15Cr-5Ti	BL 23-3	520	360	567	21	27
V-15Cr-5Ti	BL 23-4	600	384	610	25	31
V-15Cr-5Ti	BL 23-10	650	373	573	22	30
V-15Cr-5Ti	BL 23-13	700	355	519	21	32
V-15Cr-5Ti	BL 41-L1	25	570	674	26	
V-15Cr-5Ti	BL 41-12	100	494	579	23	29
V-15Cr-5Ti	BL 41-1	225	399	525	22	27
V-15Cr-5Ti	BL 41-5	325	348	500	19	26
V-15Cr-5Ti	BL 41-2	420	346	524	20	26
V-15Cr-5Ti	BL 41-3	520	350	538	19	25
V-15Cr-5Ti	BL 41-4	600	335	560	21	25
V-15Cr-5Ti	BL 41-3	650	356	575	22	27
V-15Cr-5Ti	BL 41-2	700	339	564	22	28
V-15Cr-5Ti	BL 24-18	25	545	634	23	32
V-15Cr-5Ti	BL 24-31	100	439	545	22	31
V-15Cr-5Ti	BL 24-12	225	370	478	17	25
V-15Cr-5Ti	BL 24-1	325	317	449	17	23
V-15Cr-5Ti	BL 24-11	420	341	518	21	27
V-15Cr-5Ti	BL 24-15	520	326	502	17	23
V-15Cr-5Ti	BL 24-13	600	342	555	21	26
V-15Cr-5Ti	BL 24-26	650	342	559	25	30
V-15Cr-5Ti	BL 24-25	700	337	544	21	26
V-10Cr-10Ti	BL 44-7	25	534	628	24	34
V-10Cr-10Ti	BL 44-12	100	469	571	24	36
V-10Cr-10Ti	BL 44-8	225	387	516	21	29
V-10Cr-10Ti	BL 44-5	325	367	532	23	30
V-10Cr-10Ti	BL 44-9	420	364	570	23	30
V-10Cr-10Ti	BL 44-10	520	349	560	23	29
V-10Cr-10Ti	BL 44-11	600	352	565	23	30
V-10Cr-10Ti	BL 44-3	700	328	492	20	28
V-7.5Cr-15Ti	BL 10-12	25	636	717	20	28
V-7.5Cr-15Ti	BL 10-13	100	556	647	21	28
V-7.5Cr-15Ti	BL 10-6	225	490	618	20	25
V-7.5Cr-15Ti	BL 10-5	325	487	682	21	25
V-7.5Cr-15Ti	BL 10-T1	420	471	695	22	29
V-7.5Cr-15Ti	BL 10L-2	520	468	730	24	28
V-7.5Cr-15Ti	BL 10-3	600	469	738	26	27
V-7.5Cr-15Ti	BL 10-10	650	441	661	23	28
V-7.5Cr-15Ti	BL 10T-2	700	404	584	18	30
Vanstar-7	BL 28-1	25	411	571	25	37
Vanstar-7	BL 28-12	105	337	501	28	35
Vanstar-7	BL 28-5	225	279	462	24	31

Appendix 1 (cont'd)

Alloy	ANL 1.0.	Test Temp. (°C)	Strength Yield (MPa)	Strength Tensile (MPa)	Elongation Uniform (%)	Elongation Total (%)
Vanstar-7	BL 28-10	325	249	455	23	29
Vanstar-7	BL 28-2	425	240	467	27	33
Vanstar-7	BL 28-9	520	239	450	27	33
Vanstar-7	BL 28-4	600	251	413	26	34
Vanstar-7	BL 28-3	700	219	355	20	35

Appendix 2. Parametric Equations for Tensile Properties of V and V Alloys.

V:

$YS = 280.5361 - 0.9310\,T + 3.0696 \times 10^{-3}\,T^2 - 5.0275 \times 10^{-6}\,T^3 + 2.9672 \times 10^{-9}\,T^4.$

$UTS = 318.1652 + 0.0420\,T - 1.0887 \times 10^{-2}\,T^2 + 9.4389 \times 10^{-5}\,T^3 - 2.9203 \times 10^{-7}\,T^4 + 3.7539 \times 10^{-10}\,T^5 - 1.7195 \times 10^{-13}\,T^6.$

$E_u = 28.7597 - 0.0258\,T - 3.6173 \times 10^{-4}\,T^2 + 2.3309 \times 10^{-6}\,T^3 - 4.1639 \times 10^{-9}\,T^4 + 2.3513 \times 10^{-12}\,T^5.$

$E_t = 51.6945 - 0.2133\,T + 4.2811 \times 10^{-4}\,T^2 + 3.7401 \times 10^{-7}\,T^3 - 7.2051 \times 10^{-10}\,T^4.$

V-1Ti:

$YS = 277.9337 - 0.2050\,T - 3.5612 \times 10^{-3}\,T^2 + 1.7758 \times 10^{-5}\,T^3 - 2.8609 \times 10^{-8}\,T^4 + 1.5118 \times 10^{-11}\,T^5.$

$UTS = 348.8706 + 0.6850\,T - 2.2112 \times 10^{-2}\,T^2 + 1.4430 \times 10^{-4}\,T^3 - 3.7135 \times 10^{-7}\,T^4 + 4.2220 \times 10^{-10}\,T^5 - 1.7822 \times 10^{-13}\,T^6.$

$E_u = 23.3521 + 0.0246\,T - 4.7876 \times 10^{-4}\,T^2 + 2.0429 \times 10^{-6}\,T^3 - 3.1249 \times 10^{-9}\,T^4 + 1.5761 \times 10^{-12}\,T^5.$

$E_t = 34.7157 - 0.0119\,T + 1.7919 \times 10^{-4}\,T^2 - 2.9519 \times 10^{-6}\,T^3 + 1.2072 \times 10^{-8}\,T^4 - 1.8329 \times 10^{-11}\,T^5 + 9.4216 \times 10^{-15}\,T^6.$

V-3Ti:

$YS = 346.9919 - 2.2804\,T + 1.1814 \times 10^{-2}\,T^2 - 2.9158 \times 10^{-5}\,T^3 + 3.4116 \times 10^{-8}\,T^4 - 1.5171 \times 10^{-11}\,T^5.$

$UTS = 452.3741 - 1.6660\,T + 4.7036 \times 10^{-3}\,T^2 + 2.5825 \times 10^{-6}\,T^3 - 1.7670 \times 10^{-8}\,T^4 + 1.2786 \times 10^{-11}\,T^5.$

$E_u = 24.9571 - 0.0479\,T + 3.2117 \times 10^{-4}\,T^2 - 1.1513 \times 10^{-6}\,T^3 + 1.8343 \times 10^{-9}\,T^4 - 1.0395 \times 10^{-12}\,T^5.$

$E_t = 34.3398 - 0.0974\,T + 4.8241 \times 10^{-4}\,T^2 - 1.2177 \times 10^{-6}\,T^3 + 1.4665 \times 10^{-9}\,T^4 - 6.7836 \times 10^{-13}\,T^5.$

V-5Ti:

$YS = 365.6995 - 1.0681\,T + 2.7639 \times 10^{-3}\,T^2 - 3.3882 \times 10^{-6}\,T^3 + 1.6123 \times 10^{-9}\,T^4.$

$UTS = 433.6693 - 0.7653\,T + 1.8555 \times 10^{-4}\,T^2 + 7.4088 \times 10^{-6}\,T^3 - 1.4475 \times 10^{-8}\,T^4 + 7.8862\,10^{-12}\,T^5.$

$E_u = 24.4427 - 0.2368\,T + 2.9157 \times 10^{-3}\,T^2 - 1.4176 \times 10^{-5}\,T^3 + 3.2307 \times 10^{-8}\,T^4 - 3.4788 \times 10^{-11}\,T^5 + 1.4298 \times 10^{-14}\,T^6.$

$E_t = 36.3672 - 0.0084\,T - 3.4774 \times 10^{-3}\,T^2 + 3.8201 \times 10^{-5}\,T^3 - 1.6593 \times 10^{-7}\,T^4 + 3.4850 \times 10^{-10}\,T^5 - 3.5319 \times 10^{-13}\,T^6 + 1.3852 \times 10^{-16}\,T^7.$

V-10Ti:

$YS = 474.6698 - 1.2694\,T + 3.4138 \times 10^{-3}\,T^2 - 3.5874 \times 10^{-6}\,T^3 + 9.8045 \times 10^{-10}\,T^4.$

$UTS = 556.1722 - 1.0022\,T + 2.8386 \times 10^{-3}\,T^2 - 9.7134 \times 10^{-7}\,T^3 - 1.8422 \times 10^{-9}\,T^4.$

$E_u = 25.7510 - 0.0181\,T + 2.1923 \times 10^{-4}\,T^2 - 1.7848 \times 10^{-6}\,T^3 + 5.3763 \times 10^{-9}\,T^4 - 6.6679 \times 10^{-12}\,T^5 + 2.9020 \times 10^{-15}\,T^6.$

$E_t = 34.1689 - 0.0285\,T + 4.8961 \times 10^{-6}\,T^2 + 7.6127 \times 10^{-8}\,T - 7.7651 \times 10^{-11}\,T^4.$

V-20Ti:

$YS = 678.5068 - 2.2060\,T + 7.1177 \times 10^{-3}\,T^2 - 9.4733 \times 10^{-6}\,T^3 + 4.2350 \times 10^{-9}\,T^4.$

$UTS = 727.5363 - 1.4861\,T + 4.9091 \times 10^{-3}\,T^2 - 3.2259 \times 10^{-6}\,T^3 - 2.0458 \times 10^{-9}\,T^4.$

$E_u = 22.7197 - 0.0081\,T - 1.6138 \times 10^{-5}\,T^2 - 4.0723 \times 10^{-7}\,T^3 + 3.5996 \times 10^{-9}\,T^4 - 7.4898 \times 10^{-12}\,T^5 + 4.5893 \times 10^{-15}\,T^6.$

$E_t = 32.7755 - 0.0018\,T - 5.4265 \times 10^{-4}\,T^2 + 2.8059 \times 10^{-6}\,T^3 - 4.7104 \times 10^{-9}\,T^4 + 2.5382 \times 10^{-12}\,T^5.$

V-5Cr-5Ti:

$YS = 417.5058 - 1.1834\,T + 3.1426 \times 10^{-3}\,T^2 - 3.7434 \times 10^{-6}\,T^3 + 1.7062 \times 10^{-9}\,T^4.$

$UTS = 469.1526 - 0.4914\,T - 1.1537 \times 10^{-3}\,T^2 + 1.0563 \times 10^{-5}\,T^3 - 1.8035 \times 10^{-8}\,T^4 + 9.4017 \times 10^{-12}\,T^5.$

$E_u = 25.4657 - 0.0083\,T + 1.7387 \times 10^{-4}\,T^2 - 1.0392 \times 10^{-6}\,T^3 + 1.8711 \times 10^{-9}\,T^4 - 1.0732 \times 10^{-12}\,T^5.$

$E_t = 34.8165 - 0.0326\,T + 2.1877 \times 10^{-4}\,T^2 - 1.0407 \times 10^{-6}\,T^3 + 1.8034 \times 10^{-9}\,T^4 - 1.0372 \times 10^{-12}\,T^5.$

V-7Cr-5Ti:

$YS = 431.8805 + 0.4110\,T - 1.4031 \times 10^{-2}\,T^2 + 5.7204 \times 10^{-5}\,T^3 - 8.5862 \times 10^{-8}\,T^4 + 4.4159 \times 10^{-11}\,T^5.$

$UTS = 509.1205 + 2.0489\,T - 3.9845 \times 10^{-2}\,T^2 + 2.0835 \times 10^{-4}\,T^3 - 4.7235 \times 10^{-7}\,T^4 + 4.9498 \times 10^{-10}\,T^5 - 1.9692 \times 10^{-13}\,T^6.$

$E_u = 27.0407 - 0.0284\,T - 3.3045 \times 10^{-4}\,T^2 + 1.8948 \times 10^{-6}\,T^3 - 3.2819 \times 10^{-9}\,T^4 + 1.8622 \times 10^{-12}\,T^5.$

$E_t = 36.7240 + 0.0188\,T - 1.6886 \times 10^{-3}\,T^2 + 1.0893 \times 10^{-5}\,T^3 - 2.8338 \times 10^{-8}\,T^4 + 3.3014 \times 10^{-11}\,T^5 - 1.4258 \times 10^{-14}\,T^6.$

Appendix 2 (cont'd)

V-10Cr-5Ti:

YS = 459.3969 - 0.8836 T + 1.6721 x 10^{-3} T^2 - 1.2942 x 10^{-6} T^3 t 2.9462 x 10^{-10} T^4.

UTS = 572.4420 - 1.2367 T t 3.9440 x 10^{-3} T^2 - 4.5781 x 10^{-6} T^3 t 1.7865 x 10^{-9} T^4.

E = 24.3990 - 0.0923 T t 8.4192 x 10^{-4} T^2 - 3.1271 x 10^{-6} T^3 t 5.0581 x 10^{-9} T^4 - 3.3081 x 10^{-12} T^5 t 5.3878 x 10^{-18} T^6.

E_T = 34.0122 - 0.0358 T + 2.3972 x 10^{-5} T^2 + 9.8989 x 10^{-7} T^3 - 4.9285 x 10^{-9} T^4 + 8.1672 x 10^{-12} T^5 - 4.4263 x 10^{-15} T^6.

V-12Cr-5Ti:

YS = 536.4005 - 1.7625 T t 5.1917 x 10^{-3} T^2 - 6.8368 x 10^{-6} T^3 + 3.3373 x 10^{-9} T^4.

UTS = 618.7231 - 1.7193 T t 5.8324 x 10^{-3} T^2 - 7.2205 x 10^{-6} T^3 t 3.0146 x 10^{-9} T^4.

E = 24.1740 - 0.0744 T t 7.8946 x 10^{-4} T^2 - 4.0637 x 10^{-6} T^3 t 9.4966 x 10^{-9} T^4 - 1.0014 x 10^{-11} T^5 + 3.9017 x 10^{-15} T^6.

E = 32.2659 - 0.0772 T + 4.3345 x 10^{-4} T^2 - 1.4030 x 10^{-6} T^3 + 2.1049 x 10^{-9} T^4 - 1.1221 x 10^{-12} T^5.

V-15Cr-5Ti (BL 23):

YS = 558.1555 - 0.9369 T t 1.0829 x 10^{-3} T^2 + 6.1968 x 10^{-7} T^3 - 1.1653 x 10^{-9} T^4.

UTS = 642.1572 - 0.4584 T - 1.4787 x 10^{-3} T^2 t 8.2521 x 10^{-6} T^3 - 7.9167 x 10^{-9} T^4.

E = 26.1669 - 0.0530 T t 5.8246 x 10^{-4} T^2 - 3.1406 x 10^{-6} T^3 + 7.7426 x 10^{-9} T^4 - 8.6763 x 10^{-12} T^5 t 3.6042 x 10^{-15} T^6.

E_T = 37.9524 - 0.0067 T - 2.3498 x 10^{-4} T^2 t 7.2171 x 10^{-7} T^3 - 7.4625 x 10^{-10} T^4 t 2.6945 x 10^{-13} T^5.

V-15Cr-5Ti (BL 24):

YS = 577.7104 - 1.7651 T t 4.7219 x 10^{-3} T^2 - 5.5200 x 10^{-6} T^3 + 2.3873 x 10^{-9} T^4.

UTS = 663.0236 - 1.1326 T - 1.0901 x 10^{-3} T^2 t 1.5361 x 10^{-5} T^3 - 2.6239 x 10^{-8} T^4 t 1.3376 x 10^{-11} T^5.

E = 23.3113 t 0.0512 T - 1.3537 x 10^{-3} T^2 t 8.0229 x 10^{-6} T^3 - 2.0702 x 10^{-8} T^4 t 2.4785 x 10^{-11} T^5 - 1.1214 x 10^{-14} T^6.

E_T = 32.2701 t 0.0525 T - 1.3020 x 10^{-4} T^2 t 7.1133 x 10^{-6} T^3 - 1.7357 x 10^{-8} T^4 t 2.0015 x 10^{-11} T^5 - 8.8343 x 10^{-15} T^6.

V-15Cr-5Ti (BL 41):

YS = 601.3434 - 1.2868 T + 1.7554 x 10^{-3} T^2 t 5.9653 x 10^{-9} T^3 - 9.1031 x 10^{-10} T^4.

UTS = 711.0014 - 1.5990 T + 3.9811 x 10^{-3} T^2 - 3.2279 x 10^{-6} T^3 + 5.5023 x 10^{-10} T^4.

E = 27.0546 - 0.0495 T t 2.2923 x 10^{-4} T^2 - 7.9673 x 10^{-7} T^3 t 1.3356 x 10^{-9} T^4 - 7.7245 x 10^{-13} T^5.

E = 34.3628 - 0.0789 T t 3.8941 x 10^{-4} T^2 - 1.0786 x 10^{-6} T^3 t 1.4192 x 10^{-9} T^4 - 6.7346 x 10^{-13} T^5.

V-3Ti-0.25Si:

YS = 408.4735 - 1.5563 T t 4.8229 x 10^{-3} T^2 - 6.3509 x 10^{-6} T^3 + 3.0017 x 10^{-9} T^4.

UTS = 494.2046 - 0.8883 T - 2.7576 x 10^{-3} T^2 t 2.8078 x 10^{-5} T^3 - 5.5458 x 10^{-8} T^4 t 3.3216 x 10^{-11} T^5.

E = 25.3403 - 0.0643 T + 4.9184 x 10^{-4} T^2 - 1.8284 x 10^{-6} T^3 + 2.9627 x 10^{-9} T^4 - 1.7046 x 10^{-12} T^5.

E = 35.4150 - 0.1244 T t 6.8719 x 10^{-4} T^2 - 1.8712 x 10^{-6} T^3 t 2.3929 x 10^{-9} T^4 - 1.1597 x 10^{-12} T^5.

V-3Ti-0.54Si:

YS = 519.2681 - 1.6547 T + 4.4194 x 10^{-3} T^2 - 4.5625 x 10^{-6} T^3 + 1.3895 x 10^{-9} T^4.

UTS = 602.8017 - 1.8894 T t 6.5021 x 10^{-3} T^2 - 8.0703 x 10^{-6} T^3 + 3.1241 x 10^{-9} T^4.

E = 22.1016 - 0.0889 T + 7.2714 x 10^{-4} T^2 - 2.4146 x 10^{-6} T^3 + 3.4680 x 10^{-9} T^4 - 1.8075 x 10^{-12} T^5.

E = 30.1291 - 0.1864 T t 1.5033 x 10^{-3} T^2 - 4.8683 x 10^{-6} T^3 t 6.7998 x 10^{-9} T^4 - 3.4484 x 10^{-12} T^5.

V-3Ti-0.99Si:

YS = 428.7190 - 0.2835 T - 5.1251 x 10^{-3} T^2 t 2.3242 x 10^{-5} T^3 - 3.5433 x 10^{-8} T^4 + 1.8278 x 10^{-11} T^5.

UTS = 513.4361 - 1.2006 T t 2.5549 x 10^{-3} T^2 + 4.3093 x 10^{-6} T^3 - 1.5163 x 10^{-8} T^4 t 9.9096 x 10^{-12} T^5.

E = 23.9030 + 0.0253 T + 1.9155 x 10^{-4} T^2 - 3.1484 x 10^{-6} T^3 + 1.1512 x 10^{-8} T^4 - 1.6484 x 10^{-11} T^5 t 8.2217 x 10^{-15} T^6.

E = 30.8089 + 0.1117 T -1.1126 x 10^{-3} T^2 + 3.6624 x 10^{-6} T^3 - 5.0042 x 10^{-9} T^4 t 2.3985 x 10^{-12} T^5.

Vanstar-7:

YS = 452.7675 - 1.3682 T t 2.9941 x 10^{-3} T^2 - 2.2686 x 10^{-6} T^3 t 1.5111 x 10^{-10} T^4.

UTS = 603.5484 - 1.2726 T t 2.5941 x 10^{-3} T^2 t 3.0798 x 10^{-6} T^3 - 1.2964 x 10^{-8} T^4 t 8.4617 x 10^{-12} T^5.

E_U = 24.5940 t 0.1000 T - 1.0758 x 10^{-3} T^2 t 3.8668 x 10^{-6} T^3 - 5.5711 x 10^{-9} T^4 t 2.7662 x 10^{-12} T^5.

E_T = 37.5226 t 0.0109 T - 5.4647 x 10^{-4} T^2 t 2.2930 x 10^{-6} T^3 - 3.4305 x 10^{-9} T^4 t 1.7492 x 10^{-12} T^5.

V-Ti Alloys:

YS (0-20% Ti, 420-600°C) = 145 t 15.9 (C_{Ti}).

UTS (1-20% Ti, 420-600°C) = 331 + 18.5 (C_{Ti}).

E (0-20% Ti, 600°C) = 23.6 $(C_{Ti})^{-0.062}$.

E (0-20% TI, 600°C) = 36.5 $(C_{Ti})^{-0.175}$.

V-Cr-5Ti Alloys:

YS (0-15% Cr, 420-700°C) = 204 + 10.3 (C_{Cr}).

UTS (0-15% Cr, 420-700°C) = 365 t 13.3 (C_{Cr}).

E (0-16% Cr, 600°C) = 25.6 - 3.37 (C_{Cr}) t 0.5770 $(C_{Cr})^2$ - 0.0236 $(C_{Cr})^3$.

E (0-16% Cr, 600°C) = 19.3 - 2.59 (C_{Cr}) t 0.4985 $(C_{Cr})^2$ - 0.0215 $(C_{Cr})^3$.

V-3Ti-Si Alloys:

YS (0-1.3% Si, 420-700°C) = 295 $(C_{Si})^{0.16}$.

UTS (0-1.3% Si, 420-700°C) = 468 $(C_{Si})^{0.86}$.

E (0-1.3% Si, 600°C) = 21.4 t 17.7 (C_{Si}) - 114.6 $(C_{Si})^2$ + 169.6 $(C_{Si})^3$ -73.0 $(C_{Si})^4$.

E (0-1.3% Si, 600°C) = 28.1 - 30.1 (C_{Si}) - 48.6 $(C_{Si})^2$ - 21.4 $(C_{Si})^3$.

REVISED CALCULATIONS FOR THE DYNAMIC HELIUM CHARGING EXPERIMENT IN FFTF/MOTA 28 - L. R. Greenwood, Pacific Northwest Laboratory[a]

OBJECTIVE

To simulate fusion reactor-like helium-to-displacement damage ratios in vanadium-based alloys irradiated in FFTF.

SUMMARY

Calculations of the initial tritium loading, lithium isotopic ratio, and helium pressure have been revised for the planned dynamic helium charging experiment (DHCE) in FFTF/MOTA-2B based on current neutronic information regarding the neutron flux spectrum.

PROGRESS AND STATUS

The basic idea of the DHCE experiment, as published previously,[1] is to simulate fusion reactor-like helium-to-displacement damage production rates in vanadium-based alloys irradiated in the Fast Flux Test Facility - Materials Open Test Assembly (FFTF/MOTA). Vanadium alloys in the form of tensile specimens and transmission electron microscope (TEM) disks are immersed in liquid lithium and encapsulated in TZM (Ti-Zr-Mo alloy) tubing. Under irradiation, tritium is generated in the lithium from the $^{6}Li(n,a)t$ reaction and diffuses into the vanadium. The tritium then decays to ^{3}He. In order that helium generation start immediately after reactor startup, the capsules are given an initial tritium loading. Calculations are then required to attempt to maintain a nearly constant rate of tritium in the vanadium alloys. This rate is dictated by the fusion reactor condition of about 5-to-1 for helium-to-dpa (displacement per atom) production in vanadium alloys.

Originally. calculations were performed by the author at Argonne National Laboratory. Since that time, new information has become available regarding the reactor fluxes and energy spectra as well as tritium leakage rates, and it was decided that new calculations were required to ensure proper operation of the experiment.

The calculations must provide a delicate balance between several competing factors. Tritium is lost from the capsule by decay and leakage. Tritium is produced by reactions on lithium. ^{6}Li is also burned up during the course of the experiment and the final complication is that ^{3}He has a high burnup cross section for conversion back to tritium. All of these factors must be considered over the reactor power history, which was assumed to be 100 days of operation at 291 MW followed by a 40-day outage. After the calculations were completed, a decision was made to change the schedule to 50 days of operation rather than 100. Since the net up and down time will be about the same, there should be only a minor effect on the overall helium production.

The MOTA-2B experiment is planned to operate for 300 fuli-power days (about 1 year) at a power level of 291 MW. The initial parameters were based on neutronics calculations performed by R. Simons and L. Carter.[2] The calculated neutron energy spectra were then used to calculate reaction rates and damage parameters, as listed in Table 1. A computer program was used to solve the simultaneous differential equations for these reactions.

There are several additional constraints on the calculations. Since we do not have precise knowledge of the equilibrium ratio of tritium between the vanadium and liquid lithium, calculations were performed for several different assumed weight ratios (k_w) between the values of 0.01 and 0.10. The operating temperatures of the capsules are 425, 500, and 600°C and the tritium leakage is 5.38E-10, 4.52E-9, and 4.37E-8 atoms/second, respectively, as calculated by H. Matsui.[3] Due to handling considerations in the preparation of the initial tritium loading at Argonne National Laboratory, an upper limit of 100 Ci was set on this value. As tritium is generated in the lithium, an equal amount of ^{4}He is generated. This helium, as well as some ^{3}He from tritium decay, is expected to come out of solution and collect in the capsule plenum, which was designed to be about one-half the capsule volume. This pressure can be considerable over the course of the experiment, and, based on stress calculations, it was decided to limit the pressure to 20 atm.

The results of the revised calculations are listed in Table 2. The subcapsule ID values refer to the level in the FFTF/MOTA. The design temperatures are followed by the assumed tritium weight distributions. The optimal initial tritium loading is then given in millimoles and curies followed by the recommended ^{6}Li isotopic content. The final column lists the final calculated helium pressure.

(a) Pacific Northwest Laboratory is operated for the U.S. Department of Energy by Battelle Memorial Institute under Contract DE-AC06-76RLO 1830.

Table 1. Reaction Rates and Neutron Fluxes (Rates are atom/atom-second) (dpa and helium values are for V-15Cr-5Ti)

Parameter		Level 5
$^{6}Li(n,a)t$ (xE-9)	3.98	2.65
$^{7}Li(n,n't)$(xE-12)	7.89	3.51
$^{3}He(n,p)t$ (xE-8)	1.31	0.964
dpa in V (xE-6)	1.32	0.719
He (appm)(xE-8)	2.99	1.53
Flux > 0.1 MeV (xE+15 n/cm2-2)	3.64	2.08

Table 2. Calculated Parameters for the DHCE

Subcapsule Identification	Temperature, °C	Initial K_w	Tritium, mmol	Tritium, Ci	^{6}Li, %	He Pressure, atm
4D-1	425	0.02	1.69	99	5.0	14.0
40-2	425	0.03	1.21	70	4.5	12.0
5E-1	425	0.10	0.32	18	1.0	2.3
5E-2	425	0.10	0.32	18	1.0	2.3
5D-1	500	0.01	1.69	99	6.5	14.0
5D-2	500	0.10	0.35	20	1.0	2.6
5C-1	600	0.03	0.97	56	8.0	16.0
5C-2	600	0.10	0.36	21	8.0	15.0

K_w = equilibrium ratio by weight of tritium in vanadium alloy to that in the surrounding lithium
mmol = 10^{-3} mol = 58.3 Ci of tritium (T_2)
^{6}Li = atomic ratio of 6Li atoms/total lithium atoms in %.

The detailed results of the calculations are illustrated in Figure 1, which shows helium production versus dpa in the alloy V-15Cr-5Ti, taken as a typical alloy. The straight solid line is the desired fusion reactor ratio of 5:1 helium(appm):dpa. The calculations are shown as points. As can be seen, the calculated ratios snake around the desired fusion line. The total time is about 300 days, which corresponds to about 30 dpa in level 4 of the MOTA. The steep rise at 10 dpa corresponds to the scheduled reactor down time of about 40 days. During down times, tritium decays to ^{3}He without any displacement damage, thus accounting for the steep vertical rise in helium.

These calculations have been used to guide the final loading of the DHCE capsules, which is currently in progress at Hanford.

FUTURE WORK

The DHCE capsules will be inserted into FFTF for irradiation during May 1991. The experiment should then continue for about one year. Other work in progress includes the preparation of dosimetry capsules for FFTF as well as for various experiments in the High Flux Isotopes Reactor at Oak Ridge National Laboratory.

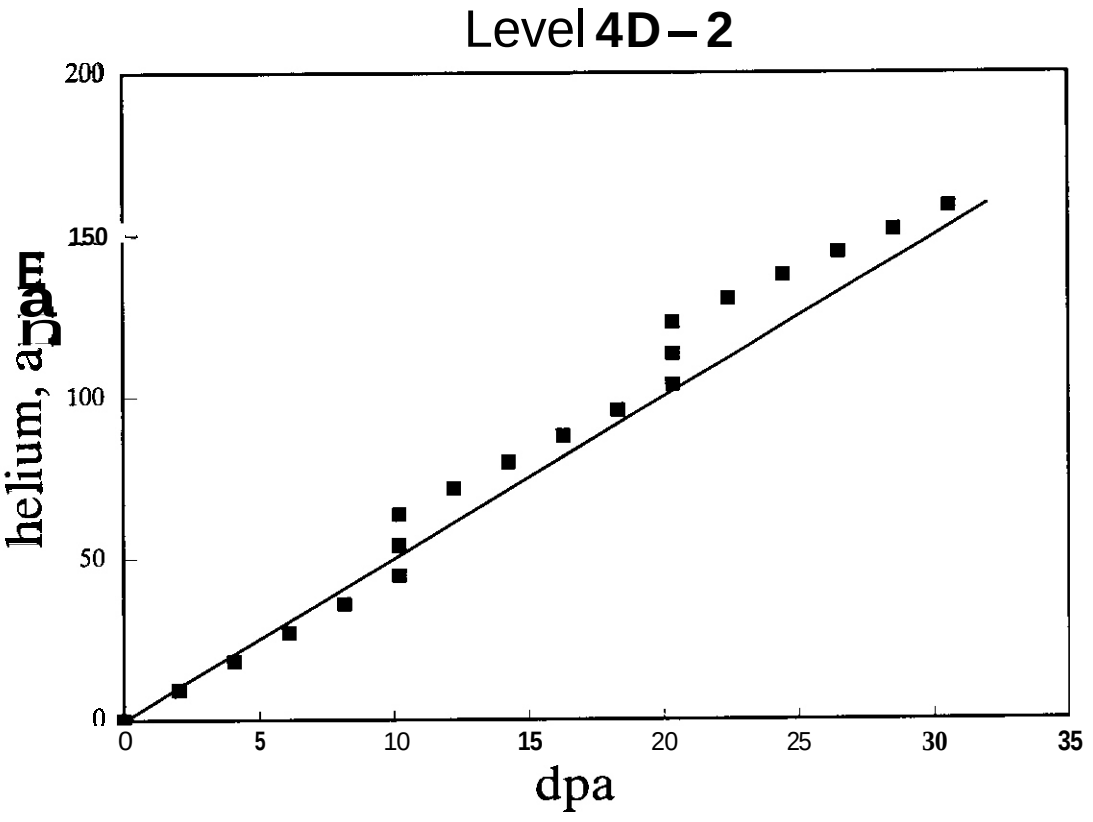


Figure 1. Results of calculations are illustrated for a DHCE capsule located in level 4D-2 of the FFTF/MOTA-2B assembly. The solid line represents the desired fusion ratio of 5:1 helium:dpa for the alloy V-15Cr-5Ti. The solid squares are calculated values using the data in Table 2. The vertical rises at 10 and 20 dpa occur when the reactor is down for maintenance and tritium decays to helium without any displacement damage.

REFERENCES

1. D. L. Smith, H. Matsui, L. R. Greenwood, and B. Loomis, Experimental Method for Investigating Helium Effects in Irradiated Vanadium, J. Nucl. Mater. 155-157, 1359-1363 (1988).

2. R. Simons and L. Carter, Westinghouse Hanford Company, private communication 1991.

3. H. Matsui, Tohoku University, private communication 1991.

STATUS OF THE DYNAMIC HELIUM CHARGING EXPERIMENT (DHCE) IN FFTF/MOTA - D. L. Smith and B. A. Loomis (Argonne National Laboratory), H. Matsui (Tohoku University), M. L. Hamilton (Pacific Northwest Laboratory), K. L. Pearce (Westinghouse Hanford Company), J. P. Kopasz and C. E. Johnson (Argonne National Laboratory), R. G. Clemmer and L. R. Greenwood (Pacific Northwest Laboratory)

OBJECTIVE

The objective of this experiment is to provide baseline irradiation data on the effects of concurrent helium production and neutron irradiation on the physical and mechanical properties of vanadium alloys. Effects of the irradiation on the alloy microstructures will also be characterized. This report documents the preparation of the experiment for irradiation.

SUMMARY

Preparation of the DHCE experiment has been completed and it has been inserted into MOTA 2B for irradiation in FFTF. The experiment will produce helium in test specimens of vanadium alloys to simulate a fusion environment.

PROGRESS AND STATUS

Introduction

The DHCE experiment[1] is designed to enhance helium production in specimens of vanadium alloys during irradiation in the FFTF/MOTA to simulate the simultaneous gas production and irradiation damage (dpa) that would be anticipated in a fusion device. In the FFTF reactor, helium is normally produced in vanadium at a very low rate, about 0.02 appm/dpa, solely by fast neutron (n,α) reactions. The ratio of helium production to dpa level in fusion reactors, however, is about 5-to-1 due to the presence of 14 MeV neutrons. Since helium will cause swelling and may influence the evolution of the microstructure, fusion simulations of helium production are needed to determine the importance of these effects. In the DHCE experiment, helium will be produced by the decay of tritium, which will be dissolved uniformly in the specimens during the irradiation. A detailed description of the technique is presented in reference 1 and nuclear parameters and calculations are presented elsewhere in this semiannual report.[1]

Experimental Procedure

Both microscopy and mechanical test specimens were encapsulated in eight TZM subcapsules along with isotopically adjusted lithium and an initial tritium source referred to as the "mother alloy." The mother alloy is a strip of pure vanadium that was doped with tritium to provide the initial tritium in the capsules. The initial tritium loading was designed to produce fusion-like helium-to-dpa ratios as soon as the irradiation starts. The lithium was enriched in ^6Li to produce sufficient tritium during irradiation to compensate for the losses due to decay and permeation through the capsule. The lithium also serves as a heat conductor and an oxygen getter. The helium generation rate is controlled by adjusting the tritium concentration in the mother alloy and the $^6Li/^7Li$ ratio. The tritium present in the lithium is expected to be in equilibrium with the tritium in the specimens due to the high diffusivity of tritium. Since the equilibrium ratio k_s of tritium in the vanadium to that in the liquid lithium is not well defined, a range of values were assumed that span the available experimental data. Details of the calculations are presented elsewhere.[2]

The mother alloy in each capsule was a coiled vanadium foil nominally measuring 2.5 cm X 3.8 cm x 0.025 cm. It was pretreated to allow easier absorption of the tritium. The pretreatment comprised evacuation at room temperature followed by heating to 900°C under vacuum and several hydrogen soak-evacuation cycles. The hydrogen soaks were performed at 400 - 500°C and the evacuations were performed at 800°C. Hydrogen absorption became increasingly more successful with repeated soaking due to the reduction of surface oxides and the removal of impurities trapped in the alloy during the high temperature evacuations.

Analysis of the tritium obtained from the supplier indicated that it was contaminated with high levels of helium as well as various carbon- and oxygen-containing compounds. While helium is not absorbed by the mother alloy, it effectively blankets the sample to be tritiated in a static apparatus, slowing the kinetics of the tritium absorption to virtually zero. The gas handling apparatus was modified to include a uranium bed to remove impurities other than helium, which was pumped away. The impurities were retained in the bed when it was heated while the tritium and hydrogen were desorbed. While this method removed most of the impurities in the tritium, it did not eliminate the H_2

The purified tritium was loaded into the pretreated mother alloy as follows: The mother alloy was heated to 900°C under vacuum to remove the hydrogen absorbed during the pretreatment. It was then evacuated for a minimum of 12 hours at this temperature and then quenched to room temperature. Tritium was desorbed from

the uranium bed into a calibrated volume to produce the desired tritium pressure and then expanded into the quartz sample tube containing the mother alloy. The mother alloy was then heated to 500°C and the pressure dropped as the tritium was absorbed. The sample was cooled slowly to 300°C, where the solubility of tritium in vanadium is higher, and the pressure was allowed to drop until the desired amount of tritium was absorbed. The valve to the quartz tube was then closed and the mother alloy cooled to room temperature. After it reached room temperature, the valve to the quartz tube was opened and the final pressure was recorded so the actual amount of tritium absorbed could be calculated. The residual gas was expanded into a vial for analysis to determine the hydrogen-to-tritium ratio. After the vial was closed, any residual tritium was adsorbed onto the uranium bed.

After the bottom end cap was EB welded onto one end of the capsules, the mother alloy was loaded into the capsules. TEM disks were dropped in on top of the mother alloy, and the remainder of the specimens were added alternating with balls of lithium. The loading was performed in a glove box inerted with argon. The capsules were maintained in an argon atmosphere until the final E8 closure weld was performed. External tritium contamination was removed using demineralized water and ethyl alcohol. The capsules were leak checked to verify that there would be no unintentional tritium release and the required nondestructive testing was performed (visual inspection, dye penetrant inspection, helium leak check, and xray radiography) to verify that the welds were satisfactory.

Results

The nominal matrix for loading the mother alloy and the lithium into the capsules is given in Table 1. Tables 2 and 3 provide a summary listing of the number and types of microscopy and mechanical test specimens loaded into the capsules. Significant difficulties were encountered during the capsule fabrication effort. Unexpected and substantial modification of the capsule welding procedures were required on short notice to avoid severe tritium contamination. As a result, only seven of the eight capsules were completed successfully. Adjustments in the matrix were therefore made to compensate for the loss of one capsule. The final matrix that was actually loaded into MOTA 2B is given in Table 4. A photograph of the completed capsules is shown in Figure 1.

Table 1. Nominal Mother Alloy and Lithium Loading in DHCE

Subcapsule ID Code	Nominal Irradiation Temp. (°C)	Initial Tritium Levels (mmol)[b]	Initial Tritium Levels (Ci)	Foil Weight (g)	^{6}Li[a] (%)	k_w[c]
401	425	**1.69**	**99**	**1.5468**	5.0	0.02
402	425	**1.21**	**70**	1.5536	**4.5**	**0.03**
5C1	425	**0.97**	**57**	**1.5651**	**8.0**	0.03
5C2	425	0.42	26	1.5657	7.5	0.10
5D1	500	**1.69**	73.5	1.5727	**6.5**	**0.01**
5D2	500	0.36	18.5	**1.5544**	2.0	**0.10**
5E1	600	0.36	16.4	**1.5656**	**1.5**	0.10
5E2	**600**	0.36	**18**	**1.5466**	**1.5**	*0.10*

(a) Atomic ratio of ^{6}Li atoms/total lithium atoms (^{6}Li + ^{7}Li) in. %.
(b) Unit: mmol (10^{-3} mol); 1 mmol = 58.3 Ci of tritium (T_2).
(c) Equilibrium ratio by weight of tritium in vanadium alloy to that in the surrounding liquid lithium.

Table 2. DHCE Specimen Description

Code	Specimen Type	Dimensions (mm)
Japanese Specimens		
A	Tensile (S)	16 x 4 x 0.25
8	TEM disk	3 (dia.) x 0.25
U.S. Specimens		
C	Tensile (SS3)	25.4 x 4.95 x 0.76
D	TEM disk	3.05 (dia.) x 0.25

Table 3. DHCE Specimen loading

Alloys	Specimen Type[a]	Specimen Quantity[b]	Nominal Irradiation Temperature (°C)
Japanese specimens[c]			
Pure Vanadium	A,B		425
V-1at.%Si	A,B	6,27	425
V-5at.%Ti	A,B	4,27	425
V-5at.%Cr	A,B	6,27	425
V-5at.%Fe	A,B	6.27	425
V-5at.%Nb	A,B	6,27	425
V-5at.%Mo	A,B	6,27	425
V-3Ti-1Si	A,B	4,27	425
V-5Cr-5Ti	A,B	18,18	425
V-15Cr-25Ti	B	12	425
Pure Vanadium	A,B	4,24	500,600
V-1at.%Si	A,B	4,18	500,600
V-5at.%Ti	A,B	8,18	500,600
V-5at.%Cr	A,B	4,18	500,600
V-5at.%Fe	A,B	4,18	500,600
V-5at.%Nb	A,B	4,18	500,600
V-5at.%Mo	A,B	4,18	500,600
V-3Ti-1Si	A,B	4,18	500,600
V-5Cr-5Ti	A,B	12,12	500,600
V-15Cr-25Ti	B	8	500,600
V-100 appm B	B	9,6,6	425,500,600
V-500 appm B	B	9,6,6	425,500,600
V-2500 appm B	B	9,5,6	425,500,600
Ti-6Al-4V	B	4,2	425,600
V-1Fe	B	2	500,600
V-3Fe	B	2	500,600
V-8Fe	B	2	500,600
V-5Fe-15Si	B	2	500,600
Ti-6Al-2Sn-4Zr-2Mo	B	2	425,600
Ti-8Al-1V-1Mo	B	2	425,600
U.S. Specimens[d]			
Pure Vanadium	D	2	425,500,600
V-5Ti	C,D	2,5	425,500,600
V-3Ti-1Si	C,D	1,5	425,500,600
V-20Ti	D	4	425,500,600
V-5Cr-5Ti	C,D	2,5	425,500,600
V-5Ti-7Cr	C,D	1,5	425,500,600
V-15Cr-5Ti	D	3	425,500,600
V-10Cr-5Ti	C,D	1,4	425,500,600
V-5Cr-5Ti	C,D	2,5	425,500,600
V-3Ti-0.1C	D	2	425,500,600
V-10Ti	C,D	1,4	425,500,600
V-3Ti-0.2Zr-0.1C	D	3,2,3	425,500,600

(a) See Table 2.
(b) Does not include specimens from cracked subcapsule (5D2).
(c) Identical heat treatment for all Japanese samples: vacuum annealed at 1100°C for 2 hours
(d) Identical heat treatment for all U.S. samples: vacuum annealed at 1125°C for 1 hour.

FUTURE WORK

This segment of the experiment will be referred to as DHCE-I. It will be irradiated during the entirety of MOTA 2B. It will be disassembled after MOTA 2B is discharged and the microscopy and mechanical test specimens contained in the capsules will be examined. Lessons learned in the fabrication of DHCE-I will be incorporated into the planning and fabrication of DHCE-II, which will be loaded into MOTA 2C on an as-yet-to-be defined schedule, pending continued FFTF operation.

Table 4. Final DHCE Test Matrix

Subcapsule Identification	Irradiation Temperature (°C)	k_w (c)	Initial Tritium mmol(d)	Initial Tritium Ci	^6Li(a) Fraction (%)	Total Number of Specimens(b) Japan TS (S)	Japan D3	U.S. SS3	U.S. TEM	Total Specimen Mass (g)(e)
4D1	425	0.02	1.69	99	5.0	24	94	8	45	5.86
4D2	425	0.03	1.20	70	4.5	16	96	8	44	5.38
5E2	425	0.10	0.45(f)	26	1.0	16	100	8	42	5.38
5D1	500	0.01	1.26	73.5	6.5	23	94	8	42	5.77
5E1	500	0.10	0.98	51	1.0	24	102	8	43	5.82
5C1	600	0.03	0.28	16.4	8.0	24	93	8	45	5.82
5c2	600	0.10	0.31	18	8.0	24	108	8	45	5.95
5D2	(g)	0.10	0.32	18.5	1.0	24	108	8	42	5.96

(a) Atomic ratio of ^6Li atoms/total lithium atoms (^6Li + ^7Li) in. %
(b) See Table 2.
(c) Equilibrium ratio by weight of tritium in vanadium alloy to that in the surrounding liquid lithium.
(d) Unit: mmol (10^{-3} mol); 1 mmol = 58.3 Ci of tritium (T_2).
(e) Does not include mother alloy.
(f) Hydrogen is added.
(g) Subcapsule not loaded into MOTA 2B due to cracked tube.

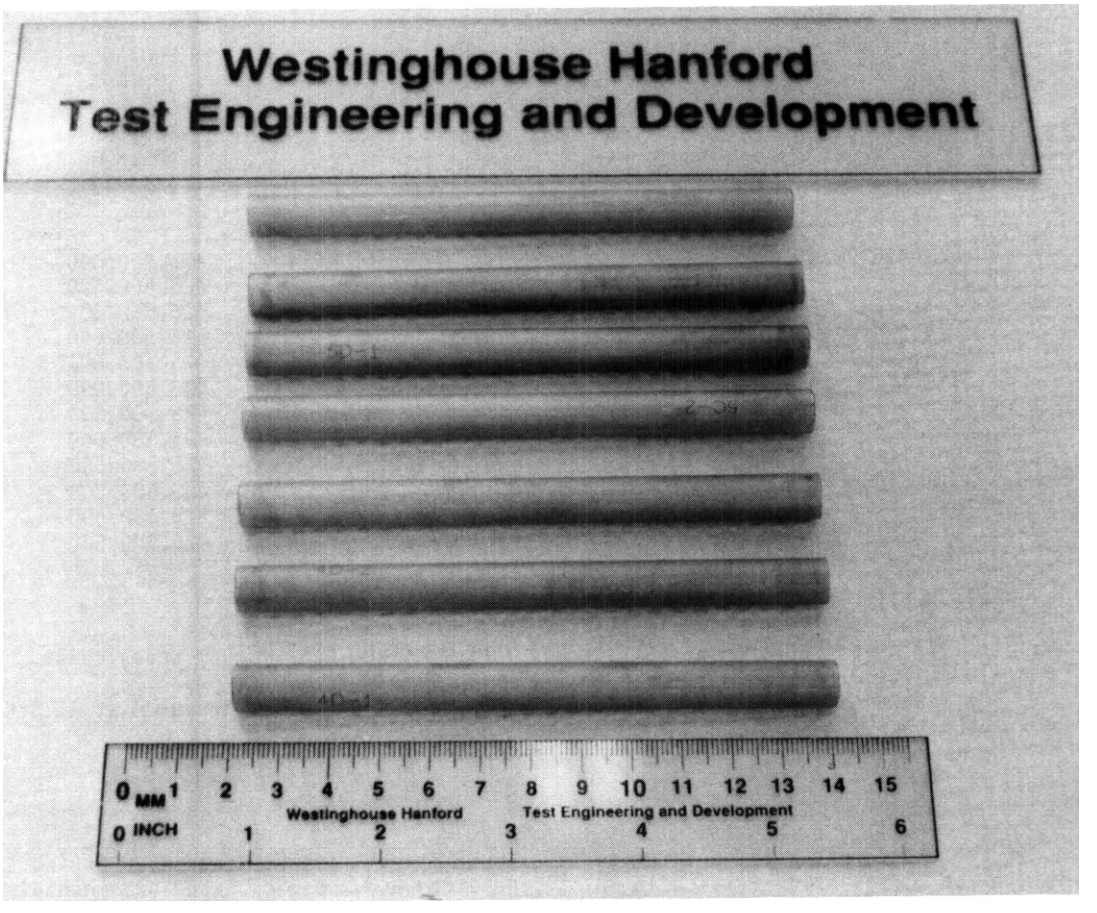


Figure 1. Seven capsules fabricated for irradiation in DHCE.

REFERENCES

1. D. L. Smith, H. Matsui, L. R. Greenwood, and B. Loomis, Experimental Method for Investigating Helium Effects in Irradiated Vanadium, J. Nucl. Mater. 155-157, pp. 1359-1363 (1988).

2. L. R. Greenwood, Revised Calculations for the Dynamic Helium Charging Experiment in FFTF/MOTA 2B, this report.

6.4 Copper Alloys

MICROSTRUCTURAL EXAMINATION OF PURE COPPER AND CU-5NI IRRADIATED WITH FISSION OR SPALLATION NEUTRONS - D. S. Gelles, Pacific Northwest Laboratory,[a] B. N. Singh and A. Horsewell, RISØ National Laboratory, Denmark, W. F. Sommer, Los Alamos National Laboratory, and F. A. Garner, Pacific Northwest Laboratory

OBJECTIVE

The object of this effort is to quantify the effect of neutron energy spectrum on damage microstructure in Cu and Cu-alloys irradiated in different neutron irradiation facilities in order to determine the suitability of copper alloys for high heat flux substructure applications.

SUMMARY

Specimens of pure copper and a copper alloy containing 5 atomic percent nickel have been examined by transmission electron microscopy following irradiation by neutrons in a mixed thermal reactor, a fast reactor and a spallation neutron source. Radiation damage microstructures have been investigated in order to identify microstructural differences and to determine suitability of copper alloys for high heat flux substructure applications in a fusion device. Most conditions developed void swelling, and all were found to contain defect clusters on a fine scale. Damage accumulation in Cu-5Ni was found to be significantly different from that observed in pure copper. Based on limited comparisons of irradiation at 335°C, high energy spallation neutrons do not appear to have any significant effect on swelling at low dose.

The results of this study confirm the need for improved temperature control of irradiation experiments in order to correlate radiation damage to fusion conditions.

PROGRESS AND STATUS

Introduction

Copper alloys will be required for high heat flux components in Tokamak Fusion Reactors. The International Thermonuclear Experimental Reactor (ITER) and Next European Torus (NET) design teams have specified a copper alloy containing Al_2O_3 dispersoid as a candidate material for high heat flux applications based on recent fast neutron irradiation experiments that show it to develop very low swelling. Pure copper will be used to mate the plasma facing tiles to the dispersion-hardened alloy. A major transmutation product of copper is nickel such that after five years in a fusion environment, pure copper will have transmuted to an alloy containing 5% Ni,[1] and therefore, studies on a Cu-5Ni alloy give some indication of the behavior in irradiated comer followins transmutation. The present effort is intended to facilitate Dredictions of irradiation response by examining a series of simple copper alloys following irradiation in three neutron irradiation facilities with very different spectra.

A large body of work exists on the effects of radiation damage on microstructure in pure copper and dilute Cu-Ni alloys. This is based on a range of radiation sources. It includes 14 MeV neutrons to low dose, but the results cannot be used to accurately predict behavior at high dose under fusion conditions. High Voltage Electron Irradiation (HVEM) studies, using 1 MeV electrons, have been performed on pure copper in order to examine dislocation climb; and swelling response,[3] and also on Cu-Ni alloys in order to examine dislocation climb[2,4-6] and swelling. More recently, dynamic defect cluster development in pure copper has been studied under dual irradiation with electrons and Xe ions.[7] Ion irradiation studies have included examination of defect clusters in pure copper at low temperature using self ions,[8] at room temperature under Ni and C ion irradiation,[10] He ion irradiation,[11] and Ne ion irradiation,[12] and void development in Cu-Ni alloys under heavy ion bombardment.[13] Neutron irradiation experiments in mixed spectrum reactors included examination of dislocations,[14] voids[14-18] and defect clusters[17-20] in pure copy and void development[21] in Cu-Ni alloys. Fast reactor neutron irradiation studies involved dislocation[22] and void[21-25] development in pure copper and swelling in Cu-Ni alloys[26,27] to doses as high as 100 dpa. 14 MeV neutron irradiation experiments have included examination of defect clusters in pure copper[20,29-36] and Cu-Ni alloys.[29,34] Defect clusters in pure copper have also been examined following high energy proton irradiation.[37]

ExDerimental Procedures

Specimens of pure copper were made from 0.25 mm thick sheet stock of 99.999% pure zone refined MARZ copper from Materials Research Corporation (lot 29/1-593-37, major impurities: <10ppm C, 4.5ppm Zn, 2ppm O, 1ppm Al, remainder <1 ppm) and were annealed at 450°C for 30 min in an argon environment and air cooled. The copper alloy contained 5 atomic percent nickel. It was originally prepared for irradiation in RTNS-II in the form of 70 g arc melted buttons made from pure starting materials from McKay Industries. The starting

---

(a) Pacific Northwest Laboratory is operated for the U.S. Department of Energy by Battelle Memorial Institute under Contract DE-AC06-76RLO 1830.

copper was 99.9975% purity with 4.5 ppm. oxygen and the nickel was of similar purity. Buttons were cold rolled to 0.25 mm sheet, and were annealed at 900°C for 15 minutes. Prior to annealing, specimens were punched from sheet, and were engraved with unique identification codes, RO for Marz copper and VP for Cu-5Ni. Identical specimens were neutron irradiated in the Los Alamos Meson Physics Facility (LAMPF), located at Los Alamos National Laboratory, Los Alamos, NM, and in the Fast Flux Test Facility (FFTF), located in Richland, WA. Specimens of 99.999% pure zone refined MARZ copper annealed at 550°C for 2 h were also irradiated in the Danish Reactor 3 (DR-3), located at RISØ National Laboratory, Roskilde. Denmark. The DR-3 provides a typical mixed thermal reactor neutron spectrum with a thermal to fast ratio of ~3:1; FFTF has a fast neutron spectrum, with mean neutron energy of ~0.5 MeV; and the Los Alamos Spallation Radiation Effects Facility (LASREF) at LAMPF, a spallation neutron source, produces neutron energies that peak at ~1 MeV but possess small numbers of neutrons with energies as high as 800 MeV. Flux comparisons are $2x10^{13}$ $cm^{-2}s^{-1}$ (E > 1KeV) for LASREF, $3x10^{13}$ $cm^{-2}s^{-1}$ (E > 1MeV) for OR-3, and $1x10^{15}$ $cm^{-2}s^{-1}$ (E > 0.1MeV) for FFTF. The OR-3 irradiations were designed to run at 250 and 400°C to doses of 0.5 dpa, LAMPF at 330 and 400°C to doses on the order of 0.25 dpa, and FFTF at 420 and 520°C to doses of 30 dpa. Irradiations in LASREF and FFTF were monitored by thermocouple, but during irradiation of the #2 capsule in LASREF, the heater failed, so that 39% of the irradiation was at 400°C ± 10°C and the remainder was at 220°C ± 30°C,[37] whereas during irradiation of the #7 capsule in LASREF the temperature was maintained at 335°C ± 10°C throughout the whole experiment. For the FFTF irradiations, specimens were in helium filled sealed capsules designated LO and ME and were irradiated in the Materials Open Test Assembly (MOTA) 1D in baskets 2-CI and 2-A4 during cycles 7 and 8 at operating temperatures of 414 and 529°C ±5 respectively, including a correction of 8°C for gamma heating while the reactor operated at full power.[38] Irradiation temperatures could not be monitored in OR-3, but temperature monitors of Pb-Au, Ag-Pb, Al-Zn and Au-Ge alloys and pure Sn and Zn were located adjacent to the specimens, and visual examination of those monitors following irradiation indicated that temperatures had exceeded design temperatures at some time during the irradiation history, so that the 250°C irradiation might have reached about 300°C for a short time, and 400°C irradiations might have exceeded 420°C for at least a short time, In both LASREF and DR-3 at the completion of the irradiation cycle, the neutron flux is reduced rapidly and the specimen temperature then drops. However, for FFTF/MOTA, it normally takes about 20 h for the specimen canisters to cool from operating temperature to the minimum in-core temperature, 225°C, and the temperature is controlled by gama heating so that as power is reduced, so is temperature. Cool down and reduction of power are approximately linear with time. Furthermore, FFTF/MOTA operation during cycles 7 and 8 was not ideal. During cycle 7, a temperature transient occurred for specimens irradiated at 529°C, so that the specimens experienced an overtemperature of 201°C lasting ~50 m when the dose was ~15 dpa. Specimens irradiated at 414°C were not affected by a temperature transient. As result of the transient in cycle 7, it was decided to proceed with various reactor tests during cycle 8 which would not significantly change the accumulated dose, including Inherent Safety Testing, Transient Testing During Shutdown, Steady State Natural Circulation Testing, and finally Loss of Flow without Scram Testing at the end of cycle 8. At the end of cycle 8 during the Loss of Flow without Scram Testing, both the 414 and 529°C conditions were held at approximately 310°C at reduced power for 21 days. At intervals lasting about two days, power was increased for one day causing specimens in canister 2C to reach approximately 340°C and specimens in canister 2A to reach approximately 390°C. Finally, the power was reduced following normal procedures and the specimens cooled to about 225°C prior to removal from reactor. Dose in dpa for DR-3 is based on the conversion by Muncie of 1 dpa per $5x10^{20}$ n/cm^2, E > 1 MeV.[39] Doses given for LASREF are only estimates; dosimetry measurements are continuing and only a minor adjustment is expected.

The specimens selected for examination are listed in Table 1. Table 1 also includes a summary of irradiation histories and results of density change measurements for specimens irradiated in FFTF.[27] Specimens were reduced in thickness by hand grinding to approximately 0.1 mm and then electropolished in a solution of 25% H_3PO_4, 25% ethylene glycol and 50% water at 11 V for about 15 s. Examinations were performed on a JEOL 2000FX at RISØ National Laboratory using either transmission or scanning modes, and compositional analysis was performed with a Tracor 5500 analyzer system.

Results

Microstructural examinations demonstrated that neutron irradiation produced coarse dislocation evolution and cavity formation for most irradiation conditions. However, most unexpectedly, defect clusters including stacking fault tetrahedra and triangular faulted loops with sizes as small as 1 nm diameter was found in all conditions examined. The microstructural observations will first be described, a summary of quantitative void and dislocation measurements will be given and then the defect cluster structure will be quantitatively described. Finally, quantitative measurements of bubbles on grain boundaries will be given.

Microstructural observations

The preirradiation microstructures of both the pure copper and Cu-5Ni specimen conditions, based on examination of FFTF control specimens, were found to contain moderate dislocation densities, consisting of dislocation tangles tending to form cell walls. Cells were on the order of 2 μm in diameter, often dislocation free within the cells. Also, weak beam dark field imaging revealed images characteristic of defect clusters. Examples of the dislocation structure and defect clusters in preirradiation microstructures are given in Figure 1. Figures 1a and c show the dislocation structures at low magnification for pure copper and Cu-5Ni respectively, and Figures 1b and d show defect clusters in weak beam dark imaging conditions at

Table 1. Specimen Conditions Examined by Transmission Electron Microscopy

Code	Material Condition	Irradiation Conditions Source	Design Temp.	Actual Conditions	Swelling due to Density Change[27]
RO	Marz copper	control			
VP	Cu-5Ni	control			
ROW7	Marz Copper	LAMPF	335%	3352, -0.25 dpa	
1 #7	Cu-5Ni				
RO#2	Marz Copper	LAMPF	400°C	400/220°C, -0.25 dpa	
1 #2	Cu-5Ni				
14	Marz Copper	DR-3	250°C	to 300°C, 1.69×10^{20} n/cm^2, E>1 MeV (0.34 dpa)	
18	Marz Copper	DR-3	400°C	to 420°C, 1.72×10^{20} n/cm^2, E>1 MeV (0.34 dpa)	
15	Marz Copper	DR-3	400°C	to 420°C, 3.86×10^{20} n/cm^2, E>1 MeV (0.77 dpa)	
ROLO	Marz Copper	FFTF	400°C	414°C, 34.1 dpa (5.5×10^{22} n/cm^2, E>0.1 MeV)	14.6, 15.5[a]
VPLO	Cu-5Ni	FFTF	400°C	414°C, 34.1 dpa "	22.0, 23.8[a]
ROME	Marz Copper	FFTF	520°C	529°C, 31.6 dpa (5.1×10^{22} n/cm^2, E>0.1 MeV)	1.76
VPME	Cu-5Ni	FFTF	520°C	529°C, 31.6 dpa "	0.56

(a) Measurements on two different specimens gave different results.

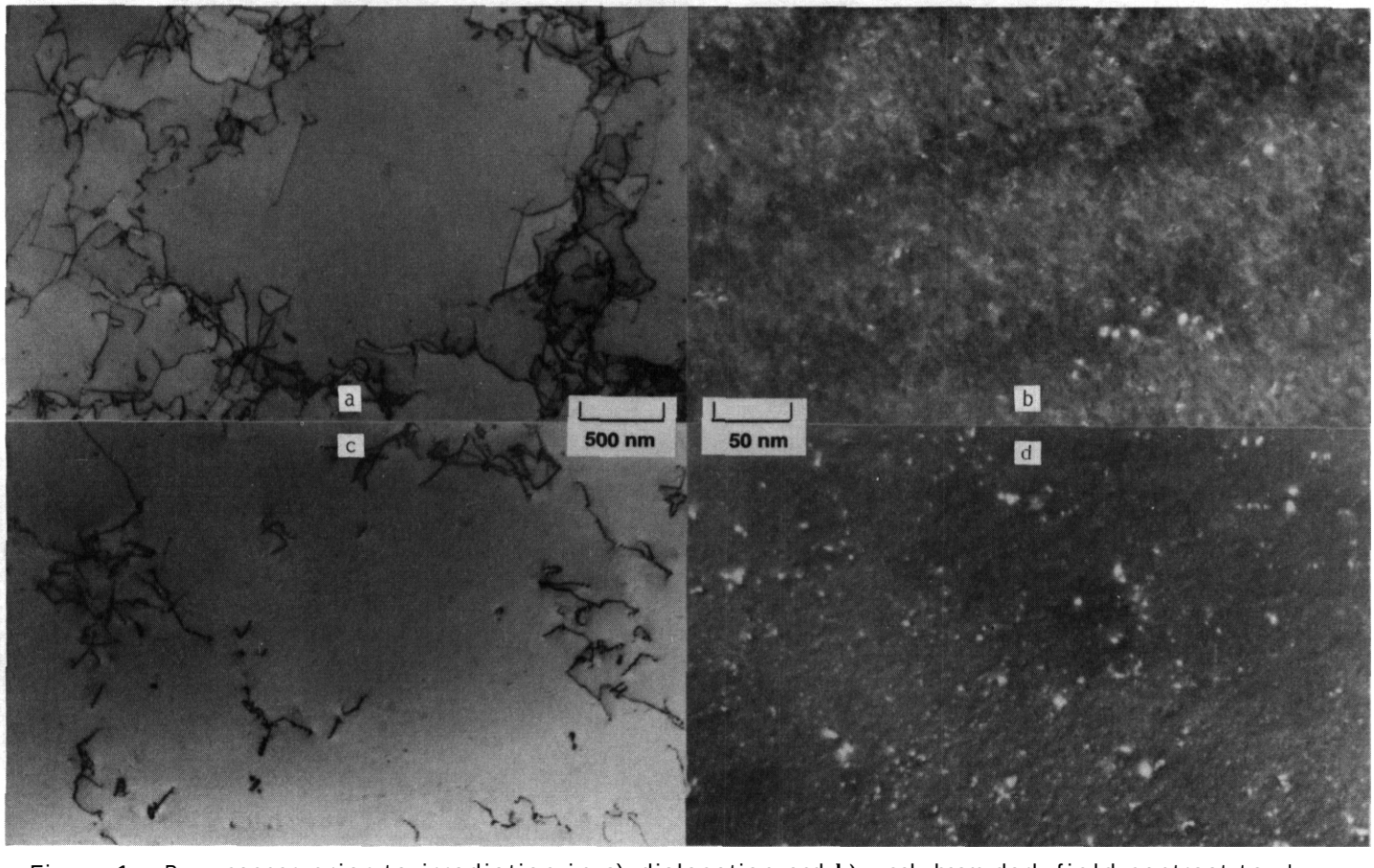


Figure 1. Pure copper prior to irradiation in a) dislocation and b) weak beam dark field contrast to show defect clusters, and Cu-5Ni prior to irradiation in c) dislocation and d) weak beam dark field contrast to show defect clusters.

high magnification. Foil orientations, in all cases, are near (001) with operating $\vec{g}$ = 200 so that 2/3 of the perfect dislocations are imaged and all faulted features with Burgers vectors of the type <111> are imaged. Weak beam images all use $\vec{g} \cdot 5\vec{g}$, the same as is used by Kiritani. Damage was not occurring during examination at 200 KeV. From these results, it is apparent that the annealing conditions used (for pure copper, 450°C for *30* minutes and for Cu-5Ni, 900°C for 15 minutes) were insufficient to anneal cold work structure, or avoid a moderate density of defect clusters. It may be noted that the structure shown in Figures la and c is typical of recovered dislocation damage and not characteristic of damage introduced during specimen preparation. In order to further understand the defect cluster observations in preirradiation microstructures, pure copper control specimens were further annealed at 800°C for 30 minutes, prepared in the usual manner and then imaged in weak beam dark field. Both the dislocation density and the defect cluster structure were significantly reduced. Also, it was found that reexamination of foils after approximately one month of storage in moderate vacuum resulted in dark field images that contained fringed structure, indicating that surface oxidation had occurred to complicate interpretation of the defect clusters. Therefore, all microscopy presented in this report was performed on specimens examined usually within a couple of hours and certainly within a day or two after specimen preparation with specimens held in vacuum storage in the interim.

Following irradiation in LASREF at 335°C to 0.25 dpa, voids within grains, bubbles on grain boundaries, unfaulted dislocation loops and defect clusters were found in both pure copper and Cu-5Ni specimens. Void swelling was greater in pure copper, consisting of a non-uniform distribution of voids with large differences in void size. The swelling was much lower in the Cu-5Ni specimens, with only a few examples of unusually shaped voids found, whereas bubbles on grain boundaries were smaller in the pure copper specimens. However, unfaulted loops and defect clusters were of comparable sizes in the two specimen conditions. Examples are given in Figure 2. Figures 2a, b and c show voids, bubbles on a grain boundary and defect clusters respectively for the pure copper specimen, and Figures 2d, e and f show similar examples for Cu-5Ni. Careful inspection of Figure 2a will reveal a bimodal void density with the large voids in the field of view of a different shape than the high density of smaller ones. The foil orientation is near (001) and the large

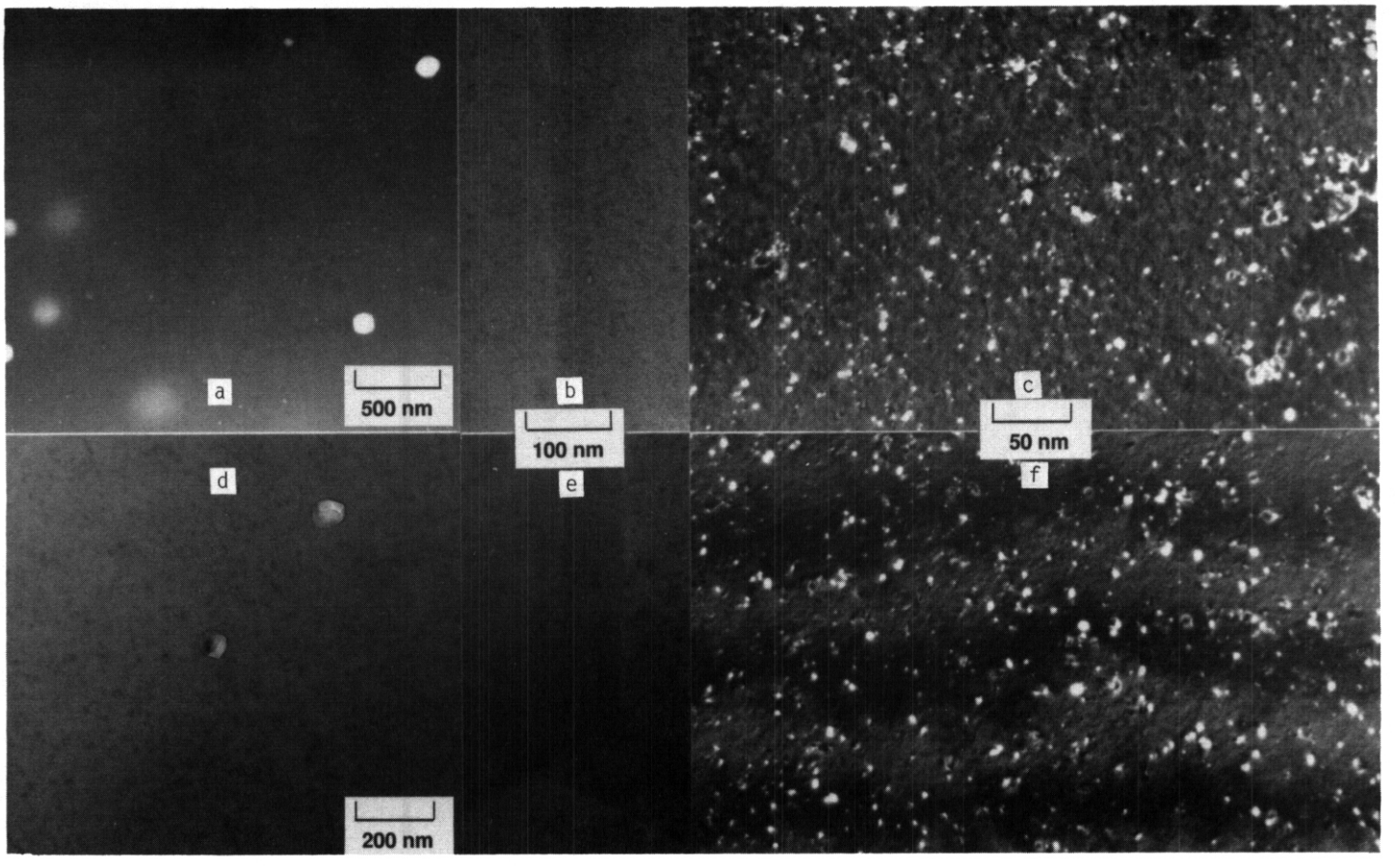


Figure 2. Following irradiation in LAMPF at 335°C to 0.25 dpa for pure copper in a) void contrast, b) void contrast to show bubbles on a grain boundary and c) weak beam dark field contrast to show defect clusters, and for Cu-5Ni in d) void contrast, e) void contrast to show bubbles on a grain boundary and f) weak beam dark field contrast to show defect clusters.

voids are truncated cubes whereas the smaller ones are octahedral. However, some large voids in other areas are also octahedral. Therefore, the more common void shape is octahedral, but large cuboidal configurations can be found. In comparison, the void shapes in Cu-5Ni were quite irregular, as shown in Figure 2d, and the void density was very low. Irregularly shaped voids and changes in void shape in a given specimen can generally be attributed to solute segregation of impurities tb void surfaces. The voids that form first are most affected. Bubbles were only identified on grain boundaries or at grain boundary nodes. The examples in Figures 2b and e, for pure copper and Cu-5Ni respectively, indicate the bubbles that formed in Cu-5Ni can be larger. However, the grain boundary node example in Figure 2e provides demonstration that bubble size varies from one boundary to another, and conclusions on bubble size as a function of composition may be misleading due to insufficient statistical information. Comparisons of defect clusters as a function of composition from Figures 2c and f show no significant differences.

Following irradiation in LASREF at 400/220°C (about 0.1 dpa at 400°C followed by about 0.15 dpa at 220°C), pure copper specimens were found to contain a moderate perfect dislocation density, a moderate density of small voids approximately 20 nm in diameter and a high density of defect clusters. Cu-5Ni irradiated under the same conditions contained no voids, a perfect dislocation loop structure formed in association with preexisting dislocations and defect clusters at a lower density that in pure copper. Examples are given in Figure 3. Figure 3a shows voids in pure copper following irradiation to 0.25 dpa at intermediate magnification. At lower magnifications, the void density was found to be quite uniform. Figure 3c shows dislocations in Cu-5Ni using $\vec{g}$ = 200 contrast for a (001) foil orientation, so that 2/3 of the perfect dislocations are visible. Figures 3 b and d allow comparison of the defect clusters in pure copper and Cu-5Ni respectively, in $\vec{g}$ = 200 weak beam dark field contrast for foil orientations near (001) and similar thicknesses of about 70 nm. Figure 3b contains void images marked by arrows. Nearby, groups of larger defect clusters can be identified. The nature of these larger features, or their significance, is not yet understood. It is anticipated that void development in pure copper and dislocation loop development near preexisting dislocations in Cu-5Ni occurred during irradiation at 400°C whereas the defect clusters are probably a result of irradiation at 220°C.

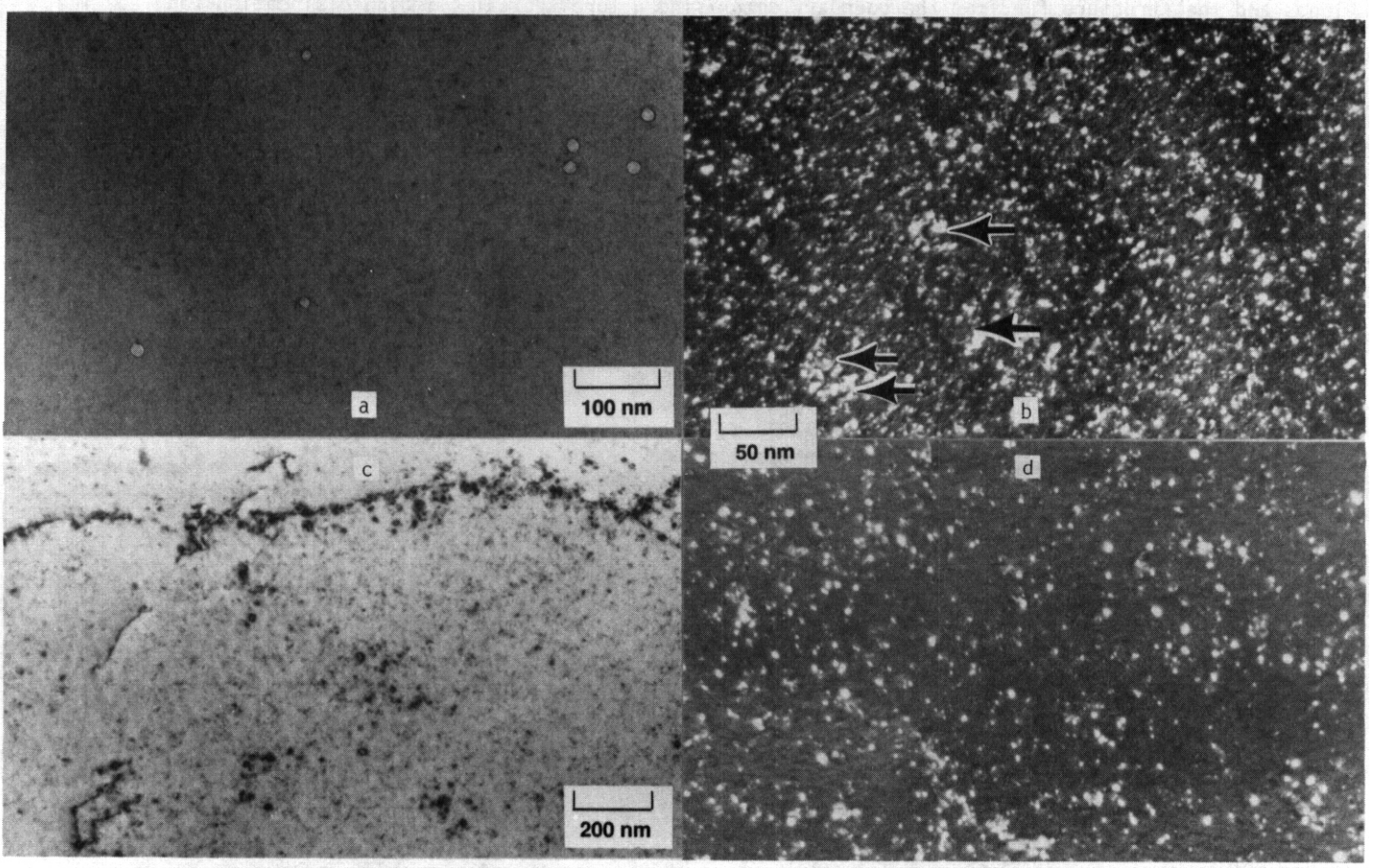


Figure 3. Following irradiation in LAMPF at 400/220°C to 0.25 dpa for pure copper in a) void contrast and b) weak beam dark field contrast to show defect clusters, and for Cu-5Ni in c) dislocation contrast and d) weak beam dark field contrast to show defect clusters.

Following irradiation in OR3 both at 250 and 400°C, the major result of irradiation was dislocation and defect cluster formation. Two regions were found containing voids in the specimen irradiated at 250°C to 0.3 dpa. The voids were of unusual shape, and the distribution was very nonuniform, both factors indicative of the initial stages of void development or of compositional inhomogeneities. Also, following irradiation at 400°C to 0.8 dpa, bubbles or voids were found to be uniformly distributed, with sizes approximately 3 to 7 nm in diameter, indicating the onset of swelling. Microstructural examples are given in Figures 4, 5 and 6. Figure 4 shows pure copper following irradiation at 250°C to 0.3 dpa. Figures 4a and b have been prepared to examine the same region in void and dislocation contrast. Voids are non-uniformly distributed,with large variations in size and shape. The largest voids show the greatest variation in shape, indicative of impurity segregation, but the foil surfaces in this region contain atypical pitting, possibly indicating that this region of the specimen is relatively impure. The dislocation structure in this part of the specimen is typical of other regions examined. The structure consists of climbing perfect dislocation segments forming a complex network, but the imaging is difficult due to strong background contrast presumably related to defect clusters. This structure is shown at higher magnification using $\bar{g}$ = 200 contrast for a foil near (011) in Figure 4c. The dislocation segments are found to be imaged as shorter segments associated with small loops, but the contrast is very difficult to understand. Similarities can be identified by comparison with the structure following irradiation in LASREF at 335-C. In both cases, the dislocation line segments are being fragmented but the process is more advanced in the DR-3 irradiation to 0.3 dpa at 250°C. Figure 4d provides an example of defect clusters in $\bar{g}$ = 200 weak beam dark field contrast for a foil near (013). Many examples of triangular and diamond shaped features can be identified, indicating that both triangular loops and stacking fault tetrahedra are present following irradiation. Therefore, the complex dislocation structure that is observed in this specimen may have arisen from the interaction of the cascade damage with the preexisting dislocation structure.

Microstructural examples of pure copper irradiated at 400°C in DR-3 to 0.3 dpa are given in Figure 5. Figure 5a shows the dislocation structure in the vicinity of a grain boundary located towards the lower left at low magnification. Distinctly different dislocation configurations developed near the boundary and far from the boundary, with the structure near the boundary consisting of what appear to be elongated dislocation loops and the structure far from the boundary comprising a more typical climbing dislocation tangle. The

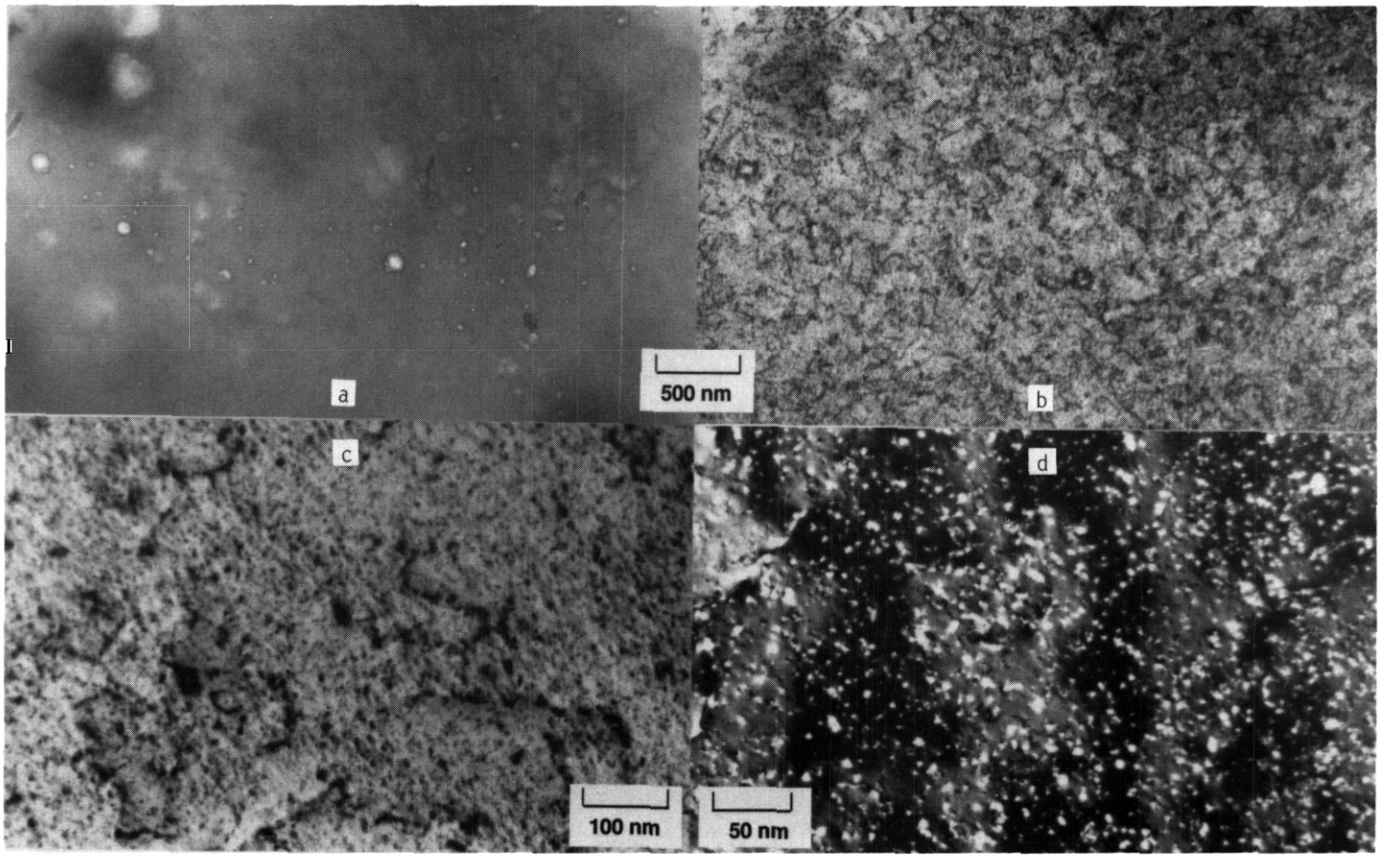


Figure 4. Following irradiation in DR-3 at 250°C to 0.34 dpa for pure copper in a) void contrast and b) dislocation contrast for the same area, c) dislocation contrast at higher magnification and d) weak beam dark field contrast to show defect clusters.

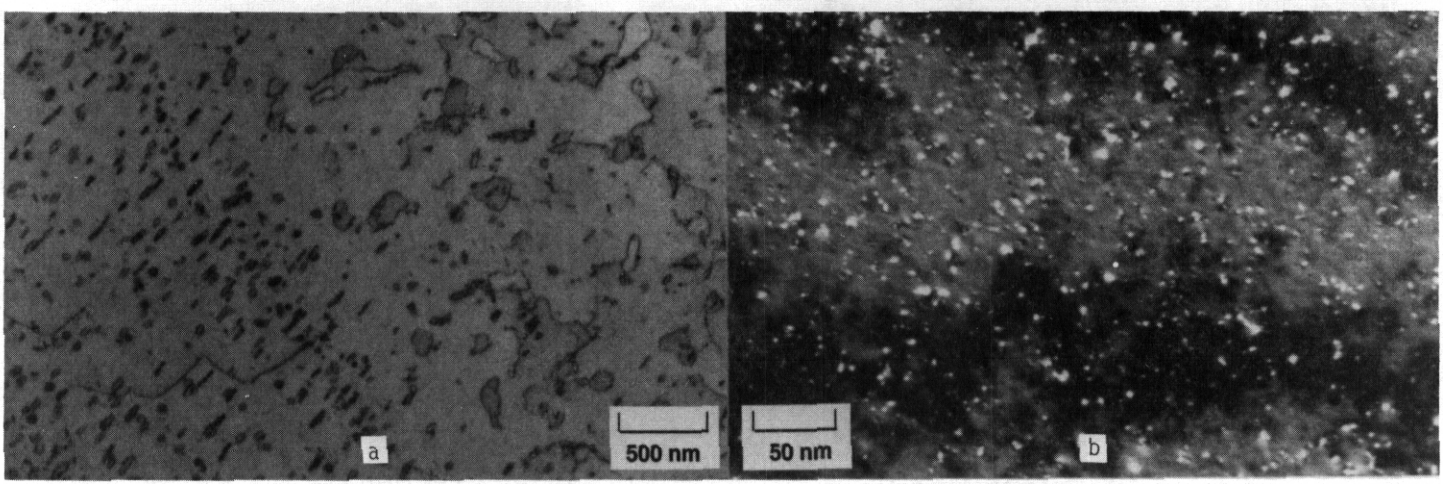


Figure 5. Following irradiation in DR-3 at 400°C to 0.34 dpa for pure copper in a) dislocation contrast near a grain boundary located at the lower left and b) weak beam dark field contrast to show defect clusters.

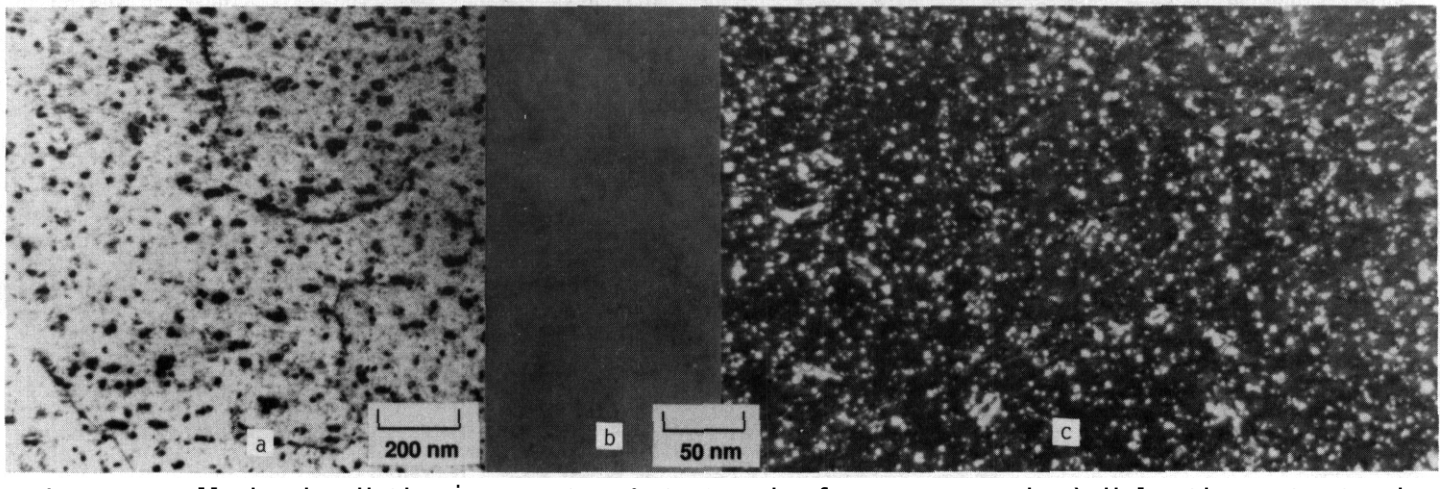


Figure 6. Following irradiation in DR-3 at 400°C to 0.77 dpa for pure copper in a) dislocation contrast and b) void contrast and c) weak beam dark field contrast to show defect clusters.

band containing loops was about 1.5 μm wide with the direction of loop elongation approximately normal to the boundary. This structure is believed to be a result of grain boundary migration during irradiation. The dislocation structure far from the boundary was more typical of the rest of the specimen. However, it is of interest to note that the imaging is much more clear, unlike the example in Figure 4b, using similar imaging conditions. No void swelling was identified in this condition. The defect clusters are shown in Figure 5b in $\bar{g}$ = 200 weak beam dark field contrast for a foil near (001). In this case, only a few examples of stacking fault tetrahedra can be identified and the defect density appears to be much lower.

Examples of the microstructural changes resulting from irradiation to a higher dose of 0.8 dpa at 400°C in DR-3 are given in Figure 6. As shown in Figure 6a, the dislocation structure still contains the preexisting dislocation structure, but now small loops dominate the microstructure. Therefore, the loops only formed after a dose of 0.3 dpa in regions containing preexisting dislocations. It can be argued that the preexisting dislocations have delayed loop nucleation and growth, but did not prevent it, whereas in the grain boundary region in Figure 5a, preexisting dislocations were not retained and loop nucleation developed at lower dose. Figure 6b shows an example of small voids found uniformly distributed in this specimen. The voids are on the order of 5 nm or less in diameter. Figure 6c shows defect clusters in $\bar{g}$ = 200 contrast for a foil near (001). A number of stacking fault tetrahedra can be identified.

The microstructures developed as a result of irradiation in FFTF were dominated by void swelling. A wide range of void sizes were observed, and the largest voids were too large for standard transmission microscopy examination. As a result, optical and scanning techniques were employed. The dislocation structure consisted of climbing dislocation tangles, often with dislocations attached to voids. However, in all cases, examples of defect clusters were found following irradiation.

Examples of optical and scanning electron microscopy images of specimens irradiated at 414°C in FFTF are provided in Figure 7. Figures 7a and d show optical microscopy of pure copper and Cu-5Ni, respectively. Grain boundaries have been selectively etched during the electropolishing procedure, so that grains 0.1 to 1 mm in diameter can be identified. These micrographs were selected to show examples of grain boundary migration, and demonstrate that migration distances of up to 0.025 mm occurred at some grain boundaries in both pure cooper and Cu-5Ni during irradiation at 414%. The texture within grains that is observed by optical microscopy is found by scanning electron microscopy to be due to voids intersecting specimen surfaces, as shown in Figures 7b and e for pure copper and Cu-5Ni, respectively. The voids in Cu-5Ni are found to be larger and more facetted but at lower number density than those in pure copper. Void shape is shown more clearly in the higher magnification scanning micrographs given in Figures 7c and f. In both cases, voids have grown larger than 1 μm in diameter. Examinations using transmission microscopy for these microstructures are very difficult because specimens must be at least 1 μm thick in order to retain such large voids. and images are unclear in such thick specimens. Therefore, transmission microscopy was restricted to dislocation and defect cluster examinations in limited thin regions near voids, with the understanding that the regions immediately adjacent to void surfaces had been removed by electropolishing.

Figure 8 provides examples of dislocation and defect cluster images in pure copper and Cu-5Ni following irradiation at 414°C in FFTF. In both cases, the dislocation structure consists of tangles of climbing perfect dislocations, often connected to voids, as shown in Figures 8a and c for pure copper and Cu-5Ni respectively. However, in both cases, voids much smaller than those found by scanning microscopy are present. Therefore, estimates of void density based on scanning microscopy will underestimate void density, and void nucleation is continuing during irradiation in both pure copper and Cu-5Ni. Examples of defect clusters in pure copper and Cu-5Ni are given in Figures 8b and d. Both regions were thin enough for examination because voids happened to be either above or below these regions, and these regions were locally thinner following electropolishing, so that this microstructural information is for regions close to voids. The defect clusters are at lower density than that found following irradiation in DR-3, but it is quite different from the unirradiated microstructures and typical of radiation damage. Examples can even be found of triangular and diamond shaped images, suggesting that both triangular loops and stacking fault tetrahedra are present in pure copper and Cu-5Ni after irradiation in FFTF at 414°C.

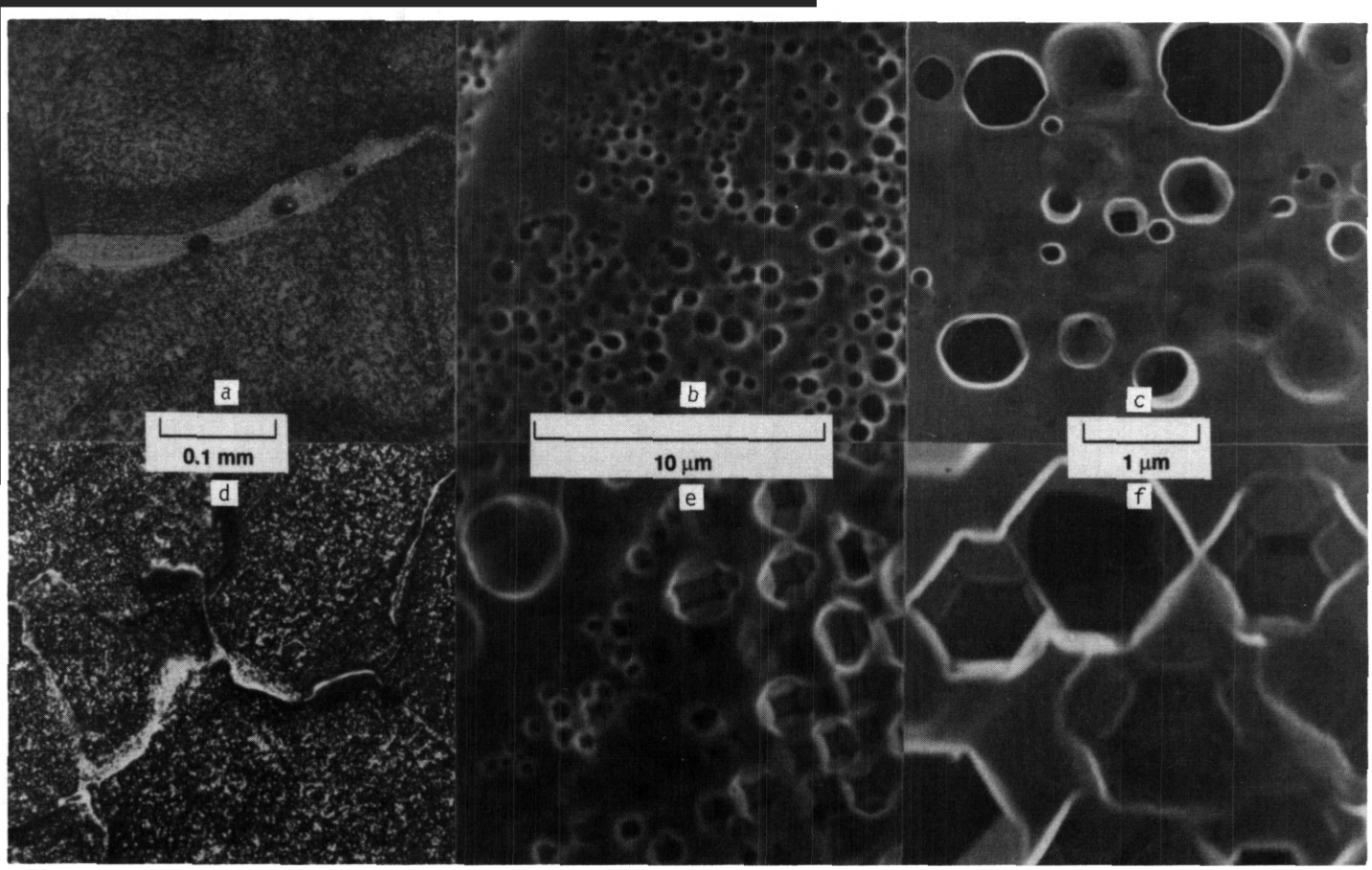


Figure 7. Following irradiation in FFTF/MOTA at 414°C to 34.1 dpa for pure copper using a) optical imaging, b) low magnification SEM and c) higher magnification SEM to show void swelling and for Cu-5Ni using d) optical imaging, e) low magnification SEM and f) higher magnification SEM to show void swelling.

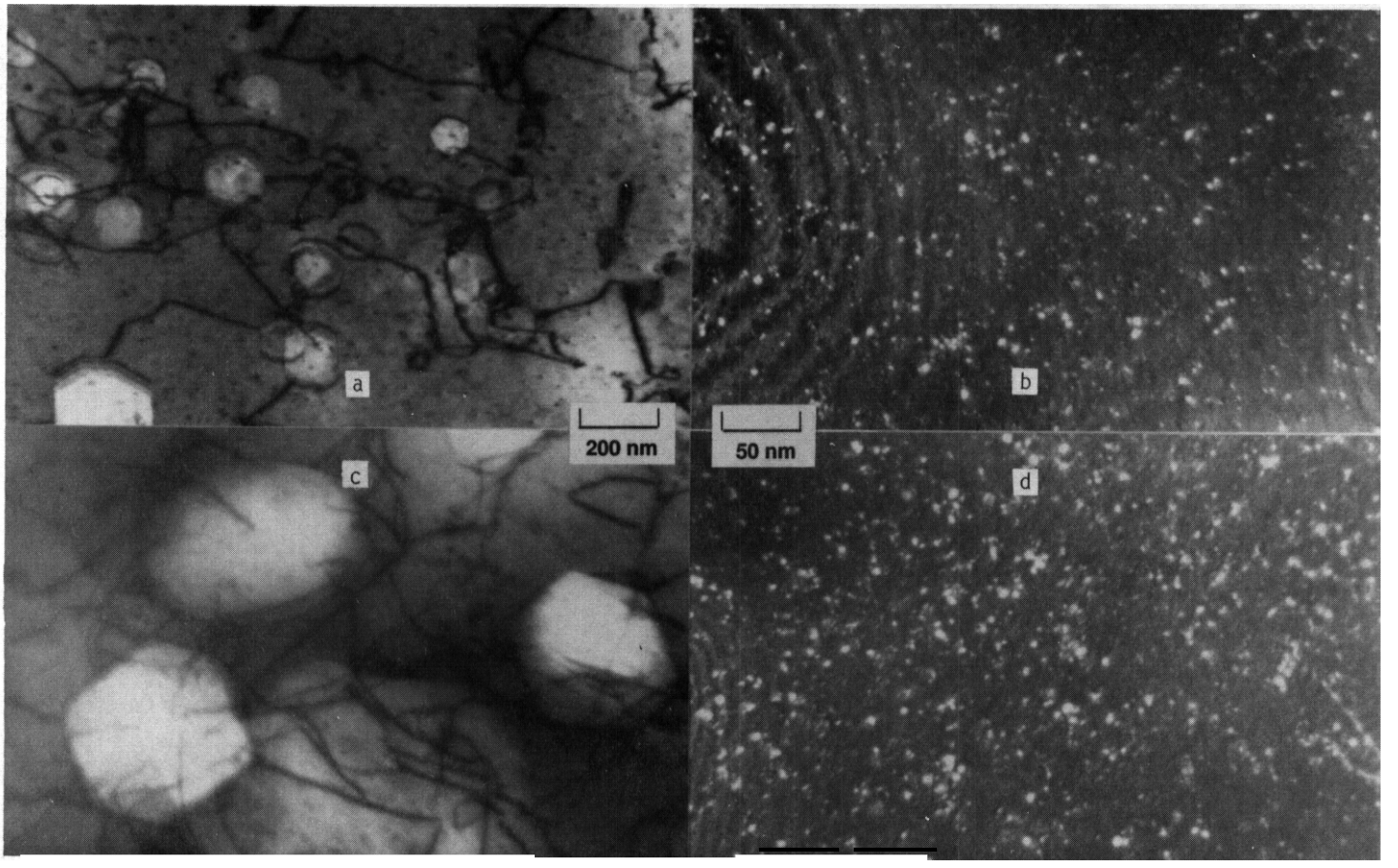


Figure 8. Following irradiation in FFTF/MOTA at 414% to 34.1 dpa for pure copper in a) dislocation contrast and b) weak beam dark field contrast to show defect clusters, and for Cu-5Ni in c) dislocation contrast and d) weak beam dark field contrast to show defect clusters.

Following irradiation at 529°C to 31.6 dpa, the major effect of irradiation was void swelling and dislocation evolution. However, no examples were found of grain boundary migration, voids did not form near grain or twin boundaries, and the largest voids tended to form in strings, suggesting that compositional or microstructural inhomogeneities present prior to irradiation encouraged void formation. As in the case of specimens irradiated at 414°C, void sizes varied considerably, including some areas containing high densities of small voids. Examples of the microstructures following irradiation at 529°C are provided in Figure 9. Figures 9a and f give examples of the void structures obtained by scanning electron microscopy at low magnification for pure copper and Cu-5Ni, respectively. Examples of larger voids are found in the Cu-5Ni specimen, but the void density is more uniform in the pure copper condition. In both figures, towards the upper part of the micrograph, examples have been selected to show groups of larger voids in stringer arrangements. All void stringers were found to be parallel in a given specimen. These voids are considerable larger than those found following irradiation at 414°C. Therefore, pure copper and Cu-5Ni follows the normal sequence of void growth as a function of temperature, but swelling is lower at 529°C because void density is reduced.

Figures 9b and g show the dislocation and void structure at higher magnification following irradiation at 529°C in pure copper and Cu-5Ni, respectively. In pure copper, the dislocation structure is found to be a tangle of climbing perfect dislocations, often connected to voids, and examples of small voids were often found. In Cu-5Ni, the dislocation structure included many examples of unfaulted loops up to about 100 nm in diameter, and examples of small voids were also often found. Even following irradiation at 529°C, defect clusters were found as shown in Figures 9c and h. The structures are characteristic of radiation damage and some of the features can be interpreted as triangular loops. Further understanding of the void development at 529°C is provided in Figures 9d and e, showing void and dislocation imaging ($\bar{g}$ = 200 near (013) so that 2/3 of the perfect dislocations should be visible), for the same area in pure copper following irradiation at 529°C to 31.6 dpa. The area on the left of Figure 9d is found to contain a high density of relatively small voids whereas the area on the right contains no voids in that size range. Dislocation imaging reveals that the array of small voids has formed in association with a high dislocation density. Therefore, void nucleation occurs in the vicinity of dislocations present in pure copper specimens. The dislocations were probably present prior to irradiation. These observations indicate that preirradiation microstructures will likely affect high temperature swelling behavior in copper alloys.

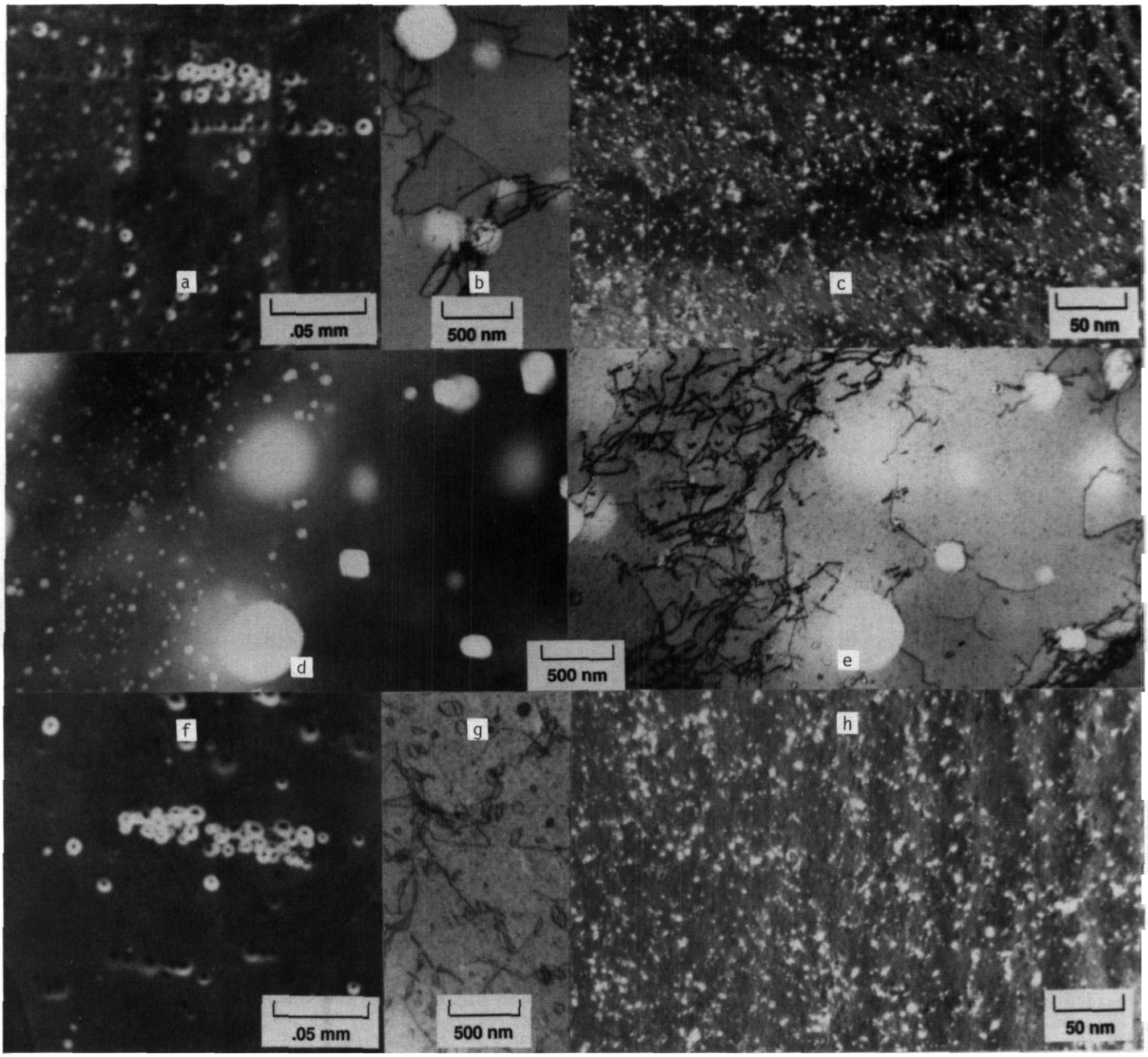


Figure 9. Following irradiation *in* FFTF/MOTA at *529°C* to 31.6 dpa for pure copper in a) low magnification SEM, b) dislocation contrast c) weak beam dark field contrast to show defect clusters and d) and *e)* showing the same area in void and dislocation contrast, and for Cu-5Ni in f) low magnification *SEII,* g) dislocation contrast and h) weak beam dark field contrast to show defect clusters.

Quantitative microstructural analysis

Void, dislocation, bubble and defect cluster images were all taken as stereo pairs so that stereoscopic estimates for foil thickness could be made and microstructural features quantified. Also, defect cluster images were taken for foil orientations near (001) using $\bar{g}$ = 200 so that triangular loops could be differentiated from stacking fault tetrahedra (tetrahedra appear as square images and planar triangular loops as triangles for orientations near {001}.) Also, defect clusters were recorded as 2% D images so that differences in stress fields around defects could be assessed.

The results of quantitative microstructural measurements are included in Table 2 and the results of quantitative measurements on defect cluster structures are summarized in Table 3. Table 2 includes each of the

Table 2. Microstructural Results for Specimen Conditions Examined by Transmission Electron Microscopy

		Voids			Dislocations	
Code	Neg #	S (%)	$\bar{d}$[(a)] (nm)	ρ (#/cm^3)	ρ (cm/cm^3)	Other
RO	1772				6.8 x 10^8	
	38825				8.0 x 10^8	
VP	1785				4.5 x 10^8	
RO#7	1140	0.265	32.7	9.2 x 10^{13}		
	1090	0.320	44.0	3.1 x 10^{13}		
	1142	0.540	45.3	8.1 x 10^{13}		
	1091/3	0.123	23.9	5.3 x 10^{13}	1.3 x 10^8	
	1146	0.278	27.2	3.6 x 10^{13}		
	1144	0.179	21.4	7.0 x 10^{13}		
RO#2	1046a	0.017	11.2	3.5 x 10^{14}		
	" b	0.015	10.4	3.6 x 10^{14}		
	949/7	0.006	10.9	1.2 x 10^{14}	8.3 x 10^8	
		0.011	14.5	9.8 x 10^{13}		
I #2	989				1.2 x 10^9	loops: 8.9 x 10^{13}/cm^3, 3.5 x 10^8/cm^2
14DR3	1701	0.26	22.9	1.3 x 10^{14}		
15DR3	1751			1.2 x 10^{10}		
	1747	0.002	2.4	6.8 x 10^{14}		
	1755	0.0009	2.9	3.7 x 10^{14}		
	1239				9.1 x 10^9	
	1215				1.02 x 10^{10}	
	1272				3.1 x 10^{10}	
ROLO	1388	11.9	196.6	1.2 x 10^{13}		
	1422/0	7.6	339.3	7.2 x 10^{12}	4.2 x 10^8	
	1383/4	9.2	228.1	6.1 x 10^{12}	5.3 x 10^8	
	1397	16.1	373.1	3.6 x 10^{12}	2.4 x 10^8	
	1394	8.8	111.9	9.2 x 10^{13}	8.5 x 10^8	
VPLO	1456				1.6 x 10^8	
	1711	16.3	432.4	2.3 x 10^{12}	1.2 x 10^9	
	1706	2.6	322.5	1.3 x 10^{12}	3.4 x 10^8	
	1710	17.8	380.0	2.0 x 10^{12}	8.6 x 10^8	
	1455	21.3	1393.3	1.2 x 10^{11}		
	1433	24.0	1336.7	2.7 x 10^{11}		
	1436	52.6	1640.7	2.6 x 10^{11}		
	1447	36.7	1523.3	2.0 x 10^{11}		
	1541	30.8	1638.9	1.5 x 10^{11}		
ROME	1507	0.7	172.5	2.7 x 10^{12}		
	1593/88	1.6	224.1	1.6 x 10^{12}	2.3 x 10^8	
	1592/87	2.3	231.8	2.2 x 10^{12}	3.8 x 10^8	
	1499	1.0	180.0	3.4 x 10^{12}		
	1597a	8.3	267.1	2.6 x 10^{12}	6.7 x 10^8	
	" b	9.9	72.3	3.6 x 10^{13}	1.7 x 10^9	
	1598/5	4.3	118.9	8.5 x 10^{12}	4.8 x 10^8	
	1599/6	2.0	225.4	2.5 x 10^{12}	4.7 x 10^8	
	1613/5	1.5	338.5	7.5 x 10^{12}	3.5 x 10^8	
	1606/4	1.2	247.5	1.8 x 10^{12}	1.1 x 10^9	
	1614/9	0.4	66.9	1.6 x 10^{13}	1.5 x 10^9	
	1494	1.0	231.6	1.4 x 10^{12}	3.1 x 10^8	
VPME	1560	0.39	218.7	4.2 x 10^{11}		
	1557			8.6 x 10^8		
	1553			7.3 x 10^8		
	1573			1.0 x 109		
	1509	0.41	257.7	2.6 x 10^{11}		
	1554	0.95	338.1	2.7 x 10^{11}		
	1556/7	1.73	309.7	4.5 x 10^{11}	7.0 x 10^8	

(a) The $\bar{d}$ given is the average void diameter, not the diameter of the average void volume.

measurements made in order to emphasize area-to-area differences whereas Table 3 only contains averages of the measurements made on a given specimen, and, for example, when micrograph quality was not good enough to allow unambiguous identification of triangular loops or stacking fault tetrahedra, measurements of those

Table 3. Results of Quantitative Measurements of Defect Clusters

			Defect Clusters			Triangular Loops			Stacking Fault Tetrahedra		
Code	Condition	Irradiation Conditions	d (nm)	Density (cm^{-3})	Vol. Fract. (%)	d (nm)	Fract. (%)	Oisl ρ (cm^{-3})	$\bar{d}$ (nm)	Fract. (%)	Vol. Fract. (%)
RO	Marz capper	control	2.6	$2.7x10^{15}$	.008		0.0			0.0	
RO800	Marz copper	800°C/30 min	4.8	$1.7x10^{15}$	.015		0.0			0.0	
VP	Cu-5Ni	control	1.7	$1.3x10^{17}$	.065	2.9	1.3	$1.5x10^{9}$		0.0	
RO#7	Marz Copper	LAMPF 335°C, 0.25 dpa	2.6	$7.4x10^{16}$	.19	3.0	3.0	$1.7x10^{9}$	2.3	5.3	.003
1 #7	1Cu-5Ni		2.9	$1.5x10^{17}$	.53	3.5	3.1	$6.0x10^{9}$	4.2	7.8	.011
RO#2	Marz Copper	LAMPF 400/220°C, 0.25dpa	2.6	$2.9x10^{17}$	.70	3.1	0.8	$2.3x10^{9}$	1.8	2.1	.000
1 #2	1Cu-5Ni		2.5	$1.0x10^{17}$	.21	3.0	3.7	$3.0x10^{9}$	3.5	4.8	.002
14	Marz Copper	OR-3, 250°C, 0.34 dpa	2.9	$7.9x10^{16}$	2.4	3.3	7.3	$6.5x10^{10}$	2.4	3.2	.012
18	Marz Copper	DR-3, 400°C, 0.34 dpa	2.4	$1.8x10^{17}$	.30		0.0			0.0	
15	Marz Copper	DR-3, 400°C, 0.77 dpa	3.1	$2.3x10^{17}$	.84	0.0	0.0		2.9	15.4	.014
ROLO	Marz Copper	FFTF, 414°C, 34.1 dpa	2.1	$5.3x10^{16}$	.09	2.9	3.3	$1.9x10^{9}$	4.0	1.1	.000
VPLO	Cu-5Ni	FFTF, 414°C, 34.1 dpa	2.6	$6.6x10^{16}$	.15	4.3	1.0	$7.6x10^{8}$	3.5	1.4	.000
ROME	Marz Copper	FFTF, 529°C, 31.6 dpa	2.5	$1.4x10^{17}$	.31	3.4	1.7	$2.5x10^{9}$	3.5	1.0	.001
VPME	Cu-5Ni	FFTF, 529°C, 31.6 dpa	2.5	$2.1x10^{17}$	.40	3.6	3.3	$8.1x10^{9}$	4.2	1.1	.002

features were ignored. In general, each entry includes measurements on about 100 features, unless the density of features was very low. The dislocation densities given are not corrected for features that should be out of contrast, and therefore they underestimate the correct value by about 33%.

From Table 2, a number of observations may be demonstrated. Void swelling measurements were made for two LASREF samples, two OR-3 samples and all four FFTF/MOTA conditions. Swelling levels in pure copper irradiated in LASREF at 335°C to 0.25 dpa were between 0.12 and 0.54%, but irradiation at 400°C to 0.1 dpa and then at 220°C to 0.15 dpa gave measurements between 0.06 and 0.17. Therefore, swelling was about three times higher following irradiation at 335%. The number density was higher in the 400/220 case. As void density is generally inversely proportional to temperature, it is reasonable to assume that void nucleation and growth, during the irradiation where the temperature changed from 400 to 220°C, is characteristic of 220°C and not 400°C. Therefore, the 400/220 LASREF irradiation microstructure is probably characteristic of irradiation at 220°C to a dose less than 0.25 dpa. For specimens irradiated in OR-3, the measurements provided in Table 2 do not follow the normal trend expected for void density. Void swelling is found to be locally higher for the 250°C condition, due to larger voids at a lower number density. However, it must be emphasized that swelling in the specimen irradiated at 250°C showed a very non-uniform distribution of voids, characteristic of a material not yet in steady state swelling, Therefore, void nucleation is probably not complete in the 250°C condition, even in the area analyzed that contained a reasonable void distribution. At higher dose, further void nucleation would be expected. Measurements of swelling in FFTF/MOTA irradiated specimens, gave a wide range of swelling values for a given irradiation condition, as would be expected for high swelling materials with large voids. However, the average values agree closely with density change results. Void densities for FFTF/MOTA irradiated specimens followed the usual trend as a function of temperature. Comparison of the effect of nickel addition to copper on swelling shows inconsistent trends. Following irradiation in LASREF or following irradiation in FFTF/MOTA at 529°C, nickel additions result in reduced swelling, whereas in FFTF/MOTA at 419°C, nickel additions result in higher swelling. Dislocation densities appear to be insensitive to irradiation, on the order of $5x10^{8}$ cm^{-2}, except in cases where small loops were present. This is likely due to the fact that the dislocation structure present prior to irradiation is retained and dominates the irradiation induced structure.

Table 3 provides the result that defect clusters found in irradiated copper and Cu-5Ni are insensitive to composition, irradiation temperature and neutron energy. Mean defect diameters vary between 2.4 and 3.1 nm, and defect densities are all in the range $5x10^{18}$ to $3x10^{17}$ cm^{-3}. In comparison with the preirradiation structures, this represents about two orders of magnitude increase in density of defect clusters for pure copper but comparable levels for Cu-5Ni. In the case of Cu-5Ni, the preirradiation defects are significantly smaller in average size, but it is not yet known what is the origin of these small defects, or whether they are retained following irradiation. It may be reasonable to speculate that defect clusters found in irradiated Cu-5Ni are due to irradiation because of their similar size and density to those produced in pure copper under identical irradiation conditions. However, some differences in the defect cluster structure can be identified as a function of composition and neutron energy. The parameter "defect clusters, volume fraction" given as a percent is intended to indicate how much of the structure is filled with cascade damage by assuming that spherical regions corresponding to the defect sizes have been affected. (Such an assumption may result in an overestimation. because the defects are likely to be loops.) This fraction is generally found to be about 0.4%. but significantly higher values are found for DR-3 irradiated specimens. Why DR-3 at 250°C gives higher values is not yet understood. Measurements for triangular loops and stacking fault tetrahedra also vary as a function of irradiation condition. In general. values for the fraction (the ratio of features compared to the total counted expressed as a percentj are on the order of 1% or less, which is considered to be about the uncertainty of the precision for differentiating triangular loops and tetrahedra from image overlaps, etc. However, values for triangular loops as high as 1% were found for OR-3 irradiated pure copper at 250°C, and for stacking fault tetrahedra as high as 15% were found for OR-3 at 400°C. (Results for specimen condition #8 in DR-3 at 400°C to 0.3 dpa are probably a consequence of insufficient image quality.)

In order to allow further comparison of the defect cluster structure, Figure 10 has been prepared to show the cluster size distribution as a function of relative frequency for each condition analyzed. Each distribution also includes the total defect density, the fraction of stacking fault tetrahedra and/or triangular loops measured, and arrows showing the mean diameter measured for the entire distribution, $\bar{d}$, stacking fault tetrahedra, $\bar{t}$, or triangular loops, $\bar{a}$. Distributions for the defect clusters present prior to irradiation are included. Comparison of the size distributions in Figure 10 reveals the unexpected result that all irradiation conditions have similar response. However, unirradiated pure copper is markedly different because the defect density is lower and the unirradiated Cu-5Ni is different because the distribution is skewed to smaller sizes. Also, in most cases, the mean size for the entire distribution is below that for the faulted features (triangular loops and stacking fault tetrahedra.) This latter observation may well be because smaller defects could not be unambiguously identified as tetrahedra or triangular loops.

Images of helium bubbles on grain boundaries were analyzed for pure copper and Cu-5Ni following irradiation in LASREF at 335°C to 0.5 dpa. For pure copper, two boundaries were analyzed in different regions of the specimen, giving mean bubble sizes of 5.2 and 5.0 nm, and corresponding bubble densities of $2.2x10^{9}$ and $8.2x10^{9}$ bubbles/cm^{2}. Three boundaries about a node in Cu-5Ni gave mean bubbles sizes of 3.4, 4.2 and 3.3 nm and corresponding bubble densities of $5.71x10^{9}$, $6.51x10^{9}$ and $3.1x10^{9}$ bubbles/cm^{2}. Therefore, bubble sizes were somewhat larger in the case of pure copper and the bubble densities were similar.

Discussion

This experiment, as originally conceived, was intended to provide results on pure copper at one temperature in three quite different neutron spectra that encompassed that for 14 MeV neutrons, with subsidiary investigations on the effect of transmutation, dose rate, dose and temperature in order to extend those results to a much wider range of conditions. Unfortunately, one of the experiments had a temperature control problem; control was lost 40% of the way through the experiment, and as a result, microstructural development was characteristic of a lower temperature. Also, temperature monitors indicate that a second test operated at temperatures significantly higher than planned.

Comparison with previous results

The present results are in reasonable agreement with previously published results with regard to swelling and dislocation evolution. For example, Singh et al,[4] and Wolfenden[21] have reported dislocation structures similar to those found in DR-3 following irradiation at 250°C. Wolfenden[21] reported zero swelling for pure copper in a mixed spectrum at 175°C to about 10 dpa, but Zinkle and Farrell[18] reported void swelling following irradiation of pure copper in a mixed spectrum reactor at 250°C to 1.3 dpa at about 0.23% with a void density of $1.5x10^{14}$ cm^{-3}, Labbe et al.[23] reported void swelling following irradiation in pure copper in a mixed spectrum reactor at 250°C to about 0.5 dpa with void densities on the order of 10^{14} cm^{-3}, and swelling between 0.03 and 0.32% and Brimhall and Kissinger[11] reported void swelling following irradiation in pure copper in a thermal reactor at 285°C in the range 0.01 to 0.1 doa to as high as 0.4% with void densities on the'order of 10^{14} cm^{-3}. Brimhall and Kissinger also showed that' the addition of 2%Ni decreased void density to about 10^{13} cm^{-3}. These results span the response from DR-3 at 250°C, and LASREF at 400/220°. At 350°C, Zinkle and Farrell[18] reported void swelling following irradiation to 1.2 dpa at about 0.35% with a void density of $4x10^{13}$ cm^{-3}, and Labbe et al.[23] reported void swelling at 335°C to about 0.5 dpa between 0.07 and 0.35%. with void densities on the order of $2x10^{13}$ cm^{-3}, in good agreement with results from LASREF at 335°C. They also describe denuded zone behavior at 335°C, possibly related to grain boundary migration response

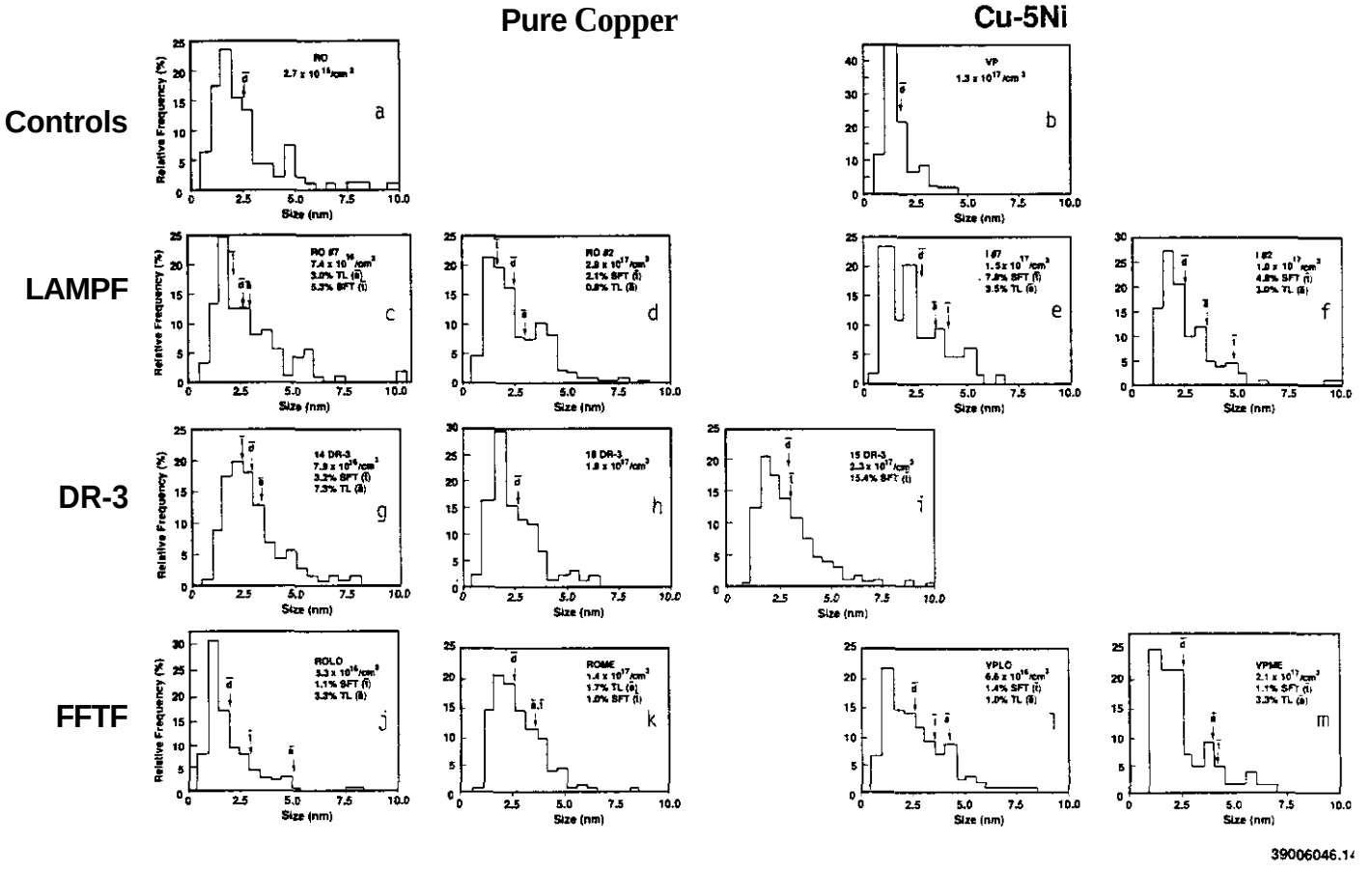


Figure 10. Defect cluster size distributions for a) unirradiated pure copper control, b) unirradiated Cu-5Ni control, c) pure copper irradiated in LAMPF to 0.25 dpa at 335°C and d) to 1.0 dpa at 420°C followed by 1.5 dpa at 200°C, e) Cu-5Ni irradiated in LAMPF to 0.25 dpa at 335°C and f) to 1.0 dpa at 420°C followed by 1.5 dpa at 200°C, g) pure copper in OR-3 to 0.3 dpa at 250°C, h) to 0.3 dpa at 400°C and i) to 0.8 dpa at 400 °C, j) pure copper in FFTF/MOTA to 34 dpa at 414°C, k) Cu-5Ni in FFTF/MOTA to 34 dpa at 414°C, 1) pure copper in FFTF/MOTA to 32 dpa at 529°C, and m) Cu-5Ni in FFTF/MOTA to 32 dpa at 529%.

described 'in the present work, and Zinkle and Farrell[18] reported differences in void development in the vicinity of a grain boundary. For 400°C to 1.3 dpa, Zinkle and Farrell[18] reported void swelling at about 0.26% with a void density of $2x10^{12}$ cm^{-3}, and for 435°C, Labbe et al[23] found void swelling between 0.1 and 0.25% with void densities on the order of $7x10^{12}$ cm^{-3}, somewhat higher and at somewhat lower density that results from DR-3. Brager[22] reported dislocation and void development at 450°C to 16 dpa in FFTF/MOTA in a precursor experiment to the present that was very similar to the present results except that the dislocation structure did not appear to contain unfaulted dislocations. Therefore, except for the results from irradiation in OR-3 and 400°C where an unusual region was analyzed, all swelling response found agrees well with published data from thermal spectra.

However, fine structure determinations reported previously were either for temperatures or doses below those of the present study or are still in progress, so that direct comparison is not informative. Brager reported a low density (about 10^{14} cm^{-3}) of small unidentified defect clusters present in his specimens following irradiation in FFTF/MOTA at 450°C[22,25] and statements by Zinkle and Farrell[18] indicated that stacking fault tetrahedra may have been present following irradiation over the whole temperature range 220 to 450°C, but detailed analysis was only in progress, and a example of fine structure has only been given for pure copper irradiated at 182°C.[40] However, the work of Yoshida et al[30] shows a very strong temperature dependence of fine structure density as a function of irradiation temperature using 14 MeV neutrons at low dose. Fine structure that formed at 200°C to a dose of 10^{22} n/m^2 was similar to that formed at room temperature but densities of radiation induced defect clusters decreased drastically at 400°C. This was in agreement with results reported by English for fission neutron irradiation.[19]

Microstructural evolution

The original experimental design provided for four dose levels in pure copper at 400°C: 0.25 dpa in LASREF, 0.34 dpa in OR-3, 0.71 dpa in OR-3 and 34.1 dpa in FFTF/MOTA, and two dose levels in Cu-5Ni at 400°C:

0.25 dpa in LASREF and 34.1 dpa in FFTF/MOTA. However, the temperature dropped in the LASREF experiment to 220°C after 0.1 dpa, and remained there for another 0.15 dpa, and comparison of void density information suggests that void structure found in pure copper irradiated during that experiment is characteristic of 220°C. Also temperature monitors for the OR-3 irradiation indicated that the operating temperature exceeded 420°C.

The following summary of microstructural evolution at about 400°C is possible. After the 400/220°C irradiation in LASREF, the microstructure was dominated by the 220°C irradiation, so that the effects of dose to about 0.1 dpa at 400°C were obscured. At a dose of 0.34 dpa in DR-3, the major effect of irradiation in pure copper was perfect dislocation loop evolution in regions were dislocations were not present. Voids were not found. Void formation occurred following a dose of 0.77 dpa, creating a uniform distribution of voids or bubbles with mean diameter of 2.4 nm at a density of 7×10^{14} cm^{-3}. By 0.77 dpa, perfect dislocation loop formation had spread to those regions containing dislocations prior to irradiation. Therefore, minor differences in specimen composition or specimen preparation could explain delay of microstructural development. However, irradiation to 34.1 dpa at 414% in FFTF/MOTA produced a large increase in swelling, at a much lower void density, generally about 10^{13} cm^{-3}, but in one case as high as 10^{14} cm^{-3}. Large differences were found in void size suggesting that void nucleation continued as swelling developed. Dislocation density was at a level similar to that present prior to irradiation. It may be noted that the lower void density found for FFTF/MOTA would not normally be attributed to void coalescence at high dose or to a higher dose rate. Therefore, again minor differences in specimen composition, specimen preparation or neutron spectrum are most likely to provide explanation for unexpected response.

Irradiation at a lower temperature, as was done in OR-3, or at a higher temperature, as in FFTF/MOTA, altered void and dislocation development. Irradiation in OR-3 at 250°C to 0.34 dpa resulted in swelling in two regions of the specimen and reduced dislocation evolution, whereas at 400°C in OR-3, no swelling was found and unfaulted loop nucleation and growth was clearly identified. The voids were of unusual shape and the distribution was characteristic of the nucleation stage of swelling possibly affected by chemical inhomogeneity. However, it can be concluded that the lower irradiation temperature reduced the dose needed for void nucleation. Irradiation in FFTF/MOTA at 529°C in comparison with 414°C resulted in less void swelling due to reduced void nucleation, but some regions contained voids at densities only slightly below levels found from 414°C. Therefore, reduced swelling can be attributed to a swelling incubation effect and again, lower irradiation temperature reduced the dose needed for the onset of swelling. Furthermore, the largest voids found following irradiation at 529°C are significantly larger than those formed at 414°C, so it is possible that swelling rates may eventually be comparable at higher dose.

Information from Cu-5Ni specimens irradiated in FFTF/MOTA follows similar trends but at lower void density. However, conclusions from LASREF irradiated specimens were very limited because void development was restrained and omission of Cu-5Ni from the OR-3 specimen matrix limits the extent of comparisons of microstructural evolution as a function of irradiation dose and temperature any further.

Consequences of transmutation on microstructural development

As pure copper is irradiated in a fusion environment, nickel and zinc will be created at a linear rate, so that initially, microstructural response will be governed by pure copper, but at higher dose, behavior will be more characteristic of Cu-5Ni. The above discussion indicates that microstructural evolution could be worse in a fusion environment than in the experimental cases studied to date. Nucleation of microstructural features occurs more rapidly in pure copper than in Cu-5Ni, but voids grow more rapidly (and as a consequence, the swelling may be higher) in the Cu-5Ni alloy. Therefore, unless factors other than just the presence of nickel (such as starting dislocation density) cause the increased growth rate, swelling in pure copper in a fusion environment could be higher than that predicted by behavior in a non-fusion environment where transmutation does not occur.

Explanations for unexpected defect cluster observations

Defect clusters have been observed in all specimen conditions examined in this study. Defect cluster observations were negligible in a specimen of pure copper heat treated for 30 min. at 800?, low for the pure copper control specimen, with a different size distribution for Cu-5Ni control specimen, and otherwise very similar for all irradiation conditions irrespective of spectrum, dose temperature or composition. Descriptions of damage as a function of irradiation temperature using 14 MeV neutrons at low dose indicate that at 400°C, defect cluster development is negligible. Also, irradiation damage at 400°C promotes both void swelling and dislocation evolution on a coarse scale so that development and retention of defect clusters was not anticipated. Therefore, it is necessary to identify the source of the defect clusters observed in the present study. Possibilities are 1) experimental procedure artifacts, 2) structure formed during reactor cool down operations as the specimen was removed from the irradiation system or 3) damage inherent in copper alloys even at high temperatures.

Several specimen handling procedures could have introduced defect clusters. Damage due to electron irradiation while the specimens were examined in the microscope, damage introduced during specimen preparation, or faulty imaging procedures, for example. However, during examinations, no increase in defect density was

ever observed. In fact, stacking fault tetrahedra occasionally were seen to suddenly disappear, so defect densities err on the low side rather than being too high. Also, it may be argued that as the control specimens of pure copper were satisfactorily examined and analyzed, giving results very different from the irradiated specimens that were prepared for microscopy and examined in exactly the same way, it is unlikely that the damage was introduced after the specimens were irradiated. Microscopy procedures incorporated stereoscopic examination so that we are sure that the defect clusters were definitely within the foil, and examples of stacking fault tetrahedra and triangular loops at densities as high as 15% of the total defect population were found confirming that handling and examination procedures can be eliminated as the source of defect clusters.

The possibility that defect damage was created during cool down following irradiation is also thought to be unlikely based on LASREF and DR-3 operating conditions. At the completion of the irradiation cycle, neutron flux is reduced rapidly and the specimen temperature then drops in both LASREF and OR-3. In the LASREF case, neutron flux and temperature are controlled independently, so that when irradiation is completed, the neutron flux drops almost instantaneously, and then the specimen temperature is allowed to decrease. In DR-3, shutdown is also rapid but the temperature is controlled in part by the neutron flux. However, reactor operators at DR-3 confirm that even though specimens from the present study were in reactor core during shut down, reactor cool down occurs in about 30 min., and therefore, dose accumulation below operating temperatures of 250 to 400°C would be limited. Studies of damage build up have shown that to reach defect cluster densities of 10^{17} cm^{-3} requires at least 10^{21} n/m^2 or 10^{17} n/cm^2 [30,34]. Therefore, at a flux rate of $3x10^{13}$ n/cm^2s, several thousand seconds at full power is required to produce the defect cluster densities observed in our study. Therefore, cool down effects are not believed to offer a consistent explanation for the creation of the defect clusters found in all irradiated specimens examined in this study.

The defect cluster damage found in FFTF/MOTA specimens probably did not arise from irradiation at 414 and 529°C. Completion of the irradiation cycle included a hold at approximately 310°C at reduced power for 21 days. At intervals lasting about two days, power was increased for one day causing specimens in the 414°C canister to reach approximately 340°C and specimens in the 529°C canister to reach approximately 390°C. Therefore, defect clusters found in specimens irradiated in FFTF/MOTA are probably characteristic of temperatures between 310 and 390°C and not the reported irradiation temperatures of 414 and 529%. Also, care must be taken in interpreting void and dislocation secondary nucleation behavior, as these may also be a consequence of shutdown procedures.

Implications of defect cluster development following irradiation at temperatures as high as 400°C

It is of interest to speculate on the consequences of defect cluster stabilization of neutron damage at temperatures on the order of 400°C. If cascade damage is able to stabilize at high temperature to densities of IO" cm^{-3} at high dose, then it is unlikely that the structure is identical to that found at low dose and shown to consist of a large fraction of vacancy clusters. Low fractions of stacking fault tetrahedra and triangular loops were found, unlike the case at lower dose. Therefore, the damage is probably interstitial in character, (not yet demonstrated in the present work) and is very different from the low dose case. Continued interstitial cluster development would provide an explanation for the observation of continued dislocation loop nucleation and growth at 529%. The loops would continue to grow from the defect clusters even though a well developed population of climbing dislocations was established. Also, the observation of continued void nucleation may be related. In effect, stabilization of defect clusters to high temperature may result in an extension of the swelling regime, beyond preconceived expectations, as was found in the present results at 529°C.

Consequences of different neutron spectrum and/or dose rate on microstructure and defect cluster development

A second surprising result from this work is that where it has been possible to compare the effect of neutron spectrum on microstructural development, little difference can be identified. Defect cluster development appears to be insensitive to neutron spectrum, dose rate or composition. Void number density response follows the trend identified by Brimhall and Kissinger," Labbe et al.[23,24] and Zinkle and Farrell[8], except for the DR-3 400°C result, and therefore appears to be insensitive to neutron spectrum. This is demonstrated in Figure 11, showing the present results of void density as a function of irradiation temperature in comparison with those of Brimhall and Kissinger based on irradiation to about 0.1 dpa in the Advanced Test Reactor (ATR), those of Labbe et al. to about 0.4 dpa in Siloe and Melusine, and those of Zinkle and Farrell based on irradiation to about 1.2 dpa in the Oak Ridge Reactor (ORR). The DR-3 result for 250°C and the LASREF irradiation at 400/220 agree very well with the other data sets, and the LASREF result for 335% overlaps the other data sets and fits directly in line with the FFTF data for pure copper. (The FFTF data for Cu-5Ni is also plotted to emphasize the consequence of nickel additions to void nucleation and agrees well with the Brimhall and Kissinger result.)

Therefore, irradiations in different neutron environments appear to give similar microstructural development, and predictions of behavior in a fusion environment may be adequately based on many irradiation facilities, irrespective of spectrum or dose rate, providing void nucleation is properly controlled, for example by maintaining the proper helium to dpa ratio for fusion.

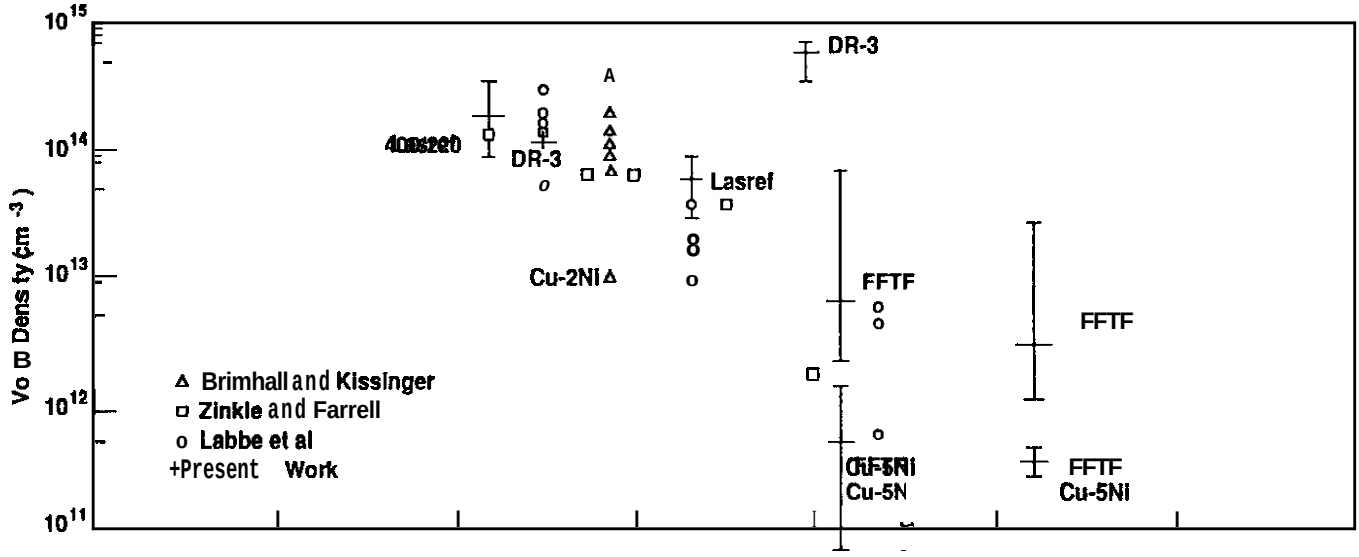


Figure 11. Void density as a function of irradiation temperature in comparison with earlier results from ATR, Siloe, Mélusine and ORR.[18,23,24]

Implications to ITER design

Several results obtained from this work are of particular note for ITER design. This work has shown that heat treatment (or retained dislocation density) plays an important role in controlling void nucleation and growth in pure copper and Cu-5Ni. Void size, void distribution and total swelling accumulation are therefore expected to be affected by processing parameters. Therefore, it will be necessary to test prototypic materials in order obtain accurate dimensional stability predictions.

However, this effort has also shown that defect cluster formation is insensitive to neutron energy, and therefore, the neutron spectrum selected for testing prototypic materials may not be important, as long as void nucleation is maintained at levels characteristic of the ITER environment.

Swelling is found to develop at temperatures as high as 529°C as a result of growth from a few very large voids, and evidence for continued void nucleation suggests that the swelling rate can be expected to increase with increasing dose. Therefore, swelling response in copper and copper based alloys may be of concern at higher temperatures than had previously been expected. If ITER applications require doses higher than 30 dpa, further high dose tests are needed. Effects due to transmutation on enhanced high temperature swelling should be reinvestigated when a fusion irradiation environment is available.

CONCLUSIONS

Specimens of pure copper and a copper alloy containing 5 atomic percent nickel have been examined by transmission electron microscopy following irradiation in DR-3, FFTF/MOTA and LAMPF at about 400°C, in OR-3 at 250°C, in LAMPF at 335°C and in FFTF/MOTA at 529°C. Most conditions developed void swelling, all were found to contain defect clusters, but the initial dislocation structure controlled the irradiated dislocation microstructure. Also, comparisons between response in pure copper and Cu-5Ni indicate that transmutation will affect microstructural development and bulk properties. Based on limited comparisons of irradiation at 335°C, high energy spallation neutrons do not appear to have any significant effect on swelling at low dose. The observations of defect clusters in all conditions examined and significant swelling at 529% were unexpected and demonstrate the need for further research in order to predict performance in ITER.

FUTURE WORK

This work will be continued when specimens become available.

ACKNOWLEDGEMENTS

This work was performed at RISØ National Laboratory and partly funded by that institution. One of the authors, D. S. Gelles, would like to thank the Danish authorities for helping to sponsor this work, his Danish colleagues for their kind hospitality and the U.S. Department of Energy for allowing the assignment in Denmark.

REFERENCES

1. F. A. Garner, H. L. Heinisch, R. L. Simons and F. M. Mann, Rad. Eff. and Defects in Solids, 113 (1990) 220.

2. T. Leffers, B. N. Singh, S. N. Buckley and S. A. Manthorpe, J. Nucl. Mater., 118 (1983) 60.

3. P. Barlow, T. Leffers and 8. N. Singh, "The Activation Energy for Loop Growth in Cu and Cu-Ni Alloys," Riso-M-2129, August 1978.

4. T. Leffers, J. B. Bilde-Sorensen and P. Barlow, Scand. J. Metall., 6 (1977) 29.

5. P. Barlow and T. Leffers, Phil. Mag., 36 (1977) 565.

6. J. B. Bilde-Sorensen, T. Leffers and P. Barlow, Phil. Mag., 36 (1977) 585.

7. T. Leffers, B. N. Singh and P. Barlow, "Void Formation and Growth in Copper-Nickel Alloys During Irradiation in the High Voltage Electron Microscope," RISO-M-1937 May (1977). Alternatively, see: B. N. Singh and T. Leffers, in High Voltage Electron Microscoov 1977, Proc. 5th Int. Conf. on High Voltage Electron Microscopy, Kyoto, Aug. 29 - Sept. 1, 1977, Eds. T. Imura and H. Hashimoto, Japanese Society of Electron Microscopy, Tokyo (1977) 581.

8. N. Sakaida, N. Sekimura and S. Ishino, J. Nucl. Mater., to be published in the ICFRM-4 proceedings.

9. T. Bullough, C. A. English and B. L. Eyre, in Vacancies and Interstitials in Metals and Allovs, (Trans Tech. Publications, Ltd., Switzerland, 1987) 1069.

10. T. Muroga, N. Yoshida, N. Tsukuda, K. Kitajima and M. Eguchi, Ibid, 1087.

11. I. Ishida, T. Yoshiie, S. Sasaki, A. Iwase, T. Iwata and M. Kiritani, J. Nucl. Mater., 155-157 (1988) 417.

12. G. Szenes, K. Havancsak, T. Ungar, A. Cziraki and V. A. Schegolev, J. Nucl. Mater., 155-157 (1988) 1089.

13. D. J. Mazey and F. Menzinger, J. Nucl. Mater., 48 (173) 15.

14. B. N. Singh, T. Leffers and A. Horsewell, Phil. Mag., 53 (1986) 233.

15. J. L. Brimhall and H. E. Kissinger, Rad. Eff. 15 (1972) 259.

16. R. 8. Adamson, W. L. Bell and P. C. Kelly, J. Nucl. Mater., 92 (1980) 149.

17. S. J. Zinkle and R. L. Sindelar, J. Nucl. Mater. 155-157 (1988) 1196.

18. S. J. Zinkle and K. Farrell, J. Nucl. Mater. 168 (1989) 262.

19. C. A. English, J. Nucl. Mater., 108-109 (1982) 104.

20. A. Horsewell, B. N. Singh, S. Proennecke, W. F. Sommer and H. L. Heinisch, J. Nucl. Mater., to be published in the ICFRM-4 proceedings, PNL-SA.

21. A. Wolfenden, Rad. Effects, 15 (1972) 255.

22. H. R. Brager, J. Nucl. Mater., 141-143 (1986) 163.

23. M. Labbe and J. P. Poirier, J. Nucl. Mater., 46 (1973) 86.

24. M. Labbe, G. Brebec and J. P. Poirier, J. Nucl. Mater., 49 (1973/74) 232.

25. H. R. Brager, J. Nucl. Mater., 141-143 (1986) 79.

26. F. A. Garner, H. R. Brager and K. R. Anderson, J. Nucl. Mater., to be published in the ICFRM-4 proceedings, PNL-SA-16984.

27. F. A. Garner, H. R. Brager and K. R. Anderson, "Density Changes Of Generation 1.5 and 2.0 Copper Alloys Irradiated at 411-414 and 529°C in FFTF-MOTA," in Fusion Reactor Materials Semiannual Progress Report for Period ending September 30, 1989, DOE/ER-0313/7, 223.

28. K. E. Anderson, Ph. D. Thesis, U. of Illinois, 1990

29. H. R. Brager, F. A. Garner and N. F. Panayotou, J. Nucl. Mater., 103 & 104 (1981) 955.

30. N. Yoshida, Y. Akashi, K. Kitajima and M. Kiritani, J. Nucl. Mater., 133 & 134 (1985) 405.

31. S. J. Zinkle, J. Nucl. Mater., 150 (1987) 140.

32. S. J. Zinkle, J. Nucl. Mater., 155-157 (1988) 1201.

33. M. Kiritani, J. Nucl. Mater., 155-157 (1973) 113.

34. Y. Satoh, I. Ishida, T. Yoshiie and M. Kiritani, J. Nucl. Mater., 155-157 (1988) 443.

35. H. Fukushima, Y. Shimomur and M. W. Guinan, J. Nucl. Mater., 155-157 (1988) 1205.

36. S. Kojima, S. J. Zinkle and H. L. Heinisch, J. Nucl. Mater., to be published in the ICFRM-4 proceedings, PNL-SA-18234.

37. Fax of August 24, 1989 from B. Thiele, Kernforschungsanlage Julich, West Germany to W. F. Sommer, Los Alamos National Laboratory on the temperature history of KFA capsule #2.

38. K. R. Anderson, "The Properties of Oxide Dispersion and Spinodally Strengthened Copper Alloys Following High Temperature Neutron Environment Exposure," Ph. D. Thesis, U. of Illinois, 1990.

39. J. M. Muncie, D. Phil Thesis, University of Sussex, U.K., 1971.

40. K. Farrell and S. J. Zinkle, "Void Swelling and Defect Cluster Formation in Reactor-Irradiated Copper," Fusion Reactor Materials Semiannual Progress Report for the Period Ending September 30, 1987, DOE/ER-0313/3, 90.

STATUS OF COPPER IRRADIATION EXPERIMENTS - F. A. Garner and M. L. Hamilton (Pacific Northwest Laboratory)[a], D. J. Edwards (University of Missouri-Rolla), B. N. Singh (RISØ National Laboratory), J. F. Stubbins (University of Illinois), T. Shikama (Tohoku University), S. J. Zinkle (Oak Ridge National Laboratory), P. Samal, (SCM Metal Products)

OBJECTIVE

The objective of this effort is to provide data on the radiation and thermal response of copper alloys intended for both near term and long term applications in fusion systems.

SUMMARY

A variety of FFTF irradiation studies and out-of-reactor studies are in progress to determine the response of copper alloys to the environment anticipated for fusion service. An updated review of these various studies is Dresented.

PROGRESS AND STATUS

Introduction

In a previous report an overview was presented of copper irradiation programs in progress in FFTF that were directed toward fusion applications.[1] These included a Generation 1.0 exploratory experiment to ~100 dpa, several more focused experiments (Generations 1.5 and 2.0) to 150 dpa, a recent PNL/RISØ lower fluence experiment to complement studies in other irradiation facilities, and another PNL/RISØ experiment involving a series of simple copper alloys addressing solute and helium effects. Considerable progress has been achieved in these studies in the intervening period and several new studies have been initiated. A brief review of these is presented below.

Generation 1.0 Exploratory Experiment

The irradiated specimens have all been examined and the results reported in references 2-4. The major conclusion of this experiment is that internally oxidized dispersion strengthened alloys appear to offer the most promise for fusion applications. The only work remaining to be completed is the measurement of tensile properties and electrical conductivities of control specimens aged at temperatures from 300 to 700°C for times as long as 10,000 or 30,000 hours. This effort will focus on discriminating between the effects of radiation and temperature in determining the response of irradiated Generation 1.0 alloys. This work will be completed at Pacific Northwest Laboratory (PNL) during the summer of 1991 by NORCUS students D. J. Edwards (University of Missouri-Rolla) and M. B. Toloczko (University of California at Berkeley) working with F. A. Garner and M. L. Hamilton.

Generation 1.5 and 2.0 Experiments

These two experiments focus primarily on various methods of dispersion strengthening of copper. The major conclusions to date are that no dispersion strengthened alloys yet tested outperform the Glidcop alloys produced by SCM Metal Products and that the swelling of these alloys depends inversely and strongly on the amount of dispersoid. It was also shown that high oxygen levels destroy the resistance to swelling in some dispersion strengthened alloys. Some precipitation strengthened alloys also show promise for fusion applications. The results of these studies were published in refs. 3 and 5-8. Additional data on the behavior of pure copper and several spinodally strengthened alloys were published in other reports.[9,10]

Analysis up to 50 dpa is complete on these experiments. The Generation 2.0 experiment continued on to 100 and 150 dpa in FFTF cycles 10 and 11 and is now undergoing examination at the 100 dpa level. Density measurements are complete and are reported in reference 6.

Helium Effects ExDeriment in MOTA-IF

As shown in Table 1, high purity copper with and without ~100 appm helium was irradiated to ~30 dpa at 385°C and also at 410°C. The helium was introduced in two ways. One set of specimens were implanted by a cyclotron (VEC Harwell) at ~50%. The others were irradiated in the LAMPF Spallation Radiation Effects Facility, also at ~50°C, to produce helium and other transmutation products. Microscopy data are now available at RISØ for the 410°C irradiation experiment and data analysis is in progress. The results will be presented at the Fifth International Conference on Fusion Reactor Materials. Cu-5Ni, Cu-5Al and Cu-5Mn were also irradiated in this experiment and will be examined later.

(a) Pacific Northwest Laboratory is operated for the U.S. Department of Energy by Battelle Memorial Institute under Contract DE-AC06-76RLO 1830.

Table 1. Copper Alloys Irradiated in RISØ/PNL Experiment[a] on Pure Metals and Model Alloys in MOTA-IF

Alloy[b]	Packet LM2 385°C	Packet LN3 410°C
Cu (OFHC)	1[c]	1
cu (99.999%)	1	1
Cu (100 appm He implanted)	--	1
Cu (100-150 appm He produced by irradiation in LAMPF)	--	1
Cu-5Ni	2	1
Cu-5Al	2	1
Cu-5Mn	2	1

(a) Other specimens are pure metals (Ni, W, Mo, Pt, Au, Ag), some with helium preinjection.
(b) All copper alloys are in the annealed condition.
(c) Number of TEM disk specimens in each packet.

Table 2. Copper Alloy Specimens in MOTA-1G

Alloy	Condition	Specimen Engraving Code[a]	3 dpa 373°C (OE01/OE03)[b]	10 dpa 418°C (OE02/OE0U)[b]
Marz Cu	Annealed	1	3/2[c]	3/2
Cu-5Ni	Annealed	2	3/2	3/2
Cu-5Ni	40% CW	3	3/2	3/2
Cu-5Mn	Annealed	4	3/2	3/2
Cu-5Mn	40% CW	5	3/2	3/2
CuBe	Solutionized	6	3/2	3/2
CuBe	Solutionized and Aged	7	3/2	3/2
CuBeNi	Solutionized	8	3/2	3/2
CuBeNi	Solutionized and Aged	9	3/2	3/2
CuAl20	20% CW	10	3/2	3/2
CuAl25	50% CW	11	3/2	3/2
CuAl20	Stress Relieved	12	3/2	3/2
CuAl25	Stress Relieved	13	3/2	312

(a) This simple code is not a standard MOTA code. These specimens will be de-encapsulated and examined at RISØ.
(b) These designations are packet codes. There are two identical packets at each temperature, allowing for the possibility of not only reaching 3 and 10 dpa, but 6 and 20 dpa as well.
(c) This code means 3 TEM disks in each of two identical packets.

Low Fluence Studies in MOTA-1G and MOTA-2B

The RISØ group is particularly interested in the relatively lower displacement levels that are relevant to NET applications. They are also interested in both technologically and fundamentally oriented alloys.

A series of alloys (Cu, Cu-5Ni, Cu-5Mn, CuBe, CuBeNi, CuAl20, CuAl25) in a variety of starting conditions were therefore irradiated in MOTA 1G to ~3 dpa at 313°C and ~10 dpa at 418°C. An identical set of specimens will be carried on in MOTA 2B to ~6 and 20 dpa respectively. The MOTA 1G experiment has been removed from reactor and will be examined both at PNL and RISØ in the next reporting period.

Generation 3.0 ExDeriment in MOTA-2B

Due to the uncertainty in continued FFTF operation beyond Cycle 12, the Generation 3.0 experiment was targeted for a single discharge only. This experiment explores a variety of questions that arose from previous irradiation experiments. One of these questions concerns the role of oxygen in radiation-induced microstructural evolution and uses specimens identical to those employed in an earlier ion irradiation study.[11] The role of cold work level on swelling of pure copper will also be studied, using materials prepared for an earlier electron irradiation study.[12] As shown in Figure 1, the effect of cold work on electron-induced swelling is not monotonic.

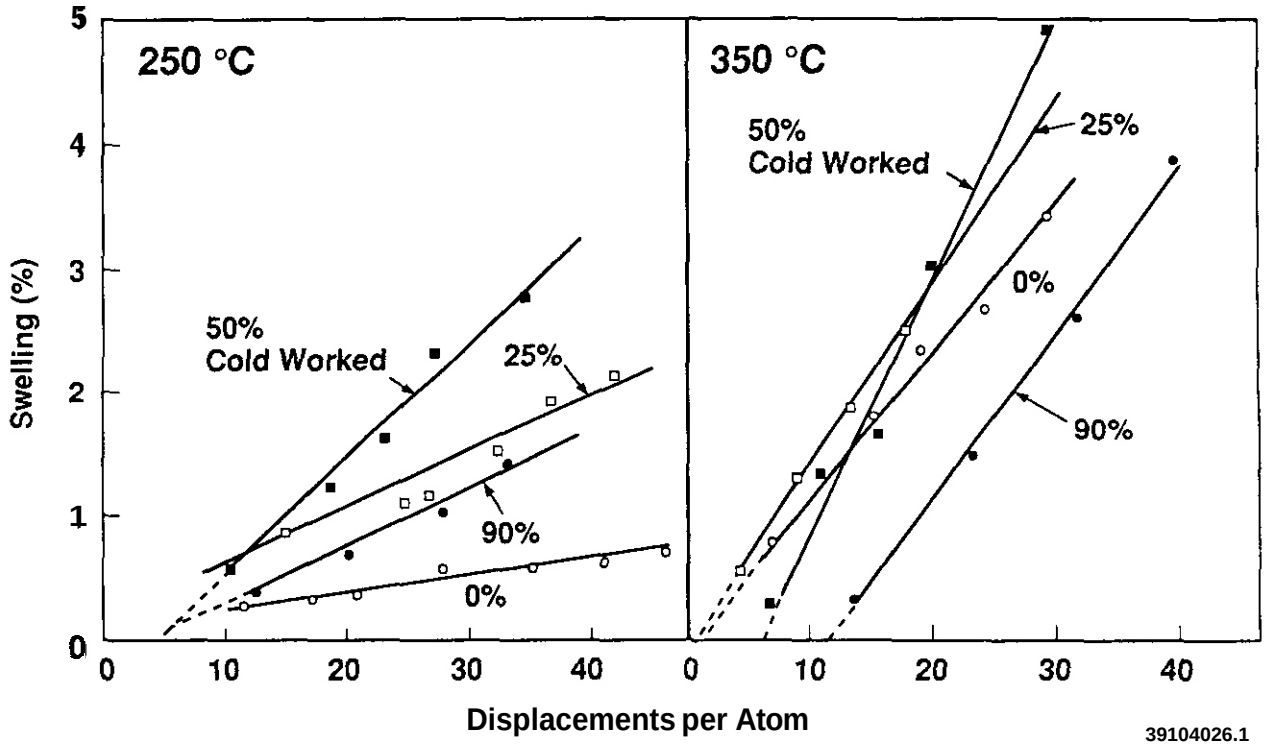


Figure 1. Effect of cold work level on electron induced swelling of 99.999% copper.[12]

Table 3. Braze Alloy Compositions and Braze Temperatures[a]

Ag-Cu Eutectic:	Ag-72%, Cu-28% Eutectic m.p. - 780°C Braze Temp. - 796°C
Au-Cu (50/50):	Au-50%, Cu-50% Solidus - 995°C, Liauidus - 970°C Braze Temp. - 980°C
TiCuSil:	Ti-4.5%, Cu-26.7%, Ag-68.8% Solidus - 830°C, Liquidus - 850°C Braze Temp. - 870°C
TiCuNi:	Ti-70%, Cu-15%, Ni-25% Solidus - 910°C, Liauidus - 960°C Braze Temp. - 980°C

(a) All brazes were performed by SCM Metal Products.

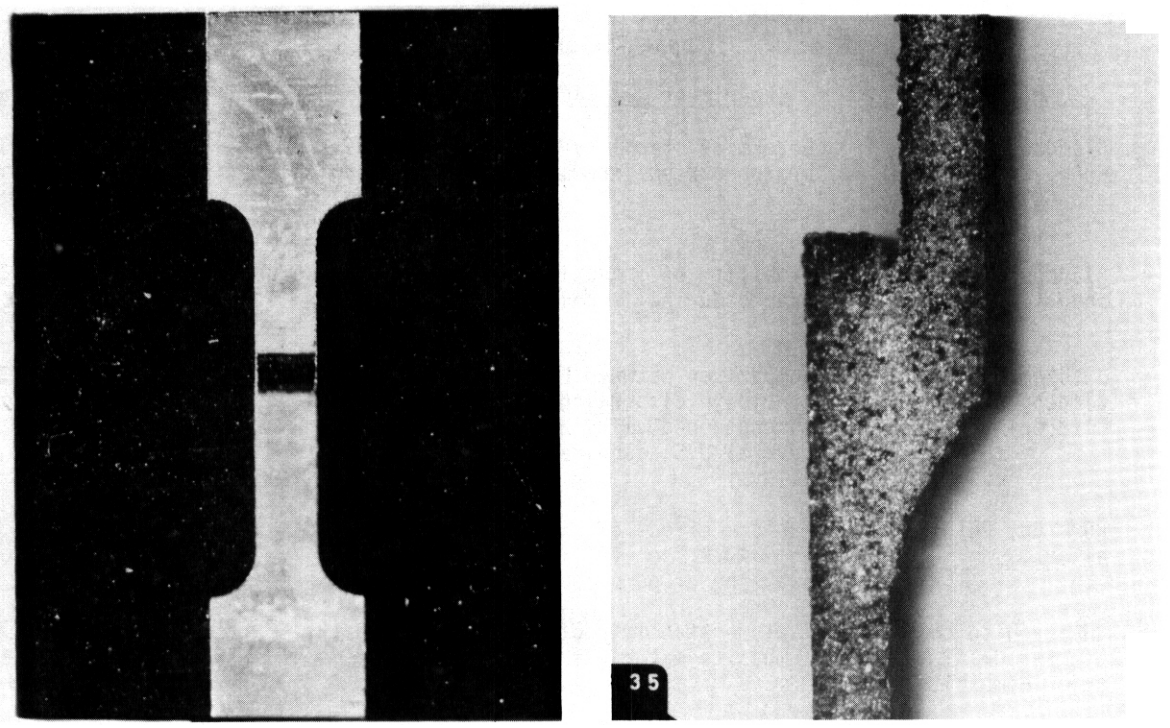


Figure 2. Lapped miniature tensile specimen (1.7 mm long, gauge section 5.1 mm long by 1.0 mm wide) produced by electrical discharge machining from brazed, overlapped sheet stock.

Another study addresses the stability of various brazing methods for copper alloys. Both induction brazing and various brazing alloys (Table 3) will be investigated. The latter were prepared either as sandwiches or lapped sheets by SCM Metal Products. TEM disks were then punched from the former and miniature tensile specimens were produced by electrical discharge machining (EDM) from the latter. Figure 2 shows the miniature tensile specimens. After irradiation these specimens will be tested on a precision horizontal tensile frame used for previous studies on copper and other alloys.

A variety of new materials will also be irradiated in Generation 3.0. Two of these are composite materials supplied to Oak Ridge National Laboratory (ORNL) by the MER Corporation. In addition, a comparative irradiation experiment in Generation 3.0 will involve the Glidcop A125 alloy used in previous studies, a new Glidcop alloy containing both Al_2O_3 and Nb "fibers" and the European candidate alloy supplied by the RISØ laboratory. The latter alloy utilizes ZrO_2 as the dispersoid. Table 4 describes both the Generation 3.0 experiments and other copper experiments that will be irradiated with Generation 3.0 in MOTA 2B.

Irradiation Tests in Other Reactors

Since FFTF operates only at temperatures ≥365°C, irradiation tests for ITER application are required in other reactors with lower coolant inlet temperatures, Negotiations are now in progress to conduct joint copper irradiation studies in HFR (Petten, Netherlands) and SM-2 (Dimitrovgrad, USSR).

Thermal Stability Study of Glidcop CuAl25

The onset of swelling in Glidcop alloys appears to be related to their thermal stability and potential for recrystallization.[8] A study has therefore been initiated which explores the thermal response of CuAl25 during aging at temperatures from 400 to 900°C for times as long as 1000 hours. Punched TEM disks and miniature tensile specimens made by EDM were prepared at PNL and are currently being aged at the University of Illinois. Tensile tests will be conducted at PNL in the summer of 1991 by M. A. Mitchell and J. F. Stubbins (both on NORCUS appointments), working with M. L. Hamilton and F. A. Garner. Hardness measurements and microscopy analysis will be conducted at the University of Illinois.

Fatigue Testing of Copper Alloys

The RISØ Laboratory is committed to providing fatigue data on copper alloys for the European Community (E.C.) fusion materials effort. In areas where U.S. and E. C. interests coincide, such work will be conducted jointly. The currently proposed specimen matrix includes pure copper, one or more dispersion strengthened alloys, and CuBeNi. Based on the results of recent development efforts there is still Some

Table 4. Copper Experiments in MOTA 2B

Lab	Materials	Experiment description	Specimen types	Irradiation conditions
PNL/SCM	Glidcop A125 with CuAg, CuAu, CuTiNi, and CuTiAg brazes	Determine stability of brazes during irradiation	TEM disk sandwiches, lapped minitensiles	10-30 dpa at 365-600°C for discharge after MOTA 2B
ORNL/PNL	Glidcop All5 induction brazes	Stability of induction brazes during irradiation	transverse braze TEM disks	10-30 dpa at 365, 400°C for discharge after MOTA 2B
PNL/RISØ	Ottokempu Cu-ZrO_2 Glidcop A125, Glidcop-Nb	Comparison between European candidate dispersion strengthened alloy and several U.S. candidate alloys	TEM disks, minitensiles (Glidcop-Nb only)	10-30 dpa at 365-600°C for discharge after MOTA 2B
PNL/RISØ/ ORNL	Pure Cu, Cu binary alloys	Explore effect of oxygen, cold work, solutes, etc. on swelling of pure copper	TEM disks	10-30 dpa at 365-500°C for discharge after MOTA 2B
ORNL/PNL	tu-graphite composite and Cu-A1 0,-W fiber composite	Explore stability of new composite materials	TEM disks	10-20 dpa at 365, 400°C for discharge after MOTA 2B
PNL/RISØ	Pure Cu and various Cu alloys	Low exposure data on alloys used in European/U.S. spectral effects' experiments in other reactors; also solute segregation to enable extrapolation of transmutation effects to other spectral environments	TEM disks	3-10 dpa at 373-418°C after MOTA 2A; for discharge after MOTA 2B at 6-20 dpa

flux in the choice of a European candidate dispersion strengthened alloy. Working with PNL, researchers at RISØ and the University of Illinois have agreed to conduct tests of fatigue (room temperature to 400°C) and fatigue-creep interaction (hold times up to one hour at 250°C). Most of the specimens will be made in Denmark. Assistance will be provided to the University of Illinois by PNL and the NORCUS program for that fraction of the work conducted in the U.S.

FUTURE WORK

This effort will continue with a strong emphasis on planning for irradiation in other reactors at temperatures below 350°C.

REFERENCES

1. F. A. Garner, M. L. Hamilton, K. R. Anderson, J F. Stubbins, B. N. Singh, A. Horsewell and W. F. Sommer "Overview of Copper Irradiation Programs", Fusion Reactor Materials Semiannual Progress Report DOE/ER-0313/6, pp. 351-356.

2. F. A. Garner and K. R. Anderson, "Conductivity Changes Observed in Generation 1.0 Copper Alloys Irradiated at 430°C TO 16-98 dpa", Fusion Reactor Materials Semiannual Progress Report DOE/ER-0313/7, Sept. 30, 1989, pp. 220-227.

3. F. A. Garner, K. R. Anderson and T. Shikama "Radiation-Induced Changes in Electrical Conductivity of a Wide Range of Copper Alloys", Fusion Reactor Materials Semiannual Progress Report DOE/ER-0313/9, (in press).

4. F. A. Garner and H. R. Brager, "Neutron Induced Changes in Density of Copper Alloys", in ref. 3.

5. K. R. Anderson, F. A. Garner, M. L. Hamilton and J. F. Stubbins, "Electrical Resistivity Changes Induced in Copper Alloys by Fast Neutron Irradiation", in ref. 1, pp. 357-369.

6. F. A. Garner, H. R. Brager and K. R. Anderson, "Density changes of Generation 1.5 and 2.0 Copper Alloys Irradiated at 411-414°C and 529°C in FFTF/MOTA", in ref. 2, pp. 223-231.

7. K. R. Anderson, F. A. Garner, M. L. Hamilton and J. F. Stubbins, "Tensile Properties and Fracture Behavior of Dispersion Strengthened Copper Alloys Irradiated in FFTF/MOTA", in ref. 2, pp. 213-219.

8. K. R. Anderson, F. A. Garner, M. L. Hamilton and J. F. Stubbins, "Mechanical Property Changes and Microstructure of Dispersion Strengthened Copper Alloys After Neutron Irradiation at 411, 414 and 529°C", in ref. 3.

9. K. R. Anderson, F. A. Garner and J. F. Stubbins "Unusual Tensile and Fracture Behavior of Pure Copper at High Levels of Neutron-Induced Swelling", Fusion Reactor Materials Semiannual Progress Report DOE/ER-0313/8, March 31, 1990, pp. 243-253.

10. K. R. Anderson, J. F. Stubbins and F. A. Garner, "The Properties of Selected Spinodally Strengthened Copper Alloys Following High Temperature Neutron Irradiation", submitted to Nuclear Science and Engineering.

11. S. J. Zinkle and E. H. Lee, "Effect of Oxygen on Vacancy Cluster Morphology", Met. Trans. A, 21A (1990), pp. 1037-1051.

12. T. Leffers, B. N. Singh and P. Barlow, RISØ-M-1937, May 1977.

NEUTRON-INDUCED CHANGES IN DENSITY OF COPPER ALLOYS - F. A. Garner, Pacific Northwest Laboratory,(") and H. R. Brager, Westinghouse Hanford Company

OBJECTIVE

The objective of this effort is to identify those copper alloys which offer promise as high heat flux materials for fusion applications.

SUMMARY

Density change measurements have been completed on the Generation 2.0 copper alloy experiment at 411°C after reaching 100 dpa. The Glidcop alloy CuAl25 continues to exhibit excellent resistance to void swelling. Welding and high oxygen levels both degrade the swelling resistance of oxide dispersion- strengthened alloys. The alloy Cu-2.0Be also resists swelling and appears to be densifying in response to the continued formation of the transmutant nickel.

PROGRESS AND STATUS

Introduction

In an earlier report, the neutron-induced swelling was reported for a number of copper alloys included in a first generation exploratory program designed to assess the suitability of such alloys for high heat flux diverter applications.[1] These allays reached 16, 47, 63 and 98 dpa in FFTF/MOTA at a reported temperature of ~450°C. This temperature assignment included an upper bound estimate of 30°C gamma heating above the ambient coolant temperature of 420%. More recent calculations now yield 8-10°C gamma heating such that 430°C is a better temperature assignment for that experiment.

As documented in a separate report, the earlier results of the first generation experiment led to two successively more focused experiments, designated Generation 1.5 and 2.0.[2] These experiments involved the irradiation of some but not all of the Generation 1.0 alloys, but also included a wider variety of alloys hardened either by dispersed oxides of various types or by spinodal decomposition. While Generation 1.5 reached 34 dpa at 414°C and 32 dpa at 529°C, Generation 2.0 has reached 50 and 100 dpa at 411°C and is still being irradiated. The last specimens of Generation 2.0 alloys at ~400°C and 150 dpa will be discharged from the current MOTA cycle.

An earlier report presented the results of density change measurements for the Generation 1.5 and 2.0 alloys for displacement levels of 50 dpa or lower.[3] Measurements are now complete for the Generation 2.0 specimens at 411°C and 100 dpa. A list of the alloys and their processing conditions is presented in Table 1.

Results

Figures 1 and 2 present the accumulated swelling data for all fluences and temperatures measured in Generations 1.5 and 2.0. While some alloys have yet to show swelling at 100 dpa, others have reached levels of 50 to 70%. The highest swelling levels were reached by a group of oxide dispersion-strengthened (ODS) alloys known to have high oxygen levels, while the lowest swelling alloy is the dispersion-strengthened Glidcop alloy CuAl25, which has a relatively low level of oxygen.

Figure 3 compares the swelling observed in pure copper and Cu-5Ni in five separate irradiation tests conducted in three different reactors at ~400°C. Adding the most recent datum for pure copper at 100 dpa confirms the reproducibility of the swelling phenomenon at ~400°C. Both Cu and Cu-5Ni swell at a rate of ~0.5%/dpa.

As shown in Figure 4, the swelling of Glidcop alloys depends on the oxide content and possibly on the cold work level. These alloys are designated by their aluminum content. CuAl25 contains 0.25 wt.% of aluminum in the form of Al_2O_3 and CuAl15+8 contains 0.15 wt.% aluminum and ~100 appm boron. The progressive densification observed in CuAl25 may represent the influence of accumulating transmutants, primarily nickel and zinc. Laser welding was found to completely destroy the swelling resistance of the Glidcop alloy and accelerate the swelling of the ODS alloy. The behavior of the welded Glidcop alloy is shown in Figure 5. Several other ODS alloys prepared by mechanical alloying (CuCr and CuHf) were found to swell at levels intermediate to those of the Glidcop and ODS alloys, as shown in Figure 6. The post-irradiation microstructures of all the dispersion-strengthened allays are discussed in reference 4.

(a) Operated for the U.S. Department of Energy by Battelle Memorial Institute under Contract DE-AC06-76RLO 1830.

Table 1
Composition and Final Processing Conditions of Copper Alloys

Allov	Composition (wt%)	Final Processina Condition
Marz Cu	99.99 Cu	Annealed
Cu-5Ni	Cu - 5% Ni	Annealed
Cu-Be	Cu - 2% Be	Annealed, Aged 2 hr 320°C
CuNiBe	Cu-1.8% Ni-0.3% Be	Annealed, Aged 3 hr 482°C
CuNiBe	Cu-1.8% Ni-0.3% Be	20% CW, Aged 3 hr 482°C
CuNiBe	Cu-1.8% Ni-0.3% Be	20% CW, Aged 9 hr 540°C
MZC	Cu-0.9% Cr-0.1% Zr-0.05% Mg	90% CW, Aged 1/2 hr 475°C
MZC	Cu-0.9% Cr-0.1% Zr-0.05% Mg	90% CW, Aged 1 hr 500°C
MZC (MIT #2)	Cu-0.9% Cr-0.1% Zr-0.05% Mg	50% CW. Aaed 1 hr 500°C
MZC (MIT #3)	Cu-0.9% Cr-0.1% Zr-0.05% Mg	Annealed,-Aged 1 hr 500°C
CuAl25	0.25% Al as Alumina	50% CW
CuAl25	0.25% Al as Alumina	50% CW + welded
CuAl20	0.20% Al as Alumina	20% CW
CuAl15+B	0.15% Al as Alumina <200 ppm Boron	Annealed
CuCr	3.5% Cr as Cr Oxide	20% CW, 1/2 hr 450°C
CuHf	1.1% Hf as Hf Oxide	20% CW, 1/2 hr 450°C
ODS-l	0.25% Mg, 1% Alumina	40% CW
ODS-1	0.25% Mg, 1% Alumina	40% CW t welded
ODS-2	0.25% Mg, 1% Alumina	40% CW
ODS-3	0.5% Mg 1% Zr Oxide	40% CW
ODS-4	0.5% Mg, 1% Alumina	40% CW
CuNiTi (VK)	Cu-5.0% Ni-2.5% Ti (MIT #3)	Solutionized and Aged
CuNiTi (VL)	Cu-5.0% Ni-2.5% Ti (LASL)	Solutionized and Aged

Figure 6 also shows the swelling behavior for those alloys involving solute modification and precipitation-strengthening. Note in some precipitation strengthened alloys that cold working prior to irradiation actually increases swelling. This behavior was also observed in the Generation 1.0 study and reflects the influence of cold work on precipitation.' Densification of Cu-2.0Be at higher fluence probably reflects additional precipitation of Be from solution as nickel is formed via transmutation. The phenomenon was also observed in the Generation 1.0 experiment.[5]

CONCLUSIONS

Density change measurements at 411°C and 100 dpa confirm the superiority of the Glidcop alloys for resistance to void swelling. Welding or lowering of the oxide dispersoid level leads to higher swelling in the Glidcop alloys. There may also be some influence of the cold work level.

FUTURE WORK

This work will continue, focusing on measurements of radiation-induced microstructure, changes in electrical resistivity, and changes in tensile properties and fracture mode.

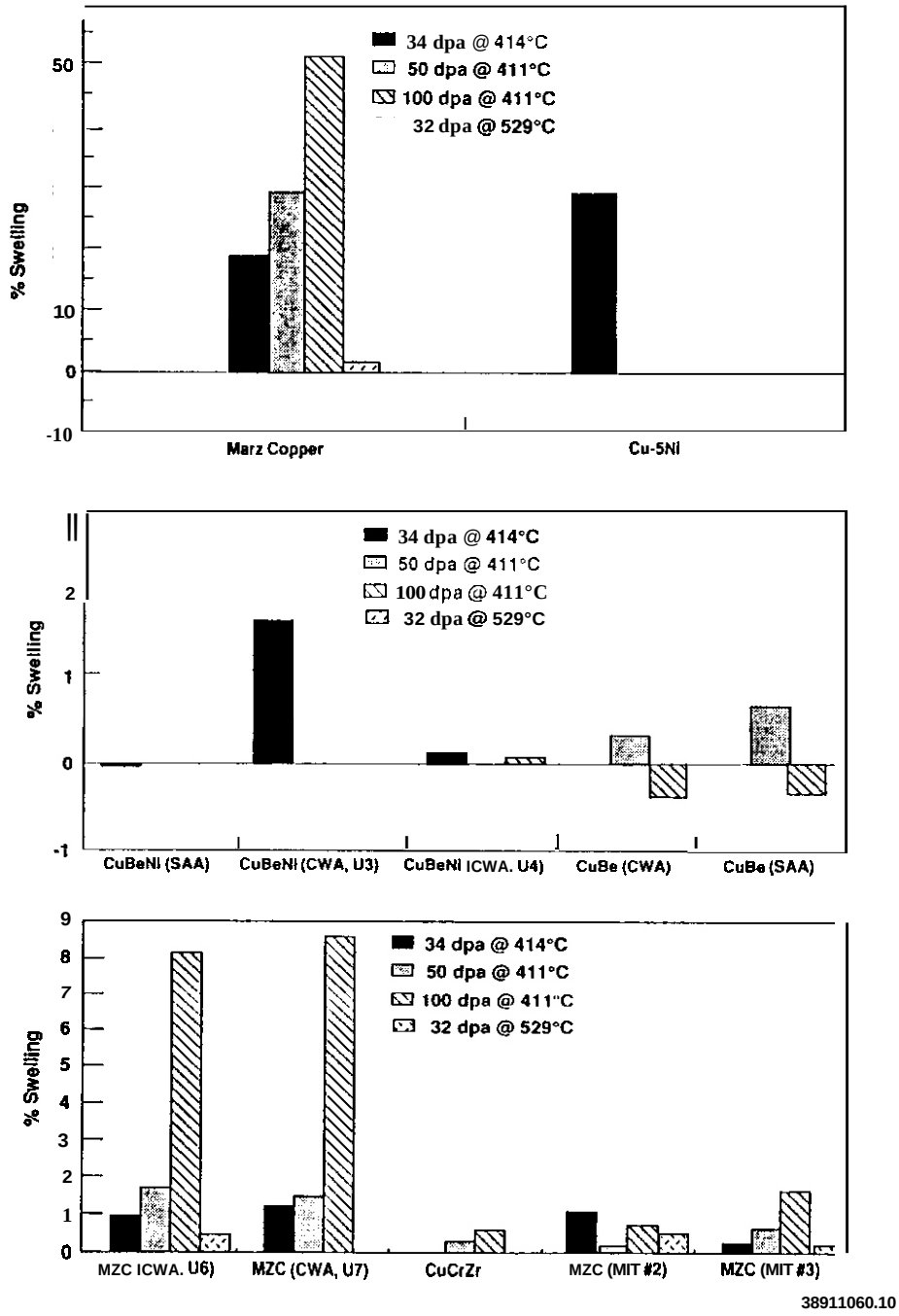


Figure 1. Swelling observed in various copper alloys irradiated in Generations 1.5 and 2.0.

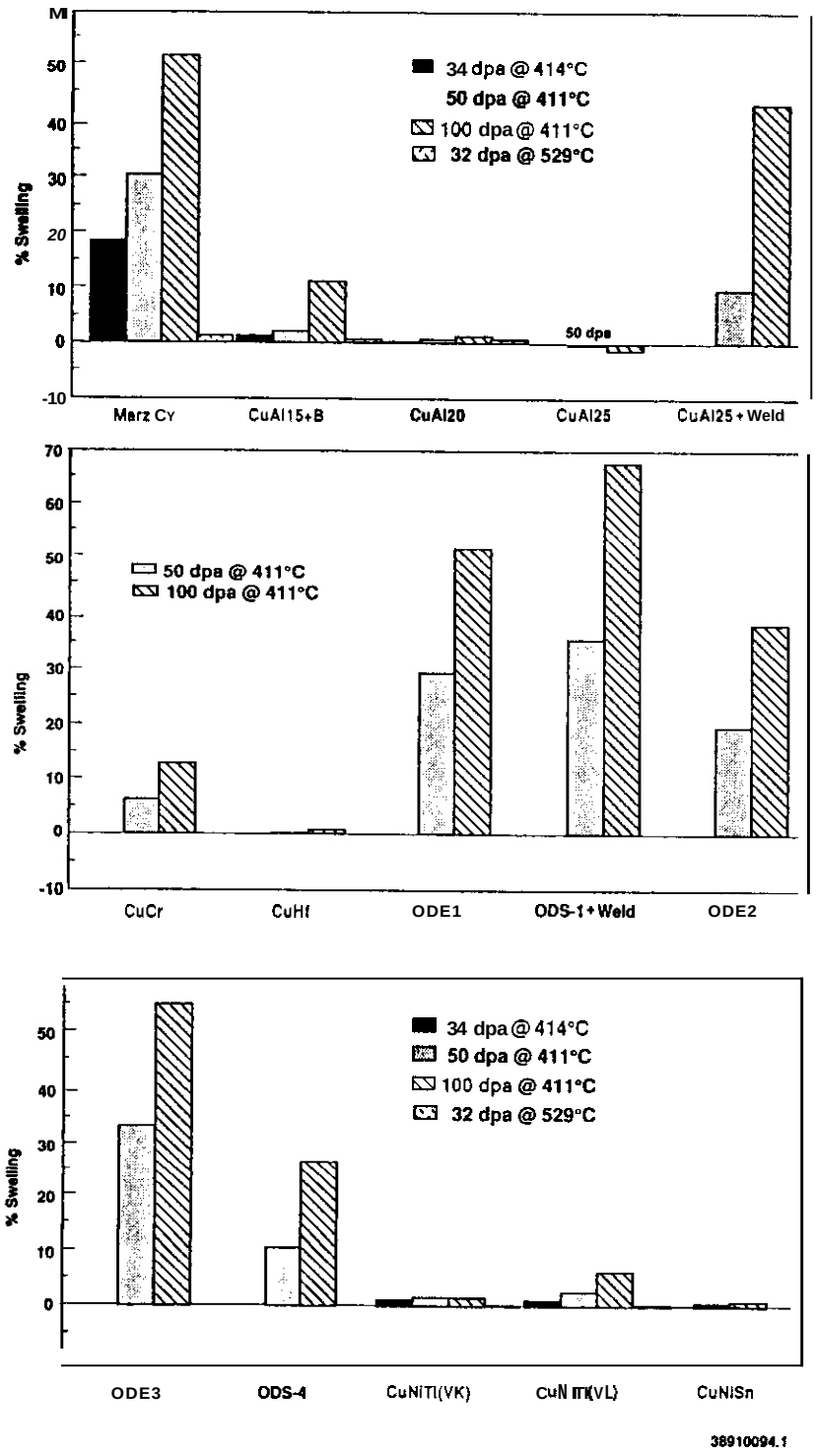


Figure 2. Swelling observed in various copper allays irradiated in Generations 1.5 and 2.0.

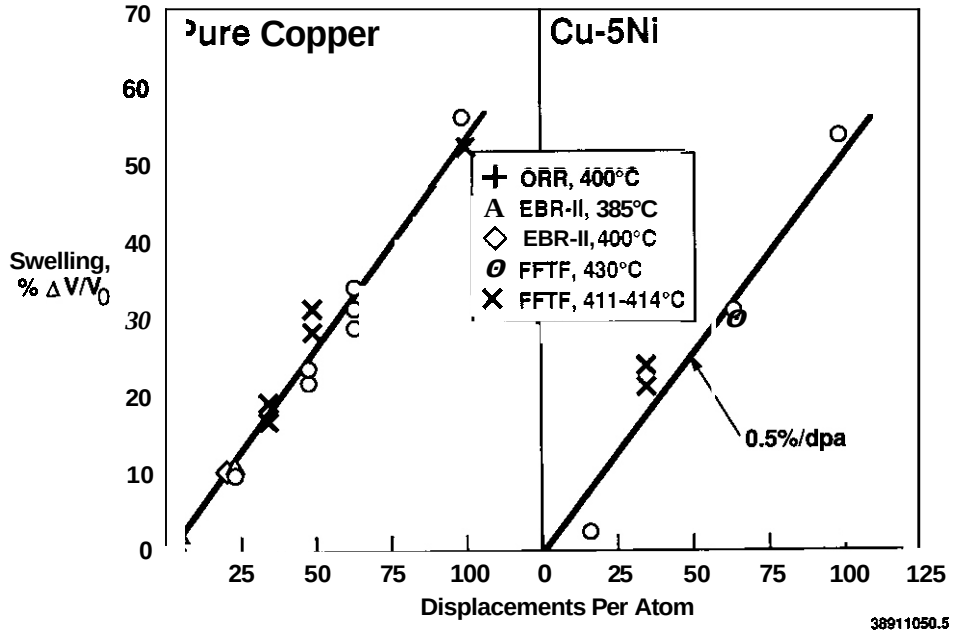


Figure 3. Comparison of swelling behavior at 385-430°C of pure copper and Cu-5 wt% Ni in various irradiation experiments.

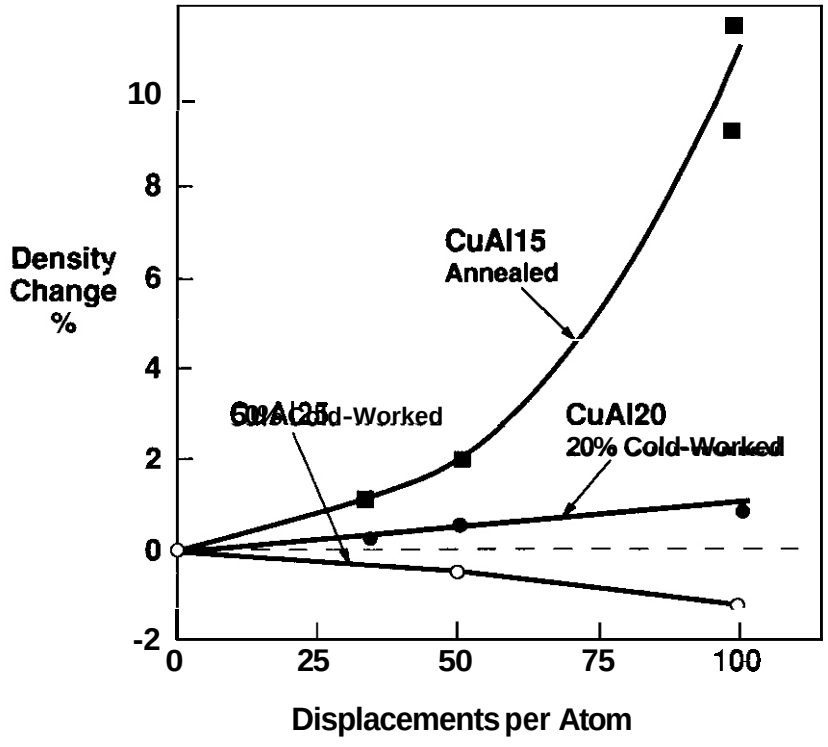


Figure 4. Dependence of swelling of Glidcop alloys at 411-414°C on Al_2O_3 content and starting condition

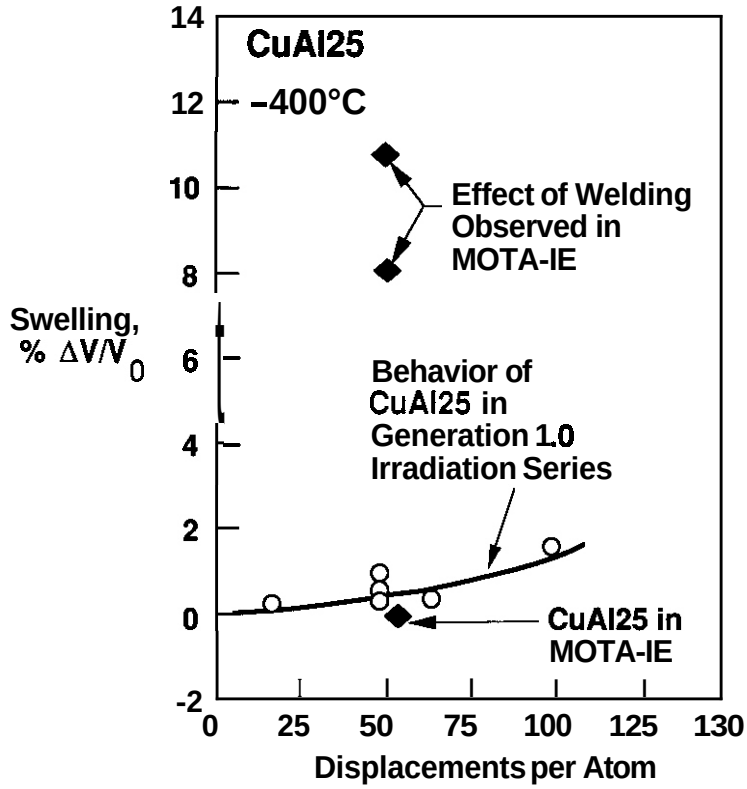


Figure 5. Loss of swelling resistance in CuAl25 upon laser welding prior to irradiation. MOTA-1E refers to the Generation 2.0 experiment. The swelling at 100 dpa of the welded alloy was rather variable, ranging from 19 to 43% while the unwelded alloy densified, as shown in Figure 4.

REFERENCES

1. H. R. Brager and F. A. Garner, "Neutron Induced Swelling of Copper Alloys at 98 dpa and 450°C," in Fusion Reactor Materials Semiannual Progress Report, DOE/ER-0313/3 (September 30, 1987) pp. 254-259.

2. F. A. Garner, M. L. Hamilton, K. R. Anderson, J. F. Stubbins, B. N. Singh, A. Horsewell and W. F. Sommer, "Overview of Copper Irradiation Programs," in Fusion Reactor Materials Semiannual Progress Report, DOE/ER-0313/6 (March 31, 1989) pp. 351-356.

3. F. A. Garner, H. R. Brager and K. R. Anderson, "Density Changes of Generation 1.5 and 2.0 Copper Alloys Irradiated at 411-414°C and 529°C in FFTF/MOTA," in Fusion Reactor Materials Semiannual Progress Report DOE/ER-0313/7 (September 30, 1989) pp. 223-230.

4. K. R. Anderson, F. A. Garner, M. L. Hamilton and J. F. Stubbins, in this Semiannual report.

5. F. A. Garner, "The Influence of Transmutation and High Neutron Fluence of Materials Used in Fission-Fusion Correlation Experiments," J. Nucl. Mater. 175 (1990) in press.

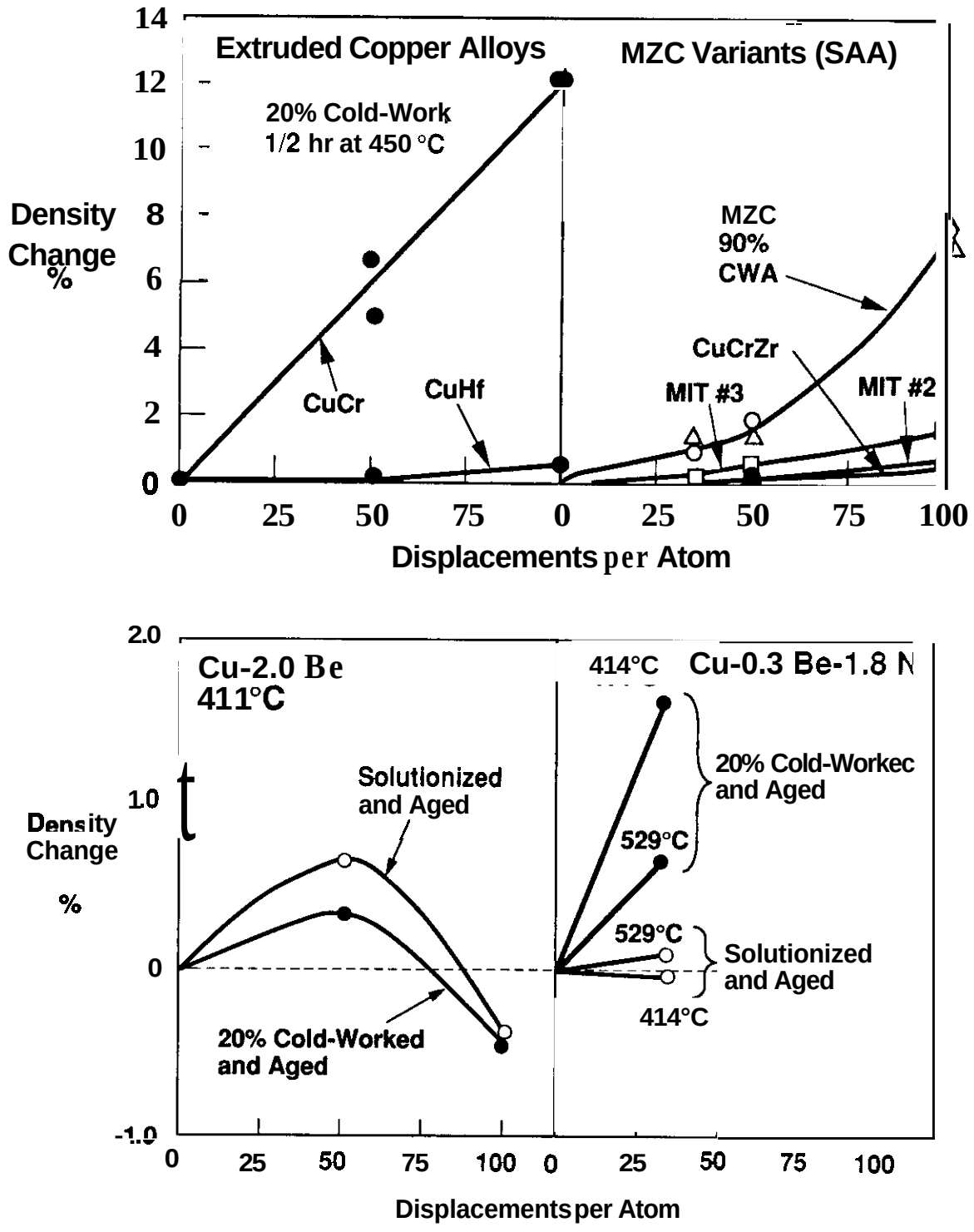


Figure 6. Swelling observed in various copper alloys irradiated in the Generation 1.5 and 2.0 experiments.

RADIATION-INDUCED CHANGES IN ELECTRICAL CONDUCTIVITY OF A WIDE RANGE OF COPPER ALLOYS - F. A. Garner, Pacific Northwest Laboratory,[a] K. R. Anderson, University of Illinois, and T. Shikama, Tohoku University

OBJECTIVE

The objective of this effort is to identify those copper alloys that offer promise as high heat flux materials for fusion application.

SUMMARY

A wide variety of radiation-induced changes in electrical conductivity was observed in a series of irradiation experiments conducted on copper alloys in FFTF/MOTA. The behavior of each alloy was found to depend on the alloy composition, starting state, irradiation temperature, and the sometimes complex interaction of three radiation-driven processes. These processes are transmutation, void swelling, and solute redistribution.

PROGRESS AND STATUS

Introduction

A variety of copper alloys have been proposed for high heat flux applications for both near-term and long-term fusion goals. In response to these proposals, a series of exploratory irradiation experiments are being conducted in FFTF/MOTA.[1] One property being measured in this experimental series is the electrical conductivity, a property that often changes substantially in response to the combined influence of void swelling, transmutation, and solute redistribution.

Several generations of FFTF copper irradiation experiments have been conducted, and the latest of these, designated Generation 2.0, continues to accumulate exposure in FFTF. Changes in conductivity of some but not all alloys measured in Generations 1.0, 1.5, and 2.0, have been reported previously,[2,3] and conductivity measurements continue to be performed on alloys that were bypassed in the first series of measurements. Measurements of conductivity for all alloys irradiated in the 430°C Generation 1.0 series at 16, 41, 63, and 98 dpa, the Generation 1.5 experiment at 414°C, 34 dpa and 529°C, 32 dpa, and the 411°C Generation 2.0 experiment at 50 dpa have now been completed and are reported here.

Measurements of the 411°C Generation 2.0 alloys at 100 and 150 dpa will be performed during 1991. Anderson et al.[2] present the details of the experimental technique and Garner et al.[1] provide a detailed description of the materials studied.

Some data presented in this report are reevaluations of previously reported data, based on refinements in the measurement technique and involving changes usually on the order of 10% or less. At the higher fluence levels of the Generation 1.0 experiment it was also found to be necessary to remeasure some previously reported specimens after mechanically removing a surface layer of aluminum. This layer had formed on closely packed specimens by diffusion bonding with aluminum spacers inserted between the specimens.[1] This problem became more pronounced as void swelling caused an increasingly tighter packing of the specimens. After removing the aluminum, a significant improvement was observed in the reproducibility of the measurements and in their consistency with data taken at lower fluence levels.

Results and Discussion

A compilation of the new and revised conductivity data measured in the various generations of the FFTF/MOTA copper irradiation experiments is presented in Tables 1 and 2.

Pure copper has been used as a standard reference material in the various generations of the FFTF copper irradiation program as well as in programs conducted in other reactors. For this purpose, we have chosen to examine the reproducibility of its electrical conductivity in these FFTF studies and in another fast reactor irradiation experiment conducted in EBR-II.[4] The major transmutation product in copper is nickel and its production rate is very dependent on neutron spectra. Nickel additions to copper have a substantial impact on the electrical and thermal conductivities. Both nickel and the second major transmutant, zinc, strongly depress the conductivities of copper.[4,5] Void swelling also decreases both types of conductivity.

Figure 1a shows that fast reactor irradiations of pure copper at 385-430°C yield electrical conductivity changes that are very consistent. Since the neutron spectra of EBR-II and FFTF are very similar, the consistency is not unexpected. Also shown in Figure 1a is electrical conductivity data for pure copper

---

(a) Operated for the U.S. Department of Energy by Battelle Memorial Institute under Contract DE-AC06-76RLO 1830.

Table 1.
Electrical Conductivities (%IACS) of Generation 1.0 Copper Alloys Irradiated as TEM Disks in FFTF/MOTA at ~430°C

Material Alloy	Code	0 dpa	16 dpa	47 dpa	63 dpa	98 dpa
MARZ Cu (SA)	RO	100.9	88.0	61.1	55.0[b]	32.7[b]
Cu-5Ni (SA)	R7	29.2	23.0[a] 25.0[a]		19.8	13.9[b]
CuBe (HTB)	R3	20.2[a]	32.0[a]	32.6[b]	29.1[a] 32.6[b]	32.8[b]
CuBe (HTA)	R1	19.3[a]	31.1[a]	29.2[a]		27.3[b]
CuNiBe (HTB)	RT	54.5[a]	64.0")	54.2	45.7[b]	
CuNiBe (HTA)	RR	66.8[a]	75.9[a]	53.0	47.3[b]	24.1[b]
CuAg (SA)	RX	94.1[a]	74.5[b]	46.6	45.2[b]	29.0[b]
CuAgP (SA)	RV	86.4[a]	71.9[a]	42.8	-	27.5[b]
MZC (CWA)	RU	83.3[a]	71.1	59.6		
Cu-5Al (SA)	R9	(c)	27.7			12.6[b]
CuAl25 (CW)	R4	85.5[a]	-14	-50	~61[b]	36.4[b]
CuAl25 (CWA)	R5	-79			~59[b]	58.2[b]

(a) Reevaluation of previously published data.
(b) Value measured after removing aluminum-contaminated surface.
(c) Not yet measured.

derived from FFTF irradiation at 529°C. Since the swelling at this dose and temperature is only 1.8% (a factor of ten lower than at ~400°C) most of the observed conductivity loss arises from transmutation to nickel and zinc, a process that is independent of temperature.

In pure copper it was found that the effects of transmutation and voidage on electrical resistivity were directly additive in accordance with Matthiesson's rule, indicating that no significant interaction between the two processes has occurred.[4,5] Two other alloys in the Generation 1.0 study involved relatively low levels of solute and one might expect a similar lack of interaction. These alloys are CuAg and CuAgP. Note in Figure 1b that the addition of solutes in CuAg and CuAgP lowered the preirradiation conductivity from the 101% IACS of pure copper to 94 and 86% IACS, respectively. This difference in conductivity was maintained relative to that of pure copper with little change throughout the first generation experiment, indicating that these solutes probably stayed in solution. The initially low conductivity of Cu-5Ni reflects the influence of nickel and decreases further with irradiation, as is also shown in Figure Ib. Much of the radiation-induced decrease in Cu-SNi is due to void swelling, the development of which appears to be unaffected by the presence of the nickel.[6]

There are some kinds of nonadditive behavior that can occur, however. In most solute-modified alloys, radiation-induced redistribution of initial solutes also leads to modifications in conductivity, particularly if the solute levels are relatively large. A previous paper[5] showed that the electrical conductivity of Cu-2.0Be initially increased slightly with irradiation, but remained constant thereafter (see Figure 2). The initial increase might be attributed to radiation-induced acceleration of precipitation and aging, but the constant conductivity thereafter was thought to be inconsistent with the continued accumulation of nickel and zinc via transmutation. It now appears that the transmutant nickel drives some of the beryllium out of solution as it forms, and the two effects compensate. The strongly reduced solubility of beryllium in copper-containing nickel is the principle on which the higher conducting CuBeNi (Cu-0.3Be-1.8Ni) alloy was developed to replace Cu-2.0Be. In CuBeNi, the lower level of beryllium compared to that of Cu-2.0Be leads to a much higher level of initial conductivity. The conductivity is increased slightly by solute redistribution in the early stages of irradiation, but this trend is reversed at a relatively low exposure by accumulating levels of transmutants and swelling. Microstructural observations show that CuBeNi swells relatively easily and that CuBe does not swell.[7,8]

Table 2

Electrical Conductivities (% IACS)[a] of Generation 1.5 and 2.0 Copper Alloys Irradiated in FFTF/MOTA

Alloy	Material Code	0 dpa	34 dpa	414% 50 dpa	411°C 529°C 32 dpa
MARZ Cu	RO	100.9	70.4	58.1	82.7[b]
		100.9	70.1	58.1	90.8[b]
CuAl25	R4	85.7		83.2	
		85.2		81.6	
CuAl25 (welded)	3N	73.9	77.7	57.7	59.6
CuAl20	UX	88.5	81.6	72.7[b]	84.0
		88.4	85.4	76.3[b]	86.4
CuAl20	UZ	84.9	82.0		
CuAl15B	VO	91.6	80.0	74.7[b]	85.8[b]
			83.6	73.8[b]	88.6[b]
ODS-1	3F	80.6		63.7	
				59.3	
ODS-1 (welded)	3H	88.5	88.4	64.9	67.9
ODS-2	3K	85.7[b]		67.2[b]	
		88.7[b]		73.6[b]	
		91.3[b]		68.0[b]	
ODS-3	3L	86.0		59.0[b]	
		89.0		57.0[b]	
ODs-4	3M	79.8		67.4	
		78.5		72.0	
CuCr	3A	89.4		77.9	
		90.2		79.4	
CuHf	3B	88.8		77.6	
CuNiTi	VK	40.4[b]	52.3	48.7[b]	68.7[b]
		40.9[b]	52.9	47.3[b]	65.0[b]
		37.5[b]		46.2[b]	
		42.0			
		40.5			
		40.8			
CuNiTi	VL	31.4	56	48.6[b]	67.2[b]
		32.9	59	49.8[b]	68.9[b]
		31.0			
CuNiSn	VN	15.8	40.8		
		16.5			
		16.5			
		18.0[b]			27.9[b]
		18.2[b]			25.3[b]
		18.6[b]			27.7[b]
CuBe (HTB)		R3	20.7		31.8
				30.8	
Cu-5Ni	VP	29.2	18.4		
			17.3		
CuNiBe (AT)		U1	58.2	67.9	
			66.3		
CuNiBe (½HT)		U3	71.0	78.8	66.5
			74.8		
CuNiBe	U4	73.6	82.5		
			74.5		
MZC	U6	88.2	88.0		90.5
			77.9		91.1
MZC	u7	86.7	88.0		
			85.1		
MZC (MIT #2)		U9	84.3	85.7	81.083.6
			88.6	71.9	86.2
MZC (MIT #3)		VB	87.3	85.2	80.391.8
			86.1	78.7	90.5

(a) Multiple values represent measurements from separate specimens.
(b) Indicates TEM disks; no notation denotes measurements made on gage section of miniature tensile specimen.

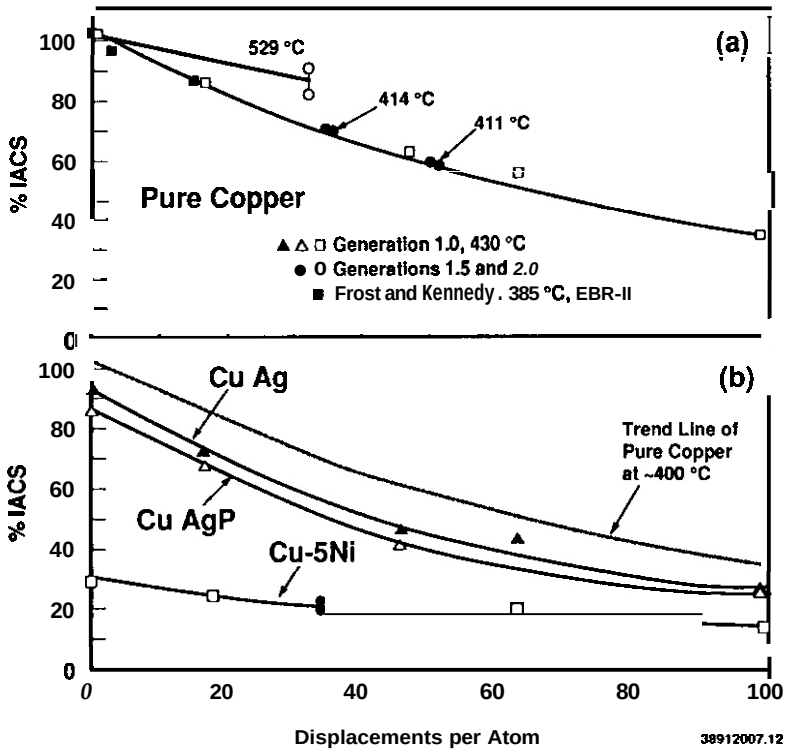


Figure 1. a) Neutron-Induced Changes in Electrical Conductivity of Pure Copper in Various Fast Reactor Irradiation Experiments in FFTF and EBR-II, b) Changes Observed in Cu-5Ni, CuAg, and CuAgP Irradiated in FFTF.

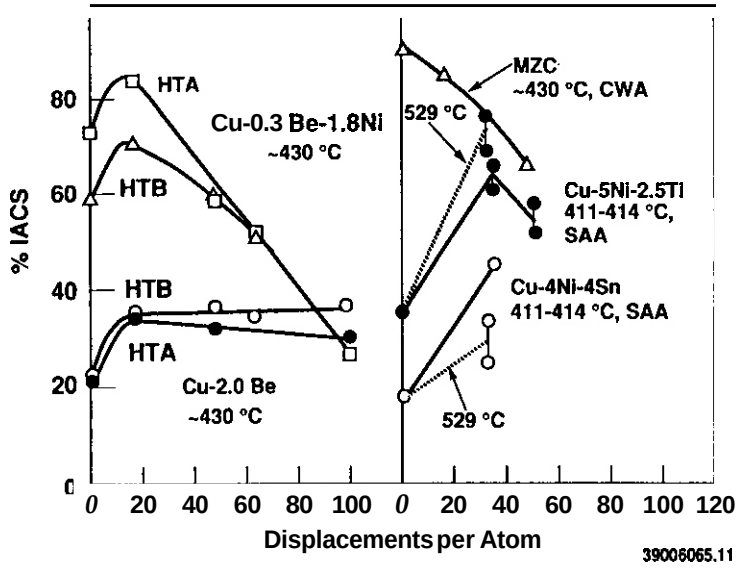


Figure 2. Wide Variety of Electrical Conductivity Behavior Observed in Five Alloys Irradiated in FFTF, Illustrating the Range of Interactions Between Precipitation , Solute Redistribution, Transmutation, and Void Swelling. The designations HTA, HTB, SAA, CWA denote Cold-Worked, Annealed, Annealed and Aged, and Cold Worked and Aged, respectively.

The complexity and variety of solute-related changes in conductivity for various copper allays is also illustrated in Figure 2. The large increases in conductivity observed in the CuNiTi and CuNiSn spinodally strengthened alloys are due to the dominant effect of radiation-induced and temperature dependent overaging of precipitates formed by spinodal decomposition, but at higher fluence the influence of void swelling and precipitation eventually begins to overwhelm the influence of solute redistribution and the conductivity begins to decline.[9]

Internally oxidized alumina alloys exhibited the best overall performance in the Generation 1.5 and 2.0 experiments, retaining the largest fractions of their electrical conductivity,[2] strength[10,11] and swelling resistance.[6,10,11] Swelling in this class of alloys was found to be very low, dependent on oxide content, and possibly dependent an cold work level. There is essentially no dependence of the electrical conductivity of these alloys on irradiation temperature since, in the absence of substantial void swelling, transmutation accounts for the majority of the decrease in conductivity.[2,9] The conductivity behavior of this class of alloys was covered in more detail elsewhere.[2] Some of these data are reproduced in Figures 3 and 4 for comparison with. the behavior of the solute-strengthened alloys.

Conclusions drawn in this report concerning the origin of the conductivity change of a given alloy are derived not only from microstructural observations but also from changes in mechanical properties and density.[7-9,11-13] At higher exposure levels in alloys that do not resist swelling, microstructural examination is not always feasible, and the behavior must be inferred from changes in the macroscopic properties.

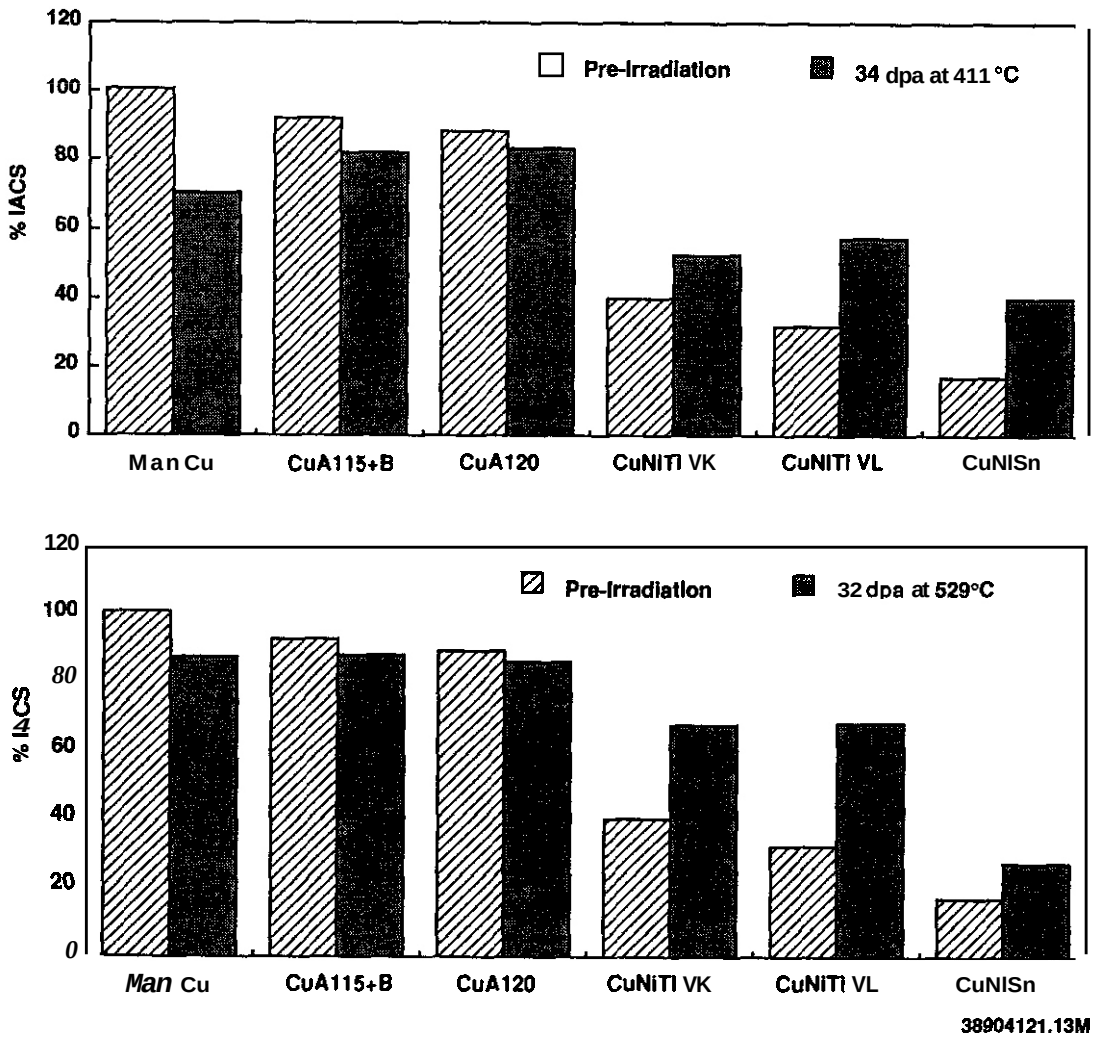


Figure 3. Measurement of Electrical Conductivity of Both Unirradiated and Irradiated (34 dpa at 411°C and 32 dpa at 529°C) Dispersion-Strengthened and Spinodally-Strengthened Alloys from Generation 1.5.

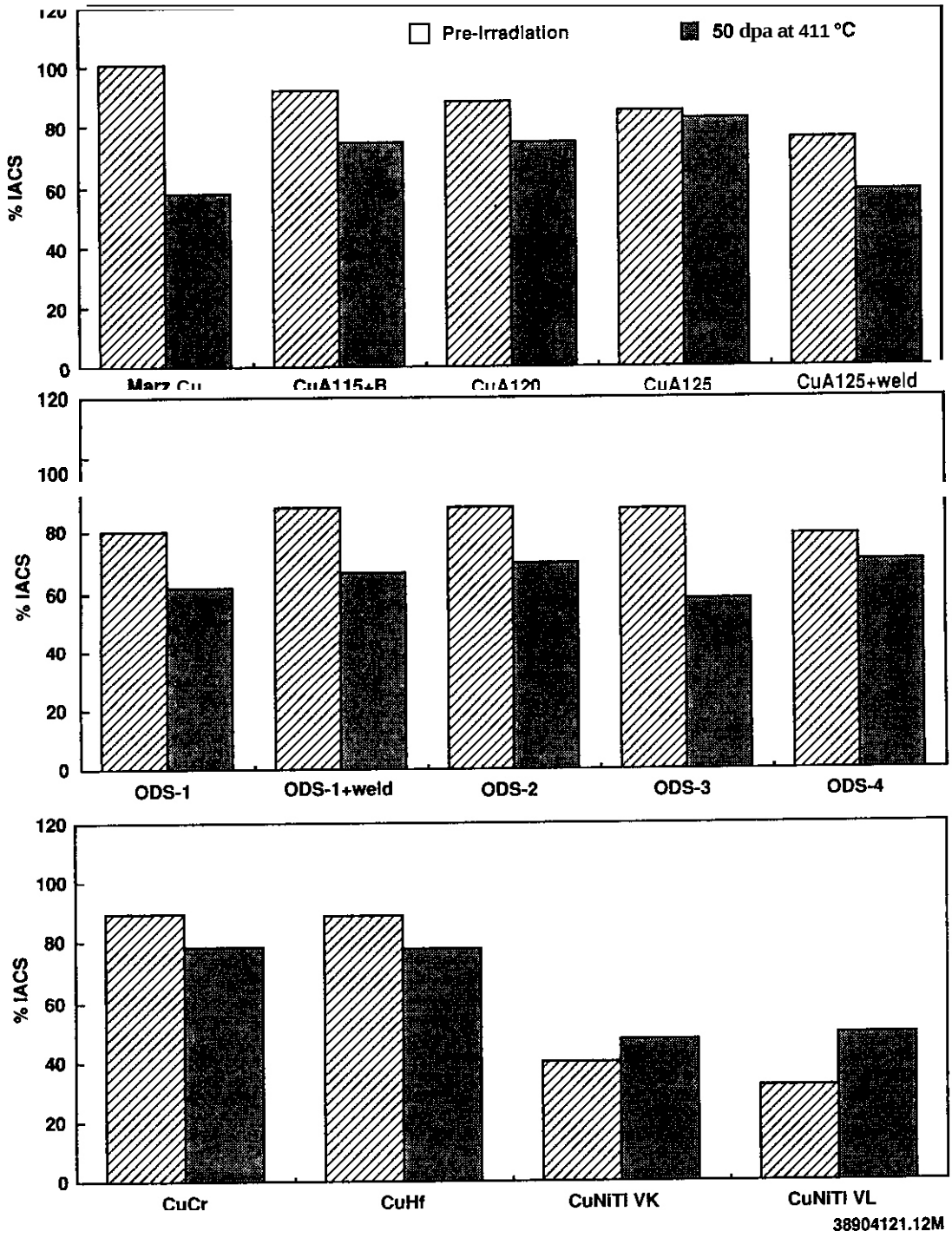


Figure 4. Measurements of Electrical Conductivity of Both Unirradiated and Irradiated (50 dpa at 411°C) Dispersion-Strengthened and Spinodally-Strengthened Alloys from Generation 2.0.

CONCLUSIONS

A wide variety of radiation-induced behaviors was observed in the electrical conductivity of various copper alloys irradiated in FFTF/MOTA. This complexity arises from the sometimes interactive effects of composition, starting state and temperature on three competing processes: transmutation, void swelling, and solute redistribution. The latter process can either increase or decrease the conductivity, while swelling and transmutation in general decrease the conductivity. In some cases these various contributions to conductivity can interact strongly to yield unanticipated results.

FUTURE WORK

Conductivity measurements will proceed on Generation 2.0 alloys irradiated at 411°C to 100 and 150 dpa. Specimens for irradiation in Generation 3.0 are now being prepared.

REFERENCES

1. F. A. Garner, M. L. Hamilton, K. R. Anderson, J. F. Stubbins, 8. N. Singh, A. Horsewell and W. F. Sommer, "Overview of Copper Irradiation Programs," Fusion Reactor Materials Semiannual Progress Report, DOE/ER-0313/6 (1989), pp. 351-356.

2. K. R. Anderson, F. A. Garner, M. L. Hamilton and J. F. Stubbins, "Electrical Resistivity Changes Induced in Copper Alloys by Fast Neutron Irradiation," Fusion Reactor Materials Semiannual Proaress Reoort, DOE/ER-0313/9, pp. 357-369.

3. F. A. Garner and K. R. Anderson, "Conductivity Changes Observed in Generation 1.0 Copper Alloys Irradiated at 430°C to 16-98 dpa," Fusion Reactor Materials Semiannual Reoort, DOE/ER-0313/7 (1989), pp. 220-222.

4. H. M. Frost and J. C. Kennedy, J. Nucl. Mater. 141-143 (1986) 169-173.

5. F. A. Garner, H. L. Heinisch, R. L. Simons, and F. M. Mann, Radiation Effects, 113 (1990) 229-255.

6. F. A. Garner and H. R. Brager, "Neutron-Induced Changes in Density of Copper Alloys," in this semiannual report.

7. H. R. Brager, J. Nucl. Mater. 141-143 (1986) 79-86.

8. H. R. Brager, J. Nucl. Mater. 141-143 (1986) 163-168.

9. K. R. Anderson, "The Properties of Oxide Dispersed and Spinodally Strengthened Copper Alloys Following High Temperature Neutron Environment Exposure", Doctoral Thesis, University of Illinois at Urbana-Champaign, 1990.

10. H. R. Brager, H. L. Heinisch and F. A. Garner, J. Nucl. Mater. 133 & 134 (1985) 676-679.

11. K. R. Anderson, F. A. Garner, M. L. Hamilton and J. F. Stubbins, in this semiannual report.

12. T. Shikama, F. A. Garner, M. L. Hamilton, and K. R. Anderson, "Tensile and Fracture Behavior of Cu-5Ni and Various Precipitation-Strengthened Copper Alloys After High Fluence Irradiation", PNL-SA-17549, to be included in the Proceedings of the 15th ASTM International Symposium on Effects of Radiation on Materials, Nashville, TN, June 17-21, 1990.

13. H. R. Brager and F. A. Garner, "Effects of Neutron Irradiation to 98 dpa on the Swelling of Various Copper Alloys," ASTM STP 1046 (vol. II), N. H. Packan, R. E. Stoller, and A. S. Kumar, eds. 1990, pp. 599-604.

BRAZING OF COPPER-ALUMINA ALLOYS - B. A. Chin, C. K. Lee (Auburn University), S. J. Zinkle (Oak Ridge National Laboratory), and R. C. Wilcox (Auburn University)

OBJECTIVE

The objective of this research is the development of an induction brazing process for GLIDCOP AI-15 using a silver-base brazing alloy. This objective centers on minimizing the time required at elevated temperatures during the brazing process in order to eliminate two major problems of furnace brazing.

SUMMARY

An induction braze has been developed to join copper-alumina alloys to eliminate the requirement for either plating the joining surfaces prior to brazing or the use of an inert cover gas or a vacuum pump to prevent excessive oxidation. Preliminary tensile tests of induction lap joints and fatigue tests of induction brazed butt joints have been conducted. A theoretical study of the diffusion of silver into the alloy has been compared to experimental EDX analysis.

PROGRESS AND STATUS

Introduction

The economic feasibility of generating electricity using tokamak fusion reactors requires an increase in the ratio of energy output to the energy input of the reactor.[1] This increased ratio will require minimizing energy losses associated with particle drift and sputtering. These losses are associated with the method used by tokamaks to confine the plasma. The energy losses associated with particle drift and sputtering are significant![1] Currently, Oak Ridge National Laboratory (ORNL) is investigating the design and material selection for three components that help combat these energy losses: magnets, limiters, and diverters. ORNL has established design criteria for the materials being considered for use. In addition, ORNL has targeted cold-worked GLIDCOP AI-15 as a possible structural material for all three devices because of the outstanding properties of this alloy[2]

GLIDCOP AI-15 contains 0.15 wt % AI in the form of aluminum oxide particles[4] 60 to 200 Å in diameter. The particles are evenly dispersed and incoherent with the copper matrix. The ability of GLIDCOP AI-15 to retain a cold-worked microstructure (and the high strength associated with this structure) is due to the presence of the aluminum oxide particles. The alloy has an extremely stable microstructure, and can withstand extended periods of time at high temperatures without recrystallization[2] The ability to retain a cold-worked high-strength microstructure after high temperature braze cycles, coupled with their high thermal and electrical conductivities, makes the alloy attractive for tokamak limiters[6] as well as for other fusion energy-related applications.[7,8]

Previous attempts for brazing GLIDCOP AI-15 have centered on furnace brazing techniques. The heat for this process is provided by placing the entire assembly to be brazed in a furnace. Several problems have arisen due to this method of brazing. The amount of time at elevated temperatures causes excessive oxidation of the base metal. Thus, in furnace brazing, either an inert cover gas must be blown through the furnace to displace the oxygen or a vacuum furnace must be used. Both methods are troublesome and time-consuming, requiring the monitoring of another set of parameters while brazing.

If a silver-based filler material is used during furnace brazing, the joining surfaces of the cold-worked GLIDCOP AI-15 must first be plated with annealed copper or nickel to prevent loss of filler material. Silver diffuses very rapidly through cold-worked copper alloys at high temperatures. Enough silver may actually diffuse away from the joining surfaces, if they are not plated, so that an insufficient amount of tiller would be left for brazing.

Experimental procedure

Brazed joints of GLIDCOP AI-15 using the BAg-5 brazing alloy (45 wt % Ag, 30% Cu, 25% Zn)[9] were produced by using a 50-kW induction furnace with an oval-shaped helical coil. A range of braze times and power settings for consistent brazing were developed. Lap joints required 25 s to reach the melting point (745°C) of BAg-5 and 4 s to obtain 1000°C. For butt joints, the melting point of BAg-5 was reached in 9 s, and 12 s was required to obtain 1000°C. Several furnace-brazed joints were produced using the standard Ticusil cycle[10] which was utilized for the Tore Supra limiter program. This cycle is as follows:

1. Heat at 25°C/min to 815°C, hold at 815°C for 20 min
2. Heat at 5°C/min to 870°C, hold for 5 min.
3. Cool at 2.5°C/min to room temperature.

Overlap SS-1 type tensile specimens were machined from rectangular strips of GLIDCOP 4-15 obtained from ORNL in the form of cold-worked plates 0.762 mm thick. An Instron testing machine (crosshead speed was 0.254 mm/min) was used to evaluate tensile properties.''

Subsize cantilever type fatigue specimens were prepared by cutting rectangular pieces from butt joints with dimensions slightly greater than the actual dimensions. Each piece was then milled to size. The specimens were 0.762 mm thick and had two circular notches of 6.35 mm radius. The gage length was 6.35 mm. Because the endurance at room temperature is sensitive to the surface finish, the subsize fatigue specimens were polished by hand using polishing papers and then electropolished using a 50% phosphoric acid, 50% water electrolyte at room temperature. The results yielded a polished surface completely free from machining effects.

Recent Results

SS-1 specimens were tested for evaluating the strength of brazed joints in shear. For each specimen, the average unit shear stress in the filler metal at failure and the average unit tensile stress in the base metal at failure were calculated as follows:[12]

$$\text{Average unit shear stress} = \frac{\text{Breakins load}}{\text{Length of overlap} * \text{Width}} \quad (1)$$

$$\text{Average unit tensile stress} = \frac{\text{Breakins load}}{\text{Thickness of base metal} * \text{Width}} \quad (2)$$

Average unit shear stress and average unit tensile stress as a function of overlap distance for SS-1 specimens are shown in Fig. 1. For an overlap length of less than 1.5 times the thickness of the base metal, the samples failed in the braze or in the joint. For an overlap length larger than 1.5 times the thickness of the base metal, all specimens failed outside the joint.

The preliminary results of fatigue testing of butt joints are shown in Fig. 2. On a log-log plot the fatigue results can be represented by a straight line. The two fatigue tests shown as solid circle data points in the figure were terminated after 20 and 45 days without failing. The fatigue results were calculated using the moment-deflection relationship for a cantilever beam and the value of 2.76 x 10' MPa (4 x lob psi) for the modulus of elasticity for the BAg-5 filler alloy. The major cause of concern is the presence of about 40% voids in the brazed butt joints. Experimentation is being conducted to determine the origin of these voids. Additional butt joints are being designed in an effort to possibly eliminate the majority of these voids.

The following assumptions were made to estimate the amount of silver filler that diffuses into the GLIDCOP AI-15 microstructure.

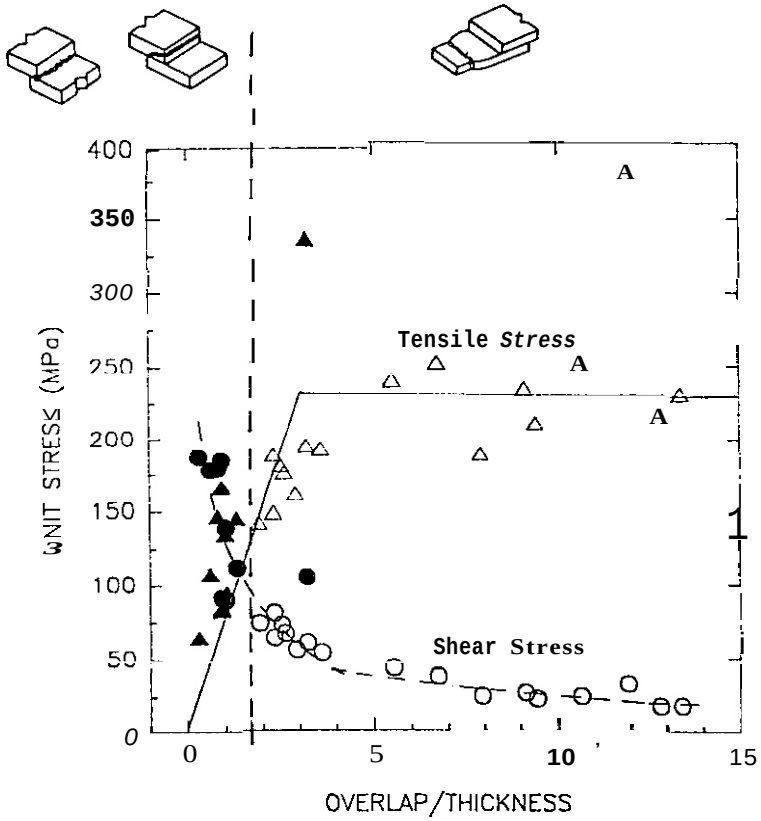


Fig. 1. Average unit shear stress and average unit tensile stress as a function of the overlap distance for SS-1 specimens.

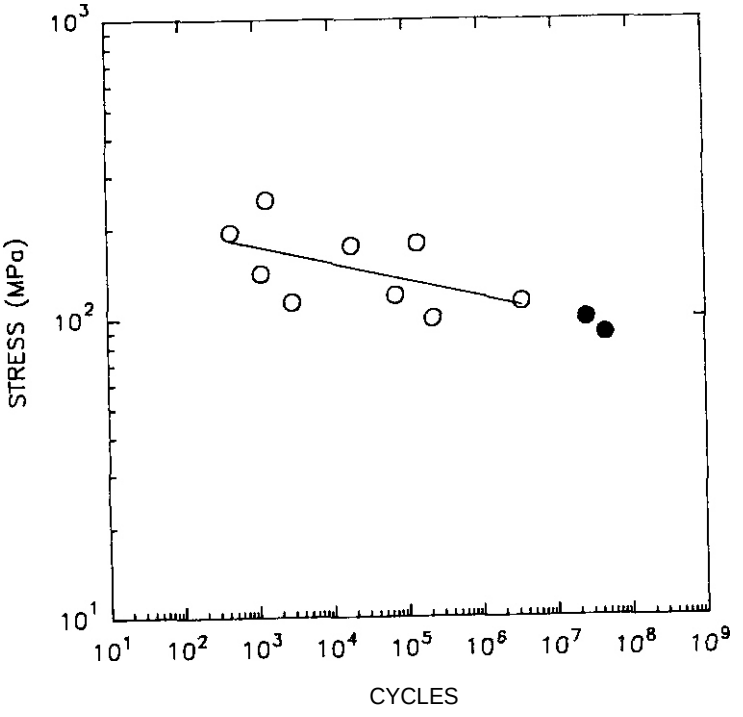


Fig. 2. Fatigue data for induction brazed butt joints.

1. The diffusion condition may be approximated as silver impurities in pure copper.

2. The original concentration of silver in GLIDCOP AI-15 is 0.0%.

3. The concentration of silver in the BAg-5 brazing alloy is 45% (ref. 9).

4. Fick's second law applies and can be simplified to

$$\partial c/\partial t = \partial(D\ \partial c/\partial x)/\partial x\ , \qquad (3)$$

where c is the concentration of diffusing species, t is time, and x is the distance from the interface, and D is the diffusion coefficient. The diffusion coefficient was assumed to be independent of concentration gradient and time so Fick's second law reduces to:

$$\partial c/\partial t = D\ \partial^2 c/\partial x^2\ , \qquad (4)$$

where D is calculated from:

$$D = D_0 \exp(-Q/RT)\ . \qquad (5)$$

D_0 is 0.63 cm^2/s (constant for Ag in Cu),[13] Q is the activation energy for diffusion, R is the ideal gas constant (1.987 cal/mole/K), and T is the absolute temperature.

5. The activation energy for surface diffusion may be taken as one half of the activation energy for volume diffusion which is 46.5 Kcal/mole (a constant for Ag impurities in Cu).[13]

6. The effective temperature at which diffusion occurs is in the 800 to 1000°C range. So, calculations were made for constant temperature diffusion at 1000°C. The brazing times were 3.5 to 4.5 s for the overlap tensile test samples, 14 s for butt joint fatigue samples, and 69 min for furnace brazing. Thus, diffusion times of 2, 4, and 943 s, respectively, were used in the calculations.

7. The silver diffusion is a relaxation of an initial rectangular pulse of the form $C_0 = 45\%$ for $-a<x<a$ and 0 elsewhere. At $t = 0$, the Fourier integral transform for this function is $\sin(\beta a)/\beta$. Thus, the solution for Fick's second law can be written."

$$C(x,t) = [Co/\pi] \int_{-\infty}^{\infty} \{[\sin(\beta a)/\beta][\cos(\beta x)\exp(-\beta^2 Dt)]\}\ d\beta \qquad (6)$$

Co = source Ag concentration (45%)
C(x,t) = Aq concentration at a distance x from the interface.

A scanning electron microscopy examination of the brazed interface revealed a small diffusion zone adjacent to the interface in both the induction brazed overlap and butt joints. On the other hand, a furnace brazed sample contained a large interdiffusion zone at the GLIDCOP AI-15 -- BAg-5 interface indicating considerable diffusion of silver into the copper alloy.

Figures 3 to 8 show the results of real and theoretical diffusion measurements made for the diffusion of silver impurity atoms into copper. The calculations were made to get an estimate of the amount of silver filler that diffused into the GLIDCOP AI-15 microstructure. The calculations for pure volume diffusion indicated that practically none of the silver would diffuse into the GLIDCOP AI-15. Calculations based on pure surface diffusion suggested significant amounts of surface diffusion could occur. Figure 3 shows that the real diffusion (real line), the theoretical pure volume diffusion (sharp peak), and the theoretical pure surface diffusion for a furnace brazed sample. Figure 4 shows the theoretical silver diffusion based on the maximum silver concentration at the joint center being dropped to the same value as that of real measurement for the furnace brazed sample. This calculation utilized Eq. (6). The calculated diffusion coefficient at 1000°C from Fig. 4 is 2×10^{-7} cm^2/s. Figures 5 and 6 show the silver concentration at the center of the lap joint is still 45 wt % and the diffusion distance is less than 0.1 mm because only small amounts of silver could diffuse in the short time of 4 s. The calculated diffusion coefficient at 1000°C for the induction lap joint was 6×10^{-7} cm^2/s. Figures 7 and 8 show the silver concentration at the center of a butt joint has dropped to 30 wt %; however, the diffusion distance is very small (0.05 mm). The diffusion coefficient calculated at 1000°C for a butt joint was 6×10^{-7} cm^2/s.

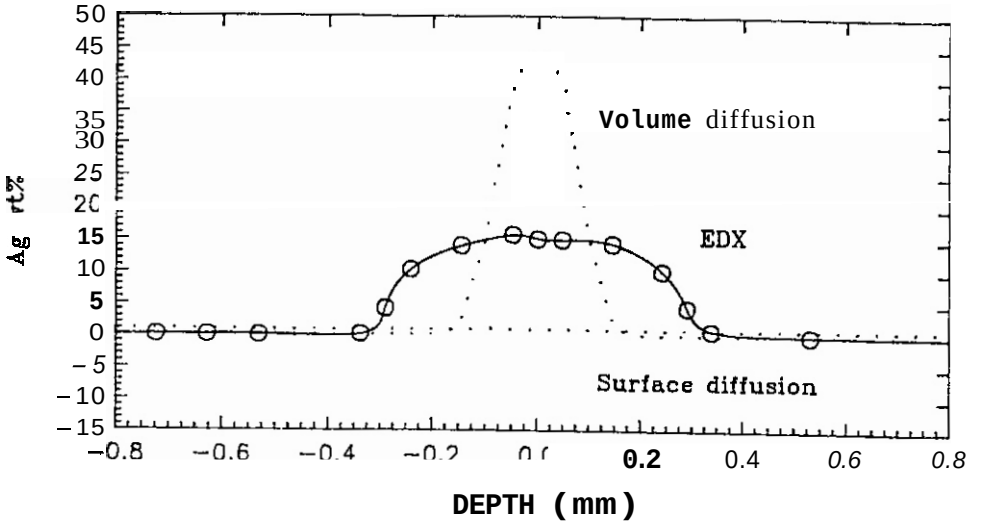


Fig. 3. The real diffusion (solid line) of silver, the theoretical pure volume diffusion (sharp peak) and the theoretical pure surface diffusion within a furnace brazed joint.

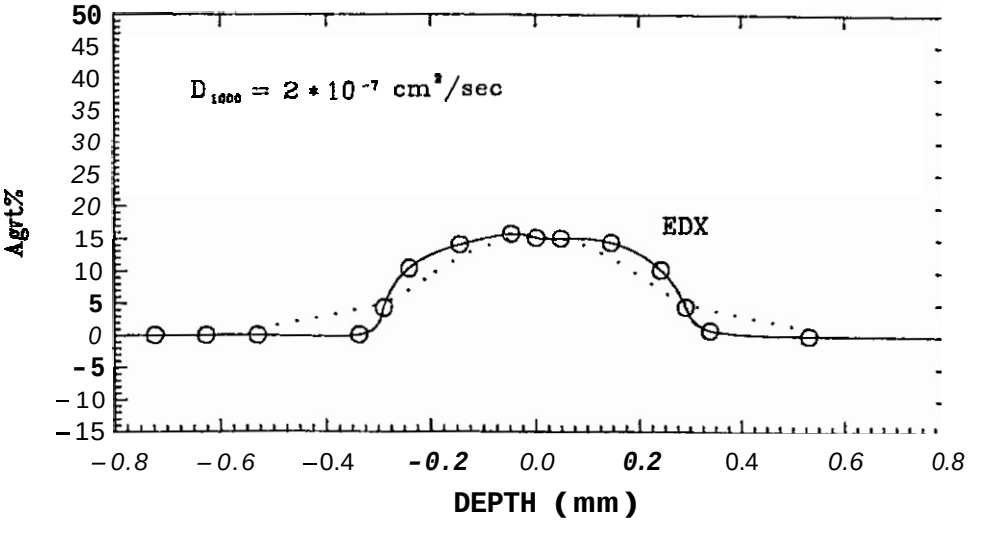


Fig. *4.* Theoretical diffusion for a furnace brazed joint compared to the real diffusion of silver.

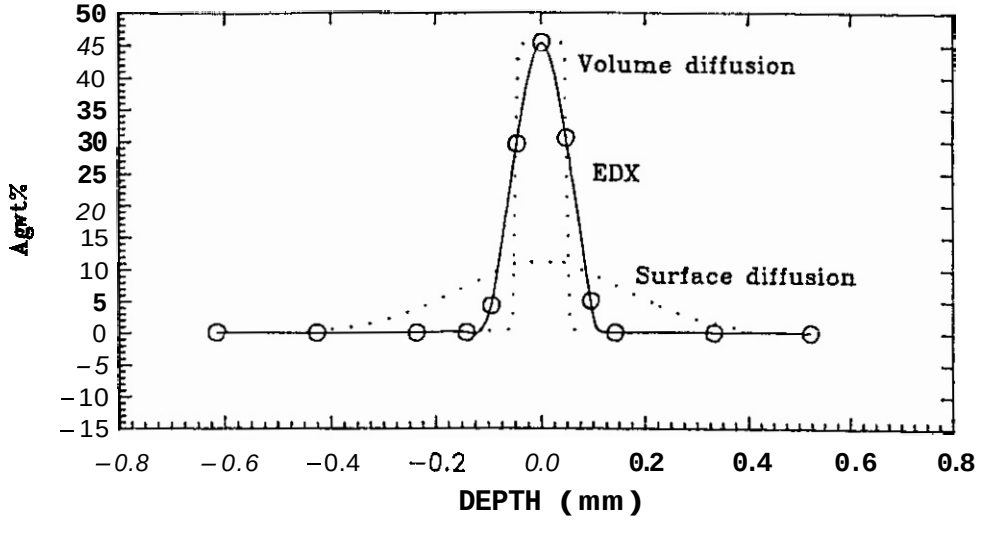


Fig. *5.* The real diffusion (solid line) of silver, the theoretical pure volume diffusion (sharp peak) and the theoretical pure surface diffusion within an induction brazed lap joint.

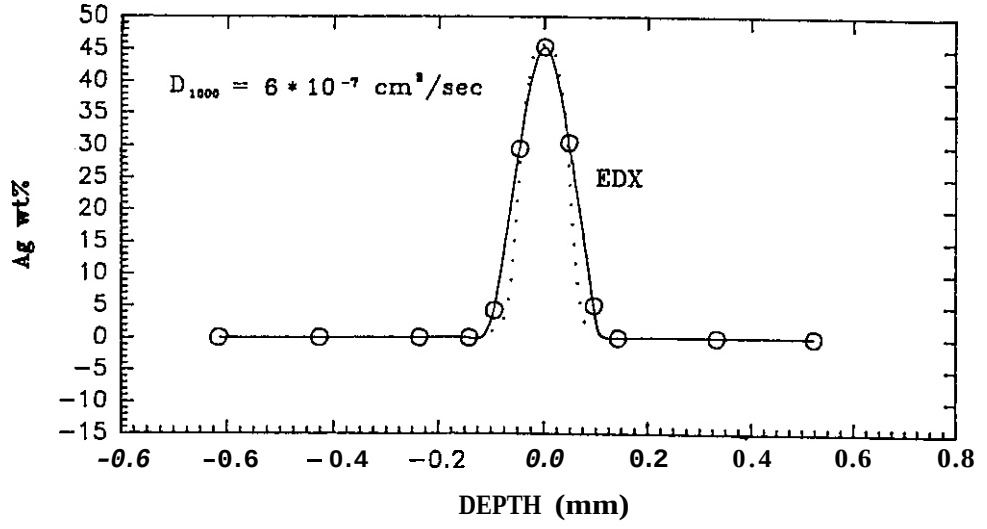
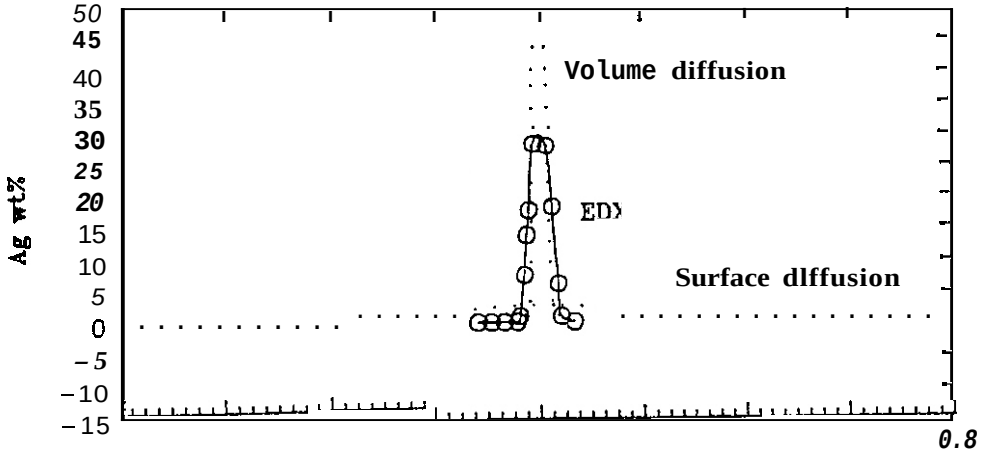


Fig. 6. Theoretical diffusion within an induction brazed lap joint compared to the real diffusion of silver



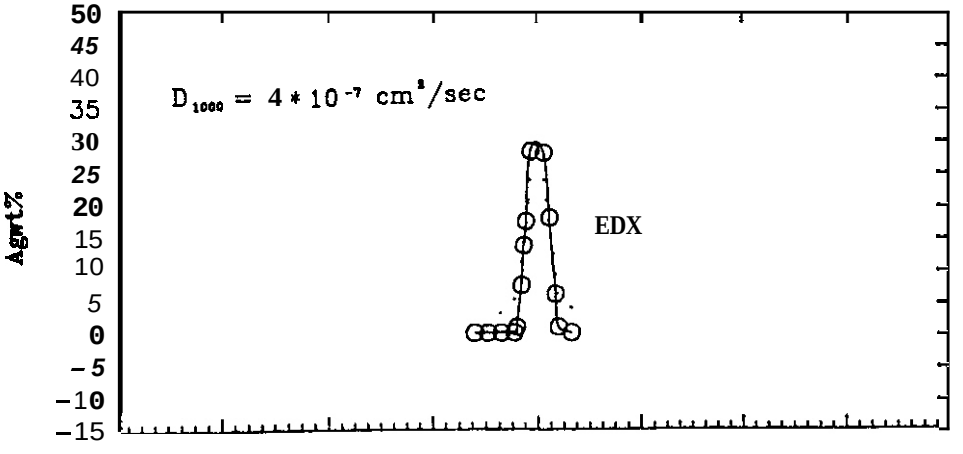


Fig. 8. Theoretical diffusion within an induction brazed lap joint compared to the real diffusion of silver.

The calculated diffusion coefficients at 1000°C based on Figs. 3 through 5 are between 2 to 6×10^{-7} cm^2/s, which are between the pure volume diffusion coefficient of 6.3×10^{-9} cm^2/s and the pure surface diffusion coefficient of 6.3×10^{-5} cm^2/s. Therefore, grain boundary diffusion must play an important role during the diffusion process.

Discussion

The results indicate that a satisfactory induction brazing process can be achieved. Satisfactory tensile and fatigue properties can be obtained through the use of a silver filler alloy and induction brazing techniques. These mechanical properties are obtained without the use of a protective atmosphere. EDX composition analysis supported the idea that only a minor amount of silver diffusion occurred during induction brazing.

REFERENCES

1. W.M. Stacey Jr., Fusion - An Introduction to the Physics and Technology of Masnetic Confinement Fusion, John Wiley and Sons, Inc., New York, 1984, pp. 4-7, 11-19, 88-99.

2. K. Niu, Nuclear Fusion, Cambridge University Press, New York, 1989, pp. 18-21, 25-50, 179-187.

3. Oak Ridge National Laboratory internal memorandum dated March 1, 1989, from E.E. Bloom to Dr.T.C. Reuther, Fusion Technologies Branch.

4. K.M. Zwilsky and N.J. Grant. "Dispersion Strengthening in the Copper-Alumina System," Tran. A.I.M.E., 221, pp. 371-377, (1961).

5. Low Oxygen Grade Glidcop A1-15 Information Brochure, SCM Metals, Inc., Cleveland, Ohio, 1985.

6. J.A. Koski, R.D. Boyd, S.M. Kempka, A.D. Romig Jr., M.F. Smith, R.D. Watson, J.B. Whitley, R.W. Conn and S.P. Grotz. "Preliminary Design Analysis of the ALT-II Limiter for TEXTOR," Journal of Nuclear Materials, 121, pp. 309-315 (1984).

7. J.J. Stephens and D.T. Schmale, The Effect of High Temuerature Thermal Braze Cycles on Mechanical Properties of a Dispersion Strensthened Copper Alloy, self-printed, undated.

8. E.N.C. Dalder, W. Ludeman and B. Schumacher. "Thermal Stability of Four High Strength, High Conductivity Copper Sheet Alloys" Lawrence Livermore National Laboratory, UCRL-89034, April, 1984.

9. Metals Handbook, Ninth Edition, Volume 6 : Welding, Brazing, and Soldering, American society for Metals, 1983, pp. 965-972, 1042-1045.

10. J.J. Stephens and D.T. Schmale. "The Effect of High Temperature Braze Thermal Cycles on Mechanical Properties of a Dispersion Strengthened copper Alloy" Oak Ridge National Laboratory, SAND87-1296.

11. "Standard Methods of Tension Testing of Metallic Materials" ASTM E8-84. 1985 Annual Book of ASTM Standards. Philadelphia: American society for Testing and Materials, 1985. Vol. 1.02, p. 609.

12. "Standard Method for Evaluating the Strength of Brazing Joints in Shear", American Welding Society, ANSI/AWS C3.2-82,1982

13. Paul G. Shewman, Diffusion in Solids, McGraw-Hill, New York, p.111.

14. J.S. Kirkaldy and D.J. Young. "Diffusion in the Condensed State" The Institute of Metals, London, 1987, pp. 25-26.

7.0 ENVIRONMENTAL EFFECTS ON STRUCTURAL MATERIALS

ENVIRONMENTAL EFFECTS ON SIC/SIC COMPOSITES FOR FUSION STRUCTURAL APPLICATIONS - R. H. Jones, Pacific Northwest Laboratory[a]

OBJECTIVE

The purpose of this study is to evaluate the data base and identify critical data needs on high temperature corrosion and environment-induced crack growth of SiC/SiC composites in relation to their potential use as structural materials in fusion reactors.

SUMMARY

The chemical stability of SiC/SiC composites in fusion relevant environments has been evaluated from the database available in the literature for monolithic SiC. The results of this assessment suggests that the primary chemical reactions that will limit the stability of these materials are: 1) Li reduction of surface and grain boundary glass phases in a liquid Li coolant, 2) impurity effects on oxidation and the oxidation of the fiber/matrix interfacial layer in a He coolant and 3) H reduction of the "passive" SiO_2 layer and the reaction of the H with SiC to form gaseous reaction products. Strength degradation has been observed for each of these reactions under certain conditions, but the database is insufficient to predict whether similar property changes will occur in fusion relevant environments. Clearly, more experimental data is needed to evaluate the stability of SiC/SiC composites for long-term exposures in fusion relevant environments.

Introduction

Ceramic matrix composites (CMC) are being evaluated for their potential use as a structural material in fusion reactors. The clear advantages for the use of CMCs such as SiC/SiC are high temperature operation and low activation; however, potential limitations are material cost, fabrication complexity, lack of design experience and the lack of data on radiation stability at relevant temperatures and fluences. Their use is proposed on the assumption that CMCs have sufficient strength and toughness to meet the design requirements; this assumption holds for unirradiated material but remains to be demonstrated for irradiated material.

Recommendations for the use of SiC as a low activation material in fusion reactors have been presented by Hopkins et al.[1] More recently, the ARIES I[2] design was based on the use of SiC/SiC composites for the diverter and first wall. The ARIES I design considered the use of SiC/SiC composite at conditions that are well within their stress and temperature limits. The maximum diverter stress and temperature would be 121 MPa and 700°C, respectively, while the maximum first wall stress and temperature would be 77 MPa and 940°C, respectively. Fracture tests conducted recently at PNL at 800°C on SiC/SiC composites obtained from several vendors showed them to have strengths ranging from 302 to 589 MPa in the unirradiated condition and 120 to 303 MPa for material irradiated at 800°C to 10^{22} n/cm^2. The irradiated material retained R curve fracture behavior. Therefore, at fluences about 1/10 of that needed for fusion first wall design, the SiC/SiC composite material exhibited properties that meet the ARIES I design requirement.

A recent DOE workshop[3] to address the feasibility issues associated with structural applications of CMCs in fusion reactors raised the following issues: 1) hermetic and vacuum properties related to matrix porosity (10-15%) and matrix microcracking from design stress and thermal cycles, 2) chemical compatibility with coolant, tritium and breeder and multiplier materials, radiation effects on compatibility, 3) radiation stability and integrity and 4) ability to join CMCs in the shop and at the reactor site and radiation stability of the joints. A number of other issues were considered generic to the developing of CMCs whereas those listed above are considered specific to fusion and therefore shoulu be addressed by the fusion community. Radiation induced microcracking of the matrix is a more recently identified issue that must also be considered. Differential radiation induced dimensional changes in the fibers and matrix could induce this microcracking.

The purpose of this report is to present the results of a survey of the corrosion characteristics of SiC in fusion relevant environments. Environments of interest include liquid lithium and helium gas. Potential chemical reactions include SiC with lithium (solid and liquid), oxygen, water vapor, hydrogen and beryllium. Data on the stability of SiC in these environments is being evaluated for other programs such as the National Aerospace Plane (H_2), the ceramic Stirling engine (H) and the Advanced Gas Turbine (molten salt). Data on SiC/SiC composite material is negligible so it is necessary to extrapolate data from monolithic material. Recent research on molten salt corrosion of SiC/SiC composite material conducted at PNL will also be reported.

(a) Operated for the U.S. Department of Energy by Battelle Memorial Institute under Contract DE-AC06-76RLO 1830.

PROGRESS AND STATUS

Corrosion Reactions for Silicon Carbide

Silicon carbide will chemically react with O_2, H_2, and H_2O according to the following reactions:

$$SiC(s) + O_2(g) = SiO(g) + CO(g): \text{ Low } P_{O_2} \quad (1a)$$

$$SiC(s) + 3/2O_2(g) = SiO_2(s) + CO(g): \text{ High } P_{O_2} \quad (1b)$$

$$SiC(s) + 2\,H_2(g) = Si + CH_4(g) \quad (2)$$

$$SiC(s) + 2\,H_2O(g) = SiO(g) + CO(g) + 2\,H_2(g) \quad (3)$$

Silicon carbide is thermodynamically unstable in O_2, H_2, and H_2O environments under certain conditions. However, the kinetics of these reactions can be affected by the formation of a protective layer of SiO_2 at high P_{O_2} such that SiC is stable in many corrosive environments. The stability of this "passive" layer then becomes critical to the stability of SiC. The O_2 pressure for the SiC active-passive transition was determined by Gulbransen and Jansson[4] as shown in Figure 1. At fusion relevant temperatures (800-1000°C) this transition occurs at O_2 pressures of 10^{-10} to 10^{-8} atm. Therefore, the pertinent reactions then become those between SiO_2 and specific gaseous or molten salt environments, except in molten Li with a low O_2 activity where SiO_2 is unstable. Relevant reactions with SiO_2 are given below:

$$SiO_2(s) + H_2(g) = SiO(g) + H_2O(g) \quad (4)$$

$$M_2O(l) + SiO_2(s) = M_2SiO_3(s) \quad (5)$$

$$xSiO_2(s) + Na_2SO_4(l) = Na_2O \cdot x(SiO_2)(l) + SO_3(g) \quad (6)$$

where M is an alkali element such as Na and Li. A phase diagram for Na_2O-SiO_2 system is shown in Figure 2 and a phase diagram for the Li_2O-SiO system is shown in Figure 3. Both diagrams are given since most of the corrosion data is for SiC in Na bearing environments while Li is of interest for the application of SiC in a lithium cooled fusion reactor. Alkali elements such as Na and Li cause a breakdown of the "passive" SiO_2 film by forming low melting alkali silicates such as those that occur at 800% in the Na_2-SiO_2 system

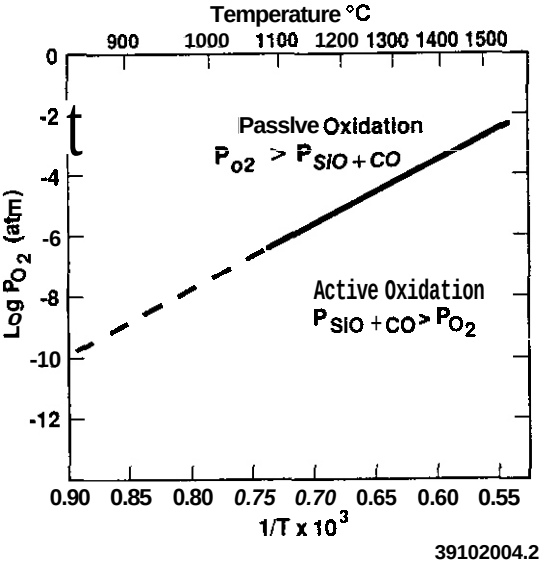


Figure 1. Transition pressures for SiC active-passive oxidation versus temperature, according to Gulbransen and Jansson.[4]

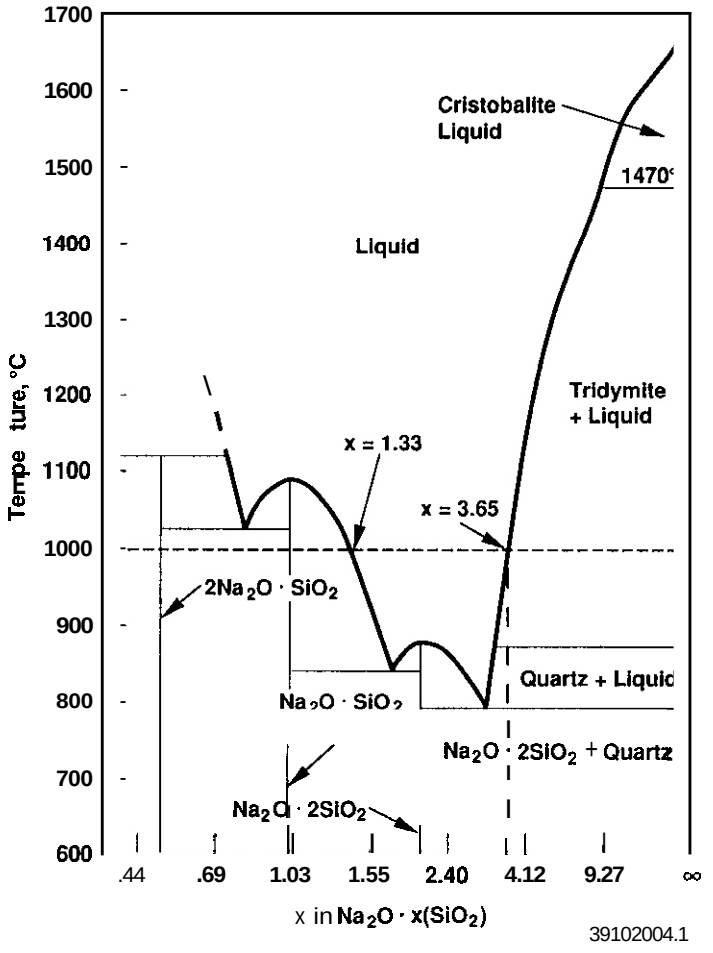


Figure 2. Phase diagram for the system Na_2O-SiO_2.[18]

and 1024% in the Li_2O-SiO, system. The eutectic temperature in the Li_2O-SiO_2 system is about 250°C higher than that in the Na_2O-SiO_2 system and, therefore, Li is expected to have less effect on the "passive" film on SiC at temperatures below 1000°C than is Na.

A summary of the behavior of SiC in gas-molten salt environments as presented by McKee and Chatterji[5] is shown in Figure 4. Passivation occurs at high Po, while active oxidation (formation of gaseous SiO) occurs at low Po_2. A basic salt or salt melt with low Po, at the salt/SiC interface will cause active corrosion as depicted by reaction scheme 4 and 5. McKee and Chatterji suggest that SiC will not react with H_2; however, more recent analysis by Herbell et al.[6] indicates that the equilibrium partial pressure of CH_4 (Eq. 2) is 10^{-4} atm at temperatures of 850 to 1400°C for a H_2 pressure of 1 atm. While McKee and Chatterji measured the sample weight change in the test environment as a function of time in 1 atm of H_2 at 900°C, they observed no reaction between SiC and H_2 (scheme 1-Figure 4). However, their gas may have had sufficient O_2 or H_2O to cause passivation. Herbell et al.[6] calculated the SiO(g) partial pressure for reaction 4 with 1 atm of H_2 containing 1 ppm of H_2O to be 10^{-7} atm. Therefore, it would appear that a very small amount of H_2O mixed with O, to promote SiO_2 formation would be sufficient to significantly reduce the reaction rate of SiC.

Stability of SiC in Liquid Lithium

The corrosion and fracture behavior of SiC in molten Li has been evaluated by Curran and Amateau[7] and Cree and Amateau.[8] Both studies were conducted on α-SiC exposed to a thin layer of molten Li on the sample surface. Fracture strengths and toughness were determined at room temperature. A Li sheet was placed on the upper horizontal surface of the sample prior to their placement in a furnace while a flowing argon atmosphere was maintained in the quartz tube containing the sample. This surface was then used as the tensile surface in a four point bend test. A decrease in the room temperature fracture strength from about 350 MPa to about 150 MPa was found in both studies for exposures exceeding 500°C. The strength loss was related to Li penetration down SiC grain boundaries. Reaction with the glass phase in the SiC grain boundaries was considered to be the primary cause of the rapid intergranular penetration. Uniform corrosion rates were reported as being extensive but with no apparent effect on the fracture strength. In the study

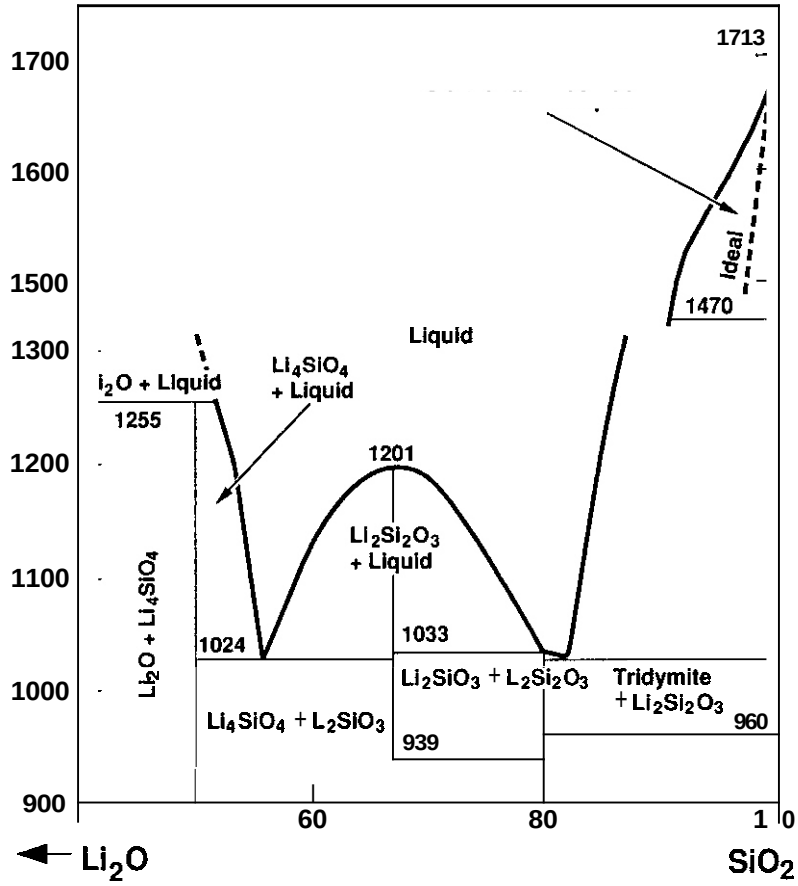


Figure 3. Phase diagram for the system Li_2O-SiO_2.

by Cree and Amateau,[8] they found a bi-modal distribution in the fracture strengths where the low strength group was related to intergranular Li penetration and the high strength group associated with the absence of grain boundary penetration. In the absence of intergranular penetration, the fracture strength decreased slightly with increasing exposure temperature to a value of about 300 MPa after exposure at 800 and 1000°C.

Fracture toughness values were also reported by Curran and Amateau[7] using the direct-crack-measurement indentation method. The fracture toughness was determined from this method by measuring the crack length produced by indentation of the surface. This method is very sensitive to changes in the properties of the material near the surface and is subject to errors associated with the compressive stresses created by the indentation process. The indentation fracture toughness measurements made by Curran and Amateau were sensitive to the effects of surface corrosion reactions. They observed a decrease in the room temperature fracture toughness from about 4 MPa$\sqrt{m}$ to about 2 MPa$\sqrt{m}$ following exposure to molten Li for 30 min at 600°C. A 30 min exposure to Ar at 800°C caused a decrease to about 3 MPa$\sqrt{m}$, so the effects of Li are not due solely to a corrosion reaction but to changes in the properties of the near surface material.

The studies by Curran and Amateau[7] and Cree and Amateau[8] were conducted for relatively short exposure periods of 30 to 60 min. It was concluded in both studies that exposure time within these limits did not affect the properties; however, these exposure times are too short to suggest that further changes will not occur during extended fusion reactor operating times. Also, the reported studies were conducted with the SiC exposed to a limited supply of liquid Li. Exposure to a flowing lithium coolant would likely produce a higher corrosion rate because the corrosion rate would be expected to decrease as the Li became saturated with SiC/SiO_2.

The results reported by Curran, Cree and Amateau are useful for estimating the potential effect of Molten Li on monolithic SiC; however, molten Li coolant in a fusion reactor environment would be maintained at a very low O_2 activity while the data of Curran, Cree and Amateau was not. In low O_2 activity Li, Li reduced SiO_2 so that reaction 5 is not appropriate for a Li coolant in a fusion reactor. It is likely that Li in a low activity O_2 environment would reduce the grain boundary glass phase and produce intergranular penetration and crack growth. Therefore, data on SiC/SiC composite material in a fusion relevant molten Li environment is needed for a correct assessment. Also, the reported data does not consider dynamic stress corrosion

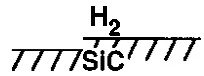
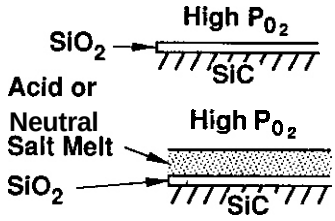
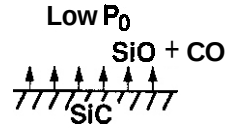
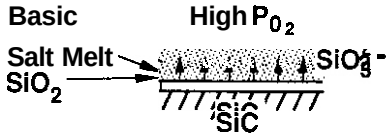
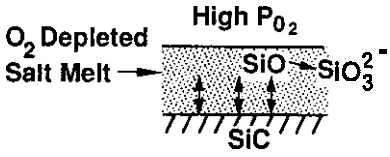
Environment	Reaction Mode	Effect
	No Reaction	No Material Loss Inert
	Passivatlon	Forms Protective SiO_2 Scale, Almost Inert to Salt Melt
	"Active" Oxidation	Evolution of SiO (g) and CO(g) at SiC Surface
	Accelerated Corrosion	Formation of Soluble ionic Species
	Gasification and Active Corrosion	Formation of SiO, SiO_2 Scale Absent or Ruptured, Silicate Formation in Melt

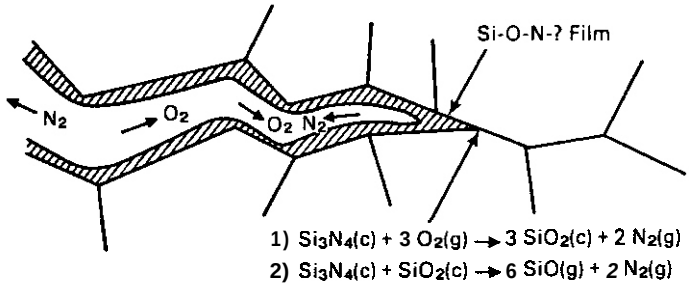
Figure 4. Possible modes of behavior of SiC in gas-molten-salt environments.

processes but only corrosion induced (flaw-induced) strength decreases. Examples of the type of reactions that are thought to be significant in stress corrosion of ceramics and ceramic composites are shown in Figure 5. Reactions with Q are shown, but other reactions such as those given by Equations 1-6 could induce crack growth. For a composite material, reactions with the fibers or whiskers bridging the crack behind the crack tip, the fiber/matrix interface of these bridging fibers and the grain boundaries ahead of the crack tip are all important. Although data on the corrosion rates of composite materials in fusion relevant environments is limited, specifics on the rate limiting corrosion step is even more limited. Information on the specific rate determining reactions in SiC/SiC composites will be needed to develop materials that are stable in specific fusion relevant environments.

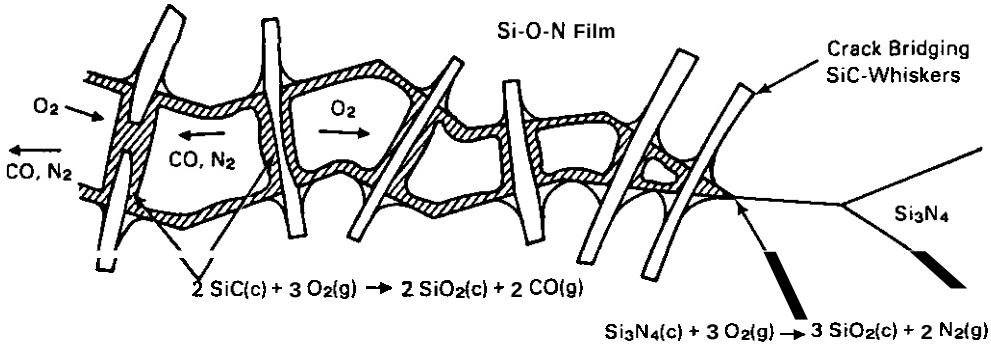
Data on the effect of environments containing Na on the corrosion and crack growth behavior of SiC is considerably more plentiful than that for molten Li or Li containing environments. This data is useful for estimating the effects of Li containing environments on the corrosion and crack growth of SiC/SiC composites because the phase diagrams for Na O and Li_2O with SiO_2 are quite similar, Figures 2 and 3. This suggests their effects on the "passive" Sib, layer and grain boundary glass phase will be similar. As mentioned previously, Na is expected to be more detrimental than Li because of the lower temperature eutectic formed in the Na O-SiO_2 system. Jacobson[9] evaluated the kinetics and mechanisms of the corrosion of sintered α-SiC in molten salts at 1000°C. In the reaction of Na_2SO_4/O_2 with SiC, the reaction occurred primarily in the first few hours with the formation of a protective SiO_2 layer. This observation was demonstrated with results showing the total weight of the corrosion products/unit area reaching 6 mg/cm^2 (SiO_2 t Na_2O- X (SiO_2) after a few hours and remaining constant up to 20 hrs.

However, as in the study by Curran and Amateau,[8] a limited amount of salt was added to the surface. This type of experiment is likely to give much lower corrosion rates than is possible in a flowing liquid Li coolant. Jacobson and Smialek[10] also noted that SiC is subject to pitting corrosion in molten salts. Pits occurred at structural discontinuities and bubbles formed during the formation of SiO . Pitting corrosion is detrimental because it demonstrates that the "passive" SiO_2 layer has been degrade8 and because the pits act as flaws resulting in reduced fracture strength.

Monolithic Si_3N_4



Sic-Whisker Reinforced Si_3N_4 Composite



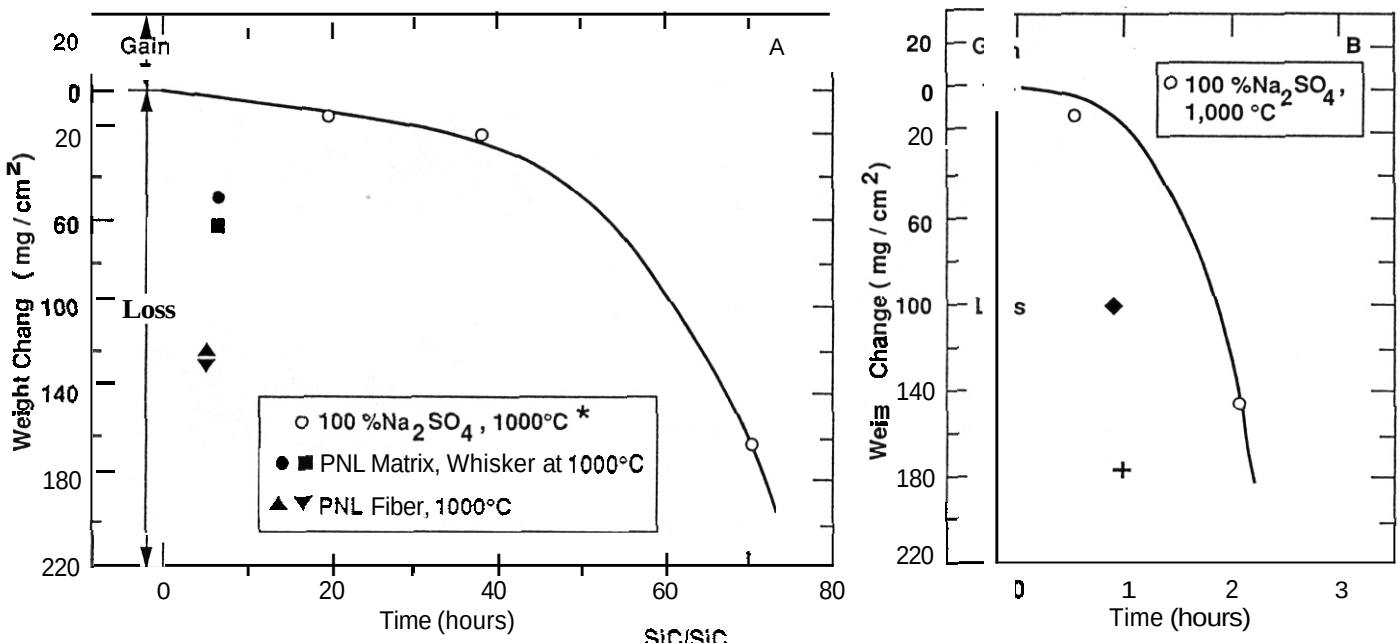
Rate Processes

1) O_2 transport to film
2) Oxidation process of matrix and whiskers
3) Deformation rate of film at crack-tip
4) Deformation rate of film at matrix-whisker interface

Figure 5. Schematic of potential environment-crack tip reactions in monolithic Si_3N_4 and Sic-whisker reinforced material.

Corrosion measurements of SiC immersed in a crucible of molten Na_2SO_4 were conducted by Tressler et al.[11] Weight change results for both SiC and Si_3N_4 in 100% Na_2SO_4 at 1000°C are given in Figure 6 where it is evident that considerable corrosion occurs for both materials with SiC showing a higher corrosion rate than Si_3N_4. . Both materials exhibited a weight loss because the reaction product was removed prior to measuring the weight change. An in situ measurement would probably exhibit a weight gain up to the time at which reaction product spallation occurs. These results illustrate the concern expressed earlier that a larger quantity of Li or Na_2SO_4 could result in a higher corrosion rate. Clearly, if the corrosion rate of SiC/SiC composites in liquid Li approach that of the molten salt, then these materials would be unstable in a liquid Li environment at 1000°C. It is not likely that Li would be used at a temperature as high as 1000°C, so corrosion data on SiC/SiC must be obtained at the relevant use temperature.

Corrosion data obtained at PNL on SiC/Si_3N_4 and SiC/SiC composite materials is also presented in Figure 6. The corrosion rate of the composite material was found to exceed that of the monolithic material for a Nicalon-SiC reinforced, hot-pressed Si_3N_4 and a Nicalon SiC reinforced, CVI SiC. A SiC whisker reinforced, hot-pressed Si_3N_4 exhibited a corrosion rate similar to the unreinforced hot-pressed Si_3N . The activation energy for the corrosion of the fiber reinforced material was 880 kJ/mol, while the whisker reinforced and matrix material had an activation energy of 1280 kJ/mol, Figure 7. The difference in corrosion rate and activation energy for the fiber reinforced material was associated with preferential corrosion of the Nicalon fiber. The fiber reinforced material had a carbon interfacial layer between the fiber and matrix while the whisker reinforced material had a thin amorphous glass layer. However, the difference in corrosion behavior is not thought to be associated with the interfacial layer but the structure of the Nicalon fiber following hot-pressing, Figure 8. As produced, Nicalon has an amorphous/microstryalline structure; the hot-pressed structure was crystallized with evidence for a Mg silicate in the grain boundaries. The source of



SiC/SiC Material	Wt. Loss/8 hr-900 °C, mg/cm^2	900 °C/1 hr	1000 °C/1 hr
BN	414	426	
No Interface	462	◆ 103	◇ 215
C	233	402	
C-B_4C-BN	298	+ 172	354

* R.E.Tressler, M.D.Meiser and T.Yonushonis J.Amer. Cer. Soc. Voi. 59 Page 278,1978

Figure 6. Molten salt corrosion data for a) monolithic Si_3N_4 (PNL data) and b) monolithic SiC (Tressler et al.) and SiC/SiC composites (PNL data).

the Mg was the MgO sintering aid used for the hot-pressing process. Corrosion of the Nicalon fiber along the glass enriched grain boundaries probably accounted for the high corrosion rate of the Nicalon fiber reinforced composite material.

The corrosion rate of a SiC/SiC composite produced by the CVI process was also greater than that of monolithic SiC, Figure 6. Microstructures of CVI SiC/SiC composites made by the ORNL process, Figure 9, and the DuPont process, Figure 10, show the porosity that exists in materials made by this process. The corrosion tests were conducted on material with porosity similar to that shown in Figure 10 but with variable fiber coatings. Composites containing fibers coated with C, BN, C-B_4C-BN and no coating were evaluated. The corrosion rate was highest for the material made with fibers with no coating and the BN coating while composites made with C and C-B_4C-BN coatings exhibited smaller corrosion rates. However, the corrosion rate of these materials at 900°C was considerably greater than that of monolithic material at 1000S. Matrix corrosion contributed to the majority of the weight change while some fiber corrosion was noted although this was a relatively small factor compared to the matrix corrosion. The open porosity and penetration of the molten salt into the composite are considered the primary factors causing the high corrosion rates for the SiC/SiC. The extrapolation of these results to that of liquid Li is difficult, especially since Li would be used at lower temperatures. However, these results demonstrate the need to measure the corrosion rate of composite materials and to make these measurements under conditions relevant to fusion reactors.

Fox, Jacobson and Smialek[12] found results in burner rig corrosion studies of CMCs similar to those obtained in the PNL molten salt studies sumnarized above. The burner rig tests utilize a hot combustion gas and would be expected to differ from a molten Li or He gas environments; however, molten deposits are only one mechanism for corrosion in hot combustion gas studies. Fox et al. evaluated Si_3N_4 reinforced with 30 vol% SiC whiskers and fibers. The method of processing for the whisker reinforced materials was not reported; however, it was probably hot-pressed while the fiber reinforced material was reaction bonded and had a residual porosity of 30%. Tests were conducted for 40 h at 1000°C in an environment containing 2 ppm Na added as NaCl. Monolithic Si_3N_4 exhibited a 10% decrease in the fracture stress while the whisker reinforced material exhibited a 35% decrease. The fiber reinforced material exhibited an excessive corrosion rate, but no fracture studies were conducted. The high residual porosity in the reaction bonded material and the free C from the carbon coated fibers were postulated as the cause for the high corrosion rate in the fiber reinforced material. In the molten salt corrosion studies conducted at PNL, the more porous CVI composite material also exhibited a higher corrosion rate than did the hot-pressed Si_3N_4/fiber or whisker reinforced material.

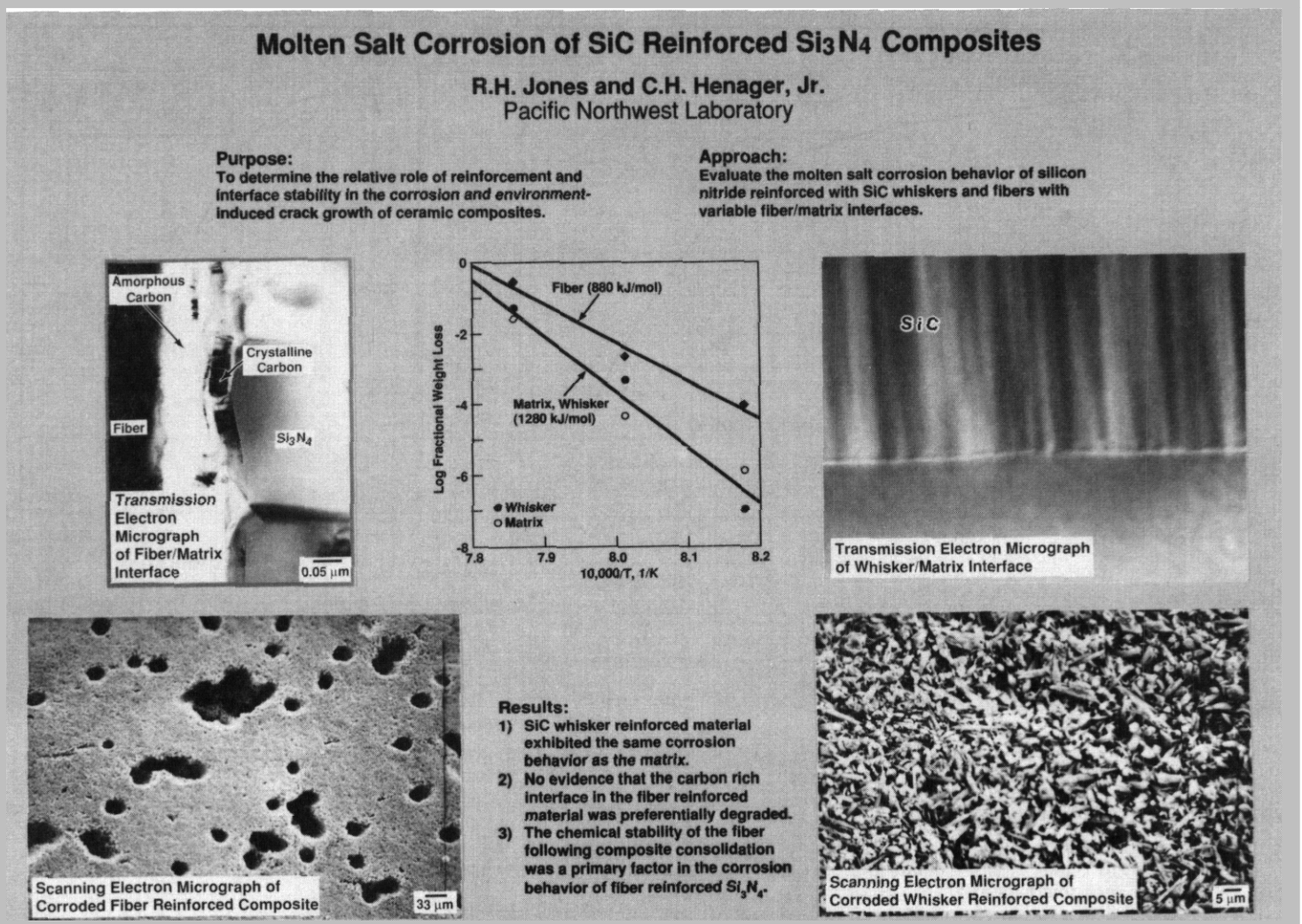


Figure 7. Molten salt corrosion data for SiC fiber and whisker reinforced Si_3N_4.

The effect of corrosion on the mechanical integrity of SiC/SiC structural components is an important factor in the durability of a fusion reactor first wall constructed of SiC/SiC. Decreases in the fracture strength would be possible by corrosion penetration along grain boundaries as noted for Li corrosion of monolithic SiC. Smialek and Jacobson[13] also found that molten salt induced pits were responsible for up to 50% of the observed strength reduction of SiC after 48 hr at 1000°C in Na_2SO_4/SO_3. A relationship between fracture stress and (pit illustrated the flaw induced fracture process. Henshall et al demonstrated that combustion gases containing alkali salts also contribute to accelerated subcritical crack growth of monolithic SiC, Figure 11. The crack velocity in the hot combustion gas was several orders of magnitude faster at a 50 K lower temperature than in air. The primary mechanism for this accelerated crack velocity is penetration of alkali ions into the grain boundary glass phase and the reduction in the viscosity of this phase. The reduced viscosity causes increased crack tip creep rates and creep damage.

During this review, no data was found in the literature on radiation effects on molten salt corrosion, although some information on radiation effects on the active-passive transition was available. Radiation induced phase changes of SiC or phases present in grain boundaries or interfaces could alter the stability of these materials in molten Li, although any discussion of this topic would be speculation without further experimental data.

The stability of SiC/SiC composites in a He coolant will depend primarily on the O_2 and H_2O partial pressures. A partial pressure of 10^{-10} to atm of O_2 will stabilize a "passive" SiO_2 layer at fusion blanket temperatures. The He coolant in a fusion reactor will undoubtedly have far more O_2 than 10^{-8} atm so that the primary corrosion issue will be the stability of this "passive" film. However, many SiC/SiC composites

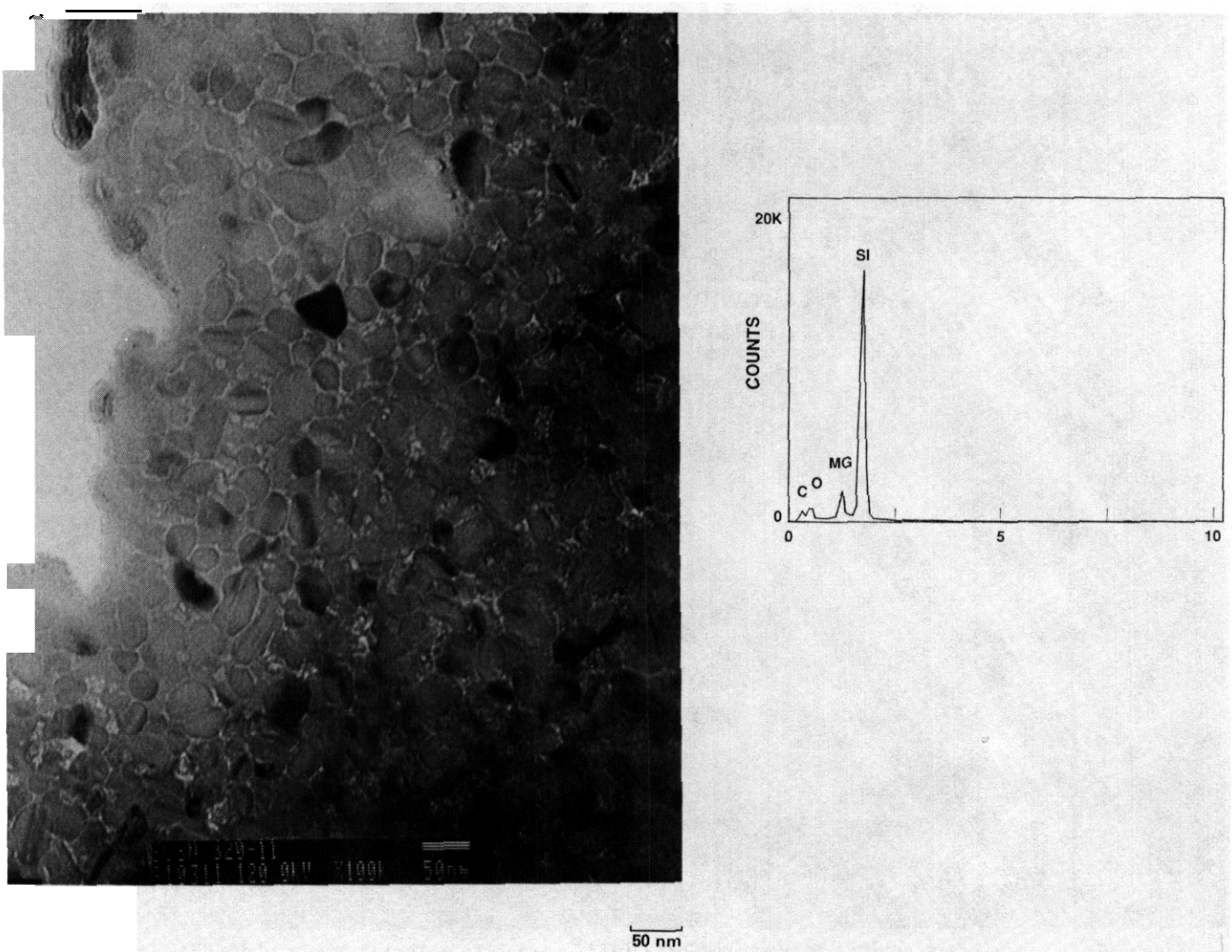


Figure 8. Transmission electron micrograph of a SiC fiber following consolidation in a SiC/Si_3N_4 composite produced by hot-pressing

rely on a fiber/matrix interfacial layer such as C, BC or BN for their fracture resistance, so the stability of this layer in O_2 and H_2O will also be important. Also, in the tritium breeding sections of the reactor, where He will be a carrier gas, the reaction of tritium with the SiC/SiC composite must be considered. Hydrogen formed by (n,p) reactions within the SiC/SiC will also react and contribute to mechanical property changes and subcritical crack growth. So reactions with hydrogen and its isotopes are potentially very significant for these materials.

Spear et al.[15] measured the oxidation rate of hexagonal, α-SiC platelets with both (0001) C and (0001) Si faces. The only solid corrosion product observed was SiO_2, as given by equation 1b, with CO(g) formed at the SiC-SiO_2 interface. The O_2 pressure was 10^{-3} to 1 at 1200 to 1500°C which is above the active-passive transition so the presence of SiO(g) would not be expected. An activation energy of 120 kJ/mol was found for SiC which is very comparable to the value of 112 kJ/mol found for Si. Silicon nitride has a much higher activation energy of 486 kJ/mol because of the formation of a silicon oxynitride phase between the Si_3N_4 and the SiO_2 phases. A growth rate of 1.1 nm/min was determined for SiC at 1300°C in 1 atm of O_2. Oxygen diffusion was postulated as the rate limiting process up to 1350°C whereas above 1350°C ionic oxygen diffusion was rate controlling.

The protective properties of the "passive" SiO_2 film are very sensitive to the impurities of the SiC from which the film is formed. Fergus and Worrell[16] compared the oxidation behavior of several batches of SiC to that of very high purity SiC produced by chemical vapor deposition; these authors observed an activation energy of 142 kJ/mol for CVD SiC and 217 kJ/mol for sintered α-SiC. This compares with the value of 120 kJ/mol reported by Spear et al. for single crystal SiC platelets. Both the CVD and SiC platelets are much higher purity than the sintered α-SiC to which sintering aids were added. Vaughn and Maahs[17] in a

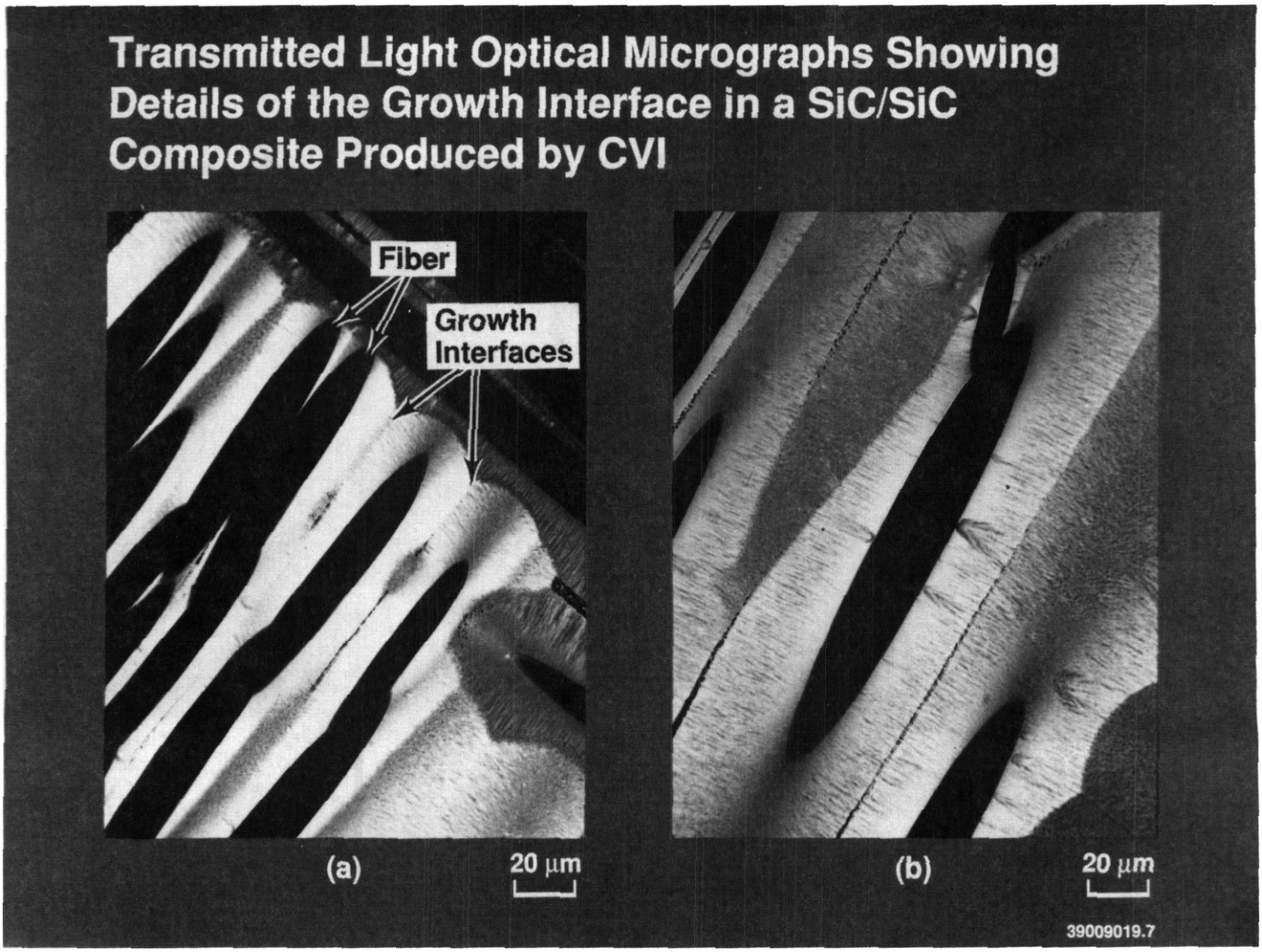


Figure 9. Transmission optical micrographs of SiC/SiC composite material produced by CVI (ORNL material)

review of the active-passive transition for SiC showed that this transition was quite variable depending on the source of the SiC and other experimental conditions such as the gas flow velocity. The Gulbransen data, Figure 1, was very close to that determined theoretically, but most other materials exhibited much higher transition temperatures, presumably caused partially by variable impurity concentrations in the materials. Therefore, it will be necessary to obtain chemical compatibility data for material-environment combinations at fusion-relevant conditions.

Results of oxidation studies of ceramic composites have not been reported, although Luthra[18] has presented some theoretical concepts on the oxidation of ceramic composites. Luthra assessed the gas phase diffusion of oxygen through microcracks, the solid state diffusion of oxygen through protective oxide layers, the formation of gaseous reaction products and the combined reaction of the matrix/reinforcement and oxygen. While the specific details of Luthra's analysis are not germane to SiC/SiC composites being proposed for fusion reactor applications, the concepts are relevant. In particular, the diffusion of oxygen through microcracks to react with the reinforcing fiber or the interface between the fiber and matrix is likely since SiC/SiC composites produced by the CVI process will have at least 10% residual porosity and there is evidence that irradiation and/or the design stresses will induce matrix microcracks. Thermal cycling is also likely to induce matrix microcracking because of the thermal expansion mismatch between the reinforcing fiber and the matrix. For SiC fibers in a CVI SiC matrix, this mismatch will be small but is not zero. Luthra's analysis applies primarily to oxide matrix composites, where the oxygen will not react with the matrix. For SiC, where the oxygen could react with the matrix, the transport would be considerably slower. In the case of SiC/SiC, Luthra's analysis should be extended to consider the reaction of oxygen with the matrix.

The formation of gaseous reaction products is a definite concern for SiC/SiC composites in an O_2 bearing environment such as a He coolant. The O_2 pressure will be maintained sufficiently high to passivate the

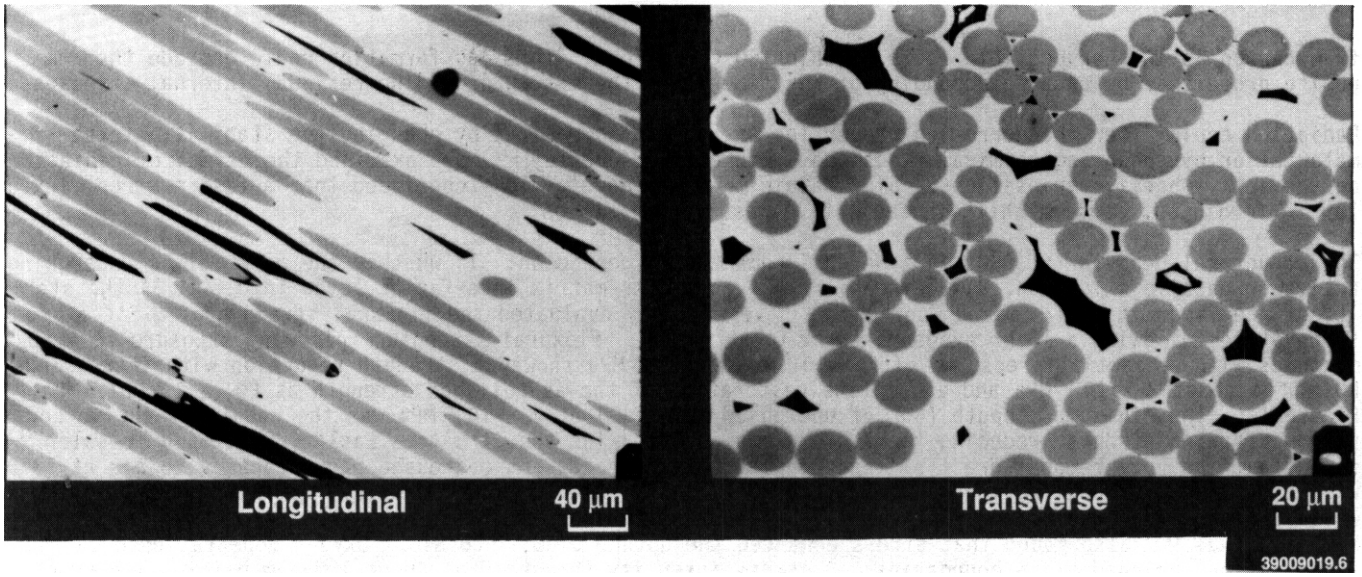


Figure 10. Reflected light optical micrographs of a) longitudinal and b) transverse cross-sections of a SiC/SiC composite produced by CVI

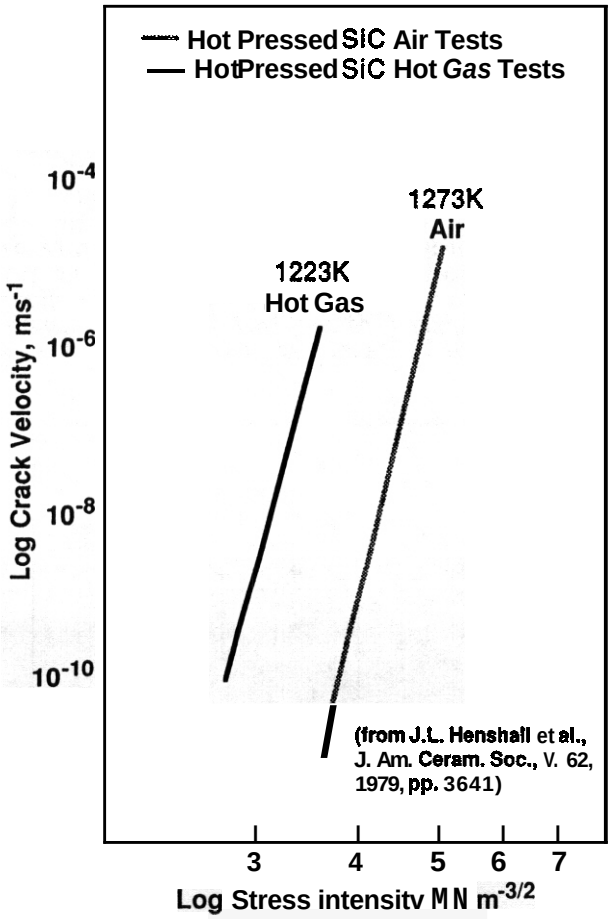


Figure 11. High temperature crack growth behavior for hot-pressed SiC in air and a combustion gas

surface of the SiC/SiC composite, but the activity within microcracks or ahead of a diffusion profile will likely drop below the active-passive transition. The formation of SiO or CO gas would then be possible at the interface between subsurface fibers and the matrix. Oxygen reacting with a carbon interfacial layer or

free carbon is another possible route by which CO could form. This gas formation could degrade the composite properties by causing debonding of the fiber from the matrix or adding residual internal stresses.

Radiation could alter the corrosion properties of SiC/SiC composites by changing the stability of the material or by enhancing chemical reactions. Bennett and Chaffey[19] have examined the effect of radiation on the active-passive transition of SiC containing 16% free Si. They concluded that a fast neutron flux of 10^{11} n/cm^2 did not cause a shift in the active-passive transition.

The structural behavior of CMCs in a He environment will depend on: 1) whether the material is undergoing active or passive oxidation, 2) the stability of the fiber-matrix interfacial layer in O_2 and 3) the stability of the fiber in O_2. Kim and Moorhead[20] have recently evaluated the flexural strength of α-SiC at room-temperature following a 10-hr exposure to Ar-O_2 at '1400°C. Flexural strengths following exposure to Ar-O_2 mixtures with O_2 partial pressures of 7 x 10^{-7} to 2 x 10^{-4} MPa showed a strength reduction with increasing PO_2 up to about 2 x 10^{-5} MPa and a complete restoration of the as-polished strength at PO_2 > 2 X 10^{-5} MPa, Figure 12. The minimum strength (60% of unexposed material) at 2 x 10^{-5} MPa was the result of active corrosion creating strength reducing flaws along grain boundaries and at pits. Easler, Bradt and Tressler[21] found that the room temperature flexure strength both increased and decreased upon exposure to air at 1370°C with and without an applied load. The strength increases were thought to result from oxidative blunting, while the decreases that occurred under load were caused by subcritical crack growth producing larger flaws. Minford et al.[22] also found that stress enhanced the uptake of O into SiC. Oxygen penetration occurred along cation enriched grain boundaries. A stress intensity threshold of about 1 MPaJm below which crack blunting occurred and above which crack extension occurred was found. At fusion relevant temperatures, active oxidation is not expected because the PO_2 in the He coolant is expected to exceed the active-passive transition. However, 10-hr exposure tests, as conducted by Kim and Moorhead, are an insufficient basis for determining the stability of SiC/SiC composites for a power plant that must operate for 1000s of hours.

Oxidation can alter the dynamic crack growth behavior of SiC as well as reduce the fracture strength caused by corrosion induced flaws. A reduction in the K_{th} of α-SiC after being loaded to different stress intensities for 4 hr at 1200 and 1400°C was reported by Minford et al.[23] They reported a reduction in the K_{th} from 2.25 in the unoxidized condition to 1.75 MPa$\sqrt{m}$ in the oxidized conditions at 1200°C and from 1.75 to 1.25 MPaJm at 1400°C for samples tested in air or pre-oxidized. They concluded that O_2 caused a change from diffusion controlled crack growth to viscous cavity growth and linkage with a corresponding reduction in K_{th}. The K_{th} was defined as the transition between crack blunting and growth as determined from the fracture strength following the 4-hr static loading at various K values. McHenry and Tressler[24] found that the K_{th} and subcritical crack growth rate was independent of the PO_2 for pressures ranging from 10^{-8} to 10^{-4} atm and temperatures of 900 to 1100°C. The crack growth rate exhibited an Arrhenius temperature dependence with an activation energy of 20 kcal/mol that is consistent with viscous flow of a grain boundary glass phase. The lack of a dependence on PO_2 does not necessarily indicate that O_2 did not induce crack growth, but that the effect of O_2 was saturated at pressures above 10^{-8} atm. Again, these results suggest a possible concern for

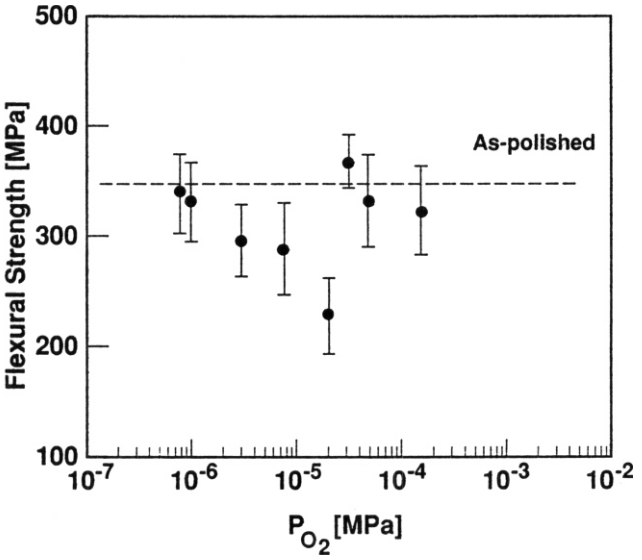


Figure 12. Room-temperature flexural strength of sintered α-SiC after exposure for 10 h at 1400°C in Ar atmospheres with various PO_2.

the use of SiC/SiC CMCs in a He environment, but the temperatures are higher than expected for a He cooled reactor (probably < 1000°C), the tests were conducted for relatively short times and the data is for monolithic SiC and not for CMCs.

Stability of SiC in $He/H_2/H_2O$ Mixtures

As mentioned previously, H and H_2O will be present in some quantities in certain sections of the reactor blanket. Water will resul? from the reaction of H_2 with residual O, while H_2 will be present as an additive to the carrier gas in the breeding blanket and from (n,p) reactions and the plasma in the first wall materials. Studies on the stability of SiC in H_2 environments have been conducted primarily for application in the National Aerospace Plane and in a ceramic Stirling engine where the H_2 chemical activities are considerably greater than expected in a fusion blanket.

Herbell, Eckel, Hull and Misra[25] have evaluated the thermodynamic stability of SiC in pure H_2 at 1 atm as shown in Figure 13. The primary gaseous reaction product is CH_4 as described by Equation 2 while other reactions that produce SiH_4 and SiH are also possible at temperatures as low as 900°C. At fusion relevant temperatures (900-1000°C), the reaction to form CH_4 is 100 times greater than that for SiH_4 and 10^6 times greater than for SiH. A small amount of H_2O can after the phase stability such that at 1400°C, and about 1000 ppm of H_2O, the dominant gaseous reaction products become SiO and CO, Figure 14. Results for lower temperatures were not reported but the reaction of H_2O with Sit occurs at much lower temperatures so similar reaction products would be expected at lower temperatures. No loss in the room-temperature flexural strength of sintered SiC was noted by Herbell et al.[25] for samples exposed to H_2 saturated with H_2O for 100 h at temperatures from 800 to 1400%. In dry H_2 (25 ppm H_2O), Hallum and Herbell[26] noted a 33% decrease in the fracture strength of sintered SiC after exposures of 500 h at 1100 and 1300°C. A statistically significant decrease in flexural strength was also observed after 50 h at 1000°C. The stability of SiC in an $Ar/H_2O/5\%$ H_2 mixture was calculated by Jacobson, Eckel, Misra and Humphrey[27] in the same manner as the H_2/H_2O mixtures, with the result shown in Figure 15. Except for the lower gas pressures and the

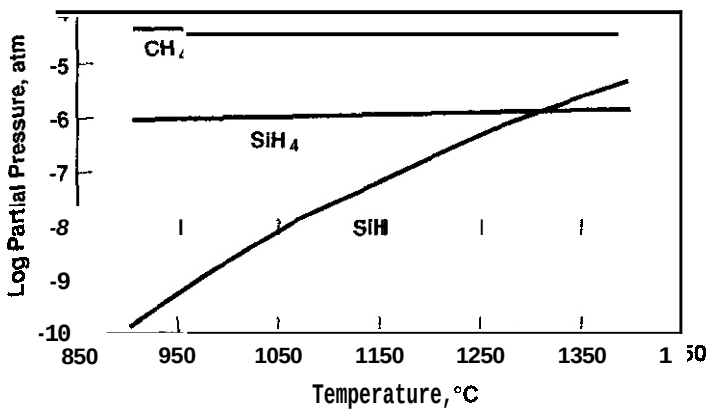


Figure 13. Partial pressures for gases in equilibrium with SiC in pure H_2 at 1 atm.

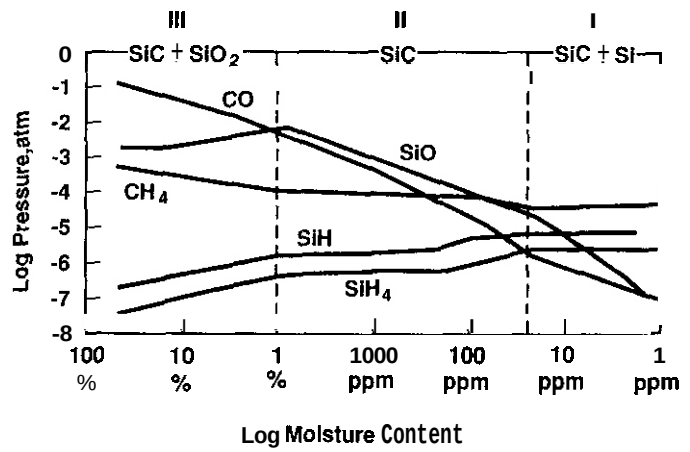


Figure 14. Stability of SiC at 1400°C in H_2 t H_2O at 1 atm.

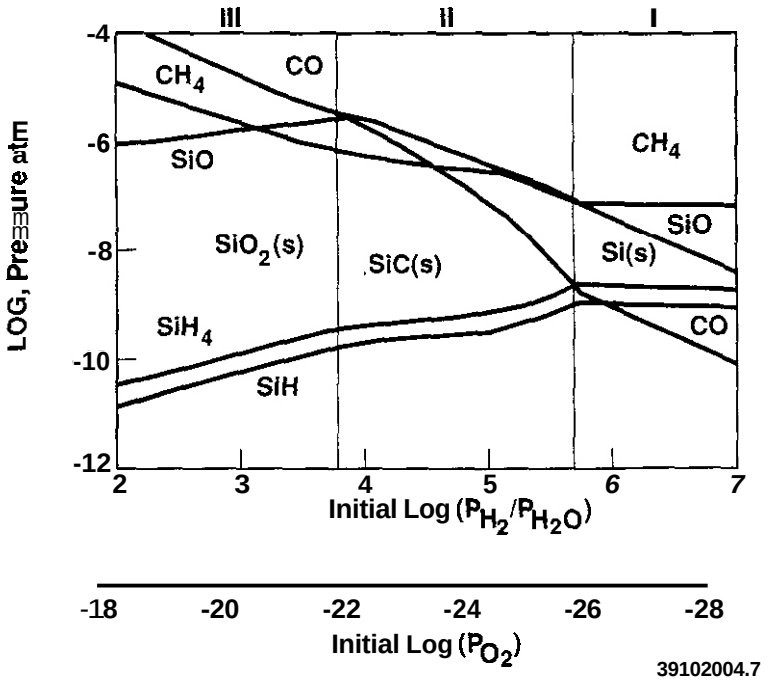


Figure 15. Thermodynamic analysis of SiC t 5% H_2/Ar at 1300°C. All pressures are in atmospheres.

shift in the relative activities of SiO and CH, in region III, the results are essentially identical. At 1300°C, Jacobson et al.[26] measured a weight loss of around 1 mg/cm² after 24 h in a region II Ar/H_2/H_2O mixture.

CONCLUSIONS

SiC/SiC composites have very attractive high temperature properties and fracture resistance coupled with low activation characteristics. However, there are a number of issues related to the application of these materials for structural applications in a fusion reactor first wall and blankets. The chemical stability of these composites in the reactor coolants and in H, is a key question that must be answered before further development of these materials for fusion reactors is warranted. The data base available in the literature is inadequate to provide a quantitative assessment but is adequate to provide some guidance. The environments evaluated in this review include: 1) liquid Li, 2) He/O_2 and 3) He/H_2/H_2O. The first environment relates to a liauid lithium cooled system, the second to a He cooled svstem and the third to a varietv of environments to which the composite material could be exposed including D/T from the plasma, internal-H from (n,p) reactions and T_2/T_2O/HTO in a sweep gas in the T breeding blanket. Essentially all of the available corrosion data is for monolithic SiC with little data available for comoosite materials. This assessment was therefore based on this data for monolithic materials with suggestibns made for composite behavior where possible. However, before SiC/SiC composites can be utilized, it will be necessary to obtain chemical compatibility data for the desired material (from a specific vendor) in the fusion relevant environment.

Corrosion and strength degradation of monolithic SiC has been observed after only short exposures to liquid Li at temperatures exceeding 500%; however, these studies were conducted in an environment with a relatively high PO_2. A low melting silicate, formed by reaction of Li_2O and surface and grain boundary glass phases, could have caused this reduction in strength. A liquid Li coolant in a fusion reactor will be maintained at a very low PO, so that the primary reaction with a SiC/SiC composite will be with grain boundary or surface glass phases, since SiC is relatively stable in liquid Li at fusion relevant temperatures. *Also*, the effects of corrosion-induced flaws on fracture strength has been evaluated but the synergistic effects of stress corrosion cracking have not been determined. Data from molten salt corrosion studies, shows that SiC/SiC composites are more severely degraded than monolithic SiC at temperatures of 900°C and above. However, this result must be viewed skeptically with respect to application in liquid Li because molten salt corrosion is expected *to* be far more severe than liquid Li at low PO_2.

Oxidation of SiC in a He coolant is another possible reaction that could degrade its properties. However, it is expected that a reactor He loop will contain sufficient O_2 that SiC will be in the "passive" oxidation range in which oxidation is kinetically limited. Under these conditions it is expected that the stability of the composite material will depend on the impurities in the material and the stability of the fiber/

matrix interfacial layer. One study showed that radiation did not alter the PO, necessary for passive oxidation of SiC t 16% Si at temperatures up to 950°C. A carbon interfacial layer will be unsuitable since it will readily oxidize, while other compounds used for the interfacial phase, such as B C and BN, will be unsuitable from a He transmutation or activation standpoint. Selection or development of this interfacial layer that is crucial to the toughness of these materials will be very crucial to the qualification of SiC/SiC composites for fusion applications. Strength reductions have been reported for monolithic SiC at PO, values below the active to passive transition while strength increases were noted for pressures above the transition. However, these were short-term exposures on the order of hours and the effect of long-term exposures (1000s of hrs), such as in a reactor, must be evaluated before SiC/SiC composites will qualify for these applications.

The stability of these materials in hydrogen is important because of the prevalence of hydrogen in a fusion reactor. SiC will react with H_2 under a variety of conditions with the formation of gaseous reaction products. A weight loss of 1 mg/cm^2 was measured after 24 h in a $Ar/H_2/H_2O$ environment at 1300°C. Although this temperature is somewhaf high for a fusion blanket, thermodynamic calculations predict that similar reactions will occur at temperatures as low as 900°C. No loss in the room temperature flexural strength was found for water saturated H_2 after an exposure of 100 h at temperatures ranging from 800 to 1400°C, but a 33% decrease was found for a 500 h exposure to dry H_2 at 1100°C and 1300°C. Under certain conditions, H_2 could reduce the protective SiO_2 layer and cause active oxidation of SiC. Therefore, the stability of SiC/SiC composites in H_2 bearing fusion reactor environments must be carefully assessed.

FUTURE WORK

Assessment of the suitability of SiC/SiC composites for fusion reactor applications will continue as time permits. Data on the oxidation, hot-gas crack growth, and radiation effects on fracture of SiC/SiC composites being conducted for other programs will be evaluated in terms of its relevance for fusion applications. Also, assessment of the leak rate of gases through SiC/SiC composites is being considered and will be undertaken if possible.

REFERENCES

1. G. R. Hopkins, and J. Chin, J. of Nuclear Materials, Vols 141-143 (1986) p. 148.

2. R. W. Conn, et al., ARIES I design report, UCLA, U.S. Department of Energy/OFE, 1990.

3. "Proceedings of the Office of Fusion Energy/DOE Workshop on Ceramic Matrix Composites for Structural Applications in Fusion Reactors," R. H. Jones and G. E. Lucas, eds., held in Santa Barbara, CA, May 21-22, 1990, PNL-SA-18743, CONF-9005225.

4. E. A. Gulbransen and S. A. Jansson, Oxid. Met., 4 (1972) p. 181.

5. D. W. McKee and D. Chatterji, J. Am. Ceram. Soc., Vol. 59 (1976) p. 441

6. T. P. Herbell, A. J. Eckel and D. R. Hull, "Effect of Hydrogen on the Strength and Microstructure of Selected Ceramics," in proceedings of the symposium on Environmental Effects on Advanced Materials, R. H. Jones and R. E. Ricker, eds., Oct. 1990, Detroit, MI, TMS, 420 Commonwealth Dr., Warrendale, PA, 15086.

7. D. R. Curran and M. F. Amateau, Am. Ceram. Soc. Bull., 65 (1986) p. 1419.

8. J. W. Cree and M. F. Amateau, J. Am. Ceram. Soc., 70 (1987) p. C-318.

9. N. S. Jacobson, J. Am. Ceram. Soc., 69 (1986) p. 74.

10. N. S. Jacobson and J. L. Smialek, J. Electrochem. Soc., Vol. 133 (1986) p. 2615.

11. R. E. Tressler, M. D. Meiser and T. Yonushonis, J. Am. Ceram. Soc., Vol. 59 (1976) p. 278

12. D. S. Fox, N. S. Jacobson and J. L. Smialek, Ceramic Transactions, Corrosion and Corrosive Degradation of Ceramics, R. E. Tressler and J. J. McNallen, eds., 1990, The American Ceramic Society, Westerville, OH, p. 227.

13. J. L. Smialek and N. S. Jacobson, J. Am. Ceram. Soc., 69 (1986) p. 741.

14. J. L. Henshall, D. J. Rowcliffe and J. W. Edington, J. Am. Ceram. Soc., Vol 62 (1979) p. 36.

15. K. E. Spear, R. E. Tressler, Z. Zheng and H. Du, ibid Ref. 12, p. 1.

16. J. W. Fergus and W. L. Worrell, ibid *Ref.* 12, *p.* 43.

17. W. L. Vaughn and H. G. Maahs, J. Am. Ceram. Soc., 73 (1990) p. 1540.

18. K. L. Duthra, ibid Ref. 12, p. 183.

19. M. J. Bennett and G. H. Chaffey, J. of Nucl. Materials, 52 (1974) p. 184.

20. H. E. Kim and A. J. Moorhead, ibid Ref. 12, p. 81.

21. T. E. Easler, R. C. Bradt and R. E. Tressler; J. Am. Ceram. Soc. 64 (1981) p. 731.

22. E. J. Minford, J. A. Costello, I. S. T. Tsong and R. E. Tressler, in Fracture Mechanics of Ceramics, V. 6. Eds. R. C. Bradt, A. G. Evans, O. P. H. Hasselmann and F. F. Lange, Plenum Publishing Corp. New York, NY, 1983.

23. E. J. Minford, D. M. Kupp and R. E. Tressler, J. Am. Ceram. Soc. 66 (1983) p. 769.

24. K. 0. McHenry and R. E. Tressler, J. Am. Ceram. Soc. 63 (1980) p. 152.

25. T. P. Herbell, A. J. Eckel, D. R. Hull and A. K. Misra, in proceedings of Environmental Effects on Advanced Materials, R. H. Jones and R. E. Ricker, eds., TMS, Warrendale, PA, in press.

26. G. W. Hallum and T. P. Herbell, Adv. Cer. Matls., 3 (1988) p. 171.

27. N. S. Jacobson, A. J. Eckel, A. K. Misra and D. L. Humphrey, J. Am. Ceram. Soc., 73 (1990) p. 2330.

EFFECT OF GAMMA IRRADIATION ON STRESS-CORROSION BEHAVIOR OF AUSTENITIC STAINLESS STEEL UNDER ITER-RELEVANT CONDITIONS--R. H. Jones and C. H. Henager, Jr., Pacific Northwest Laboratory[a]

OBJECTIVE

The objective of this research was to evaluate the role of radiolysis on stress corrosion of austenitic stainless steels under conditions typical of those expected in a water-cooled ITER.

SUMMARY

This study coupled with other published data supports the conclusion that gama irradiation will not induce stress corrosion cracking if the oxygen activity in the ITER water coolant is maintained at a low level. This conclusion is based on stress corrosion cracking tests conducted at 100°C in deionized water with 10 ppm Cl^- on solution annealed and sensitized Type 316 SS and PCA. The material was sensitized to about 5 C/cm^2 and fatigue crack growth tests were conducted in an autoclave exposed to a ^{60}Co source with tests conducted at 0, 2.3 X 10^2 and 6.5 x 10^5 rad/h. The material and water chemistry conditions were chosen to represent the worst case condition expected in an ITER resulting from poor welding and water chemistry control. Crack growth rates were found to decrease by about a factor of 2 in the presence of both gamma fluxes. Average crack velocities were 2.0 and 1.5 x 10^{-5} mm/cycle for Type 316 ss and PCA, respectively, in the absence of gamma irradiation and 1.3 and 0.74 X 10^{-5} mm/cycle at both gamma fluxes. These results suggest, for the limited conditions examined in this study, that radiolysis alone will not cause stress corrosion cracking of slightly sensitized Type 316 SS or PCA in water with 10 ppm Cl^- at 100°C. Other conditions that have not been examined and may cause crack growth include: radiolysis effects in high O_2 activity water, hydrogen induced cracking of radiation hardening Type 316 ss and PCA and irradiation-assisted stress corrosion'cracking (IASCC).

PROGRESS AND STATUS

Backsround

Stress corrosion cracking occurs when specific combinations of material microchemistry, material microstructure, environment chemistry and mechanical stress occur simultaneously. In austenitic stainless steels, the most severe material condition occurs when the precipitation of chromium-rich carbides at the grain boundary produce a condition known as sensitization. Important environmental variables include the concentration of oxygen, chloride, fluoride and sulfur ions in the water; temperature and pH. The mechanical stress may be static or cyclic resulting from externally applied loads or static stresses from residual stresses caused by welding or cold work. Stress or stress-intensity thresholds, below which stress corrosion cracking is negligible or non-existent, exist.

In previous assessments[1,2] it was shown that stress corrosion cracking of austenitic stainless steels will occur at ITER temperatures if: 1) the material is sufficiently sensitized during fabrication and 2) the water chemistry is not controlled such that impurities such as Cl^- are allowed to exist in the coolant. Other processes such as the presence of radiolysis, hydrogen generation and uptake, IASCC are also important in stress corrosion of austenitic stainless steels; however, these processes have not been previously assessed for ITER relevant conditions. The effect of gamma radiolysis on the stress corrosion cracking of thermally sensitized Type 304 SS has been examined in water at 288°C.[3] This study found that the strain to failure in a slow strain rate test was about 1/2 in the presence of gamma radiation relative to the non-irradiation environment. This suggests that radiolysis increased the crack growth rate by a factor of 2. Although this is not a major increase, the temperature dependence of this response was unknown, therefore tests were conducted at 100°C to assess the effect of radiolysis under more ITER-relevant conditions.

IASCC is a phenomenon that results from an irradiation-assisted change in the grain boundary microchemistry. Chromium depletion by an inverse Kirkendall process or impurity segregation by a point-defect binding/enhanced diffusion mechanism are two processes considered to be the primary microchemical changes responsible for IASCC. Electrochemical experiments performed by Bell et al.[4] to estimate the onset of IASCC in 25% CW PCA irradiated to 7 dpa at 60 to 400°C, found no response in material irradiated at 60°C but a significant response at 200°C. Therefore, IASCC may occur at temperatures between 60 and 200°C; however, there was some evidence that the increased corrosion current in these irradiated materials resulted from a bulk corrosion phenomenon and not a grain boundary process. Since ITER is expected to operate around 70°C, IASCC is not expected to be a major problem; however, thermal gradients and alterations in operating conditions could result in temperatures exceeding 70°C. Additionally, with the uncertainties in the temperature threshold for this phenomenon, experimental verification is necessary.

(a) Pacific Northwest Laboratory is operated for the U.S. Department of Energy by Battelle Memorial Institute under Contract DE-AC06-76RLO 1830.

Exoerimental Approach

Crack growth tests were conducted in a stainless steel autoclave, Figure 1, immersed in a ^{60}Co source. Constant K specimens, Figure 2, were cyclically loaded at 1 Hz with a sine waveform. The R ratio was 0.5 and the ΔK was 11 $MPa\sqrt{m}$. The water was deionized and deaerated before being placed in the autoclave without water recirculation. The test temperature was 100°C and a Cl^- concentration of 10 ppm was added. This was done to simulate the "worst" case situation should the ITER experience a period of poor water chemistry control. Tests were conducted at 3 gamma flux levels of 0, 2.3 x 10^2 and 6.5 x 10^5 rad/h. The variable gamma fluxes were achieved by tests conducted in the same autoclave at varying distances away from the ^{60}Co source.

The material used in this study was obtained from ORNL and was fusion heats, X-15893, Type 316 SS and K-280, PCA. The samples were solution annealed at 1100°C, quenched and sensitized at 625% for a short period of time to develop an EPR value of 5 C/cm^2.

Water Chemistry Changes from Radiolysis

Water coolant in an ITER blanket will undergo radiolysis primarily from energetic neutrons and gamma/betas. Although the radiolysis products far the ITER blanket spectrum have not been accurately determined, Fox et al.[5] have made some calculations for an aqueous environment under ITER-type conditions. They concluded that the dissolved O_2 concentration from gamma and neutron radiolysis were 30 and 50 ppb, respectively.

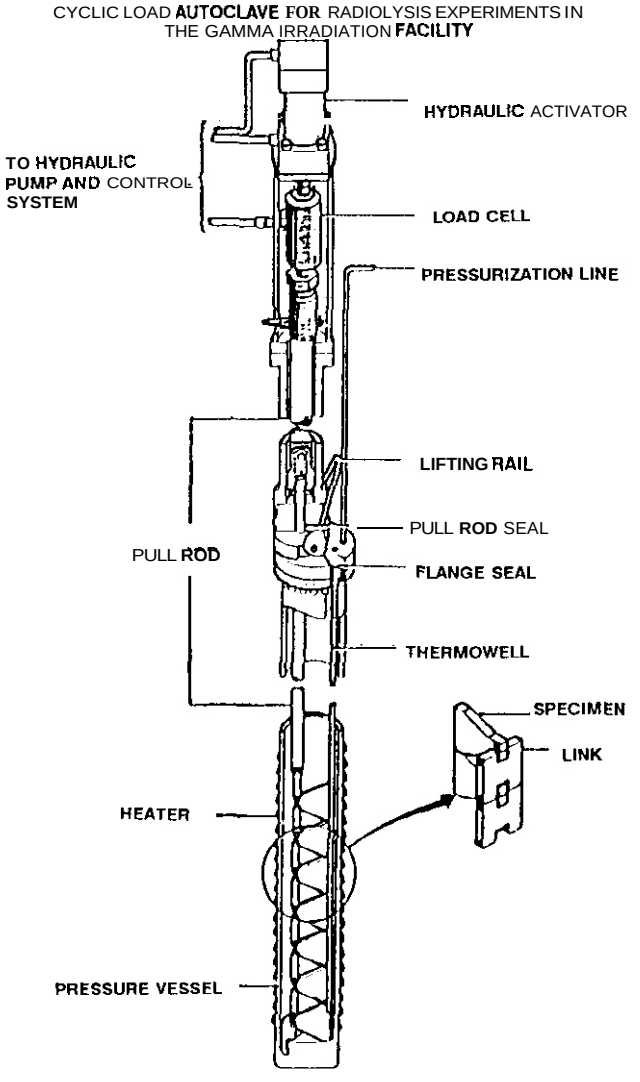


Figure 1. Experimental apparatus to conduct fatigue-crack propagation tests in an aqueous environment undergoing gamma radiation.

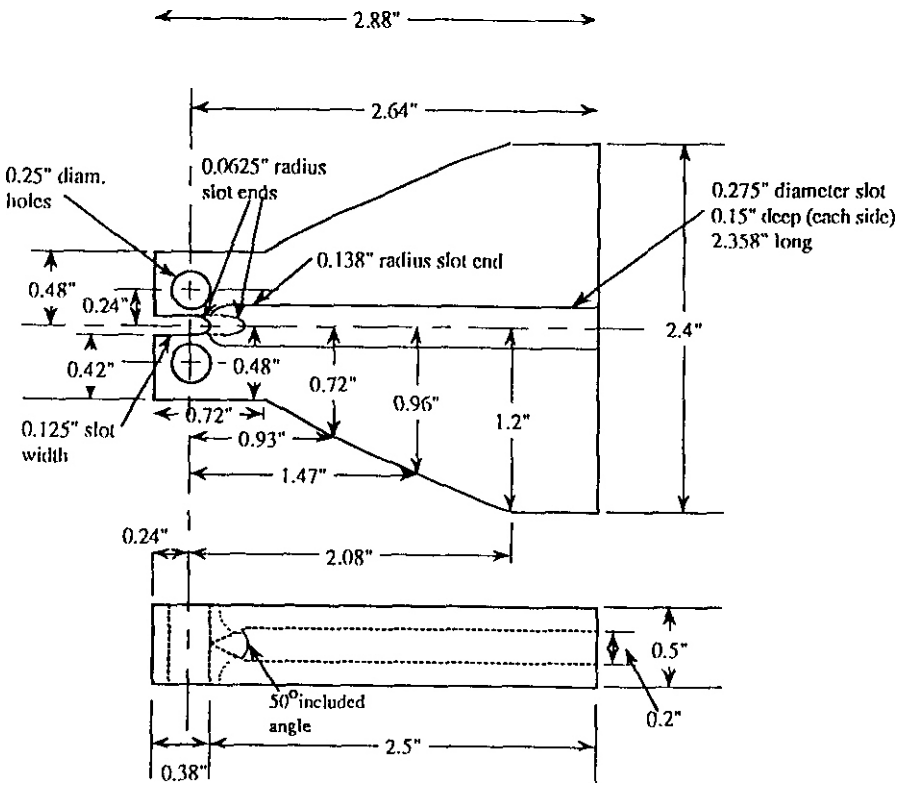


Figure 2. Constant K specimen for gamma pit testing

They also noted similar values for the H_2O concentrations. Gamma radiation is more efficient than energetic neutrons at producing e^-, H^+ and OH, but slightly less efficient at producing H_2O_2, H and H. Table 1. The differences between the production rate for these chemical species from irradiation with gamma/beta and 18 MeV neutrons is relatively small, so it is expected that the water chemistry of the tests conducted in a ^{60}Co source closely approximate those that will be present in an ITER blanket.

The major effect of radiolysis on corrosion and stress corrosion is expected to be the shift in electrochemical potential. Fox et al.[5] observed shifts of up to 100 mV in the open circuit potential of Type 304 SS with the addition of 5 ppm H_2O_2 to air saturated water at 25°C to which a small quantity of H_2SO_4 was added. Shifts of up to 300 mV in the open circuit potential have been reported[6] for Type 304 SS in the core of an LWR at 288°C relative to its out-of-reactor open circuit potential. These shifts in electrochemical potential are in a direction that could make the ITER structural material more susceptible to stress corrosion cracking.

Results

Crack growth rate results for the three test conditions are given in Table 2. A few of the test results are uncertain because the crack grew out-of-plane but their results are reported for completeness. Two tests were conducted for each condition. If the possible effects of the out of plane crack growth is ignored (PCA-8 shows the largest effect) the average crack growth rates are 1.5 x 10^{-5} and 0.74 x 10^{-5} mm/cycle for PCA without and with gamma irradiation and 2.0 x 10^{-5} and 1.3 x 10^{-5} mm/cycle for Type 316 SS without and with gamma irradiation. Clearly, there is no evidence for gamma irradiation accelerating the crack growth rate, although there is a possibility that it suppressed the crack growth rate by about a factor of 2.

Table 1. Gamma (and Beta) and Fast Neutron ($H^+ + D^+$) Radiolysis Yields (#/100eV) at Low (25-90°C) Temperatures

	$G(e^-)$	$G(H^+)$	$G(H_2O_2)$	$G(OH^-)$	$G(HO_2)$	$G(H)$	$G(H_2)$
Gamma	2.7	2.7	0.61	2.8	0.03	0.61	0.43
18 MeV Neutron	1.48	1.48	0.91	1.7	--	0.64	0.68

Table 2. Results of Crack-Growth-Rate Tests in DI Water with 10 ppm Cl^- at 100°C

Specimen Number	Crack Growth Rate, mm/cycle	ΔK	Radiation Intensity, Rad/h
PCA-2	2.3×10^{-5}	10.8	0
PCA-8	0.74×10^{-5}(a)	10.5	0
ORNL-9	1.9×10^{-5}	10.9	0
ORNL-12	2.1×10^{-5}	9.5	0
PCA-4	0.71×10^{-5}	10.9	2.3×10^{2}
PCA-5	0.86×10^{-5}	10.5	2.3×10^{2}
ORNL-7	1.2×10^{-5}(a)	11.1	2.3×10^{2}
ORNL-8	0.99×10^{-5}(a)	10.8	2.3×10^{2}
PCA-1	0.61×10^{-5}(a)	10.6	6.5×10^{5}
PCA-3	0.79×10^{-5}	10.5	6.5×10^{5}
ORNL-5	1.22×10^{-5}	10.5	6.5×10^{5}
ORNL-6	1.75×10^{-5}	11.0	6.5×10^{5}

(a) May be invalid due to off-planar cracking.

DISCUSSION

The stress intensity, water Cl^- concentration and material sensitization used in the gamma irradiation tests are expected to be more extreme than those encountered in the ITER structural first wall. Since the ITER coolant will be maintained below boiling, the coolant channels will be non-pressurized. The primary stresses will result from component loads, thermal strains, and residual stresses and vibrational stresses from the coolant. The maximum stress intensity is related to the delta stress intensity by the following relationship: $\Delta K = K_{max} (1-R)$. For a ΔK of 11 $MPa\sqrt{m}$ and R of 0.5 as used in these tests, the K_{max} was 22 $MPa\sqrt{m}$. The fracture toughness of unirradiated Type 316 SS at 100°C exceeds 100 $MPa\sqrt{m}$ but is expected to decrease with irradiation. Tensile property data reported by Grossbeck showed uniform tensile elongations of less than 1%and total elongations of about 1% following irradiation to 10-15 dpa at 50°C in HFIR. The total elongation of unirradiated, cold worked Type 316 SS is about 30% at 15°C; thus, ITER irradiation conditions caused a decrease of about a factor of 4 in the total elongation. This decreases in elongation was accompanied by an increase in the yield strength. Similar decrease in the fracture toughness are expected, but the magnitude of the fracture toughness following irradiation at ITER conditions has not been reported. If the fracture toughness decreases by a factor of 4, then a fracture toughness of about 25 $MPa\sqrt{m}$ is possible. If the ITER structural first wall reaches a fracture toughness of 25 $MPa\sqrt{m}$, then the gamma irradiation test conditions, with K_{max} equal to 22 $MPa\sqrt{m}$, would represent a test conducted very close to the end-of-life toughness for the ITER structural first wall. The ITER design will be sufficiently conservative that stress intensities within the structural first wall will be a small fraction of the end-of-life toughness. As discussed previously, the material used in this study was moderately sensitized and 10 ppm Cl^- was added to the water to simulate the "worst" case conditions resulting from poor fabrication and water chemistry control. Because an enhancement in the crack growth rate was not observed for gama irradiation for these "worst" case conditions, it is expected that gamma irradiation will not enhance the crack growth rate for more conservative material, water chemistry, and stress intensity conditions.

Crack velocities can be estimated from fatigue crack growth rates by multiplying da/dn times the test frequency. In this case, the test frequency was 1 cycle/s so the corrosion fatigue crack growth rates equal the stress corrosion crack growth rates. The stress corrosion crack growth rates calculated in this manner for the PCA and Type 316 SS are plotted along with other stress corrosion data for Type 304 SS in Figure 3. The range of crack velocities of 0.75 to 2.0×10^{-5} mm/s covers the PCA and Type 316 SS data both with and without gamma irradiation. The results are consistent with those expected for sensitized austenitic stainless steel with Cl^- impurities, although the results are slightly on the high side for 15 ppm Cl^- at 100°C. This is likely due to the more dynamic crack tip conditions existing in a corrusion fatigue test compared to a statically based stress corrosion test. In the figure, the data represented by the solid circles and squares is for 0, saturated and deionized water with low impurity concentrations. The effect of impurities on the crack velocity at ITER-relevant temperatures is clearly demonstrated by this data as the crack growth velocity decreases drastically at 100°C in high-purity water. A crack growth rate of 10^{-5} mm/s would require only 28 hrs to penetrate a 1-mm thick structure. Material selection and fabrication procedures to eliminate sensitization and water chemistry control to maintain impurities well below 1 ppm are clearly needed to ensure the structural integrity of the ITEK structural-blanket components.

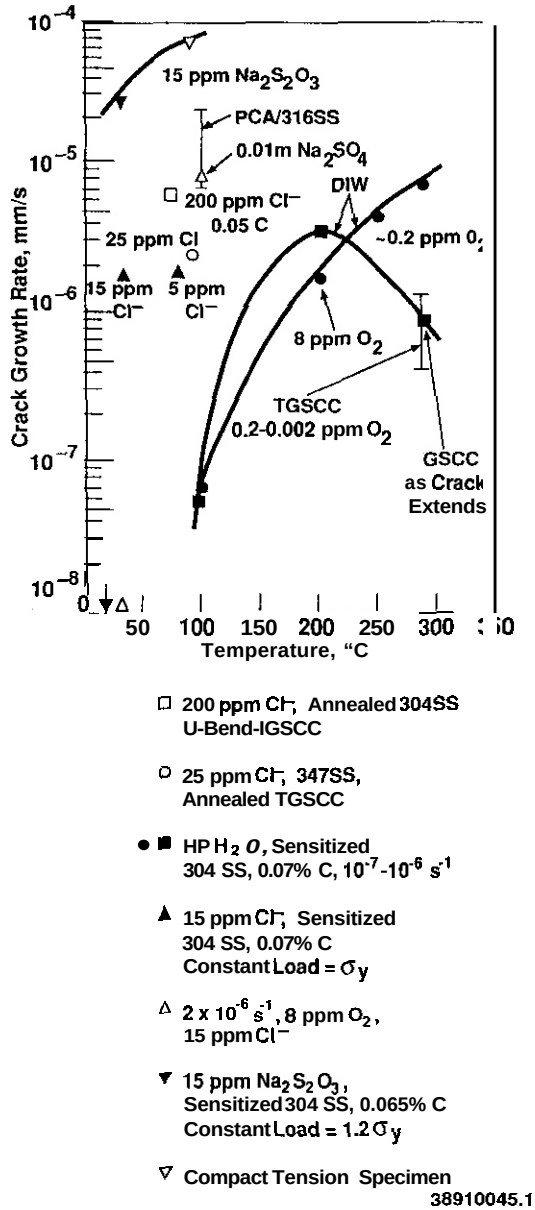


Figure 3. Stress-corrosion crack growth rate versus water temperature for austenitic stainless steel showing the effect of impurities in the water.

Fatigue loading will occur in the ITER from start-up/shut-down cycles, plasma cycles and coolant flow. How these cycles correspond to those used in the gamma stress corrosion tests is uncertain, but the cyclic loading from the plasma cycles and coolant flow will be high R ratio type loading while start-up/shut-down cycles are low R ratio type cycles. A comprehensive data set for ITER should include tests at a range of frequencies, R values and ΔK's since this study only considered one value for each of these variables.

Fujita et al.[3] and Saito et al.[8] observed a decrease in the crack velocity in tests conducted in deoxygenated water with gamma irradiation relative to tests conducted without gamma irradiation. However, an increase was observed for tests conducted in oxygenated water with gamma irradiation relative to tests without gamma irradiation. A 25%-increase in the elongation of a constant extension rate test specimen of Type 304 SS was observed for deoxygenated water in a gamma flux relative to tests without the gamma flux. In oxygenated water, gamma irradiation caused a decrease in the total elongation. The oxygen concentration in the water was controlled by bubbling H_2, N_2 or O_2 through the water before circulation through the autoclave. Saito et al. used a RADIOLYSIS MODEL to calculate the chemical species expected in oxygenated and deoxygenated water as a result of gamma irradiation. These calculations suggested that deoxygenation of the

water with H_2 resulted in a reducing environment during irradiation with gamma irradiation while the oxygenated system became more oxidizing. The reducing environment resulted from the production of e_{aq}^- and H with a significant reduction in the O concentration, whereas the oxidizing environment resulted from the increase in H_2O_2. The present test results were conducted with a static autoclave environment in which the water had been deoxygenated prior to starting the test. This is not the same as a dynamically deoxygenated system with H_2 bubbling through water flowing through the autoclave. However, the suppression in the crack velocity is consistent with the calculation of Saito et al.[8] which suggests that the environment was less oxidizing in the presence of the gamma irradiation than in its absence.

A comprehensive database on stress corrosion for ITER must include tests conducted at: 1) higher oxygen concentrations at which gamma irradiation could cause more oxidizing cunditions and 2) a wider range of temperature, ΔK and R values. Hydrogen-induced, subcritical crack growth of stainless steels is a greater concern for the integrity of ITER structural materials than aqueous stress corrosion cracking. Polusuhin et al.[9] demonstrated that H diffusivity is greatly enhanced in austenitic stainless steel during neutron irradiation. Extrapolation of their data to 100°C suggests a factor of 10^3 increase during irradiation relative to the nonirradiated material. Since H-induced crack arowth is a function of H diffusion to the crack tip, the H-induced crack velocity at ITER-relevant conditions could be substantially higher than values obtained out of reactor. The fluence for the onset of IASCC at 70 to 100°C has also not been established. The results of Bell et al.[4] suggest that this threshold exceeds 10-15 dpa at 60°C but may be less than this value at 200°C. Therefore, there is a critical need to identify this limiting threshold since the ITER operating conditions include material temperatures of up to 350°C and fluences of 30 dpa. These parameters are greater than those needed for IASCC of austenitic stainless steel which has been thoroughly documented to occur in 1 dpa at 288°C.

FUTURE DIRECTION

Further experimental work on this task is on hold pending an increase in the neutron interactive materials budget. Analysis of IASCC and hydrogen induced crack growth will be continued. Model calculations of Cr depletion by the inverse Kirkendall process will be conducted for temperatures of 60 to 200°C to evaluate the temperature and fluence threshold for IASCC for ITER-relevant conditions. These calculations will be conducted at PNL in collaboration with a BES/DOE funded program on IASCC. Also, the possible influence of neutron enhanced diffusivity of H on crack growth rate will be evaluated using existing models of H-induced crack growth for fcc metals.

REFERENCES

1. R. H. Jones, "Assessment of Stress-Corrosion Cracking for Near-Term Fusion Reactors, Fusion Reactor Materials Semiannual Report for Period ending March 31, 1988, DOE/ER-0313/4, p. 184.

2. R. H. Jones and S. M. Bruemmer, "Assessment of Stress-Corrosion Cracking of a Water-cooled ITER", Fusion Reactor Materials Semiannual Report far Period ending March 31, 1989, DOE/ER-0313/6, p. 389.

3. N. Fujita, M. Akiyama and T. Tamura, Corrosion, 37 (1981) p. 335.

4. G.E.C. Bell, E. A. Kenik and T. Inazumi, "Detection of Radiation-Induced Segregation in Austenitic Steels using Electrochemical Methods" presented at the U.S. ITER Aqueous Corrosion Workshop, August 1990, Argonne National Laboratory.

5. M. R. Fox, A. B. Hull and T. F. Kassner, "Stress Corrosion Cracking of Candidate Structural Materials in Simulated First-Wall/Aqueous Coolant Environments", 9th Topical Meeting on the Technology of Fusion Energy, in press.

6. P. L. Andresen, F. P. Ford, S. M. Murphy and J. M. Perks, "State of Knowledge of Radiation Effects on Environmental Cracking in Light Water Reactor Core Materials" in proceedings of the Fourth International Symposium on Environmental Degradation of Materials in Nuclear Power Systems-Water Reactors, Jekyll Island, Georgia, August 6-10, 1989, National Association of Corrosion Engineers, 1440 S. Creek Or. Houston, TX 77084, p. 1-83.

7. M. L. Grossbeck, "Development of Tensile Property Relations for ITER Data Ease", Fusion Reactor Materials Semiannual Report for Period ending March 31, 1989, DOE/ER-0313/6, p. 243.

8. N. Saito, N. Ichikawa, Y. Hemmi, A. Sudo, M. Itow and T. Okada, Corrosion, Vol 46 (1990) p. 531.

9. B. G. Polusuhin, A. P. Zyryanov, E. P. Baskakov, M. G. Golovachev, G. M. Kalanin, Yu. S. Strebkov, Yu. S. Shestakov, A. G. Dobrynskih and A. V. Sidornekov, "Hydrogen Permeability of Austenitic Steels Under Neutron Irradiation", presented at the Conference on Radiation Damage, PM-90, Alushta, USSR, May 22-25, 1990.

RADIATION-INDUCED SEGREGATION IN IRRADIATED TYPE 304 ALLOYS FOR THE ICG-IASCC ROUND ROBIN

-- E. A. Kenik (Oak Ridge National Laboratory)

OBJECTIVE

Comparative studies of radiation-induced segregation (RIS) produced in two type 304 alloys by low temperature (288° C) irradiation are under way utilizing analytical electron microscopy for comparison with the observed propensity toward irradiation-assisted stress corrosion cracking in austenitic stainless steels.

SUMMARY

Grain boundary RIS in two neutron-irradiated type 304 stainless steels has been investigated by X-ray microanalysis. In the conventional alloy (LC), narrow (≤5 nm width) RIS zones depleted in chromium and iron and enriched in silicon, phosphorus, and nickel were observed near grain boundaries. For the higher purity alloy (QC), similar width (56 nm) RIS zones depleted in chromium and iron and enrichment in nickel were observed at boundaries, though at reduced magnitudes relative to those in the LC material. No significant segregation of silicon or phosphorus was observed in the QC material. RIS zones associated with faulted dislocation loops in the LC material were detected and shown to be depleted in chromium and enriched in nickel and iron relative to the matrix.

PROGRESS AND STATUS

Introduction

The International Cooperative Group on Irradiation-Assisted Stress Corrosion Cracking (ICG-IASCC) is concerned with the possihility of irradiation-enhanced sensitization and stress corrosion cracking in commercial nuclear ower reactors. While IASCC is a current materials problem for fission reactors, it has ramifications for proposed water-cooleifusion machines such as the International Thermonuclear Experimental Reactor (ITER). One of the concerns is that radiation-induced segregation (RIS) could result in sensitization and stress corrosion cracking of austenitic stainless steels. The relationship between grain boundary chemistry and the propensity toward IASCC is being studied. The analytical techniques being applied to the measurement of near-grain boundary chemistry include analytical electron microscopy (AEM), Auger electron spectroscopy (AES), and atom probe field ion microscopy. Grain boundary chemistry of both thermally aged and irradiated materials will he studied. The current report is based on the preliminary X-ray microanalysis study of two irradiated materials.

Experimental Procedure

Table 1 gives the compositions of the alloys studied. The LC material is a commercial purity level type 304 stainless steel; the QC material is a higher purity version of a type 304 stainless steel with lower levels of silicon, phosphorus, sulfur, and carbon with some nitrogen added to offset the reduced carbon level. The two alloys were irradiated in different commercial boiling water reactors at 288° C nominally to the same fast neutron fluence [2.0 x 10^{21} m^{-2} (E > 1 MeV)].

Analytical electron microscopy was performed on a Philips EM400T/FEG in the scanning transmission electron microscopy mode with a probe diameter of <2 nm.[1] Subtraction of "in-hole" spectra from the measured EDS spectra corrected for (1) the normal "in-hole" counts associated with uncollimated radiation from the microscope illumination system and (2) radiation associated with the radioactivity of the specimen induced by neutron irradiation (predominantly Mn K X rays). A liquid nitrogen cooled specimen holder was employed for X-ray microanalysis in order to minimize contamination under the focussed spot. The quoted compositions are in atomic % as measured, and no attempt has been made to deconvolute the effect of excited volume size on the actual composition or profiles. However, X-ray microanalysis was generally performed in foil thicknesses ≤50 nm, in order to minimize the effect of beam broadening on the measured composition at the grain boundary. Manganese is not included in the analyses as a result of the interference of Mn X rays associated with the decay irradiation-produced ^{55}Fe. The presence of a surface film enriched in chromium resulted in measured matrix levels of chromium that were ~2.5 at. % high relative to the alloy composition. In addition, the presence of sulfur in that surface film associated with electropolishing in a sulfuric acid/methyl alcohol electrolyte interfered with the measurement of sulfur segregation to grain boundaries.

Results

Figure 1 illustrates the composition profiles measured near a grain bounda in the irradiated commercial purity LC material. Similar profiles were observed for other boundaries. A very narrow (2.53 nm width) zone of RIS was observed at the boundary with fast-diffusing chromium exhibiting the widest profile. The grain boundary is depleted of chromium and iron by ~4.5 and ~3.5 at. %, respectively; whereas silicon, phosphorus, and nickel were enriched by approximately 3.0, 0.8, and 4.0 at. %. The average composition changes for the boundaries measured were 2.6 (Si), 0.6 (P), -4.8 (Cr), -2.8 (Fe), and 4.3 at. % (Ni), where positive values indicate enrichment at the boundary and negative values indicate depletion. No statistically significant segregation of sulfur was detected.

Increased beam broadening associated with increased foil thickness has a strong effect on ihe compositions measured at grain boundaries, which is especially pronounced as a result of the very narrow width of the observed profiles. As the excited

Table 1. Alloy Composition (at. %)

Heat	Cr	Ni	Mn	Si	C	N	P	S	Fe
LC	19.95	8.60	1.99*	1.94	0.36*		0.08*	0.05*	67.03
QC	19.73	8.88	1.23	0.04	0.08	0.15	0.004	0.005	69.88

*Maximum permitted.

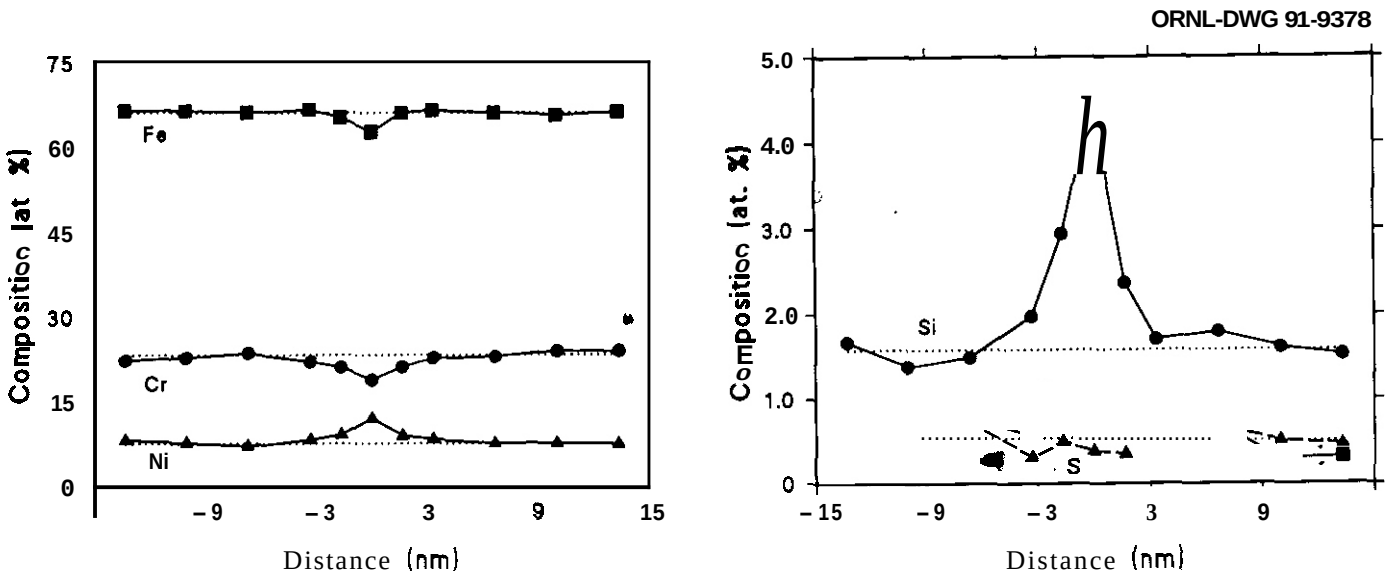


Fig. 1. (a,b) RIS profiles measured by X-ray microanalysis at grain boundary in LC material irradiated to nominal fast neutron flux of 2.0×10^{25} m^{-2} (E > 1 MeV) at 288 °C. Dotted lines indicate average matrix composition away from boundary.

volume increases in size (either from beam hroadcning or larger incident probe size), regions further from the grain boundary are included in the measured composition. This results in a lower degree of segregation being indicated hy the measurements. Table 2 illustrates the magnitude of the effect for a 25% decrease in foil thickness from ~60 nm to ~45 nm. The measurements made in foil thicknesses of ~45 nm more closely approximate the actual composition at the grain boundary than do those made at ~60 nm foil thickness. The enrichment of silicon. phosphorus, and nickel and the depletion of chromium and iron arc more pronounced for the smaller foil thickness

Table 2. Measured Grain Boundary Composition (at. %) Versus Foil Thickness

Foil Thickness (nm)	Cr	Ni	Si	P	S	Fe
45	17.95	13.07	3.59	0.77	0.33	64.29
60	18.75	11.90	2.33	0.53	0.14	66.35

Figure 2 illustrates composition profiles typical of grain boundaries in the irradiated higher purity QC material. A narrow (4-6 nm width) RIS zone is observed with chromium again exhibiting the widest profile. Though the measurements were performed in similar foil thicknesses and under similar experimental conditions, the QC material exhibits a lower degree of RIS to grain houndanes than does the LC material. No statistically significant segregation of silicon, phosphorus, or sulfur was detected. The average composition changes for the boundaries measured were 0.0 (Si), 0.0 (P), 0.0 (S), -1.7 (Cr), -0.9 (Fe), and 2.6 at. % (Ni), where positive values indicate enrichment at the boundary and negative values indicate depletion.

Another difference between the LC and QC materials was noted during the AEM examination, a marked difference in grain size. One might expect the higher purity QC alloy to exhibit the larger grain size for equivalent heat treatments. However, the QC material had an average grain size of ~8 μm (linear intercept method), whereas the LC material had a grain size of ~16 μm. This difference in grain size may indicate a difference in prior cold-workingheat treatment between the two materials or some less obvious effect of the difference in alloy composition.

As a result of the relatively low irradiation dose at 288°C, both materials exhibited moderate densities of small faulted dislocation loops (diameters ranging from 8 to 40 nm) and other extended defects too small to be identified by bright-field imaging. Figure 3 illustrates the microstructure of the QC material, which is also typical of the LC material. Little or no grain boundary denuding was observed for these defects. X-ray microanalysis of edge-on faulted dislocation loops in the irradiated LC material was performed in foil thicknesses <20 nm, in order to minimize the effect of beam broadening on the diameter of the excited volume. Table 3 gives the average composition (Cr + Fe + Ni = 100 at. %) for several dislocation loops with diameters ≥25 nm, and the adjacent matrix. The measured chromium levels are high as a result of the chromium enriched surface film present and the small foil thickness of the analyzed regions. RIS to the faulted dislocation loop results in depletion

ORNLDWG 91-9379

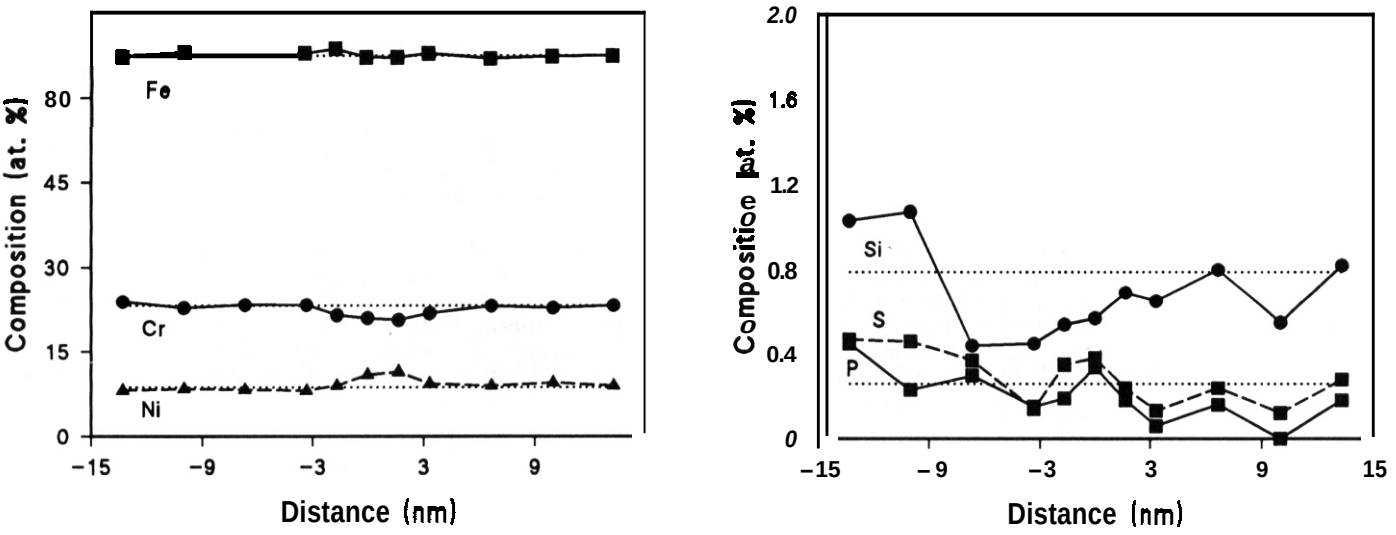


Fig. 2. (a,b) RIS profiles measured by X-ray microanalysis at grain boundary in QC material irradiated to nominal fast neutron flux of 2.0 x 10^{25} m^{-2} (E > 1MeV) at 288 C. Dotted lines indicate average matrix composition away from boundary.

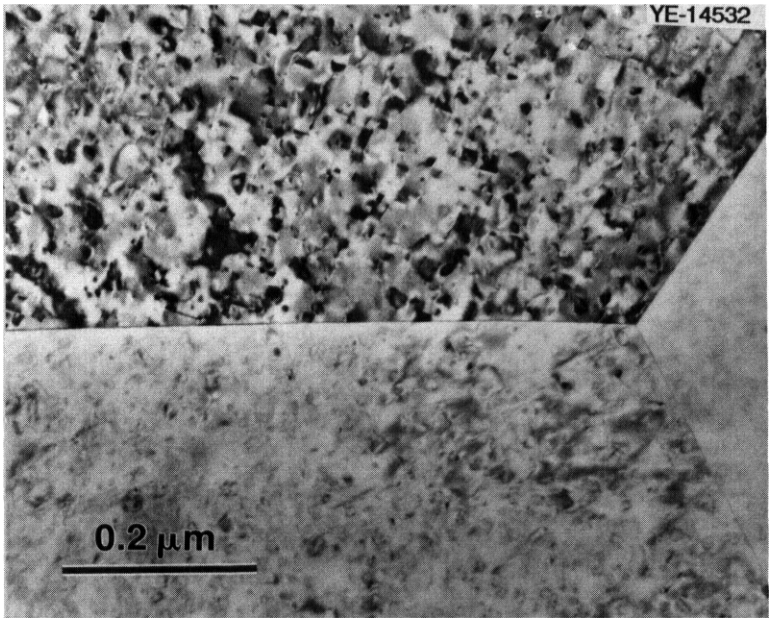


Fig. 3 Microstructure of QC material irradiated to nominal fast neutron flux of 2.0 x 10^{25} m^{-2} (E > 1 MeV) at 288 ' C. Note both moderate density of small faulted dislocation loops and other extended defects in matrix and the absence of significant denuding of extended defects at grain boundary.

Table 3. Average Composition Near Faulted Dislocation Loops (at. %) (Cr + Fe + Nl = 100 at. %)

	Cr	Fe	Nl
Dislocation Loop	21.57	65.94	12.49
Adjacent Matrix	24.64	64.52	10.84

of chromium by −3 at. % and enrichment of nickel and iron by ~1.5 at. %. There is an indication of silicon segregation to some of the dislocation loops. However, the detection limit for small silicon segregation was poor as a result of the low X-ray count rate associated with the small foil thicknesses analyzed, and both the high background and poor energy resolution (−250 eV) associated with the induced radioactivity of the specimen.

Discussion and Conclusions

Though both materials exhibit very narrow (−5 nm width) RIS profiles at grain boundaries, the magnitude of the segregation in the commercial purity LC material is more pronounced than in the high purity QC material. Depletion of chromium and iron and enrichment of silicon, phosphorus, and nickel are obvious in the LC material, whereas less oronounced depletion of chromium and iron and the'enrichment of nickel are observed in the QC material with no significant segregation of silicon or phosphorus. Detection of sulfur segregation was hampered hy the presence of a surface film enriched in sulfur and chromium. When the influence of this surface film is eliminated, the average chromium levels indicated at the grain boundaries are −15 at. % for the LC material and 18 at. % for the QC material. While these values are upper hounds for the actual grain boundary compositions as a result of relative sizes of the actual composition profiles and the excited volume, it is evident that the boundaries in the LC material are more depleted of chromium and as such should he more sensitive to irradiation-assisted stress corrosion cracking.

Two obvious differences between the two materials are the higher purity and smaller grain size of the QC material. It seems unlikely that a difference in grain size of the magnitude observed should have any effect of RIS, especially for the low irradiation temperature. This conclusion is consistent with the absence of any significant denuding of extended defects near the grain boundaries. This observation indicates that the mean free path of point defects is less than 20 nm, significantly smaller than the grain sizes. However, the difference in grain size may simply reflect the difference in alloy composition, which may be the actual origin of the difference in RIS observed between the two materials.

Certainly the reduced levels of silicon, phosphorus, and sulfur in the QC material eliminate significant RIS of silicon and phosphorus (and presumably sulfur) to grain boundaries. However, the reason is less clear for the reduced magnitude of grain boundary RIS for chromium, iron, and nickel in the QC material relative to that in the LC material. The presence of ~3.2 at. % of silicon and phosphorus segregated to boundaries in the LC material would reduce the levels of the other elements present, as the sum of all elements is constrained to 100%. While this effect could explain the reduced magnitude of RIS of chromium and iron in the QC material, it does not explain that of nickel. If silicon and nickel compete for RIS to the boundaries, it would be expected that the absence of silicon segregation in the QC material would result in increased nickel segregation (which is not observed). As such, there appears to be some synergism between RIS enrichment of silicon and possibly other elements and that of nickel. The enhanced enrichment of silicon and nickel in a material (LC) containing both elements would result in enhanced depletion of chromium and iron relative to that observed in a material (QC) containing only nickel.

The pronounced grain RIS observed in the irradiated LC material and the low irradiation dose prompted the investigation of possible RIS to faulte dislocation loops in the same material. RIS to dislocation loops has been observed for both ion and neutron irradiations at higher temperatures.[1,2] The current study shows that RIS to both grain boundaries and dislocation loops is still detectable by X-ray microanalysis for materials neutron-irradiated as low as 288 °C. It is possible that the zone of RIS around each dislocation loop may affect the pinning strength or tendency toward unfaulting of such small dislocation loops. As such, RIS to dislocation loops may affect the mechanical properties of stainless steels irradiated at such low temperatures.

FUTURE WORK

Different specimen preparation is required to minimize the thickness of the surface film associated with electropolishing and to eliminate sulfur from the film. The possibility of defecting segregation of silicon and other minor elements to both dislocation loops and grain boundaries will be investigated with parallel detection electron energy loss spectroscopy (PEELS) in order to avoid the problems of high background, poor energy resolution, and extraneous signals associated with X-ray microanalysis of radioactive specimens. These further studies will be aimed at understanding the origin of the difference in grain boundary RIS in these two alloys.

REFERENCFS

1. E. A. Kenik, Materials Problem Solving with the Transmission Electron Microscope, vol. 62, eds. L. W. Hobbs, K. H. Westmacott, and D. B. Williams, Materials Research Society, Pittsburgh, PA, 1986, p. 209.

2. E. A. Kenik, J. Nucl. Mater. 183 (In Press).

AQUEOUS STRESS CORROSION OF CANDIDATE AUSTENITIC STEELS FOR ITER STRUCTURAL APPLICATIONS – A. B. Hull and T. F. Kassner (Argonne National Laboratory)

OBJECTIVE

The corrosion resistance of the structural material to be used in an aqueous environment characteristic of candidate first wall/blanket systems in the International Thermonuclear Experimental Reactor (ITER) has not been quantified. Information obtained on the stress corrosion cracking (SCC) susceptibility of several candidate stainless steels under ITER-relevant conditions will help to identify an optimal combination of structural materials, coolant chemistry, and operational conditions for the ongoing ITER design work. The objective of this task is to provide baseline information on the SCC susceptibility of these candidate stainless steels in high-purity oxygenated water that simulates many important parameters1 anticipated in ITER first wall/blanket systems. This particular evaluation has been done to assess the role of hydrogen in environmental cracking of austenitic stainless steels in an ITER-relevant aqueous environment. Material chemistry, threshold stress conditions, and irradiation-assisted stress corrosion cracking (SCC) could influence the performance of structural materials.

SUMMARY

Hydrogen embrittlement of candidate first–wallmaterials (e.g., stainless steel, or SS) is a key issue for ITER because of hydrogen production due to (n,p) transmutation reactions; hydrogen generation of up to 2500 appm is anticipated. Material composition, changes in composition caused by transmutation reactions, irradiation damage, environment, and expected loading conditions were reviewed to assess the relative importance of various degradation processes for a fusion reactor first wall. The stability of austenite with regard to creation of deformation– or stress–induced martensite, α', was considered in relation to SCC and hydrogen-assisted crack growth in SSs at low temperatures (<150°C).

PROGRESS AND STATUS

Continuing Baseline Studies

Earlier work focused on developing criteria to define the simulated ITER water chemistry for SCC testa on candidate steels.[2,3] Interim results from a series of experiments to evaluate SCC susceptibility of Types 316NG, 316, and 304 SS have been reported previously.[4] No indication of SCC was observed in testa conducted at a strain rate of 3×10^{-7} s^{-1} in oxygenated water with sulfate additions (0.1-1.0 ppm) at temperatures of 95 and 150°C.

Additional testa[5] were performed on these steels under more severe conditions, namely, lower strain rates and the addition of hydrogen peroxide to the oxygenated water. Predominantly ductile fracture was observed in crevice specimens of Type 316NG SS strained to failure in a reference ITER water chemistry. The failure behavior of Type 304 SS crevice specimens heat-treated to yield sensitization values of 2, 3, or 20 C/cm^2 by the electrochemical potentiokinetic reactivation technique demonstrated that the degree of sensitization had a dramatic effect on susceptibility to intergranular SCC (IGSCC). Type 304 SS specimens sensitized to the higher value exhibited shorter failure times, lower maximum stresses, and lower reduction in area values than did less-sensitized Type 304 SS or Type 316NG SS specimens.

Susceptibility of the steels, including weldments, to SCC under conditions that cause radiolysis of the coolant[6] and embrittlement by hydrogen from n,p transmutation reactions in the steel during irradiation are currently being investigated. Crevice and noncrevice base metal and weldment specimens are being strained at rates of 1 to 3×10^{-7} s^{-1} in oxygenated water with H_2O_2 and/or H_2SO_4 at temperatures between 60 and 288°C. Ultimate strength, total elongation, reduction in area, and fracture surface morphology are being evaluated to determine the nature and extent of SCC.

Background: Effects of Hydrogen on Mechanical Properties of Austenitic SS

Hydrogen effects on the properties of austenitic SSs and ferritic steels have been the topic of considerable research over the past 30 years. Some of the work[7,8] is relevant to materials selection and long–term performance of fusion reactor components such as the first wall. Irradiation-enhanced diffusion of hydrogen and hydrogen–assisted crack growth in austenitic SSs may be of interest in assessments of tritium containment and integrity of irradiated structural components in a fusion reactor.

Regarding degradation of austenitic SS, many properties and failure mechanisms must be considered in a performance analysis of the first wall.[9] Hydrogen production due to (n,p) transmutation reactions, primarily in Fe and Ni, occurs at a rate of ≈540 appm/yr in Type 316 SS for a time–averaged neutron wall loading of 1 MW/m^2 (14 MeV).[9] The corresponding helium production rate from the (n,α) transmutation reaction is ≈240 appm/yr. Other transmutation products are formed at significant rates (e.g., Mn at ≈1200 appm/yr). Hydrogen and helium in the steel could influence mechanical properties[10] and make welding repair of the structure difficult.

Stress Zone Intensity Thresholds for Crack Growth and Fracture

Stress intensity thresholds for crack growth are useful in assessing maximum mechanical loads for a component containing a small crack or flaw such that failure of the component will not occur over the design life. SCC is ubiquitous because the threshold stress intensity factors, K_{th}, for crack growth are, in many instances, much lower than those for other modes of crack propagation. The implication is that under nominal loading conditions (i.e., tensile stresses well below allowable code values), small flaws (weld cracks, weld overlaps, corrosion pits, crevices, etc.) can provide both the local environment and stress intensities for crack initiation and growth. For example, K_{th} for intergranular SCC of sensitized Type 304 SS[11] in oxygenated water at 289°C is ≈10 $MPa \cdot m^{1/2}$ and the value for transgranular SCC of Type 316NG SS[12] is higher by a factor of only 2 (e.g., ~20–22 $MPa \cdot m^{1/2}$) under constant load or high–R cyclic loading. Crack propagation rates for SSs and nickel–base alloys are similar in light–water reactor (LWR) environments; consequently, efforts are made to control cracking by modifications in water chemistry and reduction of residual (and applied) stress levels.[13]

Austenite Stability in Stainless Steels

Another material parameter that can influence SCC and hydrogen–assisted crack growth in SSs at low temperatures (<150°C) is the stability of austenite with regard to formation of deformation– or stress–induced martensite, α'. The transformation from austenite to martensite ($\gamma \Rightarrow \alpha'$) occurs almost instantaneously by a diffisionless nucleation and homogeneous shear process brought about by mechanical stresses and strains, where the composition of the resulting martensite is identical to that of the predecessor austenite but the transformation involves ≈2 % increase in volume. Because of the higher diffusivity of hydrogen in the bcc phase (by 6 orders of magnitude at ≈25°C), transport of hydrogen in martensite is rapid and this could facilitate hydrogen–assisted cracking,[10] fatigue crack propagation,[14] and SCC.

As in the case of forecasting the probability of austenitic SSs to hot-crack and fissure during welding on the basis of material chemistry (ratio of Cr_{eq}/Ni_{eq}, where Cr_{eq} and Ni_{eq} are the chromium and nickel equivalents on a Schaeffler diagram),[15] a correlation has been developed to predict the stability of austenite at low temperatures from the composition of the steel.[16]

Results and Discussion

Both hot-cracking and α' formation must he considered in the selection of a "nuclear-grade" steel for the ITER first wall; the carbon concentration must he <0.025% in order to mitigate sensitization (grain–boundary Cr depletion) of the heat–affected zone of welds and IGSCC. The degree of sensitization (DOS) has been demonstrated to be a key parameter correlating grain-boundary microchemistry to SCC resistance. A high DOS corresponds to high susceptibility to IGSCC at temperatures <100°C.[5,17]

When the correlations discussed above are used to assess the susceptibility of commercial heats of AISI 300–series SSs to hot cracking and α' formation as described in actual chemical analysis reports (Table 1), one finds that most low–sulfur, low–phosphorus (S + P <0.02 wt.%) heats have a Cr_{eq}/Ni_{eq} >1.48 and consequently will exhibit good weldability (Fig. 1). In contrast, austenite stability at low temperatures (arbitrarily defined as the characteristic temperature at which 50% of the austenite transforms to martensite under a tensile true strain of 0.30 and termed M_{d30})[16] varies over a surprisingly wide range (Fig. 2). Because carbon, nitrogen, and molybdenum are more effective in stabilizing austenite at low temperatures than are nickel, silicon, and manganese, Types 301,304, and 304L SS (with lower nitrogen) have a higher susceptibility for α' formation. Types 316L and 304LN (low carbon, high nitrogen) and 316NG SS exhibit relatively good stability, as does Type 317LN SS (0.1% N and 4% Mo). However, nitrogen is not a good alloying element to provide strength or austenite stability in SSs exposed to a fast–neutron flux because of the (n,α) transmutation reaction.

Table 1. Austenite stability of different heats of AISI 300–series stainless steels

Grade	Heat	Composition (wt.%) C	N	P	S	Si	Ni	Cr	Mo	Mn	Cr_{eq}/Ni_{eq} (P + S)	Cr_{eq}/Ni_{eq} (wt.%)	$M_{d(30)}$ (°C)
301	–[2]	0.052	0.038	–	0.009	0.48	7.25	17.10	0.24	1.28	1.91	0.009	49.1
304	–[6]	0.060	0.024	–	–	0.39	8.60	18.40	0.06	0.33	1.80	–	33.0
304	9T2796	0.046	0.038	0.026	0.012	0.47	9.30	17.70	0.33	1.17	1.66	0.038	23.4
304	–[2]	0.061	0.041	0.025	0.010	0.58	8.54	18.00	0.18	1.72	1.70	0.035	15.5
304	82103	0.050	0.028	0.022	0.008	0.45	9.80	18.28	0.09	1.52	1.58	0.030	15.3
304	–[2]	0.061	0.027	0.023	0.020	0.59	9.42	18.20	0.14	1.33	1.61	0.043	14.7
304	53319	0.060	0.029	0.024	0.013	0.59	8.88	18.33	0.14	1.69	1.68	0.037	14.7
304	30956	0.060	0.100	0.019	0.007	0.48	8.00	18.70	0.20	1.63	1.91	0.026	–22.1
304LN	–[5]	0.025	0.139	0.014	0.009	0.78	9.55	18.54	0.20	1.77	1.80	0.023	–30.9
304L	05895	0.011	0.075	0.024	0.029	0.36	9.53	18.03	0.11	1.80	1.74	0.053	15.8
304L	V70200	0.023	0.079	0.03	0.018	0.39	8.25	18.15	0.30	1.79	1.94	0.048	15.2
304L	–[5]	0.024	0.074	0.021	0.010	0.51	8.64	18.7	0.20	1.63	1.93	0.031	7.9
304L	18491	0.016	0.090	0.028	0.013	0.46	8.87	18.42	0.35	1.67	1.91	0.041	3.2
304L	G351	0.016	0.089	0.028	0.028	0.30	9.82	18.41	0.35	1.78	1.72	0.054	–4.7
316L	92106	0.015	0.040	0.022	0.002	0.49	11.15	16.33	2.06	1.59	1.54	0.024	2.4
316L	16650	0.018	0.054	0.026	0.013	0.43	10.39	16.50	2.09	1.78	1.63	0.039	–2.1
316NG	P91576	0.015	0.088	0.020	0.010	0.42	10.95	16.42	2.14	1.63	1.57	0.030	–11.0
316NG	13198	0.013	0.085	0.022	0.017	0.64	10.70	16.51	2.08	1.63	1.64	0.039	–17.7
316NG	18474	0.009	0.110	0.029	0.002	0.39	10.20	16.31	2.07	1.75	1.67	0.031	–18.4
316NG	467958	0.020	0.069	0.029	0.008	0.64	12.74	17.14	2.43	1.51	1.46	0.037	–47.0
316NG	D442604	0.014	0.100	0.018	0.002	0.46	12.85	17.29	2.52	1.66	1.45	0.020	–62.9
316NG	D440104	0.015	0.098	0.011	0.002	0.49	13.25	17.91	2.48	1.75	1.45	0.013	–75.0
316NG	NDE–28	0.014	0.110	0.020	0.0002	0.52	13.58	17.79	2.59	1.77	1.42	0.020	–84.1
317LN	-	0.025	0.140	0.016	0.010	0.61	13.66	19.32	4.54	1.69	1.62	0.026	–161.0

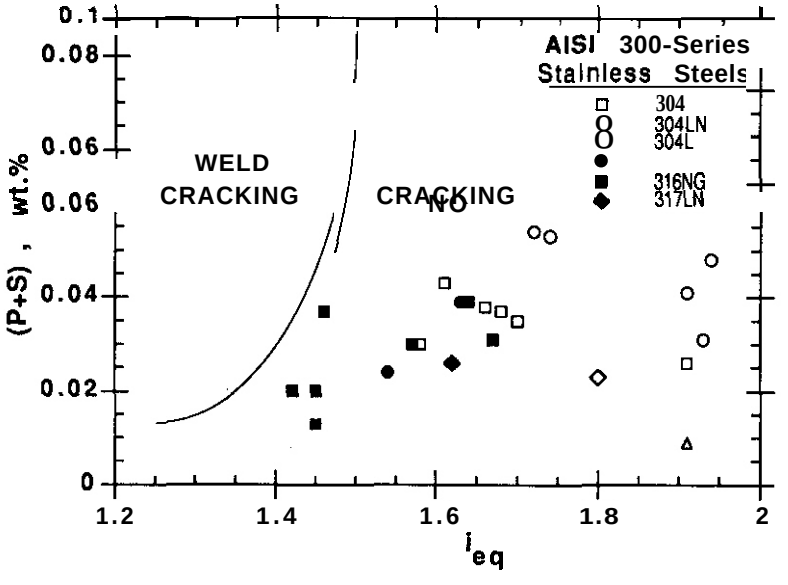


Fig. 1. Hot–cracking susceptibility of various heats of SSs.

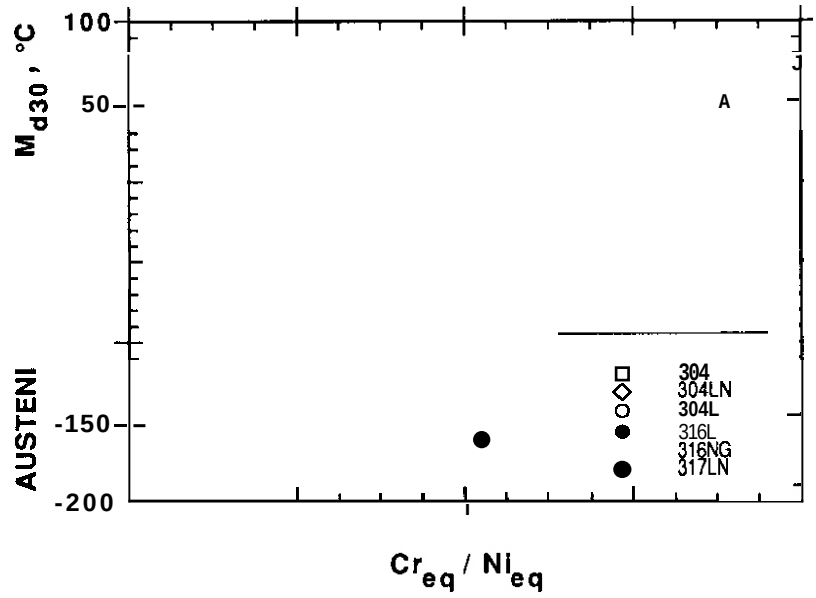


Fig. 2. Austenite stability (M_{d30}) vs. Cr_{eq}/Ni_{eq} ratio for various heats.

Regarding the effect of hydrogen on crack growth in Types **301, 304,** and **310** SS,[10] the conclusions are: (1) the amount of deformation–induced ***a'*** in Type **304** SS is not affected by hydrogen concentration up to ≈40 wppm (≈2230 appm), (2) second-stage crack growth rates increase with hydrogen concentration and austenite instability, (3) threshold stress intensity for slow crack growth and the critical stress intensity for rapid ductile fracture decrease with increasing hydrogen concentration and decreasing stability of the austenite phase, and (4) a threshold hydrogen concentration exists below which embrittlement does not occur.

These results have several implications in an assessment of hydrogen–induced cracking of a fusion reactor first wall.

1. Although the two heats of Type **304** SS used in the crack growth study'" were very susceptible to ***a'*** formation (as quantified by magnetometer measurements and substantiated by calculated M_{d30} values from the alloy compositions in Table 1), a Type **316** SS for the ITER first wall would'have a greater austenite stability at low temperatures by controlling the alloy composition. (Cold working for strength or stability under fast–neutron irradiation is not necessarily consistent with a low ***a'*** content in the steel.)

2. Although there is a threshold hydrogen concentration below which embrittlement of Type **304** SS does not occur (≈7 wppm, or ≈390 appm),[10] this threshold value would be exceeded before end–of–life of the first wall at a hydrogen production rate of ≈540 appm/MW–y/m^2. The threshold hydrogen value for less-susceptible materials must be defined.

3. The decrease in the threshold stress intensity, K_{th}, to an asymptotic value of ≈65 MPa·m$^{1/2}$ as the hydrogen concentration increases to values >50 wppm in Type **304** SS has interesting implications for the integrity of a first wall subjected to static and cyclic stresses. The ASME code limits the primary stress for an SS component to **0.9** times the yield stress or **0.33** times the ultimate strength of the steel, whichever is lower (i.e., ≈200 MPa). Although the peak thermal stress for a 5–mm–thick Type **316** SS fusion reactor first wall (approximated by a long cylinder with free ends) at a neutron wall loading of 2 MW/m^2 is ≈544 MPa,[9] this occurs only in a thin surface layer and the stresses are relieved by small amounts of plastic deformation and cracking. Thus the crack is driven by the primary stress. A simple analysis indicates that a crack must be approximately one–half the wall thickness to exceed the threshold stress intensity for hydrogen–induced slow crack growth at a design stress of 200 MPa. This implies that relatively deep cracks (a significant fraction of the wall thickness) must be present initially, or must grow by other mechanisms (e.g., fatigue or SCC), before the cracks could grow by a hydrogen–induced mechanism. In other words, because of the relatively high threshold stress intensity (≈65 MPa·m$^{1/2}$), the first wall would be flaw–tolerant from the standpoint of "failure" by hydrogen–induced cracking even at high hydrogen concentrations (≈2800 appm) in the material.

4. Because second-stage crack growth rates are so high ($\approx 10^{-6}$ m·s^{-1}), the time required for a crack to penetrate the remaining ligament is very short, <1 h. Consequently, efforts to further quantify crack growth rates of that magnitude in stainless steels would not contribute significantly to assessments of component performance. For comparison, stress corrosion crack growth rates in SSs are lower by 4 to 6 orders of magnitude, and consequently are an important consideration in evaluating the remaining useful life of flawed components.

5. In this analysis, a thumbnail-shaped through-wall crack from SCC or a hydrogen-induced cracking process would produce a small water leak into the vacuum chamber that would be readily detected; the location of the leak would be more difficult to determine. To determine whether a catastrophic failure could occur, the resistance of the steel to tearing (J_R curve) must be determined for use in safety analyses. It is likely that hydrogen and neutron damage will decrease the fracture toughness properties of the steel. Accelerated crack growth associated with stage-2 crack growth under high loads would also lead to a further apparent decrease in the J_R curve under most loading rates. J_R-curve data on steels with a range of hydrogen concentrations, a' content, and loading rates are needed to assess the resistance to fracture under various plant loading conditions, including dynamic (seismic) loading.

6. Crack growth tests should be performed on hydrogen-charged SS specimens with different compositions (austenite stability) in oxygenated water to confirm that the aqueous environment does not significantly decrease the threshold stress intensity values compared to those in air.

7. Austenitic SSs in LWR components are susceptible to irradiation-assisted stress corrosion cracking (IASCC) at very low stress intensity values after accumulation of a critical fluence (>5 x 10^{20} n/cm^2, E >1 MeV). IASCC has been associated with radiation-induced segregation (RIS) of alloy and impurity elements at grain boundaries in the materials. RIS is strongly dependent on fast-neutron flux and temperature. The flux/temperature conditions in LWRs are conducive for RIS and may contribute to IASCC of the steels (Fig. 3). However, the first wall may be less susceptible to IASCC because the lower temperatures and higher flux in ITER may decrease the degree of RIS. Further testing and evaluation will be required to determine if this is in fact the case.

CONCLUSION

An analysis was made of hydrogen effects and transport in austenitic stainless steels. Experience and understanding gained from fission reactor technology were applied to fusion reactor conditions.

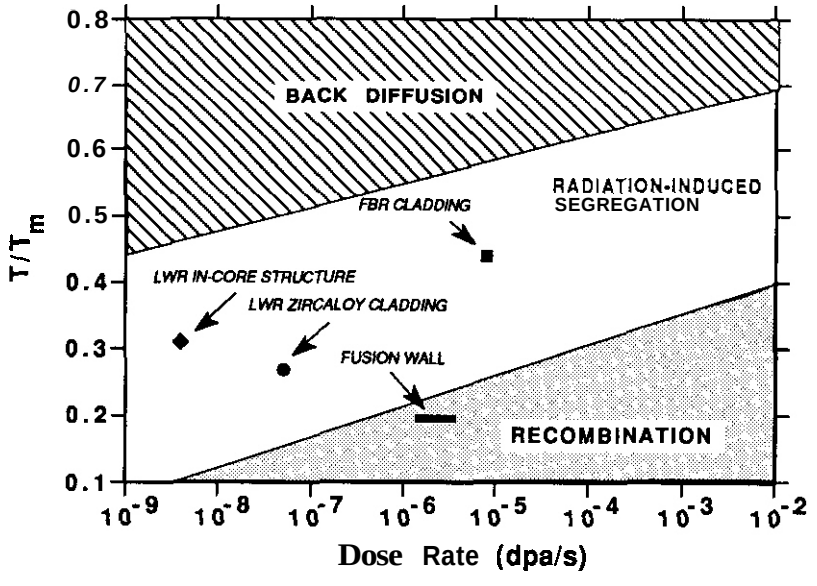


Fig. 3. Radiation response as a function of temperature and fast neutron flux.

FUTURE WORK

SCC susceptibility of selected austenitic steels (such as Types 316, 316L, and 316NG SS) in the solution-annealed, solution-annealed and cold-worked, and solution-annealed and moderately sensitized conditions will be determined for ITER materials selection. The data base will be extended from 95 to ≈ 250°C.

Crack growth testa will be initiated on fracture-mechanics-type specimens under cyclic loading conditions. Crack growth tests will also be conducted on H-charged specimens with a range of austenite stability in oxygenated water to determine threshold stress intensity values. J_R-curve data will be obtained on steels with a range of hydrogen concentrations and α' contents to assess resistance to fracture.

REFERENCES

1. A. B. Hull, M. R. Fox, J. W. Pascoe, and T. F. Kassner, Environmental Effects on Aqueous Stress Corrosion of Candidate Austenitic Steels for ITER Structural Applications, Ninth Fusion Reactor Materials Semiannual Progress Report for Period Ending September 30,1990, DOE/ER-0313/9, Oak Ridge National Laboratory (1991).

2. H. G. Khalak, Computer Simulation of Water Coolant Chemistry in a Fusion Reactor. Proceedings 3rd Natl. Conf. on Undergraduate Research, April 27-29, 1989, University of North Carolina, Asheville, p. 287 (1990).

3. H. Khalak, A. B. Hull, and T. F. Kassner, Aqueous Stress Corrosion of Austenitic Steels, Sixth Fusion Reactor Materials Semiannual Progress Report for Period Ending March 31, 1989, DOE/ER-0313/6, Oak Ridge National Laboratory, p. 379 (1989).

4. A. Patel, A. B. Hull, and T. F. Kassner, Aqueous Stress Corrosion of Structural Materials, Seventh Fusion Reactor Materials Semiannual Progress Report for Period Ending September 30, 1989, DOE/ER-0313/7, Oak Ridge National Laboratory, p. 250 (1990).

5. M. R. Fox, A. B. Hull, and T. F. Kassner, Stress Corrosion Cracking of Candidate Structural Materials under Simulated First-Wall/Aqueous Coolant Environments, Fusion Technology, in press, (1991).

6. A. B. Hull, T. F. Kassner, and M. R. Fox, Stress Corrosion Susceptibility of Austenitic Stainless Steels, Including Weldments, in Oxygenated Water, accepted for oral presentation at Fitth International Conference on Fusion Reactor Materials, Nov. 17-22, 1991, Clearwater, FL., U.S.A.

7. W. E. Ruther, T. F. Kassner, and F. A. Nichols, The Role of Hydrogen Embrittlement in Intergranular Stress Corrosion Cracking of Sensitized 304 Stainless Steel, in Pmc. 2nd Int. Symp. on Environmental Degradation of Materials in Nuclear Power Systems-Water Reactors (1985).

8. R. H. Jones, Application of Hydrogen Embrittlement Models to the Crack Growth Behavior of Fusion Reactor Materials, J. Nucl. Mater. 141-143.468-475 (1986).

9. T. J. Dolan. Fusion Research, Vol. 111—Technology, Pergamon Press, Inc., New York, pp. 678–696 (1982).

10. S. Singh and C. Altstetter, Effects of Hydrogen Concentration on Slow Crack Growth in Stainless Steels, Met. Trans. 13A, 1799–1808 (1982).

11. R. M. Horn, Evaluation of Crack Growth in Oxygenated High Temperature Water Using Full Size Pipe Testa, J. Eng. Mat. &Tech. 108, 50-56 (1986).

12. T. F. Kassner, et al., in Environmentally Assisted Cracking in Light Water Reactors: Semiannual Report, October 1988-March 1989, NUREG/CR-4667, Argonne National Laboratory Report ANL-90/4, June 1990.

13. P. L. Andresen, et al., State of Knowledge of Radiation Effects on Environmental Cracking in Light Water Reactor Core Materials, in Proc. 4th Int. Symp. on Environmental Degradation of Materials in Nuclear Power Systems-Water Reactors (1990).

14. Z. Mei and J. W. Moms, Jr., Influence of Deformation–Induced Martensite on Fatigue Crack Propagation in 304–Type Steels, Met. Trans. 21A, 3137–3152 (1990).

15. T. Takalo, N. Suutala, and T. Moisio, Austenitic Solidification Mode in Austenitic Stainless Steel Welds, Met. Trans. 10A, 1173–1181 (1979).

16. T. Angel, Formation of Martensite in Austenitic Stainless Steels—Effects of Deformation. Temperature, and Composition, J. Iron and Steel Inst., May, 165–174 (1954).

17. R. H. Jones and S. M. Bruemmer, Assessment of Stress-Corrosion Cracking in a Water-cooled ITER, Sixth Fusion Reactor Materials Semiannual Progress Report for Period Ending March 31, 1989, DOE/ER-0313/6, Oak Ridge National Laboratory, p. 389 (1989).

PRELIMINARY ASSESSMENT OF AQUEOUS CORROSION OF NIOBIUM ALLOYS FOR STRUCTURAL APPLICATIONS IN THE ITER DIVERTOR – A. B. Hull, B. A. Loomis, and L. J. Nowicki (Argonne National Laboratory)

OBJECTIVE

The objective of the program is to obtain information on baseline mechanical properties, chemical compatibility, and radiation damage of selected niobium alloys under conditions of interest for fusion reactors. The purpose of this task is to assess the compatibility of niobium alloys with high-temperature water for the divertor in ITER.

SUMMARY

Niobium and Nb-base alloys are under consideration as candidate materials for the ITER divertor structure. Unalloyed Nb and binary alloys of Nb-2.5Ti, Nb-2.5Zr, Nb-2.5Hf, Nb-2.5V, Nb-2.5Ta, Nb-2.4Mo, Nb-2.5W, Nb-2.5Fe, Nb-2.5Ni, Nb-2.5Ti, and ternary alloys of Nb-2.5Ti-2.5Ta, Nb-2.5Ti-2.5Mo, Nb-2.5Hf-2.5Mo, (expressed in terms of atomic percent alloy addition) were exposed to high-purity water with <30 ppb dissolved oxygen in a refreshed stainless steel autoclave (with a 1300-psi overpressure) to determine the extent of oxidation as a function of time at 300°C. Corrosion data are presented for pure Nb and for ten binary and three ternary Nb-base alloys exposed for up to 2906 h. All alloys exhibited weight gains except Nb-2.5Ni, Nb-2.5Ta, and Nb-2.5Fe, which lost weight after 0, 1500. and 2200 h, respectively. Of the alloys that gained weight, the V and Mo additions were the most effective in minimizing weight gain. The ternary alloys incorporating Mo were superior in terms of both resistance to weight gain and embrittlement.

PROGRESS AND STATUS

Introduction and Background

The recommended divertor concept for the technology phase of the ITER consists of a water-cooled Nb alloy divertor plate with a relatively thin W coating as the plasma facing material. The divertor plate in ITER will be subjected to high heat loads, radiation damage, and surface erosion. Niobium alloys. along with Cu and Mo alloys, have been selected as primary candidate materials for the divertor structure.'

Niobium alloys offer considerable advantages over Cu and Mo alloys for first-wall and high heat-flux applications. Serious limitations of Cu alloys are their low melting temperature and their susceptibility to accelerated erosion-corrosion where high water velocities are encountered.2 A Nb alloy allows a better thermal expansion match between the thin (<2 mm) W coating and the substrate; thus, interfacial stresses are reduced. Niobium (z=41) has advantageous thermophysical properties similar to those of Mo (z=42): low thermal expansion coefficient. and high melting point (2467°C). In addition, Nb alloys are more easily fabricated and appear to be much less susceptible to radiation-induced embrittlement than are the Mo alloys.

On the basis of a more extensive data base, Nb-1Zr was considered as the lead Nb-base alloy option for the divertor structure material. The fusion-relevant properties of Nb-1Zr were reviewed in detail earlier.3

Because low-temperature water (≈60°C) has been selected as the reference coolant, most of the divertor structure will operate at temperatures below 200°C. Temperatures of several hundred degrees will be reached in areas exposed to peak heat fluxes of 10-15 MW/m^2. Hydrogen embrittlement due to hydriding as a result of the aqueous corrosion is a major concern. Erosion/corrosion is also a concern because of the high coolant velocities required for heat removal.4 Tritium permeation into the coolant and tritium inventory in the alloy are also of concern.

Experimental Procedures

Sheet material5 was sheared into test specimens –7.4 x 25.4 x 0.1 mm. The specimens were annealed at 1000°C for 1h to remove any intrinsic H. To avoid reintroduction of H, the samples were not polished but used in the as-received condition after 30-s ultrasonic cleaning with methanol.

Because of the individual variations in specimen geometry and through-hole dimensions, the surface area was determined by image analysis techniques. The images were transferred to a Macintosh II computer by

means of the Image 1.35 pmgram.5 Surface area values computed by this technique deviated little fmm the values obtained by the standard technique, based on multiple measurements with a sensitive micrometer.

The corrosion exposures were conducted in a refreshed autoclave system. The tests were conducted at 300°C (±2°C) and a system pressure of 1300 psi, well above the 1250-psi equilibrium pressure corresponding to saturated steam. The water flow rate through the system was ≈11 cm^3/min.

The dissolved oxygen content of the exit stream from the reservoir was monitored with an Orbisphere oxygen indicator, Model 26075, sensor 21152. The oxygen level in the inlet water was also checked intermittently, and adjustments to this inlet oxygen level were made to maintain a constant outlet level of <30 ppb O_2. The corrosion specimens were supported from wires of matching composition to avoid the possibility of any galvanic action between Nb and stainless steel wire in high-temperature water. A more complete description of the experimental procedure and a schematic diagram of the autoclave system were presented earlier.[6]

The corrosion tests, which extended for a total of 2906 h, were interrupted after approximately 168, 736, 1453, and 2189 h for removal of the specimens from the test (Table 1). Weights were determined to ± 0.001 mg with a Mettler microbalance. A modified bend test was performed to screen the samples for variations in ductility.

Results and Analysis

The weight-change data from the tests are summarized in Table 1. Weight gains were observed in all alloys for exposure times up to 1500 h except for the Nb-2.5Ni, which lost weight immediately.

The fracture susceptibility upon bending the specimens is shown in Table 2. When the ductility of a specimen was considered good, i.e., when the specimen fractured only after unbending a fold, did not fracture on unbending, or exhibited neither fracturing or cracking of the corrosion layer (fracture index <4), the surface layer was microscopically examined. Severity of corrosion-layer cracking can be defined in terms of the depth of corrosion scale; in decreasing order, cracking indexes 4 to 1 signify deep cracking to no cracking.

As can be seen in Table 2, the ternary Nb-alloys exhibited good resistance to embrittlement. As shown in Fig. 1, next in fracture resistance were the binary Nb alloys including Group IVa elements. The relative corrosion layer cracking of the better alloys is shown in Fig. 2 for exposures up to 120 days. In both Figs. 1 and 2, an average was plotted from Table 2 of the fracture and corrosion layer cracking index.

Discussion

The oxidation and corrosion susceptibility[8] of niobium and niobium alloys are complex phenomena with various rate-determining processes. These can include a chemisorption reaction at the metal surface, anion or

Table 1. Influence of alloy composition and time on weight change (g/m^2) in Nb-base specimens

Exposure Time (h)	Nb	Binary Alloys[a]									Ternary Alloys[a]		
		Group IVa			Group Va		Group VIa		Group VIII				
		Ti	Zr	Hf	V	Ta	Mo	W	Fe	Ni	Ti-Ta	Ti-Mo	Hf-Mo
168	3.14	--[b]	1.85	1.97	1.73	1.69	1.99	3.03	2.16	--[b]	--[b]	--[b]	--[b]
736	12.50	9.77	4.96	5.75	3.03	11.62	4.85	10.34	5.39	-1.43	5.27	2.20	2.85
1453	--[c]	14.49	8.87	9.04	3.61	19.29	6.68	--[c]	8.85	-2.58	8.31	2.81	3.58
2189	--	--	9.73	10.72	3.79	16.72	8.96	--	9.27	--	9.64	3.23	3.40
2906	--[b]	--	10.58	12.34	3.66	--[b]	9.93	--[b]	4.70	--[b]	9.90	3.15	3.58

[a] Containing 2.5 at.% of the additional alloying element.
[b] No test was run under these conditions.
[c] Specimen fragmented.

Table 2. Phenomenological observations of fracture susceptibility and corrosion-layer cracking

Structural Material	Exposure Time (days) 7 Fract. Index[a]	7 Crack. Index[b]	30 Fract. Index	30 Crack. Index	60 Fract. Index	60 Crack. Index	90 Fract. Index	90 Crack. Index	120 Fract. Index	120 Crack. Index
Nb	2	2	5	--	6	--	--	--	--	--
Binary Alloys										
Nb-2.5Ti	--	--	3	3	4	4	--	--	5	4
Nb-2.5Zr	1	1	1	1	2	2	3	4	3	3
Nb-2.5Hf	1	1	2	2	3	3	3	4	3	4
Nb-2.5V	1	1	5	--	5	--	5	--	5	--
Nb-2.5Ta	2	2	5	--	5	--	5	--	5	--
Nb-2.4Mo	1	1	5	--	5	--	5	--	5	--
Nb-2.5W	1	1	5	--	5	--	--	--	--	--
Nb-2.5Fe	4	--	4	--	4	--	5	--	4	--
Nb-2.5Ni	--	--	6	--	6	--	--	--	--	--
Ternary Alloys										
Nb-2.5Ti-2.5Ta	--	--	2	3	3	3	3	3	3	4
Nb-2.5Ti-2.5Mo	--	--	2	3	3	4	3	4	3	4
Nb-2.5Hf-2.5Mo	--	--	2	2	2	3	3	4	3	4

[a]Fracture susceptibility *can* be defined by the mechanical response upon bending specimens: a fracture index of **6** indicates brittleness and breakage before bending test began: 5, fracture at 90° bend; 4, fracture after 180° bend 3, specimen fractured only after unbending of a fold; 2, ductility was such that no fracture occurred even on unbending of a fold; 1, there was neither fracturing nor surface cracking of the corrosion layer.

[b]When the ductility of a specimen was considered good, **i.e.,** fracture index of <4, the surface layer was microscopically examined. Severity of corrosion-layer cracking can be defined in terms of depth of corrosion scale: a cracking index of 4 indicates deep cracking: 3, moderate cracking: 2, minor cracking; and 1, no cracking.

cation diffusion through the bulk oxide, and interfacial mass or electron transport.9 If an over-all reaction proceeds through two consecutive steps. e.g., diffusion-induced metal oxidation followed by interface reaction, the step with the smaller activation energy will be rate-limiting at higher temperatures. The linear oxidation rates observed for Ti, one of the alloying elements in the present study, represent a phase boundary reaction at a metal-oxygen interface.[10]

Alloys in which both the base metal and the alloying metal are oxidizable, as is the case in this study, may form either a single-phase or composite oxide. The presence of small **amounts** of alloying elements *can* significantly reduce the oxidation rate of the base metal because of the retarded diffusion through the oxide of the alloying element.[11] On the other hand, an unstable composite scale with an outer homogeneous oxide and an inner heterogeneous layer consisting of oxide and base-metal enriched alloy may occur when the oxidation rate of the more reactive alloying component considerably exceeds that of the more stable base metal.[12]

Although acknowledging the importance of the governing processes discussed briefly above, the niobium alloys are grouped in **the** following discussion, primarily for simplification, in the context of the electronic configuration of the alloying elements.

The Group N a metals, as defined by IUPAC **notation,**[13] Ti, Zr, and Hf, have an outer electronic configuration of d^2s^2 and although possessing multiple oxidation states, the most common and important valence, especially in aqueous chemistry, is +4. In general, the Group IVa metals are subject to greater reactivity with both O and H than metals with higher valency.[14] ***As*** shown in Fig. 3, Ti is intrinsically very reactive in the presence of O and forms a tenacious passivating film, giving it corrosion resistance in a range of media. The corrosion mechanisms for Zr **and** Hf are very similar[15] but Hfis considered superior **to** Zr in corrosion resistance in both water and steam.[16]

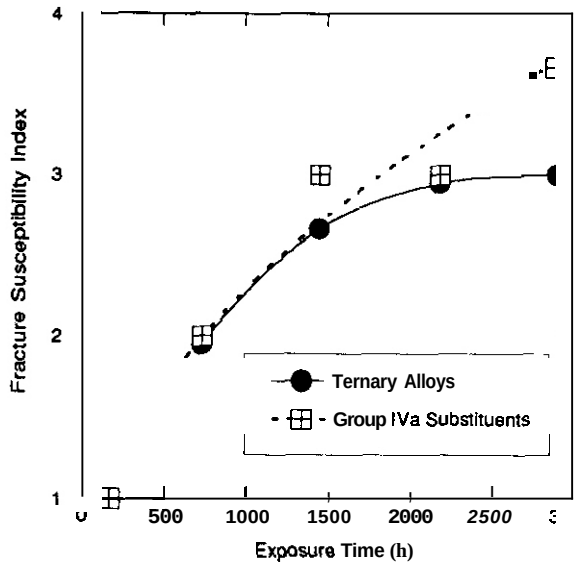


Fig. 1. Fracture susceptibility index for Nb–base alloys. The closed symbols represent an average value for the ternary alloys under consideration: Nb–2.5Ti–2.5Ta, **Nb–2.5Ti–2.5Mo,** Nb–2.5Hf–2.5Mo. The open symbol represents an average value for the Group IVa binary alloys under consideration: **Nb–2.5Ti, Nb–2.5Zr,** Nb–2.5Hf. Notation is defined in Table 2.

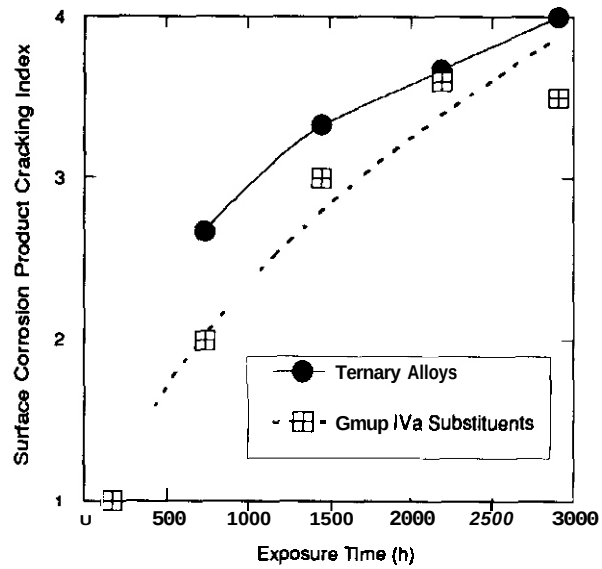


Fig. **2.** Corrosion layer cracking index for Nb–base alloys. The closed symbols represent **an** average value for the ternary alloys under consideration. Nb–2.5Ti–2.5Ta, **Nb–2.5Ti–2.5Mo, Nb–2.5Hf–2.5Mo.** The open symbol represents an average value for the Group IVa binary alloys under consideration: **Nb–2.5Ti, Nb–2.5Zr,** Nb–2.5Hf. Notation is defined in Table 2.

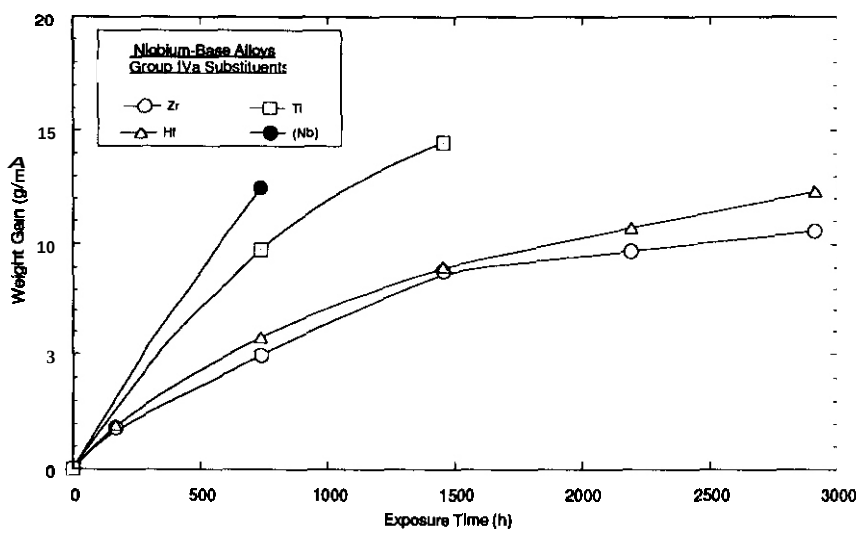


Fig. 3. Weight gain versus time for binary Nb-base alloys containing Group IVa alloying elements exposed to pure water at 300°C. Each symbol represents weight gain for a single specimen after a specific exposure time.

The Group Va metals (V, Nb, and Ta), with d^3s^2 outer electronic configurations and valences defined as 5, react exothermally with H and easily form hydrides. In general, the corrosion rate is determined hy the defect structure of the oxide film; for this reason, as shown in Fig. **4,** the corrosion resistance of Nb is slightly less than that of Ta. The superior oxidation resistance of V in Fig. **4** can be attributed to its low ionic radius. Vanadium has an ionic radius of **0.59Å,** compared to 0.69Å for Nb and 0.68Å for Ta.[13] Unalloyed Nb has rather poor resistance to gaseous oxidation and corrosion by high-temperature water.[17]

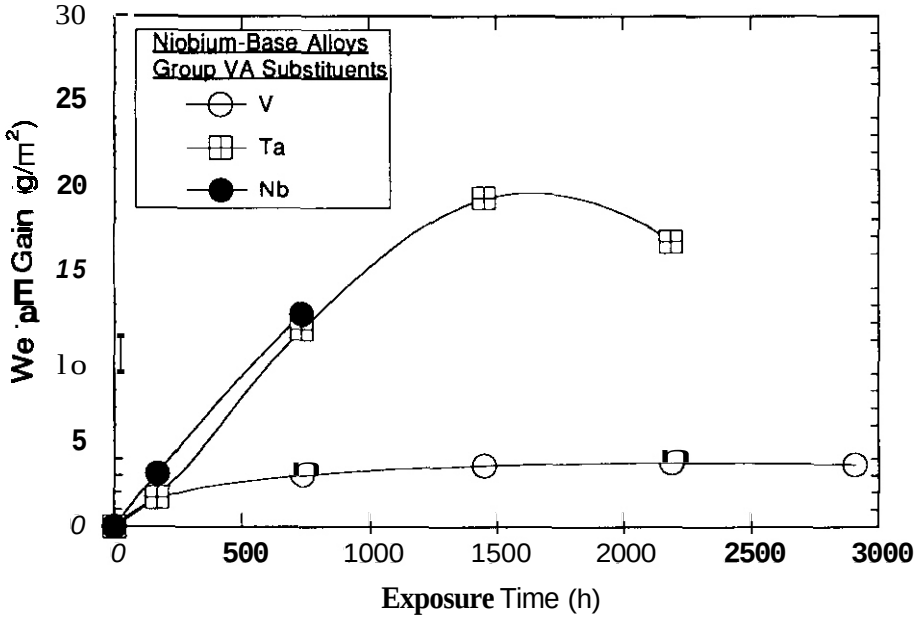


Fig. 4. Weight gain versus time for binary Nb-base alloys containing Group Va alloying elements exposed to pure water at 300°C. Each symbol represents weight gain for a single specimen after a specific exposure time.

The Group VIa metals (Mo and W), with d^5s^1 outer electronic configurations, may be hypothesized to be not as subject to oxidation or H embrittlement as the Group IVa or Group Va metals. However, in reality, Mo is very oxidation-prone with its corrosion-resistance decreasing in oxidizing environments.[18] Both Mo and W have ionic radii smaller than that of Nb, but the differenceis not as great as with V. The main effect observed in Fig. 5 is oxide stability. Both the the W and Nb oxides are more stable than the Mo oxide. As can be seen in Figs. 4 and 5, the general corrosion of Mo is lower than that of Nb and significantly less than that of Ta.[19]

The Group VIII metals (Fe and Ni) are characterized by valences of 3 and 2, respectively. The addition of Ni and Fe have a pronounced deleterious effect on Nb-base alloys (Fig. 6). The adverse effects of Ni can be related to its valence of +2, lower than that of the other alloying elements. The film formation in the Nb-2.5Fe alloy was initially stable, but after 2200 h, the adherent film apparently degraded. This may involve the formation of internal oxidation[12] in which the faster growing iron oxide buries the niobium oxide. The instability of the oxidation film may be due to slow diffiion in the Nb relative to diffusion in the iron oxide. There was apparently no protective film forming on the Nb-2.5Ni alloy.

Generally, the corrosion behavior of most ternary systems appears to be an average of the corrosion behaviors in the respective binary systems. In terms of both weight change (Fig. 7) and fracture and surface cracking (Figs. 1 and 2), the ternary alloys are considerably better. An earlier study[20] indicated that although none of the commercial alloys met all of the requirements for fusion, a combination of a solid-solution strengthener (Mo, W, or V) and a reactive metal (Ti, Zr), for oxidation resistance and creep rupture strength, would yield the best alloy for fusion applications. It was suggested that strengtheners be kept to ~3-5 w/o to improve fabricability. Zirconium, although a potent strengthener, reduces the solubility of interstitials by acting as an interstitial sink; thus, it should be kept to <2 w/o. Within these concentrations of alloying elements, Nb-5Mo-1Zr and Nb-5V-1Zr were considered particularly applicable. Our results are consistent with these findings.

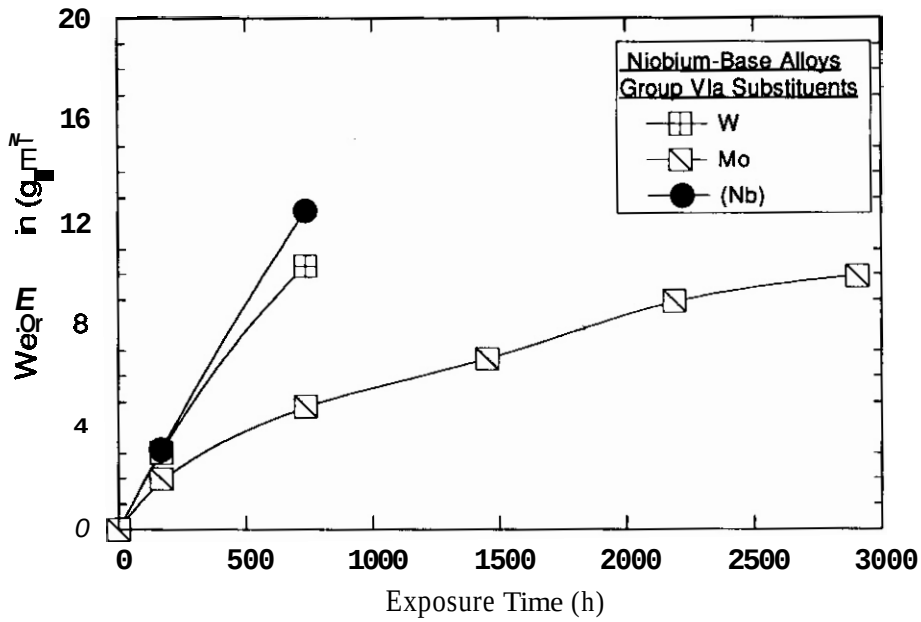


Fig. 5. Weight gain versus time for binary Nb-base alloys containing Group VIa alloying elements exposed to pure water at 300°C. Each symbol represents weight gain for a single specimen after a specific exposure time.

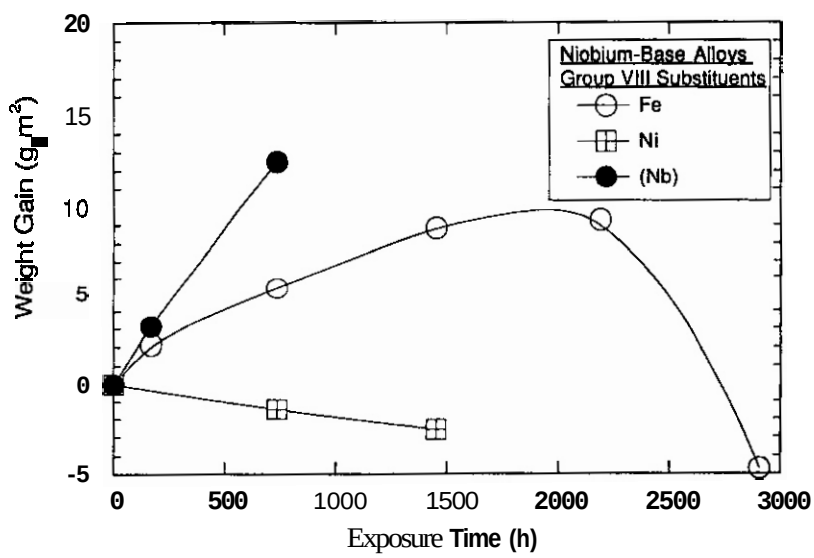


Fig. 6. Weight gain versus time for binary Nb-base alloys containing Group VIII alloying elements exposed to pure water at 300°C. Each symbol represents weight gain for a single specimen after a specific exposure time.

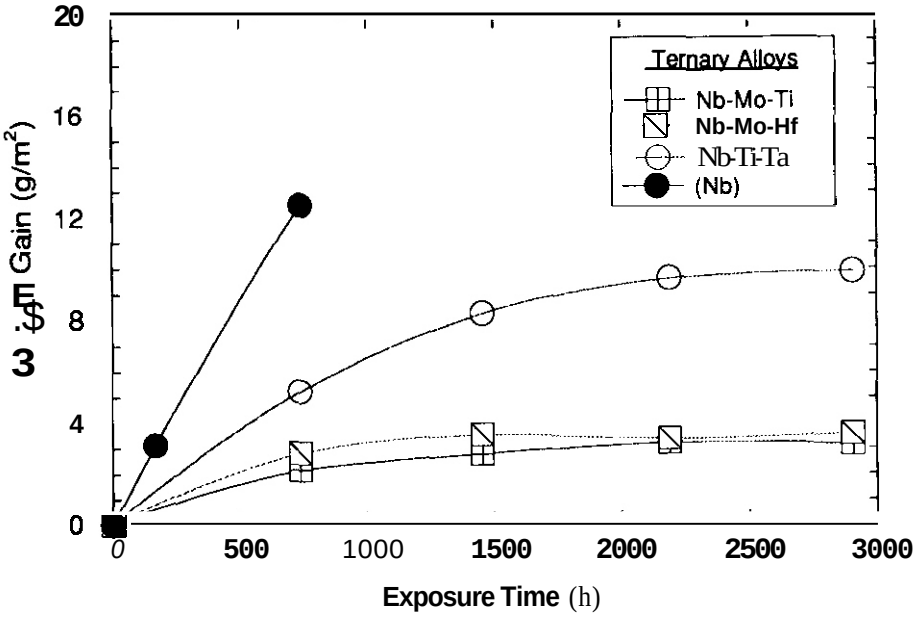


Fig. 7. Weight gain versus time for ternary Nb-base alloys exposed to pure water at 300°C. Each symbol represents weight gain for a single specimen after a specific exposure time.

CONCLUSIONS

A preliminary corrosion study of various Nb-base alloys in high-temperature deoxygenated water indicates that the ternary Nb-2.5Mo-2.5Ti alloy was the most promising of the 13 alloys examined. Binary alloying additions that improved the high-temperature oxidation resistance of Nb included Ti, Zr, Hf, V, Mo. and W. Because of instability of the protective oxide film, alloying additions of Ni and Fe produced weight loss in the corrosion specimens.

FUTURE WORK

After exposure to high-temperature water, the surface layers will be microscopically characterized and the depth of internal penetration will be determined. Alloy specimens will be analyzed for oxygen and hydrogen concentration.

The alloys Nb-2.5Mo-2.5Ti, Nb-6V-8Ti, and Nb-5V-1.25Zr will be investigated further. Tensile and ductile-brittle-transition-temperature properties will he evaluated before and after long-term corrosion testing.

REFERENCES

1. D. Smith et al., ITER Blanket, ***Shield and Material Data Base,*** ITER Documentation Series. No. 29, International Atomic Energy Agency, Vienna 1991.

2. A. B. Hull and T. F. Kassner, ***Copper Corrosion,*** in US. Contribution to the ITER Plasma Facing Components Engineering Homework Task, June 1989, Garching, Germany, p. 129-142.

3. R. F. Mattas, International Thermonuclear Experimental Reactor (ITER) Divertor Plate Performance and Lifetime Considerations, ANL/FPP/TM-246, March 1990.

4. A. B. Hull and D. L. Smith, ***Aqueous Corrosion of Niobium,*** in Proceedings of ITER PFC Meeting, May 9, 1990, MDAC, St. Louis. May 1990.

5. B. A. Loomis and S. B. Gerber, *Swelling of 58Ni+ and 3He+ Ion–Irradiated Nb and Nb Alloys,* J. Nucl. Mater. **103 & 104,1193–1198 (1981).**

6. W. Rasband, *Image. Public Domain Program for the Macintosh Computer,* distributed by Twilight Clone BBS, Silver Spring, MD (301) 946-5032,1990.

7. D. R. Diercks and D. L. Smith, *Environmental Effects on the Properties of Vanadium-Base Alloys,* in Alloy Development for Irradiation Performance: Semiannual Progress Report for Period Ending March **31, 1984,** Oak Ridge National Laboratory, Oak Ridge, TN, DOE/ER-0045/12, pp. **75-79.**

8. W. D. Klopp, W. E. Berry, and D. J. Maykuth, *The Hot Water Corrosion of Columbium and Columbium Alloys,* in Columbium Metallurgy, eds. D. L. Douglas and F. E. Kunz, Intersdence, New York, NY, **1961,** pp. 685-718.

9. K R. Lawless, *The Oxidation of Metals,* Rep. Prog. Phys. **37,231-316 (1974).**

10. W. J. Moore, *Oxidation of Metals at High Temperature,* J. Electrochem. Soc. *100,* **302-313 (1953).**

11. C. Wagner, *Theoretical Analysis of the Diffusion Processes Determining the Oxidation Rate of Alloys,* J. Electrochem. Soc. *99,* 369-380 (1952).

12. C. Wagner, *Oxidation of Alloys Involving Noble Metals,* J. Electrochem. Soc. **103, 571-580 (1956).**

13. D. R. Lide, ed., *CRC Handbook of Chemistry and Physics,* **71st** Edition, Cleveland, OH, **1990-1991,** p. 1-10.

14. W. K. Boyd, *The Use of Titanium, Zirconium, Tantalum. and Columbium in Chemical Environments,* in Process Industries Corrosion, NACE, Houston, TX, **1975,** pp. **207-212.**

15. R. Kuwae, T. Hatanaka, and J. Kawashima. *Hafnium Corrosion Behavior in High-Temperature Steam,* J. Nucl. Mater. **139,4247 (1986).**

16. Anon., *Hafnium,* Properties Data Brochure, Teledyne Wah Chang Albany, Albany, OR, **23** pp. Jan. **1987.**

17. H. A. Fisch, D. L. Douglas, and B. E. Dearing, *The High Temperature Steam Corrosion of Columbium-Vanadium Alloys,* in Columbium Metallurgy, eds. D. L. Douglas and F. E. Kunz, Interscience, New York, **1961,** pp. 597-613.

18. L. L. Shreir, ed., Corrosion Vol **1:** Metal/Environment Reactions, Newnes-Butterworths Ltd., London, England **(1976).**

19. C. A. Hampel, *Corrosion Properties of Tantalum. Colombium. Molybdenum, and Tungsten,* Corrosion *16,* 29-32 (1959).

20. L. J. Pionke and J. W. Davis, Technical Assessment of Niobium Alloys Data Base for Fusion Reactor Applications, McDonnell Douglas Astronautics Company, St. Louis, Mo., **COO-4247-2. 1979.**

8.0 SOLID BREEDING MATERIALS

IRRADIATION EXPERIMENT DESIGN FOR IN SITU TRITIUM RECOVERY FOR Li_2O ANU Li_2ZrO_3: BEATRIX-II, Phase II

0. 0. Slagle, Pacific Northwest Laboratory,(a) Richland, Washington, USA; T. Takahashi, Japan Atomic Energy Research Institute, Tokai-mura, Ibaraki-ken, Japan; J. 0. Sullivan, AECL Research, Chalk River, Ontario, Canada; R. C. Knight, Westinghouse Hanford Company, Richland, Washington, USA

OBJECTIVE

To design and fabricate the BEATRIX-II, Phase II canisters for irradiation in the FFTF/MOTA Cycle 12.

SUMMARY

BEATRIX-II is an irradiation experiment designed to study the in situ tritium release behavior from selected ceramic solid breeder materials. The second irradiation cycle of the experiment, Phase II, will include a temperature change capsule with a ring specimen of Li_2O and a temperature gradient capsule with Li_2ZrO_3 spheres. The temperature change capsule is designed to achieve temperatures in the range from 485 to 650°C while the temperature gradient capsule will include a temperature range from 450 to 1200°C. The effect of specimen temperature, sweep gas composition, irradiation damage, and sweep gas flow rate on the tritium recovery behavior will be determined in a fast neutron flux to burnups of 8%.

PROGRESS AND STATUS

Introduction

The BEATRIX-II irradiation experiment is an in situ tritium release experiment to evaluate the tritium release characteristics of fusion solid breeder materials under fast neutron irradiation.',' The participants in this International Energy Agency (IEA) sponsored experiment are the Japan Atomic Energy Research Institute (JAERI), AECL Research, Canada, and the United States Department of Energy (US/DOE). The experiment is being carried out in the Materials Open Test Assembly (MOTA] within the FFTF reactor. A sophisticated tritium gas handling system has been developed to continuously monitor the tritium release rate from the specimens and facilitate tritium removal from the reactor.

The previous phase of the experiment, Phase I, consisted of 300 Effective Full Power Days (EFPO) of neutron irradiation and was carried out from January 1990 to March 1991.[3,4] This phase of the experiment contained two Li_2O in situ tritium recovery specimens: a temperature change canister containing a thin annular ring specimen operating at nearly a uniform temperature and a temperature gradient capsule containing a solid pellet specimen. The specimens were irradiated under various temperature and sweep gas conditions to a 4% lithium burnup. Phase II of the BEATRIX-II experiment will extend the Li_2O in situ tritium recovery data base obtained in Phase I to higher burnups and possibly lower temperatures. The temperature gradient canister will consider an alternative solid breeder material, Li_2ZrO_3 that could be a candidate fusion blanket material.

ExDeriment Descriotion

Phase II of the BEATRIX-II experiment contains a Li_2O ring specimen and a Li_2ZrO_3 solid specimen. The Phase I Li_2O ring specimen was prepared in the U.S. while the ring specimen for Phase II was prepared in Japan. Improved fabrication techniques were expected to give a higher density, larger grain size material which would allow fabrication of a ring specimen with a thinner wall. Li_2ZrO_3 was chosen as the alternative ternary breeder material most suitable for additional characterization. In previous vented[5] and non-vented[7] tests, Li_2ZrO_3 had been found to be dimensionally and chemically stable during irradiations and to have relatively short tritium residence times. The material used was 1-1.5 mm diameter Li_2ZrO_3 spheres prepared by AECL, Research. This form of solid breeder is a potential candidate for use in future blanket designs. An additional objective for Phase II was to reach burnups of 8% or twice that of Phase I.

Temperature Chanse Canister

The Phase II temperature change canister is very similar to the Phase I temperature change canister. The primary emphasis is to reach higher burnups. This requirement together with some desired improvements found necessary during the operation of Phase I, presented a challenge to the designer.

(a) Pacific Northwest Laboratory is operated for the U.S. Department of Energy by Battelle Memorial Institute under Contract DE-AC06-76RLO 1830.

Design Requirements

The design requirements for the Phase II temperature change specimen were very similar to those for Phase I and included considerations such as the sensitivity of tritium measurements, minimizing the loss of tritium to the reactor, and the temperature of the specimen. A major change in the requirements was the increase in lithium burnup from 4 to 8%. This was partially achieved by increasing the ^{6}Li enrichment from 61 to 95 at%.

The temperature of the ring specimen is controlled by changing the thermal conductance of a gas gap by varying the mixture of helium and argon in the gap. The design objectives of both Phase I and Phase II were to achieve temperatures in the range from 450 to 650°C. The pre-test thermal analysis for the Phase I design had predicted temperatures in the range from 468 to 645°C. The actual temperatures achieved were in the range from 510 to 680°C. The reason for these higher temperatures was attributed to the existence of larger than expected gaps between the capsule and the specimen wall. Achieving lower temperatures for the ring specimen was given a high priority in Phase II.

Figure 1 is a schematic diagram of the temperature change canister for Phase II. The tritium sweep gas enters and exits at the bottom end of the canister after flowing along the inner diameter of the specimen. A perforated inner stainless steel sleeve insures that if the specimen should fracture during testing, the cylindrical geometry would be maintained. This sleeve also positions the inner thermocouples. The temperature in the specimen is controlled by varying the conductance of thermal gap in which the conductance is varied by the composition of the argon-helium gas in the gap. A computer controlled gas blending system allows temperature control continuously throughout the 300 day irradiation.

Figure 2 is a simplified cross section of the Phase I temperature capsule showing the individual components and possible thermal gaps. The specimen to inner capsule gap at room temperature was designed so that at the operating temperature (500°C) the specimen would be in contact with the outer wall. The occurrence of temperatures higher than the design temperatures in Phase I was attributed to several factors:

1. A gap between the outer specimen diameter and inner capsule wall could have existed at certain areas along the length of the specimen. The maximum outer specimen diameter was within the design dimension and hence was expected to close by thermal expansion. The 0.013 cm variation in diameter along the length of the specimen could have resulted in a specimen to capsule wall gap at positions where the specimen diameter was at its minimum.

2. The inner capsule wall was treated with a barrier coating to reduce the permeation of tritium and then a layer of nickel was put into place to prevent interaction of the capsule and the specimen. Nickel has a lower thermal expansion than stainless steel and as the temperature was increased the nickel layer would not increase in diameter as much as the capsule. If the specimen pressed

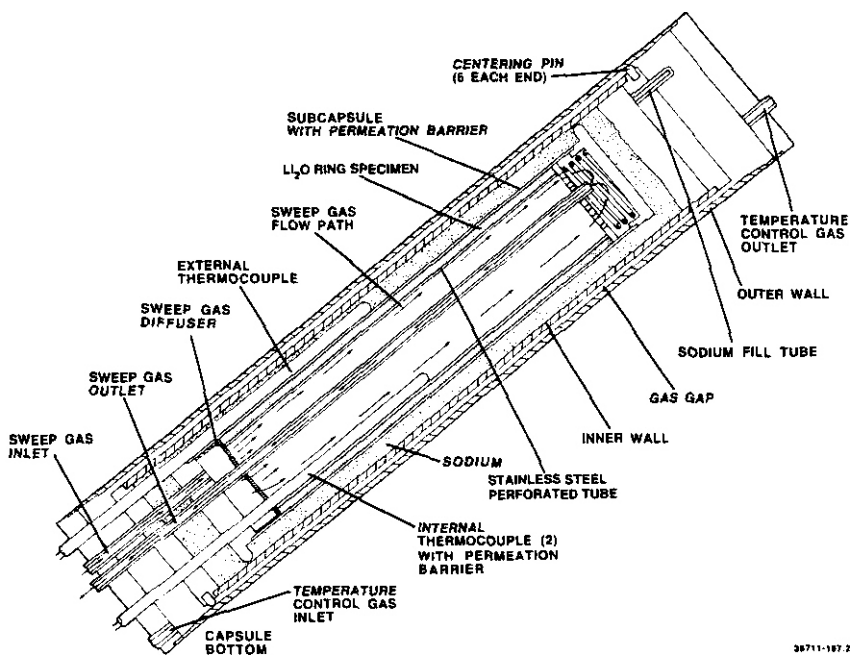


Figure 1. Schematic diagram of the temperature change canister for Phase II.

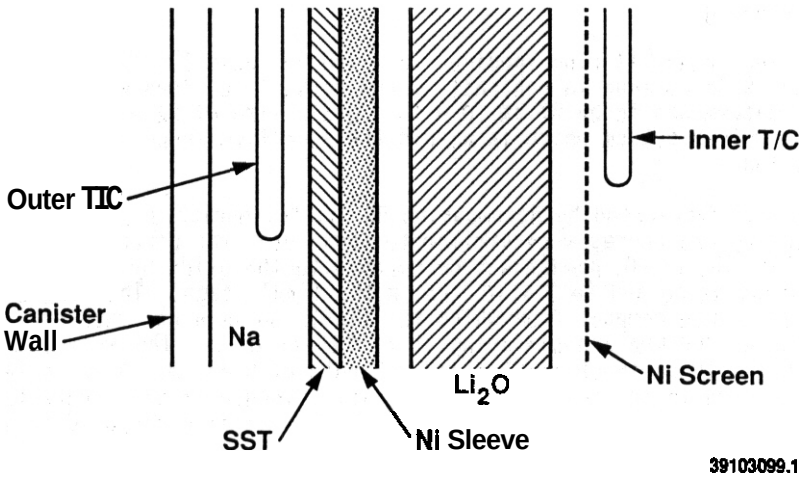


Figure 2. Simplified cross section of the temperature change canister.

firmly against the outer wall or if the nickel was strongly bonded to the capsule, the nickel liner was soft and would be expected to deform to remain in contact with the capsule. However because of the potential gap expected in case (1) above, the nickel layer may not have been held in contact with the inner capsule wall and an additional thermal gap could have resulted.

3. The specimen design was based on a thermal conductivity for an 85% TD specimen. The actual specimen density was 80% and the thickness was increased to give the same total amount of ^6Li. The increase in thickness and the decrease in density would contribute to the temperature increase.

The actual temperature increase in Phase I due to factors 1 and 2 cannot be determined quantitatively because the gap width is not known. However any gaps are calculated to give a temperature increase equivalent to 2.5°C/0.001 cm of gap. The lower density and larger specimen thickness was expected to contribute approximately 10°C.

Design of Phase II

The 8% burnup for the Li_2O ring specimen for Phase II compared to 4% for Phase I was partially achieved by increasing the ^6Li enrichment from 61 to 95 at%. However, this increase in enrichment and subsequently in the heating rate makes it even more difficult to attain lower temperatures desired in Phase 11. To offset such an increase in heating rate the total amount of ^6Li, and, thus the heating rate, in the specimen was kept constant by decreasing the volume. Specifically the thickness was decreased from 0.15 cm in Phase I to 0.10 cm in Phase 11.

A major goal of Phase II was to achieve temperatures as low as possible for the ring specimen. The three previous problem areas were addressed in the following manner:

1. The specimen-capsule gap was minimized by placing a closer tolerance on the specimen outer diameter. The previous tolerance of 0.013 cm was reduced to 0.005 cm. The inner diameter of the capsule was machined 0.010 cm larger than the largest specimen diameter. This radial gap (0.005 cm) is predicted to close at 500°C due the differential expansion between the capsule and the specimen. Final machining on the capsule was done to fit the as-fabricated specimen. This required that the tritium barrier coating previously applied to both sides of the inner capsule be applied only on the outer diameter of the capsule.

2. The potential gap between the capsule and the nickel liner was eliminated by removing the inner nickel liner. This liner was used previously as a compatibility barrier between the specimen and the capsule. The expected interaction was estimated to be 2-10 microns of general surface corrosion and possibly 25 microns of intergranular attack.[8,9]

3. The temperature drop across the specimen will be substantially less than in Phase I because the density of the specimen will be greater than 85% TD and the thickness of the specimen has been reduced by 1/3.

Specimen Fabrication/Loading

A description of the final Phase II ring specimen is given in Table 1. The Phase II ring specimen was a single section of tube, 8.85 cm long in contrast to the Phase I specimen which consisted of two sections. The final density was determined to be 87.3% TD with a grain size of 22 microns. The variation in diameter along the specimen was only 0.003 cm which is within the specified range of 0.005 cm. The wall thickness was 0.10 cm, as specified.

The Li_2O ring specimen was fabricated by decomposing 95 at% ^6Li enriched Li_2CO_3 to a Li_2O powder. The powder preparations and sintering procedures were similar to those used for preparing the temperature gradient specimen in Phase I.[10,11] The Li_2CO_3 powder was decomposed to the oxide by heating to 700°C in a vacuum of 6×10^{-2} Pa in the initial stage and to 5×10^{-5} Pa in the final stage. The ring specimen was fabricated by sintering a cylindrical shaped compact from which the final specimen was machined. The compact was formed by hydrostatic pressing at 200 MPa and sintering at 1170°C for 8 hr. The as-sintered compact was a 2.1 cm diameter cylinder with a 1.15 cm inner annulus and a length of 9.43 cm. A "rock lathe" was used to machine the final thin wall specimen in an atmosphere of dry air. Because of the inherently fragile nature of the thin ring specimen, a second specimen of the same dimensions was also prepared to serve as a backup.

Figure 3 shows the capsule with the specimen in place, the "backup" specimen, and the inner perforated sleeve prior to final loading. The specimen slid easily into the capsule which had an inner diameter of 1.863 cm or a 0.010 diametral clearance. The Phase I capsule used an inner sleeve of nickel screen but for Phase II this was replaced by a perforated stainless steel tube. Stainless steel was used to minimize the interactions of the metal surfaces with the purge gas. A perforated tube was chosen over the screen because of problems in Phase 1 with thermocouple location. The tube was a more rigid structure than the screen used previously and allowed a more definite positioning of the thermocouples.

Figure 4 is a radiograph of the capsule after loading. This shows clearly the relationship of the different components. The positioning of the inner thermocouples in the slots provided by the inner sleeve can be seen. The thermocouple in the center of the radiograph is the outer thermocouple which measures the

Table 1. Description of BEATRIX-II, Phase II Ring Specimen

^6Li Enrichment	95 at%
Outer Diameter	1.850 - 1.853 cm
Inner Diameter	1.651 - 1.653 cm
Straightness	0.003 cm
Wall Thickness	0.10 cm
Length	8.85 cm
Weight	8.103 g
Density	87.3% TD
Grain Size	22 microns

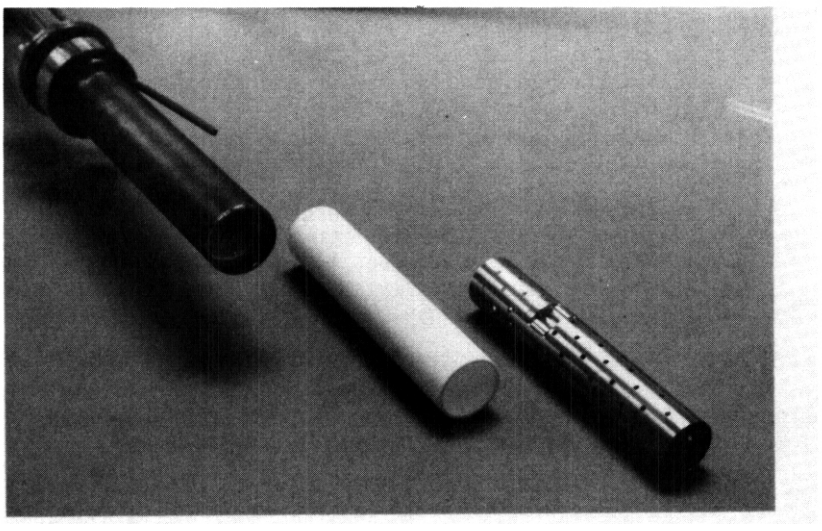


Figure 3. Temperature change capsule with the loaded specimen, the "backup" specimen, and the inner perforated tube prior to final assembly.

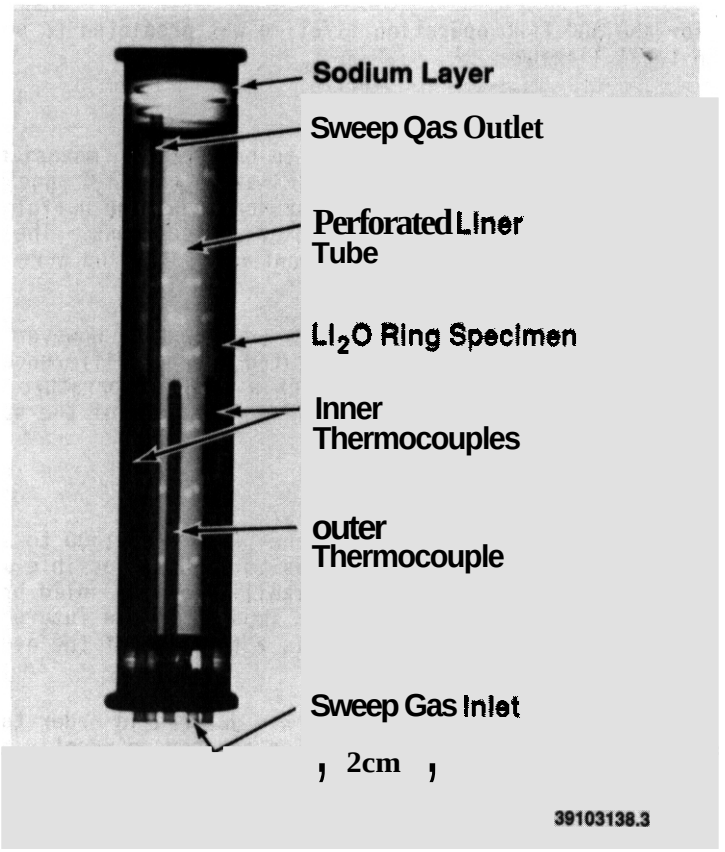


Figure 4. X-ray radiograph of the temperature change canister as-fabricated.

temperature in the sodium used as a thermal contact. The assembly shown in Figure 4 was thermally bonded inside the gas-gapped thermally controlled canister with sodium. The sodium also serves to minimize axial temperature gradients.

Predicted Performance

The thermal and neutronic performance of the ring specimen was calculated on the basis of the expected neutron flux in the MOTA cycle 12 and the heat generation in the Li_2O ring specimen (110 W/g). Using this heat generation rate, the specimen temperatures were calculated for two different control gases in the canister temperature control gap. The results are summarized in Table 2. The minimum temperatures were calculated for 100% helium and the temperature range across the specimen was determined to be 485-503°C. This is substantially less than the temperatures achieved in Phase I which were 500 to 540°C across the specimen. The upper temperature in our current test matrix is 650°C and this temperature was found to be achievable with a 1:7 ratio of He:Ar temperature control gas.

Table 2. Thermal and Neutronic Performance of BEATRIX-II Ring Specimen in FFTF/MOTA Cycle 12

Thermal Heat Generation	110 W/gm
Specimen-Capsule Diametral Gap	0.005 cm
Specimen Minimum Temperature (100% He)	
Outer Diameter	485°C
Inner Diameter	503°C
Specimen Maximum Temperature (1:7, He:Ar)	
Outer Diameter	632°C
Inner Diameter	654°C
Tritium Generation (300 EFPD)	1250 Ci
Total Lithium Burnup	7.8 at%

The total tritium generation for the 300 EFPD operating lifetime was predicted to be 1250 Ci. This corresponds to a 7.8% burnup in the total lithium.

Temperature Gradient Canister

The material in the temperature gradient canister was chosen to be a Li_2ZrO_3 monosize sphere bed. This "solid" specimen with its inherent temperature gradient is similar to the Li_2O specimen used in phase I and provides a comparison of the two breeder forms. Such a comparison should be useful in evaluating the relative merits of the two breeder forms proposed for fusion blanket applications. The sphere diameters were specified to be in the range from 1-1.5 mm with a ^6Li enrichment of 85 at% and were provided by AECL Research.

During the initial stages of planning a ring type specimen was considered. However the low thermal conductivity of a lithium zirconate sphere bed resulted in a calculated thermal difference across the ring that was on the order of 100°C for a single-sphere-thick ring. Such a large temperature difference limits the usefulness of a temperature change canister. The low thermal conductivity of the sphere bed also places restraints on the maximum diameter of a "solid" specimen.

Design Requirements

The desired centerline temperature in the sphere bed was in the range from 1000 to 1200°C. These limits were chosen based on the desire to obtain data at temperatures as high as possible without changing the microstructure of the lithium zirconate. Confirming the reliability of the solid breeder material over a broad range of temperatures minimizes the design restrictions imposed in the future when actual blanket designs are being considered. Achieving these temperatures is a function of the neutron environment and the diameter of the sphere bed or capsule.

A total tritium generation of 1000 Ci for the 300 EFPD cycle was desired in order to achieve tritium concentration levels compatible with the flow rates and ionization chambers currently being used in the tritium measurement system. Because of the lower lithium density in Li_2ZrO_3 relative to Li_2O, the temperature gradient canister was placed in a higher flux position, nearer the center of the reactor core than the temperature control canister, to increase the tritium production rate.

Canister Design

The design of the temperature gradient canister is shown schematically in Figure 5. The Li_2ZrO_3 sphere bed was contained in a stainless steel capsule between porous nickel end screens. The porous nickel screens allow the passage of sweep gas into and out of the bed. A high temperature spring was used to hold the sphere bed in place during handling operations prior to loading the MOTA into the reactor. The spring was designed to withstand the 600°C outgassing of the canister prior to irradiation. A center tube is used for inserting the thermocouple into the centerline of the specimen after the sphere bed has been loaded to the required density by vibrating.

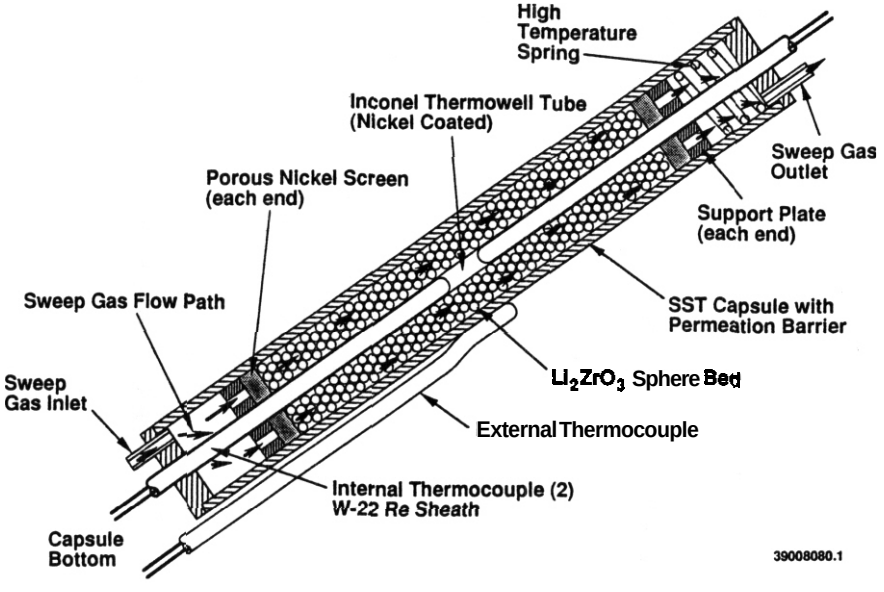


Figure 5. Schematic diagram of the temperature gradient canister for BEATRIX-II, Phase II.

Type K thermocouples have performed well up to fluences equivalent to 300 EFPD in FFTF but have a limited lifetime as temperatures approach and exceed 1200°C. A type K thermocouple was chosen for one of the thermocouples with an alternative higher temperature thermocouple for the other end of the canister. A Nb-1%Zr/Mo thermocouple has been under development and appeared to offer good stability in a neutron field plus reliability at the higher temperatures. This thermocouple was used as the alternative thermocouple for the solid specimen canister. The experiment will provide additional confirmation of the applicability of this thermocouple for high temperature applications in a high fluence neutron environment.

Calculated Performance

From the predicted heat generation and the thermal conductivity of the sphere bed, a sphere bed diameter was determined that would result in the desired centerline temperatures. The specimen parameters and the resulting operational predictions are given in Table 3. The thermal conductivity of the individual Li_2ZrO_3 spheres was taken from the data for 80 %TD polycrystalline Li_2ZrO_3 obtained by Hollenberg et al[12] and Kennedy.[13] The data were interpolated to the anticipated experimental conditions using the expression.[14]

$$k_{sphere} = (1-p)^{5/3}\left(\frac{3.643}{(1 + 0.001549\ T)} + 7.579 \times 10^{-10}\ T^3\right)$$

where p is the fractional porosity of the spheres, in this case 20%. The thermal conductivity of the predominantly helium sweep gas was calculated from the following expression from Gandhi and Saxena:[15]

$$k_g = 3.36 \times 10^{-3}\ T^{0.688}$$

Packing tests were performed using a Plexiglas model of the capsule, employing both steel and zirconia spheres. It was found that both sphere types packed to a packing fraction of 60% in this geometry.

The thermal conductivities of the packed bed were calculated using the model proposed by Hall and Martin.[16] The results of these calculations indicated that for a canister inner diameter of 33.5 mm, a centerline temperature in the range from 1030 to 1160°C would be expected. The uncertainties include both thermal conductivity and neutronic heating.

The calculated tritium generation for the temperature gradient canister during the 300 EFPD cycle was 828 Ci. This tritium production is less than one-fourth the tritium generated in the Phase I Li_2O solid specimen. The factors tending to increase the tritium production such as higher neutron flux and ^6Li enrichment are not sufficient to offset the smaller volume and lower lithium density in the Li_2ZrO_3 sphere bed. However, the tritium generation rate is not much smaller than that of the temperature control capsule, and it should be adequate to allow characterization of the tritium recovery from the temperature gradient canister during the Phase II irradiation.

Specimen Fabrication/Loading

The Li_2ZrO_3 spheres are shown in Figure 6(a) as received from AECL prior to loading. The diameters of the slightly non-spherical Li_2ZrO_3 spheres fall approximately in the range of 1 to 1.5 mm with a nominal diameter of 1.2 mm. Figure 6(b) shows the top of the sphere bed as loaded into the temperature change canister.

Table 3. Predicted Thermal and Neutronic Performance of the BEATRIX-II Li_2ZrO_3 Sphere Bed Canister

Thermal Heat Generation	27.3 W/gm
Properties of the Sphere Bed	
Sphere Diameter	1-1.5 mm
^6Li Enrichment	85 at%
Sphere Matrix Density	80% TD
Sphere Packing density	60%
Outer Diameter	1.32 cm
Inner Diameter	0.23 cm
Specimen Centerline Temperature	
Maximum	1160°C
Minimum	1030°C
Tritium Generation (300 EFPD)	828 Ci
Total Lithium Burnup	8.9 at%

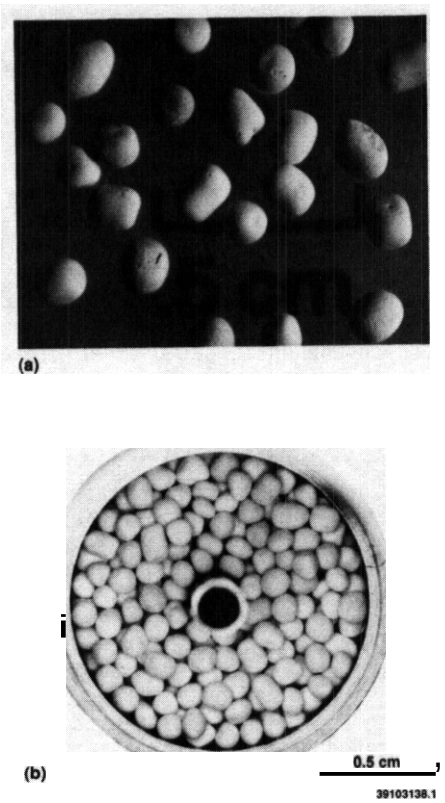


Figure 6. Li_2ZrO_3 spheres (a) As-fabricated by AECL, (b) As-loaded in the temperature gradient canister.

This view gives an indication of the sphere diameters relative to the capsule dimensions. The center tube is the thermal well into which the upper thermocouple was inserted to complete the assembly.

The sphere porosity was characterized by a mercury porosimeter analysis. The density of the individual spheres was 80-82% TD and of the total porosity of 18-20%, approximately 4.5% was closed. Open porosity was found to be in the range of 0.03 to 2.0 microns. Two SEM microstructures (See Figure 7) of a fracture surface in an individual Li_2ZrO_3 sphere indicates that the grain size is approximately 10 microns with an intergranular porosity consistent with the 2 microns upper limit determined from the porosimetry results.

Prior to loading, the spheres were vibrated into volumes from 2.0 to 6.0 cd. As indicated above, packing densities of 60% are expected for these spheres in the volumes involved. The resulting packing densities ranged from 2.03 to 2.08 g/cm^3. The capsule was loaded by vibrating 29.471 g of spheres into the 13.754 cc volume. The resultant density was 2.143 g/cm^3. Assuming the density of the individual spheres is 80% TD (TD = 4.112 g/cm^3) implies that a packing density of 65.1% was achieved. Such a high packing density may be attributable to the deviation of the material from perfect spheres and/or to the sphere density being larger than 80% TD.

The higher density of Li_2ZrO_3 in the capsule is not expected to significantly change the resulting temperature distribution. The increase in heat generation from the higher ^6Li loading is offset by the anticipated increase in thermal conductivity. The resulting centerline temperatures achieved during the irradiation testing will be a check on the effect of this increased packing density and on the assumptions made in the design calculations.

Figure 8 is an x-ray radiograph of the final assembled canister. The sphere bed nature of the specimen and the relative size of the spheres relative to the total sphere bed dimension can be seen. Because of the small size and brittle nature of the W-Re thermocouple sheath, it is to be noted that the alignment of the thermocouples relative to the end caps was a very critical operation to assure that the thermocouple sheathes remained intact during assembly.

CONCLUSIONS

Phase II of the BEATRIX-II experiment will extend the data base for in situ tritium recovery established in Phase I to higher burnups and to alternate fusion solid breeder forms and materials.

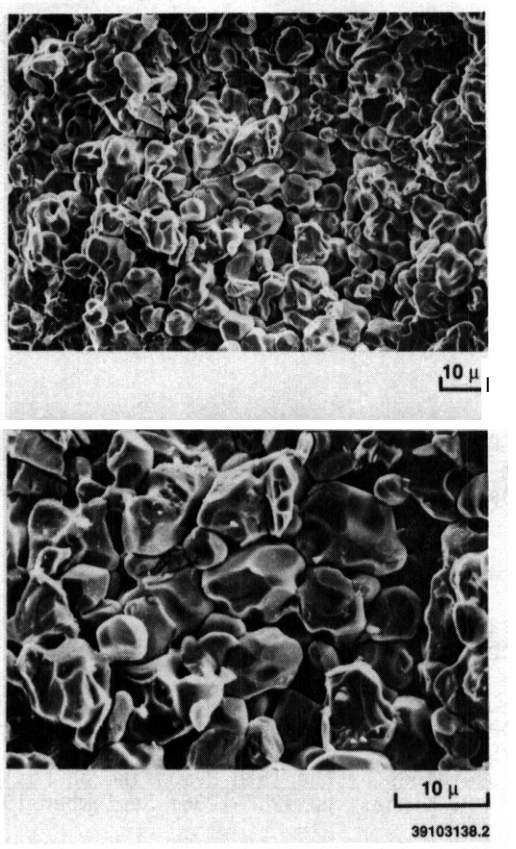


Figure 7. SEM microstructures of a fracture surface for the Li_2ZrO_3 spheres as-fabricated by AECL.

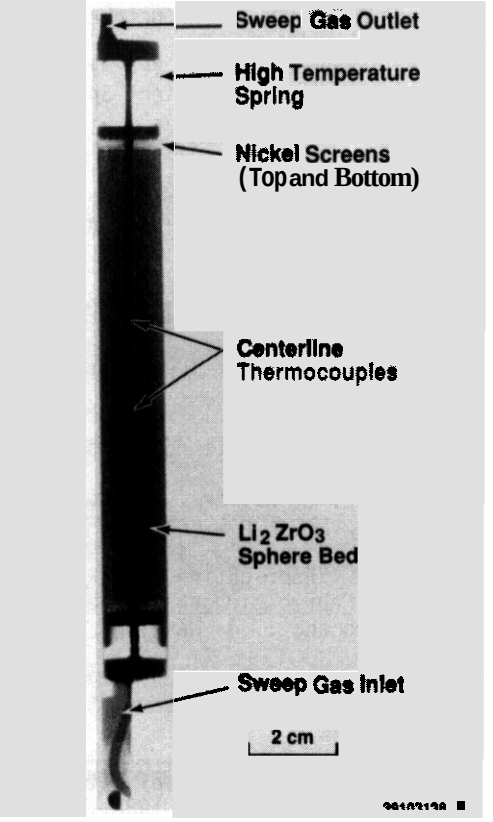


Figure 8. X-ray radiograph of the temperature gradient canister as-fabricated.

In the temperature control specimen minimizing the thermal gaps between the Li_2O specimen and the capsule is expected to result in lower temperatures than achieved in Phase I. A higher lithium burnup is achieved by using a higher ^6Li enrichment and the higher thermal generation density is offset by using a thinner-walled specimen.

For the ternary capsule the diameter of the capsule was limited by the low thermal conductivity of the Li_2ZrO_3 sphere bed together with the maximum temperature limit. These constraints resulted in the volume of the temperature change specimen being nearly half that of Phase I. This smaller volume, together with the lower lithium density in a Li_2ZrO_3 sphere bed results in a tritium generation rate that is only 25% of the rate for the Phase I temperature gradient canister. However, the tritium generation rate is not much smaller than that of the temperature control canister and it should be adequate to allow characterization of the tritium recovery during the Phase II irradiations.

FUTURE WORK

The irradiation of BEATRIX-II, Phase II will begin with the start of FFTF Cycle 12 scheduled to start in June 1991. The in situ tritium recovery will be detetmined as a function of the specimen temperature, neutron intensity, sweep gas composition, sweep gas flow rate, and burnup.

REFERENCES

1. G. W. Hollenberg, T. Kurasawa, H. Watanabe, S. E. Berk, I. J. Hastings, and D. E. Baker, "A Fast Neutron, In situ Tritium Recovery Experiment on Solid Breeder Materials," Fusion Technoloay ,15, 1349-1354 (1989).

2. R. J. Puigh, G. W. Hollenberg, T. Kurasawa, H. Watanabe, I. J. Hastings, J. M. Miller, S. E. Berk, R. E. Bauer, and D. E. Baker, "BEATRIX-11: In situ Tritium Recovery from a Fast Neutron Irradiation of Solid Breeder Materials," In Proceedings of the 15th Symposium on Fusion Technoloay, edited by A. M. Van Inger, A. Nigsen-Vis, and H. P. Kippel, pp 1282-1286, September 19-23, 1988, Utrecht, The Netherlands. Elsevier, Netherlands.

3. T. Kurasawa, O .D. Slagle, G. W. Hollenberg, and R. A. Verrall, "Insitu Tritium Recovery from Li_2O Irradiated in Fast Neutron - BEATRIX-II: In Situ Tritium Test Operation," Presented at the Ninth Topical Meeting on the Technology of Fusion Energy Oak Brook, Ill, October 7-11, 1990.

4. T. Kurasawa, O. D. Slagle, G. W. Hollenberg and R. A. Verrall, "Insitu Tritium Recovery from Li_2O Irradiated in Fast Neutron - BEATRIX-II: Temperature Gradient Specimen." Presented in another paper in this proceedings.

5. M. Briec, J. J. Abassin, C. E. Johnson, M. Amasson, N. Roux and H. Watanabe, "The MOZART Experiment: In-Pile Tritium Extraction from Lithium Oxide, Aluminates' Zirconates,' In Proceedinas of the 15th Symposium on Fusion Technoloay, edited by A. M. Van Inger, A. Nigsen-Vis, and H. P. Kippel, pp 1105-1111, September 19-23, 1988, Utrecht, The Netherlands. Elsevier, Netherlands.

6. O. D. Slagle, G. W. Hollenberg, and D. L. Baldwin, "The FUBR-1B Experiment - Tritium Release and Physical Stability of Solid Breeder Materials," to be published in J. Nucl. Mater. 1991.

7. G. W. Hollenberg and O. L. Baldwin, "The Effect of Irradiation on Four Solid Breeder Materials," J. Nucl. Mater., 133 & 134, 242-245 (1985).

8. C. E. Johnson, Argonne National Laboratory, private communication (1990).

9. D. L. Porter, J. R. Krsul, M. T. Lang, L. C. Walters, and M. Tetenbaum, "Neutron Irradiation and Compatibility Testing of Li_2O," J. Nucl. Mater., 122 & 123 (1984) 923-933.

10. O. D. Slagle, K. Noda, and T. Takahashi, "Fabrication of Lithium Ceramic Pellets, Rings and Single Crystals for Irradiation in BEATRIX-II," in Fabrication and Properties of Lithium Ceramics 11: Advances in Ceramics, Vol. 27, edited by G. W. Hollenberg and I. J. Hastings, The American Ceramic Society, Westerville, Ohio (1990).

11. T. Takahashi and H. Watanabe, 'Preparation and Characterization of Lithium Oxide," Fusion Enaineering and Design, 8, 399-405 (1989).

12. G. W. Hollenberg and D. E. Baker, "Thermal Properties of Lithium Ceramics for Fusion Applications," presented at the American Ceramic Society Meeting May 2-5, 1982, HEDL-SA-2674-FP.

13. P. Kennedy, "The Preparation, Characterization and Properties of Lithium Oxide and Lithium Meta-Zirconate Irradiated in the HFR Petten in the Second and Third Exotic Experiment," Fusion Technology, 2, 1013, 1989.

14. K. Noda, M. Billone, et. al., Summary Report for the ITER Specialist Meeting on Blanket Materials Data Base, February 7-9, 1990, Garching, FRG, April 1990.

15. J. M. Gandhi and S. C. Saxena, "Correlated Thermal conductivity Data of Rare Gases and their Binary Mixtures at Ordinary Pressures," J. Chem. Eng. Data, 13, 3, (1968).

16. R.A.O. Hall and D. G. Martin, "The Thermal Conductivity of Powder Beds. A Model, Some Measurements on UO_2 Vibro-compacted Microspheres and their Correlation," J. Nucl. Mater., 101, 172 (1981).

IN SITU TRITIUM RECOVERY FROM Li_2O IRRADIATED UNDER A LARGE TEMPERATURE GRADIENT: BEATRIX-II SOLID SPECIMEN - T. Kurasawa, Japan Atomic Energy Research Institute, Tokai-mura, Iharaki-ken, Japan; O. D. Slagle and G. W. Hollenberg, Pacific Northwest Laboratory,(a) Richland, Washington, USA; and R. A. Verrall, AECL Research, Chalk River, Ontario, Canada

OBJECTIVE

To characterize the in situ tritium recovery behavior of Li_2O irradiated under a temperature gradient in Phase I of the IEA sponsored experiment BEATRIX-II.

SUMMARY

BEATRIX-II is an in situ tritium recovery experiment to determine the tritium release characteristics of Li_2O in a fast neutron flux. A large diameter specimen of Li_2O has been irradiated under a steep temperature gradient to 4% burnup in a variety of sweep gas compositions and flow rates. Decreasing the amount of hydrogen in the sweep gas significantly decreases the tritium recovery rate. During irradiation the temperature of the specimen has remained stable and the results suggest that Li_2O is a viable fusion solid breeder material.

PROGRESS AND STATUS

Introduction

BEATRIX-II, Phase I is an International Atomic Energy (IEA) sponsored irradiation experiment to evaluate the tritium release characteristics of Li_2O and its stability under fast neutron irradiation to extended burnups.[1,2] It is an in situ tritium recovery experiment being carried out in the Fast Flux Test Facility (FFTF) as a collaborative effort by the Japan Atomic Energy Research Institute (JAERI), the Atomic Energy of Canada, Ltd., (AECL) and the United States Department of Energy (US/DOE). The first cycle or Phase I which consisted of 300 effective full power days (EFPD) of operation has been completed.

The experiment included two capsules containing different Li_2O specimens each with a separate sweep gas and tritium measurement system. This paper describes the results obtained from one of these specimens: a solid cylinder of pellets operated under a temperature gradient. The other specimen was in the form of a thin annular ring operated at a nearly uniform temperature. The initial results obtained from this ring specimen have been described elsewhere.[3] The experiment used a sophisticated tritium gas handling system to both monitor the release of tritium from the two solid breeder specimens and recover the tritium in specially designed getter beds.[4]

ExDeriment Design

The irradiation was carried out in the Materials Open Test Assembly (MOTA) of FFTF. The solid specimen capsule was positioned near the bottom of the core in level 1 of the MOTA. This position was selected to achieve a lower sample temperature since the reactor coolant was at a minimum at this point. At this position the predicted lithium burnup for a 300 EFPD cycle was approximately 4%.

A tritium measurement system provided continuous monitoring of the sweep gas recovered from each capsule. This included the flow rate, total moisture, and tritium concentration. Splitting the flow into two individual flow streams allowed determination of the amount of tritium in the oxidized versus the reduced form. The sweep gas inlet system provided for the selection of the sweep gas composition which included helium with various levels of hydrogen. Hydrogen levels were 0, 0.01, 0.1 and 1.0%. A complete description of the system has been presented elsewhere.'

Figure 1 is a schematic diagram of the capsule. The specimen was a 8.9 cm long stack of 11 pellets with a diameter of 1.70 cm. Table 1 is a listing of the important design parameters. The four pellets on the top and bottom of the stack have a 0.27 cm center hole for accommodating centerline thermocouples. The density of the individual pellets varied from 84.5 to 92.6 %TO. The grain size increased with increasing density from 25 to 45 microns.[5] Depleted Li_2O pellets were used to thermally insulate the hot center sections of the pellets columns from the metal end caps. A porous nickel liner in the capsule served as the primary pathway for the sweep gas from the bottom to the top of the capsule.

The temperature distribution calculated for the initial design of the specimen predicted a surface temperature of 440°C and a centerline temperature of 900°C. The observed centerline temperature was on the order

---

(a) Pacific Northwest Laboratory is operated for the U.S. Department of Energy by Battelle Memorial Institute under Contract DE-AC06-76RLO 1830.

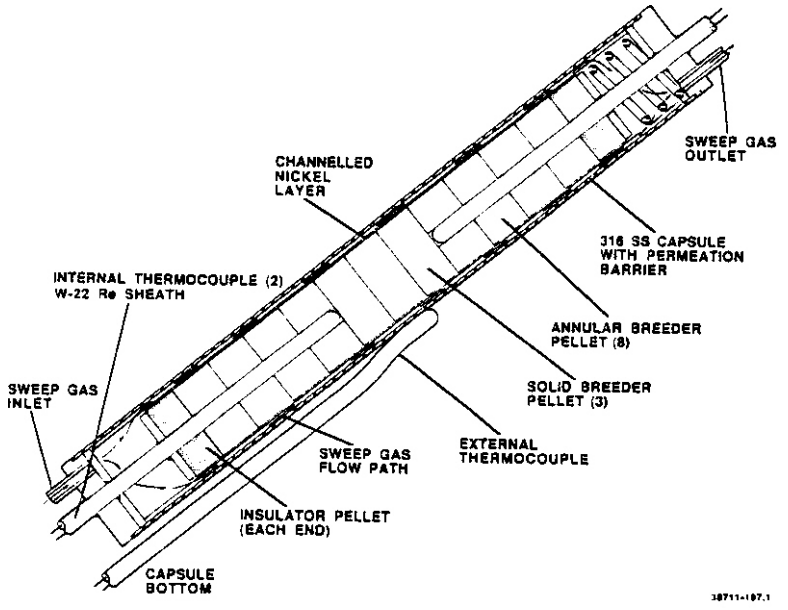


Figure 1. BEATRIX-II, Phase I temperature gradient capsule.

Table 1. Materials and Environmental Conditions for BEATRIX-II

Dimensions	
Length	8.92 cm
Outer diameter	1.70 cm
Inner diameter	0.27 cm
Weight	34.31 g
Density (%TD)	
Minimum	84.5 %TD
Maximum	92.6 %TD
Grain Size	25-45 um
^{6}Li enrichment	
Solid Breeder	61 at%
Insulator	t0.5 at%
Temperature	
Center	1000-c
Edge	440°C
Total Tritium Generation	3640 Ci (300 EFPD)

of 1000°C and the higher temperatures were attributed to higher neutron flux than originally predicted and pellet densities greater than the design density of 85 %TD. The higher temperatures were not expected to result in any damage to the capsule and will actually provide a test of the operation of Li_2O under more stringent thermal conditions. An axial temperature gradient also existed along the capsule and the temperature of the upper thermocouple was typically 40-50°C higher than the temperature of the bottom thermocouple. Such a temperature gradient was due to the increase in the neutron flux at positions closer the core center.

Experimental Test Plan

The two primary experimental parameters available for studying the performance of the solid specimen were the neutron flux which changed during reactor startup/shutdown and the sweep gas which has variable composition and flow rate.

The experimental test plan for the solid specimen is summarized in Table 2. In this table the parameter change represents a change from the reference condition which was a sweep gas composition of He-0.1% H, at a

Table 2. Experimental Test Plan for the Solid Specimen. Parameter changes indicate changes from the reference state of He-0.1% H_2 sweep gas at a flow rate of 100 mL/min.

Test No.	Parameter Change from Reference State, Duration in days (d)
Cycle 11-8.1	
1	50 mL/min (7d)
2	He-0.01% H_2 (2d)
3	He (2d)
Cycle 11-8.2	
A	He-0.01% H_2 (2d)
5	He-0.01% H_2 (4d)
6	He (2d)
7	He (4d)
8	He (4d) plus He-0.01% H_2 (2d)
9	He (2d) plus He-0.01% H_2 (4d)
10	He (4d) plus He-0.01% H_2 (2d)
11	He (2d) followed by reactor shutdown
Cycle 11-C	
12	Reactor startup followed by He (1d) plus He-0.01% H_2 (2d)
13	He (4d) plus He-0.01% H_2 (6d)
14	He (8d) plus He-0.01% H_2 (2d)-reactor shutdown
15	He-1.0% H_2 (1d)

flow rate of 100 mL/min. Cycle 11 of FFTF consisted of 300 EFPD of irradiation. Three subcycles: 11-8.1 (85 EFPD), 11-8.2 (134 EFPD) and 11-C (81 EFPD) provided essentially constant reactor power levels.

The first parameter change for the solid was a change in the flow rate from 100 to 50 ml/min. The remaining tests were changes in gas composition. The initial tests (Tests #2-7) were changes from the reference sweep gas (He-0.1% H_2) to an alternate gas (He and He-0.01% H_2) for a pre-determined period of time and then a return to reference gas. Later tests (Tests #8-10, 13 and 14) involved changes between alternate gases (He to He-0.01% H_2), before returning to the reference state. The last test was a change to He-1.0% H_2 to determine the effectiveness of higher H_2 levels in the recovery of tritium.

During reactor startup at the start of each new cycle, the reactor power was successively increased to higher power levels before reaching full power. This gave the opportunity to study the tritium recovery under different tritium generation rates and specimen temperature. Reactor shutdowns were typically over a shorter time period than startups but also provided conditions of rapidly changing neutron flux. By using different gas compositions during individual startups/shutdowns, the additional effect of sweep gas could be observed.

Results and Discussion

A primary objective of this experiment was to determine viable operating parameters for a solid breeder blanket and the associated tritium inventories. Because the results of the experiment reflect the tritium recovery rates for the total system, interpretation of the results in terms of tritium release from the solid breeder involved a number of uncertainties. However, the observed steady state tritium recovery rates and the shape of the recovery peaks did permit general observations to be made concerning the tritium recovery from Li_2O.

Throughout the test sequence there was a slow buildup of background on the ionization chambers. At the end of Cycle 11-C this buildup resulted in a background on the order of 30-35 Ci/m^3 on the ion chamber measuring total tritium from the solid specimen. Throughout this paper the tritium concentration levels listed are those measured, including the backgrounds. For any given measurement in the reference sweep gas, the amount of background can be estimated by assuming that the recovery rate is equal to the recovery rate determined early in the test when the background correction was small. At later times in the operational cycle after larger backgrounds had developed, background levels were more difficult to determine. The tritium recovery rate, determined early in the test sequence, was equivalent to a tritium concentration of 84.2 Ci/m^3 at the reference flow rate of 100 mL/min. Using this as the steady state recovery rate for the reference condition provides a means for estimating the effect of background and furthermore provides a first approximation for comparing the recovery behavior for data taken at different times in the experiment with different backgrounds.

The measured tritium recovery rate was equivalent to a total tritium generation of 3640 Ci for a 300 EFPD cycle. An analysis based on the reactor core configuration in Cycle 11-8.1 was carried out to calculate the

tritium generation of the temperature gradient specimen. The calculated generation rate was 12% less than the measured recovery rate. This is within the expected uncertainties of the measurements and the calculations.

Form of the Recovered Tritium

The tritium measurement system allowed the determination of the distribution of the recovered tritium between its chemical forms, specifically the oxidized (HTO or T_2O) or reduced form (HT or T_2). Because this determination required using the difference between two ion chambers, the background changes occurring during the experiment interfered with determining the absolute quantities of the two forms of tritium. However large or relative changes were still discernable.

During the initial stages of the experiment it was determined that for the reference sweep gas of He-0.1% H_2 greater than 95% of the recovered tritium was in the reduced form. This is the same type of behavior noted for the temperature change specimen operated in the temperature range from 500 to 640°C[3].

Temperature History

One of the observable indicators of the physical stability of the specimen was the long term stability of the specimen temperature during irradiation. Figure 2 is a plot of the two measured centerline temperatures for the first 85 EFPD. The top thermocouple was closer to the center of the reactor core and was at a level of higher neutron flux. Initially the reactor operated at 95% power before a step rise in power to 100%. During the first ten days of operation after reaching 95% power the temperature of both thermocouples appeared to drop, with the top thermocouple temperature dropping as much as 30°C. Other than this initial drop there was, in general, only a slow steady drop in the temperatures throughout the reactor cycle both at 95% and 100% power. This temperature drop can be partially attributed to a slow decrease in the neutron flux at the capsule as the reactor control rods were pulled out to maintain constant power with fuel burnout.

For the first operational cycle, Cycle 11-B.1 (Figure 2), when the reactor reached 100% power, the average inner temperature was 998°C, dropping to 952°C at the end of the cycle. In the two successive reactor cycles a similar type of behavior was observed. In Cycle 11.B-2, the average inner temperature at 100% power dropped from an initial temperature of 1006°C to 961°C at the end of the 134 EFPD cycle. For Cycle 11-C the temperature dropped from an initial temperature of 1027% to 995°C after an 81 EFPD cycle. The temperature difference between cycles resulted from the change in neutron environment brought about by the refueling that occurred between cycles.

Fracturing of the specimen due to thermal gradients would increase the temperature difference across the specimen and raise the center temperatures. The initial drop in temperatures at the start of the experiment may indicate some restructuring in the specimen has occurred but is not indicative of any internal fracturing. From the overall stability of the temperature it is inferred that the microstructure of the specimen

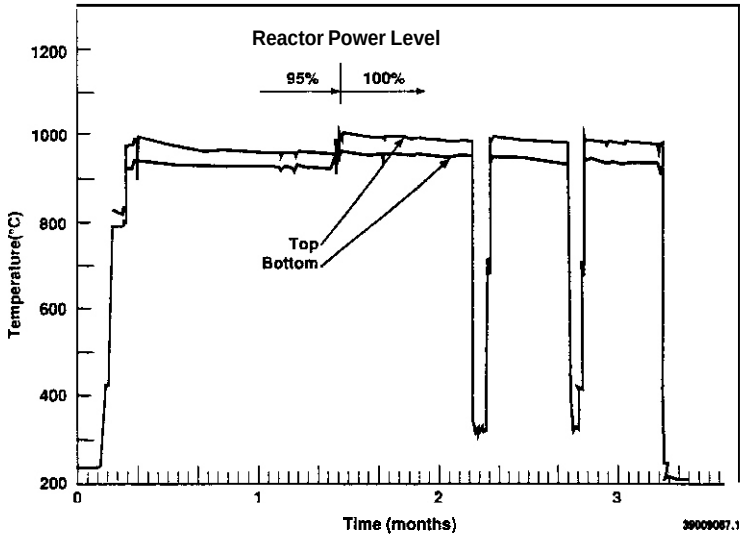


Figure 2. Center temperatures for the temperature gradient capsule during the first operational cycle of BEATRIX-II.

has remained relatively stable and has not undergone any drastic changes such as thermal shock fracturing. Postirradiation examination will provide the final assessment of the microstructural changes that have occurred during the experiment.

Sweep Gas Flow Rate

The change in the recovered tritium during the changes in sweep gas flow rate between 100 and 50 mL/min are shown in Figure 3. The shape of the transient recovery curve was dependent on the rate at which equilibrium could be established and therefore changing to 100 mL/min resulted in a sharper transient recovery curve than the change to 50 mL/min. The recovery rate at the lower flow rate of 50 mL/min after 7 days (left side of Figure 3) was 1% less than the initial recovery rate for the reference flow rate of 100 mL/min. A similar type behavior was observed for the temperature change specimen.[3] Whether this change in recovery rate was related to a dynamic interaction between the sweep gas flow rate and the specimen or was due to permeation losses through the cladding cannot be determined at this time.

Sweep Gas Composition Effects

Sweep gas composition, in particular the amount of H_2 in He, was found to have a major effect on the steady-state tritium recovery. Determining this effect was the primary objective of the test plan in Table 2.

The initial gas composition changes involved a change in sweep gas from the reference gas of He-0.1% H_2 to an alternate gas containing less H_2. These alternate sweep gases were He-0.01% H_2 and pure He. In the first test cycle the alternate gases were used for a duration of two days. For the second cycle the two day tests were repeated and then extended to four days.

Figure 4 compares the observed recovered tritium concentration for the four-day tests in He-0.01% H_2 and in He (Tests #5 and 7). In general the change from reference to the alternate gas with less hydrogen resulted in a sharp drop in the tritium recovery. The tritium concentration then increased to a pseudo-equilibrium rate where the tritium release rate was increasing very slowly. The rate of increase was initially faster for He-0.01% H_2 than He but after four days the recovery rates appeared to be nearly equal. The recovery rates after four days in the alternate gases were compared to the initial recovery rate in reference gas. The resultant ratios were 2/3 for He and 3/4 for He-0.01% H_2. For the ring specimen similar tests were carried out for shorter times,[3] the recovery rates were found to be approximately one-half and two-thirds for He and He-0.01% H_2 respectively. Return to the reference gas resulted in a large, sharp peak in the recovered tritium. After the four day period in helium the change to reference gas resulted in a tritium recovery peak height of 1400 Ci/m^3. This recovery peak was equivalent to 19 Ci of tritium.

The next series of tests (Tests No #E-10) involved a combination of alternate gases in the sequence of He-0.1% H_2, He, He-0.01% H_2 to He-0.1% H_2. During Cycle 11-B.2, the duration times in the two alternate gases (He and He-0.01% H_2) was varied from two to four days. The tritium concentration versus time for these tests is shown Figure 5. The tritium recovery behavior for the first portion of the tests in He is

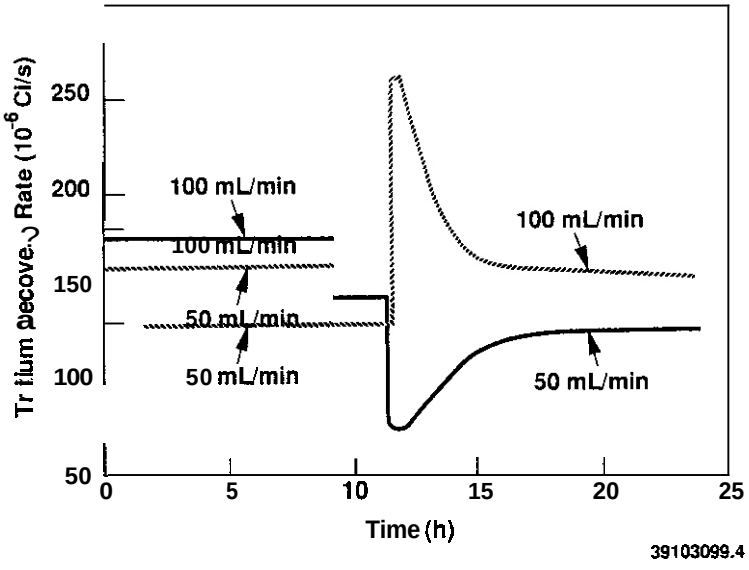


Figure 3. Tritium recovery rate during the change in sweep gas flow rates in Test #1.

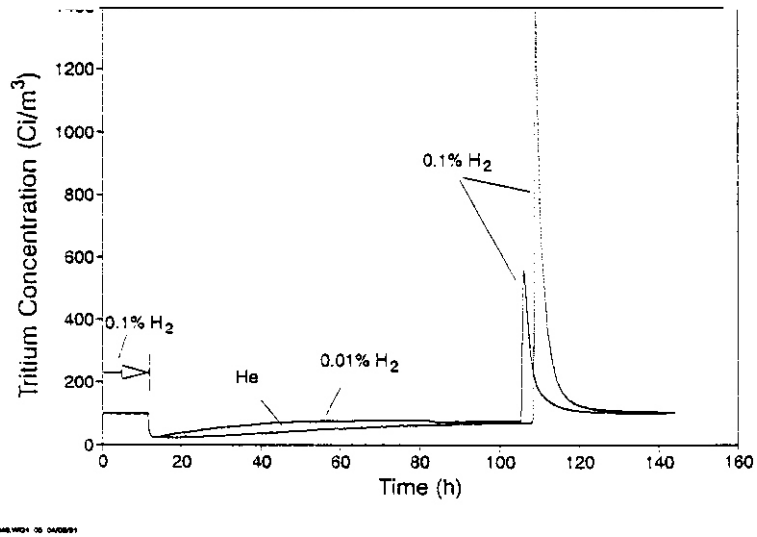


Figure 4. Tritium recovery concentrations during sweep gas composition changes in Tests #5 and #7.

similar to that observed previously in the two and four day tests (Figure 4). The transition from He to He-0.01% H_2 results in a lower, longer peak than the transition from He to He-0.1% H_2. The height and duration of He to He-0.01% H_2 peaks after both 2 and 4 day periods in helium were similar. The transition from He-0.01% H_2 to He-0.1% H_2 resulted in a sharp transition peak similar to that seen previously in Tests #2, 4 and 5 (Figure 4). However the size of the observed peaks did not seem to increase with increasing time in the alternative gases. This independence of tritium recovery peak size with time in the alternate gases suggests that for longer times the tritium inventories may have been saturating for the given gas composition. Thus the changes in tritium inventories that were occurring for specific gas composition changes were similar for the three different tests.

The other characteristic of these curves in Figure 5 is that, if the recovery peaks from the sweep gas changes are neglected, the recovery rate appears to hdve been increasing with increasing time even through the transition from He to He-0.01% H_2. This suggests that with longer times the recovery rate in He-0.01% H_2 would have approached the recovery rate in He-0.1% H_2. To test this hypothesis, two additional tests, #13 and #14, were carried out for extended times in alternate gases. The resulting curves of recovered tritium are shown in Figure 6. Test #13 was run 4 days in helium and then for 6 days in He-0.01% H_2. The resulting recovery rate in He-0.01% H_2 at the end of this run (after subtracting the background) was 78% the

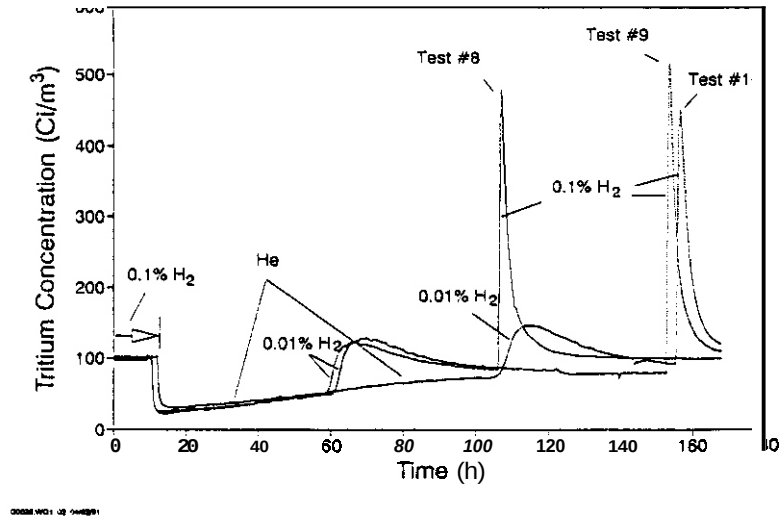


Figure 5. Tritium recovery concentrations during sweep gas composition changes for Tests #8, #9, and #10.

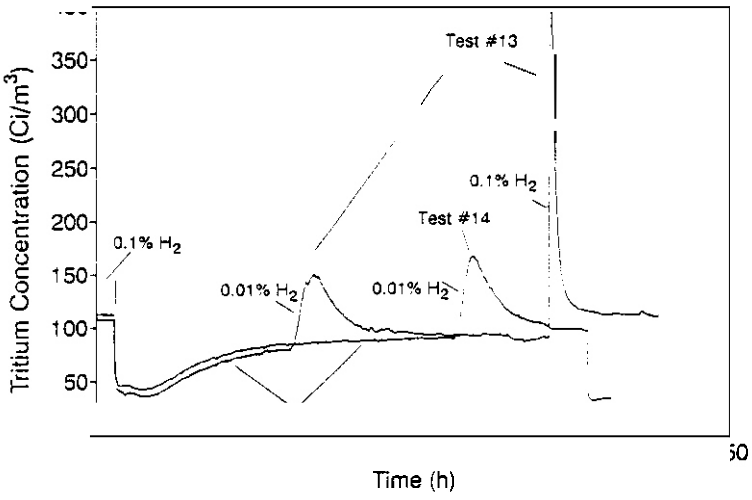


Figure 6. Tritium recovery concentrations during sweep gas composition changes in Tests #13 and #14.

recovery rate in reference gas at the start of this test. Test #14 was run with an even longer time in He extending the time to 8 days. After 2 days in He-0.01% H_2 the recovery rate was 83% of the recovery rate in reference gas at the start.

It is concluded from the results of these tests (Tests #13 and 14) with the alternate sweep gases that for time periods up to 10 days the observed recovery rates were always less than the recovery rates in reference gas. Possible explanations are that the release rate from the specimen was less than the generation rate and that a buildup of tritium was occurring in the specimen or that tritium was accumulating in other regions of the system. The continuation of this low recovery rate for an indefinite period of time would suggest that a change in the specimen tritium inventory was occurring. The reduction in recovery rates with lower concentrations of hydrogen in the sweep gas has also been observed in the VOM experiment.[6] In the CRITIC-1 test on Li_2O,[7] this effect was not seen directly, but was inferred from a buildup in the tritium inventory over long periods of time using low H_2 concentrations in the sweep gas.

The significant changes in tritium recovery observed by decreasing the hydrogen in the sweep gas to less than 0.1% H_2 suggested that an increase in the hydrogen should be considered. Test #15 was carried out using He-1% H_2 as the sweep gas. The results are shown in Figure 7. For the change from He-0.1% H_2 to He-1.0% H_2 there was an initial decrease in the recovered tritium concentration followed by a small peak and an approach to steady state. This increase in the apparent steady state recovery in He-1.0% H_2 was 21% of the initial measured recovery rate (corrected for background) in the reference sweep gas.

Taken at face value, the increase in the recovery rate in He-1.0% H_2 versus the reference gas has significant implications. One possible explanation is that the recovery rate for the reference sweep gas of He-0.1% H_2 was less than the generation rate. Another possible explanation is that the response of the ionization chambers is not independent of the H_2 content of the gas and the addition of H_2 results in a higher indicated concentration of tritium. This explanation would also explain the failure for the recovery rates in the alternate gases to reach the recovery rate in the reference gas. The possibility of the ionization chamber response being affected by the gas composition will be characterized in future testing.

In addition to changes in the tritium recovery rate for a sweep gas of He-1.0% H_2 the moisture in the recovered sweep gas increased from 25 ppm for the reference gas to 440 ppm for He-1.0% H_2. This moisture level was much higher than observed previously in the experiment. The recovered HTO did not show any comparable increase and was proportional to the total recovered tritium curve. Because of the overwhelming large amount of hydrogen compared to tritium (200:1), it is difficult to draw any conclusions as to whether this moisture was released from the specimen or from other components of the system.

Reactor Startup/Shutdown

Reactor startup and shutdown provide opportunities to study the effect of changes in the tritium generation rate and temperature on tritium recovery from the solid specimen. During reactor startup/shutdown in reference gas, the observed tritium release behavior was as expected, with increasing/decreasing reactor power the temperature and tritium recovery increased/decreased almost proportionately. Temperature being related directly to heat generation and tritium recovery related directly to tritium generation. However

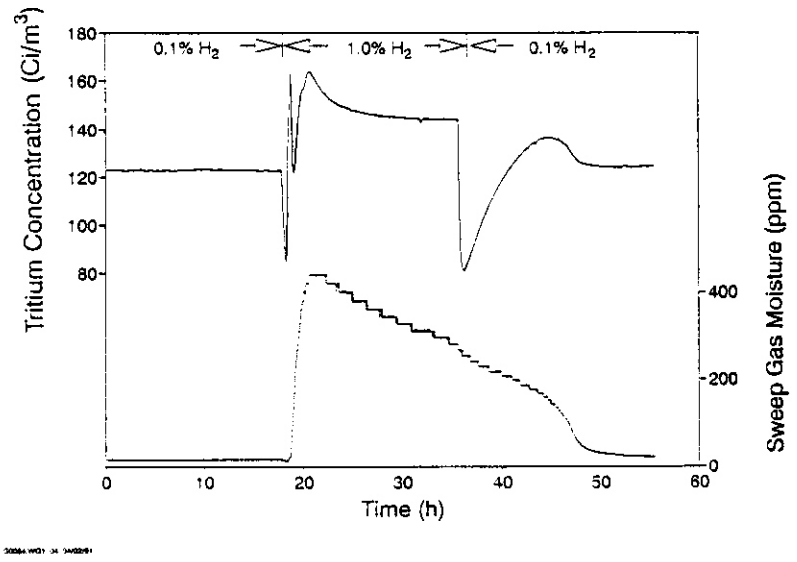


Figure 7. Tritium recovery concentrations and sweep gas moisture for a change from He-0.1% H_2 to He-1% H_2 sweep gas (Test #15).

using helium as sweep gas during reactor shutdown was found to significantly effect the tritium recovery behavior. Figure 8 is a plot of tritium concentration and neutron level for reactor shutdown in a He-0.1% H_2 and He sweep gas. Although the neutron intensity is shown here for comparison, the temperature of the specimen also decreased in direct response to the decrease in neutron intensity. The tritium recovery for a shutdown in He-0.1% H_2 was as expected, with a steady decrease in the tritium concentration as the power was reduced. For He sweep gas, the behavior was drastically different. As the neutron level decreased, the tritium generation rate and specimen temperature decreased but the recovered tritium concentration increased.

During reactor startup in helium, the recovered tritium with increasing neutron intensity was also found to be different than observed for He-0.1% H_2. Figure 9 is a plot of recovered tritium and neutron flux during a reactor startup in helium. After increases in neutron intensity the recovered tritium decreased as the tritium generation and specimen temperature increased. When the reactor had reached full power, the sweep gas was changed to He-0.01% H_2. This change resulted in the typical tritium release peak. Before the peak

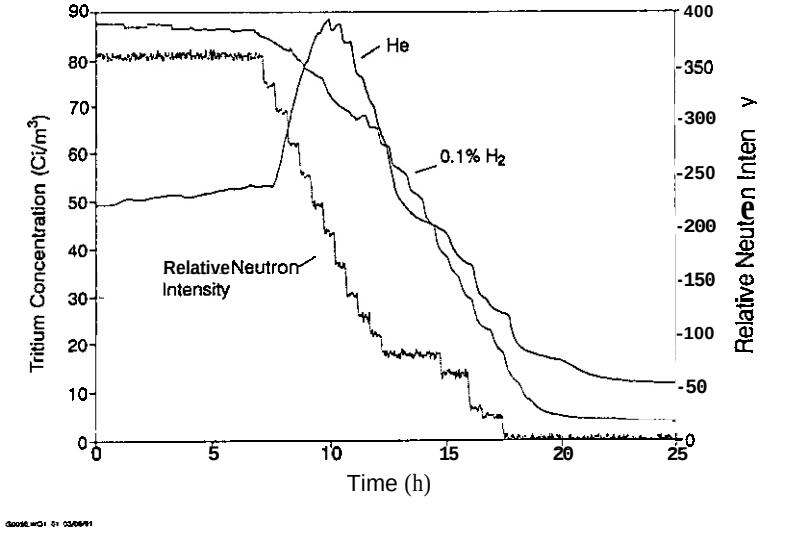


Figure 8. Tritium recovery concentrations and neutron flux during a reactor shutdown in He and He-0.1% H_2 sweep gases.

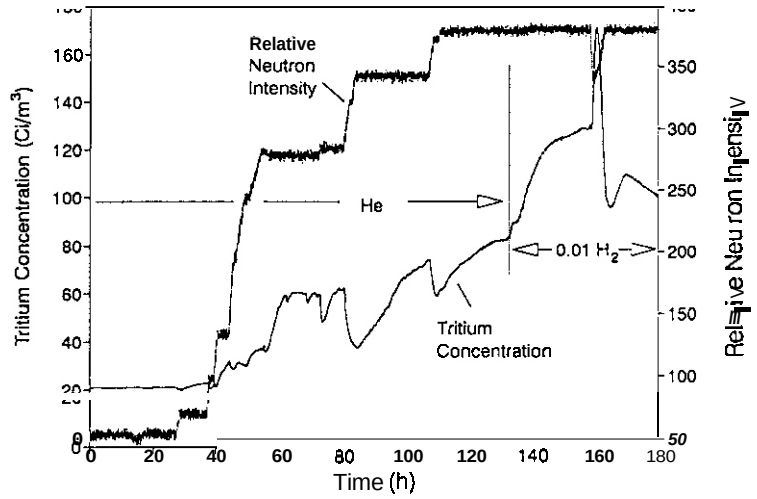


Figure 9. Tritium recovery concentrations and neutron flux during a reactor startup in He sweep gas.

was finished, the reactor power decreased. This power decrease/increase was accompanied by an increase/ decrease in the recovered tritium, similar to the behavior observed for helium sweep gas.

One possible explanation for the behavior of the specimen during power changes in a helium sweep gas is related to hydrogen/tritium solubility in Li_2O. The amount of hydrogen/tritium dissolved in Li_2O increases with increasing temperature.[8,9] An increase in reactor power effects an increase in the dissolved tritium/hydrogen inventory and a possible decrease in the tritium recovery rate.

The difference between the reference sweep gas and helium sweep gas was the relative amounts of tritium and hydrogen in the sweep gas. The recovered tritium concentrations in He-0.1% H_2 sweep gas were equivalent to approximately 65 ppm of tritium atoms. For the He-0.1% H_2 sweep gas, the concentration of hydrogen atoms is 2000 ppm. Thus the ratio of tritium to hydrogen is roughly 1:30 at steady state. For He as the sweep gas, the hydrogen concentration would theoretically approach zero. Hence for He-0.1% H_2 sweep gas, any dissolved hydrogen/tritium will be predominately hydrogen while for a helium sweep gas the dissolved hydrogen/ tritium will be predominately tritium. Thus an increase in the tritium release rate due to the dissolution of hydrogen/tritium from the Li_2O matrix would be most likely to be observed when tritium is a significant proportion of the dissolved hydrogen/tritium as is the case when the sweep gas contains a low concentration of H_2. Such an effect could be contributing to the difference in startup/shutdown tritium recovery behavior observed for He versus He-0.1% H_2 sweep gases. Since the tritium recovery in a helium sweep gas is opposite to that anticipated from the change in generation rate, surface controlled release or a diffusional controlled mechanism, the observed anomalous recovery during startup/shutdown may be related to the behavior of tritium dissolved in the Li_2O.

CONCLUSIONS

The BEATRIX-II, Phase I experiment provided data for in situ tritium recovery from a Li_2O specimen irradiated under a large thermal gradient typical of fusion blanket designs. This test has provided additional verification of the viability of Li_2O as a candidate for a fusion solid blanket. Results from the 300 EFPD of operation can be summarized as follows:

1. Throughout the 300 EFPO of irradiation, the temperature of the specimen was nearly constant or decreasing slowly throughout the cycle. From the stability of the temperature it is inferred that the microstructure and the thermal properties of the specimen have also remained stable and that the specimen has remained physically intact.

2. The composition of the sweep gas was found to be a critical parameter in the recovery of tritium from Li_2O. In general, decreasing the amount of hydrogen in the sweep gas decreased the recovery rate of tritium. The conclusion is that for sweep gases having smaller amounts of H_2 than the reference gas the recovery rates are always less than the recovery rates in reference gas for time periods up to 10 days.

3. During reactor startup/shutdown the composition of the sweep gas has been found to be an important factor in the tritium recovery.

FUTURE WORK

The tritium recovery data will be more extensively analyzed to characterize the tritium release behavior during sweep gas composition changes. Postirradiation examination of the specimen will be used in coordination with the in situ tritium recovery data to characterize the operational behavior of Li_2O during the 300 EFPD irradiation cycle. BEATRIX-II, Phase II is a follow-on experiment which will involve the irradiation of a Li_2O temperature change specimen and a Li_2ZrO_3 sphere bed.

REFERENCES

1. Hollenberg, G. W., T. Kurasawa, H. Watanabe, S. E. Berk, 1. J. Hastings, and D. E. Baker, "A Fast Neutron, In Situ Tritium Recovery Experiment ON Solid Breeder Materials," Fusion Technology, 15, 1349-1354 (1989).

2. Puigh, R. J., G. W. Hollenberg, T. Kurasawa, H. Watanabe, I. J. Hastings, J. M. Miller, S. E. Berk, R. E. Bauer, and 0. E. Baker, "BEATRIX-II: In Situ Tritium Recovery from a Fast Neutron Irradiation Of Solid Breeder Materials," In Proceedings of the 15th Svmoosium on Fusion Technolosv, edited by A. M. Van Inger, A. Nigsen-Vis, and H. P. Kippel, pp 1282-1286, September 19-23, 1988, Utrecht, The Netherlands. Elsevier, Nether1ands.

3. Kurasawa, T., 0. 0. Slagle, G. W. Hollenberg, and R. A. Verrall, "In Situ Tritium Recovery from Li_2O Irradiated in Fast Neutron Flux - BEATRIX-II Initial Results," Presented at the Ninth Topical Meeting on the Technology of Fusion Energy Oak Brook, IL, October 7-11, 1990.

4. Baker, 0. E., T. Kurasawa, J. M. Miller, and 0. D. Slagle, "BEATRIX-II: In Situ Tritium Test Operation," Presented at the Ninth Topical Meeting on the Technology of Fusion Energy Oak Brook, IL, October 7-11, 1990.

5. Takahashi, T., and H. Watanabe, "Preparation and Characterization of Lithium Oxide," Fusion Engineering and Desian, 8, 399-405 (1989).

6. Kurasawa, T., et al., "The Time Dependence of In-Situ Tritium Release from Lithium Oxide and Lithium Aluminate (VOM-22H Experiment)," J. Nucl. Mater., 141-143, 265 (1986).

7. Verrall, R. A., J. M. Miller, D. S. MacDonald, and S. R. Bokwa, "CRITIC-1 Irradiation of Lithium Oxide," J. Nucl. Mater., 155-157, 553-557 (1988).

8. Smith, D., et al, "Tritium Breeding Blanket," Presented at the Ninth Topical Meeting on the Technology of Fusion Energy Oak Brook, IL, October 7-11, 1990.

9. Billone, M. C., C. C. Lin, H. Attaya, and Y. Gohar, "Tritium Retention and Release Analysis for the U.S.-ITER Blanket." Presented at the Ninth Topical Meeting on the Technology of Fusion Energy Oak Brook, IL, October 7-11, 1990.

INVESTIGATION OF TRITIUM RELEASE AND RETENTION IN LITHIUM ALUMINATE - J. P. Kopasz (Argonne National Laboratory). S. Tistchenko and F. Botter (Commisariat a L'Energie Atomique, Centre de Saclay, Gif-sur-Yvette, CEOEX, France)

SUMMARY

Tritium release from single crystal lithium aluminate has been investigated by a series of isothermal anneal and constant rate heating experiments. The results of these experiments indicate that after anneals at low temperature, a large fraction of the tritium present before the anneal remains in the sample. We have modeled this behavior based on first order release from three types of sites. At low temperature the release is dominated by one site, while the tritium in the other sites is retained in the solid. Dopants appear to alter the distribution of tritium between the sites. Adding MgO decreases the fraction of tritium released at 777°C, while increasing the fractions released at 538 and 950°C.

PROGRESS AND STATUS

Introduction

Tritium release from lithium aluminate is of interest due to the potential use of the aluminate as a tritium breeding material in a fusion device. Several previous experiments have investigated tritium release from lithium aluminate, however, there is little agreement in the data.[1,2,3] In addition, the rate controlling mechanism is still under debate, with some claiming diffusion is rate controlling while others claim desorption is rate controlling.[4,5]

In an attempt to increase our understanding of tritium release from lithium aluminate we have performed several postirradiation annealing experiments on pure lithium aluminate and lithium aluminate doped with Magnesium. Magnesium should substitute for lithium in the lattice and increase the number of lithium vacancies present in the crystal. If tritium release is diffusion controlled and tritium diffusion is correlated with lithium diffusion as has been postulated, the magnesium dopant should improve tritium release. The results of these anneals have indicated that the tritium is released from several different sites, with different activation energies and that tritium release was not diffusion limited under the conditions studied. In the single crystal samples at low temperature, release was dominated by release from one type of site while the tritium from the other sites remained in the solid. Doping appears to alter the distribution of tritium between the different types of sites. We have analyzed tritium release based on first order kinetics from three types of sites.

Experimental

Pure single crystals and single crystals doped with magnesium were prepared using the Czochralski method. The details of the preparations have been reported previously.6 Sintered pellets of pure and doped aluminate were prepared by B. Rasneur.[7] The annealing apparatus and procedure are identical to those reported in reference 6. Two types of tritium release experiments were performed. The first type of experiment is a series of isothermal anneals, performed on the same sample. The furnace is preheated to temperature T1, and the sample is moved into the heated portion of the apparatus. The tritium release is recorded as a function of time, for a fixed time or until the release approaches the baseline. The temperature is then raised to a new temperature T2, and the tritium release observed as a function of time. The temperature may be increased again to a third temperature after a specified time. The second type of experiment is a constant rate heating or temperature programed desorption experiment. In this experiment the sample is placed in a furnace under flowing purge gas (Ar ± 0.1% H_2). The temperature is then raised to give a linear temperature versus time profile, while the tritium released is detected downstream by a proportional counter.

Results and Discussion

Successive thermal anneals were performed on single crystals of $LiAlO_2$ with a radius of 1 mm. A typical example is illustrated in Figure la. The anneals are at 538, 777, and 950°C. The rapid initial release at 538°C followed by a return to baseline, suggests that the majority of tritium has been released. However, when the temperature is increased to 777°C, a large tritium release peak is observed. The tritium released at 538°C is only a small fraction of the total tritium in the sample. This type of release is inconsistent with a diffusion controlled release mechanism and with a simple desorption mechanism with one activation energy. The fraction of the total tritium released was analyzed as a function of time to determine the effective diffusion coefficient at the initial anneal temperature. This treatment resulted in an effective diffusion coefficient which varied by up to an order of magnitude over the time of an anneal at a single temperature, indicating the tritium release was not diffusion controlled under these conditions. Similar analyses of the fraction released at the temperature of the anneal result in effective first order desorption rate constants which are fairly constant over the time of the anneal. However, the values at the same temperature differ depending on the history of the anneal. These results suggest that tritium is released from several types of sites on the surface, each exhibiting a different activation energy.

Work supported by the U.S. Department of Energy, Office of Fusion Energy, under Contract W-38-109-Eng-38.

Constant rate heating experiments were performed on the samples to investigate the hypothesis that tritium is released from several types of sites. The results show the presence of several overlapping peaks, again suggesting that the tritium is released from several types of sites with different activation energies.

Activation energies for desorption or other first order processes can be obtained from constant rate heating experiments performed at two heating rates using equation 1 below.

$$Ea/RT = \ln(T_m^2/\beta) - \ln(Ea/AR) \quad (1)$$

where β = heating rate
Ea = activation energy
E = temperature degrees Kelvin
A = preexponential
T_m = temperature of peak maxima
R = gas constant

For the pure single crystal, peak maxima appear at approximately 666° and 780°C for a heating rate of 2°C/min, while the maximum for the largest peak has not been reached at 950°C. At a heating rate of 0.5°C/min, these peaks appear at 602° and 706°C, and the main maxima appears at 904°C. These data provide activation energies of 132.6 Kj/mol (31.7 kcal/mol) and 143.5 kj/mol (34.3 kcal/mol) for the two lower temperature peaks. These values are in ood agreement with activation energies determined for the desorption of water from $LiAlO_2$ by A. Fischer.! Analysis of constant rate heating experiments for Mg doped single crystals at heating rates of 1.0 and 0.5°C/min result in activation energies of 150 and 181 kj/mol (36.3 and 43.2 kcallmol). The activation energy for the last peak could not be determined for either the pure or doped material. At the higher heating rates, the maximum of the peak was not reached before the maximum temperature of the experiment.

To further test our hypothesis, the tritium release curves from the isothermal anneal experiments were modeled as combinations of several first order processes. The tritium release at each temperature was fit to a linear combination of two first order release processes. The rate constants calculated from the individual anneals were used to calculate activation energies and preexponential terms. These terms plus a term describing the distribution of tritium between the three types of sites were then used to calculate the release for an experiment with three successive anneals of 538, 777, and 950°C. The fit to the experimental data was optimized by varying the distribution term and making small adjustments in the rate constants. The results are shown in Figures 1a and 2a (pure and Mg doped single crystals, respectively). The best fits were obtained with following rate constants (calculated as desorption rate constants) : $H_a = 0.039\ e^{(-63\ kj/mol/RT)}$ for the low temperature or type A sites, $H_b = 16.25\ e^{(-133\ kj/mol/RT)}$ for the type B sites in the pure material, $H_b = 32.5\ e^{(-133\ kj/mol/RT)}$ for the type B sites in the doped material, $H_c = 70\ e^{(-142\ kj/mol/RT)}$ for the type C sites in the pure material and $H_c = 164\ e^{(-181\ kj/mol/RT)}$ for the type C sites in the doped material. The same distribution, preexponential terms and activation energies were then employed to model the results from experiments with successive anneals of 777 and 950°C. The results are illustrated in Figures 1b and 2b. The activation energy of 62.8 kj/mol is in good agreement with the lowest activation energy reported for desorption of H_2O from $LiAlO_2$, while the values of 133 and 142 kj/mol are in agreement with energies obtained for desorption from a higher energy site.[8] The values of 133. 142 and 181 kj/mol are also in agreement with those obtained from the constant rate heating experiments. Attempts to fit the release from samples annealed only at 950°C with these same parameters failed. The 950°C first anneal curves were better fit by a single first order rate constant. This may be due to tritium being released during the time the sample is heating up to 950°C and to a redistribution of the tritium between the different sites at the higher temperature.

The magnesium doping was found to have a small effect on the tritium release. For the magnesium doped samples, a slightly larger fraction of the total tritium was released at 538°C and 950°C than for the pure materials, while less tritium was released at 777°C than was observed in the pure samples (see Table 1 and Figures 1a and 2a). This

Table I
Comparison of Fraction of Tritium Released at Various Temperatures for Pure or Mg Doped $LiAlO_2$

Fraction Released		Temperature
Pure	Doped	°C
.035	.085	538
.920	.635	777
.045	.280	950

indicates that the magnesium doping changes the distribution of the tritium between the three types of sites, decreasing the amount at type B sites while increasing the amounts at type A and C sites. In addition, the doping increased the tritium release rate at 777°C. The increase appears as an increase in the preexponential term for the release from site B, from 16.25 to 32.5. Doping also decreases the release rate at 950°C and increases the activation energy for release from type C sites. The increased activation energy is observed in the constant rate heating experiments and the isothermal anneals.

Recent results with small grain size sintered pellets also suggest the presence of several different tritium sites. However, release from small grain size samples occurs at lower temperatures than for the single crystals or large grain size material.

This is also consistent with a desorption model. For desorption controlled release the fraction of tritium released increases with decreasing grain size according to the equation:

$$f = 1-\exp(-3Ht/a)$$

where f = fraction of tritium removed
H = desorption rate constant and
a = grain radius.

CONCLUSION

Tritium release from lithium aluminate is a complex process. The release was not diffusion controlled under the conditions investigated. The data is consistent with first order release occurring from three sites. At low temperatures (538°C and below), release is dominated by release from type A sites, while release from the type B and C sites is very low. At these temperatures the tritium in the type C sites is effectively retained in the solid. At higher temperatures tritium release from the type B and C sites dominates. Doping the material can influence the distribution of tritium between the three types of sites and can change the activation energy or preexponential term for the release rate constant for release from a particular site.

FUTURE WORK

Tritium release will be studied by isothermal anneals and constant rate heating experiments as a function of grain size to determine the relationship between the various tritium sites, the release rate constants and the grain size. Of particular interest is whether the activation energies remain the same when changing grain sizes. This would indicate that release is occurring from the same types of sites for the different grain sizes and and only the preexponential terms which provide information on the number of sites is changing.

REFERENCES

1. R. G. Clemner, P. A. Finn, B. Misra, M. C. Billone, A. K. Fischer, S. W. Tam, C. E. Johnson and A. E. Scandora, J. Nucl. Mater. 133/134 (1985) 171.

2. F. Botter, D. Cherquitte, and N. Roux, Fusion Technology, 2 (1986) 357.

3. C. E. Johnson, G. W. Hollenberg, N. Roux, and H. Watanabe. Fusion Engineering and Design 8 (1989) 145.

4. H. Kudo, Radiochimica Acta 50 (1990) 71.

5. M. Briec, F. Botter, J. J. Abassin, R. Benoit, P. Chenebault, M. Masson, B. Rasneur, P. Sciers, H. Werle, and E. Roth, J. Nucl. Mater 141/143 (1986) 357.

6. F. Botter, J. Mougin, B. Rasneur, S. Tistchenko, and J. Kopasz, Proceedings of the 16th Symposium on Fusion Technology, 3–7 September 1990.

7. B. Rasneur, A. M. Lejus, and R. Collongues, Proceedings of the 16th Symposium on Fusion Technology, 3–7 September 1990.

8. A. K. Fischer, Proceedings of the Ninth Topical Meeting on the Technology of Fusion Energy, October 1990 (in press).

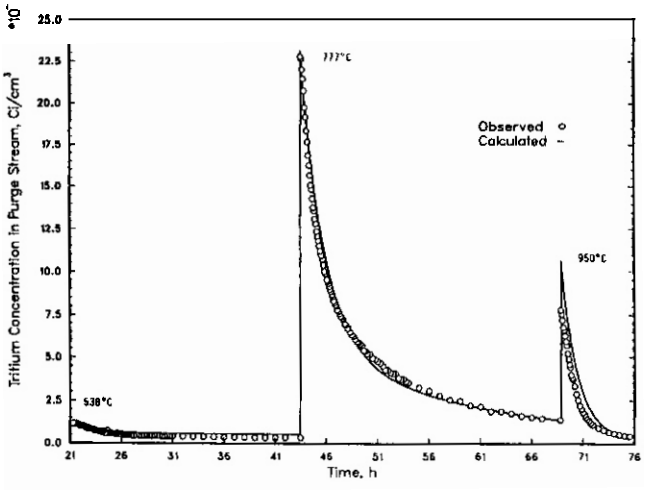


Fig. 1a. Calculated and Observed Release of Tritium from "pure" $LiAlO_2$ for Successive Anneals at 538, 777 and 950°C.

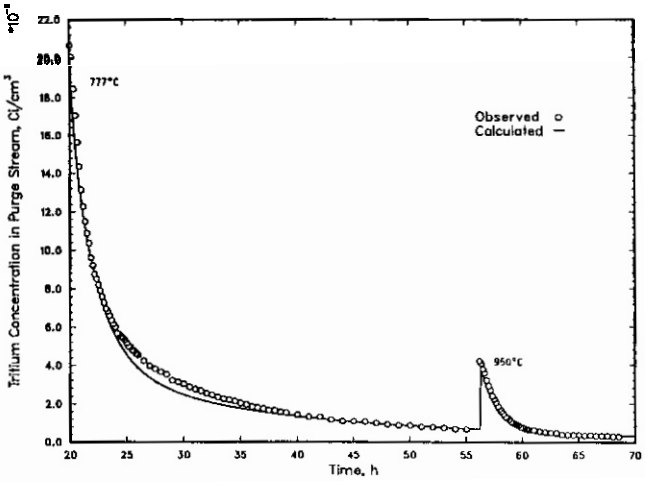


Fig. 1b. Calculated and Observed Release of Tritium from "pure" $LiAlO_2$ for Successive Anneals at 777 and 950°C.

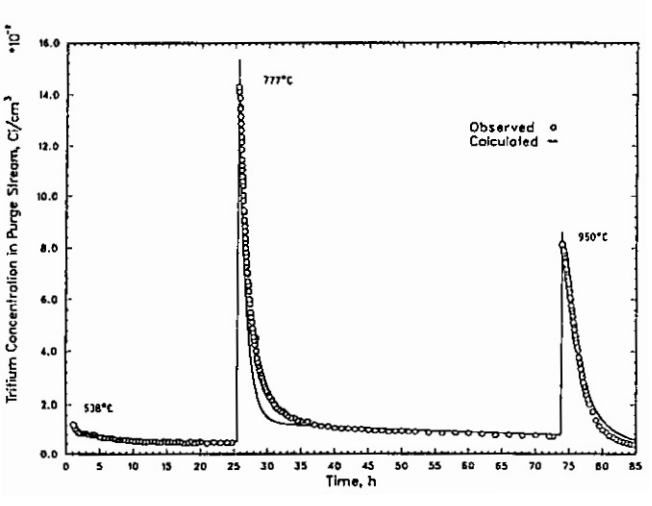


Fig. 2a. Calculated and Observed Release of Tritium from Magnesium Doped $LiAlO_2$ during Successive Anneals at 538. 777 and 950°C.

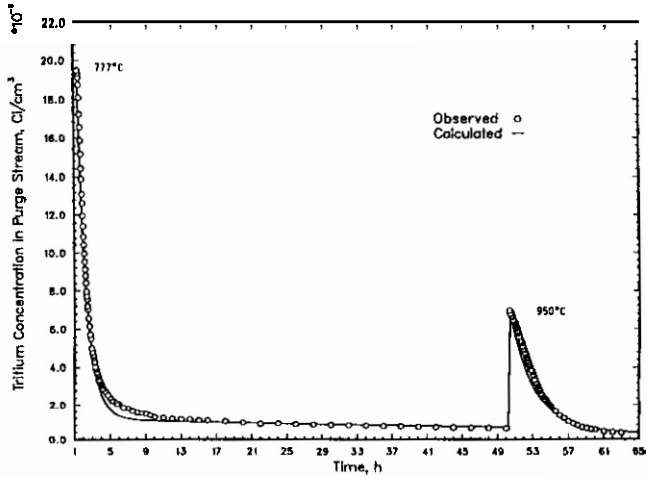


Fig. 2b. Calculated and Observed Release of Tritium from Magnesium Doped $LiAlO_2$ during Successive Anneals at 777 and 950°C.

DESORPTION CHARACTERISTICS OF THE $LiAlO_2$-H_2-$H_2O(g)$ SYSTEM - A. K. Fischer and C. E. Johnson (Argonne National Laboratory)

OBJECTIVE

The objective is to describe the energetics and kinetics of desorption of $H_2O(g)$ and H_2 from the surface of ceramic tritium breeders ($LiAlO_2$ in the present case) in a form that enables predictions of the characteristics of tritium release.

SUMMARY

The energetics and kinetics of the evolution of H_2O and H_2 from $LiAlO_2$ have been studied by the temperature programmed desorption technique. After treating the sample with helium containing 990, 495, or 247 vppm H_2 at 923 K, H_2O and H_2 evolution was observed during 473 to 1073 K (200 to 800°C) ramps at rates of 5.6 K/min. The sweep gas was either pure helium or the same He-H_2 mixture that was used in the preliminary treatment. The H_2O and H_2 desorption peaks were shown to be the sums of first order subpeaks which had reproducible activation energies and pre-exponential terms. For H_2O desorption, these peaks, of types labelled B, C, and O had activation energies of 22, 28, and 32 kcal/mol. (Earlier work identified type A peaks with an activation energy of 18 kcallmol.) Enhancement of desorption of H_2O in rate and quantity by H_2 in the sweep gas was confirmed. It appears that the effectiveness of H_2 in this enhancement is not in modifying the activation energy and pre-exponential term for a given kind of site, but rather in changing the populations of sites participating in the desorption processes so that sites with lower activation energies are increasingly involved. Only C and D subpeaks were involved in H_2 desorption and they had activation energies close to and perhaps only 1 kcal/mol higher than the analogous peaks for H_2 evolution.

PROGRESS AND STATUS

Introduction

Earlier reports in this series discussed the background for the temperature programmed desorption (TPD) technique for measuring the activation energy and pre-exponential terms for the desorption rate equation and also presented results for TPD runs on $LiAlO_2$ that had been pretreated with H_2 at 673 K. It was not clear whether H_2 in the gas stream facilitated desorption under those pretreatment conditions; a higher pretreatment temperature was seen as possibly necessary to reveal the enhanced release that was observed with irradiated samples. In the present report, results are presented for TPD runs on $LiAlO_2$ that was pretreated with H_2 at 923 K.

Experimental

TPD experiments were run on $LiAlO_2$ that had been pretreated at 923 K (650°C) overnight or, in a few cases, for a week or 12 days in a gas stream containing H_2 at concentrations of 990, 495, and 247 vppm. The system was cooled quickly to 473 K while maintaining the equilibrating gas composition. The temperature ramp was from 473 to 1073 K at a ramp rate of 5.6 K/min. The sweep gas during the TPD run was either pure helium or the same He-H_2 mixture that was used in the preceding treatment. When pure helium was to be the sweep gas, the gas composition was switched from the He-H_2 mixture to pure helium just before or as the ramp began. Differences in the desorption peaks allowed comparisons to be made that express the impact of H_2 in the sweep gas on the desorption processes.

The gas conposition was monitored with a mass spectrometer to provide continuous traces for H_2, H_2O, N_2, and O_2. The N_2 and O_2 data provided ongoing evidence for the absence of leaks. The O_2 trace remained at baseline. At the end of the ramp, there was a soaking period of 10 min at 1073 K followed by cooldown to 923 K. This was the temperature during the succeeding equilibration with the desired He-H_2 mixture for the next run.

TPO peaks for the evolution of both H_2 and H_2O were obtained during the runs of desorption into pure helium. During runs of desorption into He-H_2 mixtures, peaks due to desorption of H_2 would be obscured against the strong background of H_2 in the sweep gas mixture. Nevertheless, some significant hydrogen effects were observed.

Results and Discussion - Desorption of H_2O

Figures 1-3 show TPD curves from runs for desorption of H_2O into pure He sweep gas and desorption of H_2O into a He-H_2 mixture; in a given figure, the pretreatment gas composition was the same whether the desorption was into helium or into the mixture. The y-axis gives the rate of evolution from the particular sample in units of mol/min-m^2. The areas under the curves reflect the amounts of evolved material. It is evident in each case that the rates and amounts of desorption of H_2O are enhanced substantially over the values for desorption into pure helium. Earlier it was shown that the desorption process involves multiple processes reflecting desorption from different kinds of sites on the surface of the $LiAlO_2$.[1] The desorption peaks were analyzed to derive values for the kinetic parameters of the contributing subpeaks.

This work supported by the U.S. Department of Energy, Office of Fusion Energy, under Contract W-31-109-Eng-38.

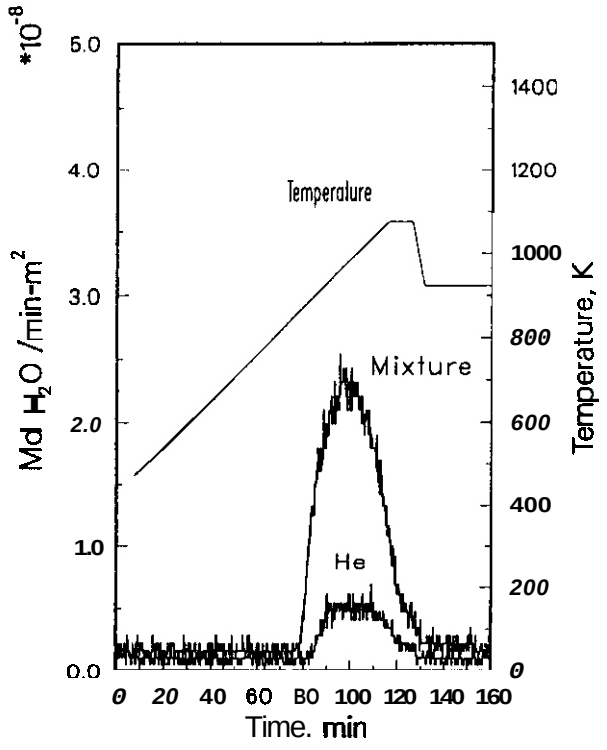


Figure 1. TPD of H_2O from $LiAlO_2$ treated with 247 vppm H_2; into helium or into same gas mixture.

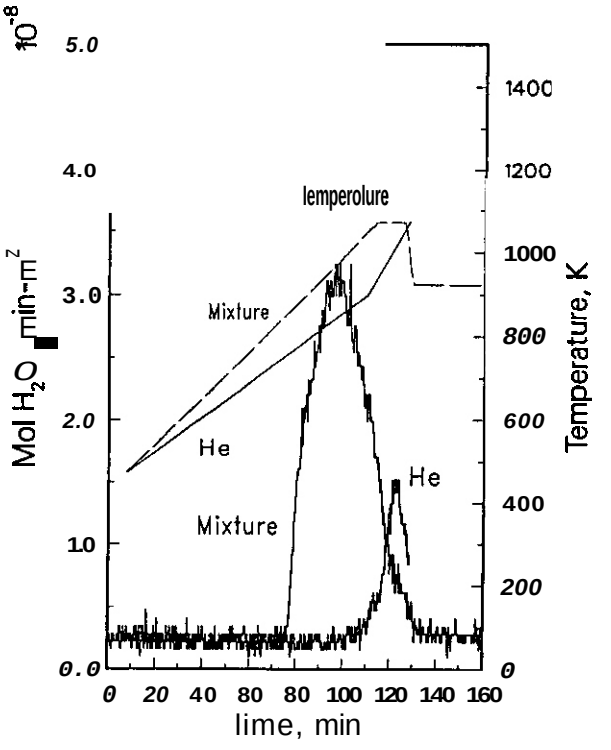


Figure 2. TPD of H_2O from $LiAlO_2$ treated with 495 vppm H_2; into helium or into same gas mixture.

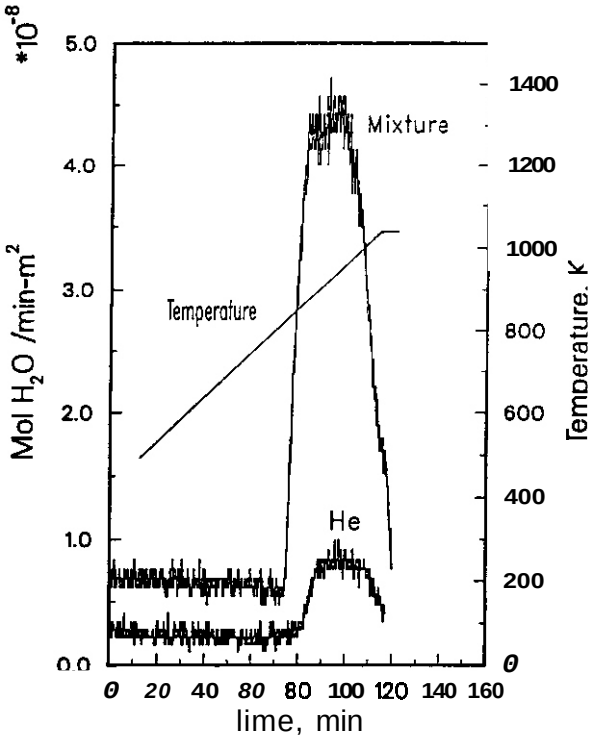


Figure 3. TPD of H_2O from $LiAlO_2$ treated with 990 vppm H_2; into helium or into same gas mixture.

The method of analyzing the peaks was to synthesize them from the subpeaks of the functional form for a first order desorption process:

$$r = \Sigma \nu_i a_i \exp(-E_{di}/RT) \quad (1)$$

where r is the overall rate of desorption of $H_2O(g)$ expressed by the measured curves in mol/min and is comprised of the sum of desorption from the individual types of sites identified by subscript i, ν_i, is the pre-exponential term for a given type of site in units of mol H_2O/min/mol occupied site, i, a_i is the amount in mol of H20 adsorbed on a given type of site at a given time, and E_{di} is the activation energy of desorption in units of kcal/mol.

Figures 4 and 5 show deconvoluted TPD spectra for an example of desorption into He and into He-495 vppm H_2. Consistently. the curves for desorption into He-H_2 mixtures contained two types of peaks labelled B and C, and the curves for desorption into pure helium contained C and D peaks. (In earlier work dealing with desorption from samples soaked at 400°C, A, B, and C peaks were identified.)[2] Results for all runs are shown in Table 1 which also lists the pre-exponential terms. The activation energies of the B, C, and D peaks are close to 23, 28, and 32 kcal/mol. (The A peaks have a desorption activation energy of 18 kcallmol.) The data indicate that the H_2 in the sweep gas causes precursors of desorbed H_2O, namely the OH- population, to shift and to build up in the B and C sites, which provide an activation energy mixture that is lower than that which prevails in the absence of H_2 when the higher activation energy combination of C and D sites is involved. It is important to note that the activation energies of the sites do not change significantly.

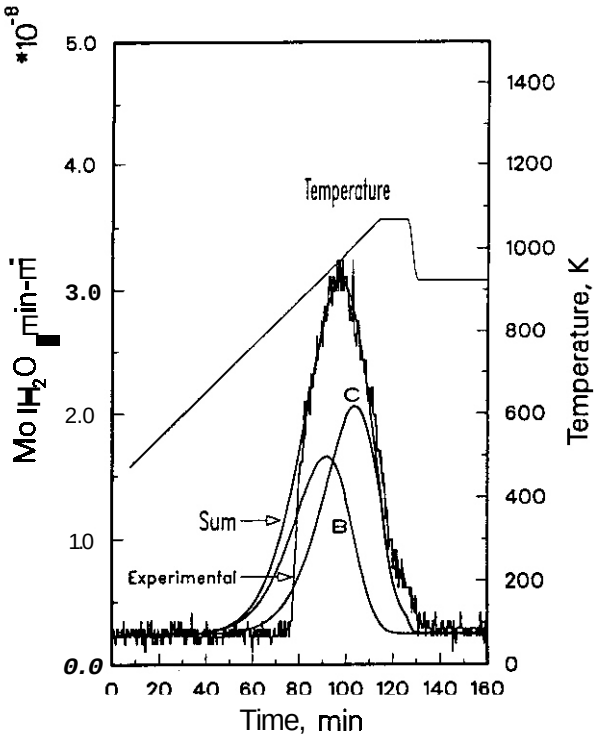


Figure 4. TPD of H_2O into 495 vppm H_2; deconvolution into B and C subpeaks.

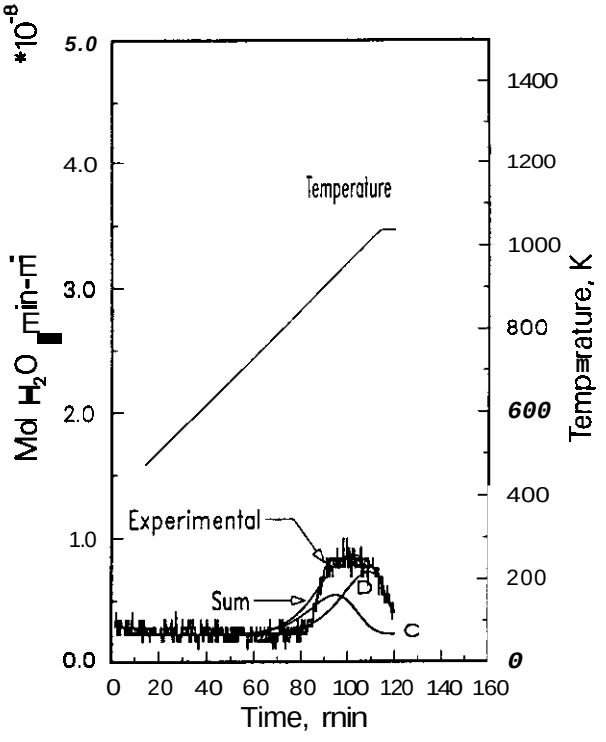


Figure 5. TPD of H_2O into pure helium from $LiAlO_2$ treated with 495 vppm H_2; deconvolution into C and D subpeaks.

The pre-exponential terms are not as constant as the activation energies. Standard deviations of the sets of ν_i range from 13 to 52%of the respective mean values. Where the ν values may be compared to determine the effect of H_2 on pre-exponentials, namely for the C peaks, the values of (2.22 ± 1.16)E5 vs (8.91±1.14)E4 for pure He and for the gas mixture, respectively, can just about be called different at the lo level. It appears, therefore, that the effect of H_2 makes a small change in the pre-exponential term for the C sites, which is in the direction of reducing the overall desorption rate: however, this effect is overcome by the entry of substantial coverage in the lower activation energy B sites when H_2 is in the sweep gas.

Table 1. Kinetic Parameters for First Order Desorption of H_2O from B, C. and D Sites on $LiAlO_2$. Duration of soak in h: H_2 concentration in soak and in sweep gases in vppm.

Soak time	Soak gas	Sweep gas	ν_B	E_{dB}	ν_C	E_{dC}	ν_D	E_{dD}
20	247	0	-	-	1.90E5	28.2	3.51E5	32.3
170	495	0	-	-	1.25E5	28.0	9.91E5	32.0
20	990	0	-	-	3.51E5	28.0	7.51E5	32.0
20	247	247	2.22E4	23.0	8.82E4	28.0	-	-
20	495	495	1.07E4	22.0	7.62E4	28.0	-	-
20	495	495	1.62E4	23.0	8.78E4	28.0	-	-
290	990	990	2.75E4	22.8	1.04E5	28.0	-	-

These data are sumnarized in the form of the mean values of the ui and E_{di} values in Table 2.

Table 2. Averaged Kinetic Parameters for B, C, and D Peaks for H_2O Desorption from $LiAlO_2$ into H_2 Mixtures and into He

	ν_B	E_{dB}	ν_C	E_{dC}	ν_D	E_{dD}
He	-	-	2.22E5	28.1	6.9E5	32.1
Mixture	1.91E4	22.7	8.91E4	28.0	-	-

Utility for Designers and Modelers

The areas under the H_2O desorption curves, represented by the sums of the B and C peaks or the C and D peaks, were converted to values of fractional surface coverage, θ, on the assumption of 1E19 sites per m^2 of surface. This θ value is for the total evolvable H_2O under the given conditions, either into the respective $He-H_2$ mixtures or into pure He. It is distinguished from a θ value that would include all sites that might be covered but which did not participate in the desorption processes that were measured. Such sites are those that would have been activated only at temperatures higher than those in the range of the experimental temperature ramp. The H_2 adsorption process (leading to surface OH- groups which combine bimolecularly on reversal to adsorption) was regarded as disassociative chemisorption so that it and the H_2O coverage should vary as the square root of the H_2 partial pressure. Therefore, the observed total evolvable H_2O coverage, θ, was plotted against the partial pressure of H_2 in $Pa^{1/2}$. Figure 6 shows the linear relationship followed.

As an example, a designer interested in the rate of desorption of H_2O at steady state from a breeder at 650°C into a helium stream carrying H_2 in the measured range would be dealing with a steady state coverage of desorbable H_2O indicated by Figure 6. To calculate the desorption rate requires knowledge of the values of a_B and a_C for the rate equation. These may be calculated from:

$$a_i = 1.66\times10^{-5} m \sigma_s \theta_i \qquad (2)$$

where the factor $1.66\times10^{-5} = 10^{19}/6.02\times10^{23}$, m is the mass of the breeder in g, σ is the specific surface area in m^2/g, and θi is the fractional surface coverage by evolvable H_2O on sites of type i. The last quantity is derived from the curve in Figure 6 by allocating portions of the indicated total θ to the B and C sites. The exact relationship between B and C site populations still requires study, but for the present purpose it is useful to assume the ratio of B to C sites as approximately 0.5; the observed ratios ranged from 0.38 to 0.79. That is, 1/3 of the θ from Figure 6 is assigned to the B peak and 2/3 to the C peak. (For desorptions into pure helium, the ratio of C to D peaks was in the range from 0.24 to 1.18.) The rate of desorption can be calculated by substitution of these values into equation 1.

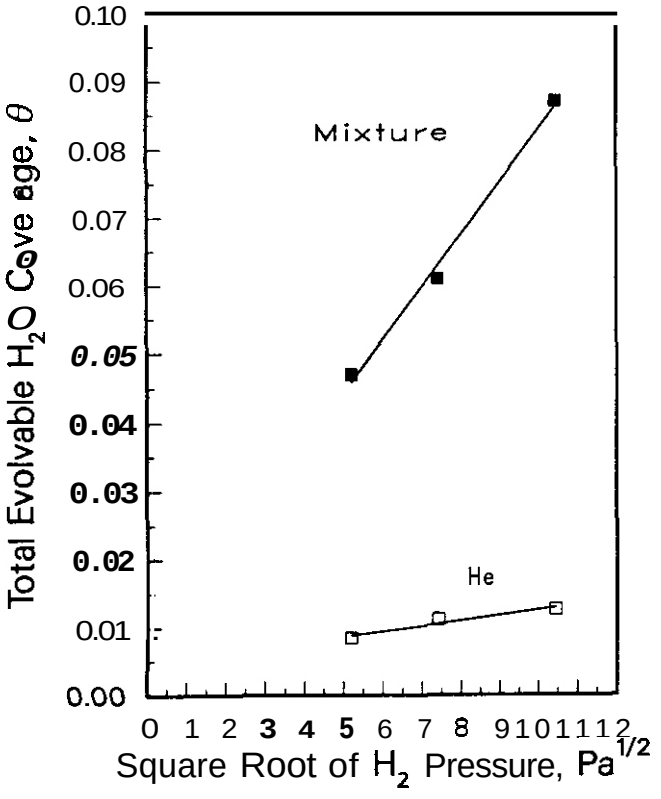


Figure 6. Fractional surface coverage by H_2O desorbed in the 200 to 800°C TPD ramp: desorption into H_2 mixture or into pure helium.

Results and Discussion - Desorption of H_2

Some data for the TPD of H_2 were also obtained. Desorption into pure helium provided desorption peaks which were deconvoluted. The results from this analysis are presented in Table 3.

Table 3. Kinetic Parameters for First Order Desorption of H_2 into He from C and D Sites on $LiAlO_2$. Duration of soak in h and H_2 concentration in soak gas in vppm.

Soak time	Soak gas	ν_C	E_{dC}	ν_D	E_{dD}
20	247	1.61E5	28.2	6.35E4	33.5
170	495	1.30E5	28.5	5.00E5	32.5
20	990	4.68E5	28.5	8.91E5	33.0
	Average	2.5E5	28.4	4.8E5	33.0

It is striking that the kinetic parameters are very similar to those for H_2O. The subpeaks are labelled C and D to indicate their similarity to the ones for H_2O, though it is not implied at this time that the sites are the same. Figure 7 shows the deconvolution for the most prominent H_2 peak observed with excellent fit of the data. However, there are still puzzling aspects for which further study is planned. For example, Figure 8 compares the evolution of H_2 in a pure helium stream and the changes in H_2 level in the sweep gas that is introduced initially with a concentration of 247 vppm. Ignoring the first 10 minutes or so, which is a warmup period for a mass spectrometer, the droop in the upper curve indicates that H_2 is being taken up by the system until a temperature of approximately 1080 K (710°C) is reached whereupon H_2 evolution commences. This behavior roughly parallels the lower curve for desorption into pure He. One question is how much of the H_2 in the gas stream after passing the sample originates from the sample and how much from the input stream. The forthcoming work with deuterium-loaded samples (but with Li_2O as the sample) and H_2-containing sweep gas should cast light on this. It would provide a direct isotopic analog for questions of tritium behavior.

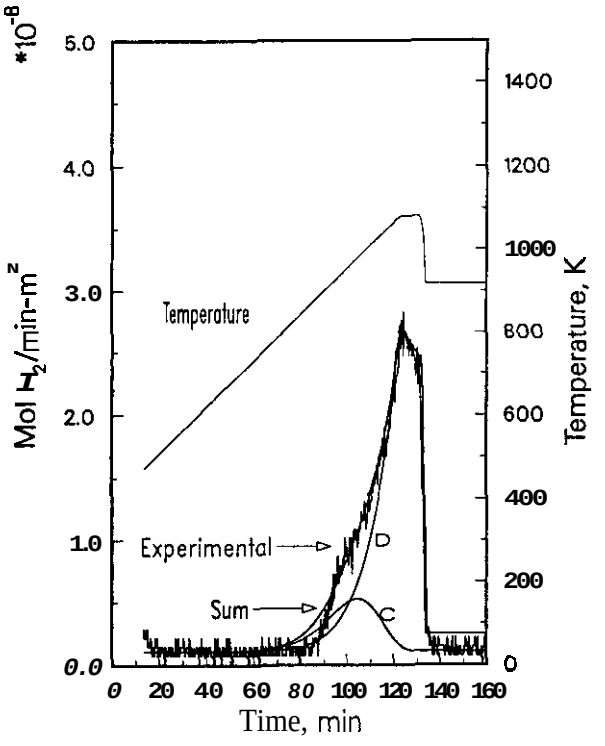


Figure 7. TPD of H_2 into pure helium from $LiAlO_2$ treated with 247 vppm H_2; deconvoluted into C and D subpeaks.

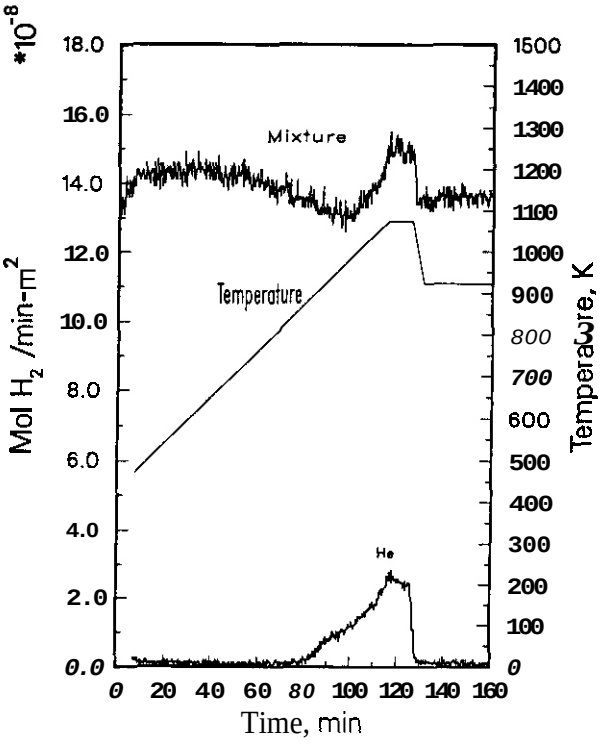


Figure 8. TPD of H_2 into pure helium or into 247 vppm H_2 mixture from $LiAlO_2$ treated with 247 vppm H_2.

Other matters may be developed by examination of Figure 9 in which the coplotted H_2 and H_2O peaks for a single run are shown for desorption into a stream of 247 ppm H_2. (The H_2-into-He curve in Figure 8 has been replaced by the H_2O-into-mixture curve.) Here, it appears that H_2O desorption lags behind the onset of H_2 uptake. Adsorbed H_2 builds up before H_2O appears. A question is whether to regard the process as reduction by H_2 to make H_2O or as displacement of H_2O from the surface. Along with this is the question of the oxygen and/or water source, since H_2O peaks are observed repeatedly on the same sample. It has been suggested that an experimental approach to identify the oxygen source is to perform the TPD measurements on a sample labelled with ^{18}O. However, the practicality of this in terms of expense and sensitivity has not been explored yet.

At the time of writing, further numerical analyses of the data are still possible. One task is to compare the areas of H_2 uptake and the areas of H_2 and H_2O desorption; they appear similar in size. However, some inexactness in the comparison is expected from uncertainty due to the small-number changes in a large-number variable. Though the program plan calls for no further experimental work with $LiAlO_2$, the issues raised here indicate the need in the forthcoming work with Li_2O not only for the new innovations in experimental technique (use of deuterium for sure and possible use of ^{18}O) but also for extension of the basic experimental variables of changes in ramp rate and the temperature limit of the ramp, variables that form the core of a comprehensive TPO study.

FUTURE WORK

The next phase of the TPO measurements will center on the breeder, Li_2O, in order to provide data that are of current interest for ITER.

REFERENCES:

1. J. P. Kopasz, A. K. Fischer, and C. E. Johnson, "Multiple Activation Energies for Tritium Release from Ceramic Breeders.' Adv. Ceram. 27, 317 (1990).

2. A. K. Fischer, "Processes for Desorption from $LiAlO_2$ Treated with H_2 as Studied by Temperature Programmed Desorption," Proceedings of the Ninth Topical fleeting on the Technology of Fusion Energy, Accepted for publication in Fusion Technology.

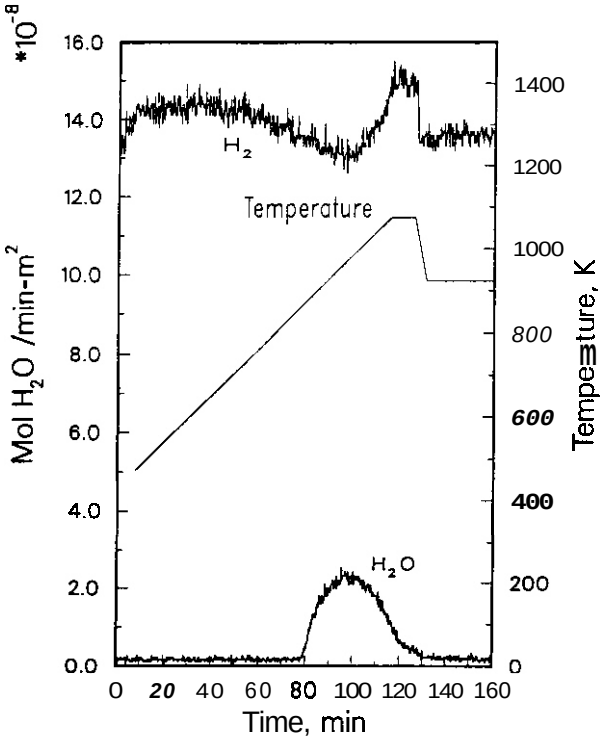


Figure 9. TPD of H_2O and H_2 into pure helium or into 247 vppm H_2 from $LiAlO_2$ treated with 247 vppm H_2.

9.0 CERAMICS

MICROSTRUCTURE OF Al_2O_3 AND $MgAl_2O_4$ PREIMPLANTED WITH H, He, C AND IRRADIATED WITH Ar^+ IONS

Reiji Yamada [Japan Atomic Energy Research Institute (JAERI)], Steven J. Zinkle (Oak Ridge National Laboratory), and G. Philip Pells (Harwell Laboratory)

OBJECTIVE

To examine the microstructural changes in ceramic insulators following irradiation at fusion-relevant transmutation products (H, He, C) per dpa ratios.

SUMMARY

Polycrystalline spinel ($MgAl_2O_4$) and alumina (Al_2O_3) were irradiated under three different sets of ion irradiation conditions in order to examine the effects of displacement damage and transmutation product formation on their microstructural evolution. Specimens were implanted with H, He and *C* alone, or irradiated with 4 MeV Ar^+ ions alone, or preimplanted with H, He, *C* and subsequently irradiated with 4 MeV Ar^+ ions. Irradiated specimens were observed with transmission electron microscopy following irradiation to damage levels of *0.6* to 30 dpa at *260* to *630°C* for spinel and *0.6* to 18 dpa at *260* to 810°C for alumina. In both spinel and alumina, no radiation effects were observable in specimens implanted with H, He and *C* alone, and the preinjected transmutation products did not have a significant effect on dislocation loop size or density in Ar^+ irradiated specimens. In alumina, cavities were formed in all of the observed Ar^+ irradiated specimens for both the preimplanted H, He and C case and the Ar^+ alone case. In spinel, cavity formation was only observed in preimplanted specimens irradiated with Ar^+ ions at relatively high temperatures and/or doses.

PROGRESS AND STATUS

1. Introduction

Ceramic materials have been proposed for fusion applications as special purpose materials like insulators, rf windows, etc., from the point of view of their insulating and dielectric properties. In addition, the advantages of low activity materials in future fusion reactors like DEMO are so attractive that ceramic and/or composite materials may he applied not only for a specialized purpose but more broadly for first wall and structural materials.

Concerning the radiation damage of ceramics, most of the experiments so far have utilized fission reactors or ion accelerators. One of the largest differences between fission and fusion reactors in radiation damage on ceramics is that, in the case of fusion reactors, a fairly large number of transmutation products will be produced. For example, the amounts of H, He and C production in units of atomic concentration per displacements per atom (appm/dpa) were each estimated as approximately 100 appm/dpa for alumina (Al_2O_3) and for magnesium aluminate spinel ($MgAl_2O_4$) due to irradiation with 14 MeV neutrons.[1,2] Compared to other ceramics, microstructural evolution of alumina and spinel during neutron or ion irradiation have been fairly well studied.[3-5] Related phenomena such as hardening and amorphization have also received attention.[11-16] These studies have revealed that spinel has higher resistance to aggregate damage accumulation than alumina under fast neutron (>0.1 MeV) (refs. 3-5) or self-ion irradiation.[6,7] For irradiation relevant to fusion reactors, the effects of helium-doping in alumina was investigated under 4 MeV Ne+ and Ar^+ ion irradiation; helium-doped specimens exhibited an increased number and diameter of voids as well as total swelling.[8] The presence of a sufficient concentration of helium can lead to the formation of a dense dislocation network as well as of a cavity array along the c axis of alumina during O^+ plus He^+ irradiations[9] A similar alignment of cavities is observed following simultaneous irradiation of Al^+, O^+ and He^+ ions[10] and coimplantation of helium assists the development of cavity formation.[12] Cavity alignment in alumina is also seen in other ion and neutron studies (e.g., refs. 3,7). In spinel, cavity formation occurs preferentially at dislocation loops and grain boundaries following irradiation at fusion-relevant He/dpa ratios[3] As far as the authors know, however, there is still a lack of knowledge on how the multiple transmutation products of H, He and C affect the radiation damage of alumina and spinel.

In order to examine the effect of multiple transmutation products on microstructural evolution, we performed three types of irradiation on Al_2O_3 and $MgAl_2O_4$: (1)Pre-implantation of H^+, He^+, C^+ ions and successive Ar^+ ion irradiation; (2) Ar^+ ions alone; and (3) H, He and C ions alone.

In this report we present the results of the temperature and dose dependence of the cavity and dislocation loop microstructure which were examined in cross-section with a transmission electron microscope (TEM).

2. Experimental

The 99.9% pure, polycrystalline alumina, trade name Vitox, was supplied by Anderman & Ryder. Vitox was of near theoretical density with an average grain size of 1.5 μm. The 99.9% pure polycrystalline spinel was supplied by Baikowski International Corporation and had an average grain size of 0.6 pm.

The targets of alumina and spinel, mechanically polished to a 1 μm finish, were irradiated using the Harwell Van de Graaff accelerator. The irradiation of 4 MeV Ar^+ ions was used to create collisional displacement damage to simulate the damage due to neutron irradiation. For simulating the effects of transmutation products on radiation damage, H, He and C ions were pre-implanted at room temperature. The ion energies of preimplantation were adjusted to be equivalent to the range of 4 MeV Ar^+: 580 keV H^+, 820 keV He^+ and 3.0 MeV C^+, and they were implanted in the order of H, He and C. The ratios of atomic concentration of H, He and C to displacements per atom were each set at 100 appm/dpa, which is nearly equal to the calculated ratios for 14 MeV neutron irradiation.[1,2] The value of the displacement threshold used in the calculations was 53 eV.

In order to obtain a uniform damage profile of 4 MeV Ar^+ ions as well as a uniform implantation profile of H^+, He^+ and C^+ ions, the targets were irradiated at several angles: The angles through which the sample was tilted for pre-implantation as well as 4 MeV Ar^+ irradiation, starting with the sample normal to the beam, were 0, 24, 33.5, 40, 46, 50, 54, 58, 61, 64, 66, 68, 70 deg. The same dose was given at each angle. The damage profiles of 4 MeV AI' irradiation in alumina were calculated by using the EDEP-1 code'' as well as the TRIM code.'' Tilting at the above angles gave a uniform distribution of dpa for depths from 0.4 to 1.4 μm, as shown in Fig. 1. This figure was taken from Pells et al.[19]

The target size was 10 x 10 mm. Selective masking was used to produce three different irradiation conditions on each target: (1) implantation of transmutation products alone, (2) 4 MeV Ar^+ ions alone, and (3) preimplantation of transmutation products plus 4 MeV Ar^+ ion irradiation. The target area exposed to each irradiation condition was approximately 3 x 3 mm. The implantation of transmutation products for (1) and (3) was first carried out at room temperature at the same time, and then the 4 MeV Ar^+ ion irradiation for (2) and (3) was performed together. Different targets were irradiated at 260 to 630°C to damage levels of 0.66 to 30 dpa for spinel and at 260 to 810°C to damage levels of 0.66 to 18 dpa for alumina where the damage levels were taken from a flat-top position of Fig. 1. During the 4 MeV Ar^+ ion irradiation the whole target for conditions (1)-(4) was annealed at that higher temperature. Table 1 summarizes the experimental conditions for the TEM specimens irradiated in this study.

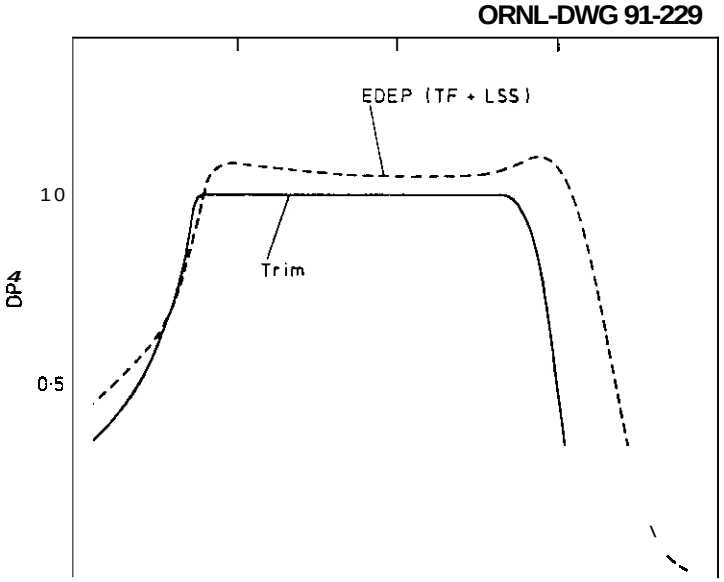


Table 1. Ion irradiation conditions for TEM study

H, He, and C preimplantation* + 4 MeV Ar^+ ion irradiation

Material	Temperature (°C)	Damage Level (dpa)						
$MgAl_2O_4$	260	0.6	3.2	4	6.2	12		
$MgAl_2O_4$	420		2.6			12.5		
$MgAl_2O_4$	630		3		6	12		30
Al_2O_3	260	0.66	2.7			12.5		
Al_2O_3	420					12	18	
Al_2O_3	620		3			12		
Al_2O_3	810		3					

4 MeV Ar^+ ion irradiation alone

Material	Temperature (°C)	Damage Level (dpa)						
$MgAl_2O_4$	260					12		
$MgAl_2O_4$	420		2.6			12.5		
$MgAl_2O_4$	630		3					
Al_2O_3	260	0.66	2.7					
Al_2O_3	420		3			12	18	
Al_2O_3	620		3			12		
Al_2O_3	810		3					

*Preimplanted concentration is 100 appm/dpa for each H, He, and C

The cavity and dislocation loop microstructure of the irradiated specimens was examined with a Philips CM 12 transmission electron microscope operating at 120 keV. The TEM specimens were prepared by the cross-sectioning method. An irradiated target was cut into four parts, the piece containing the preimplanted transmutation products plus Ar^+ irradiation condition was glued face-to-face with the piece exposed to the transmutation products alone, and similarly the piece exposed to argon irradiation alone with the unirradiated piece. These sandwiched specimens were sliced perpendicular to the irradiated surface, mechanically dimpled and ion-milled using procedures described elsewhere.[7,8]

3. Results

The general cross-section microstructure of spinel preimplanted with H, He, C and subsequently irradiated with 4-MeV Ar^+ ions to 3 dpa at 630°C is shown in Fig. 2. Since the target was tilted at several angles during irradiation, the microstructure was distributed rather uniformly. Evidence of radiation damage extends to a depth of 2 μm, which is in good agreement with the theoretical calculations of EDEP-1 and TRIM codes.

3.1 Cavity formation

The cavity observation was performed as a function of temperature and dose and the results are summarized in Table 2. In order to observe cavities, we examined areas of the near-surface, midrange and end of range. If the range is not specified, TEM micrographs were taken from near the middle range.

3.1.1. $MgAl_2O_4$

The TEM examination revealed that cavities were only observed in specimens preimplanted with H, He, C and subsequently irradiated with 4 MeV Ar^+ ions at a higher dose and/or higher target temperature. Within the present experimental conditions, the cavities were not observed at a dose less than 12 dpa over the temperature range of 260 to 420°C, but at 630°C cavities were observed even at 3 dpa. Figure 3 shows cavities at under- and over-focus conditions for a specimen after H, He, C preimplantation and subsequent Ar^+ ion irradiation to 3 dpa at 630°C. For this irradiation condition the cavities were uniformly distributed, and their diameter was approximately 1.5 nm. At a higher dose of 30 dpa at 630°C the cavities were not distributed uniformly, but had a tendency to line up along grain boundaries, as shown in Fig. 4. The size of cavities at this irradiation condition increased slightly to be about 2.4 nm. In general, the effect of temperature and dose on the size of cavities was not significant.

We could not observe any cavities within the resolution of TEM in any of the observed specimens irradiated with Ar^+ ions alone, as summarized in Table 2. Although it is not listed in Table 2, the specimens irradiated with H^+, He^+ and C^+ ions alone also did not show any cavities.

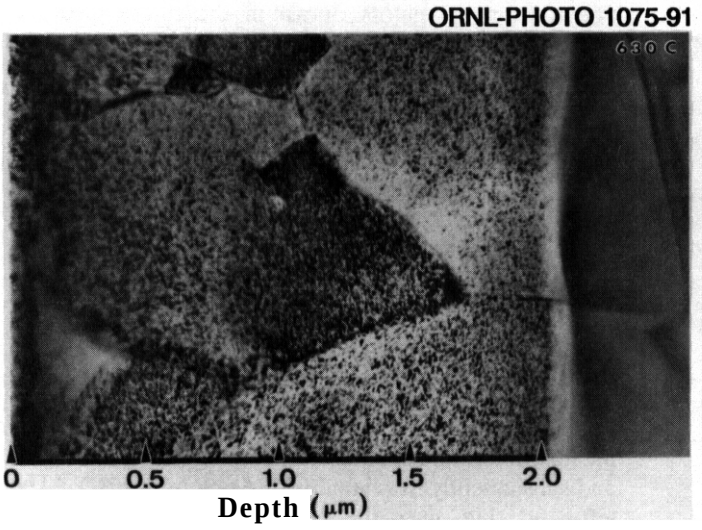


Fig. 2. Cross section microstructure of $MgAl_2O_4$ preimplanted with H, He and C, and subsequently irradiated with 4 MeV Ar^+ ions to 3 dpa at 630°C.

Table 2. The results of cavity formation

H, He. and C preimplantation + 4 MeV Ar^+ ion irradiation

	Damage level (dpa)										
Al_2O_3					Spinel ($MgAl_2O_4$)						
260°C	0.66*	2.7			260°C	0.6	3.2	4		12	
420°C			12	18	420°C		2.6			12.5	
620°C		3	12		630°C		3		6	12	30
810°C		3									

4 MeV Ar^+ ion irradiation alone

	Damage level (dpa)										
Al_2O_3					Spinel ($MgAl_2O_4$)						
260°C	0.66	2.7			260°C					12	
420°C		3	12	18	420°C		2.6			12.5	
620°C		3	12		630°C		3				
810°C		3									

*Cavities were observed at underlined doses.

ORNL-PHOTO 1073-91

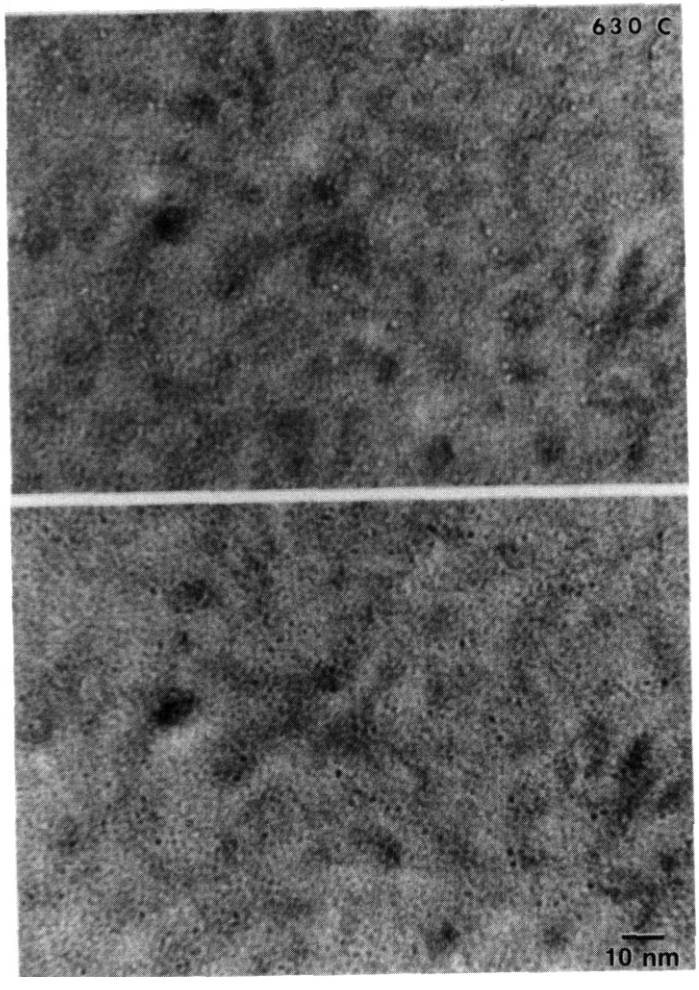


Fig. 3. TEM micrographs of cavities in $MgAl_2O_4$ at under-(bottom picture) and over-(upper picture) focus condition. The specimen was preimplanted with H, He and C and subsequently irradiated with 4 MeV Ar^+ ions to 3 dpa at 630°C.

ORNL-PHOTO 1316-91

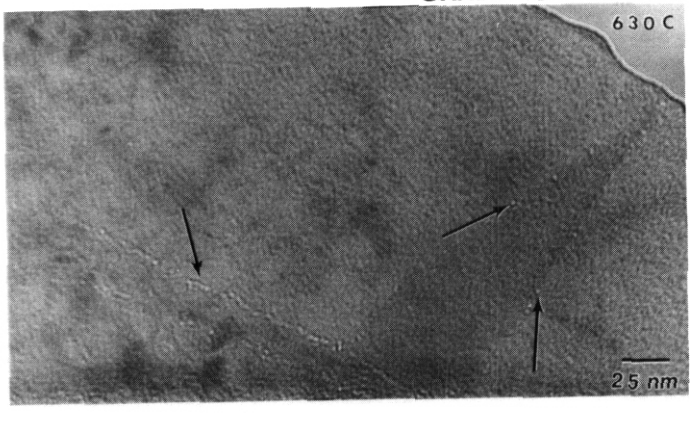


Fig. 4. TEM micrograph of cavities in $MgAl_2O_4$ preimplanted with H, He and C and subsequently irradiated with 4 MeV Ar^+ ions to 30 dpa at 630°C.

We observed depth dependent cavity formation in spinel following H, He, C preimplantation and 4-MeV Ar^+ ion irradiation to 3 dpa at 630°C, as shown in Fig. 5. In the middle of the damage region (about 1.2 μm depth; the cavity density is much larger than that at a depth of 0.5 μm, in agreement with the calculated irradiation profile (Fig. 1). The size of cavities, however, did not vary with depth by any significant amount.

3.1.2. Al_2O_3

In Al_2O_3, cavities were formed in all of the observed specimens with and without pre-implantation of H, He and C. However, no cavities were observed in the specimens implanted with H, He and C alone. Figure 6 shows the TEM observation of cavities for an mer-focus condition for implanted and non-implanted specimens irradiated with Ar^+ ions to 3 dpa at 810°C. Contrary to the results for spinel, the size and density distribution of cavities did not show any significant difference between preimplanted H, He and C specimens and non-preimplanted ones. The cavity size was approximately 15 nm for both cases.

The cavities in alumina also showed a tendency to line up along grain boundaries in the case of high temperature and high dose irradiation. Similar to spinel, cavities form preferentially near a grain boundary in the specimen irradiated with Ar^+ ions alone, as shown in Fig. 7. It should be noted that cavities only lined up near the grain boundary of the grain on the left-hand side of Fig. 7. There is a denuded wne of cavities next to the grain boundary of width 5 nm. In order to investigate how the orientation of grain boundary affects cavity formation, tilting experiments were performed at several grain boundaries. The left-hand side of Fig. 8 shows the same grain boundary as Fig. 7, and the right-hand side of Fig. 8 shows another grain boundary in the same specimen. The diffraction vectors drawn in the figure give the information of orientation of grains. The results of Fig. 8 indicate that if a grain boundary lies nearly parallel to the basal plane (hexagonal crystal structure), cavity formation is enhanced adjacent to the grain boundary, and that if a grain boundary lies nearly parallel to a prism plane, the lining-up of cavity formation along the grain boundary is much less pronounced.

3.2 Dislocation loop microstructure

3.2.1 $MgAl_2O_4$

Figure 9 shows the effect of dose on the microstructure of spinel preimplanted with H, He and C and subsequently irradiated with Ar^+ ions at 630°C. The left-hand side gives the result after 3 dpa, and the right-hand side 30 dpa. The specimen was tilted to observe the dislocation loops in an edge-on configuration. For both doses the habit planes of the dislocation loops were {110} and {111} planes, and the

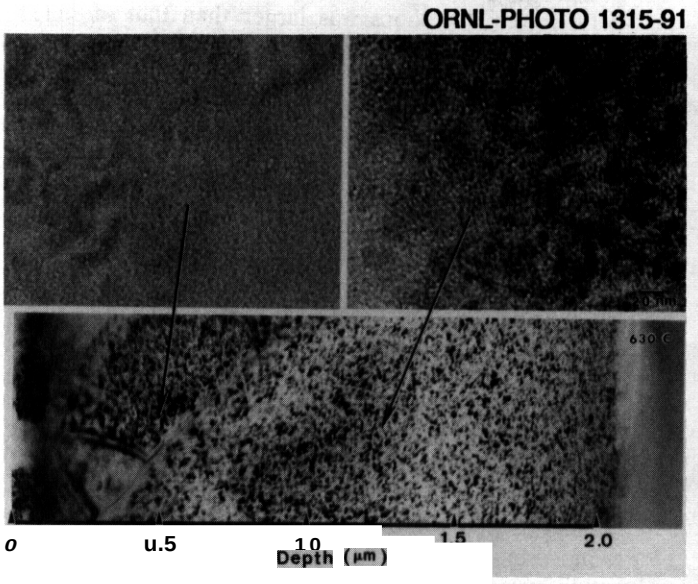


Fig. 5. Depth-dependent cavity formation (two upper pictures) and microstructure (bottom picture) in $MgAl_2O_4$ preimplanted with H, He and C and subsequently with 4 MeV Ar^+ ions to 3 dpa at 630°C.

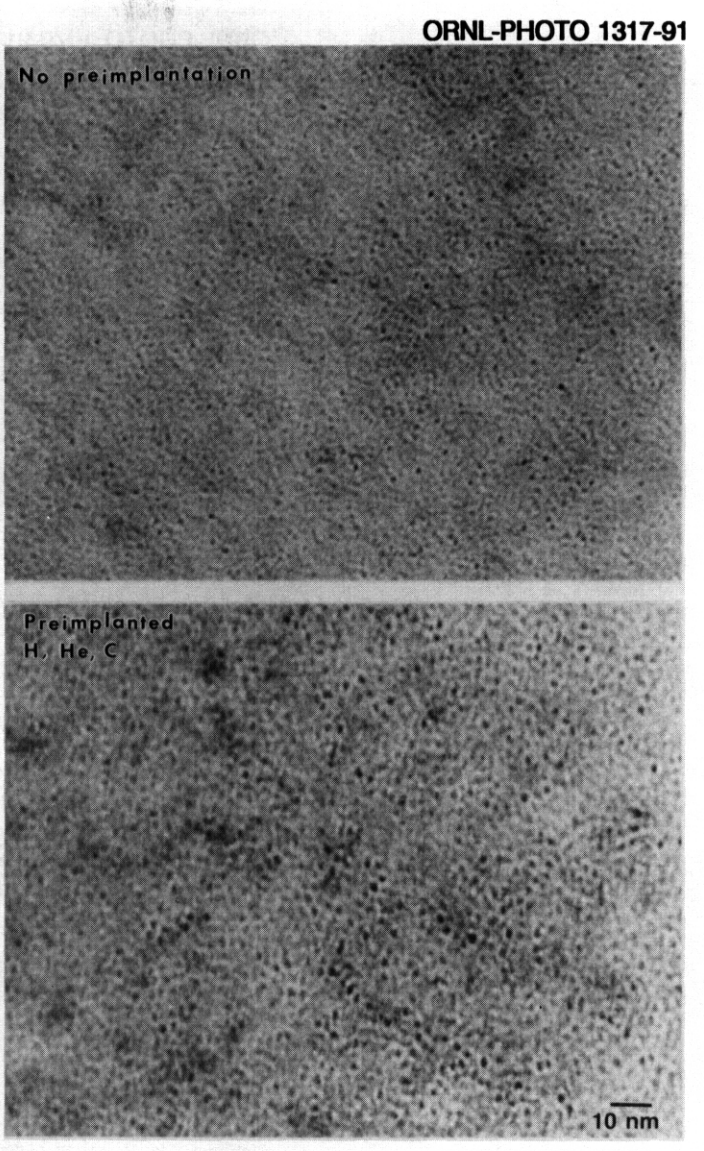


Fig. 6. TEM micrographs of cavities in Al_2O_4 at over-focus condition. The specimen was irradiated with 4 MeV Ar^+ ions alone (upper), and preimplanted with H, He and C and subsequently irradiated with 4 MeV Ar^+ ions (bottom) to 3 dpa at 810°C.

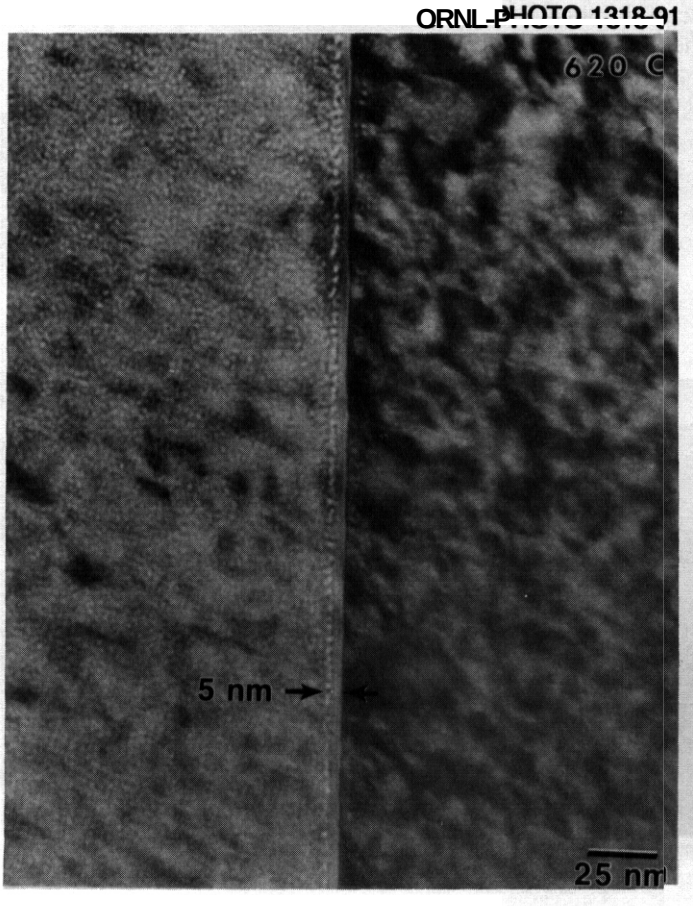


Fig. 7 Cavity formation near a grain boundary in Al_2O_3 irradiated with 4 MeV Ar^+ ions alone to 12 dpa at 620°C.

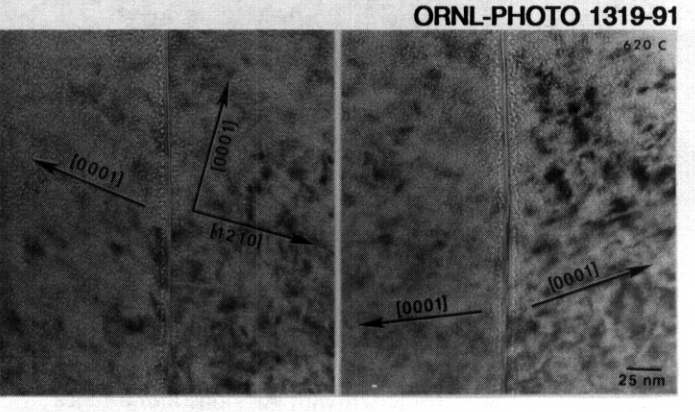


Fig. 8. Orientation dependence of grain boundary cavity formation in Al_2O_3 irradiated with 4 MeV Ar^+ ions alone to 12 dpa at 620°C.

ORNLPHOTO 1079-91

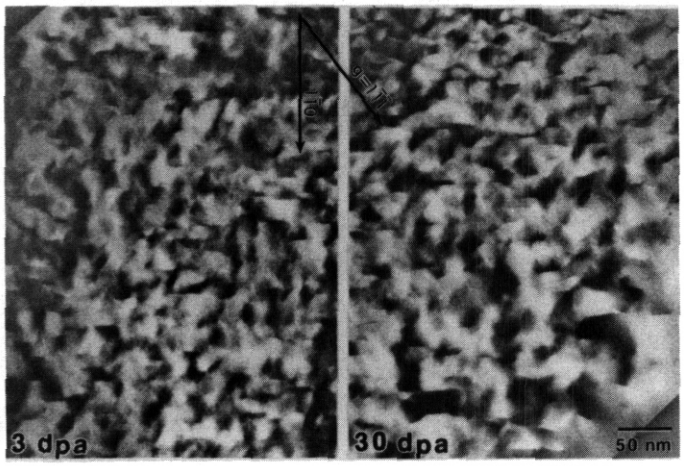


Fig. 9. Effect of dose on the microstructure of $MgAl_2O_4$ preimplanted with H, He and C and subsequently irradiated with 4 MeV Ar^+ ions at 630°C (centered dark field image). The dose of Ar irradiation is 3 dpa (left) and 30 dpa (right).

density of {110} loops was larger than that of {111} loops. The average loop diameter was about 22 nm for {110} loops and 15 nm for {111} loops at 30 dpa, and about 16 nm for {110} loops and 13 nm for {111} loops at 3 dpa. The loop densities were similar for both doses.

Figure 10 shows the effect of irradiation temperature on the microstructure in spinel. The left-hand side gives the microstructure irradiated with Ar^+ ions alone at 260°C, and the right-hand side shows a specimen preimplanted with H, He and C and subsequently irradiated with Ar^+ ions at 630°C The habit planes at 260°C were also {110} and {111} planes, and the density of {110} loops was larger than that of {111} loops. The average loop diameters were about 21 nm for {110} loops and 12 nm for {111} loops at 260°C, and 22 nm for {110} loops, and 15 nm for {111} loop at 630°C. The number density of dislocation loop was almost same as those in Fig. 9. We also examined many other specimens to confirm the results implied by Fig. 10, which revealed that the target temperature did not significantly affect the loop diameter or size. Contrary to the void formation results, Fig. 10 also implies that there is no significant effects of the preinjected transmutation products on loop size or density when spinel was irradiated with Ar^+ ions to a dose of 3 dpa or more.

Low dose irradiations resulted in a different type of microstructure, as shown in Fig. 11, where spinel was preimplanted with H, He and C and subsequently irradiated with Ar^+ ions to 0.6 dpa at 260°C. The dislocation loops were very small after this low dose, with an average diameter of about 2 nm. Because of the small loop size, their habit planes were not identified, but it seems that habit planes other than {110} and {111} planes may exist during irradiation to a small dose.

ORNL-PHOTO 1078-91

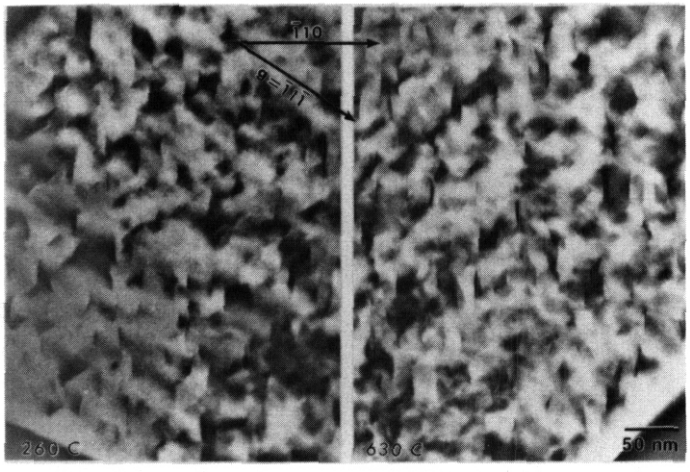


Fig. 10. Effect of irradiation temperature on the microstructure of $MgAl_2O_4$ (centered dark field image). The specimen was irradiated with Ar^+ ions alone to 12 dpa at 260°C (left), and preimplanted with H, He and C and subsequently with Ar^+ ions to 30 dpa at 630°C (right).

ORNL-PHOTO 1077-91

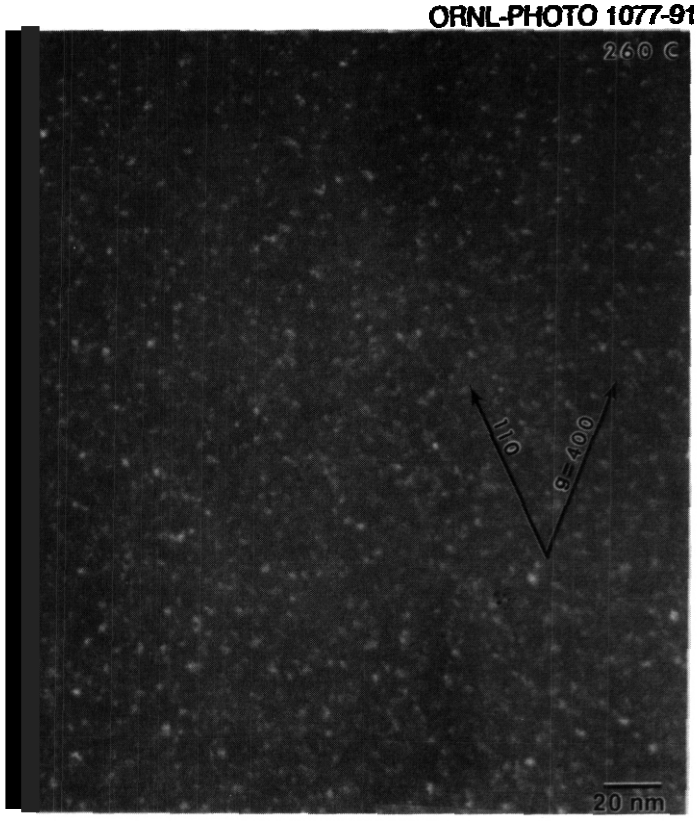


Fig. 11. Weak beam (g, 5g) microstructure of $MgAl_2O_4$ preimplanted with H, He and C and subsequently irradiated with Ar^+ ions to 0.6 dpa at 260°C.

3.22. Al_2O_3

In the case of Al_2O_3, the dislocation loop structure induced by preimplantation of H, He and C and subsequent Ar^+ irradiation was similar to that for Ar^+ irradiation alone. This suggests that the preinjected transmutation products do not have a significant effect on loop size or density, which is the same as the results for spinel.

Figure 12 shows the microstructure of alumina irradiated with Ar^+ ions alone to 12 dpa at 620°C, where the specimen was tilted to observe the dislocation loops in an edge-on configuration. It is seen that the habit planes of dislocation loops are (0001) and {1$\bar{1}$00} planes, and that the (0001) habit plane is preferred.

4. Discussion

Cavity formation did not occur in any of the observed specimens of spinel irradiated with Ar^+ ions alone for the experimental conditions that we employed, whereas cavities were observed in H, He, C preimplanted spinel following high dose or high temperature Ar^+ irradiation. This indicates that the transmutation products may have a significant effect on cavity swelling in ceramics. The enhancement of cavity formation and void swelling due to helium-doping or coimplantation of helium has already been studied in alumina and spinel.[6,7,9,12] In the case of spinel, the transmutation products of H, He, C seem to play a much more vital role on the formation of cavities. In this connection it should be noted that the specimens irradiated with H^+, He^+ and C^+ ions alone did not show any cavities. Since the doses of implantation of H, He and C and also their masses were smaller than those of Ar^+ ions, the displacement damage due to transmutation products was negligible compared with that of argon irradiation. In this experiment, the implantation of transmutation products 'has only an kffect of introducing light impurity atoms into the specimens. It is, therefore, indicated from the lack of cavities in the preimplanted-alone specimens that displacement damage is also necessary and a dominant factor for cavity formation. It should be mentioned here that Knight et al. reported that cavities are formed in spinel at 800°C due to 4 MeV Ar^+ ion irradiation alone to 1 dpa.[10] As previously mentioned we have not observed cavities in spinel irradiated with 4 MeV Ar^+ ions alone at temperatures up to 630°C. Compared to the size of cavities observed for our preimplanted spinel (1.5-14 nm), the size of cavities observed by Knight et al. is much larger (about 25 nm). The above results imply that a critical temperature for cavity growth in spinel may exist at a temperature between 630 to 800°C.

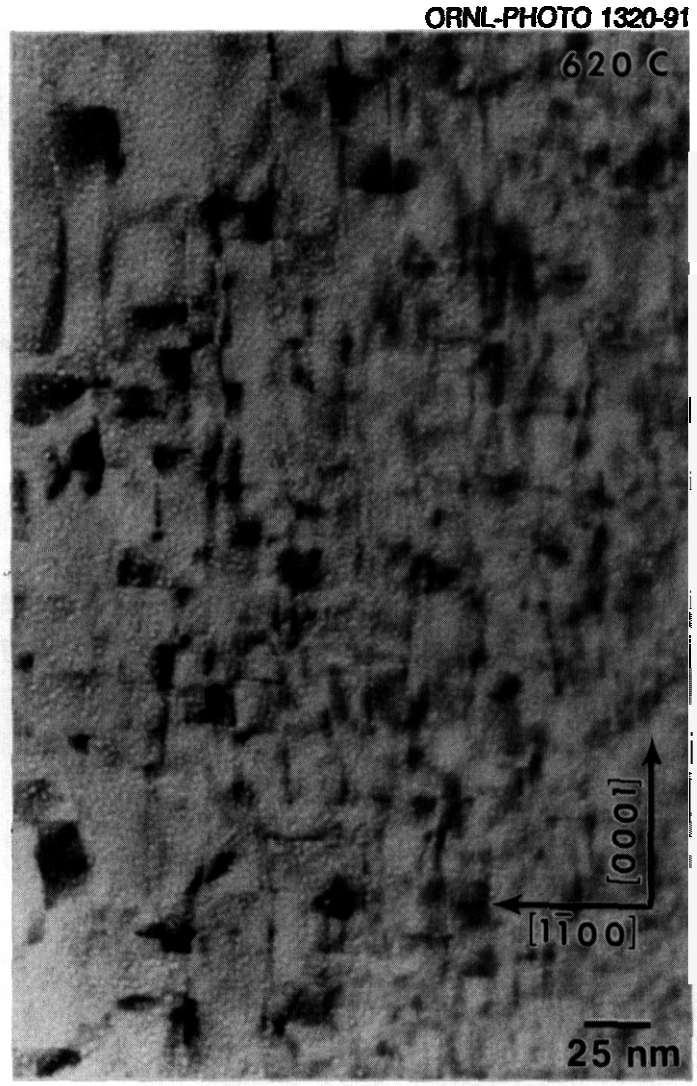


Fig. 12. Centered dark field microstructure of Al_2O_3 irradiated with Ar^+ ions alone to 0.6 dpa at 620°C.

The result of depthdependent cavity formation, as shown in Fig. 5, is also evidence that a certain amount of displacement damage as well as transmutation products are necessary for the formation of cavities in spinel. In our experimental condition-the amount of displacement damage decreases around a depth of 0.5 μm, as shown in Fig. 1 (Fig. 1 actually gives the damage profile of alumina, but almost the same profile is obtained for spinel). The amounts of implanted H, He, C atoms also decrease around a depth of 0.5 μm. The depth-dependent cavity formation can be ascribed to the decrease of both displacement damage and transmutation products.

The orientation dependence of grain boundary cavity formation in alumina in Fig. 8 may originate from the anisotropy of the hexagonal crystal structure. It has already been reported that cavities are aligned along [0001] axis in irradiated alumina.[3,6,7,9] The present results reveal another feature that cavity swelling is enhanced adjacent to grain boundaries in grains with grain boundaries nearly parallel to the basal plane. The

anisotropic diffusion of vacancies and interstitials should be taken into account to explain these phenomena, and further study is needed.

As for microstructure, the dislocation loop formation in both spinel and alumina is not influenced by preinjected transmutation products, which is very different from void formation. Target temperature also has a minor effect on dislocation loops for the temperature range studied here. There is a dose dependence at a small dose (less than 3 dpa) although it is saturated by 3 dpa, judging from the similar loop microstructures between 3 and 30 dpa (Fig. 9). It appears that damage level has an effect on loop size, density or habit planes in spinel and alumina only during low dose irradiation.

We observed defect-free and/or nearly defect-free grains in spinel irradiated with Ar^+ ions alone to 12 dpa at a nominal temperature of 420°C and also preimplanted with H, He and C and subsequently irradiated with Ar^+ ions to 12 dpa at 630°C. Figure 13 shows the results at 420°C. We can see that the denuded wne at grain boundaries is about 100 nm, and that there is a defect-free grain whose size is comparable to the size of denuded zone. On the other hand, the typical denuded zone at grain boundaries was about 10 to 15 nm for spinel irradiated at temperatures between 260 and 630°C, as shown in Fig. 14. These two observations of extended defect-free zones at grain boundaries are rather unusual, and it is still unclear under what conditions we can observe such a defect-free grain. Moreover, in those two specimens, there is a possibility that a "hot spot" had occurred at some time during the argon ion irradiation, which would give a localized increase in dose rate and probably temperature. It can be said, nevertheless, from the result of Fig. 13 that if the grain size is small and the temperature is high, defect-free or nearly defect-free grains can be expected in spinel.



Fig. 13. Defect-free regions adjacent to grain boundaries in $MgAl_2O_4$ irradiated with Ar^+ ions alone to 12 dpa at a nominal temperature of 420°C.

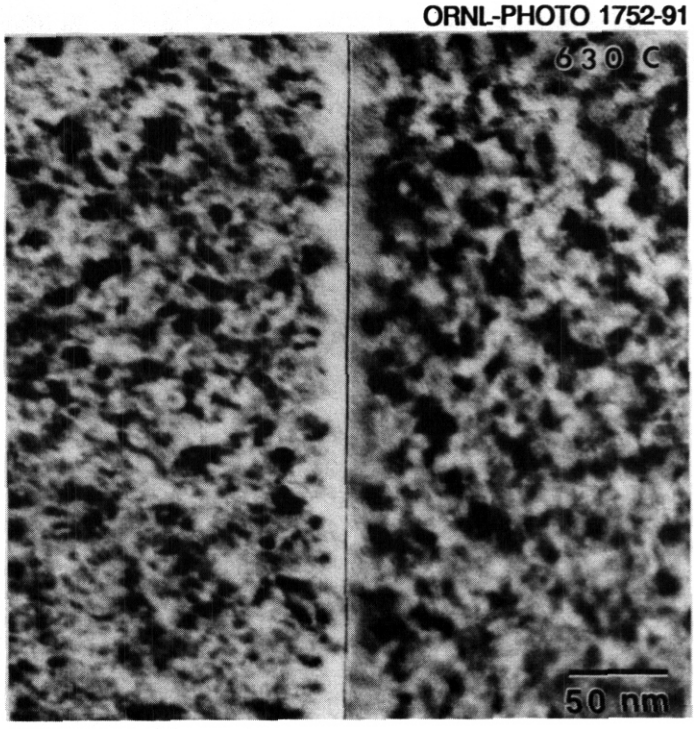


Fig. 14. A typical defect-free zone adjacent to a grain boundary in $MgAl_2O_4$ preimplanted with H, He, C and subsequently irradiated with Ar^+ ions to 3 dpa at 630°C.

5. Summary and Conclusions

The effect of the transmutation products of H, He and C on microstructural evolution in Al_2O_3 and $MgAl_2O_4$ specimens during irradiation can be summarized as follows:

1. No radiation effects were observable in specimens implanted with H, He and C alone.
2. The preinjected transmutation products did not have a significant effect on loop size or density for Ar^+ irradiated specimens.

3. In Al_2O_3, cavities were formed in all of the observed Ar^+ irradiated specimens for both the preimplanted H, He and C case and the Ar^+ alone case.

4. In $MgAl_2O_4$, cavities were not observed unless the specimens were preimplanted with H, He and C and irradiated with Ar^+ ions at relatively high temperatures or doses.

5. Larger cavities occur preferentially near grain boundaries after high dose irradiation at elevated temperatures for both $MgAl_2O_4$ and Al_2O_3. For Al_2O_3 its preference depends on grain orientation, which should originate from the anisotropy of the hexagonal crystal structure.

6. $MgAl_2O_4$ forms loops preferentially on {111} and {110} planes at a dose of more than 3 dpa, and also other habit planes may exist at lower doses.

7. Al_2O_3 forms loops on (0001) and $\{1\bar{1}00\}$ planes, and the (0001) habit plane is preferred.

8. The denuded zone at grain boundaries in $MgAl_2O_4$ is about 10 to 15 nm, but in some cases becomes 100 nm which may be due to a higher irradiation temperature than the nominal value.

Fission reactor irradiation of spinel does not accurately simulate its swelling response during fusion neutron irradiation due to the low concentration of H, He and C produced. For Al_2O_3, the microstructure changes following fission and fusion irradiation might be similar since H, He, and C apparently have a small effect on the irradiated microstructure.

Acknowledgments

The authors thank A. M. Williams for preparing the TEM specimens. One of us(RY) would like to thank Dr. A. F. Rowcliffe and Dr. E. E. Bloom for their hospitality to him during his stay in ORNL, and also Dr. A. Hishinuma and Dr. T. Kondo for their support.

References

1. L. H. Rovner and G. R. Hopkins, Nucl Technol., **29 (1976) 274.**
2. G. P. Pells, J. Nucl. Mater. **155-157 (1988) 67.**
3. F. W. Clinard, Jr., G. F. Hurley and L. W. Hobbs, J. Nucl. Mater. **108-109 (1982) 655.**
4. F. W. Clinard, Jr., G. F. Hurley and L. W. Hobbs, D. L. Rohr and R. A. Youngman, J. Nucl. Mater. **122-123 (1984) 1386.**
5. C. A. Parker, L. W. Hobbs, K. C. Russell and F. W. Clinard Jr., J. Nucl. Mater. **133-134 (1985) 741.**
6. M. D. Rechtin, Rad. Effects **42 (1979) 129**
7. W. E. Lee, M. L. Jenkins and G. P. Pells, Phil. Mag. **A51 (1985) 639.**
8. Y. Katano, H. Ohno and H. **Katsuta,** J. Nucl. Mater. **155-157 (1988) 366.**
9. S. J. Zinkle and S. Kojima, J. Nucl. Mater. **176 (1991)** (in press).
10. P. A. Knight, M. L. Jenkins and G. P. Pells, Mat. Res. Soc. Symp. Proc., **Vol 152,** Optical Materials: Processing and Science **(1989)** p. 135.
11. S. J. Zinkle, NATO-Adv. Study Inst. on Structural-Property Relationships in Surface Modified Ceramics, edited by C. J. McHargue et al. (Kluwer Academic Publishers, **1989)** p.219.
12. S. J. Zinkle, in: Mat. Res. Soc. Symp. Proc, **Vol.128 Eds.** L. E. Rehn et al. (MRS, Pittsburgh, **1989) p363.**
13. S. J. Zinkle, J. *Am.* Ceram. Soc. **72 (1989) 1343.**
14. S. J. Zinkle, 15th Intern. Symp. on Effects of Radiation on Materials (1990) (in press).
15. C. J. McHargue, G. C. Farlow, C. W. White, B. R. Appleton, J. M. Williams, P. S. Sklad, P. Angelini and C. S. Yust, J. Materials for Energy Systems **8 (1986) 255.**
16. P. J. Burnett and T. F. Page, Rad. Effects **97 (1986) 283.**
17. I. Manning and G. P. Meuller, Computer Phys. Comm, **7 (1974)** 85.
18. J. P. Biersack and L. G. Haggmark, Nucl. Instrum. and Methods, **174 (1980) 257.**
19. G. P. Pells, S. N. Buckley, P. Agnew, A. J. E. Foreman, M. J. Murphy and S. A. B. Staunton-Lambert, AERE-R13222 **(1988).**
20. S. J. Zinkle, C. P. Haltom, L. C. Jenkins and C. K. H. DuBose, J. Electron Microscopy Tech. **(1991)** (in press).

MICROSTRUCTURAL CHANGES IN OXIDE CERAMICS FOLLOWING LIGHT ION IRRADIATION - S. J. Zinkle (Oak Ridge National Laboratory)

OBJECTIVE

The objective of this study is to investigate the microstructure of oxide ceramics following irradiation with various light ions, in order to determine if the observed radiation effects can be correlated with heavy ion and neutron irradiation results.

SUMMARY

Irradiation of ceramics such as Al_2O_3 and $MgAl_2O_4$ with energetic light ions causes a suppression in the nudeation of dislocation loops. The results of recent electron microscope studies on ion irradiated oxide ceramics are summarized. It is proposed that the anomalous suppression of dislocation loop formation may be associated with the high proportion of energy lost to electronic ionization events compared to displacement damage events during light ion irradiation.

PROGRESS AND STATUS

Introduction

It has become increasingly apparent in recent years that radiation effects in ceramics will have a significant impact on the design of D-T fusion plasma physics machines. Large flux dependent changes in electrical properties will occur during irradiation,' which may cause modification in the design and operation of even near-term, low fluence machines such as the Burning Plasma Experiment (BPX). Recognition of the need for in situ measurements of various physical properties of ceramics during irradiation has stimulated a modest amount of worldwide activity in this radiation effects area.'" Many of these studies have utilized accelerator-based sources due to the obvious difficuities associated with in situ electrical property measurements in fission reactors.

The present study was initiated in order to gain a better understanding of the fundamental processes that occur during particle irradiation of ceramics. There are two distinct differences between light ion irradiation sources and heavy ion or neutron-based sources. First, the mean energy imparted to primary knock-on atoms (PKAs) is significantly smaller for light ion irradiation compared to heavy ion or neutron irradiation.[12] For example, the mean PKA energy for 1 MeV neutrons or Al+ ions incident on Al_2O_3 is ~10 keV, whereas the mean PKA energy for 1 MeV protons is ~300 eV (assuming a displacement energy of 40 eV). In essence, light ions produce isolated Frenkel defects whereas heavy ions and energetic neutrons produce displacement cascades. A second consideration is that proportionately more energy is lost to electronic excitation events during light ion irradiation compared to heavy ion or neutron irradiation. Table 1 compares the ratio of ionizing to displacive energy losses for several different irradiation sources.

There is a surprising lack of microstructural studies on ceramics irradiated with protons or alpha particles--only three open-literature publications[13-15] were found during a computer literature search. Small dislocation loops were Observed in the He-implanted region of Al_2O_3 following He^+ ion irradiation to 0.3 dpa at 230°C,[13] and 750–950°C.[14] Loops were also observed at depths midway between the surface and the He-implanted region in the Al_2O_3 specimen irradiated at 230°C.[13] Lee et al.[15] reported the formation of a low density of large interstitial loops in Al_2O_3 following He^+ irradiation to a damage level of ~0.04 dpa. Unpublished research by Knight[16] indicated that no detectable loop formation occurred in $MgAl_2O_4$ following irradiation at 600°C with 3 MeV protons to 0.1 dpa. In this study.'" the sample thickness was less than the proton range so that the protons were transmitted through the specimen.

ExDerimental procedure

Polycrystalline blocks of Al_2O_3 (GE Lucalox), MgO (Ube) and $MgAl_2O_4$ (Ceradyne) were sliced into foils of 0.5 mm thickness, and 3-mm-diam TEM disks were cut from the foils. The disks were mechanically polished with 0.5 μm diamond paste, and then bombarded in a 3 x 3 array at 650°C in the triple ion beam accelerator facility'" at Oak Ridge National Laboratory. The irradiation temperature was determined from a thermocouple spot-welded to the face of a stainless steel specimen that occupied one of the positions in the 9-specimen array. The thermocouple reading at this position during irradiation was about 5°C higher than the recorded temperature from a thermocouple embedded in the base of the sample holder.

Tabla 1. Approximate ratios of ionizing to displacive energy for Al_2O_3 exposed to different irradiation sources

Irradiation Source	Gamma Dose Rate/ Neutron Dose Rate (Gy/s)	$\left(\frac{dE}{dX}\right)_{ion}/\left(\frac{dE}{dX}\right)_{disp}$
1-MeV H^+ (4 μm depth)		2800
2-MeV Al^+ (0.6 μm dapth)		10
TRIGA thermal reactor		
Unshielded	19	100
1-in. lead shield	1.3	10-20
Fast reactor	~2	~20
Fusion reactor (BPX)		
First wall	0.6	15
Behind magnets	2	14

Four different specimens arrays were exposed to either 1-Mev H^+ or He^+ ion beams. A masking slit was used to cover the top row of specimens at the beginning of the irradiation of each specimen array. The masking slit was removed when ~90% of the total fluence was achieved. This resulted in a factor of 10 lower fluence for the top row of specimens compared to the bottom two rows. Specimen arrays were irradiated at two different ion fluxes for both the proton and helium irradiations. Table 2 summarizes the irradiation conditions. The damage levels shown in Table 2 were calculated for Al_2O_3 from the EDEP-1 Code[11] using a threshold displacement energy of 40 eV. It should be noted that the calculated damage level (and damage rate) for 1 MeV protons and alpha particles varies by a factor of 35 and 22, respectively between the damage peak vs midway between the surface and damage peak. The calculated mean ion range for 1 MeV H^+ and He^+ in Al_2O_3 is 8.57 μm and 2.14 μm, respectively.

Table 2. Ion irradiation conditions for the Al_2O_3, MgO, and $MgAl_2O_4$ specimens irradiated at 650°C

Ion Species	Flux (10^{16}/m²-s)	Fluence (10^{20}/m²)	Midrange Dose (dpa)	Pnak Dose (dpa)	Midrange Ionizing Radiation Flux (10^6 Gy/s)	Pnak Implanted Ion Concentration (at. %)
1-MeV H^+	60	170	0.09	3.2	3	60
	60	20	0.01	0.4	3	8
	8	15	0.008	0.3	0.4	6
	8	3	0.0016	0.06	0.4	1
1-MeV He^+	40	100	1	21	10	50
	40	10	0.1	2.1	10	5
	4	10	0.1	2.1	1	5
	4	1	0.01	0.2	1	0.5

The ceramic specimens displayed luminescence during the ion irradiations (the target assembly could be viewed through a quartz window). The spinel specimens exhibited a green color, MgO was pink or orange (depending on the flux), and Al_2O_3 was white. The luminescence intensity decreased almost instantaneously when the ion beam was shuttered.

Following irradiation, the specimens were examined with an optical microscope and selected specimens were prepared as cross-section TEM specimens using techniques that are described elsewhere.[11] The TEM specimens were examined with a Philips CM-12 electron microscope, operating at 120 keV.

RESULTS

Optical examination of the as-irradiated disks revealed blister formation and exfoliation in specimens subjected to H^+ or He+ ion fluences $\geq 1 \times 10^{22}$/m². A small fraction of the grains in spinel were exfoliated following He^+ ion irradiation to 1×10^{21}/m². Blister formation was not observed by optical microscopy in the other ceramic specimens irradiated to H^+ or He* ion fluences $\leq 2 \times 10^{21}$/m². Figure 1 shows low-magnification examples of the blistering and exfoliation in $MgAl_2O_4$ and Al_2O_3 specimens subjected to high-fluence irradiation. Exfoliation was generally limited to individual grains in the He-implanted specimens, whereas the blister formation and exfoliation extended over many grains in the H-implanted specimens (Fig. 1). This difference may be attributable to the deeper range of the H^+ ions compared to the He^+ ions. Several previous studies have examined blistering and exfoliation in ceramics implanted with gaseous ions (e.g., 19-22). The present results agree with these studies that the critical fluence for the onset of blistering occurs near 3×10^{21} ions/m².

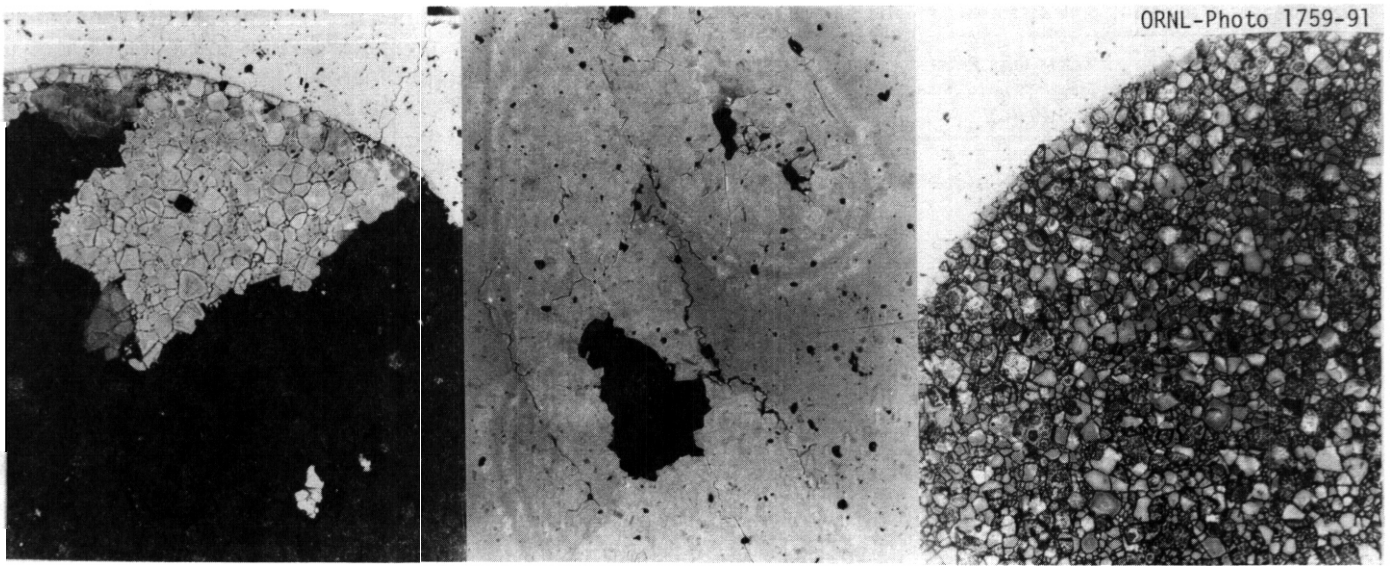


Fig. 1. Blister formation and exfoliation in $MgAl_2O_4$ and Al_2O_3 following high-flux 1 MeV H^+ or He^+ ion irradiation at 650°C. Left to right: spinel, 1.7 x 10^{22} H^+/m^2, Al_2O_3, 1.7 x 10^{22} H^+/m^2; spinel, 1.0 x 10^{22} He^+/m^2.

Preparation of the cross-section TEM specimens required special care due to the blistered and exfoliated surface. Fortunately, intact grains were located and observed in all of the specimens selected for TEM examination.

Spinel TEM observations

Figure 2 shows the cross-section microstructure for spinel following high-flux He^+ irradiation to a peak damage level of 2.1 dpa (cf Table 2). A moderate density of medium-sized dislocation loops occurred in the region where the implanted ion and damage peaks nearly coincide. The damage range was in fair agreement with that predicted by the Al_2O_3 EDEP-1 calculation (after correcting for density differences between Al_2O_3 and $MgAl_2O_4$). There was no observable defect formation at irradiation depths up to 2.0 μm. The radiation damage level in these regions was ~0.1 dpa (Table 2).

The microstructure of spinel following high-flux He^+ ion irradiation to a peak damage level of 21 dpa is shown in Fig. 3. Many of the near-surface regions of this specimen had spalled off due to the implantation of ~50 at. % He. Extensive cracking and cavitation were observed at depths corresponding to the implanted He region (~2.3 pm). Dislocation loops ware observed in the peak damage region. However, dislocation loops did not occur at irradiation depths up to 2.0 μm despite radiation damage levels of ~1 dpa.

The depth-dependent microstructure of the proton-inadiated spinel specimens was qualitatively similar to the He-irradiated specimens. with the exception that the damage peak occurred at depths of 10.5 pm. The observed damage peak occurred at a depth ~10% larger than the predicted peak calculated by EDEP-1. Figure 4 shows the cross-section microstructure of spinel following low-flux proton irradiation to a peak damage level of 0.3 dpa (c.f. Table 2). Once again, dislocation loop formation was only observed in regions close to the implanted ion and displacement damage peaks. Similar results were obtained from spinel specimens irradiated following high flux proton irradiation to a peak damage level of 3 dpa, except that the amount of cavitation in the H^+ implanted region was substantial.

ALO. TEM observations

Figure 5 shows the cross-section microstructure of Al_2O_3 following high-flux He^+ ion irradiation to a peak damage level of 21 dpa. Substantial subsurface cavitation and cracking occurred at a depth of ~2.3 μm as a result of the injection of 50 at. % He into the specimen. As shown in Fig. 6, dislocation loop formation occurred at all depths within the irradiated region. The loops in the midrange region ware larger and of lower density compared to the loops formed in the peak damage region. Similar results were obtained on Al_2O_3 specimens following either high-flux or low flux He+ ion irradiation to a peak damage level of 2.1 dpa (c.f. Table 2). However, in these lower dose specimens (0.1 dpa @ midrange), the dislocation loop sue was about half that of the high-dose specimens (1 dpa @ midrange). The observed extent of displacement damage was in good agreement with the value calculated by EDEP-1.

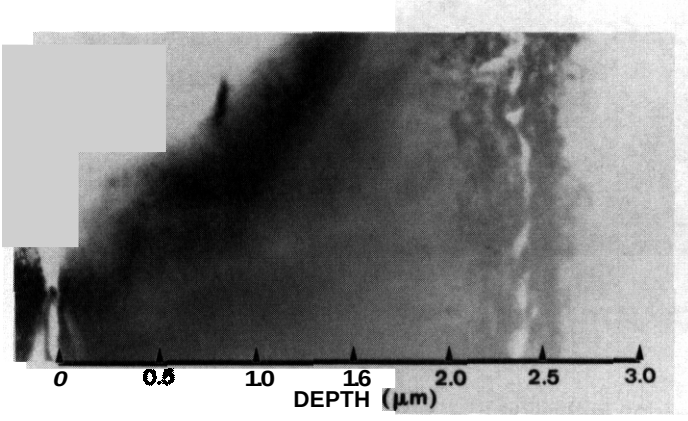


Fig. 2. Microstructure of spinel following low-flux 1 MeV He+ ion irradiation to 1 x 10^{21} He^+/m^2.

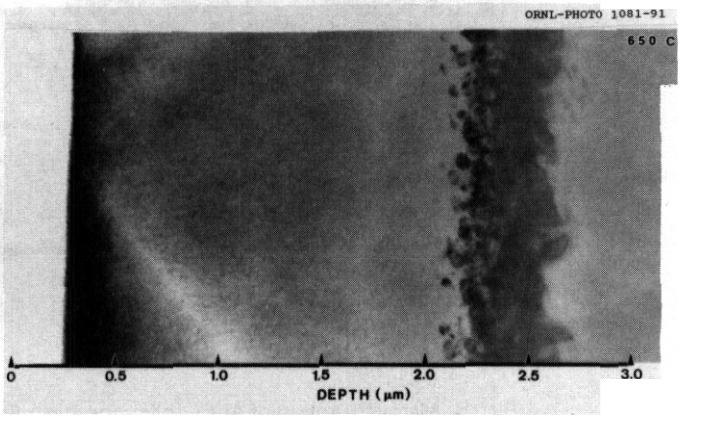


Fig. 3. Microstructure of spinel following high-flux irradiation with 1 **MeV** He+ ions to 1 x 10^{22} He^+/m^2 at 650°C.

ORNL PHOTO 1758-91

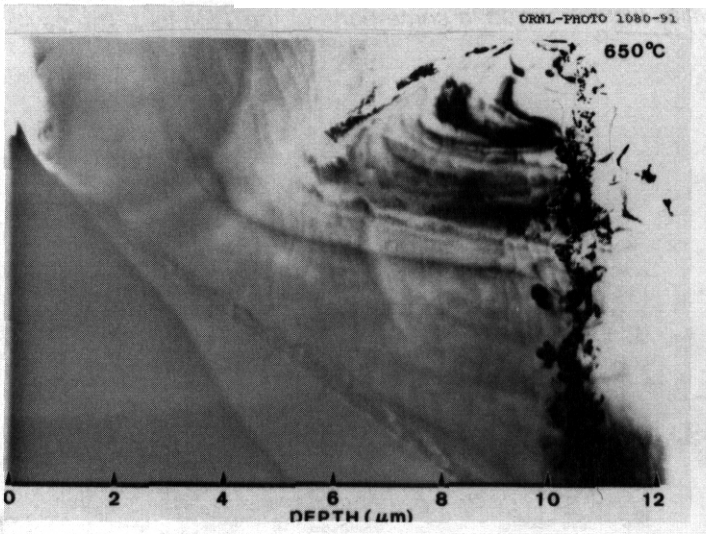


Fig. **4.** Microstructure of spinel following low-flux proton irradiation to **1.5** x 10^{21} H^+/m^2.

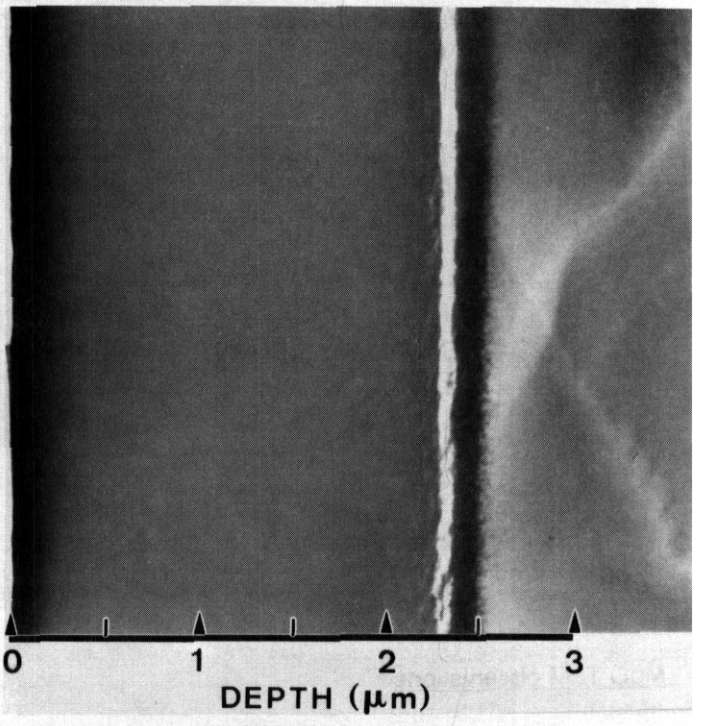


Fig. 5. Microstructure of Al_2O_3 following high-flux Irradiation at 650°C with **He'** ions to 1 x 10^{22} He^+/m^2

Dislocation loop formation was confined to regions close to the implanted ion and displacement damage peaks for Al_2O_3 irradiated with high-flux H^+ ions to a peak damage level of 3 dpa. Figure 7 shows the cross-section microstructure for this irradiation condition. The observed damage peak occurred at a depth ~10% larger than the value calculated by **EDEP-1.** The absence of resolvable dislocation loop formation in the midrange regions of the proton irradiation is in stark contrast to the copious amounts of dislocation loops observed in Al_2O_3 specimens irradiated with **He'** ions to the same midrange dose (0.1 dpa). A very low density of large dislocation loops was observed in the midrange regions of Al_2O_3 following low-flux proton irradiation to a midrange damage level of 0.008 dpa. This observation suggests that some physical process associated with proton irradiation is inhibiting the nucleation of dislocation loops in Al_2O_3, but does not suppress their subsequent growth.

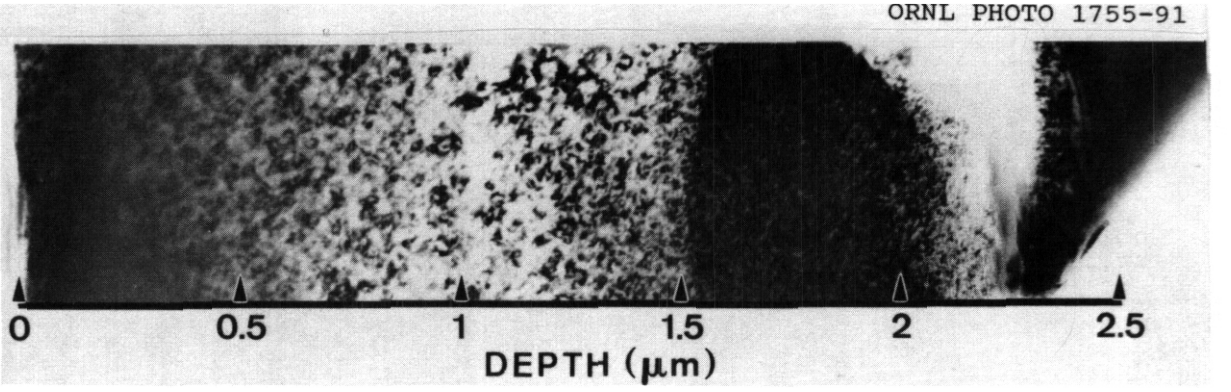


Fig. 6. Microstructure of Al_2O_3 following high-flux He^+ ion irradiation to 1×10^{22} He^+/m^2 at 650°C.

Figure 8 shows an example of the cavity formation that occurred near the implanted ion region of Al_2O_3 irradiated with high-flux protons to e peak damage level of 3 dpa. A high density of cavities are present in this region. Subsurface cracking associated with the interconnection of these cavities was observed in some parts of the TEM foil. The cavities tended to nucleate at dislocation loops.

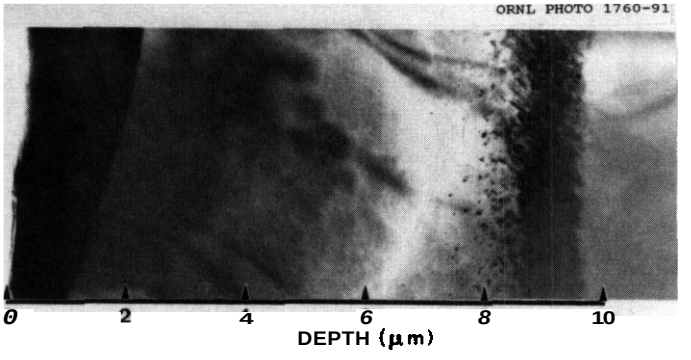


Fig. 7. Microstructure of Al_2O_3 following high-flux proton irradiation at 650°C to 1.7×10^{22} H^+/m^2.

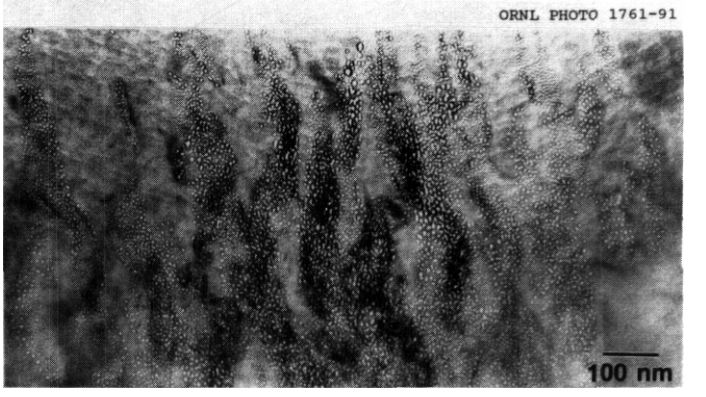


Fig. 8. Cavity formation in the implanted H^+ ion region of Al_2O_3 after 1.7×10^{22} H^+/m^2.

MgO TEM observations

High flux proton irradiation of MgO to a peak damage level of 3 dpa (Table 2) produced dislocation loops near the implanted ion and damage peaks, but no effects of displacement damage were visible at other irradiated depths. High flux irradiation of MgO with 1-MeV He^+ ions to a peak damage level of 21 dpa produced small dislocation loops at depths near the implanted ion and peak damage regions. A moderate density of loops was observed in midrange regions. Therefore, the behavior of MgO to light ion irradiation may be classified as intermediate between that of Al_2O_3 and spinel.

DISCUSSION

As mentioned in the introduction, the displacement cascade density (mean PKA energy) and fraction of energy lost to ionization events is significantly different for light ion irradiations compared to heavy ion or neutron irradiations. The lack of observable dislocation loop formation in the midrange regions of Al_2O_3 and spinel specimens following light ion irradiation suggests that these differences may be sufficient to alter the microstructural development of ceramics during irradiation. The results obtained on H^+ and He^+ ion irradiated Al_2O_3 specimens (Figs. 6 and 7) also suggests that there is a significant difference in the radiation damage processes associated with 1-MeV protons vs 1-MeV He^+ ions. A simple calculation of

the mean PKA energy" for these two irradiation conditions (assuming a threshold displacement energy of 40 eV) yields $\bar{E}_{PKA}$ ~325 eV and 370 eV for 1-MeV H^+ and He^+ ions, respectively. This small difference suggests that it may be worthwhile to concentrate on differences in the amount of ionization energy deposited during irradiation.

Figures 9 and 10 show the depth-dependent energy losses of various energetic ions in Al_2O_3 as a result of elastic collisions (displacements) and electronic interactions (ionization), respectively. The specific energy loss for both processes increases with increasing mass of the bombarding particle.[23] The partitioning of energy loss between the two processes can be seen more clearly by examining the ratio of ionizing to displacive energy losses, as shown in Fig. 11. It is clear from this figure that a substantially higher fraction of energy from the incident ion is transferred into ionization events during light ion irradiation compared to heavier ion irradiation. From Table 1, the ratio of ionizing to displacive energy losses that is relevant for fusion reactor irradiations, $(dE/dX)_{ion}/(dE/dX)_{disp}$ is ≈ 15. Medium-weight ions such as 2-MeV Al^+ and 4-MeV Ar^+ achieve this ratio in Al_2O_3 near the midpoint of their ion range. However, light ions such as 1 MeV H^+ and He^+ do not approach this value until near the ion end of range.

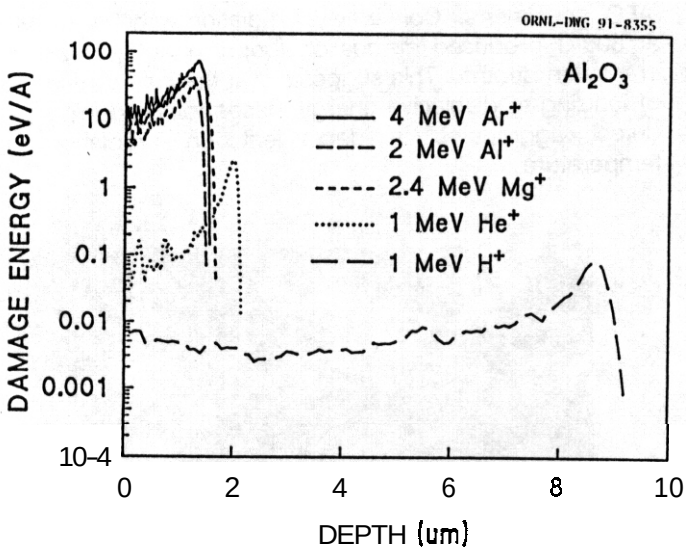


Fig. 9. Energy losses to atomic recoil processes during ion irradiation as calculated by the TRIM-90 (ref. 23) code.

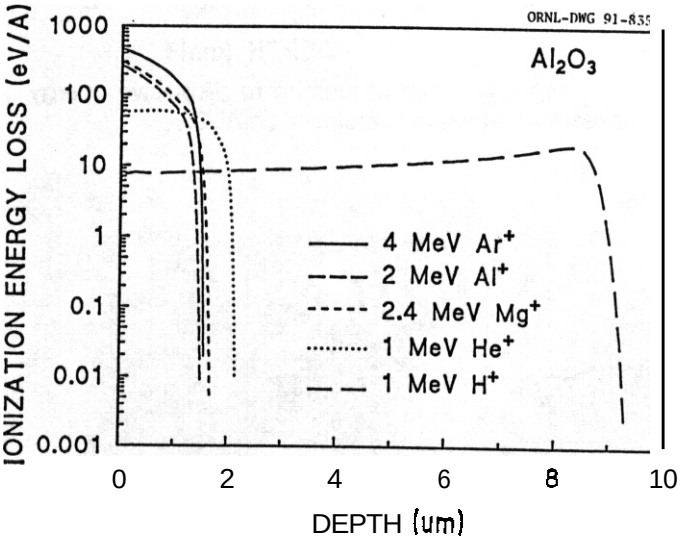
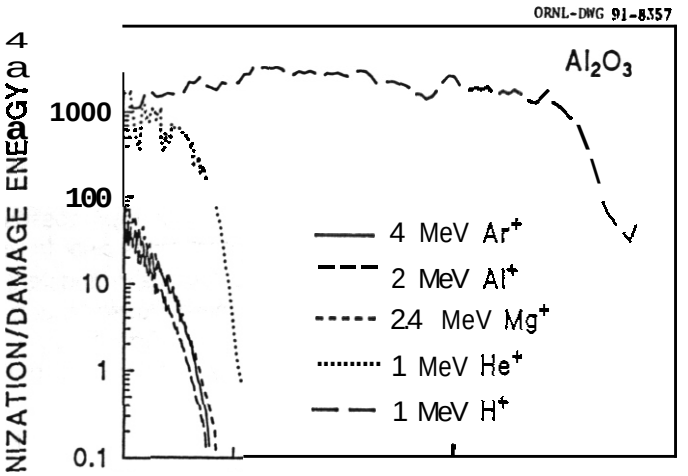


Fig. 10. Energy losses to electron ionization during ion irradiation as calculated by the TRIM-90 (ref. 23) code.

Further insight into the radiation effects associated with light vs heavy ion irradiation can be obtained by comparing the microstructural response of spinel following irradiation with Mg^+ and Al^+ ions.[24,25] As shown in Fig. 12, irradiation with 2.4 MeV Mg^+ ions produces a defect-free region within ~0.8 μm of the surface?' Dislocation loops and tangles are created at deeper layers within the irradiated region (0.8 to 2.0 μm). Irradiation of spinel at the same damage rate with 2.0 MeV Al^+ ions produced a defect-free region within ~0.4 μm of the surface (Fig. 13).[25] The extent of these surface-denuded zones was found to be independent of damage level for ion fluences in the range of 5×10^{20} to 5.5×10^{21} ions/m². Figure 14 shows the depth-dependent ratio of ionizing to displacive energy losses (calculated for Al_2O_3) for 2.4 MeV Mg^+ and 2 MeV Al^+ ions. This ratio has a value of about 10 at irradiation depths of 0.8 μm and 0.5 μm, respectively, for the 2.4 MeV Mg^+ and 2 MeV Al^+ ions, which is in reasonably good agreement with the observed extents of the surface-denuded zones in spinel following irradiation with these two ions. This empirical relationship suggests that the ratio of ionizing to displacive energy losses must be less than ~10 to produce a significant concentration of resolvable defect aggregates in spinel during ion irradiation at 650°C. On the other hand, the light ion results for Al_2O_3 suggest that defect aggregates in this material will be produced for ionizing to displacive energy ratios up to ~1000. These Observations may partially explain the relative resistance of spinel to defect aggregate formation during neutron irradiation as compared to Al_2O_3: the ratio of ionizing to displacive energy during neutron irradiation of ceramics is ~10 to 20 (Table 1), which is close to the empirical critical value for defect aggregate formation in spinel but well below the corresponding value for Al_2O_3.

Several researchers have pointed out the potential influence of electronic excitation effects on radiation damage processes in metals and ceramics.[26-35] In some ceramics, ionization can directly lead to the formation of additional Frenkel defects." Other studies have noted that electronic excitation events can lead to an annealing of pre-existing cascade damage.[28,29] Several analyses have suggested that energy transfer between ionized electrons and ions within the



surviving Frenkel defects assodated with the cascade.[30-32] It is also well-known" that ionization causes enhanced ionic diffusion in insulators during irradiation. it is clear that further research is needed to develop a better fundamental understanding of the importance of ionizing vs displacive radiation on damage accumulation in various ceramics.

We have observed that the development *of* observable defect aggregates in ceramics during light ion irradiation is strongly dependent on the irradiation temperature. Irradiations with $^3He^+$ ions performed near room temperature did not produce observable damage even in the implanted ion regions of spinel or

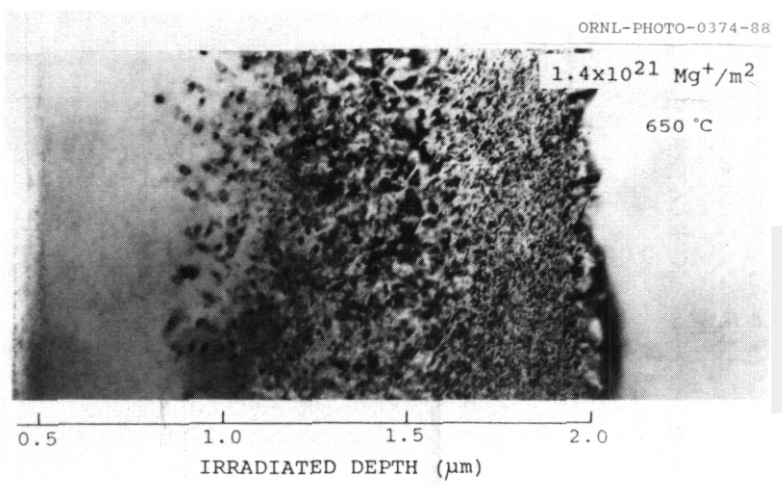


Fig. 12 Microstructure *of* spinel following 24 MeV Mg^+ ion irradiation (from ref. 24).

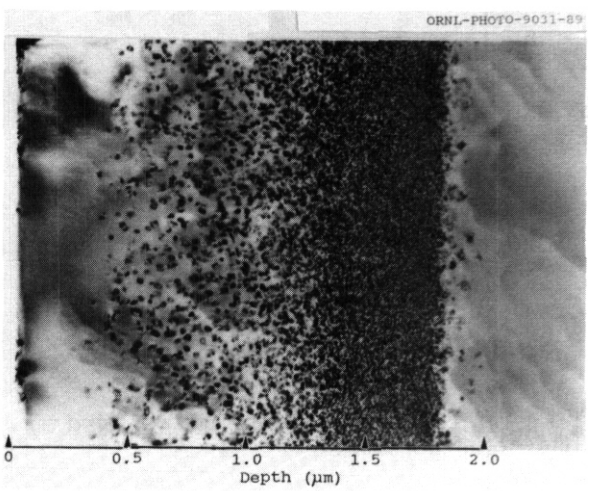


Fig. 13. Microstructure of spinel following 2-MeV Al^+ ion irradiation at 650°C to a fluence of 5×10^{20} Al^+/m^2 (from ref. 25).

it should be emphasized that another feature associated with most ion irradiation studies on ceramics involves the implantation*of* the bombarding ions. This can produce space charge effects and stimulate an electrical current associated with radiation-induced-conductivity.[36,37] Experiments are presently being performed to determine if these effects may be contributing to the anomalous suppression of dislocation loop formation in ceramics irradiated with light ions.

FUTURE WORK

Ceramic specimens will be irradiated with 3 MeV C^+ ions and 4-MeV Zr^+ ions during the next reporting period. Some of the specimens will be C-coated prior to irradiation. Plans are also underway for transmission irradiations of ceramic specimens with 10-MeV protons and 28 MeV He' ions.

ACKNOWLEDGMENTS

The TEM specimens were expertly prepared by A. M. Williams: S. W. Cook performed the bulk *of* the light ion irradiations.

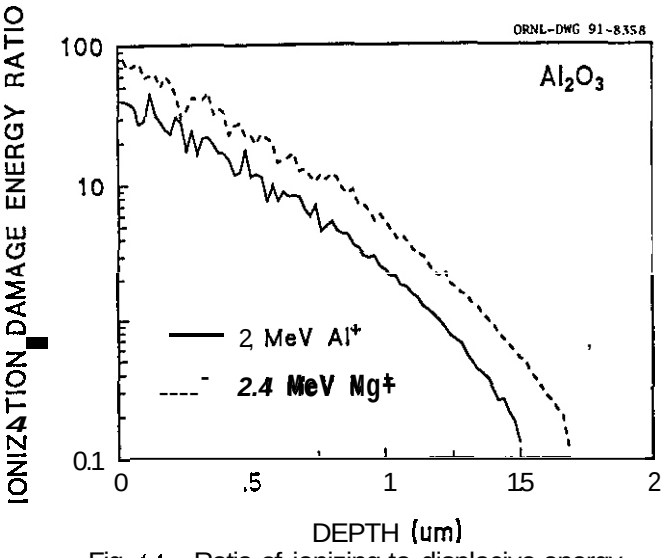


Fig. 14. Ratio of ionizing to displacive energy losses for 2.4 MeV Mg^+ and 2-MeV Al+ions incident on Al_2O_3.

REFERENCES

1. Proceedings of the IEA Workshop on In Situ Measurements of Radiation Effects in Ceramic Electrical Insulators, Los Alamos, NM, June 27-29, 1990 (Commissionof the European Communities Directorate General XII - Fusiori Programme Report EUR FU BRU/XII-6/91-MATIA, Jan. 1991).

2. R. W. Klaffky, B. H. Rose, A. N. Goland, and G. J. Dienes, *Phys.* Rev. *B* 21 8(1980) 3610-34.

3. G. P. Pells. S. N. Buckley. G. J. Hill, and M. J. Murphy, Harwell Lab. Report AERE R11715 (Nov. 1985).

4. G. P. Pells, Rad. Effects 97 (1986) 39-47.

5. G. P. Pells, et al., Harwell Lab. Report AERE R13222 (Sept. 1988).

6. E. R. Hodgson and S. Clement, Rad. Effects 97 (1986) 91-6.

7. E. R. Hodgson. *Cryst. Latt. Def. and Amorph.* Mat. 18 (1989) 169-80.

6. E. R. Hodgson, Proc. 4th Int. Conf. on Fusion Reactor Materials, Kyoto, Dec. 1989, J. Nucl. Mater. (in press).

9. T. Shikama, M. Narui. A. Ochiai. H. Kayano, and T. Endo, "Electrical Conductivity of Single Crystal α-Alumina under Neutron and y-Ray Irradiation," 14th Int. Symp. of Effects of Radiation on Materials, Nashville, TN, June 1990 (ASTM, Philadelphia. in press).

10. E. H. Farnum, H. M. Frost, and F. W. Clinard, Fusion Reactor Materials Semiann. Prog. Report ending Sept. 30, 1990, DOE/ER-0313/9 pp. 295-6.

11. R. E. Stoller, R. H. Goulding and S. J. Zinkle, Fusion Reactor Materials Semiann. Prog. Report ending Sept. 30, 1990. DOE/ER-0313/9, pp. 317-22; also R. H. Goulding, R. E. Stoller and S. J. Zinkle, this progress report.

12. M. W. Thompson, "Defects and Radiation Damage in Metals," Cambridge Univ. Press, 1969, pp. 89-142.

13. M. D. Rechtin, Rad. Effects 42 (1979) 129-44.

14. Y. Katano, H. Ohno, and H. Katsuta. J. Nucl. Mater. 155-157 (1986) 366-71.

15. W. E. Lee, M. L. Jenkins, and G. P. Pells, *Phil.* Mag. A 51, 5 (1985) 639-59.

16. M. B. Lewis, W. R. Allen, R. A. Buhl, N. H. Packan, S. W. Cook, and L. K. Mansur. Nucl. *Instr.* Meth. *B* 43 (1989) 243.

17. I. Manning and G. P. Mueller, *Comput. Phys. Commun.* 7 (1974) 65.

18. S. J. Zinkle, C. P. Haltom, L. C. Jenkins, and C. K. H. DuBose, J. Electron *Microsc.* Tech., in press; also Fusion Reactor Materials Semiannual Prog. Report ending Sept. 30, 1990, DOE/ER-0313/9, pp. 334-9.

19. W. Primak, J. *Appl. Phys.* 34 (1963) 3630-1.

20. W. Primak and J. Luthra, *J.* Appl. *Phys.* 37 (1966) 2287-94.

21. D. M. Gruen, B. Siskind, and R. B. Wright, *J.* Chem. *Phys.* 65 (1976) 363-78.

22. L. Romana, G. Fuchs, G. Massouras, and P. Thevenard, Rad. *Eff. Def.* Solids, 115 (1990) 139-43.

23. J. F. Ziegler and J. M. Manoyan, Nucl. hstr. Meth. *B* 35 (188) 21528.

24. S. J. Zinkle, *J.* Amer. *Cerm. Soc.* 72, 8 (1969) 1343-51.

25. S. J. Zinkle, "Dislocation Loop Formation in Ion-Irradiated Polycrystalline Spinel and Alumina." 14th Int. Symp. of Effects of Radiation on Materials, Nashville, TN, June, 1990, (ASTM. Philadelphia) in press; also Fusion Reactor Materials Semiann. Prog. Report ending Sept. 30, 1990, DOE/ER-0313/9, pp. 323-3.

26. N. Itoh, Rad. *Eff. Def.* Solids 110 (1989) 19-26.

27. E. P. EerNisse, J. Appl. *Phys.* 45, 1 (1974) 167-74.

28. A. Dunlop, D. Lesueur, G. Jaskierowicz, and J. Schildknecht, Nucl. Instr. Meth. *Phys.* Res. *B 36* (1989) 412-9.

29. I. P. Chernov, et al., Rad. *Eff.* 97 (1986) 155-60.

30. R. Bullough and J. J. Gilman, *J.* Appl. *Phys.* 37, 6 (1966) 2283-7.

31. C. P. Flynn and R. S. Averback, *Phys.* Rev. *B,* 38 (1988) 7118-20.

32. A. M. Stoneham, Nucl. hstr. Meth. *Phys. Res. B* 48 (1990) 389-98.

33. J. C. Bourgoin and J. W. Corbett, Rad. *Eff.* 36 (1978) 157--88.

34. H. J. Pabst, Rad. *Eff.* 25 (1975) 279-81.

35. A. Alghamdi and P. D. Townsend. Rad. *Eff.* Def. Solids 115 (1990) 73-8.

36. L. A. Harrah. *Appl. Phys.* Left. 17, 10 (1970) 421-3.

37. B. Gross, in "Electrets," Topics in Applied Physics Vol. 33, G. M. Sessler, Ed. (Springer-Verlag, New York, 1980) pp. 217-84.

PREPARATION OF $MgAl_2O_4$ **SPINEL** CONTAINING CONTROLLED AMOUNTS OF ^{17}O **ISOTOPE --** Hyoun-Ee Kim, Steven J. Zinkle, and William R. Allen (Oak Ridge National Laboratory)

OBJECTIVE

The objective of this study was to determine if magnesium aluminate spinel ($MgAl_2O_4$) could be prepared with a controlled amount of ^{17}O. This would allow fusion-relevant He:dpa ratios to be achieved during irradiation in a mixed-spectrum reactor such as HFIR.

SUMMARY

Magnesium aluminate spinel ($MgAl_2O_4$) with an ^{17}O enrichment ($^{17}O/O_{Tot}$) of about 23 at. % was prepared by reacting fine mixtures of aluminum hydroxide (enriched with ^{17}O) and MgO of normal isotopic content. The material was prepared for experiments in which the radiation damage produced in a fusion reactor is simulated by fission reactor exposures. The powder mixtures were obtained by hydrolyzing, with water containing the ^{17}O isotope, a mixture of aluminum isopropoxide and MgO powder. The mixture was converted into pure spinel by a series of heat treatments and grindings. Essentially fully dense bodies, which contained about 45% of the ^{17}O isotope initially present in the water, were successfully fabricated provided that all thermal treatments were conducted in argon or vacuum atmospheres.

PROGRESS AND STATUS

Introduction

Ceramic materials will be required in several locations within proposed fusion reactors, where they may be subjected to appreciable doses of 14-MeV fusion neutrons.[1,2] Unfortunately, at the present time there are no 14-MeV neutron sources available that have sufficient intensity to perform high-dose tests on candidate fusion reactor materials. Nuclear fission reactors have been used to expose various ceramic materials to high-dose irradiation.[3] However, these exposures are inadequate for estimating the degree of degradation to be expected in fusion reactors because the amount of transmutation products formed during fission neutron irradiation is generally much lower than that generated during deuterium-tritium (d-T) fusion neutron irradiation. For example, the amount of helium generated in a ceramic such as Al_2O_3 is, for irradiation to the same displacement damage level, more than an order of magnitude higher for d-T fusion neutron irradiation than for fission neutron irradiation.[4]

One technique that can be utilized to investigate helium effects in fission neutron irradiated oxide ceramics is to take advantage of the high helium production rate associated with the ^{17}O $(n, \alpha)^{14}C$ thermal neutron reaction? Oxygen of natural abundance contains only 0.04% ^{17}O, so this reaction does not produce significant amounts of helium during fission neutron irradiation of standard oxide ceramics. The (n,α) thermal neutron reaction cross section is very small for the other two stable oxygen isotopes, ^{16}O and ^{18}O. A technique has been recently developed for producing ^{17}O-enriched Al_2O_3 from aluminum isopropoxide and water containing enriched concentrations of the ^{17}O isotope?

Studies on magnesium aluminate spinel have indicated that this material has superior swelling resistance compared to most metals and ceramics during fission neutron irradiation.[5] Because of this behavior, spinel is considered a prime candidate insulator for fusion reactor applications. However, a recent ion irradiation study found that co-implantation of fusion-relevant amounts of helium during the irradiation of spinel resulted in the formation of large cavities on the grain boundaries.[6] Cavity formation did not occur in ion-irradiated spinel in the absence of helium co-implantation. Because of these mixed results on such a promising material, experiments are being conducted to evaluate the behavior of this ceramic material under conditions that will simulate the damage induced by fusion neutron irradiation. The technique developed for producing ^{17}O-enriched Al_2O_3 was modified to produce ^{17}O-enriched magnesium aluminate spinel from MgO powder, aluminum isopropoxide, and water containing enriched concentrations of the ^{17}O isotope, The material was evaluated for isotope enrichment using a nuclear reaction analysis technique and was characterized by transmission electron microscopy.

EXPERIMENTAL PROCEDURES

Samples of isotopically tailored spinel were prepared by hydrolyzing a mixture of submicron MgO powder and aluminum isopropoxide $[Al(OC_3H_7)_3]$ dissolved in isopropyl alcohol with ^{17}O-isotope enriched water (Monsanto Research *Corp.*, Miamisburg, OH). The aluminum isopropoxide was ground to produce a fine-grained powder that dissolved more readily in the isopropyl alcohol. The measured levels of the various oxygen isotopes in the enriched water were: 12.95% ^{16}O, 51.48% ^{17}O,

and 35.57% ^{18}O (it is difficult to completely separate ^{17}O from the ^{16}O and ^{18}O isotopes using present-day enrichment techniques). The hydrolysis reaction was conducted at 60°C in a flowing argon atmosphere while the solution was vigorously stirred. The apparatus used for this operation has been shown previously! A fine mixture of MgO and aluminum hydroxide (γ-AlOOH, boehmite) enriched in ^{17}O and ^{18}O was obtained by the following reaction:

$$2\ Al(OC_3H_7)_3 + MgO + 4\ H_2O \rightarrow 2\ AlOOH + MgO + 6\ C_3H_7OH(\uparrow) \quad . \qquad (1)$$

After the hydrolysis, the isopropyl alcohol was removed from the slurry by vacuum evaporation. The dried mixture was heat treated to induce the calcination of AlOOH into Al_2O_3 and the subsequent reaction to form spinel. All the heat treatments were performed in flowing argon to prevent the exchange of ^{17}O and ^{18}O with oxygen of normal abundance. The calcination was performed at a temperature higher than 1300°C to produce complete transformation[6] of Al_2O_3 polytypes into α-Al_2O_3. Formation of spinel was confirmed by X-ray diffraction. After the presence of pure $MgAl_2O_4$ was confirmed, 0.5 wt % CaO was added to the powder as a sintering aid. The powder mixture was milled with alumina halls as milling media for 3 h in isopropyl alcohol for mixing and particle size reduction. The size of the milled powder was measured with a particle size analyzer. Compacts were fabricated by uniaxially pressing the powders in a steel die at a pressure of 140 MPa. Sintering was performed by heating the compacts for 3 h in vacuum at 1800°C. Control specimens were fabricated using the identical synthesis and densification procedures but using non-enriched water.

After sintering, the densities of the samples were measured by the immersion technique. A specimen for examination by transmission electron microscopy was cut from the sintered 3 mm-diam cylinders of the enriched spinel. These specimens were mechanically ground and ion milled to perforation. The enrichment levels of ^{17}O and ^{18}O were determined from nuclear reaction analysis and Rutherford backscattering measurements. For the former technique, targets from the spinel specimens were bombarded with 750-keV protons (^1H) to promote nuclear reactions with the ^{17}O and ^{18}O isotopes. Details of the measurement technique have been previously reported! A recently published excitation curve[7] for the $^{18}O\ (p,\alpha)^{15}N$ reaction was used to calculate the ^{18}O concentration profile.

RESULTS AND DISCUSSION

Formation of magnesium aluminate spinel by the reaction between MgO and ^{17}O-enriched AlOOH was verified by X-ray diffraction with the results shown in Fig. 1 (A)-(C). As expected, before heat treatment only MgO peaks were detected [Fig. 1(A)]. After heat treatment for 20 h in argon at 1300°C, strong magnesium aluminate peaks were detected. However, as shown in Fig. 1 (B), there were still appreciable amounts of unreacted alumina and MgO. Upon repeated regrinding and heat treatments for longer periods of time at 1300°C, the intensities of the alumina and MgO peaks were weaker, but they still persisted. Pure $MgAl_2O_4$ phase was obtained only when a powder that had been heat treated at 1300°C and reground was pelletized and heat treated at 1400°C for ~20 h. The X-ray diffraction pattern of the powder prepared with the latter procedure, Fig. 1 (C), shows that the powder has pure $MgAl_2O_4$ phase. After heat treatment, the pellets were again crushed, and milled in isopropyl alcohol with alumina halls as the grinding media. Small amounts (~0.5 wt %) of CaO were added during milling as a sintering aid.' The average particle size of the powder after milling was 2.4 ± 0.7 pm. Sintering of the samples was performed by heating for 3 h in vacuum at 1800°C. The densities of the sintered bodies were consistently higher than 99% of theoretical.

The ^{18}O isotope concentration as a function of depth in the sintered $MgAl_2O_4$ specimens was measured for regions within 1.5 μm of the surface by collecting and analyzing the energies of alpha particles created by the 750-keV proton reaction $^{18}O\ (p,\alpha)^{15}N$. The ^{17}O enrichment level was deduced from the ^{18}O concentration measurements by assuming that the probability of replacement of the oxygen isotopes in the enriched material with levels of normal abundance was independent of isotope mass. The validity of this assumption was proved in our previous experiments[6] with isotopically tailored Al_2O_3. The measured ratio of ^{18}O to total oxygen atoms in the enriched $MgAl_2O_4$ is shown in Fig. 2, along with measurements made on spinel prepared using non-enriched water ("control $MgAl_2O_4$") and single crystal Al_2O_3. This graph shows a slight depletion of ^{18}O in the enriched spinel within 0.5 μm of the surface. The depth-averaged ratio of ^{18}O to total atoms was 9.24 ± 1.7 at. %, which corresponds to an oxygen ratio ($^{18}O/O_{Tot}$) of 16.2 ± 3.2 at. % in the enriched $MgAl_2O_4$. The hydrolysis reaction used to prepare the spinel (Eq. 1) shows that the enriched oxygen isotopes present in the water will be diluted with natural-enrichment oxygen present in the MgO and aluminum isopropoxide powders. A previous measurement on γ-AlOOH powder prepared from the hydrolysis of aluminum isopropoxide[6] indicated that the (OC_3H_7) radical is efficiently replaced by the enriched H_2O (i.e., about 62% of the enriched oxygen isotopes in the water were transferred to the γ-AlOOH powder for hydrolysis performed in an argon environment). [The data presented in ref. 6 have been reduced by 20% to allow for the revised cross-sections for the $^{18}O(p,\alpha)^{15}N$ reaction in ref 7.] Assuming that the MgO powder does not react with the H_2O during hydrolysis, and that a similar fraction of enriched oxygen isotopes are transferred from the H_2O to the γ-AlOOH powder in the present case, then the maximum fraction of enriched oxygen isotopes retained in spinel would be 50%. The measured ^{18}O ratio in the sintered spinel was 16.2 ± 3.2 at. % ($^{18}O/O_{Tot}$), which corresponds to 45 ± 9% of the ^{18}O initially present in the enriched water. This indicates

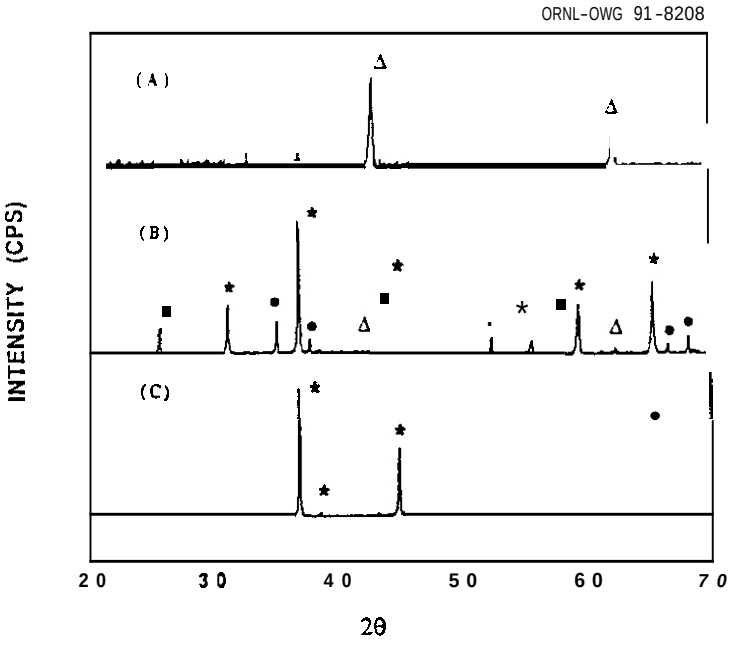


Fig. 1. X-ray diffraction patterns of the mixture of AlOOH and MgO; (A) before heat treatment showing only MgO peaks, (B) after heat treatment in Ar at 1300°C for 20 h, showing the peaks of magnesium aluminate as well as those of unreacted alumina and MgO, (C) after heat treatment at 1400°C for 20 h after pelletizing the powder which had been heat treated at 1300°C and reground, showing only $MgAl_2O_4$ peaks. (Δ) MgO, (•) Al_2O_3, (*) $MgAl_2O_4$.

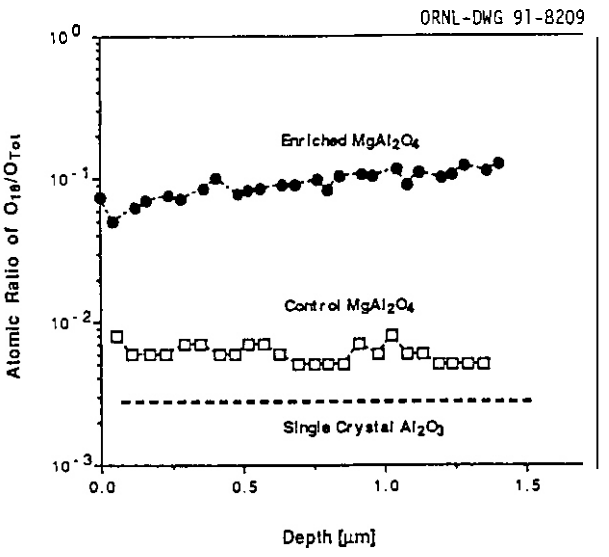


Fig. 2 Depth profile of the ratio of ^{18}O to total atoms for enriched and control $MgAl_2O_4$ and single crystal Al_2O_3 measured with the $^{18}O(p,\alpha)^{15}N$ nuclear reaction using 750-keV protons. The ^{17}O enrichment level was deduced from the ^{18}O concentration measurements.

that only minimal replacement of the enriched isotopes by natural oxygen occurred during calcination and sintering of the spinel. Assuming the same retention ratio for ^{18}O, then 23 at. % ($^{17}O/O_{Tot}$) was present in the $MgAl_2O_4$. An enrichment ratio of 17 at. % ($^{17}O/O_{Tot}$) was desired for the study on the simulation of damage in nuclear fusion reactor environments: This ratio could he achieved by simply diluting the enriched H_2O with normal H_2O. A slightly higher than expected ratio of $^{18}O/O_{Tot}$ was observed in the control $MgAl_2O_4$ specimens, as shown in Fig. 2, apparently due to the contamination of containers from prior fabrication of the enriched alumina or spinel specimens. The amount of ^{17}O present in the control spinel deduced from the ^{18}O measurement is still too low to produce significant amounts of additional helium during fission neutron irradiation.

Transmission electron microscopy revealed that the microstructure of the sintered spinel consisted of single-phase grains with a typical diameter of 15 to 20 μm. A moderate density ($\sim 5 \times 10^{16}/m^3$) of sintering pores with a mean size of ~0.7 μm was observed in the interior of the grains. There was no evidence of pore formation at the grain boundaries. The volume fraction of the intragranular pores was ~1%, which agrees with the measured bulk density of ~99% theoretical. An amorphous (glassy) intergranular phase was observed at many of the grain boundary triple point junctions in the spinel. Energy dispersive x-ray spectroscopy measurements indicated that the intergranular phase was enriched in calcium and aluminum. Figure 3 shows an example of this intergranular phase at a triple point.

SUMMARY

Polycrystalline magnesium aluminate spinel enriched in ^{17}O, necessary for the simulation of the nuclear fusion helium generation rate in a fission reactor, was successfully prepared. About 45% of the ^{17}O and ^{18}O isotopes initially present in the water used to prepare the spinel were retained in the sintered material, with most of the oxygen replacement likely occurring during hydrolysis of aluminum isopropoxide.

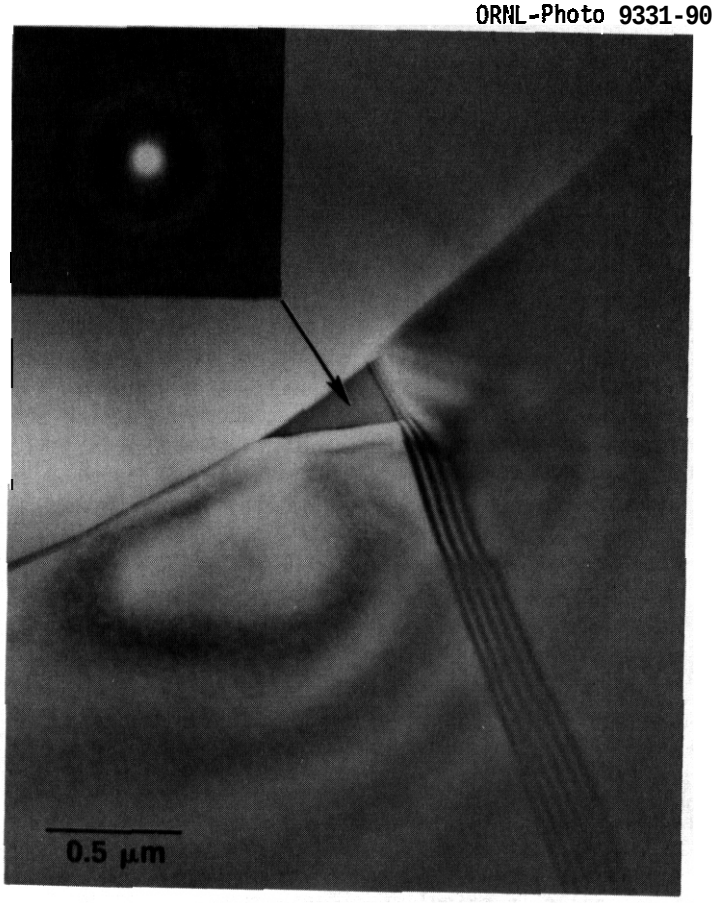


Fig. 3. Transmission electron micrograph of sintered spinel showing an amorphous intergranular phase. The inset electron microdiffraction pattern shows a diffuse ring surrounding the center transmitted beam spot, characteristic of an amorphous phase.

FUTURE WORK

The isotopically tailored $MgAl_2O_4$ and Al_2O_3 specimens will be irradiated in the HFIR to fast neutron fluences of 24 and 7.2×10^{26} n/m^2 (E > 0.1 MeV). The irradiation is scheduled to begin in early summer 1991 (see elsewhere in this volume for further details about the irradiation).

ACKNOWLEDGMENT

We thank A. J. Moorhead and T. N. Tiegs for their helpful comments when reviewing the manuscript. The ^{17}O-enriched water used to prepare the spinel specimens was purchased by Los Alamos National Laboratory (LANL) as part of a LANL/ORNL collaboration on irradiation of isotopically tailored ceramics in HFIR.

REFERENCES

1. J. L. Scott, F. W. Clinard, Jr., and F. W. Wiffen, "Special Purpose Materials for Fusion Application: J. *Nucl Mater.* 133&134, 156-63 (1985).

2. F. W. Clinard, Jr., "Ceramics for Applications in Fusion Systems," *J. Nucl. Muter.* 85&86, 393-404 (1979).

3. F. W. Clinard, Jr. and L. W. Hobbs, "Radiation Effects in Non-Metals," pp. 387-471 in Physics of Radiation Effects in Crystals, Edited by R. A. Johnson and A. N. Orlov, Elsevier Science, Amsterdam, The Netherlands, 1986.

4. R. J. LaBauve, R. J. Livak, and F. W. Clinard, Jr., "Calculations for Isotopically-Tailored Ceramics in Fission and Fusion Reactors," Adv. *Ceramic Mater.* 3, 353-56 (1988).

5. S. J. Zinkle and S. Kojima, "Helium-Assisted Cavity Formation in Ion-Irradiated Ceramics," I. *Nucl.* Muter. (1990) in press.

6. H.-E. Kim, S. J. Zinkle, and W. R. Allen, "Preparation and Characterization of ^{17}O-Enriched Alumina for Nuclear Fusion Damage Experiments," *J.* Am Cemm *Soc.*, 73 [2] 425-29 (1990).

7. N. S. Christensen, F. Jensen, F. Besenbacher, and I. Stensgaard, "Absolute Calibration of the ^{18}O (p,α) ^{15}N Nuclear Reaction," *Nucl. Instr. Meth.*, 51 [8] 97-101 (1990).

8. R. J. Bratton, 'Translucent Sintered $MgAl_2O_4$," I. Am *Ceram. Soc.*, 57 [7] 283-86 (1974).

IRRADIATION OF CONVENTIONAL AND ISOTOPICALLY TAILORED CERAMICS IN HFIR — S. J. Zinkle (Oak Ridge National Laboratory), and L. L. Snead (Rensselaer Polytechnic Institute, on assignment at ORNL), and E. H. Farnum (Los Alamos National Laboratory)

OBJECTIVE

The objective of this report is to summarize the irradiation conditions for ceramic specimens being irradiated in the High Flux Isotope Reactor irradiation capsules MFE CTR-60 and -61.

SUMMARY

Al_2O_3 and $MgAl_2O_4$ specimens containing ^{17}O isotope concentrations of 0 to 25 at. % ($^{17}O/O_{TOT}$) have been prepared for irradiation in HFIR in order to investigate the effects of helium formation on their microstructure and dielectric and mechanical properties. SiC/SiC flexure bars, ceramic fibers and a wide range of commercial ceramics TEM disks have also been included in the irradiation capsules. The specimens will be irradiated at temperatures of 100, 350, and 600°C in two irradiation capsules that will receive respective maximum neutron fluences of 2.4 × 10^{26} and 7.2 × 10^{26} n/m^2 (E > 0.1 MeV).

PROGRESS AND STATUS

Introduction

Ceramic insulators and dielectrics have several potential applications in high neutron flux regions of fusion reactors. A wide variety of ceramics have been examined following low-fluence neutron irradiation (<10^{25} n/m^2, E > 0.1 MeV),' but there are relatively few studies on the behavior of ceramics following high-fluence neutron irradiation (>10^{26} n/m^2, E > 0.1 MeV).[1,2]

It is well documented[3,4] that the helium production rate per unit displacement damage in ceramics such as Al_2O_3 is more than an order of magnitude higher during irradiation in a 14-MeV fusion neutron spectrum than the corresponding fission neutron He:dpa rate. A recent dual-beam ion irradiation study has found evidence that irradiation of $MgAl_2O_4$ at a fusion-relevant He:dpa ratio caused severe cavity swelling, particularly along grain boundaries.[5] Cavity formation did not occur in spinel specimens irradiated without helium coimplantation. As proposed by Clinard,[6] helium effects in oxide ceramics can be studied during irradiation in a mixed-spectrum reactor such as HFIR by ^{17}O isotopic tailoring techniques. A joint irradiation program has been established involving LANL and ORNL research staff members to pursue the preparation and pre- and post-irradiation characterization of ^{17}O isotopically tailored Al_2O_3 and $MgAl_2O_4$. Details of the fabrication technique and the preirradiation characterization of the isotopically tailored specimens are given elsewhere.[7-10]

Each HFIR irradiation capsule was designed to accomnodate nearly 100 ceramic TEM disks in addition to the isotopically tailored ceramic specimens. Additional space was also made available for flexural bars in the lower flux top and bottom ends of the irradiation capsule. A representative cross section of advanced ceramic TEM disks (comnercial and non-commercial) was selected for HFIR irradiation at temperatures of 100 to 600°C. This study complements a parallel study of the same ceramic materials in the FFTF,** which spans irradiation temperatures from 420 to 800°C. The overlap of irradiation temperatures in the two experiments allows a determination to be made whether the higher amount of ionizing radiation in the HFIR compared to FFTF has a significant effect on the irradiated microstructures of ceramics.

Materials and Irradiation Conditions

Two identical irradiation capsules (MFE-CTR-60 and -61) will be utilized for the irradiations in HFIR target positions. The capsules will both be inserted in May or June 1991, and will be irradiated to horizontal midplane fluences of 2.4 × 10^{26} n/m^2 and 7.2 × 10^{26} n/m^2 (E > 0.1 MeV), respectively. This corresponds to irradiation times of about 8 and 24 months. The temperature at different regions in the irradiated capsule will be controlled by gamma heating; six SiC temperature monitors from each capsule will be examined after irradiation to verify that the design irradiation temperatures were achieved. Six neutron dosimetry packets are included in each capsule to measure the axial dependence of the neutron fluence.

Table 1 summarizes the experimental matrix for the isotopically tailored Al_2O_3 and $MgAl_2O_4$ specimens. The ^{17}O concentration in the specimens varies from natural enrichment (0.04% $^{17}O/O_{TOT}$) to ~25% $^{17}O/O_{TOT}$. These enrichment levels bracket the ^{17}O concentration of 18% $^{17}O/O_{TOT}$ that is calculated[4] to produce the fusion first wall He:dpa ratio in Al_2O_3 during HFIR irradiation. TEM disks (0.25 mm thickness), flexural strength bend bars of dimensions 1.25 by 2.5 by 35 mn, and disks of dimensions 7.7 mm diam by 0.5 mm thickness are included for the nonenriched and fully enriched (25% $^{17}O_{TOT}$) Al_2O_3 conditions. Flexure bars and indentation disks were not fabricated for the spinel specimens due to time and budgetary constraints.

Table 1. Summary of ^{17}O isotopically tailored Al_2O_3 and $MgAl_2O_4$ specimens contained in each of the two irradiation capsules

	TEM Disks			Indentation Disks		Flexure Bars	
	100°C	350°C	600°C	100°C	600°C	100°C	600°C
Al_2O_3 (nonenriched)	3	3	3	3	5	8	9
Al_2O_3 (8 at. % $^{17}O/O_{TOT}$)	3	3	3	0	0	0	0
Al_2O_3 (25 at. % $^{17}O/O_{TOT}$)	3	3	3	3	5	8	9
$MgAl_2O_4$ (nonenriched)	3	3	3	0	0	0	0
$MgAl_2O_4$ (14 at. % $^{17}O/O_{TOT}$)	2	2	2	0	0	0	0
$MgAl_2O_4$(23 at. % $^{17}O/O_{TOT}$)	1	1	1	0	0	0	0
TOTALS	15	15	15	6	10	16	18

The use of multiple specimens for each irradiation condition allows several different postirradiation analysis techniques to be utilized. Postirradiation tests that are planned include chemical analysis (helium content), density, dielectric properties at ~100 GHz, flexural strength, indentation fracture toughness, and TEM.

Table 2 shows the irradiation matrix for the other ceramic TEM disks (0.25 mm thickness) included in the HFIR capsules. One of the faces of each disk was mechanically polished so that postirradiation indentation fracture toughness measurements could be easily performed. The experimental matrix includes advanced comnercial ceramics, natural diamond and CVD diamond films, and several types of transformation-toughened zirconia and SiC whisker-reinforced ceramics. The physical properties of the commercial ceramics are tabulated in an accompanying report.[10] TEM disks prepared from the same stock material are being irradiated in FFTF.[11]

Table 2. Ceramic TEM disks loaded into each of the low-dose and high-dose HFIR capsules

Ceramic and vendor	Number of Disks at Each Irradiation Temperature		
	100°C	350°C	600°C
Al_2O_3 (Wesgo 995)	2	2	2
MgO (Ube UMP-0505)	2	2	2
$MgAl_2O_4$ (Ceradyne)	1	2	2
Si_3N_4 (Kyocera SN733)	2	3	2
AlN (Cercom)	2	2	2
E-Sic (Cercom, direct sintered)	2	2	2
α-SiC (Carborundum, Hexoloy-SA)	2	2	2
$MgO{\cdot}SiO_2$ (Kyocera S-211)	2	2	1
$2MgO{\cdot}SiO_2$ (Kyocera F1123)	2	2	2
TiO_2 (Kyocera T-792)	2	2	2
$ZrO_2{\cdot}SiO_2$ (Kyocera Z-381)	1	2	1
Sialon, Al/Si = 0.33 (ORNL)	1	1	1
Macor (Oow Chemical)	0	2	0
Graphite—3% B (Toyo Tanso Co.)	0	2	0
Diamond [001] (Drukker, Type IIA)	1	1	1
CVD diamond (ORNL {100}<100>)	1	0	1
CVD diamond (ORNL {100 + 111})	0	1	0
Al_2O_3—20% SiC whiskers (ORNL)	0	2	0
$3Al_2O_3{\cdot}2SiO_2$—20% SiC whiskers (ORNL)	0	2	0
Si_3N_4—6%Y_2O_3—2% Al_2O_3 (ORNL)	0	2	0
Si_3N_4—6%Y_2O_3—2% Al_2O_3—20% SiC whiskers (ORNL)	1	1	1
ZrO_2—12% CeO_2 (ORNL)	0	2	0
ZrO_2—2% Y_2O_3 (ORNL)	1	2	1
ZrO_2—8% MgO (ORNL)	0	2	0
TOTALS	25	43	25

A total of 20 SiC/SiC composite bend bars of dimensions 1.88 by 2.5 by 35 mm have been inserted into the low flux end regions of both HFIR capsules. The composites were fabricated at ORNL using the Forced Chemical Vapor Infiltration (FCVI) process to deposit the matrix into the Nicalon fiber preform. There are two interfacial thicknesses being loaded of 0.25 and 0.35 μm, both deposited from propylene prior to SiC infiltration. Also being loaded into the end regions will be two aluminum holders each containing five chambers for ceramic fibers. The types of fibers being loaded are listed in Table 3. The irradiation temperature in the end regions will be ~350°C, and the neutron fluence will be about half that of the capsule center region.

FUTURE WORK

Postirradiation examination of the specimens irradiated to a fluence of ~2.4 × 10^{26} n/m^2 (E > 0.1 MeV) will be initiated in late summer 1992.

ACKNOWLEDGMENTS

The isotopically tailored Al_2O_3 and $MgAl_2O_4$ ceramics were prepared by H-E K*m. Most of the final specimen cutting and polishing was performed

Table 3. Ceramic fiber bundles loaded into HFIR Capsules MFE CTR-60 and -61

Vendor	Composition	Fiber Diameter (μm)	Tensile Strength (MPa)
Nippon Carbon Nicalon	SiC, SiO_2, C	12–20	~3000
MER Corp. (#071190Z)	SiC, C (sized)	3–5	3200
MER Corp. (#070690Z)	SiC, C (sized)	3–5	3000
Texton Tyranno	E-Sic, Ti, O, C	6–10	2970
DuPont (#E 105)	Graphite	15	--

by A. M. Williams, J. W. Jones, and C. P. Haltom. H. M. Frost and F. W. Clinard, Jr. of Los Alamos National Laboratory provided valuable assistance on the outlining of the test matrix for the isotopically tailored specimens. The water used to prepare the ^{17}O-enriched specimens was purchased by LANL.

REFERENCES

1. R. A. Wullaert et al., in: Effects of Radiation on Materials and Components, J. F. Kircher and R. E. Bowman, eds., Reinhold Publ. Co., New Vork, 1964, pp. 277–402.

2. F. W. Clinard, Jr. and L. W. Hobbs, in: Physics of Radiation Effects in Crystals, R. A. Johnson and A. N. Orlov, eds., Elsevier Science Publ.. 1986, pp. 387–471.

3. L. H. Rovner and G. R. Hopkins, Nucl. Technol. 29 (1976) 274–302.

4. R. J. LaBauve, R. J. Livak, and F. W. Clinard, Jr., Adv. Ceram. Mater. 3 (1988) 353–56.

5. S. J. Zinkle and S. Kojima, "Helium-Assisted Cavity Formation in Ion-Irradiated Ceramics," Proc. 4th Int. Conf. on Fusion Reactor Materials, Kyoto, 1989, J. Nucl. Mater. (in press); also Fusion Reactor Materials Semiann. Prog. Rept., Mar. 31, 1990, DOE/ER-0313/8, pp. 293–96.

6. F. W. Clinard, Jr., J. Nucl. Mater. 85&86 (1979) 393–404.

7. H-E Kim, S. J. Zinkle, and W. R. Allen, J. Am. Ceram. Soc. 73 (1990) 425–29.

8. H-E Kim, S. J. linkle, and W. R. Allen, "Preparation of $MgAl_2O_4$ Spinel Containing Controlled Amounts of ^{17}O Isotope," J. Am. Ceram. Soc, Rapid Commun. 74 (1991); also elsewhere in this progress report.

9. H. M. Frost. J. C. Kennedy, T. N. Claytor, E. F. Brown, and S. J. linkle, "Ceramic-Processing Aided by Millieter-Wave Testing," Fusion Reactor Materials Semiann. Prog. Rept., Sep. 30. 1989, DOE/ER-0313/7, pp. 289–96.

10. H. M. Frost, J. C. Kennedy, T. N. Claytor, E. F. Brown, and S. J. Zinkle, "Millieter-Wave Testing of Isotopically Enriched Alumina," Fusion Reactor Materials Semiann. Prog. Rept., Sep. 30, 1990, DOE/ER-0313/9, pp. 297–301.

11. S. J. linkle and L. L. Snead, "Irradiation of Ceramics in FFTF," this progress report.

IRRAOIATION OF CERAMICS IN FFTF — S. J. Zinkle (Oak Ridge National Laboratory) and L. L. Snead (Rensselaer Polytechnic Institute, on assignment at ORNL)

OBJECTIVE

This report summarizes the irradiation conditions for ceramic specimens being irradiated in FFTF MOTA-2B.

SUMMARY

A wide range of advanced structural ceramics have been prepared and shipped to FFTF for irradiation to a nominal fluence of ~6 × 10^{26} n/m^2 (E > 0.1 MeV) at temperatures of 420 to 800°C. Most of the ceramics will be irradiated as TEM disks, but SiC/SiC flexural bars, electrical conductivity disks, and bundles of commercial ceramic fibers will also be irradiated in separate irradiation capsules.

PROGRESS AND STATUS

Introduction

Information on the properties of nonfissile ceramics following high-dose neutron irradiation is rather limited compared to the data base that has been accumulated for metals.[1,2] The most extensive studies have been confined to a few materials, notably Al_2O_3, MgO, and $MgAl_2O_4$ (e.g., ref. 3) and to a lesser extent Si_3N_4, BeO, etc. In addition, ceramic processing techniques continue to evolve. This suggests that irradiation results obtained on ceramics of 1960s or even 1970s vintage may not accurately represent the irradiation response of materials made within the last few years.

The purpose of the present irradiation program is to obtain information on the strength, fracture toughness, density, and microstructural changes of a wide range of advanced ceramics, including representative monolithic oxides, carbides, and nitrides. A spectrum of advanced structural ceramics ranging from whisker- and transformation-toughened ceramics to SiC/SiC composites has been included along with recently developed chemical vapor-deposited (CVD) diamond films and commercial ceramic fibers.

The results obtained on specimens irradiated at 420 and 600°C will be compared to the results obtained from HFIR irradiation of the same specimens. The HFIR has a higher component of ionizing radiation than the FFTF due to an order of magnitude higher gamma ray flux. A comparison of ceramics irradiated in the two reactors will help determine whether changes in the ratio of ionizing to displacive radiation have a significant effect on the irradiation response of ceramics.

Materials and Irradiation Conditions

Table 1 summarizes the irradiation conditions for the ceramic TEH disks. All of the disks will be irradiated to a nominal fast fluence of ~6 × 10^{26} n/m^2 (E > 0.1 MeV). A total of 13 different commercial ceramics have been prepared, along with natural diamond, two types of CVD diamond films, and several types of transformation-toughened zirconia and SiC whisker-toughened ceramics. Specimens will be irradiated at 420, 600, and 800°C. One of the faces of each disk (except for diamond) was mechanically polished to allow indentation fracture toughness measurements to be performed. The TEM disk dimensions are 3 mm diam by 0.25 mm thickness.

Table 2 compares the room temperature physical properties quoted by the manufacturer for the particular grades of each commercial ceramic included in the irradiation capsules. It can be seen that the range of nominal strength and thermal conductivity values spans a factor of 10 or more for the chosen ceramics. This produces a corresponding wide range of thermal shock resistance for the nonirradiated materials. The electrical resistivity ranges from a typical semiconductor (SiC) to very good insulators.

Table 3 summarizes the irradiation conditions and nominal initial strength for the bundles of ceramic fibers. All of the ceramic fibers will be irradiated at 420 and 800°C to a nominal fluence of ~6 × 10^{26} n/m^2 (E > 0.1 MeV). The length of the fibers is about 2.5 cm.

Table 4 lists the ceramic electrical conductivity disks that will be irradiated at 800°C to a fluence of ~6 × 10^{26} n/m^2 (E > 0.1 MeV). The disks have nominal dimensions of 6 mm diam by 0.9 mm thickness. Following neutron irradiation, the electrical conductivity of the disks will be measured during x-ray irradiation and compared to the behavior of specimens not subjected to neutron irradiation.

Table 1. Type and number of ceramic TEM disks loaded into MOTA 28

Ceramic and Vendor	Number of Disks at Each Irradiation Temperature					
	420°C		600°C		800°C	
	10 mil	20 mil	10 mil	20 mil	10 mil	20 mil
Al_2O_3 (Wesgo 995)	2	2	2	2	2	2
MgO (Ube UMP-0505)	2	2	2	2	2	2
$MgAl_2O_4$ (Ceradyne)	2	2	2	2	2	2
Si_3N_4 (Kyocera SN733)	2	2	2	2	2	2
AlN (Cercom)	2	2	2	2	2	2
6-Sic (Cercom, direct sintered)	2	2	2	2	2	2
a-SiC (Carborundum, Hexoloy-SA)	2	0	2	0	2	0
$MgO{\cdot}SiO_2$ (Kyocera S-211)	2	1	2	1	2	1
$2MgO{\cdot}SiO_2$ (Kyocera F1123)	2	1	2	1	2	1
TiO_2 (Kyocera T-792)	2	1	2	1	2	1
Zircon, $ZrO_2{\cdot}SiO_2$ (Kyocera Z-381)	2	1	2	1	2	1
Macor (Dow Chemical)	2	0	2	0	2	0
Boronized graphite (Toyo Tanso)	1	0	1	0	1	0
Diamond [001] (Drukker, Type IIA	1	0	0	0	1	0
CVD diamond (ORNL {100}<100>)	0	0	0	0	1	0
CVD diamond (ORNL {100 + 111})	1	0	1	0	1	0
Al_2O_3—20% SiC whiskers (ORNL)	2	0	1	0	2	0
$3Al_2O_3{\cdot}2SiO_2$—20% SiC whiskers (ORNL)	2	0	2	0	2	0
Si_3N_4—6%Y_2O_3—2% Al_2O_3 (ORNL)	2	0	1	0	2	0
Si_3N_4—6%Y_2O_3—2% Al_2O_3—20% SiC whiskers (ORNL)	0	0	1	0	1	0
ZrO_2—12% CeO_2 (ORNL)	1	0	2	0	1	0
ZrO_2—2% Y_2O_3 (ORNL)	2	0	2	0	2	0
ZrO_2—8% MgO (ORNL)	1	0	2	0	1	0
TOTALS	53		53		55	

Table 2. Physical properties of commercial ceramics being irradiated in MOTA 28 (vendor's quoted values!

Ceramic	Density (g/cm^3)	4-Point Flexural Strength (MPa)	Fracture Toughness (MPa $\sqrt{m}$)	Young's Modulus (GPa)	Coefficient of Thermal Expansion ($10^{-6}/°C$)	Thermal Conductivity (W/m- K)	Electrical Resistivity at 25°C (Ω-m)
Al_2O_3 (Wesgo 995)	3.86	310		~360	6.9	29	$>10^{12}$
MgO (Ube UMP-0505)	3.54	300		275	13.8	42	$>10^{12}$
$MgAl_2O_4$ (Ceradyne)[a]	3.51	150		200	8.1	18	$>10^{12}$
Si_3N_4 (Kyocera SN733)	3.2	980		304	2.5	29	$>10^{12}$
AlN (Cercom)	3.25	300		300	5.7	115	$>10^{12}$
β-SiC (Cercom, direct sintered)	3.10	550	4	400	4.4	110	~100
α-SiC (Carborundum, Hexoloy-SA)	3.10	460	4.6	410	4.0	126	~1
$MgO{\cdot}SiO_2$ (Kyocera S-211)	3.1	157			8.1	3.8	$>10^{12}$
$2MgO{\cdot}SiO_2$ (Kyocera F1123)	3.0	142		147	8.8	3.3	$>10^{12}$
TiO2 (Kyocera T-792)	4.3	147		176	9.6	3.3	10^{10}
$SiZrO_4$ (Kyocera Z-381)	3.5	167		157	3.7	5.0	$>10^{12}$
Macor (Dow)	2.52	100		65	13	1.3	10^{12}
Graphite—3%B (Toyo Tanso)						~40	
Diamond (Drukker, Type IIA)	3.515	~10,000		1050	0.8	2000	10^{14}

[a]Data product sheet not available for spinel (listed values are nominal properties taken from various sources).

Table 3. Ceramic fiber bundles loaded into MOTA 28 for irradiation at 420 and 800°C

Vendor/Tradename	Composition	Fiber Diameter (μm)	Tensile Strength (MPa)
Textron Tyranno	E-Sic, Ti, O, C	6–10	2970
Textron Tyranno (LOX)	8-Sic, Ti, C (low oxygen)	6–10	>2000
MER Corp. (#0722590)	SiC, C	3–5	3000
MER Corp. (#071190Z)	SiC, C (sized)	3–5	3200
MER Corp. (#070690Z)	SiC, C (sized	3–5	3400
Textron AVCO (#SCS2)	CVO SiC on C core	140	3450
Textron AVCO (#SCS9)	CVD SiC on C core	143	3920
Nippon Carbon Nicalon	SiC, SiO_2, C	12–20	~3000
LANL VLS whiskers[a]	E-Sic	4–7	8300
3M Nextel (#440)	Mullite–2% B_2O_3	10–12	1900
DuPont (#E 130)	Graphite	15	--
DuPont (#E 105)	Graphite	15	--
OuPont (#E 75)	Graphite	15	--

[a]Fiber bundles included for F. W. Clinard, Jr. (LANL).

Table 4. Radiation-induced conductivity disks loaded into MOTA 2B for irradiation at 800°C

Vendor	Ceramic	Vendor	Ceramic
Kyocera	8-Sic	Crystal Systems	α-Al_2O_3 [0001] orientation
ORNL	SiC (CVD)/SiC (Nicalon)	Coors	Al_2O_3 (AD 994)
ORNL	0.17 μm C coated fibers	Boride Products	Si_3N_4
Thermoelectron	CVD SiC (commercial grade)	Cercom	AlN
Thermoelectron	CVO SiC (high-purity grade)		
Carborundum	a-Sic (Hexoloy-SA)		

A total of seven SiC/SiC flexural strength bars were encapsulated for irradiation at 600°C to a fluence of ~6 × 10^{26} n/m^2 (E > 0.1 MeV). The composite was prepared at ORNL from a 30 weave of Nicalon fibers coated with 0.35 μm graphite with a chemical vapor infiltrated (CVI) matrix of SiC. The dimensions of the bend bars are 1.88 by 2.5 by 35 mm.

FUTURE WORK

Measurements will be made on the microstructure, density, indentation fracture toughness, flexural strength, tensile strength, and electrical conductivity of the irradiated specimens starting in the summer of 1992.

ACKNOWLEDGMENTS

The assistance of A. M. Williams, J. W. Jones, and C. P. Haltom in preparing many of the ceramic specimens is gratefully acknowledged.

REFERENCES

1. R. A. Wullaert et al., in: Effects of Radiation on Materials and Components, J. F. Kircher and R. E. Bowman, eds., Reinhold Publ. Co., New York, 1964, pp. 277–402.

2. F. W. Clinard, Jr. and L. W. Hobbs, in: Physics of Radiation Effects in Crystals, R. A. Johnson and A. N. Orlov, eds., Elsevier Science Publ., 1986, pp. 387–471.

3. F. W. Clinard, Jr., G. F. Hurley, and L. W. Hobbs, J. Nucl. Mater. 108&109 (1982) 655–670.

4. S. J. Zinkle, L. L. Snead, and E. H. Farnum, "Irradiation of Conventional and Isotopically Tailored Ceramics in HFIR," this progress report.

CROSS SECTIONAL MEASUREMENT OF ELASTIC MODULUS FOR ION BEAM DAMAGED SILICON CARBIDE - Lance L. Snead, Steven J. Zinkle (Oak Ridge National Laboratory), and Don Steiner (Rensselaer Polytechnic Institute)

OBJECTIVE

The purpose of this work is to demonstrate that elastic modulus can be measured over very short distances and with such accuracy as to allow measurement of the material moduli along the damage path of an ion beam.

SUMMARY

The application of a microindentation technique to measure the elastic modulus of carbon beam implanted silicon carbide is presented. Samples of Chemically Vapor Deposited (CVD) Silicon Carbide/Nicalon composites have been implanted to a damage level of **30** dpa at room temperature. The samples were then prepared in cross section and the microstructure was analyzed and modulus was measured along the damage path of the carbon ions. Both CVD silicon carbide and Nicalon silicon carbide was seen to amorphize at room temperature with the threshold for the CVD being approximately **15** dpa. Amorphization of Nicalon silicon carbide fiber was seen to occur over the entire range of the carbon path implying a much lower threshold for amorphization. Elastic moduli were seen to decrease significantly (from 440 GPa to 280 GPa) for the CVD material with the minimum modulus corresponding to the maximum damage region of the carbon beam. The modulus of Nicalon showed the opposite behavior. The modulus for the fiber was increased over most of the damaged region from an undamaged value of **170** GPa to a maximum of **210** GPa.

PROGRESS AND STATUS

Introduction

The use of microindentation for the measurement of hardness and modulus is becoming a useful tool for material scientists. It has become possible to measure material properties with applied force and depth measurement sensitivities of **0.3** μN and **0.16** nm, respectively.' By taking advantage of this sensitivity, along with submicron accuracy in the placement of indents, it is possible to measure the modification of material properties over very short distances. The application of this method to ion beam implanted materials (which have been prepared in cross section) can yield material properties along the damage path of the ion.

1. Microindentation Modulus Measurement

The modulus of a material can be obtained from the unloading portion of the load-displacement curve generated during indentation. Figure 1 shows the Nanoindenter load displacement curve for CVD silicon carbide. The figure shows four separate loadings and unloading depths of **20,** 40, 80 and 160 nm.

From such a curve it is straightforward[2] to calculate the depth of plastic deformation caused in loading to a specified depth by extrapolating a tangent line from the unloading curve to its intersection with the load axis. For metals, nearly all the unloading curves are linear. For materials such as ceramics, with high hardness to modulus ratio, there is substantial curvature to the unloading curve caused by the loss in indenter contact area. Even for materials such as silicon with a very high hardenss to modulus ratio, however, the first 1/3 of the unloading curve is linear, thus an accurate determination of plastic depth can still be obtained.

For the elastic deformation of isotropic materials, Loubet[3] used the solution of Sneddon[4] for a flat-ended cylindrical punch. Relating the projected area of the flat punch to that of a Vickers pyramid the following relation was obtained for the slope of the unloading curve dP/dh:

$$dP/dh = \left(\frac{2}{\pi}\right)^{1/2} D E_r ,$$

where

$$1/E_r = \frac{1 - \nu_s^2}{E_s} + \frac{1 - \nu_i^2}{E_i}$$

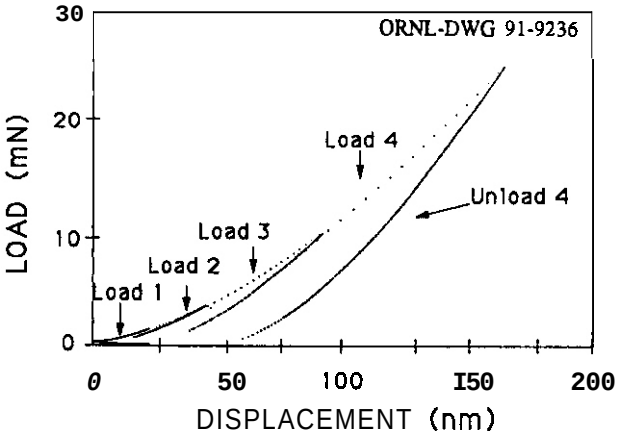


Fig. 1. Microindentation Load-Displacement Curves.

with D being the Vickers diagonal length, E and ν the Young's Moduli and Poisson ratios for the sample and indenter.

By then assuming an ideal pyramidal geometry for the Nanoindenter Berkovich diamond tip and using the relation between the D and the plastic depth (hp), the equation for the modulus is found to be:

$$E_s = \frac{dp}{d_h} \frac{1}{2hp} \left(\frac{\pi}{24.5}\right)^{1/2} .$$

2. Sensing Distance

Elastic moduli calculated from unloading curves reflect an average modulus integrated over a volume much larger than the indenter imprint. There are therefore limits to how close successive indents can be to each other and how close an indent can come to a material discontinuity, such as an edge, without interference. Samuels and Mulhearn[5] experimentally quantified these limits using Vickers-pyramid and Brinell-ball indentations for 7030 brass. Even though the Berkovich pyramid is a three sided pyramid, the results of Samuels and Mulhearn will apply as the iso-strain contours are independent of indenter geometry away from the plastic imprint.

Figure 2 shows the elastic-plastic boundaries for an infinite and semi-infinite material? The indenter geometry is that of the Berkovich pyramid which has an imprint diagonal to depth ratio of 6.5. From the figure it is apparent that for the infinite medium the elastic plastic boundary is spherical and extends radially approximately ten times the indenter depth. For the second unloading curve of Fig. 1, which corresponds to an unloading depth of 0.04 μm, this means that the plastically deformed region is 0.4 μm.

To avoid overlap of the plastically deformed zone, the infinite medium results in Fig. 2 indicate that the minimum distance between adjacent indents should be twice the radius to the elastic-plastic boundary (i. e., twenty times the indent depth apart.) When making successive loadings, however, the plastic depth of the final loading of the (previous) adjacent indent must be taken into account. For this case the minimum distance is 17.6 times the (current) indent depth plus the adjacent indent diagonal corresponding to the final loading.

The iso-strain contours are deformed significantly for indents close to the edge of a sample. From Fig. 2 it is seen that the elastic-plastic boundary for a semi-infinite sample is skewed such that the boundary contacts the edge of the sample at a distance/indenter depth ratio of 11.7, or as a distance of 0.47 μm for an indent depth of 0.04 μm. The minimum approach distance to an edge is therefore 11.7 times the depth of the indent.

This minimum distance between indents and minimum distance from an edge is given in Table 1 for the unloading depths of Fig. 1. For the case of unloading number two of Fig. 1 (0.04 μm), the minimum distance between successive indents is 0.79 μm and the minimum distance to the sample edge is (11.7 x Depth) 0.47 μm.

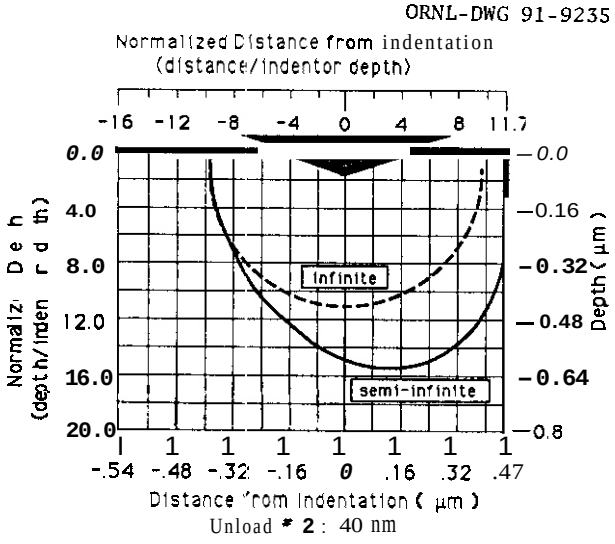


Fig. 2. Elastic Plastic Boundaries for Indentations on Infinite and Semi-Infinite Media.

Table 1. Indent Parameters

Indent Depth (μm)	Indent Diagonal (μm)	Sensing Radius (μm)	Minimum Distance, μm	
			Center-to-Center	Center-to-Edge
0.02	0.13	0.35	0.396	0.235
0.04	0.26	0.70	0.791	0.470
0.08	0.52	1.40	1.582	0.940
0.16	1.04	2.80	3.165	1.880

3. Sensing on Curved Surfaces

In the process of polishing a cross section sample, a certain degree of curvature is caused near the interface. This is primarily due to the difference in polishing rates between the SiC sample and the interface adhesive, Because the adhesive is more easily polished than the SiC, the surface of the adhesive will be lower than that of the silicon carbide, causing some polishing of the edge, therefore a negatively sloping interface.

A downward sloping interface will have the effect of causing an underestimate of material hardness and modulus. This is brought about because the contact area is calculated directly from the indenter depth as measured from the point of tip contact with the surface. Therefore, for a sloping surface the actual area will be greater than the calculated area and the modulus will be underestimated. This effect becomes significant for a negative slope of greater than 5% (underestimate of 5%) and has only a 1% underestimate in modulus for a -2.5% slope!

4. Uniformity of Material Proverties

In order to measure the radiation-induced changes in modulus from consecutive indents, it is first necessary to determine if the material is locally uniform. In many ceramic fibers (such as graphite for example), the modulus and hardness can he strongly dependent on the radial position of the fiber. It is also conceivable that for the case of CVD matrix material, which grows radially away from the fibers, that the modulus and hardness properties would be a function of the distance from the fiber.

To determine the uniformity of the silicon carbide composite materials, a matrix of indents was applied to fiber and matrix material for a fiber oriented normal to the polished surface (Fig. 3) and for a transverse fiber orientation (Fig. 4.) Moduli from unloading at a depth of 125 nm were calculated and shown in Figs. 5 and 6. From Fig. 5 it is seen that the modulus is radially constant for the fiber within an accuracy of less than 4%. This small difference could be due to material non-uniformity but is within the experimental error in measuring the moduli. Also seen from this figure is that the matrix material is fairly uniform and also shows no radial dependence of the modulus.

The moduli for the fiber oriented in the transverse direction also shows no radial dependence in either the fiber or matrix material. Both figures show sharply decreased modulus for indents close to the interface. This is caused by an averaging of the properties of the fiber (or matrix) with that of the low modulus interface.

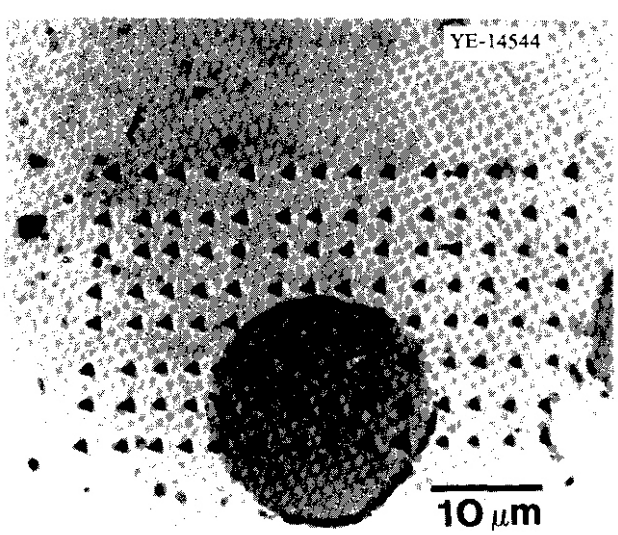


Fig. 3. Indentation Matrix for CVD SiC/Nicalon Composite for a Normally Oriented Fiber

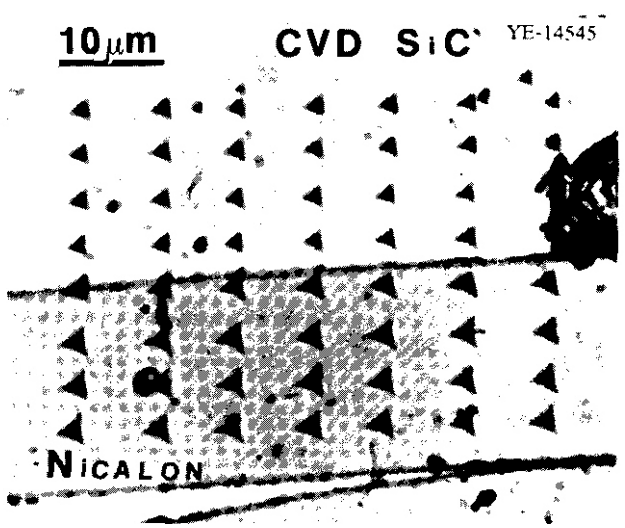


Fig. 4. Indentation Matrix for CVD SiC/Nicalon Composite for a Transverse Oriented Fiber.

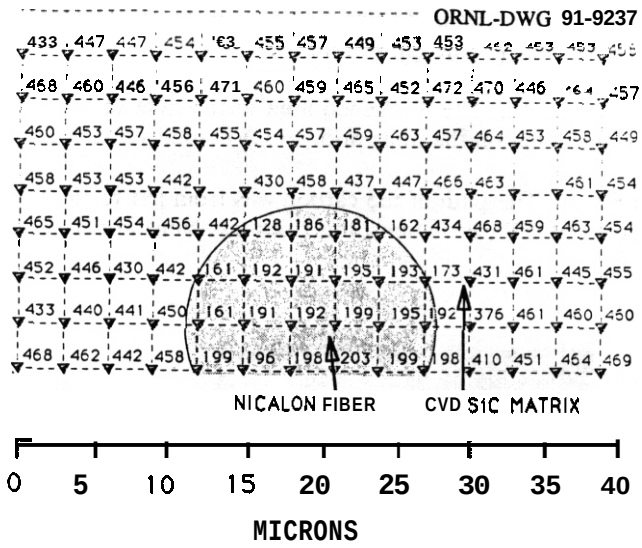


Fig. 5. Moduli Matrix for CVD SiC/Nicalon Composite with Normally Oriented Fiber.

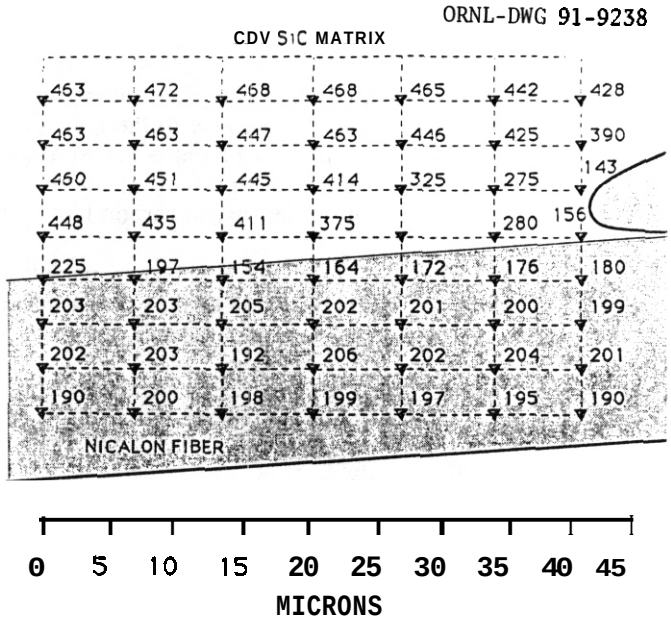


Fig. 6. Moduli Matrix for CVD SiC/Nicalon Composite with Transverse Oriented Fiber.

5. Amorphization of Silicon Carbide

Ion implantation of silicon carbide[6] has revealed that amorphization of the crystal structure occurs at a relatively low dose level and remains to relatively high temperatures as is typical of covalently bonded compounds. Early studies have shown that the threshold for this amorphous transformation occurs at about 0.2 dpa for chromium and nitrogen implantation With an associated volume change of +30%. At damage levels lower than the threshold the crystal structure was found to be highly disordered but not randomized. Recrystallization of the amorphized structure is seen to occur rapidly at temperatures above 1000°C.[7]

CVD silicon carbide, which is the structure of composite matrix material, is made up of heavily faulted crystalline silicon carbide. Silicon carbide structure is generally characterized as being a (hexagonal) or β (cubic), though there are over 60 polytypes of β with the most common being the 6H structure. CVD silicon carbide is made up of both α and β.

Nicalon fibers are made up of a mixture of β silicon carbide with approximately 25% by weight SiO_2 and 10% excess carbon. Very little work has been published on the radiation induced microstructural evolution of Nicalon fiber. Some recent work has suggested, however, that crystallization of the Nicalon structure occurs following nickel ion implantation at room temperature." The evidence supporting this work shows an increase in grain size as found by analysis of TEM dark field images. If this were true, it would be in contradiction to previous work on single and polycrystalline silicon carbide as well as what is generally seen in covalently bonded solids.

Experimental Procedure

Samples of Nicalon fiber infiltrated with CVD silicon carbide were wafered with a low speed saw and then polished to a 1/2 μm polish. The samples were then mounted and implanted with 3 MeV carbon ions in the Triple Ion Beam Facility at ORNL to a dose of 30 dpa (peak) at ambient temperature. The EDEP code was used to calculate the peak damage and the damage profile. The thickness of the implanted sections was 500 μm. Irradiated specimens were prepared in cross section' for TEM and microindentation. A Nano-Instruments Nanoindenter with a Berkovich indenter tip was used.

All transmission electron micrographs were taken at 300 keV in a Philips CM-30 microscope.

Results and Discussion

The room temperature carbon implantation of the SiC composite caused amorphization in both the CVD matrix and Nicalon material. Shown in Fig. 7 is a TEM micrograph of a cross section sample. In this micrograph the glue which bonds the polished ion irradiated surface to the unirradiated section is intact. The entire range of the carbon beam is therefore imaged and an amorphous band occurs starting at a 2.25 pm to a depth of 2.59 μm. The CVD material was grown radially from a fiber which is partially intact at the right of the photo. The blackened area to the right of the amorphous band is part of the interfacial carbon layer which was deposited on the fiber prior to CVD infiltration.

The amorphous CVD is shown at higher magnification in Fig. 8. The path of the carbon was from left to right in the photo causing a amorphous band of 0.34 μm in thickness. From EDEP calculations, this thickness band would correspond to a damage level greater than 15 dpa.

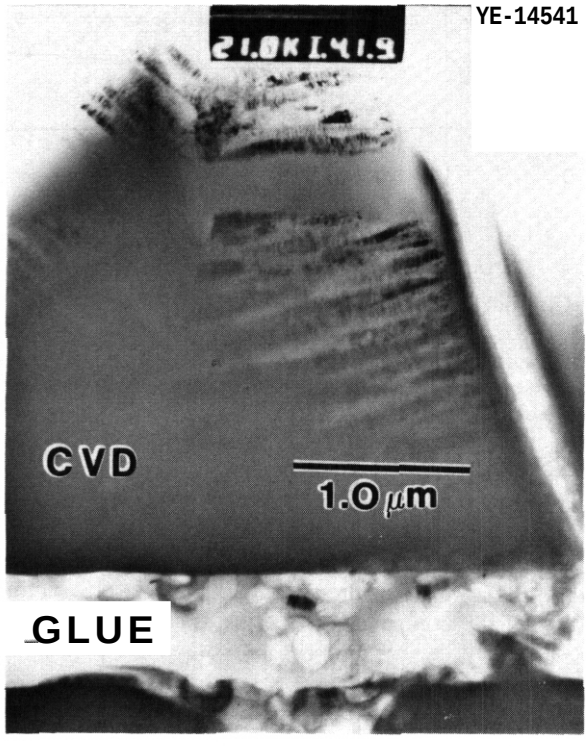


Fig. 7. Cross Section Bright Field Micrograph of Carbon Implanted CVD SiC.

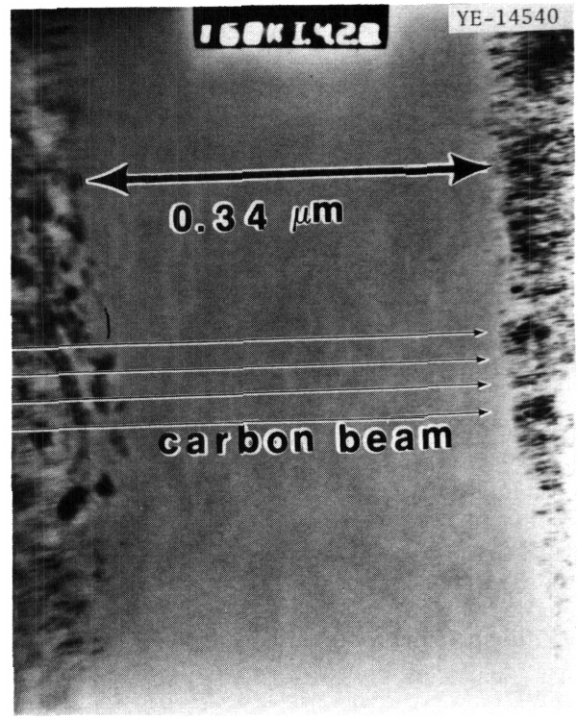


Fig. 8. Bright Field Micrograph of Amorphized Band caused by Carbon Ion Implantation in CVD SiC.

Figure 9 shows the microstructure of the Nicalon fiber at three depths : beginning of range (0.1 pm), at the peak damage region, and well past range of the implanted carbon. The middle micrograph in this figure shows the maximum damage region where the incoming carbon ion has come from the left of the photo and caused peak damage near the center of the micrograph. The micrograph suggests that the damaged Nicalon material has become finer grained in structure. At the center of the middle picture of this figure, which corresponds to the point at which the carbon beam has stopped, the structure goes from a fine-grained material to the coarser grained material of the undamaged (past range) Nicalon. Recrystallization was not found to occur anywhere in the carbon damaged region. Both dark field and diffraction pattern analysis likewise supported this observation.

Also of note in Fig. 9 is that the microstructure has been significantly changed even at the relatively low doses occurring near the implantation surface. This is seen by comparison of the beginning of range and end of range pictures.

A series of indents were taken for both the Nicalon and CVD silicon carbide implanted regions. Figures 10 and 11 show the pattern of indents taken in the matrix and fiber, respectively. It is apparent from these figures that a white band has appeared at the sample edge corresponding to the damaged region. A small difference in range between CVD SiC and Nicalon is also seen by inspection of Fig. 11. It is further seen that for the CVD silicon carbide of Fig. 10 that the region corresponding to the amorphized zone has greater contrast. The indents were spaced at a distance of 1.5 μm apart at an

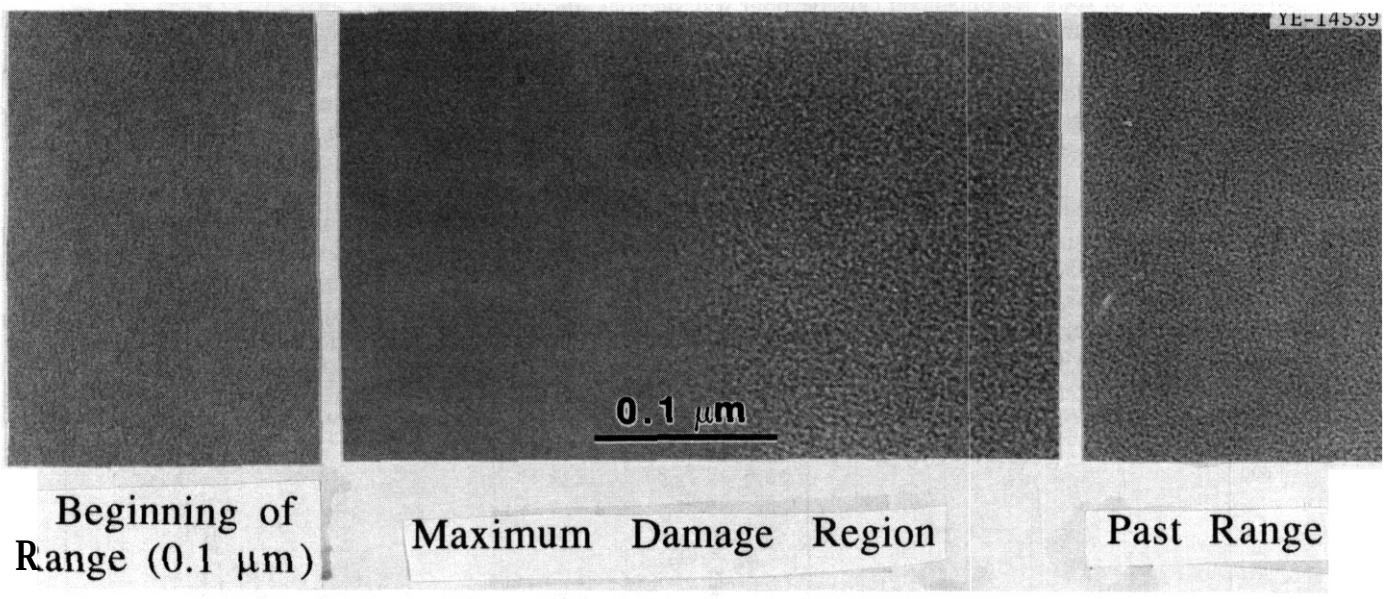


Fig. 9. Bright Field Micrograph of Structural Changes in Nicalon Fiber caused by Carbon Ion Implantation.

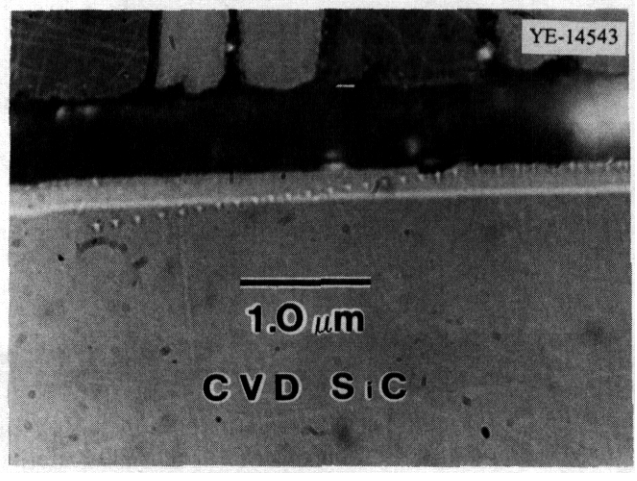


Fig. 10. Series of Indentations Across Irradiated Zone in CVD Silicon Carbide.

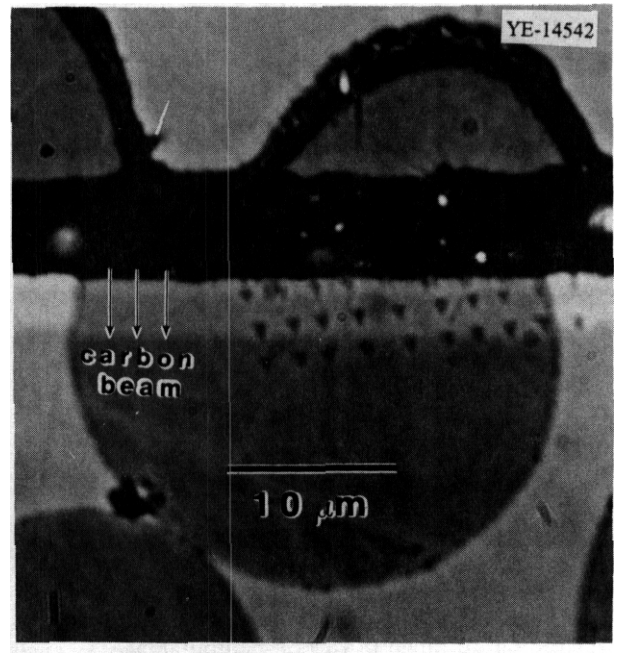


Fig. 11. Series of Indentations Across Irradiated Zone in Nicalon Fiber.

angle to the surface so that the sample edge was approached at approximately 1/10 μm per indent. Four unloadings were taken at 0.02, 0.04, 0.08 and 0.16 μm depth. Referring to Table 1 it is apparent that a 1.5 μm spacing is too close for the 0.16 μm spacing without interference from the plastically deformed region of adjacent indents. The deeper indent was required for imaging of the imprints, however.

The radiation degraded modulus for the matrix silicon carbide is shown in Fig. 12. This data is taken from the 0.04-pmdepth unloading curve which has an area-sensing radius of about 0.4 μm. At well beyond the implanted range the modulus is relatively constant at approximately 400 GPa. As the indents approach the amorphized region, which corresponds to the peak damage of 30 dpa given in the figure, the modulus degrades to a minimum of 280 GPa.

The behavior of the Nicalon silicon carbide fiber was significantly different from the CVD material. From Fig. 13 it is Seen that the material modulus increased in the damaged region from a undamaged value of 170 GPa to a maximum of 215 GPa in the damaged region. It is also interesting to note that the maximum damaged Nicalon modulus was not found to occur at the peak damage area. There was a broad peak just inside the maximum damaged region. The reason behind this is unclear, though Fig. 9 has suggested that the Nicalon morphology has been changed at a relatively low threshold damage level in which case the modulus would be constant above this threshold.

It is difficult to ascertain the material properties for this sample for distances of less than 1 μm from the sample edge. This may be attributed to the difficulties in sensing on a curved surface and the problems of the sensing volume becoming distorted approaching the edge. In the case of the CVD material of Fig. 13, it would be expected that the modulus would increase as the surface was approached and the damage was reduced. The modulus is Seen to decrease for distances less than 1.0 pm, however. This is most likely attributed to the sloping interface effect as the sensing distance of the 0.04 μm indent is only 0.4 μm.

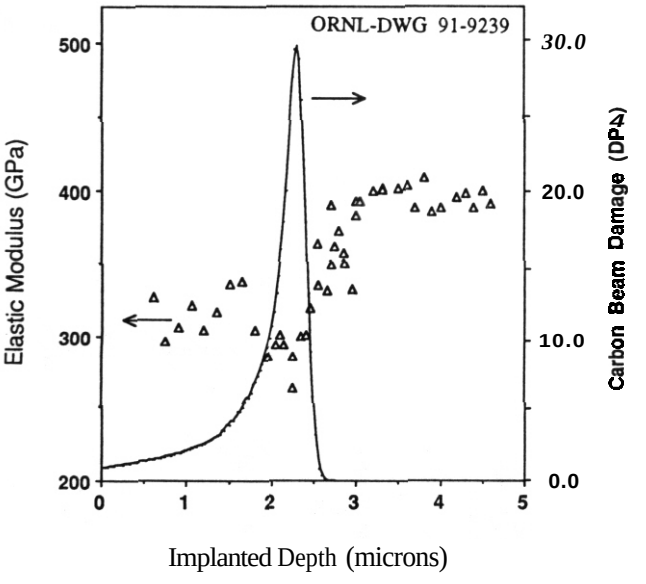


Fig. 12. Cross Sectional Modulus Profile for Carbon Ion Implanted CVD Silicon Carbide.

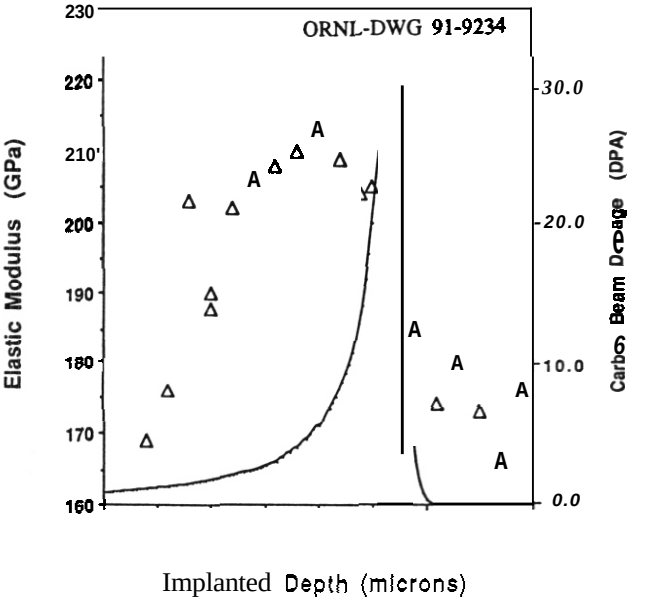


Fig. 13. Cross Sectional Modulus Profile for Carbon Ion Implanted Nicalon Fiber.

Conclusions

Microstructural changes in both CVD silicon carbide and Nicalon silicon fiber have been induced by 3 MeV carbon implantation at room temperature. The general effect is an amorphization of the silicon carbide. The CVD material has a fairly high threshold for amorphization of approximately 15 dpa while the Nicalon structure was seen to become much finer over the entire range of carbon beam damage.

The elastic modulus for both CVD and Nicalon materials was measured along the damage path of the carbon beam. The modulus of the CVD material decreases from 400 to 280 GPa inside the amorphized region. The Nicalon fiber show the opposite effect. The modulus increases from a nominal value of 170 GPa to a maximum value in the damaged region of 215 GPa.

FUTURE WORK

This technique of measuring hardness and modulus is being applied to SiC/Nicalon composite samples implanted to 1, 10 and 30 dpa (peak) with carbon beams as well as dual beam irradiated samples at the same damage levels with helium injection of 0.01, 0.1 and 1 at.%. The temperature range of implantation is from room temperature to 1100°C. This data will then be compared with neutron modified material irradiated to 1 dpa (300°C HFIR, 600°C FFTF) and 15 dpa (600°C FFTF.)

REFERENCES

1. W. C. Oliver et al., "Measurements of Hardness at Indentation Depths as Low as 20 Nanometers," pp. 90-108 in ASTM Special Technical Publication No. 889, Microindentation Techniques in Material Science and Engineering. Edited by P. J. Blau and B. R. Lawn. American Society for Testing Materials. Philadelphia Pa. (1985).

2. M. F. Doerner and W. D. Nix, "A Method for Interpreting the Data from Depth-Sensing Indentation Instruments." J. Mater Res, 1 (4), pp. 601-609. Jul/Aug, (1986).

3. J. L. Loubet et al., J. Tribology 106, 43 (1984).

4. P. E. Wierenga and A. J. J. Frenken, J. Appl. Phys. 55, 4244, (1984).

5. L. E. Samuels and T. O. Mulhearn, "An Experimental Investigation of the Deformed Zone Associated with Indentation Hardness Impressions," J. Mechanics and Physics of Solids. Vol. 5, pp. 125-131 (1957).

6. J. M. Williams et al. "Structural Alterations in SiC as a Result of Cr and N Implantation," Nucl. Intrum. and Methods, 209/210, pp. 317-323 (1983).

7. H. G. Bonn et al. "Recrystallization of ion-implanted a-Sic," J. Mater. Res. 2(1), pp. 107-117, Jan/Feb (1987).

8. A. Kohyama et al. "Radiation Induced Microstructural Evolution in SiC/Al Composite Materials," J. Nucl. Mat., 155-157, pp. 334-339, (1988).

9. S. J. Zinkle et al. 'Technique for Preparing Cross-Section Transmission Electron Microscope Specimens from Ion-Irradiated Ceramics," Sub. J. Electron Microscopy Tech. In Press 1991.

IN-SITU MEASUREMENT OF RADIATION INDUCED CONDUCTIVITY IN CERAMICS---E. H. Farnum. J. M. Kennedy and F. W. Clinard (Los Alamos National Laboratory)

OBJECTIVE

The objective of this work is to develop a data base and understanding of radiation-induced changes in the electrical properties of ceramic insulators, and then use this information to identify or design new ceramic materials that will improve the performance of magnetic fusion reactors.

SUMMARY

Recent data by E.R. Hodgson[1,2] and by G. P. Pells[3,4] shows enhanced dielectric loss and electrical breakdown in ceramics during irradiation with protons and electrons and while subject to an externally applied DC electric field. We have investigated this radiation-induced conductivity effect at frequencies between 100 Hz and 10 MHz by irradiating sapphire with 3 MeV protons at 300 K. Calculations of energy deposition and displacement damage in the sapphire were made using TRIM 90 on an IBM-AT. Results show an immediate increase in loss tangent at onset of irradiation that depends on both frequency and time.

PROGRESS AND STATUS

Method

A general description of this experiment was presented in the last Fusion Reactor Materials Semi-Annual Progress Report (for period ending September 30, 1990). We are using proton irradiation to study in-situ radiation-induced conductivity in ceramics The main advantage of proton irradiation is that the flux can be widely varied both above and below that expected in a fusion reactor. Additional advantages are that the beam can be turned on and off quickly at will, and that irradiation temperature is easily varied. While the ratio of ionizing to displacing radiation is not similar to that expected in a fusion reactor, both are present and effects from both are observable.

During the past reporting period we conducted two experiments with proton irradiation. We polished single crystal sapphire disks with face plane of (1120) to 25-μm-thickness and attached them to a copper block that kept the temperature between 298 and 302 K during the experiment. Electrodes were applied to the top surface to form a guard-ring capacitor that was measured with a frequency-swept impedance analyzer. The dielectric constant and loss tangent were calculated from complex-impedance measurements made auring the irradiation. We calculated ionization and displacement rates for the protons using the TRIM 90 code on an IBM-AT. In our first data we used a proton current of 45 nA (1 μA/cm^2) that created an ionization flux of 10^7 Rad/s and a displacement flux of 10^{-7} displacements per atom per second (dpa/s). During one of the irradiations, a DC electric field up to 1000 V/mm was applied for about 2 hours.

The proton irradiation caused a large immediate increase in the loss tangent (tan δ) that then decayed with increasing fluence. At 100 Hz. tan δ changed from 2×10^{-4} to 2.1 within seconds after onset of irradiation. The initial increase in tan δ is not as large at higher frequency. Figure 1 shows the measured tan δ vs irradiation time for several frequencies. After about 1500 seconds, the decay can be characterized with a time constant τ that is between 3000 s and 7000 s and is weakly dependent on frequency . We fit the Figure 1 data to the formula $\tan\delta = A\, e^{-t/\tau}$ and the results for A and τ are shown in Table 1. In addition, the beam-on-minus-beam-& change in tan δ, $\Delta \tan\delta$, is inversely proportional to frequency between 1 kHz and 10 MHz ($\Delta \tan\delta = 2.5 \times 10^3 F^{-1}$) where F is the frequency in Hz. Figure 2 shows $\Delta \tan\delta$ times frequency vs. frequency for three irradiation times at a flux of 1 μa/cm^2. The ohmic part of the AC conductivity. σ may be obtained from $\Delta \tan\delta = \sigma(\omega \varepsilon \varepsilon_0)^{-1}$, where $\varepsilon \varepsilon_0$ is the dielectric permittivity, and $\omega = 2\pi F$. This equation fits our data between 1 kHz and 10 MHz, and shows a purely resistive, frequency-independent, in-situ radiation-induced conductivity for the 1 μa/cm^2 flux. Measured values for σ from the fig 2 data at various times are shown in Table 2.

After the beam is turned off. the material recovers with a time constant much longer than 7000s. Preliminary data show that after five days, the increase in tan δ observed at the onset of re-irradiation has returned to its' large initial values. At early time, tanδ from 100 Hz to 1 kHz is nearly independent of frequency with a value of 2.1. but this effect soon moves to frequencies lower than 100 Hz. Application of a 1000V/mm DC electric field for up to two hours during the irradiation had no effect on the dielectric loss between 100 Hz and 10 MHz.

FUTURE PLANS

We intend to explore these prompt effects further by varying flux and also the beam-off time to determine flux dependence and recovery rates at room temperature. In addition, similar experiments will be conducted on sapphire doped with 150 ppm of titanium to explore the possible effect of additional trapping sites for the electron-hole pairs created by the ionizing part of the radiation.

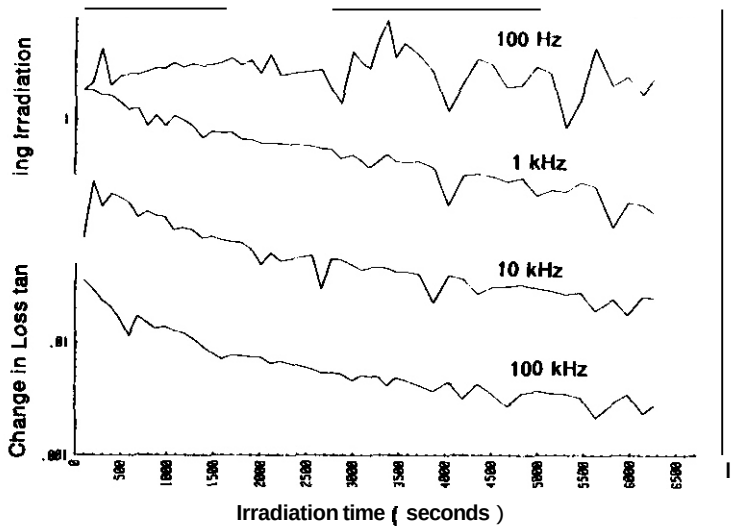


Fig. 1 Sapphire, 300 C, 3 Mev Protons, 1 μA/cm^2 , no bias

TABLE 1

Data fitted to tan 6 = A $e^{-t/\tau}$ for t > 1500s

frequency	τ (s)	A
100Hz	7000	4.7
1kHz	3100	1.2
10kHz	4200	0.1
100kHz	5600	0.009

Unirradiated
tan6 = 2 x 10^{-4}

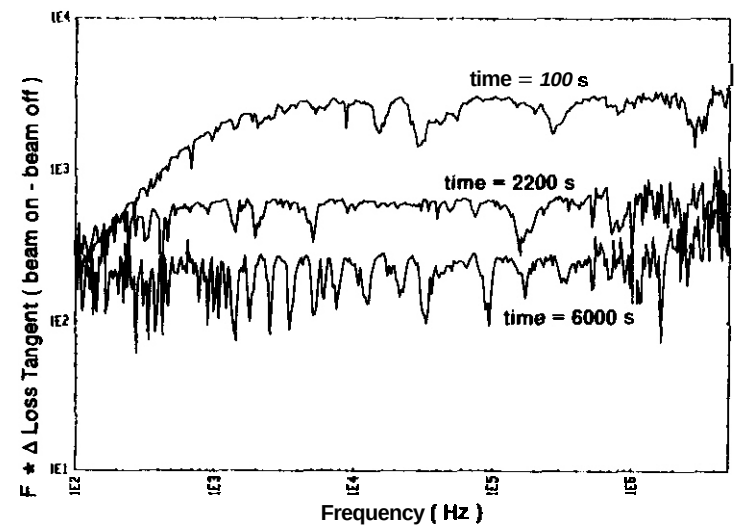


Fig. 2– Sapphire. 300 C. 3 MeV Protons, 1 μA/cm^2, no bias, beam off and on

TABLE 2

Data fitted to σ = F tan 6 ($2\pi\varepsilon\varepsilon_0$)
E = 10.5, ε_0 = 8.85 x 10^{-12} F/M

time (s)	σ (Ω M)$^{-1}$
100	1.45 x 10^{-6}
2200	3.5 x 10^{-7}
6000	1.5 x 10^{-7}

REFERENCES

1. E. R. Hodgson. IEA Workshop on In-Si Measurement of Electrical Prooerties of Irradiated Ceramics, (Los Alamos, NM, June 27-29, 1990) to be published.
2. E. R. Hodgson, Fourth International Conference on Fusion Reactor Materials, (ICFRM-4, Kyoto, Japan Dec. 4-8, 1989) To Be Published.
3. G. P. Pells et. al., Culham/EEC Fusion Technology Task MAT-13 AERE R 13222, Materials Development Div. Harwell Lab.. Oxfordshire OX11 ORA.
4. G. P. Pells et. al., IEA Workshop in In-Situ Measurement of Electrical Properties of Irradiated Ceramics, (Los Alamos, NM. June 27-29, 1990) to be published.

CORROSION AND ELECTRICAL PROPERTIES OF CERAMIC INSULATORS AFTER EXPOSURE TO FLOWING LITHIUM AT 400°C · M. R. Fox, A. B. Hull, J-H. Park, J.H. Hsieh, and G. Dragel (Argonne National Laboratory)

OBJECTIVE

Two major concerns for liquid metal blankets in magnetic fusion reactor designs are the corrosion resistance of the structural material and the magnetohydrodynamic (MHD) force and its subsequent influence on thermal-hydraulics and corrosion. The objective of this study is to develop stable ceramic coatings at the liquid metal/structural material interface, with emphasis on electrically insulating coatings that prevent adverse MHD-generated currents from passing through the structural walls.

SUMMARY

Based on a preliminary survey of more than 15 oxides and nitrides, four ceramic materials (CaO, MgO, Y_2O_3, and BN) were identified as candidates for insulator coating development. These compounds were fabricated by a variety of techniques and exposed to flowing lithium at 400°C to assess chemical compatibility. Yttrium oxide exhibited excellent corrosion resistance in flowing liquid Li at 400°C; its corrosion rate was calculated to be 0.042 μm/yr. Resistivity measurements were taken before and after Li exposure to determine the effects of Li on the electrical properties of Y_2O_3. No deterioration in the resistivity could be measured; in both cases the resistivity was $>10^{12}$ Ω·m. Boron nitride coatings on V-20Ti substrates were fabricated by the newly developed ion-beam-assisted-deposition process. These coatings are expected to exhibit better compatibility with liquid Li than the previously RF-sputtered coatings. The resistivity of *in-situ-formed* $(V,Ti)_xN$ reaction-product layers on various V-base alloys, including V-7Cr-5Ti, V-2.5Ti-1Si, and V-20Ti, is being determined.

PROGRESS AND STATUS

Introduction and Background

MHD forces and their effects on corrosion rates, heat transfer, and pressure drop are a key concern with a V/Li system for first-wall applications in a magnetic fusion reactor (MFR). The MHD effects could be significantly reduced by placing an electrical insulator coating at the V/Li interface.[1] For a material to work as an insulator coating in this environment, it must first meet two criteria: high corrosion resistance and electrical resistivity $>10^2$ Ω·m when exposed to Li and a radiation field. Preliminary evaluations of candidate coating/substrate combinations[2] were conducted on the basis of chemical stability in liquid Li and electrical resistivity of the coatings after exposure to Li. The coating materials include BN, Y_2O_3, Cr_2O_3, MgO, CaO, Si_3N_4, V_2O_5, and in-situ coatings of calcium vanadate and a V-Ti-N reaction-product layer formed in flowing Li.

Lithium compatibility studies indicated that failure resulted from one of three causes: (1) thermodynamic instability (Si_3N_4), (2) incomplete densification (CaO, MgO), or (3) impurity content in the ceramic (BN).

Currently, one of the most promising materials being considered for this application is Y_2O_3. Previous work has shown that Y_2O_3 has a low corrosion rate[2,3] and no gross loss of resistivity in static Li.[3]

Experimental Procedures and Results

1. Compatibility of Y_2O_3 with Liquid Lithium

The Y_2O_3 was prepared by hot-pressing and sintering, as described previously by Wang et al.[2] The surface area was determined by micrometer, and weight was obtained with an Ohaus GA110 balance. The Y_2O_3 was then exposed in the Li fatigue and failure testingloop 3 (FFTL-3)[4] for 675 h at 405°C. Weight loss was measured and corrosion rate was determined. One specimen with 2.34×10^{-4} m^2 surface area showed no weight loss, and the other specimen, with 6.04×10^{-5} m^2 surface area, had a weight loss of 0.0001 g and a corrosion rate of 0.042 μm/yr.

2. Resistivity Measurement

Resistivity of Y_2O_3 was measured in air at room temperature by a four-probe technique.[5] Both exposed and unexposed samples were carefully sectioned, and four platinum electrodes were attached to notched specimens using silver paint, as shown in Figs. 1 and 2. A current (I) was passed through the outside two electrodes using a

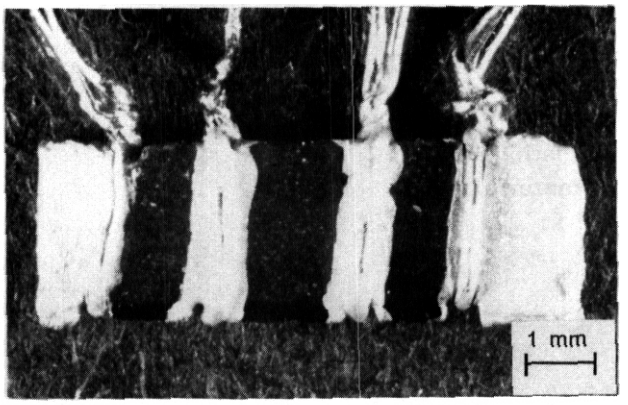


Fig. 1. Lithium-exposed Y_2O_3 specimen viewed by optical microscopy.

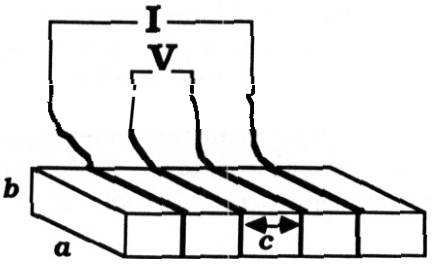


Fig. 2. Resistivity measurement by four-probe technique.

Keithley 263 Calibrator/Source, and the voltage drop (V) was measured across the two inside electrodes with a Data Precision 3500 voltmeter. Resistance (R) and resistivity (ρ) were calculated from Eqs. 1 and 2.

$$R = V/I \quad (1)$$

$$\rho = R(a*b)/c \quad (2)$$

As determined by the extrapolation of high temperature values to calculate lower temperature values, the resistivity of Y_2O_3 at room temperature is $\approx 10^{16}$ Ω·m.[6] Because of equipment and sample size limitations, the highest resistivity that could be measured was 10^{12} Ω·m. Yttrium oxide specimens both before and after 400°C Li exposure had resistivities $>10^{12}$ Ω·m.

DISCUSSION AND CONCLUSIONS

Ceramic electrical insulator coatings have great potential for MFR applications. Because of the high thermal stresses, coatings on the surface of the V-base alloys may tend to crack or spall. If this happens, the insulating and corrosion benefits are lost.

An ideal coating would regenerate in-situ by forming compounds with interstitial impurities in the Li and/or alloying elements in the V-base alloy. One coating of interest is the $(V,Ti)_xN$ reaction-product layer that forms in V-Ti alloys exposed to Li.[7] Results suggest that this layer is brittle, but that it seems to be adherent. Conductivity/resistivity tests are being performed[8] on V-7Cr-5Ti, V-2.5Ti-1Si, and V-20Ti substrates before and after exposure to flowing Li at 450°C for 2000 h. These measurements will be correlated with the thickness and composition of the deposited surface layer.

Reactive coating processes that are of interest in this context include oxidation and diffusion coating. A schematic of the coating and the diffusion zone is shown in Fig. 3. If the surface layer cracks or spalls, chemical reactions of constituents in the diffusion zone of the alloy and in the liquid metal could repair the coating. Y_2O_3 is one of the materials being considered for diffusion coating.

In earlier work,[2] 10-μm-thick BN coatings were deposited by RF-sputtering. These coatings completely dissolved in Li after 1h exposure. New BN coatings have been formed on V-base substrates by ion-beam-assisted-deposition (IBAD). By combining ion implantation and thermal evaporation, IBAD optimizes the best features of these more conventional surface modification processes.[9] Adhesion is not a problem because there is no discrete interface; because of fast deposition, the BN coating thickness was 5 μm.

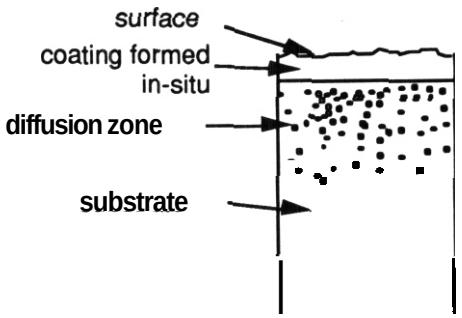


Fig. 3. In-situ-formed coating on a diffusion-coated material.

Boron nitride crystallizes in two forms, hexagonal and cubic. The two polymorphs are frequently compared[10] to the graphite and diamond forms of carbon, with which they are isoelectronic. The IBAD technique causes the BN to form a high-density, highly ordered cubic[11] crystal structure that is more stable in Li than the hexagonal crystal structure that forms during RF-sputtering.

Reaction of Li with B_2O_3 is another source of instability. Earlier studies[3] indicated that after the BN (with B_2O_3 contaminants) was subjected to a 1700°C nitrogen atmosphere for 12 h, the B_2O_3 contaminants reacted with N to form BN, and subsequently the BN was entirely stable in Li.

FUTURE WORK

Yttrium oxide will be exposed to flowing Li for longer times at higher temperatures. Attempts will be made to form a Y_2O_3 coating in-situ by diffusing Y into a V substrate. Resistivity of Y_2O_3 will be measured in-situ at high temperature.

The resistivity of in-situ-formed $(V,Ti)_xN$ reaction product layers on various V-base alloys immersed in flowing Li is being investigated at 450°C.

The stability of BN coating on V-base substrates is being readdressed in light of the advantages implicit in the new IBAD coating technology. The problem of BN purity will be avoided by heat-treating the BN-coated V-base substrates in a N atmosphere at 800°C for several days[12] to remove any B_2O_3 impurities.

Ceramic discs of AIN, $Y_3Al_5O_{12}$, $MgAl_2O_4$, CaO, $CaO{\cdot}V_2O_5$, TiC, SiC, and TiN will be immersed in flowing Li to determine their chemical compatibility with Li.

REFERENCES

1. Y. Y. Liu and D. L. Smith, Ceramic Electrical *Insulators* for Liquid Metal Blankets, J. Nucl. Mater., 141-143, 38 (1986).

2. D. Y. Wang, A. B. Hull, M. R. Fox and C. E. Campbell, Development of Ceramic Znsulator Coatings for Liquid Metal Blanket Applications, Fusion Reactor Materials Semiannual Report for the Period Ending September 30, 1990, DOE/ER-0313/9, Oak Ridge National Laboratory (1991).

3. J. E. Battles, Materials for Advanced High Temperature Secondary Batteries, Int. Mat. Rev., 34.1 (1989).

4. O. K. Chopra and A. B. Hull, Influence of Carbon and Nitrogen Impurities on the Corrosion *of Structural* Materials in a Rowing-Lithium Environment, Fus. Tech., 15,309 (1989).

5. J. H. Park and K. Natesan, Electronic Tmnsport in Thermally Grown Cr_2O_3, Oxid. Met., 33, 31 (1990).

6. W. D. Kingery et al., Introduction to Ceramics, 2nd ed., John Wiley and Sons, New York p. 905 (1976).

7. H. Borgstedt, M. Grundmann, J. Konys and Z. Peric', A *Vanadium* Alloy for Application in a Liquid Metal Blanket of a Fusion Reactor, J. Nucl. Mater., 155-157, 690 (1988).

8. A. B. Hull, M. R. Fox, and J.-H. Hsieh, *Vanadium-Base-Alloy* ***Surface Modification for Liquid Metal Blankets and First-Wall in Magnetic Fusion Reactors,*** accepted for presentation at 5th Intl. Conf. on Fusion Reactor Materials, Nov. 17-22, 1991, Clearwater, FL.

9. G. Fenske and R. Erck, ***Ion Beams 'Nail' Thin Films,*** Ceramic Industry, March, 25-28 (1991).

10. C. R. Aita, ***Sputter Deposited Boron Nitride: A Review*** in The Synthesis and Properties of Boron Nitride, J. J. Pouch and S. A. Alterovitz, eds., Trans Tech Publications, Aedermannsdorf, Switzerland, 1990.

11. Y. Andoh et al., Properties of Boron Nitride Coating Films Prepared by the Ion Beam and Vapor Deposition Method (IVD), Nucl. Instrum. & Meth. in Phys. Res. B19/20 (1987) 787-790.

12. J. Battles, Argonne National Laboratory, personal communication, 1991.

DISTRIBUTION

1–16. Argonne National Laboratory, 9700 South Cass Avenue, Argonne, IL 60439

M. C. Billone	P. A. Finn	B. A. Loomis
P. E. Blackburn	A. K. Fisher	R. F. Mattas
O. K. Chopra	A. E. Hull	L. A. Neimark
R. G. Clemner	C. E. Johnson	D. L. Smith
D. R. Diercks	F. Kassner	S. W. Tam
		H. Wiedersich

17. Argonne National Laboratory, EBR-II Division, Reactor Materials Section, P.O. Box 2528, Idaho Falls, IO 83403-2528
D. L. Porter

18. Auburn University, Department of Mechanical Engineering, 201 Ross Hall, Auburn, AL 36849
B. A. Chin

19–34. Battelle-Pacific Northwest Laboratory, P. O. Box 999, Richland, WA 09352

M. D. Freshley	M. L. Hamilton	J. M. McCarthy
F. A. Garner (5)	H. L. Heinisch	B. D. Shipp
D. S. Gelles	G. W. Hollenberg	O. D. Slagle
L. R. Greenwood	R. H. Jones	J. L. Straalsund

35–36. Carnegie Institute of Technology, Carnegie-Mellon University, Schenley Park, Pittsburgh, PA 15213
W. M. Garrison, Jr. J. C. Williams

37. Department of Energy, Richland Operations Office, Federal Bldg., MS A590, Richland, WA 99352
Paul Pak

38. EG&G Idaho, Inc., Fusion Safety Program, P.O. Box 1625, Idaho Falls, ID 83415-3523
D. F. Holland

39. GE Astrospace Division, San Jose Operations, 6835 via Deloro, P.D. Box 530954, San Jose, CA 95153-5354
Mike Kangilaski

40–43. General Atomics, P.O. Box 85608, San Diego, CA 92138

J. Baur	O. I. Roberts
T. A. Lechtenberg	K. R. Schultz

44. General Dynamics Corporation, 5001 Kearny Villa Road, San Diego, CA 92138
T. L. Cookson

45. Georgia Institute of Technology, School of Textile Engineering, Atlanta, GA 30332
D. S. Tucker

46. Grand Canyon University, Department of Natural Science, 3300 W. Camelback Rd., Phoenix, AZ 85017
W. A. Coghlan

47-48. Hokkaido University, Faculty of Engineering, Kita 13, Nishi 8, Kita-ku, Sapporo 060, Japan
Professor Heishichiro Takahashi Professor Akira Okada

49–52. Japan Atomic Energy Research Institute, Tokai Research Establishment, Tokai-mura, Naka-gun, Ibaraki-ken 319-11, Japan
Dr. Tatsuo Kondo Dr. Akimichi Hishinuma (3)

53. Kyushu University, Research Institute for Applied Mechanics, 6-1, Kasuga-Koen, Kasuga-Shi, Fukuoka-Ken 816, Japan
Professor Takeo Muroga

54-56. Lawrence Livermore National Laboratory, P.O. Box 808, Livermore, CA 94550

E.C.N. Dalder	J. Perkins
M. Guinan	

57–65. Los Alamos National Laboratory, P.O. Box 1663, Los Alamos, NM 87545

J. L. Anderson	D. J. Dudziak	C. D. Kise
L. D. Caudill	H. M. Frost	R. Liepens
F. W. Clinard	G. Hurley	T. Zocco

66. Manlabs, Inc., 231 Erie Street, Cambridge, MA 02139
O. Tognarelli

67. Massachusetts Institute of Technology. Department of Metallurgy and Materials Science, Cambridge, MA 02139
L. W. Hobbs

68–69. Massachusetts Institute of Technology, Room 13-4069, Cambridge, MA 02139
N. J. Grant — K. C. Russell

70–71. Massachusetts Institute of Technology, Plasma Fusion Center Headquarters, Cambridge, MA 02139
H. D. Becker — D. B. Montgomery

72. McDonnell-Douglas Missile Systems Company, Mail Code 306 4204, P.O. Box 516, St. Louis, MO 63166
J. W. Davis

7374. Nagoya University, Institute of Plasma Physics, Furo-Cho, Chikusa-ku, Nagoya 464-01, Japan
Professor Akira Miyahara — Dr. Chusei Namba

75. Nagoya University, Department of Nuclear Engineering, Furo-Cho, Chikusa-ku, Nagoya 464-01, Japan
Professor Michio Kiritani

76–77. National Institute of Standards and Technology, Boulder, CO 80302
F. R. Fickett — J. R. Reed

78. National Materials Advisory Board, 2101 Constitution Avenue, Washington, DC 20418
K. M. Zwilsky

79–80. National Research Institute for Metals, Tsukuba Branch, Sengen, Tsukuba-shi, Ibaraki-ken 305, Japan
Dr. Masatoshi Okada — Dr. Haruki Shiraishi

81. Naval Research Laboratory, Washington, DC 20375
J. A. Sprague

82–122. Oak Ridge National Laboratory, P.O. Box 2008, Oak Ridge, TN 37831

Central Research Library
Document Reference Section
Laboratory Records Department (2)
Laboratory Records—RC
Patent Section
D. J. Alexander
C. C. Baker
G.E.C. Bell
J. Bentley
E. E. Bloom
D. N. Braski
T. D. Burchell
R. H. Goulding
M. L. Grossbeck
E. A. Kenik
R. L. Klueh
Eal Lee
A. W. Longest
L. K. Mansur
P. J. Maziasz
T. C. Reuther
T. K. Roche
A. F. Rowcliffe (10)
R. L. Senn
J. Sheffield
L. Snead
R. E. Stoller
K. R. Thoms
P. F. Tortorelli
S. J. Zinkle
R. Yamada

123124. Princeton University, Princeton Plasma Physics Laboratory, P.O. Box 451, Princeton, NJ 08540
H. Furth — Long-Poe Ku

125–126. Rensselaer Polytechnic Institute, Troy, NY 12181
D. Steiner — David Duquette

127. Rockwell International Corporation, NA02, Rocketdyne Division, 6633 Canoga Avenue, Canoga Park, CA 91304
D. W. Kneff

128–129. Sandia National Laboratories, P.O. Box 5800, Albuquerque, NM 87185-5800
M. J. Davis — W. B. Gauster

130–131. Sandia National Laboratories, Livermore Division 8316, Livermore, CA 94550
W. Bauer — W. G. Wolfer

132. San Oiego State University, Mechanical Engineering Dept., San Oiego, CA 92182-0191
L. D. Thompson

133. Tohoku University, Institute for Materials Research, Katahira 2-1-1, Sendai 980, Japan
Professor Hideki Matsui

134. Tohoku University, Institute for Materials Research, Orai Branch, Oarai, Higashi-Ibaraki-gun, Ibaraki-ken 311-13, Japan
Professor Hideo Kayano

135. Tohoku University, Department of Nuclear Engineering, Tohoku University, Aoba, Aramaki, Sendai 980, Japan
Professor Katsunori Abe

136–137. University of California, Department of Chemical and Nuclear Engineering, Santa Barbara, CA 93106
G. E. Lucas
G. R. Odette

139140. University of California, Department of Chemical, Nuclear and Thermal Engineering, Los Angeles, CA 90024
M. B. Abduo
R. W. Conn
N. M. Ghoniem

141. University of Michigan, Department of Nuclear Engineering, Ann Arbor, MI 48109
T. Kammash

142. University of Missouri, Department of Nuclear Engineering, Rolla, MO 65401
A. Kumar

143. University of Tokyo, Oepartment of Materials Science & Technology, 2641 Yamazaki Noda City, Chiba Prefecture 278 Japan
N. Igata

144–145. University of Tokyo, Department of Nuclear Engineering, 3-1, Hongo 7-Chome, Bunkyo-ku, Tokyo 113 Japan
Professor Shiori Ishino (2)

146–147. University of Tokyo, Department of Materials Science, 3-1, Hongo 7-Chome, Bunkyo-ku, Tokyo 113, Japan
Professor Akira Kohyama
Professor Yutaka Kohno

148. University of Wisconsin, Nuclear Engineering Dept., 1600 Johnson Orive, Madison, WI 53706
G. L. Kulcinski

149–154. Westinghouse Hanford Company, P. O. Box 1970, Richland, WA 99352
H. R. Brager
A. M. Ermi
G. D. Johnson
F. M. Mann
R. J. Puigh
R. L. Simons

155. Department of Energy, DOE Field Office, P.O. Box 2001, Oak Ridge, TN 37831-8501
Assistant Manager for Energy Research and Oeveloprnent

156. Department of Energy, Oak Ridge Operations Office, P. O. Box 2001, MS 6269, Oak Ridge, TN 37831
S. D. Frey

157–162. Department of Energy, Office of Fusion Energy. Washington, DC 20585
S. E. Berk
M. M. Cohen
N. A. Davies
R. J. Dowling
R. E. Price
F. W. Wiffen

163–213. Department of Energy, Office of Scientific and Technical Information, Office of Information Services, P.O. Box 62, Oak Ridge, TN 37831
For distribution as shown in DOE/TIC-4500, Distribution Categories UC-423 (Magnetic Fusion Reactor Materials) and UC-424 (Magnetic Fusion Energy Systems)